Available online at www.sciencedirect.com

ScienceDirect

Nuclear Data Sheets

Nuclear Data Sheets 210 (2026) 1–224

www.elsevier.com/locate/nds

ENDF/B-VIII.1: Updated Nuclear Reaction Data Library for Science and Applications

G.P.A. Nobre,[1,*] R. Capote,[2] M.T. Pigni,[3] A. Trkov,[4] C.M. Mattoon,[5] D. Neudecker,[6] D.A. Brown,[1] M.B. Chadwick,[6] A.C. Kahler,[6] N.A. Kleedtke,[6] M. Zerkle,[7] A.I. Hawari,[8] C.W. Chapman,[3] N.C. Fleming,[8] J.L. Wormald,[7] K. Ramić,[3] Y. Danon,[9] N.A. Gibson,[6] P. Brain,[9] M.W. Paris,[6] G.M. Hale,[6] I.J. Thompson,[5] D.P. Barry,[10] I. Stetcu,[6] W. Haeck,[6] A.E. Lovell,[6] M.R. Mumpower,[6] G. Potel,[5] K. Kravvaris,[5] G. Noguere,[11] J.D. McDonnell,[3] A.D. Carlson,[12] M. Dunn,[13] T. Kawano,[6] D. Wiarda,[3] I. Al-Qasir,[14,3] G. Arbanas,[3] R. Arcilla,[1] B. Beck,[5] D. Bernard,[11] R. Beyer,[15] J.M. Brown,[3] O. Cabellos,[16] R.J. Casperson,[5] Y. Cheng,[3] E.V. Chimanski,[1] R. Coles,[1] M. Cornock,[17] J. Cotchen,[7] J.P.W. Crozier,[18] D.E. Cullen,[2,†] A. Daskalakis,[10] M.-A. Descalle,[5] D.D. DiJulio,[19] P. Dimitriou,[2] A.C. Dreyfuss,[5] I. Durán,[20,21] R. Ferrer,[22] T. Gaines,[17] V. Gillette,[14] G. Gert,[5] K.H. Guber,[3] J.D. Haverkamp,[10] M.W. Herman,[6] J. Holmes,[7] M. Hursin,[23] N. Jisrawi,[14] A.R. Junghans,[15] K.J. Kelly,[6] H.I. Kim,[24] K.S. Kim,[3] A.J. Koning,[2] M. Koštál,[25] B.K. Laramee,[18] A. Lauer-Coles,[1] L. Leal,[3,26] H.Y. Lee,[6] A.M. Lewis,[10] J. Malec,[4] J.I. Márquez Damián,[19] W.J. Marshall,[3] A. Mattera,[1] G. Muhrer,[19] A. Ney,[10] W.E. Ormand,[5] D.K. Parsons,[6] C.M. Percher,[5] V.G. Pronyaev,[21] A. Qteish,[27] S. Quaglioni,[5] M. Rapp,[10] J.J. Ressler,[5] M. Rising,[6] D. Rochman,[28] P.K. Romano,[29] D. Roubtsov,[30] G. Schnabel,[2] M. Schulc,[25] G.J. Siemers,[9] A.A. Sonzogni,[1] P. Talou,[6] J. Thompson,[10] T.H. Trumbull,[10] S.C. van der Marck,[31] M. Vorabbi,[1,32] C. Wemple,[22] K.A. Wendt,[5] M. White,[6] and R.Q. Wright[3,†]

[1] *Brookhaven National Laboratory, Upton, NY 11973-5000, USA*
[2] *International Atomic Energy Agency, Vienna A-1400, PO Box 100, Austria*
[3] *Oak Ridge National Laboratory, Oak Ridge, TN 37831-6171, USA*
[4] *Jožef Stefan Institute, Jamova 39, SI-1000, Ljubljana, Slovenia*
[5] *Lawrence Livermore National Laboratory, Livermore, CA 94551-0808, USA*
[6] *Los Alamos National Laboratory, Los Alamos, NM 87545, USA*
[7] *Naval Nuclear Laboratory, West Mifflin, PA 15122-0079, USA*
[8] *Department of Nuclear Engineering, Texas A&M University, College Station, TX 77843, USA*
[9] *Rensselaer Polytechnic Institute, Troy, NY 12180, USA*
[10] *Naval Nuclear Laboratory, Schenectady, NY 12301-1072, USA*
[11] *CEA, DEN, DER, SPRC, Cadarache, 13108 Saint-Paul-lèz-Durance, France*
[12] *National Institute of Standards and Technology, Gaithersburg, MD 20899-8463, USA*
[13] *Spectra Tech, Inc., Oak Ridge, TN 37830, USA*
[14] *Department of Nuclear, University of Sharjah, Sharjah, United Arab Emirates*
[15] *Helmholtz-Zentrum Dresden - Rossendorf e.V., Dresden, Germany*
[16] *Universidad Politécnica de Madrid, José Gutiérrez Abascal, 2 28006, Madrid, Spain*
[17] *AWE.plc Aldermaston, Reading, Berkshire, RG7 4PR, United Kingdom*
[18] *North Carolina State University, Department of Nuclear Engineering, Raleigh, NC 27695*
[19] *European Spallation Source ERIC, Lund, Sweden*
[20] *IGFAE-Universidad de Santiago de Compostela, 1782 Spain*
[21] *International Atomic Energy Agency (consultant), Vienna A-1400, PO Box 100, Austria*
[22] *Studsvik Scandpower, Inc., 1070 Riverwalk Dr., Idaho Falls, ID 83401, USA*
[23] *Ecole Polytechnique Fédérale de Lausanne, 1015 Lausanne, Switzerland*
[24] *Korea Atomic Energy Research Institute, Daejeon, Republic of Korea*
[25] *Research Centre Řež Ltd, Husinec-Řež, Czech Republic*
[26] *Institut de Radioprotection et de Sûreté Nucléaire, 92262 Fontenay aux Roses, Cedex, France*
[27] *Physics Department, Yarmouk University, Irbid, Jordan*
[28] *Laboratory for Reactor Physics Systems Behaviour, Paul Scherrer Institut, Villigen, Switzerland*
[29] *Argonne National Laboratory, Argonne, IL 60439-4842 USA*
[30] *Canadian Nuclear Laboratories, Chalk River, Ontario, Canada*
[31] *NRG Westerduinweg 3, 1755 LE Petten, Netherlands*
[32] *University of Surrey, Guildford, Surrey, GU2 7XH, United Kingdom*

(Dated: April 10, 2026; Received December 23, 2024; revised October 21, 2025)

https://doi.org/10.1016/j.nds.2026.04.001

0090-3752/© 2026 The Author(s). Published by Elsevier Inc.
This is an open access article under the CC BY license (http://creativecommons.org/licenses/by/4.0/).

The ENDF/B-VIII.1 library is the newest recommended evaluated nuclear data file by the Cross Section Evaluation Working Group (CSEWG) for use in nuclear science and technology applications, and incorporates advances made in the six years since the release of ENDF/B-VIII.0. Among key advances made are that the ^{239}Pu file was reevaluated by a joint international effort and that updated ^{16,18}O, ^{19}F, $^{28-30}$Si, $^{50-54}$Cr, ^{55}Mn, ^{54,56,57}Fe, ^{63,65}Cu, ^{139}La, ^{233,235,238}U, and ^{240,241}Pu neutron nuclear data from the IAEA coordinated INDEN collaboration were adopted. Over 60 neutron dosimetry cross sections were adopted from the IAEA's IRDFF-II library. In addition, the new library includes significant changes for ^{3}He, ^{6}Li, ^{9}Be, ^{51}V, ^{88}Sr, ^{103}Rh, ^{140,142}Ce, Dy, ^{181}Ta, Pt, $^{206-208}$Pb, and ^{234,236}U neutron data, and new nuclear data for the photonuclear, charged-particle and atomic sublibraries. Numerous thermal neutron scattering kernels were reevaluated or provided for the very first time. On the covariance side, work was undertaken to introduce better uncertainty quantification standards and testing for nuclear data covariances. The significant effort to reevaluate important nuclides has reduced bias in the simulations of many integral experiments with particular progress noted for fluorine, copper, and stainless steel containing benchmarks. Data issues hindered the successful deployment of the previous ENDF/B-VIII.0 for commercial nuclear power applications in high burnup situations. These issues were addressed by improving the ^{238}U and ^{239,240,241}Pu evaluated data in the resonance region. The new library performance as a function of burnup is similar to the reference ENDF/B-VII.1 library. The ENDF/B-VIII.1 data are available in ENDF-6 and GNDS format at https://doi.org/10.11578/endf/2571019.

CONTENTS

I. INTRODUCTION 4

II. OVERVIEW OF THE CURRENT ENDF/B RELEASE 4
- A. Neutron sublibrary 5
- B. Thermal neutron scattering sublibrary 5
- C. Photonuclear sublibrary 6
- D. Charged particle sublibraries 6
- E. Fission product yield sublibraries 6
- F. Migration to GitLab repository 6
- G. Review process 7

III. NEUTRON CROSS SECTIONS 7
- A. Jointly-assembled ^{239}Pu 7
  - 1. Background & Previous Evaluations 7
  - 2. (n,f) fission neutron multiplicity $\overline{\nu}$ 7
  - 3. Prompt Fission Neutron Spectrum 10
  - 4. Resonance Region 10
  - 5. Fast Region 13
  - 6. Integral benchmarks 21
- B. INDEN evaluations 21
  - 1. ^{16}O 21
  - 2. ^{18}O 21
  - 3. ^{19}F 21
  - 4. ^{28,29,30}Si 25
  - 5. ^{50,51,52,53,54}Cr 26
  - 6. ^{55}Mn 27
  - 7. ^{54,56,57}Fe 28
  - 8. ^{63,65}Cu 28
  - 9. ^{139}La 35
  - 10. ^{233}U 35
  - 11. ^{235}U 37
  - 12. ^{238}U 41
  - 13. ^{240,241}Pu 44
- C. Non-INDEN evaluations 45
  - 1. ^{3}He 45
  - 2. ^{6}Li 45
  - 3. ^{9}Be 46
  - 4. ^{51}V 47
  - 5. ^{88}Sr 49
  - 6. ^{103}Rh 51
  - 7. ^{140,142}Ce 52
  - 8. ^{156,158,160,161,162,163,164}Dy 52
  - 9. ^{181}Ta 54
  - 10. ^{190,191,192,193,194,195,196,197,198}Pt 59
  - 11. ^{206,207,208}Pb 61
  - 12. ^{234}U 62
  - 13. ^{236}U 64
  - 14. Adoption of IRDFF-II neutron dosimetry evaluations 64
- D. Fixes or improvements to existing evaluations 70
  - 1. ^{106,108,110,111,112,114,116}Cd 70
  - 2. Gamma-spectra fixes 70
  - 3. Previously missing outgoing-particle distributions 70
  - 4. Fission-product updates in the URR 75
  - 5. Prompt nubar evaluations of minor actinides 77
- E. File updates due to only minor fixes 78

IV. NEUTRON REACTION COVARIANCES 78
- A. Improved Testing of Nuclear Data Covariances 78
- B. Templates of Expected Measurement Uncertainties 82
- C. Decision Process of CSEWG to not Provide Mathematically Adjusted Libraries for ENDF/B-VIII.1 83

V. THERMAL NEUTRON SCATTERING SUBLIBRARY 83

* Corresponding author: gnobre@bnl.gov
† Retired.

A. Moderators 84
1. Light water (H_2O) 84
2. Beryllium (Be-metal) 85
3. Beryllium-Metal with Distinct Effects (Be+S_d) 86
4. Beryllium Oxide (BeO) 87
5. Calcium Hydride (CaH_2) 87
6. FLiBe Molten Salt 89
7. Nuclear/Reactor Graphite (20%) 90
8. Crystalline Graphite with Distinct Effects (graph+S_d) 90
9. Anhydrous Hydrogen Fluoride (HF) 93
10. Heavy Paraffinic Oil 93
11. Silicon Carbide (SiC) 94
12. Silicon Dioxide (SiO_2, α Phase) 95
13. Polystyrene ($(C_8H_8)_n$) 96
14. Poly(methyl methacrylate) ($(C_5O_2H_8)_n$) 98
15. Zirconium Carbide (ZrC) 100
16. Beryllium Carbide (Be_2C) 101
17. Zirconium Hydride (ZrH_x and ZrH_2) 102
18. Yttrium Hydride (YH_2) 102
19. Lithium-7 Hydride (^{7}LiH) and Deuteride (^{7}LiD) 104
B. Fuels 104
1. Plutonium Dioxide (PuO_2) 104
2. Uranium Carbide (UC) 105
3. Uranium Metal (U-metal) 107
4. Uranium Nitride (UN) 108
5. Uranium Dioxide (UO_2) 109
6. Uranium Hydride (UH_3) 110
C. Special Purpose 110
1. Liquid hydrogen and deuterium (l-H_2, l-D_2) 110
2. Sapphire Single-Crystal Neutron Filter (Al_2O_3) 111
3. Magnesium Oxide Neutron Filter (MgO) 112
4. Magnesium Fluoride Neutron Filter (MgF_2) 113
5. Beryllium Fluoride Neutron Filter (BeF_2) 114

VI. PHOTONUCLEAR SUBLIBRARY 115
A. Evaluation choices 116

VII. CHARGED PARTICLE REACTION SUBLIBRARIES 117
A. Alphas sublibrary 117
1. ^{9}Be 117
2. ^{17,18}O 118
B. Helions sublibrary 118
C. Deuterons sublibrary 119
1. ^{3}H 119
2. ^{3}He 119
3. ^{6}Li 120
D. Protons sublibrary 120
1. ^{4}He 121
E. Tritons sublibrary 121
1. ^{4}He 121

VIII. FISSION YIELDS SUBLIBRARIES 121
A. Correction to the uncertainties of cumulative yields near stability 122
B. Corrections to the thermal-neutron-induced fission yields of ^{241}Pu 122

IX. DECAY SUBLIBRARY 124

X. ATOMIC SUBLIBRARIES 124

XI. NEUTRON DATA STANDARDS 124
A. Thermal Neutron Constants (TNC) 125

XII. SUMMARY OF FORMAT CHANGES SINCE ENDF/B-VIII.0 125
A. ENDF-6 Format Changes 126
B. GNDS Format Changes 126

XIII. PROCESSING UPDATES 127
A. NJOY 128
B. FUDGE 129
C. AMPX 130

XIV. INTEGRAL DATA TESTING SUMMARY 130
A. Criticality Benchmark Experiment Results 131
1. The Mosteller Suite 131
2. Complete Criticality Testing 131
B. Delayed Neutron Experiment Results 135
C. Reaction Rate Ratio Results 136
D. Reactor Depletion 137
1. Depletion calculations using `Serpent` 138
2. Depletion calculations using `Shift` 140
3. Depletion calculations using `CASMO5` 141
4. Fuel cycle calculations using CORD-2 and WIMSD-5B 142
E. Pulsed Spheres Results 145

XV. CONCLUSIONS & FUTURE WORK 148

Acknowledgments 150

References 150

A. Provenance of evaluations in ENDF/B-VIII.1 181

B. Summary of criticality k_{eff} C/E Changes Between ENDF/B-VIII.0 and ENDF/B-VIII.1 validation results 203

C. Complete validation results from GNDS files 220

I. INTRODUCTION

This paper describes the contents of the next generation of the United States' premier nuclear data library, ENDF/B-VIII.1. The ENDF library is the product of the Cross Section Evaluation Working Group (CSEWG), a long running collaboration formed in 1968. The version numbering for the ENDF library indicates that this release is a "minor" one in that it does not include an update to the standards observables published by the International Atomic Energy Agency (IAEA) Neutron Data Standard Committee [1]. However, the version numbering does not tell the whole story: we have updated many neutron sublibrary evaluations including fissionable materials ^{233,234,235,236,238}U, ^{239,240,241}Pu and structural materials, such as F, Si, Cr, Fe, Cu, Ta, and Pb. Additionally, we have developed several thermal neutron scattering evaluations and introduced other smaller but impactful changes. We have also addressed issues with actinide resolved-resonance-region data in high burnup situations. Finally, we have adopted many of the high-quality reactor dosimetry evaluations from the IRDFF-II library [2]. These changes will be outlined in the next sections and expanded on throughout this paper.

Our main goal while developing ENDF/B-VIII.1 is maintaining and/or improving the overall quality and performance of the library while ensuring both the transparency and reproducibility of methods and decisions within the CSEWG collaboration[1]. Updating an ENDF evaluation requires a detailed study to confirm that a new proposed evaluation is indeed superior. This cautious approach helps prevent an unintended step backwards. The key principles we have followed are:

- Do no harm
- Be aware of historical and previous evaluation decisions
- Ensure proposed changes are demonstrably better
- Anticipate potential problems and conduct validation testing

For the most part, each ENDF/B-VIII.1 evaluation is "hand crafted" by nuclear data experts merging the best available experiment and theory, and in some cases, with limited Artificial Intelligence and/or Machine Learning (AI/ML) assistance. This process is unlike TENDL (which is arguably purely ML-generated) and more like the JENDL and JEFF evaluation efforts. Once the evaluator has completed their work, they upload their files to CSEWG's git repository (see Sec. II F) where a battery of automated "phase 1" tests are run on the data. The results of these tests are used in a peer review process by nuclear data subject matter experts (see Sec. II G). This review takes place directly in the git repository's web page, preserving both the file modification and review history and comments. Once the files pass this peer review step, the library is made available to data validators coordinated by the CSEWG Validation Committee. This fully online review process is new for ENDF/B-VIII.1 and is expected to smooth the development of the follow-on ENDF/B-IX.0 library.

We are in a rare moment of optimism in the field of nuclear data. While nuclear science is being recognized for its important historical impacts [3–7], in a broad sense, we are also experiencing a "nuclear renaissance" and not just for traditional nuclear reactors. Recently, the Nuclear Ignition Facility (NIF) at Lawrence Livermore National Laboratory (LLNL) achieved Lawson's criteria for ignition [8] sparking discussions about nuclear data for fusion applications. In addition, we are eagerly anticipating the possibility of human-crewed missions to the moon and Mars, all of which spark interest in space reactors [9] and nuclear propulsion [10]. Planetary science uses methods, such as active neutron interrogation which uses techniques pioneered by the petroleum industry [11] but eagerly adopted for nuclear non-proliferation [12]. Put simply, nuclear science and specifically nuclear data are being viewed as part of the solution to the world's problems in combating climate change, ensuring nuclear security, enabling space exploration and providing new radionuclides for medical applications (see recent nuclear data needs for medical applications compiled at the IAEA meeting [13]). ENDF/B-VIII.1 changes to actinides and thermal neutron scattering evaluations will aid all reactor application, both on Earth and in space. The changes to the structural materials will benefit nearly all applications. The addition/correction of outgoing particle spectra will improve energy balance in all applications. Improvements to outgoing gamma data will have a substantial impact by enabling spectroscopy applications in exploration and non-proliferation applications.

Our ability to take advantage of these opportunities is enhanced by the Nuclear Data Working Group's efforts to organize the Workshop on Applied Nuclear Data Activities (WANDA) series of workshops which helps us identify cross-cutting needs for both current and emerging nuclear data users. This has also expanded the communities' funding and brought in new members into the nuclear data workforce as reflected in several new evaluations in ENDF/B-VIII.1. These new entrants have helped preserve the expert knowledge that might have otherwise been lost when the senior members of our community have passed away.

II. OVERVIEW OF THE CURRENT ENDF/B RELEASE

Table I provides an overview of the ENDF/B-VIII.1 release and compares it to the last four ENDF/B versions.

[1] Due to the nature of the collaboration, in-development data usually cannot be made fully open to the public.

TABLE I. Overview of the ENDF/B library releases and the 15 sublibraries in ENDF/B-VIII.1. Shown in the columns are the number of materials present in each sublibrary in each release. Here Spontaneous Fission Yields is abbreviated as SFY and Neutron-induced Fission Yields as NFY.

Sublibrary	VIII.1	VIII.0	VII.1	VII.0	VI.8
Neutron	558	557	423	393	328
Thermal n-scattering	114	33	21	20	15
Proton	49	49	48	48	35
Deuteron	6	5	5	5	2
Triton	5	5	3	3	1
Helium3	4	3	2	2	1
Alpha	5	1	n/a	n/a	n/a
Photonuclear	222	163	163	163	n/a
Atomic relaxation	100	100	100	100	100
Electron	100	100	100	100	100
Photoatomic	100	100	100	100	100
Decay data	3821	3821	3817	3838	979
SFY	9	9	9	9	9
NFY	31	31	31	31	31
Standards	10	10	8	8	8

In this release, there are significant changes to most sublibraries, with only the standards and decay sublibraries remaining untouched. The sublibraries in which new evaluations were added, either by replacing existing evaluations or creating new ones are highlighted in bold font in Table I. Below, we summarize the largest changes to various sublibraries and the largest changes to the ENDF workflow.

A. Neutron sublibrary

In this release, many neutron files were reevaluated or received major changes. Below, we highlight these changes and, where appropriate, attempt to relate the evaluations to an application need, at least in broad terms. Roughly one third of the new neutron evaluations were performed as part of the International Nuclear Data Evaluation Network (INDEN) collaboration:

- **^{239}Pu:** As a product of a joint evaluation from IAEA, Los Alamos National Laboratory (LANL), LLNL and Oak Ridge National Laboratory (ORNL), a new ^{239}Pu was developed. Changes to the fission neutron multiplicity $\bar{\nu}$, Prompt Fission Neutron Spectrum, resonance region and fast region were made. The changes helped address the depletion issues noted elsewhere.
- **INDEN light isotopes:** ^{16}O, ^{18}O, ^{19}F
- **INDEN structural materials:** ^{28,29,30}Si, ^{63,65}Cu, and components of stainless steel (^{50,51,52,53,54}Cr, ^{55}Mn and ^{54,56,57}Fe)
- **INDEN detector materials:** ^{139}La is used in scintillators and other detector materials
- **INDEN actinides:** ^{233}U, ^{235}U, ^{238}U, and ^{240,241}Pu
- **Non-INDEN light isotopes:** ^{3}He, ^{6}Li, and ^{9}Be
- **Non-INDEN structural materials:** ^{51}V and ^{181}Ta
- **Dosimetry materials:** in addition to adopting IRDFF-II neutron dosimetry reactions in many materials, full evaluations were made for other dosimetry materials: ^{88}Sr, ^{103}Rh, and ^{190,191,192,193,194,195,196,197,198}Pt
- **Rare earths:** ^{140,142}Ce is often alloyed in fuel and refractory materials and ^{156,158,160,161,162,163,164}Dy is used in reactor control rods
- **Lead:** is used in shielding and in lead cooled fast reactors, so ^{206,207,208}Pb were reevaluated
- **Non-INDEN actinides:** ^{234}U and ^{236}U

In addition, there were many fixes or improvements to existing evaluations, including ^{106,108,110,111,112,114,116}Cd, gamma-spectra fixes, addition of previously missing outgoing-particle distributions, updates to the unresolved resonance region (URR) for fission products and prompt $\bar{\nu}$ evaluations of minor actinides.

Finally, we note that there was much activity addressing neutron reaction covariances, including improved covariance testing, adoption of Templates of Expected Measurement Uncertainties to identify missing components in covariance data and a major decision to not provide mathematically adjusted neutron libraries for ENDF/B-VIII.1. Covariances were corrected (some are very minor changes), updated or newly included, for many nuclei, such as ^{1,2}H, ^{6,7}Li, ^{9}Be, ^{10}B, ^{13}C, ^{23}Na, ^{24}Mg, ^{27}Al, ^{35,36}Cl, ^{29,30,32}Si, ^{31}P, ^{32}S, ^{39,41}K, $^{46-48}$Ti ^{49,51}V, $^{50-53}$Cr, ^{55}Mn, ^{54,56}Fe, ^{59}Co, ^{58,60,63}Ni, ^{63,65}Cu, ^{64,67,68}Zn, ^{75}As, ^{86}Kr, ^{86}Kr, ^{89}Y, ^{90,91,95}Zr, ^{92,97,98,100}Mo, ^{102}Ru, ^{103}Rh, ^{113,115}In, ^{127}I, ^{132}Xe, ^{139}La, ^{140,142}Ce, ^{139}La, ^{141}Pr, ^{143}Nd, ^{147}Pm, ^{155}Eu, ^{152,160}Gd, $^{156,158,160-164}$Dy, ^{169,170}Tm, ^{181}Ta, ^{199}Hg, $^{190-198}$Pt, $^{182-184,186}$W, ^{197}Au, $^{204,206-208}$Pb, ^{209}Bi, $^{233-236}$U and ^{239,240,242}Pu.

B. Thermal neutron scattering sublibrary

CSEWG has dramatically increased the number of evaluations in the thermal scattering neutron law (TSL) sublibrary:

- **Traditional moderators:** light water (H_2O), Beryllium metal, Beryllium Oxide (BeO), Calcium Hydride (CaH_2), plastics (Polystyrene ($(C_8H_8)_n$)

and Lucite ($(C_5O_2H_8)_n$)), graphite (reactor-grade graphite (20%) and crystalline graphite (graph+S_d)), anhydrous Hydrogen Fluoride (HF), and heavy paraffinic oil.

- **Exotic moderators:** Beryllium Carbide (Be_2C), Zirconium Hydride (ZrH_x and ZrH_2), Yttrium Hydride (YH_2), Lithium-7 Hydride (^{7}LiH), and Deuteride (^{7}LiD)

- **FLiBe molten salt**

- **Structural materials and cladding:** Silicon Carbide (SiC), Silicon Dioxide (SiO_2), and Zirconium Carbide (ZrC)

- **Fuels:** Plutonium Dioxide (PuO_2), Uranium Carbide (UC), Uranium metal, Uranium Nitride (UN), Uranium Dioxide (UO_2), and Uranium Hydride (UH_3)

- **Special purpose materials:** liquid hydrogen and deuterium (l-H_2, l-D_2), and neutron filters (Sapphire (Al_2O_3), Magnesium Oxide (MgO), Magnesium Fluoride (MgF_2), and Beryllium Fluoride (BeF_2))

These additions meant that number of evaluated files in the ENDF/B library is larger than the previous number of available material (MAT) numbers as allotted by the ENDF-6 manual. Therefore, CSEWG approved a format change that allows the use of all numbers from 1 to 9999. To organize and manage the administrative task of assigning unique MAT numbers to individual materials in a consistent manner within a given ENDF/B release and to ensure the user is effectively informed, we distribute alongside the TSL sublibrary of ENDF/B-VIII.1 a comma-separated file (CSV), named `TSL_MAT_numbers.csv`, which lists all evaluated files in the current release and their corresponding MAT number. In the future, as more materials evaluations are added and thus more MAT numbers are assigned, this file will be updated accordingly.

C. Photonuclear sublibrary

Around 200 evaluated files originating from the IAEA Coordinated Research Project (CRP) on photonuclear data [14] were adopted into ENDF/B-VIII.1. For a few select mission-critical materials, evaluations from ENDF/B-VIII.0, which can be traced back to an earlier CRP [15], were adopted instead. Additionally, fixes addressing format and other small issues were implemented. Lastly, ENDF/B-VIII.1 contains one new photonuclear file when compared to ENDF/B-VIII.0 – that is ^{242}Pu which was adopted from JENDL-5 [16].

D. Charged particle sublibraries

There were major and minor updates to evaluated files from the alphas, helions (^{3}He), deuterons, protons and tritons sublibraries in ENDF/B-VIII.1. Among these, we can highlight:

- For the alphas sublibrary, we adopted: the LLNL Evaluated Charged-Partilce Library (ECPL) [17] evaluation for ^{6}Li; the NNL-modified JENDL evaluation for ^{9}Be and ^{16,17}O.

- For the helions sublibrary we adopted: new ^{4}He evaluation from the INDEN collaboration; the LLNL ECPL [17] evaluation for ^{7}Li.

- For the deuterons sublibrary we adopted: additions and corrections to the ENDF/B-VIII.0 d+t file; new LANL evaluation updates for ^{3}He and ^{6}Li.

- For the protons sublibrary we adopted: evaluation updates for ^{4}He.

- For the tritons sublibrary we adopted: evaluation updates for ^{4}He.

E. Fission product yield sublibraries

There were no new complete evaluations for either spontaneous (SFY) or neutron-induced fission yields (NFY) sublibraries in ENDF/B-VIII.1. However, an important fix was implemented into the ^{241}Pu NFY file, solving a long-standing anomalous discontinuity issue introduced in ENDF/B-VI.2, decades ago. Additionally, many erroneously large uncertainties, present in both NFY and SFY from ENDF/B-VIII.0, were corrected.

F. Migration to GitLab repository

Shortly after the ENDF/B-VIII.0 release, the development version of the ENDF library was migrated from an Apache Subversion (SVN) repository to a GitLab server hosted by the National Nuclear Data Center (NNDC) [18]. This migration provided several benefits leading up to the ENDF/B-VIII.1 release. The Git versioning system has by far surpassed SVN and competitors to become the main tool for developing and maintaining versioned repositories. Git provides more flexibility than SVN in creating, editing and merging branches. This capability proved especially useful when several competing candidate evaluations were being developed and reviewed simultaneously. In addition to hosting the repository, GitLab provides a web interface with integrated issue trackers and merge requests that helped collaborators identify, document, track and resolve issues. This allowed the implementation of continuous-integrated, continuous-development tools that would automatically trigger a se-

ries of format and processing tests for every update submitted. Although access to the ENDF GitLab repository cannot be made public due to the nature of the sponsors of much of its development, any member of the CSEWG collaboration can request access to it.

G. Review process

Even though evaluation reviews have always existed in the ENDF/B library, from series of paper forms a few decades ago to something more dynamic but less structured in the recent years, for ENDF/B-VIII.1, this was the first time that a formal, streamlined, electronic/digital peer-review was completely integrated into the evaluation submission process. This was accomplished by leveraging the GitLab ENDF/B repository [18], where contributions would be directly uploaded to one branch (`phase1`) by evaluators, but could only move to a second branch (`phase2`) after being reviewed by one or more peers.

The user-friendliness of the GitLab platform, which allows for back-and-forth interactions with mark-down text, figures, file attachments, hyperlinks and GitLab cross-links, greatly encouraged iterations between evaluators, reviewers and other collaborators. The whole review discussion history, in the form of review branch merge requests, is completely preserved in GitLab, allowing for future consultation of the documentation and rationale that went into a particular decision. Although one could argue this process would slow down prompt access to the evaluations, quite often the evaluators would praise the process as it gave them a chance to find and fix errors, while users would benefit from this quality-assurance step.

This integrated process often led to issues with evaluated files being found and addressed well before beta and final releases, minimizing chances of unwanted surprises after the releases, therefore, increasing the quality and reliability of the final product. Although the details of the review process are restricted to the CSEWG collaboration, important information about the development of the files can be openly found in the change logs (`CHANGELOG.md` files) distributed within each ENDF/B-VIII.1 released sublibrary [19–34], as well as with the whole ENDF/B-VIII.1 release package [19]).

III. NEUTRON CROSS SECTIONS

A. Jointly-assembled ^{239}Pu

1. *Background & Previous Evaluations*

A joint international effort on ^{239}Pu has been adopted for ENDF/B-VIII.1. This work involved substantial contributions from LANL, LLNL, ORNL, and the IAEA-coordinated INDEN collaboration. A completely new evaluation has been developed in the whole energy range. A concerted effort has been made by the international team to include the latest measured differential data, improve the agreement with existing measurements and neutron standards, use the IAEA evaluated prompt fission neutron spectrum (PFNS) at the thermal point, make use of new and decisive LANL-LLNL Chi-Nu PFNS and CEA measurements [35–38] above the thermal point, and increase the evaluation range up to 30 MeV incident neutron energy. Additional work on resonance parameters and resulting fission, capture and total cross sections in the resolved resonance range below 2 eV was required to increase the criticality of power reactors at high burnup, a known ENDF/B-VIII.0 deficiency [39].

2. *(n,f) fission neutron multiplicity $\overline{\nu}$*

The neutron-induced average prompt fission neutron multiplicity, $\overline{\nu}$, for n+^{239}Pu in the resonance region was reevaluated to consider the Thermal Neutron Constant (TNC) values [1] as well as experimental values measured by Gwin [40, 41]. The $\overline{\nu}$ evaluation shape up to 0.8 eV is very similar to ENDF/B-VIII.0 and largely driven by Gwin 1984 data [40]. The comparison with Gwin data and other evaluations is shown in Fig. 1. The thermal $\overline{\nu}_{pr}$=2.855 is 0.6% lower than the recommended standard TNC value $\overline{\nu}_{pr}$ of 2.872 ± 0.012. The evaluated prompt $\overline{\nu}$ value is driven by lower criticality required for Pu solutions benchmarks[2] and the need to increase the criticality at high burnup, see the discussion in Section XIV D.

Note that Kahler calculated 158 plutonium thermal solutions (PST1, PST2, PST3, PST4, PST5, PST6, PST9, PST10, PST11, PST12, PST18, PST22, PST28, PST32, PST34, and PST38): the average Δk_{eff} for ENDF/B-VII.1 was 1.00451(455), for ENDF/B-VIII.0 was 0.99996(468), and for the latest ENDF/B-VIII.1 evaluation became 1.00236(493). The excellent ENDF/B-VIII.0 results were driven by the adoption of the Working Party on International Nuclear Data Evaluation Cooperation (WPEC) Sub-Group-34 (SG-34) resonance parameters, but the thermal-neutron-induced PFNS was not changed from the ENDF/B-VII.0 evaluation. The dispersion of calculated results remain at 500 pcm level for all three evaluations, which is certainly too high. Further work is needed to improve this performance considering criticality, depletion, and temperature reactivity coefficients.

A bump present in ENDF/B-VIII.0 $\overline{\nu}$ evaluation between 0.8 eV and 5 eV was reduced in this work as previously done in the JENDL-5 evaluation [16] as shown in Fig. 1. There is contradictory information from integral experiments: to increase power-reactor criticality at high burnup [39], a higher Pu thermal average neutron

[2] Private communication by A.C. "Skip" Kahler.

multiplicity is required. However, the average criticality of many well-thermalized Pu thermal solutions (as listed above) indicates a need for lower thermal average neutron multiplicity as suggested by A.C. Kahler. This contradiction required a compromise solution.

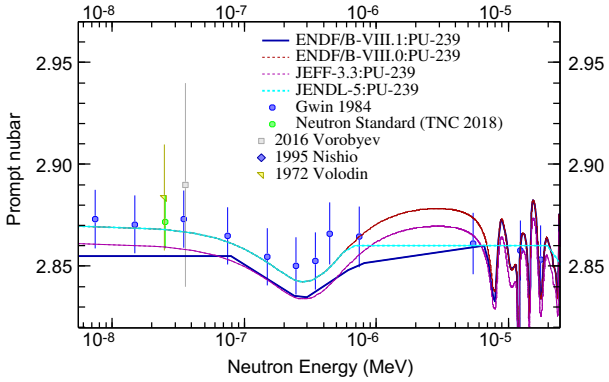


FIG. 1. Evaluated ^{239}Pu $\overline{\nu}$ in ENDF/B-VIII.1 and previous evaluations are compared with selected experimental data [42–44] from EXFOR [45]. Gwin data [40] were derived using the recommended ^{252}Cf(sf) $\overline{\nu}$ [1].

The evaluated $\overline{\nu}$ uncertainty for n+^{239}Pu is shown in Fig. 2 in a logarithmic energy scale to emphasize the resonance range. The current evaluated $\overline{\nu}$ uncertainty has increased significantly up to 1.2 MeV of incident neutron energy (minimum uncertainty around 0.44%) due to the increase in the evaluated $\overline{\nu}$ uncertainty of the ^{252}Cf(sf) standard from 0.13% up to 0.42% [1], and its impact on experimental data measured as a ratio to the ^{252}Cf(sf) $\overline{\nu}$ standard.

Additionally, the $\overline{\nu}$ uncertainty from 500 eV up to 80 keV has increased up to 1.5% to consider the Gwin 1986 experimental data [41] (also measured relative to the ^{252}Cf(sf) standard). No other measurements are available from about 10 eV up to 80 keV of neutron incident energy.

The ENDF/B-VIII.1 $\overline{\nu}$ evaluated uncertainties in the fast-neutron range in Fig. 2 are larger than in ENDF/B-VIII.0 from 80 keV to approximately 2 MeV due to the increased ^{252}Cf(sf) $\overline{\nu}$ standard uncertainty (0.42%). The evaluated uncertainties are smaller than ENDF/B-VIII.0 above 2 MeV due to high-precision data from Marini *et al.* [46, 47] as discussed below. The correlation matrix in Fig. 3 is strongly and positively correlated due to the full correlation stemming from the dominant ^{252}Cf(sf) $\overline{\nu}$ standard uncertainty. A reevaluation of the ^{252}Cf(sf) $\overline{\nu}$ standard is planned for ENDF/B-IX.0.

The neutron-induced average prompt fission neutron multiplicity, $\overline{\nu}$, for n+^{239}Pu in the fast-neutron range (above 80 keV of incident neutron energy) was reevaluated from scratch for ENDF/B-VIII.0 [38, 48]. Experimental-data uncertainties were reevaluated using templates of expected $\overline{\nu}$ measurement uncertainties [49] and information provided in EXFOR and published papers.

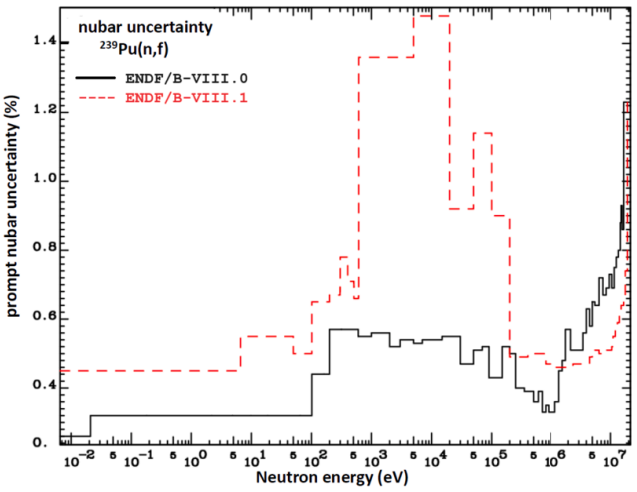


FIG. 2. Evaluated ^{239}Pu $\overline{\nu}$ uncertainty in ENDF/B-VIII.1 versus ENDF/B-VIII.0.

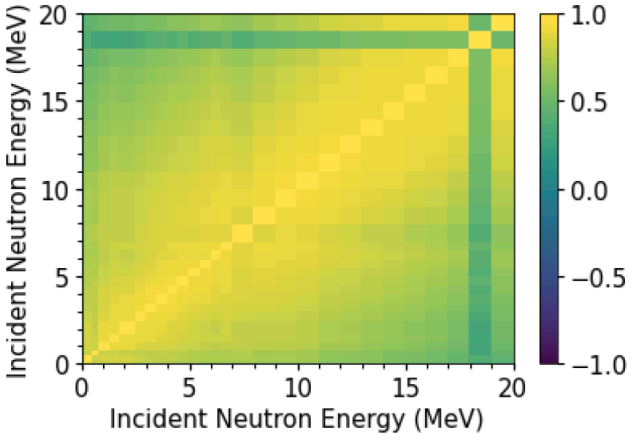


FIG. 3. Evaluated ^{239}Pu $\overline{\nu}$ correlation matrix.

The very recent high-precision data by Marini *et al.* [46, 47] for incident energies above 700 keV were included in the new evaluation. Unfortunately, no measurement was carried out at the thermal incident energy. New Marini *et al.* measurements validated the evaluated ENDF/B-VIII.0 prompt fission neutron multiplicity from 700 keV up to about 5 MeV [47].

For the very first time, the `CGMF` fission-event generator [50] was used as a model to evaluate $\overline{\nu}$. Including that model in the evaluation made it possible to employ evaluated model parameters to compute other fission quantities, such as yields as a function of mass, the average total kinetic energy of fission fragments, *etc.* It was shown in Ref. [38] that most of these predicted fission quantities agree well with experimental data except for the PFNS – a known model deficiency that is being investigated. This combined new information led to distinct $\overline{\nu}$ changes in the fast energy range from ENDF/B-VIII.0 as shown in Figs. 4 and 5.

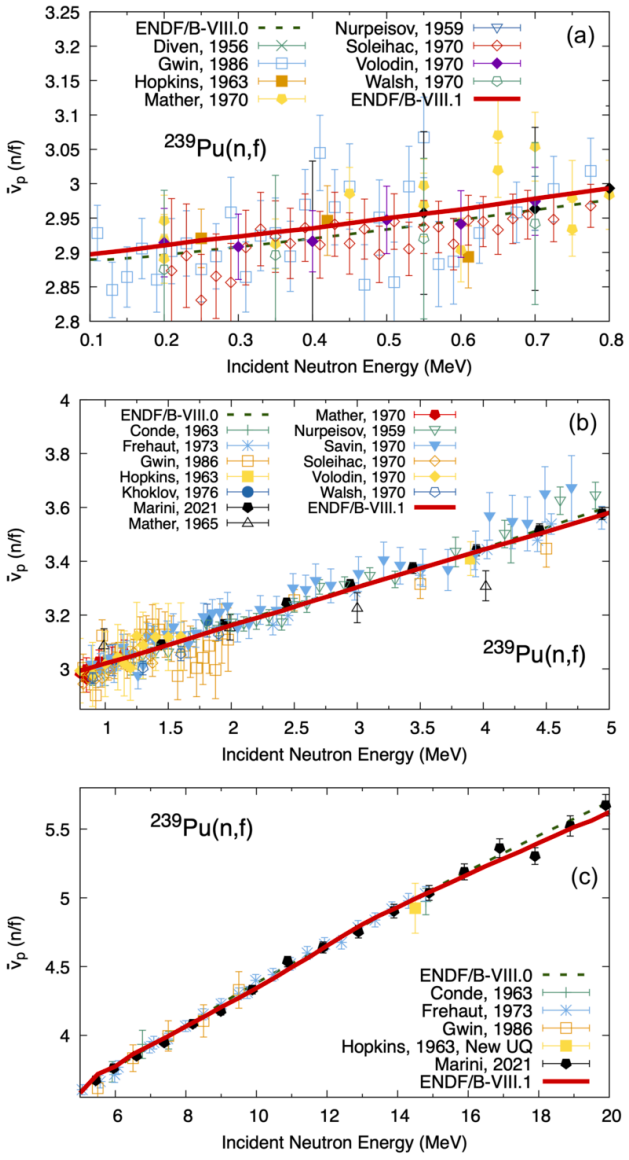


FIG. 4. Selected experimental data [51–63] taken from EXFOR [45] and evaluated ^{239}Pu $\overline{\nu}$ in the fast neutron range compared to ENDF/B-VIII.0 (dashed black line) and ENDF/B-VIII.1 (solid line) for 0.1 MeV to 0.8 MeV (a), 0.9 MeV to 5 MeV (b) and 5 MeV to 20 MeV (c) neutron incident energies.

A new $\overline{\nu}$ evaluation is compared to JENDL-5, JEFF-3.3 evaluations and selected experimental data and plotted as a ratio to ENDF/B-VIII.0 in Fig. 5. The new evaluation is up to 0.5% higher than the ENDF/B-VIII.0 below 1.5 MeV (the curves cross around 1.5 MeV) and is in reasonable agreement with Marini data [46, 47] within the experiment's uncertainties except at 2.2, 5.5, and 12 MeV.

From 5 MeV up to 5.5 MeV, the $\overline{\nu}$ jump predicted by the model at the opening of the second fission chance is barely (if at all) seen in the data. The new evaluation overestimates the Marini data around 5 MeV by about 0.5%, but the agreement with Marini data improves above 6 MeV.

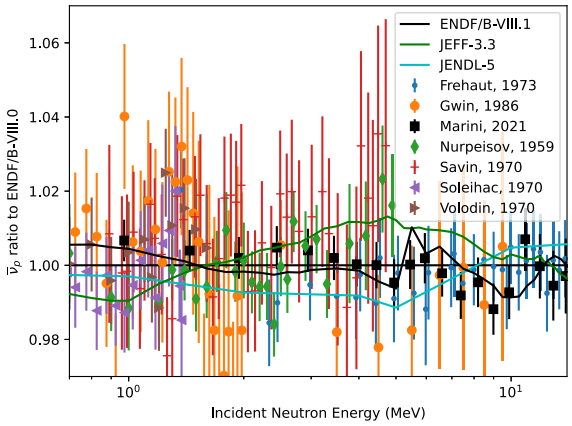


FIG. 5. Evaluated ^{239}Pu $\overline{\nu}$ ratio to ENDF/B-VIII.0 for selected experimental data [53, 54, 56–59, 62] and for JENDL-5 [16], JEFF-3.3 [64], and the new ENDF/B-VIII.1 evaluations.

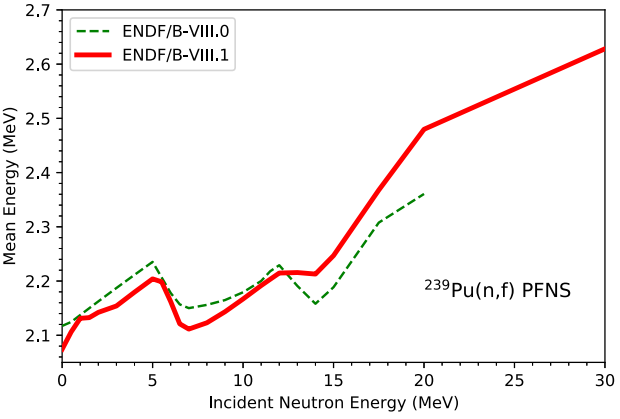


FIG. 6. Evaluated ^{239}Pu PFNS mean energy.

The changed $\overline{\nu}$ resulted in a slight increase in Jezebel k_{eff} (about 100–150 pcm) that was counter-balanced by the criticality reduction induced by a new and softer n+^{239}Pu PFNS. However, the disagreement of model-predicted PFNS versus the experimental PFNS data implies that strong correlations brought by the model into the evaluation should be reviewed and models improved.

The evaluated $\overline{\nu}$ described above was increased at the IAEA by up to 0.1%[3] in the energy range 1.5–4 MeV (scaling factors: 1.0 at 1.5 MeV, 1.001 at 2.5–3 MeV, and 1.0 at 4.0 MeV, linear interpolation) to calculate the Jezebel $k_{\text{eff}} \equiv 1$ for the Jezebel v5 of the benchmark computational model. It is worth noting that such increase improves the agreement of the evaluated $\overline{\nu}$ with Marini data [46, 47]. The Jezebel v5 "calibration" was recommended by the expert CSEWG group led by R. Little.

[3] representing about +20 pcm of reactivity worth

The $\overline{\nu}$-tweak was well within the assessed relative uncertainty of about 0.5%. No changes in the $\overline{\nu}$-covariance matrix were introduced.

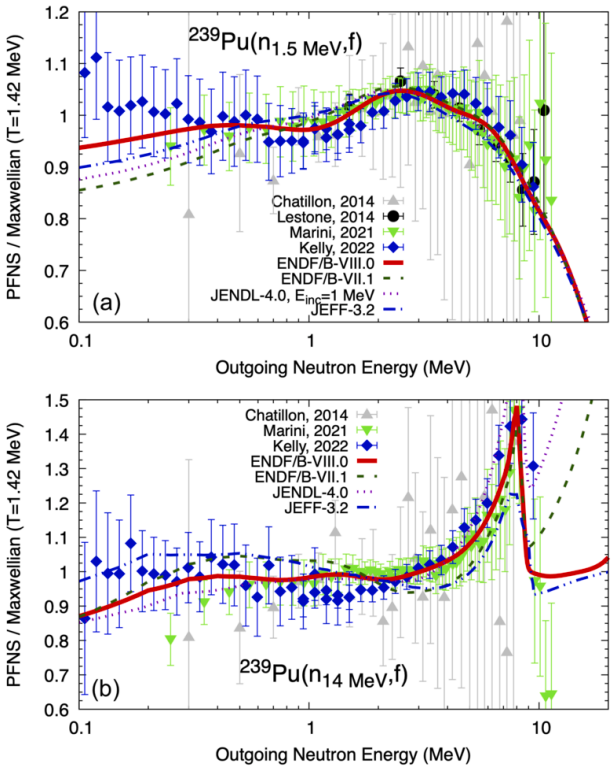


FIG. 7. Selected experimental data [37, 46, 65, 66] from EXFOR [45] and evaluated ^{239}Pu PFNS for $E_{\rm inc}$=1.5 (a) and 14 MeV (b).

3. *Prompt Fission Neutron Spectrum*

The n+^{239}Pu PFNS at thermal energies was adopted from the IAEA CRP work [44] which used a generalized least-square fit to available PFNS experimental data for the three major fissile actinides: ^{233,235}U and ^{239}Pu. A common feature of the IAEA-evaluated PFNS at the thermal point was the reduction of the PFNS average energy by about 30 keV compared to the ENDF/B-VII.1 values for all three fissile nuclei. Such reduction required important changes in the evaluated resonance parameters and neutron multiplicity below 5 eV to compensate for the increased criticality induced by softer PFNS. Those changes were introduced for ^{235}U in the ENDF/B-VIII.0 library [67, 68], but the IAEA-evaluated PFNS at the thermal point were only adopted for ^{233}U and ^{239}Pu targets in the current ENDF/B-VIII.1 library release.

PFNS at all other energies were reevaluated as described in Refs. [38, 69] and built on PFNS work included in ENDF/B-VIII.0 [70]. The main difference is the inclusion of high-precision ^{239}Pu PFNS measured by the CEA and Chi-Nu teams [35–37, 71] and Lestone data at $E_{\rm inc}$=2 MeV [65]. The evaluated PFNS differ distinctly at all incident-neutron energies from ENDF/B-VIII.0 as can be seen in the change of mean energy in Fig. 6. The new PFNS evaluation follows more closely the new experimental data sets as can be seen for $E_{\rm inc}$=1.5 and 14 MeV in Fig. 7. In Fig. 6, the average mean energy shows a nonlinear behavior from thermal to 1 MeV, where we would expect a linear one from a physics point of view. The reason for that is we prioritized following the high-precision experiments starting at 0.5 MeV rather than obtaining a smooth trend in the mean energy for the first-chance fission. New PFNS experiments would be needed in the low energy range, especially at the thermal up to 1 MeV, to better evaluate the PFNS in this energy range and confirm the IAEA PFNS evaluation at the thermal point.

This distinct change in the PFNS led to a minor decrease in Jezebel and Flattop-Pu $k_{\rm eff}$ values by 128(1) and 114(1) pcm [38, 69]. It was counter-balanced by other changes in ^{239}Pu, such as in the average prompt fission neutron multiplicity. The changes in the prediction of the Pu LLNL pulsed-sphere neutron-leakage spectra were modest [38, 69].

Evaluated PFNS covariances are provided for seven $E_{\rm inc}$ bins. Their mean energy uncertainties, $\delta\langle E\rangle$, are listed in Table II at thermal and from 0.75–3 MeV, where most experimental data are available. In the $E_{\rm inc}$ bin spanning 0.75–3 MeV (Fig. 8), the low uncertainties are driven by Marini, Chi-Nu and Lestone data at 1.5 MeV [35–37, 65].

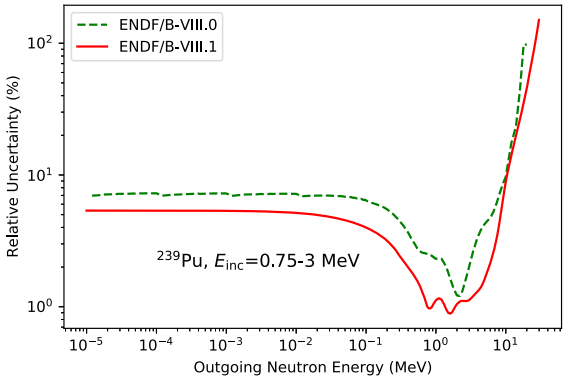


FIG. 8. Evaluated ^{239}Pu PFNS uncertainties for $E_{\rm inc}$=0.75–3 MeV.

4. *Resonance Region*

The resolved resonance region (RRR) and unresolved resonance region (URR) parameters have been updated by M. Pigni *et al.* [72] within the INDEN collaboration since ENDF/B-VIII.0.

Similar to the ^{235}U evaluation, the R-matrix analysis of the n+^{239}Pu system is an ongoing milestone of the Nuclear Criticality Safety Program (NCSP), and, in the ENDF/B-VIII.1 nuclear data library release, the major

TABLE II. The mean energy uncertainties, $\delta\langle E\rangle$, for the ^{239}Pu PFNS are listed per incident-neutron energy, $E_{\rm inc}$. For ENDF/B-VIII.0, the mean energy uncertainty was 37 keV for thermal–5 MeV.

$E_{\rm inc}$	$\delta\langle E\rangle$ (keV)
Thermal	16
0.25–0.75	37
0.75–3	15
3–5	33
5–6.5	33
6.5–13	34
13–30	40

updates in chronological order to this evaluation work were the extension of the RRR evaluation up to 5 keV and the updates in the thermal and low-energy region up to a few eVs. The extension to 5 keV of the RRR improved benchmark performance for integral experiments that are not fully thermalized. The updates below 5 eV were to guarantee an excellent performance in criticality benchmarks affected by the changes in the PFNS evaluation, together with the adoption of the thermal constants recommended by the standard evaluation [1], and to address issues in depletion calculations at high burnup, a known ENDF/B-VIII.0 deficiency [39].

Starting from energy levels and resonance widths randomly distributed from Wigner and Porter-Thomas distributions, respectively, the extension of the RRR evaluation from 2.5 keV up to 5 keV used both Harvey's thick-target data transmission and Weston's fission cross sections[4]. Due to the lack of measured capture data in this energy range, the cross sections of this reaction channel were obtained by using an average value of 40 meV assigned to the capture widths consistently with the Reich-Moore (RM) approximation of the R-matrix theory. In this regard, Fig. 9 highlights the neutron-energy region between 2.5–5 keV comparing the ENDF/B-VIII.0 (in black) and ENDF/B-VIII.1 (in red) evaluation together with Harvey's total cross sections and Weston's fission cross section. The Bayesian sequential fit of the measured data generated reasonable agreement. The fidelity of the newly released ENDF/B-VIII.1 library has been enormously improved in comparison to the ENDF/B-VIII.0 evaluation, particularly in view of the fluctuating behavior of the measured data. Although the χ^2 value for both cases is satisfactory (also most likely due to the large number of degrees of freedom), the fit of the fission cross section was easier to achieve than the fit of the transmission data.

In the low neutron-energy region below around 5 eV, the performance of the ENDF/B-VIII.1 evaluation was tested on the basis of multiple integral constraints, i.e., depletion calculations coupled to criticality safety benchmarks and the CEA Mistral-2 experiment that are particularly sensitive to the thermal and sub-thermal energy region, respectively. MISTRAL $C-E$ criticality differences as a function of temperature are compared versus the JEFF-3.1.1 reference result in Fig. 10. There is a known bias in the calculated results, but the important quantity is the slope which defines the reactivity temperature coefficient (RTC). The RTC calculated for the ENDF/B-VIII.1 evaluations is similar to the JEFF-3.1.1 RTC reference value and agrees with data within the estimated uncertainty of around 1 pcm/K.

Starting the discussion from the sub-thermal energy region, Fig. 11 shows the energy-dependent reproduction factor η-function ($\eta = \overline{\nu}\sigma_f/(\sigma_f+\sigma_\gamma)$) for three nuclear data libraries up to 10 eV. Besides non-negligible differences in both magnitude and energy shift of the resonance level at 0.3 eV, the energy behavior of the η-function for neutron incident energies below the thermal point E_n=0.0253 eV is significantly different, particularly with respect to the JEFF-3.3 library. In fact, sensitivity analyses of integral benchmarks showed that the non-linear sub-thermal energy trend of the η-function, together with

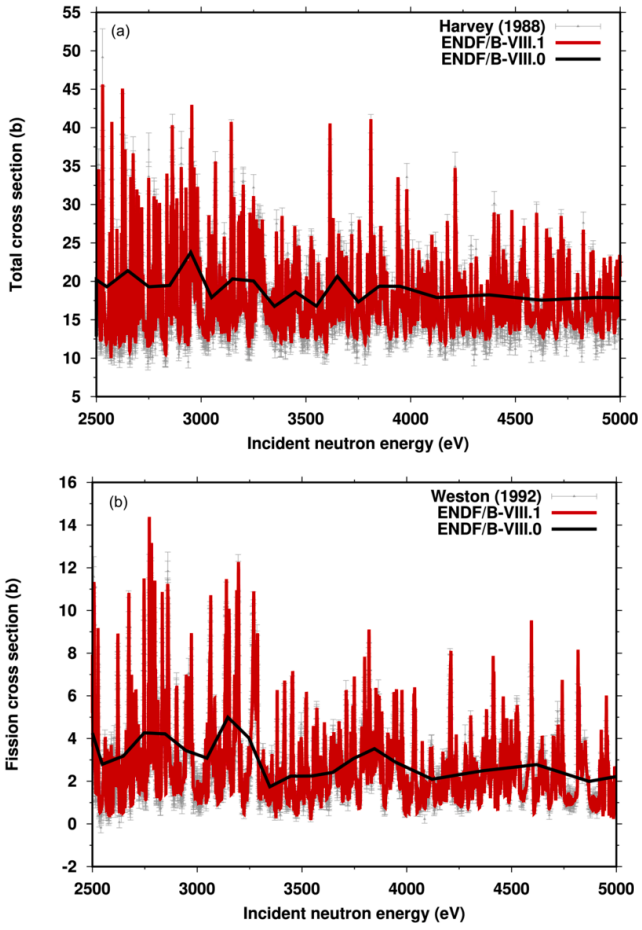


FIG. 9. n+^{239}Pu total and fission neutron cross section calculated for two nuclear data libraries together with Harvey's (a) and Weston's (b) measured data [73, 74].

[4] Weston's fission data were aligned to the Harvey's thick-target transmission data.

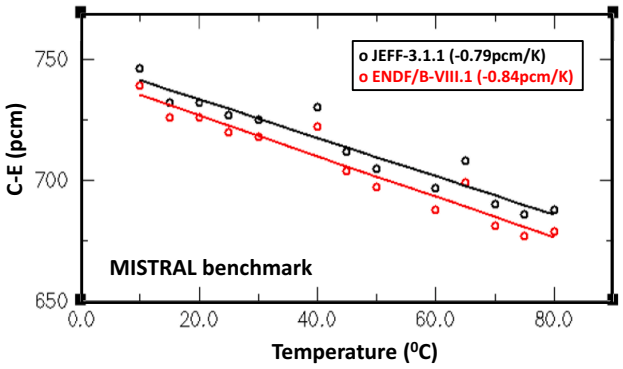


FIG. 10. MISTRAL benchmark reactivity temperature coefficient $C-E$ (pcm) for the ENDF/B-VIII.1 evaluation versus the JEFF-3.1.1 reference result.

its increased value above the thermal point up to about the 0.3 eV resonance level, are of fundamental importance to achieve a reasonable agreement with the Mistral-2 integral experiment. Overall, the energy behavior of the η-function for ENDF/B-VIII.0 and ENDF/B-VIII.1 is very similarly driven by the adopted bound states; it shows a slowly increasing trend in η up to the thermal point where all three libraries converge.

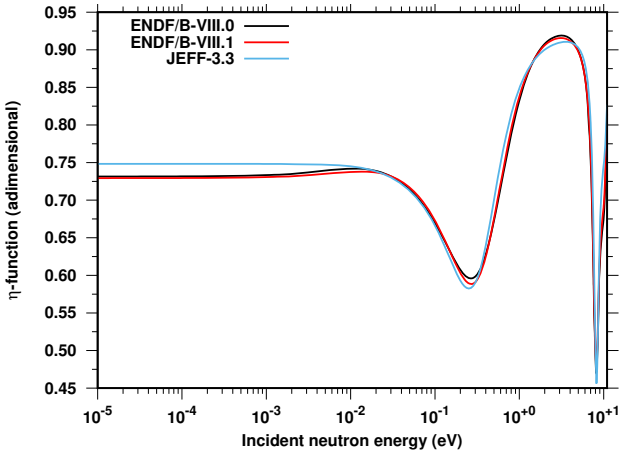


FIG. 11. ^{239}Pu energy dependent η-function for three nuclear data libraries.

Above the thermal point (in the epithermal region below 2 eV), it is important that the fission-to-capture cross-section ratio is well calibrated to achieve a local minimum of the η-function at about 0.3 eV to consistently guarantee a higher ^{239}Pu production at high burnup in depletion calculations. The correct ratio of the 0.3 eV resonance level was suggested by the fit of measured data including their scaling factors as shown in Fig. 12, while the energy trend in the sub-thermal energy region was achieved by the energy recalibration of the bound level (negative-energy level) which is very close to zero energy. As clearly shown in these figures for the JEFF-3.3 library, an energy shift of the 0.3 eV energy level would help in having a flat gradient as a function of Energy of Average Lethargy causing Fission (EALF) in criticality benchmarks. However, this choice poorly describes the measured differential data for all reaction channels, as seen in Fig. 12. We extensively discussed this issue at the INDEN meeting in Vienna in May 2024 and came to the final compromise solution used in the ENDF/B-VIII.1 evaluation. In this regard, additional sensitivity analyses suggested that the achievement of reasonable depletion calculations is anti-correlated with having a flat gradient as a function of EALF in criticality benchmarks. In Table III,

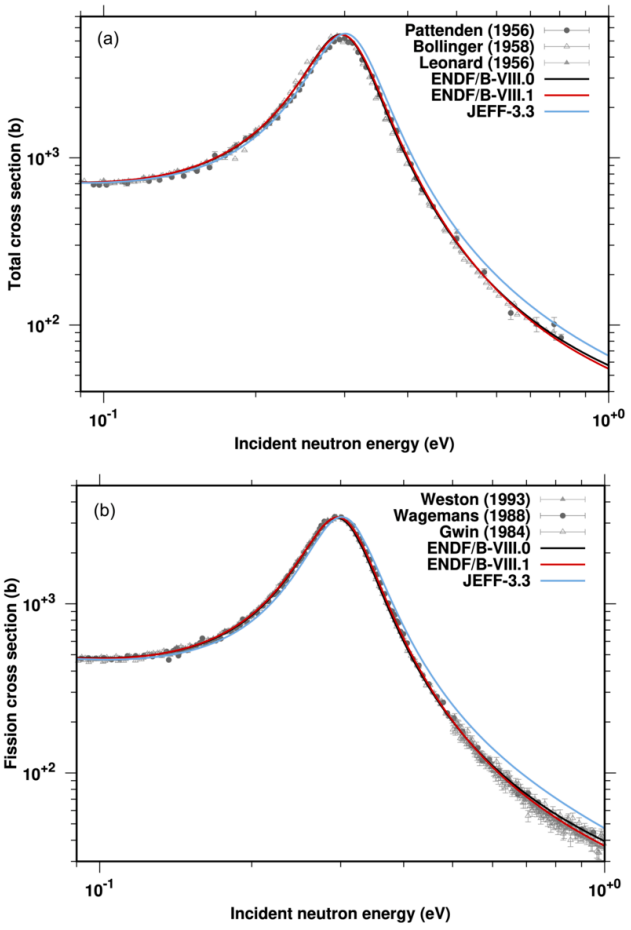


FIG. 12. n+^{239}Pu total and fission cross sections calculated for three nuclear data libraries together with selected measured data [75–80]. Impurity effects due to ^{240,242}Pu isotopes in the sample are not plotted.

the thermal constants for scattering, fission, and capture cross sections are reported for three nuclear data libraries: JEFF-3.3, ENDF/B-VIII.0 and the new ENDF/B-VIII.1 library. The thermal constant evaluated data show deviations within 1% for fission and capture cross sections. For the elastic scattering channel, there are deviations up to -6% with the JEFF-3.3 library. In the current ENDF/B-VIII.1 evaluation, the thermal-elastic scattering value was estimated to be about 8 b, similar to the ENDF/B-VIII.0 release. However, the thermal value for this reaction channel is in need of a verification measure-

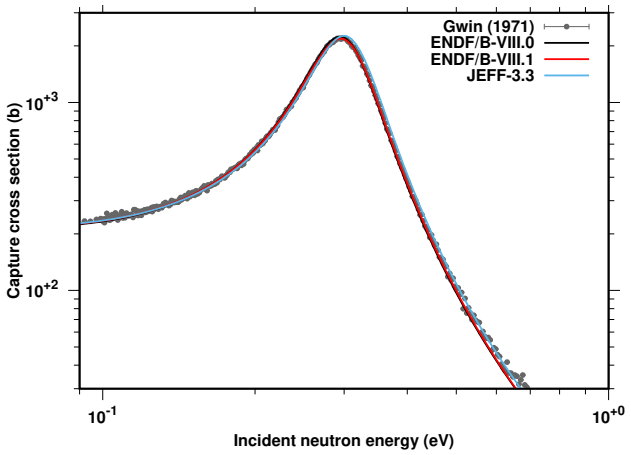


FIG. 13. n+^{239}Pu capture cross sections calculated for three nuclear data libraries together with Gwin's measured data [81]. Impurity effects due to ^{240,242}Pu isotopes in the sample are not plotted.

TABLE III. n+^{239}Pu 2200 m/s thermal cross sections for three nuclear data libraries compared with the Thermal Neutron Constants derived by the Standard group [1] and Duran *et al.* [82, 83] estimates. Available experimental data by Lounsbury *et al.* [84–86] are also listed.

Source	$\alpha_{\rm therm}$	σ_{el} (b)	σ_f (b)	σ_c (b)
ENDF/B-VIII.1	0.3600(17)	8.08(8)	751.1(22)	270.4(10)
ENDF/B-VIII.0	0.3614(535)	8.07(7)	747.4(22)	270.1(400)
JEFF-3.3	0.3622(145)	7.76(31)	749.4(64)	271.4(68)
Standards [1]	0.3586(35)	7.8(10)	752.4(22)	269.8(25)
Duran [82, 83]	0.3588(34)	8.0(10)	751.0(19)	269.5(24)
Lounsbury [84–86]	0.3555(57)	–	–	–

ment.

In fact, among transmission data measured at ORELA in the mid- to late-eighties on Pu samples of thin, medium, and thick size [73], particularly those measured at the 18-m flight path extend to low energies just below the large Pu resonance at 0.25 eV. By fitting the thick-target sample, a relatively large increase of the thermal scattering cross section was derived. The increase was estimated to be up to +19% higher than the value reported in ENDF/B-VIII.0, which stands at about 8 b. A thermal scattering cross section of 9 – 9.5 b is largely overestimating the value of the scattering cross section reported by National Institute of Standards and Technology (NIST) based on the Sears' compilation [87], which is about the value adopted by the JEFF-3.3 library and, therefore, already 3% lower than ENDF/B evaluations. A similar R-matrix analysis for the ^{238}U evaluation with transmission data extending to low energies and measured at ORELA showed similar inconsistencies. Therefore, waiting for additional experimental evidence, ORELA thick-target transmission data measured at the 18-m flight path was excluded in the current evaluation and the thermal scattering value of 8 b was adopted from the ENDF/B-VIII.0 evaluation.

The new ENDF/B-VIII.1 evaluation shows the best agreement with standard values [1] as well as with thermal cross sections recommended by Duran *et al.* [82, 83]. An excellent agreement of evaluated ENDF/B-VIII.1 α_{therm} with measurements of Lounsbury *et al.* [84–86] is observed; evaluated values of ENDF/B-VIII.0 and JEFF-3.3 α_{therm} are slightly larger than Lounsbury 1-sigma uncertainty interval.

It is worth noting that the first iteration of the INDEN ^{239}Pu RRR evaluation (ENDF/B-VIII.1β1) resulted in a MISTRAL reactivity temperature coefficient of -1.5 pcm/K, significantly worse than the JEFF-3.1.1 reference value equal to -0.79 pcm/K. This poor result was traceable to an overley large value of $\alpha_2 \equiv I_2^c/I_2^f = 0.653$ in the energy region from 0.1 up to 1 eV, being I_2^c and I_2^f – the corresponding integrals of the capture and fission cross section in the mentioned energy interval. Calculated α_2 values are listed in Table IV for ENDF/B-VII.1, ENDF/B-VIII.0, ENDF/B-VIII.1β1, and ENDF/B-VIII.1 evaluations. The α_2 integral value determines the MISTRAL reactivity temperature coefficient and, to a large extent, the reactivity at high burnup for power reactors. If we wanted to reproduce the ENDF/B-VII.1 depletion trend, then we have to reproduce the ENDF/B-VII.1 value of $\alpha_2 = 0.624$. The ENDF/B-VIII.0 value was 1.6% larger, the ENDF/B-VIII.1β1 value was an unacceptable 4.8% larger than the ENDF/B-VII.1 α_2 value.

We kept the newly fit resonance parameters in ENDF/B-VIII.1β1, but adopted the ENDF/B-VIII.0 negative resonances as discussed at the INDEN May 2024 meeting at the IAEA. As a result, we achieved the resulting ENDF/B-VIII.1 value of $\alpha_2 = 0.623$, which is in excellent agreement with the target ENDF/B-VII.1 α_2 value. Additional fitting to satisfy differential data constraints resulted in the final resonance parameters of the new ENDF/B-VIII.1 ^{239}Pu evaluation.

TABLE IV. n+^{239}Pu capture and fission cross-section integrals I_2^c and I_2^f (in eVb) in the energy interval [0.1–1] eV covering the first resonance are compared with the ratio $\alpha_2 \equiv I_2^c/I_2^f$ for ENDF/B-VII.1, ENDF/B-VIII.0, ENDF/B-VIII.1β1, and ENDF/B-VIII.1 libraries

Source	α_2 [0.1 – 1eV]	I_2^f(b.eV) [0.1 – 1eV]	I_2^c(b.eV) [0.1 – 1eV]
ENDF/B-VIII.1	0.623	564.3	351.6
ENDF/B-VIII.1β1	0.653	542.6	354.3
ENDF/B-VIII.0	0.633	553.6	350.7
ENDF/B-VII.1	0.624	558.4	348.6

5. *Fast Region*

New data have been incorporated in the fast energy range since the last ENDF/B release. Notable differential data include radiative capture from Mosby [88] (already

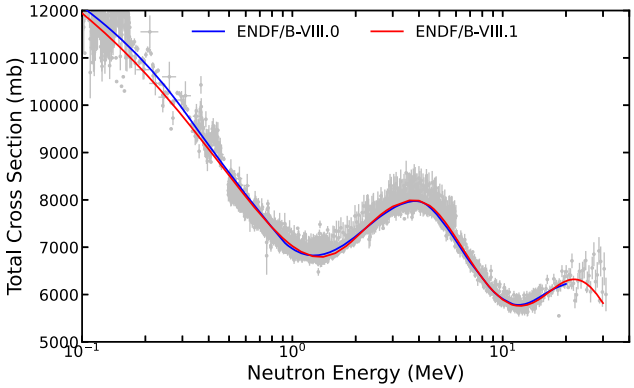


FIG. 14. The total cross section in the fast energy range for ^{239}Pu along with comparison to ENDF/B-VIII.0. The spread in experimental data in the EXFOR database is shown in grey [45].

used in the ENDF/B-VIII.0), fissionTPC data from Snyder [89] and (n,2n) data measured at CEA just above the threshold by Méot and colleagues [90].

Continual progress has been made in the fast energy region with respect to integral benchmarks. However, compensating errors in individual reaction channel data may still play a consequential role in the prediction of criticality. Capture and (n,2n) evaluations were derived by the INDEN collaboration using a least-squares fit of experimental data as described below. Elastic and inelastic data were calculated using nuclear models [91].

a. (n,tot) total cross section

The new total cross section in the fast neutron range was calculated using the modern reaction code `CoH` [92–94] with input parameters carefully adjusted to reproduce the total cross-section experimental data, see Ref. [91] for details. The evaluation of the total cross section is essentially equal to ENDF/B-VIII.0 except in the region between 100 and 400 keV where it is marginally lower. Fig. 14 highlights the present evaluation in comparison with ENDF/B-VIII.0.

b. (n,f) fission cross section

For ENDF/B-VIII.0, neutron-induced fission cross sections for ^{239}Pu were reported by the Neutron Data Standards committee [1] with covariances enlarged by a fully correlated USU (unrecognized sources of uncertainties [95]) component equal to 1.2%. This USU should account for known but missing uncertainty sources and correlations in the input to the evaluation as well as unknown uncertainties. While the latter can only be assessed by the spread of data among experiments employing different measurement techniques, the former were tackled by creating templates of expected fission cross-section uncertainties and applying them to ^{239}Pu(n,f) cross-section data in the database [96, 97]. In addition to that, fission TPC ^{238}U/^{235}U and ^{239}Pu/^{235}U [98] neutron-induced fission cross-section ratios were included into the evaluation undertaken by the Standards group [99]. These data were treated as shape data as their normalization is about 2% off from the current standard [98]. The final ^{239}Pu(n,f) cross section implemented in ENDF/B-VIII.1 was presented in Ref. [38] and is compared to fission TPC data in Fig. 15 as a ratio to ^{235}U(n,f) cross sections. Inclusion of the high-precision fission TPC data reduced the cross section above 10 MeV (see Fig. 16), while changes from ENDF/B-VIII.0 to ENDF/B-VIII.1 cross sections stem from applying templates of expected measurement uncertainties leading to an improved uncertainty estimate. In the energy region above 10 MeV, discrepant data sets led to questions on the shape of the cross section [1]; potential biases were suspected in quantifying the detector efficiency, especially the effect of angular distribution on the efficiency.

Fission TPC data were measured with a time-projection chamber, a new and different type of fission detector than previously used. This detector has a more fine-grained view of the angular distribution of fission fragments [98]. Hence, these new data lead to more confidence in the new shape of the fission cross section at higher incident-neutron energies.

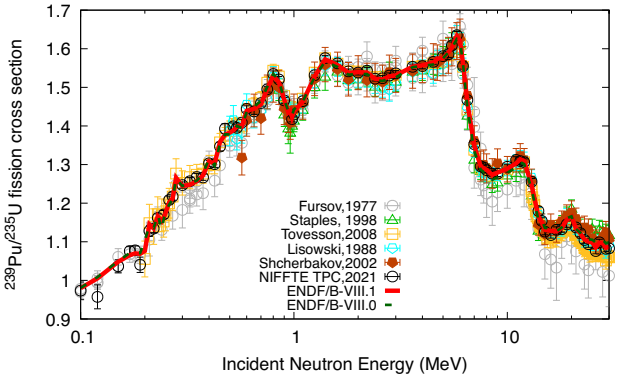


FIG. 15. Evaluated ^{239}Pu/^{235}U cross-section ratios from ENDF/B-VIII.1 and ENDF/B-VIII.0 libraries versus selected experimental data [98, 100–104] taken from EXFOR [45].

c. (n, f) fission cross-section covariances

Finally, work was done to update the USU component of the fission cross-section uncertainties to have energy-dependent correlations rather than being fully correlated. This work is motivated by the belief that ENDF/B-VIII.0 estimated USU fission cross-section uncertainty of 1.2% was probably overestimated in the very important energy region from 0.1 MeV up to 5 MeV (the first-chance fission plateau). Energy-independent USU also introduced overly strong, long-range, cross-energy correlations which were probably unrealistic. Such correlations present a challenge to data adjustment based on critical assemblies which feature sensitivities to narrow energy regions (e.g., typically fast critical assemblies – PMF – are sensitive to neutron energies from 10 keV up to 5 MeV, mostly).

The USU energy-dependence was accounted for by the

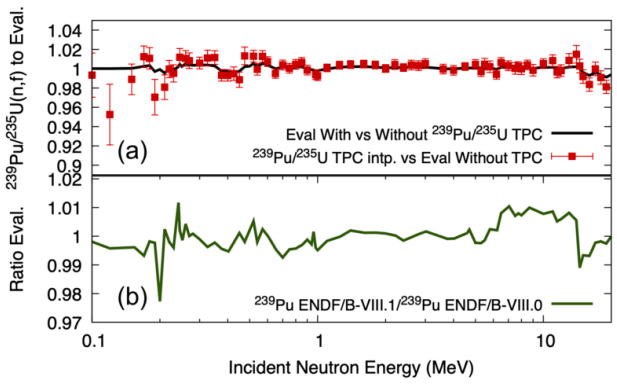


FIG. 16. ^{239}Pu/^{235}U cross-section ratios (from fission TPC [98] or ENDF/B-VIII.1) are divided by the evaluation without fissionTPC data (a) or by the ENDF/B-VIII.0 ^{239}Pu/^{235}U cross-section ratio (b).

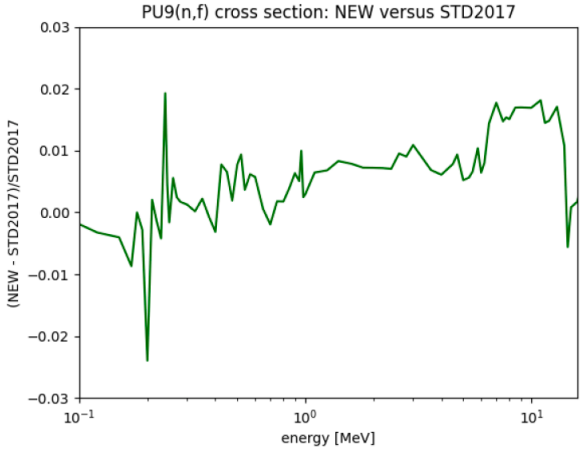


FIG. 17. Newly evaluated ^{239}Pu(n,f) cross section with latest `gmapy` code and inputs including a new USU treatment as a ratio to the ENDF/B-VIII.0 cross sections. These cross sections were not used in the ENDF/B-VIII.1 file.

introduction of additional energy-dependent bias functions for each dataset, which are parameterized as a piecewise linear functions. The same energy mesh is assumed for all datasets of the same reaction channel, but the bias function of each dataset is allowed to vary independently of bias functions of other datasets. The energy-dependent USU was then also defined as piecewise linear function using the same energy mesh as for the bias functions. At a conceptual level, the spread of the bias function at each energy mesh point informed the magnitude of the uncertainty associated with USU at the same energy.

Technically, the generalized least squares (GLS) method was further generalized to a Bayesian hierarchical model in order to also incorporate the bias functions and the associated USU uncertainties. The posterior expectation of the cross sections and associated covariance matrix was then determined by the Hamilton Monte Carlo method. A more detailed description of the procedure will be the subject of a separate publication. All changes were implemented within the open-source IAEA `gmapy` code developed by G. Schnabel, which was used for calculations. The `gmapy` code employed as input the revised and updated GMA input database already used for Neutron Data Standards [1].

Energy-dependent USU components were added to the revised GMA database used for the evaluation undertaken by the Standards group [99], which includes new relative measurements of ^{238}U(n,f) and ^{239}Pu(n,f) from the NIFFTE collaboration [98], revised uncertainty quantification of ^{239}Pu(n,f) datasets based on templates [96, 97], and revised spectrum-averaged cross sections (SACS) and SACS ratio data [105]. Additionally, datasets or parts of datasets have been removed when they were deemed inconsistent with other datasets or exhibited problematic energy behavior. In particular, datapoints from the Pankratov ^{235}U(n,f) and ^{238}U(n,f) shape datasets (GMA ID 722 and 874) above 23 MeV were removed; the absolute ^{238}U(n,f) measurement of Nolte between 34 and 200 MeV (GMA ID 8008) as well as datapoints above 27 MeV of the Carlson ^{235}U(n,f) measurement (GMA ID 524) were also discarded. At an IAEA Experts Meeting in 2023, an agreement was reached to remove these data from the analysis.

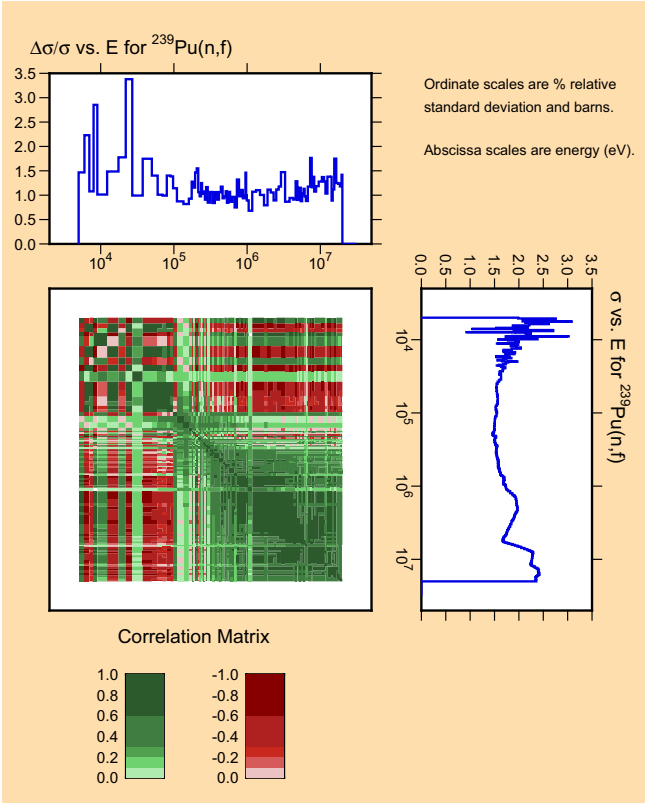


FIG. 18. The ENDF/B-VIII.1 evaluated ^{239}Pu(n,f) cross-section uncertainties and correlation matrix for incident neutron energies from 5 keV up to 30 MeV.

The energy mesh for USU components was manually defined taking into account the availability of data and features of the cross-section curve, with the lowest energy mesh point starting as low as 1 keV and going up to at least 30 MeV. USU components were defined for absolute and relative measurements as well as shape measurements of absolute and relative cross sections involving ^{235,238}U and ^{239}Pu targets and their combinations. 30000 samples were obtained from the posterior which proved to be sufficiently large for the convergence of posterior cross-section estimates and the associated covariance matrix. Note that data from the entire GMA input database was used for the fitting, not only the ^{239}Pu(n,f) data.

Due to the fact that, in this ENDF/B release, the ^{239}Pu(n,f) covariance matrix coming from a new USU treatment was introduced after the mean-value evaluation had been concluded, special care must be taken to ensure consistency between the employed mean values [99] and the updated covariance matrix using the energy-dependent USU. This was achieved by a post-processing of the covariance matrix that inflates elements in the covariance matrix based on a cross-entropy criterion.

The difference between the STD2017 evaluation [1] (part of the ENDF/B-VIII.0 release) and the newly evaluated (`gmapy`) ^{239}Pu(n,f) cross sections due to updated USU treatment and vetted data is about +0.7% larger than the standards in the first-chance plateau from 1 MeV up to 6 MeV. The fission cross-section increase reaches almost 1.8% from 7 MeV up to 13 MeV, but it vanishes at 14 MeV as shown in Fig. 17.

The final correlation plot and the associated relative uncertainties with respect to ENDF/B-VIII.1 evaluated mean values are shown in Fig. 18.

d. (n,γ) capture cross section

The INDEN evaluation of the neutron-capture channel was adopted for the ENDF/B-VIII.1 library. The INDEN evaluation is a Bayesian Generalized Least-Square Evaluation using the `GANDR` code [106] with the model prior generated using the `EMPIRE` code system [107] as described in Ref. [108].

To measure neutron capture on fissile elements, it is imperative to measure the fission-to-capture ratio (usually called the α-ratio). This implies that the systematic uncertainty from fission measurements will correlate all capture datasets derived from the measured α-ratio. Experimental data used as input for the `GANDR` system are listed in Tables V and VI.

The newest ^{239}Pu(n,γ) dataset is the one measured by Mosby and colleagues [88] at LANL which used the ENDF/B-VIII.0 fission cross section (standard) to derive the capture cross section from the measured α-ratio. This dataset also features the lowest uncertainties of about 4%, which defines the ENDF/B-VIII.1 evaluated mean values and uncertainties. There is also an extensive set of older α-ratio measurements which are listed in Table VI. We used evaluated ^{239}Pu fission cross sections for ENDF/B-VIII.1 undertaken by the Standards group [99] to derive the measured capture cross sections with uncertainties from the corresponding α-ratio listed in Table VI. Data derived in this way are automatically corrected to the latest fission standard and represent a much larger and consistent experimental database than those data listed in Table V (with the exception of Mosby 2018 which were also considered).

The ENDF/B-VIII.1 evaluated ^{239}Pu(n,γ) cross section for incident neutron energies from 9 keV up to 100 keV is compared with the data described above and ENDF/B-VIII.0 in Fig. 19. A significant decrease compared to ENDF/B-VIII.0 is observed in the whole URR up to 50 keV mainly driven by Mosby data. Fluctuations observed in the ENDF/B-VIII.0 file were related to the

TABLE V. Selection of radiative capture cross-section measurements of ^{239}Pu for incident neutron energy above 5 keV from the EXFOR database [45]. Experiments selected for fitting are marked by a "+" sign in the first column.

	Author	Year	EXFOR No.
+	Mosby *et al.* [88]	(2018)	14794002
-	Belyaev *et al.* [109]	(1970)	40087006
-	Hopkins *et al.* [110]	(1962)	12331008
-	Andreev [111]	(1958)	40385007
-	Spivak *et al.* [112]	(1956)	40350006

Systematic uncertainties:
3% for each EXFOR set
3% common to all measurements

TABLE VI. Selection of absorption (alpha ratio ≡ capture/fission) cross-section measurements of ^{239}Pu for incident neutron energy above 5 keV from the EXFOR database [45]. Experiments selected for fitting are marked by a "+" sign in the first column.

	Author	Year	EXFOR No.
+	Bolotskii *et al.* [113]	(1977)	40548002
+	Ryabov [114, 115]	(1976)	40312003
+	Gwin *et al.* [116]	(1976)	10267029
+	Kononov *et al.* [117]	(1975)	40412005
	Kononov data discarded for $E_n > 60$ keV:		
+	Bandl *et al.* [118]	(1972)	20158003
+	Kurov *et al.* [119]	(1972)	40024003
+	Weston *et al.* [120]	(1972)	10301003
-	Farrell *et al.* [121]	(1970)	10326002
+	Belyaev *et al.* [109]	(1970)	40087008
+	Schomberg *et al.* [122]	(1970)	20476005
+	de Saussure *et al.* [123]	(1966)	12409004
+	de Saussure *et al.* [123]	(1966)	12409005
+	Hopkins *et al.* [110]	(1962)	12331007
-	Andreev [111]	(1958)	40385008
-	Spivak *et al.* [112]	(1956)	40350016

Systematic uncertainties:
3% for each EXFOR set
3% common to all measurements

URR evaluation. In the region from 20 keV up to 50 keV, older measured data led to evaluated results slightly lower than the Mosby measurements. The ^{239}Pu(n,γ) ratio to ENDF/B-VIII.0 is shown in Fig. 20 from 70 keV up to 1.3 MeV. A significant increase in the capture cross section compared to ENDF/B-VIII.0 is noted in the fast neutron region from 300 keV up to 1 MeV, reaching almost 20% around 800 keV. This capture increase is driven by Hopkins and Mosby data and the impact on reducing the criticality of fast Pu assemblies is significant.

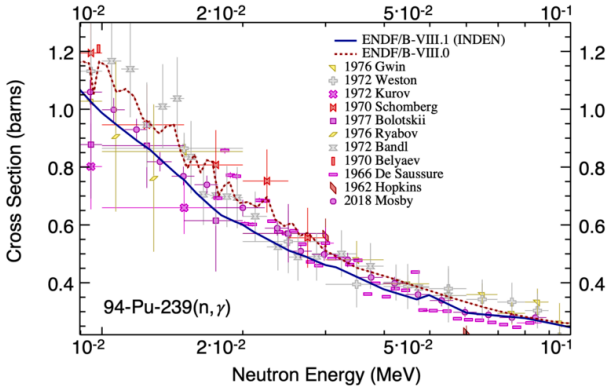


FIG. 19. The ENDF/B-VIII.1 evaluated ^{239}Pu(n,γ) cross section for incident neutron energies from 10 keV up to 100 keV along with comparison to experimental data from EXFOR [45] as listed in Tables V and VI and ENDF/B-VIII.0. Data from Refs. [88, 109, 110, 113–116, 118–120, 122, 123].

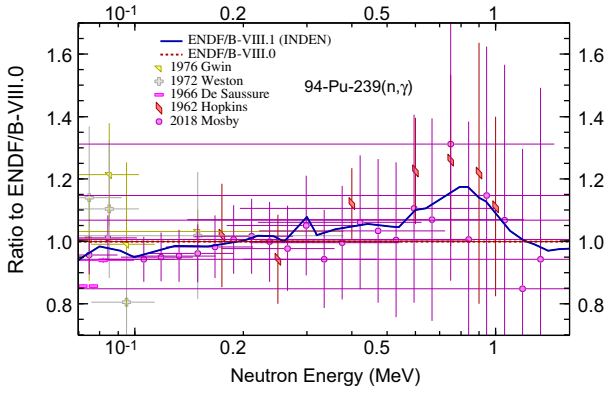


FIG. 20. The ratio of the ENDF/B-VIII.1 evaluated ^{239}Pu(n,γ) cross section to ENDF/B-VIII.0 for incident neutron energies from 70 keV up to 1.5 MeV is compared versus the same ratio using selected experimental data from EXFOR [45]. Data from Refs. [88, 110, 116, 120, 123].

e. (n,γ) covariances

The EMPIRE code system is a well-tested system package for nuclear model calculations and nuclear data evaluation [107]. Its capabilities include random sampling of

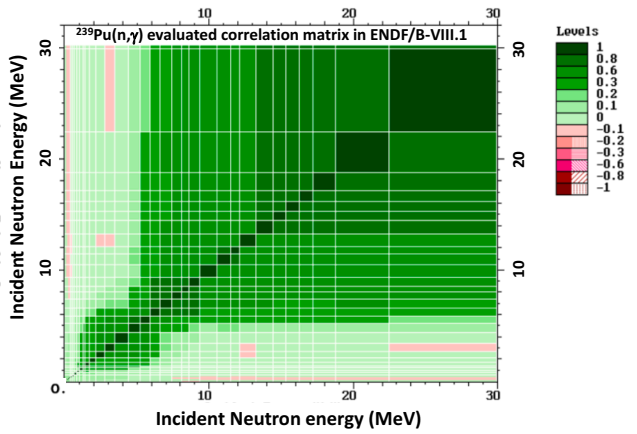


FIG. 21. ENDF/B-VIII.1 evaluated ^{239}Pu(n,γ) cross-section correlations for incident neutron energies from 5 keV up to 30 MeV.

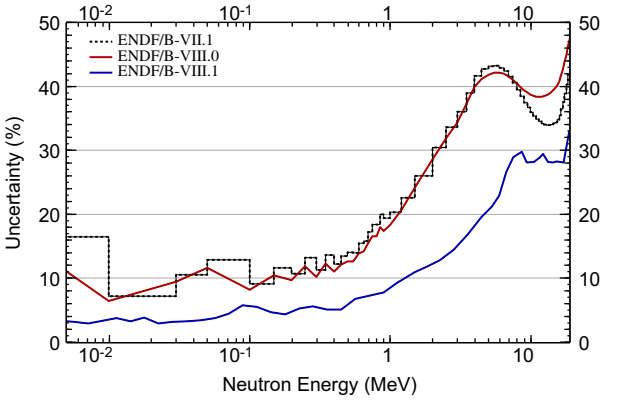


FIG. 22. ENDF/B-VIII.1 evaluated ^{239}Pu(n,γ) cross-section uncertainties for incident neutron energies from 5 keV up to 20 MeV are compared for the ENDF/B-VII.1 and ENDF/B-VIII.0 libraries.

model parameters, which can be utilized to generate a full model covariance matrix of all calculated cross sections, including cross-reaction correlations. The EMPIRE system was employed to calculate the prior covariance matrices of reaction cross sections of neutron-induced reactions on a ^{239}Pu target for incident neutron energies up to 30 MeV, including both the capture and (n,2n) cross sections. The model parameter uncertainties were conservatively estimated to get capture cross-section uncertainties covering the spread of experimental data. The resulting model prior covariance for the capture reaction features an uncertainty estimate of around 30% up to 2 MeV, and much larger for higher energies. The model prior correlations are strong and positive with near-energy correlations reaching 95% and correlations between 10 keV and 100 keV of about 50%. A typical model correlation matrix is shown in Fig. 1 of Ref. [108]. The derived modeling

prior covariance matrix was input to the GANDR system [106, 124], which is a software package based on the GLS method that makes use of the experimental data retrieved from EXFOR in the C4/C5 format [45].

By introducing the vetted experimental data from the EXFOR database listed in Tables V and VI above into GANDR, the constrained covariance matrices and evaluated cross section were obtained using the method outlined in Ref. [108]. Posterior evaluated values were subsequently formatted in ENDF-6 format. A typical evaluated correlation matrix shows negative and positive correlations due to the experimental data constraints as shown in Fig. 21.

The evaluated uncertainty of the ENDF/B-VIII.1 capture cross sections is about 4% from 5 keV up to 100 keV, being reduced by a factor of about 2 compared to ENDF/B-VIII.0 and ENDF/B-VII.1 uncertainties as shown in Fig. 22. The uncertainty increases monotonically reaching 10% at 1 MeV and 20% at 5 MeV. The uncertainty reduction is driven mostly by the lower uncertainty of the data from Mosby *et al.* [88], which is about 4% below 500 keV. The lower uncertainty of Mosby data were not properly considered in the ENDF/B-VIII.0 evaluation, therefore the evaluated uncertainty remained much larger. Below 500 keV, there is also some uncertainty reduction driven by the availability of several independent experiments derived from the measured $\alpha-$ratio data as listed in Table VI.

f. (n,2n) cross section

The INDEN evaluation of the (n,2n) channel was adopted for the ENDF/B-VIII.1 library. The INDEN evaluation is a Bayesian Generalized Least-Square evaluation using the GANDR code [106] with the model prior generated using the EMPIRE code system [107] as described in Ref. [108] and Section III A 5 d. The evaluation started from the McNabb analysis [125] which was adopted for the ENDF/B-VII.1 library. The most precise experiment considered at that time was the activation measurement done by Lougheed *et al.* and carefully analysed and corrected by McNabb and colleagues [125]. A joint LANL GEANIE experiment was coupled to a model simulation to derive the most comprehensive set of the (n,2n) cross sections over a broad energy range by Bernstein and collaborators [126]. We also used a new experiment undertaken by Méot *et al.* [90] which was normalized to the ENDF/B-VIII.0 at 9 MeV. We discarded Mather [127] and Frehaut [128] data as discussed in Ref. [125]. We have also discarded a new surrogate experiment by Ma *et al.* [129] as having very large uncertainties below 10 MeV and a shape not corresponding to the theoretical expectations. Selected experimental data for the (n,2n) evaluations are listed in Table VII.

The ENDF/B-VIII.1 evaluated $(n,2n)$ cross sections versus experimental data and ENDF/B-VIII.0, ENDF/B-VII.1, and JENDL-5 evaluations are shown in Fig. 23. Note that both the original Lougheed data [130] (yellow rhombi) and the revised data by McNabb [125] (green circles) are plotted. The highest energy point of

TABLE VII. Selection of (n,2n) cross-section measurements of ^{239}Pu from the EXFOR database [45]. Selected experiments are marked by a "+" sign in the first column.

	Author	Year	EXFOR No.	Comment
+	Méot *et al.* [90]	(2021)	23777002	New measurement
+	Bernstein *et al.* [126]	(2002)	13787006	Meas + Model
+	Lougheed *et al.* [125, 130]	(2002)	13787006	Meas + Model
-	Mather *et al.* [127]	(1972)	32815003	An outlier
-	Frehaut *et al.* [128]	(1986)	32815003	Wrong shape
-	Nanru Ma *et al.* [129]	(2020)	32815003	Surrogate

Systematic uncertainties:
1% for each EXFOR set
4% common to all measurements (altogether 4.1 %)

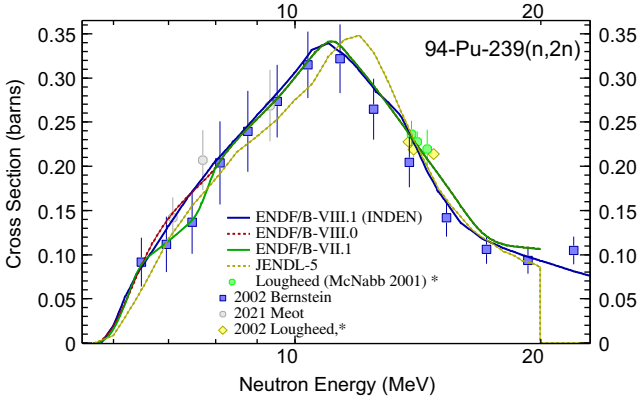


FIG. 23. ENDF/B-VIII.1 evaluated ^{239}Pu$(n,2n)$ cross sections versus selected experimental data [90, 125, 126, 130] and JENDL-5, ENDF/B-VII.1, and ENDF/B-VIII.0 evaluations up to 25 MeV.

McNabb revised data was considered an outlier and its uncertainty was doubled. Below 9 MeV, there is an excellent agreement between the ENDF/B-VIII.0 and new ENDF/B-VIII.1 evaluation which will lead to almost the same calculated ^{239}Pu(n,2n) reaction rate in a fission spectrum. The energy-dependence of the new evaluation below 10 MeV is driven by the shape of the EMPIRE model calculations used as a prior in the least-squares evaluation. This shape validates the changes in this energy region undertaken in the ENDF/B-VIII.0 evaluation. The JENDL-5 evaluation results in a much lower calculated ^{239}Pu(n,2n) reaction rate in a fission spectrum. Note that the new Méot *et al.* [90] measured shape is in excellent agreement with the new evaluation from 7 MeV up to 9 MeV. The ENDF/B-VIII.1 and JENDL-5 evaluations are in excellent agreement above 13 MeV and shows the best agreement with GEANIE-derived data [126] and a very good agreement with McNabb derived data [125]. There is a disagreement between JENDL-5 and other evaluations in the energy corresponding to the

maximum of the ^{239}Pu(n,2n) excitation function. The ENDF/B evaluated maximum energy around 11 MeV relies on the measured data while the JENDL-5 maximum of about 12 MeV aligns better with model calculations; further investigation is needed.

g. (n,2n) covariances

The (n,2n) covariance matrix and uncertainties were derived as described for the capture cross-section covariances in Section III A 5 d. A derived modeling prior covariance matrix was input to the GANDR system [106, 124]. By introducing the vetted (marked with + sign) experimental data from the EXFOR database listed in Table VII into GANDR, the constrained covariance matrix and corresponding evaluated cross section were obtained using a method described in Ref. [108] and formatted in ENDF-6 format.

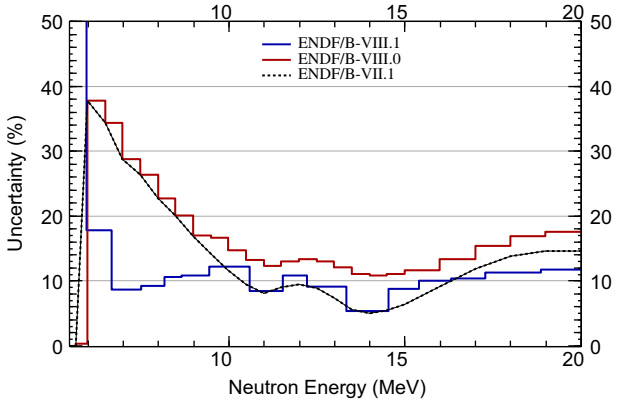


FIG. 24. ENDF/B-VIII.1 evaluated ^{239}Pu(n,2n) cross-section uncertainties for incident neutron energies from 5 MeV up to 20 MeV are compared for the ENDF/B-VII.1 and ENDF/B-VIII.0 libraries.

The evaluated uncertainty of the ENDF/B-VIII.1 (n,2n) cross sections is about 10% from 7 MeV up to 13 MeV, being reduced significantly compared to the uncertainties in the ENDF/B-VII.1 and ENDF/B-VIII.0 libraries in the region below 9 MeV due to the use of newly available Méot data [90] as shown in Fig. 24. The uncertainty reaches the minimum around 14 MeV in excellent agreement with McNabb 2001 evaluation [125] used in the ENDF/B-VII.1 library. This uncertainty reduction is driven by the lower uncertainty estimated by McNabb *et al.* [125] from the Lougheed experimental data [130]. Note that a much larger uncertainty (about 12%) defined in the ENDF/B-VIII.0 evaluation is inconsistent with the McNabb analysis [125]. The uncertainty of the current evaluation is lower at energies above 15 MeV due to the strong cross-energy correlations in the model prior and available GEANIE experimental data. Evaluated uncertainties are driven by the overall uncertainty of the best experiments and modeling as evidenced in the discussion above.

A typical evaluated correlation matrix shows negative and positive correlations due to the experimental data constraints as shown in Fig. 25.

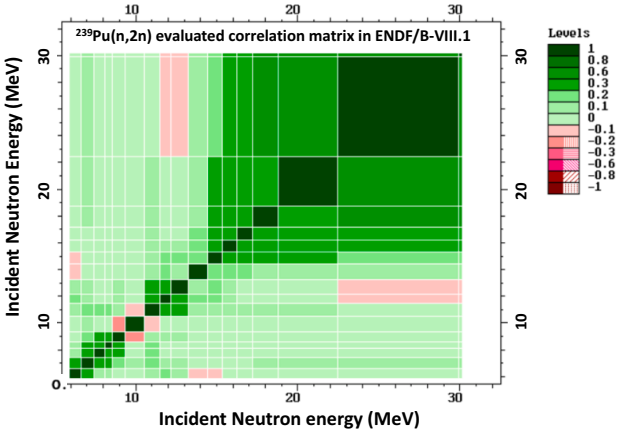


FIG. 25. ENDF/B-VIII.1 evaluated ^{239}Pu(n,2n) cross-section correlations for incident neutron energies from 5 MeV up to 30 MeV.

h. Elastic & inelastic cross sections

A theoretical improvement in the treatment of the direct reaction channels in a coupled-channel calculation is the diagonalization of the S-matrix using the Engelbrecht-Weidenmüller (EW) transformation [131]. This development was implemented in the CoH code [134],

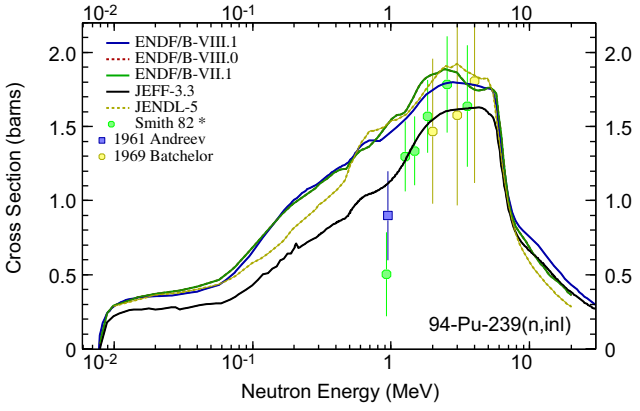


FIG. 26. The inelastic cross section in the fast energy range for ^{239}Pu along with comparison to ENDF/B-VIII.0, ENDF/B-VII.1, JENDL-5, JEFF-3.3 and selected experimental data from EXFOR [45]. Note that Smith 1982 data [132, 133] are weakly model dependent (model calculations are needed to estimate the inelastic cross section below the experimental threshold).

resulting in a more realistic treatment of the inelastic cross sections when the direct channels are strongly coupled, which is the case in the study of low-energy neutron-induced reactions on ^{239}Pu. However, this important theoretical improvement has a small impact on the calculated total inelastic cross section as shown in Fig. 26. Such small impact was expected: there are many open inelastic channels even at very low incident-neutron en-

ergy. This is due to the high level density in odd targets and reduces the predicted inelastic enhancement [134] of the EW transformation. The ENDF/B-VIII.1 evaluated inelastic cross section is very close to the ENDF/B-VII.1 evaluation (adopted for ENDF/B-VIII.0) up to 1 MeV incident neutron energy.

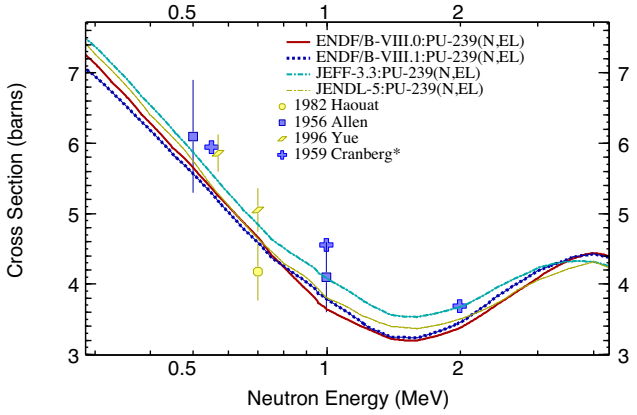


FIG. 27. The elastic cross section in the fast energy range for ^{239}Pu along with comparison to ENDF/B-VIII.0, ENDF/B-VII.1, JENDL-5, JEFF-3.3 and selected experimental data [135–139] from EXFOR [45]. Note that Cranberg 59 [136] data were reduced by 500 mb to consider the inelastic scattering to the first excited level.

The ENDF/B-VIII.1 total inelastic cross section reaches a maximum of 1.8 b from 2 MeV up to 3 MeV being about 100 mb lower than ENDF/B-VIII.0 and JENDL-5 evaluations. The JEFF-3.3 evaluation shows the best agreement with experimental data below 2 MeV, being about 200 mb lower from 2 up to 5 MeV than the ENDF/B-VIII.1 evaluation. This decrease in the inelastic channel is related to the increased JEFF-3.3 elastic cross section from 1 MeV up to 5 MeV as shown in Fig. 27. These evaluation differences deserve further study, as this energy region corresponds to the maximum number of fission neutrons; therefore, it is the most important energy region for fast reactors.

It was noted that there is the need to increase the inelastic scattering spectrum to the continuum to describe both the differential 14 MeV scattering data by Kammerdiener [140] as well as the LLNL pulsed-sphere neutron-leakage spectra [141]. Description of inelastic neutron emission scattering cross sections and spectra above 5 MeV is a long-standing issue for neutron scattering on actinide nuclei (e.g., see Ref. [142]). Different theoretical approaches have been proposed. A common empirical method used in ENDF/B-VII and ENDF/B-VIII.0 major actinide evaluations [67, 143] relies on the combination of direct excitation to the continuum treated by Distorted Wave Born Approximation (DWBA) of collective levels of the even-even core whose properties (excitation energy, spin, parity, deformation lengths) are adjusted to reproduce the 14 MeV scattering neutron spectra and time-of-flight neutron distributions from pulsed-sphere experiments [141]. The exciton model is used to describe the smooth continuum pre-equilibrium emission. A semi-microscopic approach to inelastic scattering relies on the Tamura Udagawa Lenske pre-equilibrium QRPA structure model [144]. A new empirical approach was used for calculations of the inelastic scattering in this evaluation that also relies on the exciton model with an effective 1p-1h level density at low energy that emulates the excitation of collective levels [145]. This approach results in higher total inelastic scattering cross section in ENDF/B-VIII.1 [91] compared to other evaluations above 10 MeV (including the ENDF/B-VIII.0) as shown in Fig. 26. A sound theoretical treatment of the direct inelastic neutron scattering requires a deformed QRPA calculation as discussed in Ref. [146]. Unfortunately, this is technically very challenging and is still work in progress.

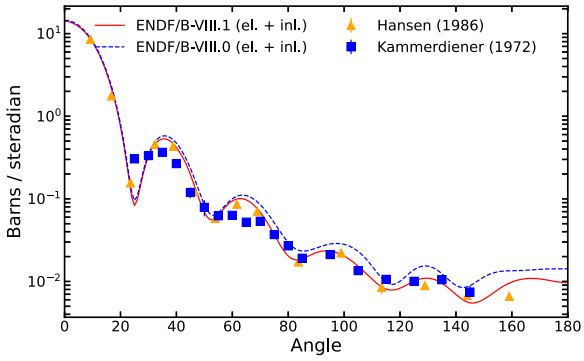


FIG. 28. The angular distribution of ^{239}Pu at incident neutron energy of 14 MeV along with comparison to ENDF/B-VIII.0 and data [140, 147].

The summed elastic and inelastic angular distribution at 14 MeV is shown in Fig. 28. A marked improvement over ENDF/B-VIII.0 is found with respect to the Hansen [147] and Kammerdiener data [140], which is due to the improved dispersive coupled-channel optical model potential (OMP) – Reference Input Parameter Library (RIPL) 2408[5] – used in the current evaluation [148–150] where those 14 MeV data were used in the fit.

Cross-section covariances for the elastic, inelastic, and total channels were estimated using a Kalman filter [151]. For these channels, the Kalman uncertainties were scaled to match the magnitude used in the ENDF/B-VIII.0 approach. For ^{239}Pu, the fission channel is evaluated independently which causes problems in developing self-consistent cross-channel covariances. Cross-channel covariances were, therefore, not included in the present effort and studies are in progress for inclusion in future releases.

[5] The OMP was slightly refitted to change the calculated total cross section [91], but those changes are not expected to effect the calculated angular distributions.

6. *Integral benchmarks*

Having a new evaluation of neutron-induced reactions on a ^{239}Pu target in this release, it was essential to perform extensive testing and validation. This comprehensive validation is documented in Section XIV.

TABLE VIII. Calculated and experimental values of effective delayed neutron fraction for selected fast plutonium benchmark experiments. The notation of * was used to signify that the uncertainty of the calculated result is less than 1 pcm. Only experimental uncertainties were provided for both assemblies, which were unrealistically small. Hence, 8% uncertainties were added to experimental ones in quadrature following IRPhEP.

Benchmark	Measured	ENDF/B-VIII.0	ENDF/B-VIII.1
A	0.00195(19)	0.00183(0)*	0.00185(0)*
B	0.00276(23)	0.00284(4)	0.00275(4)

Also included in our validation was the calculation of the effective delayed neutron fraction, which describes the fraction of delayed neutrons that contribute to the criticality of the system. Two systems were considered: (A) Jezebel (PU-MET-FAST-001-001) and (B) Flattop with plutonium core (PU-MET-FAST-006-001). The results in Table VIII show that the simulated values from the present evaluation are in better agreement with measured experimental values than ENDF/B-VIII.0.

a. Future work

The competition between the elastic and inelastic channels as well as the elastic angular distributions across a wide range of incident neutron energies remain open issues in the evaluation of ^{239}Pu. Additional targeted measurements may be required to ascertain information on these channels. Additional information may be needed to confirm the ground-breaking Lougheed $(n, 2n)$ experiment at 14 MeV [125, 130] that drove the (n,2n) evaluations and defined uncertainties since the ENDF/B-VII.0 release. In the meantime, as we work towards more self-consistent evaluations, it is important to continue to incorporate the latest experimental efforts along with advancements in theoretical modeling.

B. INDEN evaluations

1. ^{16}O

Much work has been done on the ^{17}O R-matrix analysis at LANL in the last few years: extending the data to higher energies for some reactions, and adding ^{16}O* excited states to the channel configuration. However, it was decided after preliminary data testing to carry over the ENDF/B-VIII.0 evaluation [68] to ENDF/B-VIII.1. This decision was taken because much of the new data added to the analysis was from (α, n) measurements on ^{13}C targets, and although many of these measurements are clear improvements over the earlier ones, they still suffer from difficulties in characterizing their absolute normalizations and energy calibrations to the extent that strong disagreements remain among them. Most of the experimental groups are diligently working to improve their data, and hopefully the situation concerning the (α, n) data will become clearer in the near future. We will not repeat here the discussion about the ^{16}O evaluation in Ref. [68, Section 10], but rather summarize the few changes made for ENDF/B-VIII.1.

Some of the newer (α, n_0) measurements, especially those at lower energies, confirm the normalization scale that was determined in the ENDF/B-VIII.0 analysis, which was 0.94 times the original cross-section scale of Bair and Haas [152]. This was also consistent with the $^{16}\mathrm{O}(n, \alpha_0)$ cross section measured by Giorginis [153] up to $E_n = 9$ MeV.

Therefore, no changes were made in the (n, α_0) cross section for ENDF/B-VIII.1. However, the (n, α_1), (n, α_2), and (n, α_3) cross sections were reduced by a factor of 2 relative to ENDF/B-VIII.0, as suggested by R. Capote, to agree better with experimental data from Refs. [154] and [155]. The total cross section remains identical to the ENDF/B-VIII.0 evaluation above 5 MeV.

Simakov and Fischer [156] made a comprehensive analysis of the ORNL oxygen 60" broomstick experiment [157] and demonstrated a much better performance of the JEFF-3.3 (= ENDF/B-VII.1) ^{16}O evaluation compared to ENDF/B-VIII.0 from 5.7 MeV up to 7.2 MeV [156]. Simakov and Fischer estimated the need for a 3% reduction of the ENDF/B-VIII.0 total cross section from 5.5 MeV up to 7 MeV and a 20% reduction of the (n, α_0) cross section. Capote and Trkov have found that a proposed reduction in the total cross section, especially in the region from 6.2 MeV up to 6.7 MeV is consistent with measured data by Finlay (1993), Cierjacks (1980), Larson (1980), Schracks (1972), Perey (1972) and renormalized Cierjacks (1968). This is one indication that further work needs to be done on the R-matrix analysis to accommodate experimental information about the ^{17}O system in a unitary framework that describes all the reactions well with special focus on improving the total neutron cross section and alpha emission channels.

2. ^{18}O

The evaluation was adopted from the ENDF/B-VIII.0 library, except for the radiative capture, taken from EAF-2010 as proposed by A. Trkov to improve the agreement with existing experimental data.

3. ^{19}F

LiF–NaF (FLiNa) or LiF–BeF_2 (FLiBe) salts with highly enriched ^{7}Li isotope are strong candidates for Generation IV reactor designs, such as the High Tem-

perature Graphite Reactor (HTGR) and Fluoride-cooled High-temperature Reactor (FHR) or Molten Salt Reactor (MSR). Some of those advanced reactor designs are being commercially developed, e.g., by Kairos Power and Terrapower. Fluorine is also an integral component of uranium manufacturing/enrichment process as uranium hexafluoride (UF_6) and is also used directly as nuclear fuel. Finally, fluorine is a major component of Teflon® which is commonly used to reduce the average neutron energy in critical assemblies.

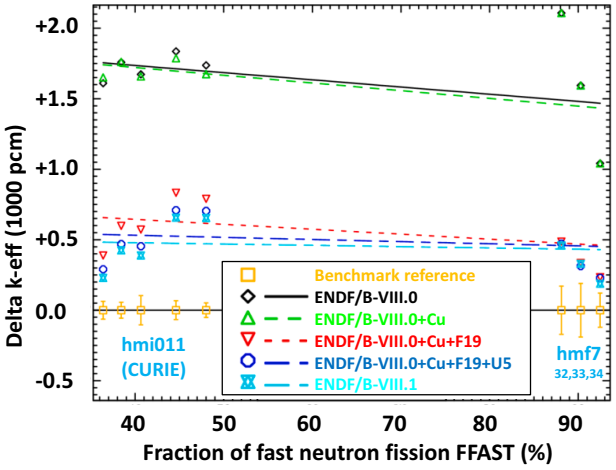


FIG. 29. Criticality differences to the experimental benchmark values $\Delta\ k_{\rm eff}$ of ^{19}F-sensitive fast ICBESP benchmarks (HMI011/1,2,3,4,5 and HMF007/32,33,34 [158]). Calculated values are given for the reference ENDF/B-VIII.0 library, then subsequently adding ^{63,65}Cu evaluations from ENDF/B-VIII.1 (+Cu), ^{63,65}Cu and ^{19}F evaluations from ENDF/B-VIII.1 (+Cu+F19), and ^{63,65}Cu, ^{19}F, and ^{235}U evaluations from ENDF/B-VIII.1 (+Cu+F19+U5) library. Finally, the full ENDF/B-VIII.1 results are also shown.

Therefore, ^{19}F nuclear data are very important for criticality safety, design, and operation of many nuclear facilities including some advanced reactor designs. ^{19}F nuclear data deficiencies have been shown in the validation of the ENDF/B-VIII.0 library [68] (e.g., for the HMF007/ cases 32,33,34 [158]) which were calculated high by 1500 pcm on average.

Fluorine also constitutes the first case of a nuclear data deficiency identified through machine learning (ML) techniques by Neudecker and collaborators [163]: the ^{19}F(n,inl) cross section from 0.4 – 0.9 MeV was shown to be problematic by a study of biases in simulating approximately 1,000 ISCBEP $k_{\rm eff}$ values. After these ML results pointed to a potential shortcoming in this cross section, evaluated ENDF/B-VIII.0 ^{19}F(n,inl) cross section were compared to associated differential experimental data and large discrepancies were found. This problematic behavior was attributed to the resonance range of the evaluation having been extended to too high incident neutron energies.

Of particular concern were the recently developed CURIE criticality experiments, which are intermediate-

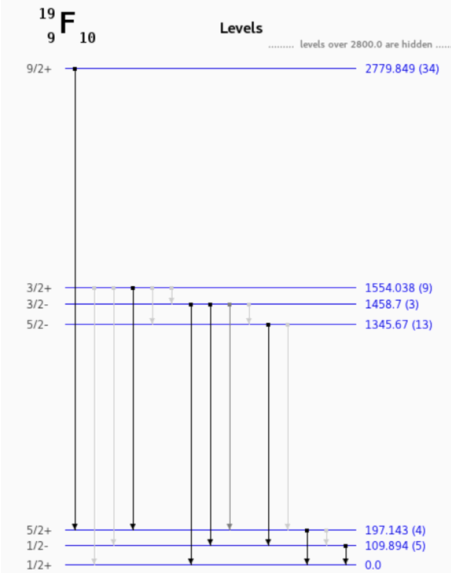


FIG. 30. Low lying nuclear levels of ^{19}F below 3 MeV of excitation energy [159].

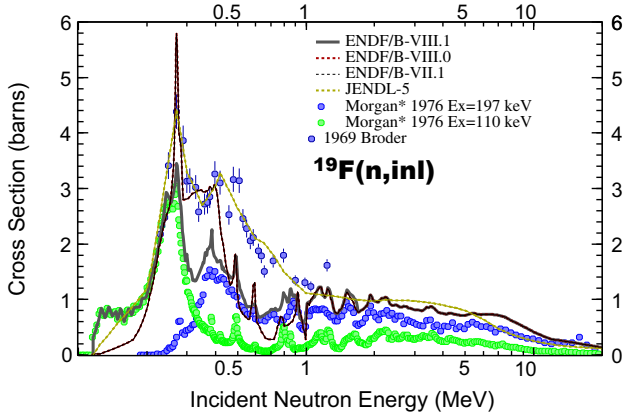


FIG. 31. Neutron induced inelastic scattering cross sections of ^{19}F up to 20 MeV. Experimental data from Broder *et al.* [160] and total inelastic data derived from Morgan *et al.* [161] are compared to JENDL-5 [16], ENDF/B-VIII.0=ENDF/B-VII.1 [68, 162] and ENDF/B-VIII.1 (INDEN) evaluations.

spectrum high-enriched uranium (HEU) teflon-reflected assemblies, which also contain a large amount of copper. They are listed in the International Criticality Safety Benchmark Evaluation Project (ICSBEP) Handbook [158] as HEU-MET-INTER-011 (HMI011) and showed an overestimation of criticality from reference benchmark values by about 1700 pcm for ENDF/B-VIII.0 as shown in Fig. 29. The impact of latest improvements in ^{63,65}Cu evaluations within the INDEN/ORNL collaboration adopted for the ENDF/B-VIII.1 library is negligible (compare green triangles versus black rhombi in the figure), and the performance remains pretty poor. ^{63,65}Cu ENDF/B-VIII.1 evaluation induced small criticality changes in HEU intermediate-spectrum assemblies (e.g., Zeus benchmarks), which is confirmed in HMI011

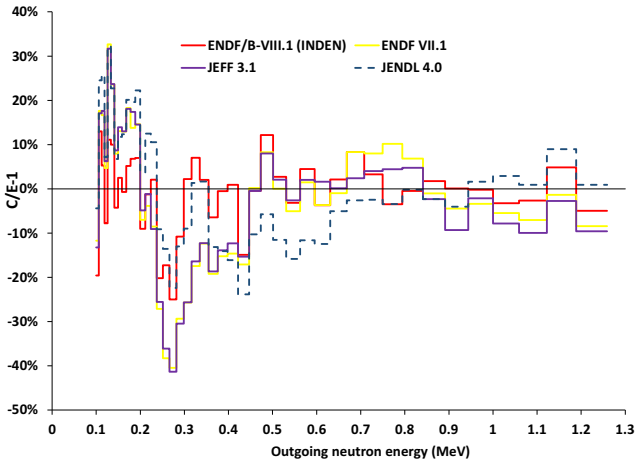


FIG. 32. LR0 reactor spectrum neutron leakage of FLINA solution from 100 keV up to 1.2 MeV of leaked neutrons measured with HPD detectors [164, 165]. Experimental benchmark values (E) are compared to calculations (C) using ENDF/B-VII.0, JEFF-3.1, JENDL-4, and the new INDEN evaluation adopted for the ENDF/B-VIII.1 library[a].

[a] private communication by M. Kostal, December 2023.

cases. The criticality overestimation of HMF007/32,33,34 cases remain between 1100 and 2000 pcm as shown in Fig. 29. The largest improvements in calculated criticality of more than 1000 pcm is due to the improvements in ^{19}F data (red triangles). Additional 100 pcm are due to ^{235}U changes (blue circles). Other materials have a very minor impact.

a. ^{19}F evaluation changes:

Starting from the ENDF/B-VIII.0 evaluation, the following cross-section changes were made:

- Japanese colleagues pointed out deficiencies of existing ^{19}F evaluations in the elastic angular distributions below 1 MeV of the neutron incident energy in the RRR [16]. In this evaluation, elastic angular distributions were derived by fitting Elwyn *et al.* data up to 2 MeV [168]; above 2 MeV, the elastic angular distributions were adopted from the JENDL-5 evaluation [16].

- The total and capture cross sections were adopted from JENDL-5 [16].

- The first two discrete level inelastic cross sections (levels at 110 and 197 keV as shown in Fig. 30) were replaced by the (n,n'γ) data of Morgan [161]. A comparison of the total inelastic experimental data versus evaluated cross sections is shown in Fig. 31. Many evaluations, including ENDF/B-VIII.0 [68] and JENDL-5 [16], followed the (n,n'γ) data by Broder *et al.* [160], which were measured relative to the ^{56}Fe(n,n'γ) data. Note that this monitor reaction was not recommended as a reference (n,n'γ) cross section by the IAEA Neutron Standard committee [1]. Therefore, Fe was considered a poor reference for (n,n'γ), which makes Broder measurement [160] questionable.

  Morgan and coworkers measured the ^{7}Li(n,n'γ) data at a given detection angle together with the ^{19}F(n,n'γ) data. Morgan measurements for ^{7}Li(n,n'γ) are in good agreement with the proposed ^{7}Li(n,n'γ) reference cross section [1]. The angular distributions of the first two ^{19}F inelastic levels are known to be almost isotropic (the first level is isotropic by definition having spin=1/2). This allows us to calculate the discrete level excitation function shown in Fig. 31 from Morgan measured data by simply multiplying the measured angular distribution by 4π. Derived inelastic cross sections for the first two levels from Morgan *et al.* [161] were used in the newly evaluated file as shown in Fig. 31 and reduced the evaluated total inelastic cross section below 1 MeV by up to 30% compared to the evaluations, which followed Broder data [160] (e.g., the ENDF/B-VIII.0 and JENDL-5 files).

- The ^{19}F(n,2n) cross sections were adopted from the IRDFF-II evaluation [2].

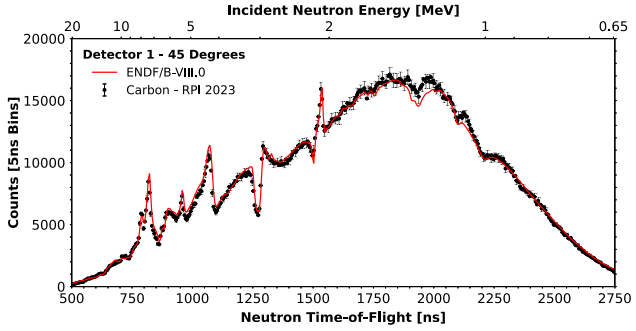
b. ^{19}F Validation

Improvements in ^{19}F evaluation, in particular the reduction of the inelastic cross section and the elastic angular distribution changes, decreased the excess criticality in fast HEU benchmarks to below 500 pcm on average as shown in Fig. 29. The average excess-criticality dependence on the fast fission neutron fraction (FFAST%) also flattened significantly. Further improvement is needed and is probably related to remaining issues in cross sections and angular distributions of excited levels above 1.3 MeV as discussed below.

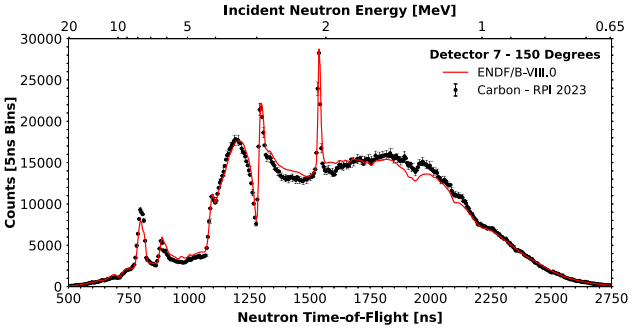
Neutron spectrum in FLINA salt for energies between 0.1 MeV and 1.3 MeV was measured using hydrogen proportional counters by Kostal *et al.* [164, 165]. The direct comparison between experimental and calculated values is realized by means of a $C/E-1$ comparison as shown in Fig. 32: a significant improvement in the C/E is observed for the new ENDF/B-VIII.1 evaluation.

An additional validation of the proposed ^{19}F changes is provided by a recent quasi-differential measurement of the scattered neutron yield from a Teflon® $(C_2F_4)_n$ sample, undertaken by Siemers and colleagues at the Rensselaer Polytechnic Institute (RPI) and presented at the WINS 2023 workshop [167] and CSEWG 2023 [166] as shown in Fig. 33. Neutron scattering and emissions were measured in time-of-flight from a 1.95" thick 3" diameter right cylinder of virgin Teflon® with an estimated 6% systematic uncertainty in the incident neutron energies range of 0.65 MeV up to 20 MeV. A 2.75" thick 3" diameter right cylinder sample of carbon was also measured as part of the Teflon® experiment to validate the experimental findings. MCNP6 was used to perform the radiation transport calculations of the experiment to compare evaluated nuclear data with the experimental data.

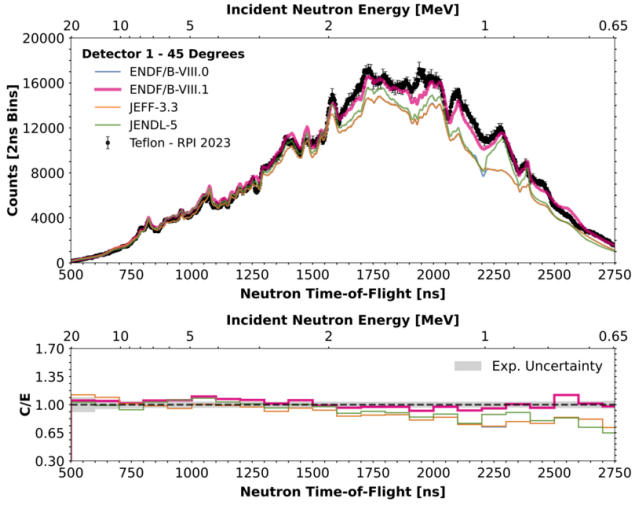
First, the measured neutron scattering yield from the



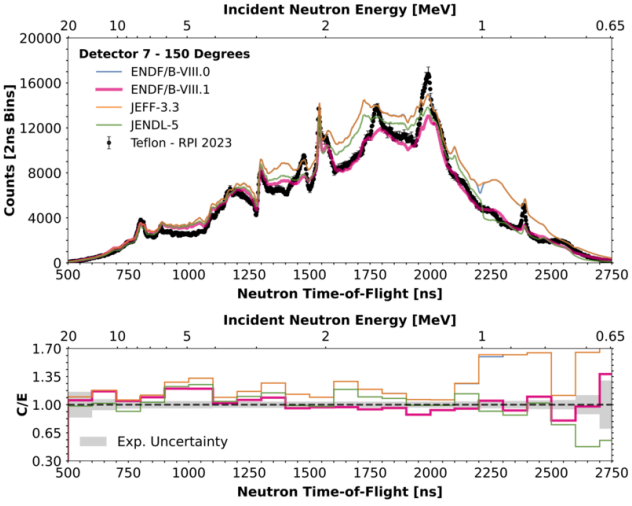
(a) Carbon measured and simulated quasi-differential neutron scattering at 45 degrees.



(b) Carbon measured and simulated quasi-differential neutron scattering at 150 degrees.



(c) Teflon® measured (E) and simulated (C) quasi-differential neutron scattering at 45 degrees.



(d) Teflon® measured (E) and simulated (C) quasi-differential neutron scattering at 150 degrees.

FIG. 33. Results from the Teflon® quasi-differential neutron scattering experiment at RPI [166, 167] in the incident neutron energy range of 0.65 to 20 MeV. Carbon neutron scattering yields, measured during the Teflon® experiment, at a forward and backward detector compared to MCNP simulations of the ENDF/B-VIII.0 carbon evaluation are presented in Figs. 33(a) and 33(b), respectively. Measured Teflon® neutron scattering yields at corresponding forward and backward detectors compared to MCNP simulations of the ENDF/B-VIII.0, JEFF-3.3, JENDL-5.0, and ENDF/B-VIII.1 ^{19}F evaluations are presented in Figs. 33(c) and 33(d), respectively. C/E ratios are provided to compare the experimental and simulated results along with the experimental uncertainty band.

carbon sample was compared to evaluated carbon nuclear data from ENDF/B-VIII.0 (which is equal to ENDF/B-VIII.1). Results for a typical forward scattering angle (45 degrees) are shown in Fig. 33(a) and for a typical backward scattering angle (150 degrees) in Fig. 33(b). Excellent agreement is observed between experiment and evaluation throughout most of the experimental energy region. Minor disagreements are noted around 2.5 MeV and 7.5 MeV at the backward angle and around 1.3 MeV and 5 MeV at both the forward and backward neutron scattering angles. Note that in another, independent, quasi-differential neutron scattering experiment from RPI (undertaken to measure the scattered neutron yield from tantalum), similarly good agreement between the measured carbon sample (same sample as measured in the Teflon® experiment) and the simulation was observed throughout the experimental incident neutron energy region at both detection angles provided (see Figs. 91(a) and 91(b) in a later section). Therefore, the minor discrepancies observed for carbon in Teflon® experiments may show deficiencies in evaluated carbon nuclear data, especially at backward angles. Note that the carbon elastic angular distributions is the only standard angular distribution up to 1.8 MeV of neutron incident energy [1].

Evaluated ^{19}F nuclear data from the ENDF/B-VIII.0, JEFF-3.3, JENDL-5, and ENDF/B-VIII.1 libraries were used to reproduce the measured Teflon® neutron scattering yield in simulation and compared with the mea-

sured data. Results for a typical forward scattering angle (45 deg) are shown in Fig. 33(c) and for a typical backward scattering angle (150 deg) in Fig. 33(d). Note that these scattering angles correspond to the angles of the aforementioned carbon validation measurement. The new ENDF/B-VIII.1 evaluation adopted from INDEN is observed to agree best with the experimental data. However, some underestimation of the measured scattered neutron yield remains between 1.3 MeV and 2 MeV at forward angles. Despite this, evaluation and experimental agreement for forward angles is acceptable.

On the other hand, significant differences are observed between the evaluation and experiment at backward angles. Particularly in the low-lying resonances corresponding to inelastic scattering to the excited ^{19}F nuclear levels from 1.3 MeV up to 3 MeV. These discrete levels of the ^{19}F nucleus are shown in Fig. 30. The third, fourth, fifth (grouped between 1.3–1.5 MeV), and sixth (2.78 MeV) excited levels are present in this region of disagreement. Although the ENDF/B-VIII.1 evaluation shows better performance at backward angles, no evaluation is able to reproduce the resonance structure observed in the experiment between 1300 and 2100 ns (roughly from 1.2 MeV up to 3.0 MeV). The results from this experiment demonstrate that we have advanced our understanding. However, new neutron inelastic scattering measurements, including angular distributions, of the third to sixth excited levels with excitation energies from 1.34 MeV up to 2.78 MeV are needed to further improve our knowledge of the ^{19}F inelastic scattering cross sections. ENDF/B-VIII.0 covariances were unchanged.

4. $^{28,29,30}Si$

The evaluation work on three major silicon isotopes was an INDEN collaboration led by ORNL/IAEA as described in Ref. [169]. In that work, resonance parameter evaluations performed at ORNL in 2002 [170] were revised in their thermal constant values following the reference values recommended by the IAEA project Evaluated Gamma-ray Activation File (EGAF) [171, 172], especially the ^{28}Si(n,γ) cross section of σ_{th} = 186 mb. The energy-dependent contribution of the `TEDCA` code for direct capture cross-section calculations in the 2002 ORNL evaluation was replaced by new `CUPIDO`[6] direct capture calculations.

Figs. 34–36, taken from Ref. [169], graphically summarize the changes in the direct capture contribution and corresponding adopted thermal capture values. It should be noted that `CUPIDO` calculations showed a better physical behavior of the capture increase in the fast neutron region. As shown in Ref. [169], results of benchmark calculations performed at the IAEA evidenced an excellent

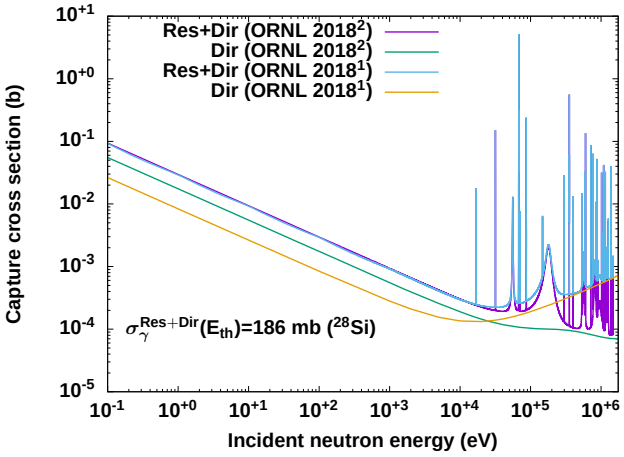


FIG. 34. ^{28}Si(n,γ) cross sections reconstructed from the ORNL (2002) evaluation and the ORNL-1/ORNL-2 (2018) evaluations in the neutron energy range up to 1.75 MeV. Figure taken from Ref. [169].

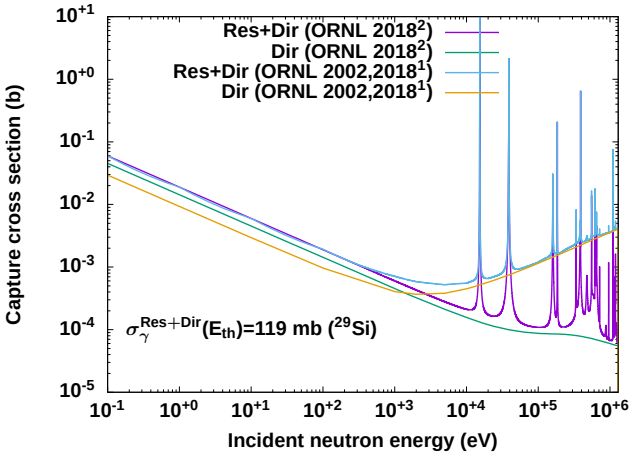


FIG. 35. ^{29}Si(n,γ) cross sections reconstructed from the ORNL (2002) evaluation and the ORNL-1/ORNL-2 (2018) evaluations in the neutron energy range up to 1.75 MeV. Figure taken from Ref. [169].

agreement with the IPPE HMM005 benchmark (BFS-079), especially designed to test silicon cross sections as shown in Fig. 37. Benchmark testing was performed for two different evaluated datafiles: ORNL-1 and ORNL-2. The first included changes only for the ^{28}Si isotope and the latter for all three isotopes – ^{28,29,30}Si. This was motivated by the unphysical behavior of the `TEDCA` calculation of the direct capture cross sections reported in the 2002 ORNL evaluation. Due to these changes, a decreased reactivity of about 800 pcm for thermal assemblies was expected by the overall increased capture cross sections in the low-energy region.

Calculated results for the HMM005 benchmark experiments from the ICSBEP compilation [158] are plotted in Fig. 37 versus measured benchmark values. Calculations were undertaken for different evaluated libraries:

[6] F. Dietrich, unpublished code.

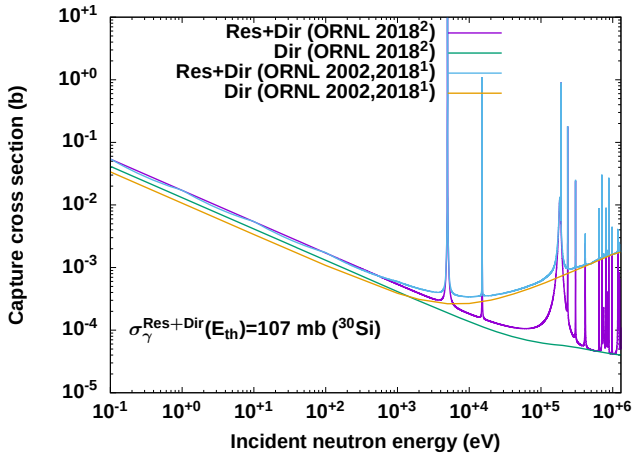


FIG. 36. ^{30}Si(n,γ) cross sections reconstructed from the ORNL (2002) evaluation and the ORNL-1/ORNL-2 (2018) evaluations in the neutron energy range up to 1.75 MeV. Figure taken from Ref. [169].

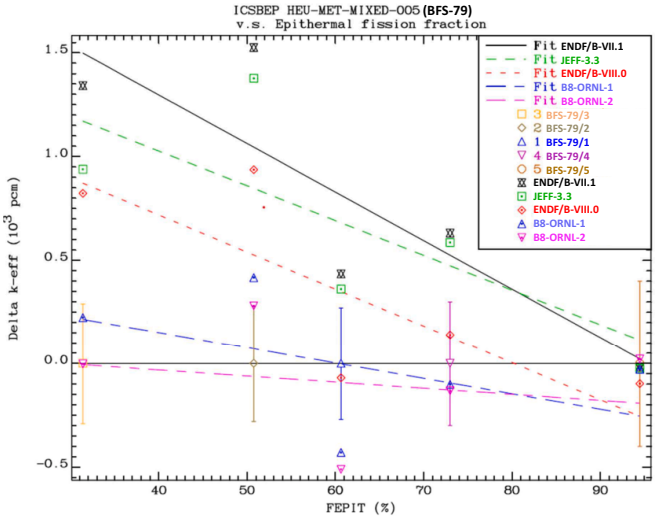


FIG. 37. Results for the HEU-MET-MIXED THERM (HMM005) experiments from the ICSBEP compilation [158] for different evaluated libraries: ENDF/B-VIII.1 (e80-ORNL-2), ENDF/B-VIII.0, JEFF-3.3, and ENDF/B-VII.1. Comparison between ORNL-1 and ORNL-2 evaluations. Figure taken from Ref. [169].

ENDF/B-VIII.1 (e80-ORNL-2), ENDF/B-VIII.0, JEFF-3.3, and ENDF/B-VII.1. It is clearly seen that the new INDEN Si evaluation adopted for the ENDF/B-VIII.1 library shows a perfectly flat trend well within experimental benchmark uncertainties as a function of the fraction of epithermal neutrons (FEPIT). This represents a big performance improvement compared to previous evaluations. ENDF/B-VIII.0 covariances were unchanged.

5. $^{50,51,52,53,54}Cr$

Chromium is present in structural materials in many nuclear systems. It is an important component in alloys with iron and other materials to form stainless steel [173]. The ENDF/B-VIII.1 evaluated files for ^{50,52,53,54}Cr, which form the natural occurrence of chromium, were mostly based on the recent evaluation by Nobre *et al.* [174], with a few minor modifications which are discussed below.

One of the main motivations behind the new set of evaluations detailed in Ref. [174] was the poor description of a cluster of large capture resonances centered around neutron-incident energy of 5 keV and going up to around 10 keV. This resonance cluster, which drives capture by elemental chromium in reactor systems, is formed by resonances from ^{50}Cr and ^{53}Cr and have been historically poorly described. Careful investigation of previous data from Refs. [175–177] allowed to fit capture more reliably in that important energy region. This directly improved the performance in criticality benchmarks sensitive to chromium, as discussed in Ref. [174]. Additionally, Ref. [174] presented complete new fast-region isotopic evaluations using modern theoretical models (e.g., soft-rotor optical model potentials [178], tuning of microscopic level densities [179]) with newer reaction isotopic data for many reaction channels, in particular inelastic and (n,p). The resulting evaluated files for ^{50,52,53,54}Cr represented a significant improvement in the description of experimental data for angle-integrated cross sections, angular distributions, energy spectra, and neutron and gamma double-differential spectra.

Updates in the evaluated files for chromium isotopes present in ENDF/B-VIII.1 done after Ref. [174] are:

- Extended model calculations in ^{50,52,53,54}Cr from 20 MeV to 65 MeV to allow its use in fusion applications. This led to the adoption of these files by the Fusion Evaluated Nuclear Data Library (FENDL) [180].

- Adoption of selected capture resonance widths from BROND-3.1 [181] for certain resonances in ^{52}Cr; namely, the resonances at neutron energies of -30.06818 keV (artificial resonance background), 1.625867 keV, 22.95014 keV, 27.59859 keV, 33.91804 keV, 47.94530 keV, 78.82184 keV, 94.94674 keV, 106.4305 keV, and 122.9100 keV. The main goal of this particular change was to increase the ^{52}Cr Maxwellian-averaged cross section (MACS) for capture, which led to improvement both in low-enriched uranium (LEU) lattices and in pmi002 criticality.

- Extrapolation of model calculations to generate a higher-fidelity evaluated file for the unstable ^{51}Cr isotope which now replaces the TENDL-based version from ENDF/B-VIII.0, taking advantage of the complete new data-driven model parametrization

from the stable isotopes done in Ref. [174]. In addition to that, exit distributions for outgoing particles were added as part of the effort described in Section III D 3.

- Covariances from ENDF/B-VIII.0 were adopted for ENDF/B-VIII.1 for chromium isotopes whenever they were available; that is, for ^{50,52,53}Cr. Unfortunately, new fast-region covariances consistent with the new fast-region evaluations were not generated in time. Also, there were no new complete resonance evaluations to justify new resonance covariances. Hence, the pragmatic choice was made of adopting ENDF/B-VIII.0 covariances when possible. A few consistency tweaks were necessary, such as removing MF=33 MT=22 in ^{50,53}Cr since MF=3 MT=22 is now not present in the current file; updating the resonance widths in MF=32 in ^{52}Cr for the resonances with widths taken from BROND-3.1 to match the new values; and other minor fixes.

Although these new evaluations for chromium isotopes incorporated into ENDF/B-VIII.1 represent a major improvement relative to ENDF/B-VIII.0, corresponding to one of the highlights of the current release, there are clear pathways for further improvements:

- Most of the performance improvement for the current set of ENDF/B-VIII.1 chromium files came from a proper fit of the 0 – 10 keV cluster of resonances from the minor isotopes ^{50,53}Cr. However, these were fits of older or corrected data. Ideally, new capture and/or transmission measurements on enriched ^{50}Cr and ^{53}Cr should be performed to guide new evaluations.

- As detailed above, the resonance evaluations for chromium isotopes in ENDF/B-VIII.1 were restricted to initial cluster of resonances in ^{50,53}Cr. New complete reevaluations of resonances in ^{50,53}Cr as well as in ^{52}Cr, preferably with the new measurements available as mentioned in the bullet above, would bring an additional round of improvements.

- New consistent covariances in the fast region and, if there are new resonance evaluations, in the resonance region as well.

- Neutron leakage experiments using natural chromium may help in improving the elastic and inelastic scattering cross sections and elastic angular distributions, which remain poorly constrained below 4 MeV of neutron incident energy. Such experiments are planned in Rez, CZ within the INDEN collaboration.

- The PETALE experimental programme [182] in the CROCUS zero power reactor at the Federal Polytechnic School of Lausanne (EPFL), Switzerland aims to measure reaction rates inside Cr plate used as reactor reflector. This experiment may provide key data to improve Cr evaluations. Results are being analyzed; preliminary data were first presented at the JEFF 2024 meeting showing some issues for the adopted ENDF/B-VIII.1 Cr evaluation. Additional work is warranted.

6. ^{55}Mn

Two updates were done to the original ENDF/B-VIII.0 evaluation [68]: dosimetry cross sections and thermal capture prompt gammas. ^{55}Mn(n,2n) dosimetry cross sections were replaced by those evaluated within the IRDFF-II library [2] as described in Ref. [183]. Thermal capture gammas were updated as described in Ref. [184]. The gamma emission changes are summarized below.

At the CSEWG meeting at BNL in November 2019, Marie-Laure Mauborgne presented results of calculations relevant to oil-well logging[7], where some evaluations showed degraded performance compared to ENDF/B-VI.3. Experimental prompt-gamma data for the thermal-capture gamma spectra were used in the ENDF/B-VI.3 evaluation.

The case of ^{55}Mn was investigated because this is an IAEA evaluation that was adopted for ENDF/B-VII.1 [162] and transferred without change into ENDF/B-VIII.0 [68]. The IAEA ^{55}Mn evaluation adopted for the ENDF/B-VII.1 library was based on `EMPIRE` modeling [107] with discrete levels adopted from the RIPL-3 (2009 release) database [185]. Unfortunately, the gamma spectra were stored on a coarse outgoing photon energy grid with more than 100 keV energy bins. That makes the resolution of the primary gammas too poor for radionuclide identification. Additionally, the probability of emission of high-energy photons (e.g., higher than 4 MeV), which are crucial for many applications, can be accurately derived from the EGAF library [171, 172], but it is not accurate to describe them with state-of-art theoretical modeling.

The EGAF library [171, 172] was used to update the evaluated gamma emission spectrum corresponding to the thermal capture for incident neutron energies below 100 eV. It is worth noticing that a more accurate update of the evaluation was recently demonstrated by RPI colleagues by combining a `DICEBOX` code simulation[8] of the thermal-capture gamma cascade with an updated MCNP gamma transport [186]. Further investigations are warranted within the GRIN project [187].

[7] see CSWEG 2019 Mauborgne presentation at https://indico.bnl.gov/event/6642/contributions/31815/attachments/25323/37862/BNL_-_Mauborgne.pptx

[8] see `DICEBOX` distribution at https://nds.iaea.org/dicebox/

7. $^{54,56,57}Fe$

A new suite of evaluations for ^{54,56,57,58}Fe isotopes was developed in the framework of the CIELO international collaboration [188, 189] and adopted for the ENDF/B-VIII.0 library [68]. New RRR were evaluated for ^{54}Fe and ^{57}Fe, while modifications were applied to resonances in ^{56}Fe. However, during the ENDF/B-VIII.0 library validation, a 30% underestimation of the fast neutron transmission through thick iron shells (for neutrons with energies between 1 and 10 MeV) was identified, see Fig. 32 of Ref. [188].

While the CIELO iron evaluation was adopted for the ENDF/B-VIII.0 library, it was recognized that these identified deficiencies need to be addressed. A new evaluation was developed by Trkov and colleagues [190] within the IAEA INDEN project [191]; for a detailed description, see the mentioned Ref. [190]. Covariances from ENDF/B-VIII.0 were adopted for ENDF/B-VIII.1 for iron isotopes which is a pragmatic choice.

Following discussions with Plompen, this new evaluation adopted the CIELO resolved resonance parameters for ^{56}Fe with one important change in the Γ_γ of the 27.7 keV resonance: the ENDF/B-VIII.0 value, $\Gamma_\gamma = 1.288$ eV, was found to overestimate Spencer ORNL data and the recommended $\Gamma_\gamma = 1.0005$ eV value used in the JEFF-3.1 evaluation was adopted. These resonance parameters were essentially those evaluated by Perey and Perey [192] for the ENDF/B-V.2 material 1326. The ENDF/B-V.2 resonance parameters were adopted by Fröhner's evaluation for the JEF-2.2 library [193]. Some typos in the original evaluation were corrected (one resonance energy was changed from 767.240 keV to 766.724 keV and the spurious resonance at 59.5 keV was deleted [188]).

a. Iron validation

In the ICSBEP Handbook [158], there are many benchmarks sensitive either to iron or stainless steel cross sections. A selection of the most sensitive benchmarks was made (see Table 1 of Ref. [190]). The comparison between the calculated values for the ENDF/B-VIII.0, JEFF-3.3 and the ENDF/B-VIII.1 evaluations is shown in Fig. 38. Current criticality performance is as good as for ENDF/B-VIII.0 (compare blue triangles versus red circles). The largest improvement is observed for the pmi002 benchmark (Case 23) mainly due to the improvement in Cr cross sections in ENDF/B-VIII.1.

We also checked the reactivity prediction of fast assemblies as a function of the stainless steel reflector thickness for values from 1.27 cm up to 28 cm thick (see Table 2 of Ref. [190]). The results are shown in Fig. 39: the ENDF/B-VIII.1 performance is very similar to the ENDF/B-VIII.0 and significantly better than the ENDF/B-VII.1 and JEFF-3.3 libraries.

For the joint validation of both Cr and Fe ENDF/B-VIII.1 evaluations in deep penetration problems, we relied on a recent experiment at Rez, CZ that uses a well-validated neutron spectrometer [194, 195]. The experiment used a 50.2×50.2×50.4 cm^3 stainless steel (SS) cube with a ^{252}Cf(sf) source located inside. The neutron leakage spectrum was measured at one meter for incident neutron energies above 1 MeV.

Calculated leaked neutron spectra through the SS cube with different libraries are compared to the measured spectrum using the $C/E - 1$ criteria for outgoing neutron energies from 1 MeV up to 10 MeV. The best results of all participating libraries were obtained with the INDEN Cr and Fe evaluations, adopted for the ENDF/B-VIII.1 library as shown in Fig. 40. The 15% underestimation of the neutron leakage through stainless steel observed in Refs. [188, 189] for the ENDF/B-VIII.0 library is clearly seen in Fig. 40 in the whole energy range. The JENDL-4 evaluation slightly overestimates the measured data around 5 MeV whilst the JEFF-3.3 evaluation overestimates the measured neutron leakage from 2 MeV up to 4 MeV of neutron leaked energy.

8. $^{63,65}Cu$

Copper is an important structural material in various nuclear energy applications, including criticality safety. A significant number of ICBESP criticality benchmarks show a large sensitivity to copper data due to the extensive use of copper reflectors in various critical assemblies (e.g., the Zeus, Comet and CURIE benchmarks in the USA and the IMF020, IMF022 series in Sweden). Significant efforts have been devoted to improving the experimental database leading to improved copper evaluations.

New experimental neutron capture data on Cu isotopes have been measured by activation and time-of-flight methods by Newsome [196], Weigand [197], and Prokop [198]. The evaluations of neutron reactions on ^{63,65}Cu have been updated within the INDEN collaboration. Cross sections for ^{63}Cu(n,α), ^{63}Cu(n,2n), and ^{65}Cu(n,2n) reactions were adopted from the IRDFF-II library [2, 183].

a. Angular distributions

Discussions within the INDEN collaboration and our previous work [199] established that the angular distributions (represented by the Legendre coefficients) and capture cross sections strongly affect integral benchmark calculations; this work continued that investigation. The angular distribution parameterization in the RRR incorporates measured data from literature that have become available since the previous ^{63,65}Cu evaluation for ENDF/B-VIII.0 [68, 200].

The μ-bar (the Legendre coefficient P_1 in the LAB system) dependence as a function of the neutron incident energy is shown in Fig. 41. A clear overestimation of the evaluated μ-bar compared to the measured data is observed in the ENDF/B-VIII.0 evaluation up to about 700 keV of neutron incident energy. The evaluated angular distributions below 300 keV in the ENDF/B-VIII.0 library, which were reconstructed from the resonance parameters [200], were found to disagree with

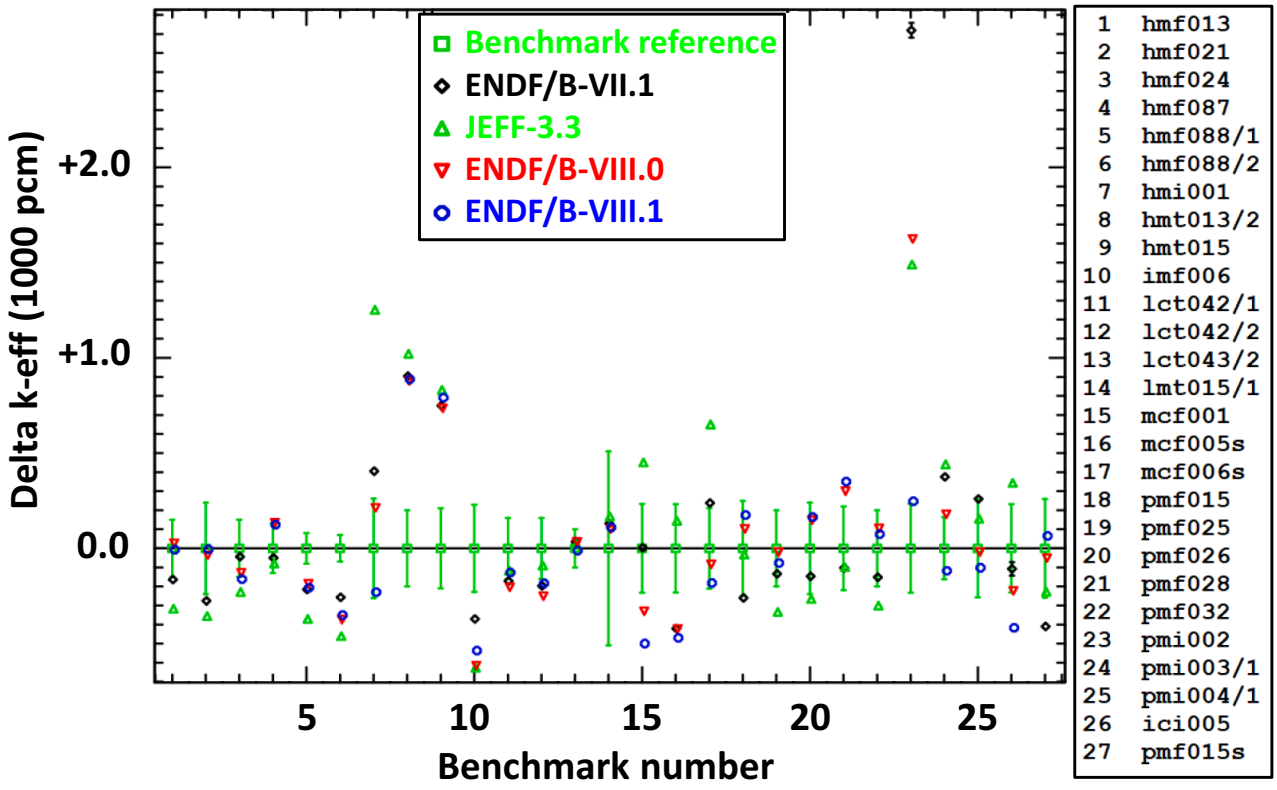


FIG. 38. Criticality differences to the experimental benchmark values C/E of selected stainless steel ICSBEP benchmarks. Experimental benchmark values are compared to JEFF-3.3, ENDF/B-VII.1, ENDF/B-VIII.0 and the new INDEN evaluation of iron (and chromium) isotopes adopted for the ENDF/B-VIII.1 library (INDEN r61).

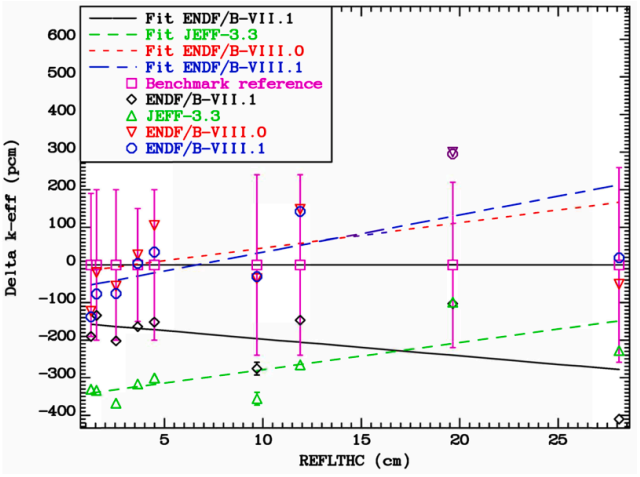


FIG. 39. Criticality differences to the experimental benchmark values C/E of stainless-steel reflected ICSBEP benchmarks [158] as a function of the reflector thickness in cm. Experimental benchmark values are compared to JEFF-3.3, ENDF/B-VIII.0 and the new INDEN evaluation of iron and chromium isotopes adopted for the ENDF/B-VIII.1 library. See Table 2 of Ref. [190] for the list of 9 benchmarks.

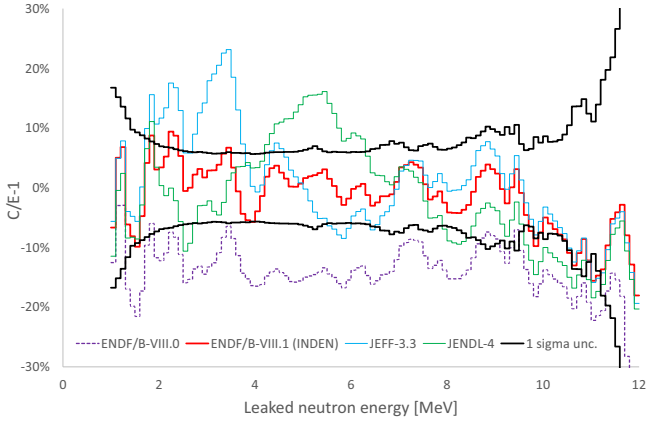


FIG. 40. Measured neutron leakage of the ^{252}Cf(sf) neutron source measured at 1 m distance from a 50.2x50.2x50.4 cm^3 stainless steel block [194, 195]. Experimental benchmark values $C/E - 1$ are compared with transport calculations using JEFF-3.3, JENDL-4.0, ENDF/B-VIII.0 and the new ENDF/B-VIII.1 library that adopted the INDEN Fe and Cr evaluations.

measured data by Popov and Samosvat [201]. The evaluated angular distributions from 300 keV up to 700 keV in the ENDF/B-VIII.0 library also disagree with Smith

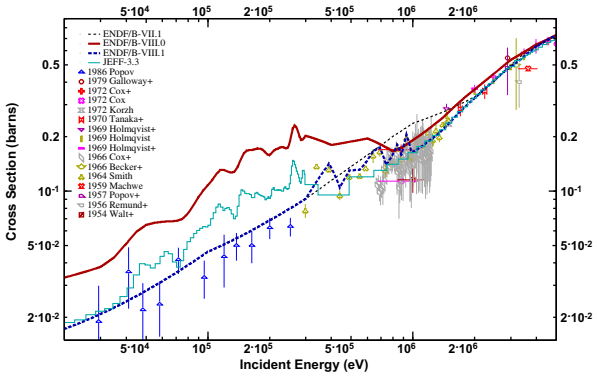


FIG. 41. ^{63}Cu μ-bar (P_1 Legendre coefficient in the LAB system) as a function of the neutron incident energy for different evaluated libraries versus selected experimental data [201–206] from EXFOR [45] up to 4 MeV.

et al. [202] data. The ENDF/B-VII.1 evaluation agrees with Popov data [201] on average, so a significant deviation from the experimental data happened during the ENDF/B-VIII.0 evaluation.

A similar disagreement between ENDF/B-VIII.0 evaluated and measured angular distribution data was shown by Blain and colleagues in RPI quasi-differential experiments [207], see Fig. 42 at forward (35 degrees) and backward (150 degrees) angles. The largest disagreement between the ENDF/B-VIII.0 simulation and measured RPI data is observed in the region near 250 keV of incident neutron energy for a 35-degree detector. Much better agreement is shown for JENDL-4.0 and JEFF-3.3 libraries. The INDEN evaluation adopted for ENDF/B-VIII.1 fitted the Legendre coefficients representing angular distributions to Popov [201] and Smith [202] data up to 1.1 MeV. The new ENDF/B-VIII.1 evaluation is in very good agreement with RPI quasi-differential data on copper which confirmed our evaluation choices.

b. Resolved Resonance parameters

The RRR in the ENDF/B-VIII.0 evaluation was limited to 100 keV [68] due to the poor integral performance traced to the decreased average capture cross section if the RRR was extended to 300 keV [68, 200]. The experimental data considered in the current R-matrix analysis were discussed in a previous work by McDonnell and Pigni [199]. Table IX summarizes (reproduced from the aforementioned work by the authors [199]) the experimental data sets measured for several sample configurations and list experimental properties, such as thickness n, target enrichment, reaction type, and energy range.

The Pandey [208] measurements are valuable for constraining the R-matrix parameters in the middle and the upper end of the RRR. At the lower end of the RRR, however, the Kauwenberghs data [209] are of a higher resolution and lower uncertainty and, thus, provide a more accurate constraint for R-matrix analysis.

The Tsuchiya [210] measurements on natural copper samples were primarily used for validation rather than fitting. The exception is that it proved useful to incorporate the data into the fit in the vicinity of the 579 eV resonance in ^{63}Cu, since this is the only measurement in which that resonance is not blacked out; thus, this measurement provides valuable information for the true shape and magnitude of that resonance.

The Guber [211] measurements provide necessary constraints for the capture widths. As discussed in our previous work [199], this experiment's measured data are estimated to be lower than the true capture yield above 100 keV. Therefore, we augmented the information with the more recent (but lower resolution) measurement by Weigand *et al.* [197]. Although the resolution of the Weigand data is too low for fitting resonance parameters, the data were used to normalize the capture cross section for incident neutron energies above 50 keV.

The additional recent measurement of the capture cross section for ^{65}Cu by Prokop [198] was found to agree well with the existing ENDF/B-VIII.0 evaluated data for ^{65}Cu, so it was used as validation rather than a fitting constraint.

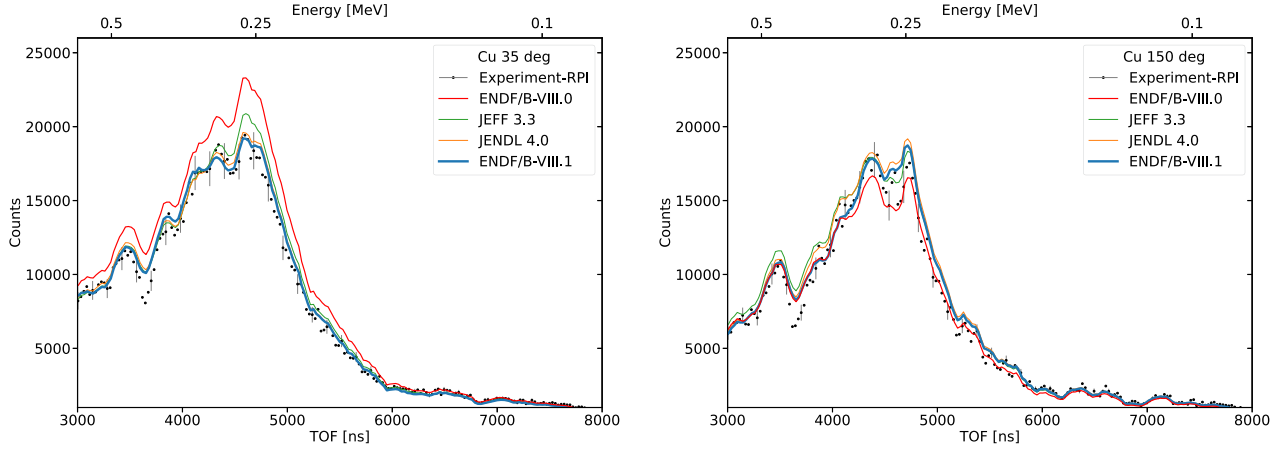
The R-matrix analysis is described in detail in Ref. [199]. We summarize the discussion and update with final parameter values here.

One feature of the ENDF/B-VIII.0 evaluations for ^{63,65}Cu is that average values were used for each isotope's capture widths. Resonance parameters for ^{63}Cu from a previous beta release of ENDF/B-VIII.0 ("revision 900") were found to describe the shapes of the resonances in the data better, and so we chose these parameters for our prior. However, the ENDF/B-VIII.0 resonance parameters themselves served as the prior parameters for ^{65}Cu as they give good agreement with recently measured Prokop capture data [198].

The comments about the underestimation of the capture yield data in Guber experiments discussed during the ENDF/B-VIII.0 evaluation, which led to cutting the RRR at 100 keV, were confirmed [199]. The measured data by Guber *et al.* [211] are thought to be too small for incident neutron energies above 100 keV due to an issue with the flux monitor during the experiment. A more recent experiment by Weigand *et al.* [197] corroborates a higher capture cross section in ^{63}Cu as suggested within the INDEN collaboration. For energies below 50 keV, the R-matrix parameters describe the increased capture cross section sufficiently well. This was accomplished by scaling the capture yield data from Guber *et al.* by a factor of 20% for energies above 19 keV, so that the magnitude of the capture cross section is similar to that of the data from Weigand *et al.* However, from 50 keV up to 100 keV, the cross section is modeled with an additional background term to reproduce Weigand data.

In this work, a refit of the capture widths below 100 keV was performed, which allows an improved description of several resonances. In contrast, the ENDF/B-VIII.0 evaluation files for ^{63,65}Cu used identical average values for the capture widths for each resonance.

The thermal values for the two isotopes, as obtained by this work and ENDF/B-VIII.0, are compared with the



(a) Detector at 35 deg

(b) Detector at 150deg

FIG. 42. Quasi differential copper scattering data measured with 35 deg and 150 deg detectors by Blain *et al.* [207] below 600 keV is compared with simulations using different evaluated libraries.

TABLE IX. Experimental data sets measured for several copper sample configurations, such as thickness n and enrichment in the RRR. These data represent the experimental database used to derive the set of resonance parameters in the RRR for ^{63,65}Cu.
Note: The Weigand [197] and Prokop [198] references do not communicate sample thickness. As such, neither data set was included in the SAMMY R-matrix analysis.

Author (year)	Facility	Sample	Type	n (10^{-3} a/b)	Energy Range	Data Points
Pandey (1977) [208]	ORELA	Enriched	Trans	78.964	1 keV–1.4 MeV 33 eV–185 keV	24086 31393
Kauwen. (2013) [209]	GELINA	Enriched	Trans	8.804	150 eV–90 keV	21528
Tsuchiya (2014) [210]	GELINA	Natural	Trans Trans	0.989 164.63	150 eV–90 keV	37673
Guber (2014) [211]	GELINA	Enriched	Capture Yield	8.804	90 eV–300 keV	31296
Weigand (2017) [197]	LANSCE	^{63}Cu	Capture	–	74 eV–690 keV	398
Prokop (2019) [198]	LANSCE	^{65}Cu	Capture	–	1 eV–933 keV	264

National Institute of Standards and Technology (NIST) recommended values by Sears [87] in Table X, showing a marginal increase of the elastic cross section and overall good agreement with NIST recommendations.

TABLE X. Thermal cross section values in barn for ^{63,65}Cu in ENDF/B-VIII.0 (labeled B-VIII.0) and ENDF/B-VIII.1 (labeled B-VIII.1) evaluations are compared with NIST [87] and Firestone recommendations [212]. ENDF/B evaluations do not feature uncertainty components. If uncertainties and covariances are needed they may be adopted from JEFF-3.3 [64].

Quantity	B-VIII.0	B-VIII.1	NIST [87]	Firestone [212]
^{63}Cu (n,γ)	4.47	4.48	4.52	4.3(3)
^{63}Cu (n,el)	5.10	5.22	5.2	–
^{65}Cu (n,γ)	2.15	2.15	2.17	2.11(17)
^{65}Cu (n,el)	13.8	13.8	14.1	–

In the analysis with the SAMMY code, both isotopes, ^{63,65}Cu, were analyzed together, accounting for the isotopic enrichment in each experimental data set. Most of the experimental data sets considered for capture used highly enriched isotopic samples (>99%), which minimized the correlation between the isotopes in the analysis. The exception was in the vicinity of the 579 eV resonance in ^{63}Cu, where the Tsuchiya data set, measured on a natural copper sample, was incorporated. This introduced a small correlation between the two isotopes in that region.

The resonance parameter covariance matrix (RPCM) was obtained in the course of the R-matrix analysis. The RPCM is reported in the ENDF File 32. The correlation matrix and uncertainties in the cross section for n+^{63}Cu are shown in Fig. 43.

c. Fast neutron region

The elastic scattering angular distributions for both ^{63,65}Cu isotopes up to 1100 keV were updated using the Legendre polynomials derived from the fit to Popov and Samosvat [201] and Smith *et al.* [202] data taken on natural copper. The same angular distributions were used for

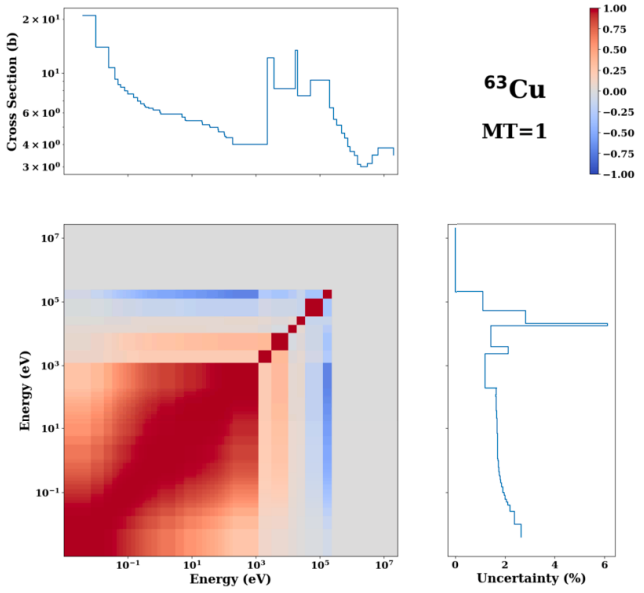


FIG. 43. Correlation matrix and uncertainties for the total cross section of n+^{63}Cu are shown.

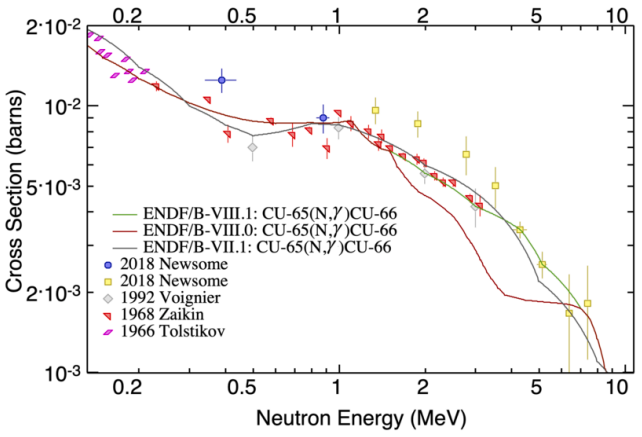


FIG. 44. n+^{65}Cu capture cross sections calculated for ENDF/B-VII.1, ENDF/B-VIII.0, and ENDF/B-VIII.1 nuclear data libraries are compared with selected experimental data [196, 213–215].

both copper isotopes. Smith and Popov angular distribution data are consistent at 300 keV. Popov data were used below 300 keV; Smith data are used from 300 keV up to 1100 keV.

From 1.1 MeV up to 3 MeV, the angular distributions were adopted from the JEFF-3.3 library, which is in better agreement with experimental data by Tanaka *et al.* [203], Becker *et al.* [204], Korzh *et al.* [205], and Popov [206], as shown in the Fig. 41. We found a huge sensitivity of the calculated criticality in fast assemblies to small differences in the evaluated μ-bar up to 3 MeV. Above 3 MeV, the JEFF-3.3 evaluation smoothly matches the ENDF/B-VIII.0 as shown in Fig. 41.

Capture cross section on ^{65}Cu have been recently measured by Newsome *et al.* [196] and Prokop *et al.* [198]. Prokop data are not yet in EXFOR, but authors showed excellent agreement in the fast neutron region with the ENDF/B-VIII.0 evaluation up to 1 MeV (see Fig. 8 of Ref. [198]). Older measurements by Voignier [213], Zaikin [214], and Tolstikov [215] are shown in Fig. 44 and agree with the ENDF/B-VIII.0 evaluation below 1.5 MeV. Unfortunately, Newsome activation measurements [196] above 1 MeV seem to be too high. Our new evaluation followed ENDF/B-VIII.0 up to 1.5 MeV in agreement with Prokop and Zaikin data. Above 1.5 MeV, the new evaluation is closer to the ENDF/B-VII.1 evaluation, being significantly higher than the ENDF/B-VIII.0 evaluation. The new evaluation agrees much better with experimental data than ENDF/B-VIII.0 as shown in Fig. 44.

Capture cross section on ^{63}Cu have been recently measured by Newsome *et al.* [196] and Weigand *et al.* [197]. Weigand data below 0.6 MeV and Newsome measured point at 0.4 MeV are significantly higher than older measurements by Voignier [213], Zaikin [214], and Tolstikov [215] in this energy region as shown in Fig. 45. For this isotope, Voignier, Tolstikov, and Zaikin data were also in good agreement and were the basis of the ENDF/B-VIII.0 and JENDL-5 evaluations. In this work we choose to follow Weigand data in the fast neutron region starting at 100 keV (and below as discussed in the RRR evaluation above). Implicitly, that means that the new evaluation is higher than older evaluations from 100 keV up to 600 keV as driving experimental data are discrepant. We significantly reduced capture cross section from ENDF/B-VIII.0 and JENDL-5 evaluations from 600 keV up to 1 MeV to better agree with Newsome and older data (especially Zaikin) in that region. From 1 MeV up to 2 MeV there is good agreement with data and the other evaluations, and the new evaluation is close to the ENDF/B-VIII.0 and JENDL-5 evaluations there. It should be noted that from 2 MeV up to 3 MeV the JENDL-5 evaluation is lower than measured datasets, but we followed newer Newsome data up to 7 MeV in agreement with the ENDF/B-VIII.0 library.

Inelastic cross section and scattering spectra (including continuum double differential cross sections and discrete level angular distributions) were adopted from the JENDL-4 evaluation. This was very important to correct deficiencies of the ENDF/B-VIII.0 evaluation in 14 MeV fusion benchmarks as shown, e.g., for the Oktavian benchmark in Fig. 46. Data issues in previous evaluations (except JENDL-4) are clearly seen from 4 MeV up to 12 MeV of the outgoing neutron energy in the above mentioned figure leading to an overestimated response compared to measured data.

d. Validation

We have selected two benchmark suites: one thermal, the second one including the intermediate and fast neutron assemblies. Criticality calculations were done by A. Trkov. A similar set of benchmarks were also calculated at ORNL in previous work [199].

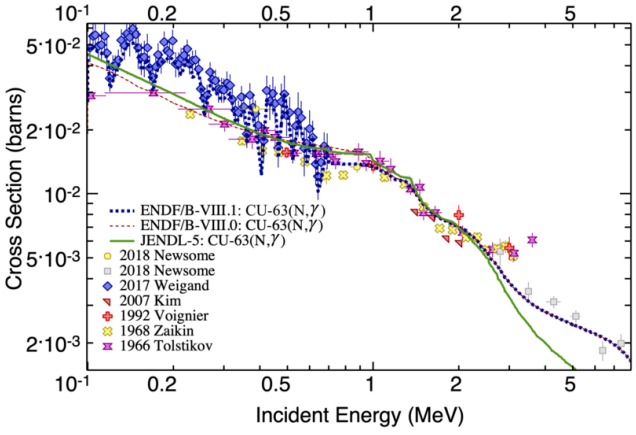


FIG. 45. n+^{63}Cu capture cross sections calculated for JENDL-5, ENDF/B-VIII.0, and ENDF/B-VIII.1 nuclear data libraries are compared with selected experimental data [196, 197, 213–215].

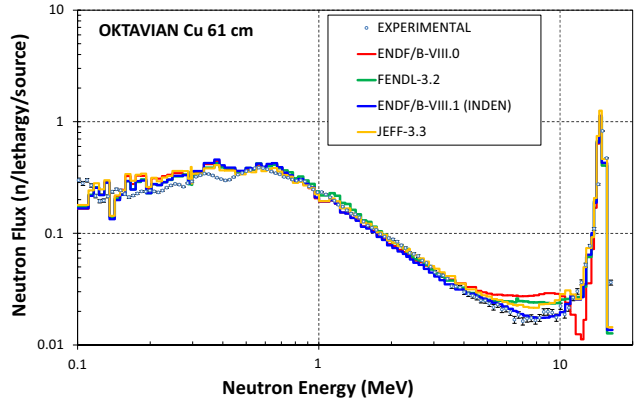


FIG. 46. The measured neutron leakage from a copper assembly using pulsed 14-MeV DT neutron beam at the Oktavian facility is compared with simulations using different nuclear data libraries. Experimental data taken from Ref. [216].

Results for the thermal set of benchmarks are shown in Fig. 47. The R-matrix parameters derived and updated in this work does improve agreement between calculated and measured criticality benchmark values compared to previous libraries – ENDF/B-VII.1, JEFF-3.3, and ENDF/B-VIII.0.

The agreement for well-thermalized assemblies with FEPIT< 20% was similar for all libraries as shown in Fig. 47. A perfectly flat trend was achieved for the ENDF/B-VIII.1 copper evaluation covering from very well-thermalized assemblies (HCT006/3 with FEPIT≈ 0) to epithermal assemblies with FEPIT≈ 40% (HCT005), clearly an improved performance for lattices and thermal benchmarks.

All previous evaluations systematically underestimated the criticality of epithermal assemblies, being ENDF/B-VIII.0 slightly better (showing smaller gradient) than ENDF/B-VII.1 and JEFF-3.3, especially for HCT007(cases 1,2,3,5,6) and HCT005, but still worse than the new evaluation.

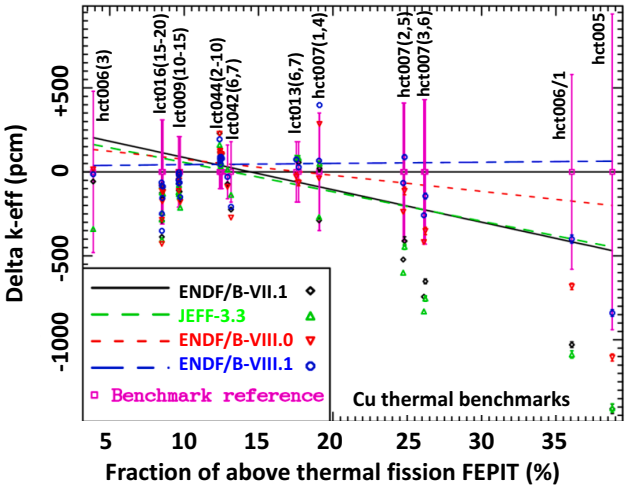


FIG. 47. The plot of Δk_{eff} comparing calculated to experimental values for the suite of thermal ICSBEP benchmarks [158] that show sensitivity to copper. The x-axis corresponds to the percentage fraction of above-thermal fissions—FEPIT.

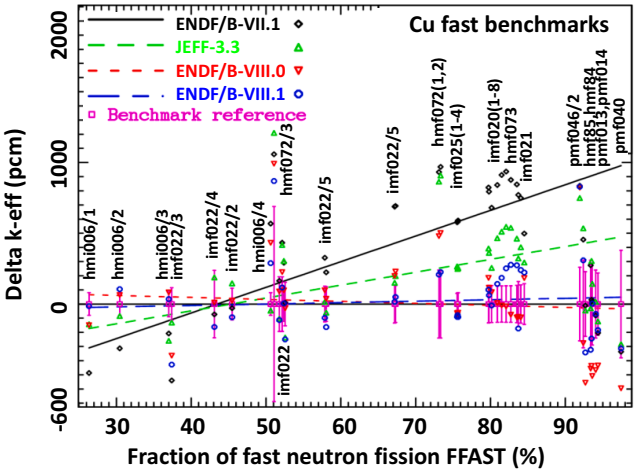


FIG. 48. The plot of Δk_{eff} comparing calculated to experimental values for the suite of fast and intermediate ICSBEP benchmarks [158] that show sensitivity to copper. The x-axis corresponds to the percentage fraction of fast-neutron fissions – FFAST.

Results for the intermediate and fast neutron spectrum set of benchmarks are shown in Fig. 48. This benchmark set covers a broad range of the percentage fraction of fast-neutron fissions FFAST from 25% up to close to 100%. Both ENDF/B-VIII.0 and the new ENDF/B-VIII.1 (INDEN) evaluations show a very flat trend as a function of the percentage of fast-neutron fissions FFAST. The new evaluation shows worse performance for the Swedish set of benchmarks IMF20,21,22, which will be

discussed in detail below. However, the new evaluation improved the ENDF/B-VIII.0 performance both for ZEUS intermediate benchmarks (e.g., HMI006) as well as for the fastest studied benchmarks (FFAST>90%) in this set (e.g., HMF084, HMF085 and PMF013, PMF014, PMF040, and PMF046/2).

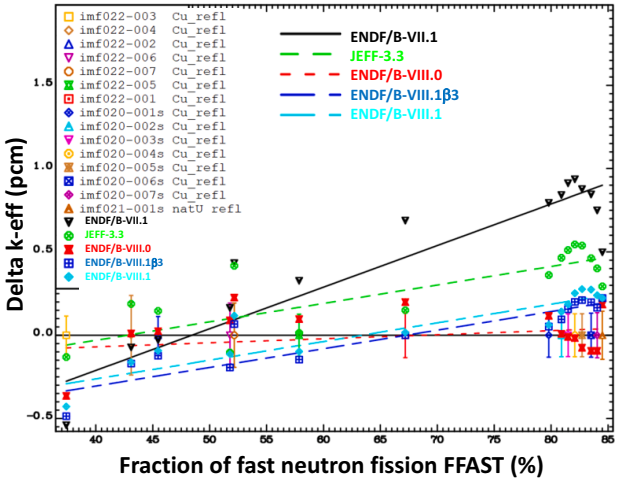


FIG. 49. Criticality of Cu-sensitive intermediate Swedish ICSBEP benchmarks (IMF020,21,22) relative to the measured benchmark values as a function of the percentage fraction of fast-neutron fission (FFAST).

As previously discussed, the Δk_{eff} calculated for the ENDF/B-VIII.1 evaluation increased for the Swedish IMF020 and IMF022 series of benchmarks compared to the ENDF/B-VIII.0 as shown in Fig. 49. In fact, the new ENDF/B-VIII.1 evaluation (dashed cyan line) shows a larger positive gradient along this benchmark series as a function of the fraction of fast-neutron fissions (FFAST). The ENDF/B-VIII.0 (dashed red line) better agreement was driven by a too large μ-bar in the RRR up to 700 keV, which was in disagreement with Popov [201] and Smith [202] data, as previously discussed. However, we noticed that the IMF021 benchmark (brown upper triangle in Fig. 49) uses exactly the same fuel as IMF020 and IMF022 benchmarks, but features a natural uranium reflector instead of the copper one. Considering how well we know uranium cross sections, the fact that the IMF021 calculates high by about +200 pcm both for ENDF/B-VIII.0 and ENDF/B-VIII.1 indicates an unidentified +200 pcm benchmark bias in the IMF020,21,22 benchmark series. If we consider this bias by subtracting 200 pcm from the C values, the ENDF/B-VIII.1 evaluation will perform perfectly for this benchmark set as well, better than the ENDF/B-VIII.0.

The preliminary calculations of the new CERBERUS integral experiments [217] also show a much improved agreement for the ENDF/B-VIII.1 evaluation.

A very important shielding benchmark was the measurement of the ^{252}Cf(sf) neutron leakage from a 48x50x50 cm^3 copper cube undertaken at the CVR Rez near Prague using stilbene scintillator detectors [218, 219]. This type of benchmark is very sensitive to the elastic and inelastic cross sections and elastic angular distributions up to 10 MeV of neutron incident energy, but it is practically insensitive to capture. It does perfectly complement the criticality benchmarks. The success of this benchmark to validate evaluated data is also driven by our excellent knowledge of the standard ^{252}Cf(sf) neutron spectrum [220].

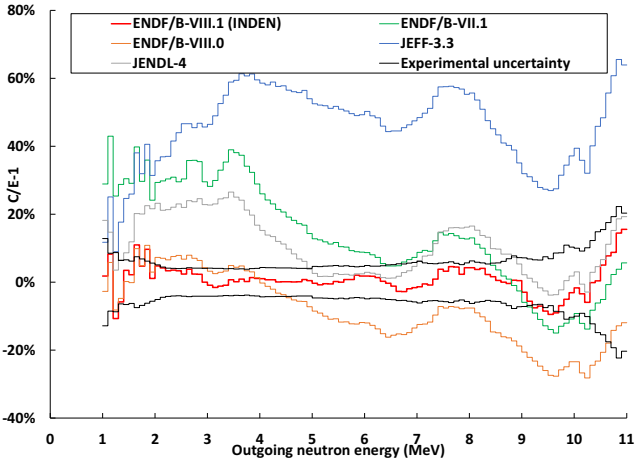


FIG. 50. Measured neutron leakage of the ^{252}Cf(sf) neutron source measured at 1m distance from a 48x50x50 cm^3 copper block [218, 219]. Experimental benchmark values are compared with transport calculations using JEFF-3.3, JENDL-4.0, ENDF/B-VII.1, ENDF/B-VIII.0 and the new ENDF/B-VIII.1 library that adopted the INDEN Cu evaluations by means of C/E-1 ratio.

Calculated leaked neutron spectrum through the copper cube with different libraries is compared to the measured spectrum using the $C/E-1$ criteria for outgoing neutron energies from 1 MeV up to 10 MeV as shown in Fig. 50. The best results of all participating libraries were obtained with the INDEN Cu evaluation adopted for the ENDF/B-VIII.1 library. JEFF-3.3 overestimated the leakage by up to +40% due to disagreement of evaluated total cross section with available experimental data. The ENDF/B-VIII.0 evaluation underestimated the measured neutron leakage above 5 MeV by up to -20 to -30% due to inappropriate description of the isotopic elastic cross section data in that energy region. ENDF/B-VII.1 and JENDL-4 showed similar performance overestimating the measured neutron leakage below 5 MeV of the outgoing neutron energy, and slightly overestimating the measured leakage around 8 MeV.

JEFF-3.3 covariances [64] are recommended to be used, if needed, as ENDF/B-VIII.0 did not include covariances for copper.

9. ^{139}La

The central values for ^{139}La were adopted from TENDL-2014, with RRR and URR resonance parameters adopted from ENDF/B-VIII.0. As for any isotopic TENDL evaluation, the fast neutron range was optimized by adjusting TALYS [221] nuclear model parameters. In the case of ^{139}La, we adjusted the photon strength function for the neutron capture cross section, the proton optical model and particle-hole densities for the (n,n'), (n,2n) and (n,p) channels, and the alpha optical model parameters for the alpha-emitting channels. The estimation of covariance data for ^{139}La was performed following an approach similar to that of the TENDL library [222]. First, the cross sections and angular distributions are obtained by adjusting model parameters in order to be close to selected experimental data. In the fast neutron range, these parameters concern the models included in TALYS, and in the resonance range, resonance parameters are adjusted with the code TARES [223]. Covariances are then obtained by randomly modifying all model parameters. In the resonance range, multi-level Breit Wigner parameters are sampled given specific widths and standard deviations, in order to reproduce recommended values for the thermal cross sections and resonance integrals. In the fast range, a Bayesian Monte Carlo approach is followed [224, 225] with the code TASMAN, based on large prior distributions for parameters. In this case, the final sampled parameters are obtained from posterior distributions updated with experimental data. Finally, covariance data from sampled cross sections and angular distributions are formatted into the ENDF-6 format with the code TEFAL.

It is worth noting that special nuclear data processing was needed when the ^{139}La evaluation was adopted for the FENDL library [180]. The analysis of a numerical benchmark for a neutron transport through a 1-meter sphere of ^{139}La proposed by C. Konno using ACE- and MATXS-formatted cross section files from the FENDL-3.1c library showed problems in the URR of ^{139}La evaluation adopted from TENDL-2014 [226]. The total neutron flux computed using MCNP/ACE differed up to 50% from the one calculated applying ANISN/MATXS deterministic transport codes. The problem arose when too small total cross section values were sampled by the PURR module of `NJOY2016` mainly due to the limitations of the processing method [226], but also due to the quality of the URR evaluated data. An `NJOY2016` (PURR) patch to correct this issue was proposed and applied, and the TENDL-2014 resonance data was replaced by the ENDF/B-VIII.0 resonance evaluation. The ENDF/B-VIII.0 data replacement and the `NJOY` patch increased the neutron flux in the URR for Monte Carlo calculations by 4%. The corresponding increase of the calculated neutron flux for deterministic codes is about 15% for the ENDF/B-VIII.0 data. The agreement between deterministic and Monte Carlo benchmark results was significantly improved.

10. ^{233}U

^{233}U evaluated data have poor performance in critical solutions, which has been well documented [68]. Performance in fast critical assemblies is much better. No change has been done to the ENDF/B-VIII.0 evaluation in the fast energy range except the capture cross section that was changed from 3 keV up to 200 keV to agree on average with new experimental data by Leal-Cidoncha *et al.* [227], and the neutron multiplicity change which is described below. A joint effort has been made by the international team led by ORNL within the INDEN collaboration to include the latest measured differential data and use the IAEA evaluated prompt fission neutron spectrum at the thermal point. Whilst performance problems remain, this new evaluation represents a step forward compared to ENDF/B-VIII.0.

a. Thermal and resonance region

Similarly to R-matrix analyses on the two major fissile actinides ^{235}U and ^{239}Pu, the resonance parameter evaluation of n+^{233}U reactions is an ongoing milestone of the US NCSP. In the ENDF/B-VIII.1 nuclear data library release, the major updates, in chronological order, to this evaluation work were the extension of the RRR evaluation up to 2.5 keV featuring an average increased fission cross section above 50 eV and the updates in the thermal and low-energy region up to a few eVs.

The extension up to 2.5 keV used transmission data and fission cross sections measured at the ORELA facility in the early 2000s [228, 229]. Due to the lack of capture measured data in the extended energy range, the cross sections of this reaction channel were obtained by using an average value of 39 meV assigned to the capture widths consistently with the RM approximation of the *R*-matrix theory. The second update was to guarantee a reasonable performance in criticality solution benchmarks affected by the changes in the thermal PFNS evaluation together with the adoption of the thermal constants recommended by the standard evaluations as discussed in the preliminary benchmark analysis found in Ref. [230].

In Table XI, the fitted cross sections calculated at the thermal energy E=0.0253 eV are reported for three libraries. A very good agreement with standard values [1] as well with thermal cross section recommended by Duran *et al.* [82, 83] is observed. An excellent agreement of evaluated α_{therm} with Lounsbury *et al.* measurement [84–86] is also seen for all libraries except ENDF/B-VIII.0, which featured too low capture cross section.

In the energy region above thermal, the evaluation procedure consisted on fitting sequentially fission and capture measured data. Among these, Berthomieux's and Weston's measurements [231, 232] are particularly relevant because the fission and capture reaction channels were measured simultaneously with anti-coincidence techniques. Although the capture channel is associated with a relatively large scaling factor of about 11%, Berthomieux's fission measured data [231] (that are consistent to other fission cross sections measured by Cal-

TABLE XI. n+^{233}U 2200 m/s thermal cross sections for three nuclear data libraries compared with the Thermal Neutron Constants derived by the Standard group [1] and Duran *et al.* [82] estimates. Available experimental data by Lounsbury *et al.* [84–86] are also listed.

Source	α_{therm} (b)	σ_{el} (b)	σ_f (b)	σ_c (b)
ENDF/B-VIII.1	0.0827(28)	12.08(24)	533.4(91)	44.1(13)
relat. uncert.	3.4%	2.0%	1.7%	2.9%
ENDF/B-VIII.0	0.0792	12.18	534.1	42.3
relat. uncert.	–	–	–	–
ENDF/B-VII.1	0.0852(19)	12.18(75)	531.4(32)	45.3(10)
relat. uncert.	2.3%	6.1%	0.6%	2.2%
Standards [1]	0.0842(17)	12.2(7)	533.0(22)	44.9(9)
relat. uncert.	2.0%	5.7%	0.4%	2.0%
Duran [82, 83]	0.0845(41)	12.4(5)	533.0(7)	44.8(22)
relat. uncert.	4.9%	4.0%	1.3%	4.9%
Lounsbury [84–86]	0.0861(21)	–		
relat. uncert.	2.4%	–	–	-

viani [233]) were taken as main reference for this evaluation because of their improved resolution and statistics over Weston's measured data. Instead, Weston's data were used for estimating the average magnitude of the capture reaction channel.

Plots in Fig. 51 show the calculated fission and capture cross sections (a) together with the η-function normalized to the average number of neutrons $\bar{\nu}$ (b). The quantity η is a measure of the average number of neutron released per neutron absorption and related to the ratio capture-to-fission α as $\eta = \bar{\nu}/(1+\alpha)$. Compared to corresponding measured data (in black), the calculated fission and capture cross sections (in red) largely differ in their average magnitude. In fact, except for the resonance levels at 2.3 eV and 7.4 eV, the fission cross section is about an order of magnitude larger than the capture cross section. This results in a capture reaction channel associated with large uncertainties and highly correlated to small variations in the fission reaction channel. This can significantly impact the magnitude of the capture cross section and, in turn, greatly affect the reactivity in criticality benchmarks.

The bottom plot of Fig. 51 is about the energy dependence of the η-function and can be used to highlight critical points of incompatibility between measured data as well as the difficulty of the R-matrix model to describe the shape of the measured data. For instance, although the relatively good fit is achieved for the fission and capture channel, the energy region marked by the first arrow at about 1.5 eV could not be perfectly optimized to describe the measured data as their energy tail augmented by not negligible deviations between Weston's and Berthomieux's measured data in the same energy region. The second arrow marking the energy region at 8 eV is also about large deviations in the small resonance levels between Berthomieux's and Weston's measured data. This represents one of the cases where the magnitude of both fission and capture cross section is small and fission

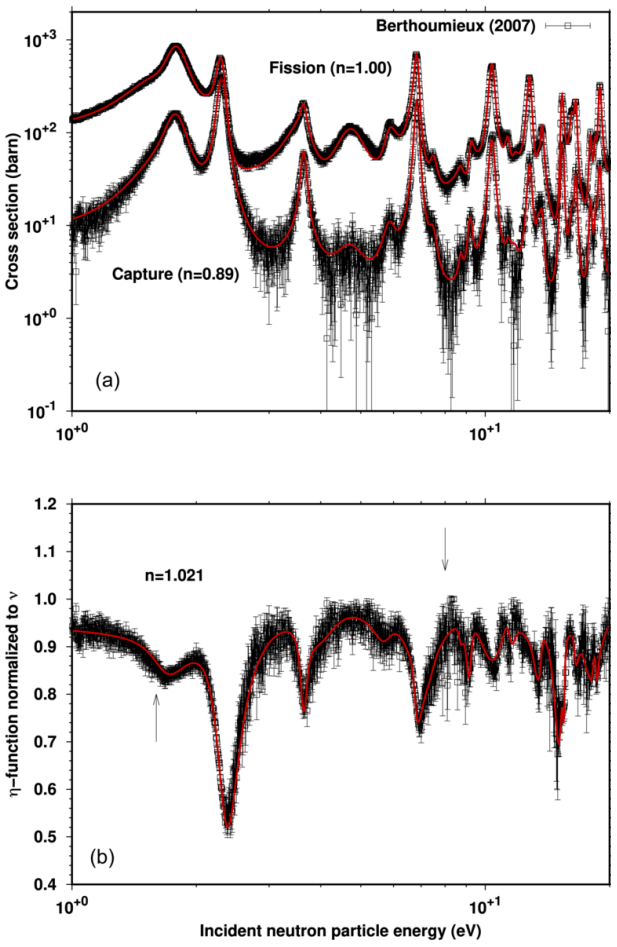


FIG. 51. n+^{233}U comparison of calculated (red) and measured (black) cross sections (a) and η-function normalized to the number of neutrons ν (b). Normalization factors to the calculated data are also reported. Measured are data from Ref. [231].

widths are much larger than the average capture width.

In addition to the η-function, average differences in the Weston's and Berthomieux's measured data are shown in Fig. 52 where the integral comparison of the ratio-capture-to-fission α is shown up to 10 eV. Not negligible deviations (up to 22%) between the reported measured data can be seen confirming the difficulties in the characterization of the capture channel among different measurements.

As in other cases of fissile actinides, an accurate and precise characterization of the capture cross sections remain elusive from the experimental point of view. For these reasons, some guidance was taken from the reactivity of criticality benchmarks as a function of the epithermal fission fraction. Evaluation of n+^{233}U reactions is one of the most challenging cases due to the large magnitude of the fission reaction channel compared to the capture cross section.

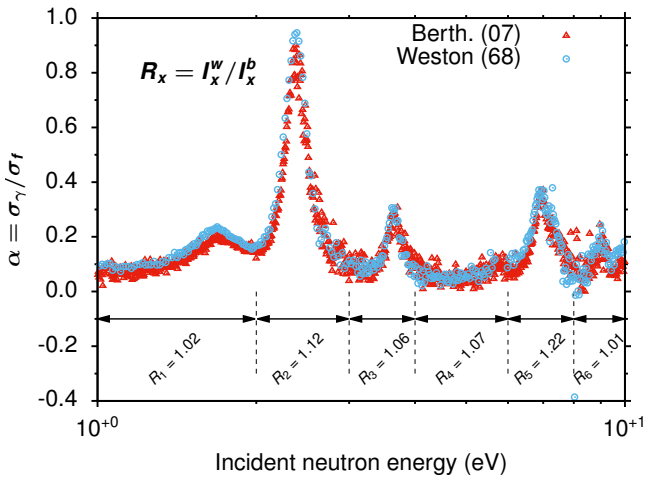


FIG. 52. n+^{233}U comparison between Berthomieux's and Weston's ratio capture-to-fission α measured data [231, 232]. The ratio R_x of Weston to Berthomieux integrals of several energy ranges up to 10 eV is also shown.

b. (n,f) Fission $\overline{\nu}$

The thermal $\overline{\nu}_{tot}$ in the new evaluation was slightly increased to 2.4869 in perfect agreement with the thermal neutron constant value of 2.487(0.011) [1]. The ENDF/B-VIII.0 value was slightly smaller 2.48524 but agrees well within estimated uncertainties of 0.42%. Gwin data [41] renormalized to the above-discussed thermal value was used to define the $\overline{\nu}$ energy dependence below 10 eV. Gwin data [40] was also employed to define the neutron multiplicity from 500 eV up to 500 keV as shown in Fig. 53.

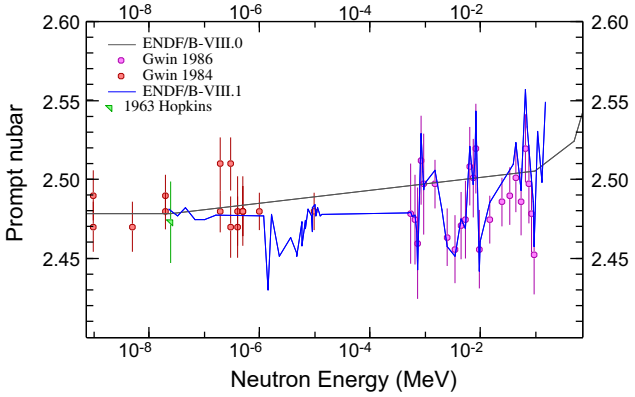


FIG. 53. Experimental data from Gwin *et al.* [40, 41] and Hopkins *et al.* [234] are compared to evaluated ENDF/B-VIII.0 and ENDF/B-VIII.1 ^{233}U $\overline{\nu}$ below 100 keV.

ENDF/B-VIII.1 neutron multiplicity was changed to optimize the agreement with Jezebel-23 benchmark and is compared to ENDF/B-VIII.0 in Fig. 54.

The ENDF/B-VIII.1 evaluated $\overline{\nu}$ uncertainties in Fig. 55 are distinctly larger up to 100 keV due to the increased $\overline{\nu}$(^{252}Cf(sf)) standard uncertainties (0.42%). The use of Gwin nubar data [40] from 500 eV up to 100 keV led to a significant increase of the nubar uncertainty to values up to 1.4% in the new evaluation (from about 0.5% in ENDF/B-VIII.0 to roughly the uncertainty of Gwin's experiment) as shown in Fig. 55. The evaluated ^{233}U $\overline{\nu}$ uncertainty was similar to ENDF/B-VIII.0 up to 3 MeV and significantly increased above.

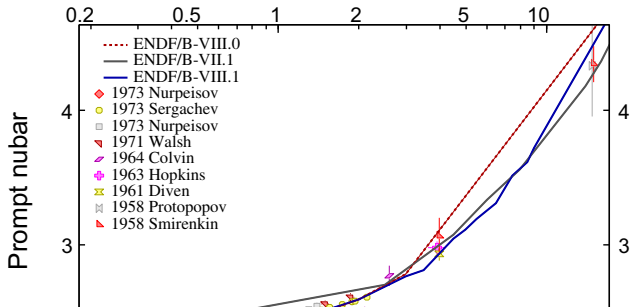


FIG. 54. Selected experimental data [234–241] from EXFOR [45] versus evaluated ^{233}U $\overline{\nu}$ from 100 keV up to 20 MeV.

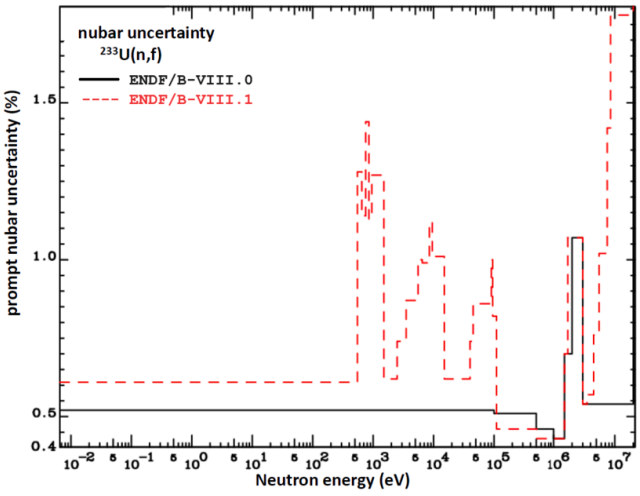


FIG. 55. Evaluated ^{233}U $\overline{\nu}$ uncertainty.

11. ^{235}U

A focused international effort on ^{235}U evaluations adopted for the ENDF/B-VIII.0 library was coordinated by the IAEA within the CIELO project [242] and comprehensively documented by Capote *et al.* [67] and Chadwick *et al.* [189]. Cross-section evaluation in the fast neutron range remains unchanged for ENDF/B-VIII.1. PFNS and $\overline{\nu}$ were revisited as described below. Minor

changes were also undertaken in the resonance region driven by newly available experimental data [243].

a. Thermal and Resonance regions

The R-matrix analysis of the n+^{235}U system is an ongoing milestone of the NCSP. In the ENDF/B-VIII.1 nuclear data library release, the major update to this evaluation work has been the inclusion of the neutron capture and fission yield data measured at the RPI Gaerttner LINear ACcelerator (LINAC) facility below 2.5 keV [243]. Two measurements were done—thermal and epithermal—that together cover the energy range from 0.01 eV to 2.5 keV. The measurements recorded gammas from ^{235}U reactions using the RPI multiplicity detectors. Fission and capture events were separated by event multiplicity and total energy deposition [243]. The importance of these yield data relies in the simultaneous measurement of both capture and fission reaction channels including the low-lying resonance at 0.3 eV. In fact, besides being extremely important for the correct quantification of reactivity coefficients in criticality benchmarks, the first ^{235}U resonance located at 0.3 eV features a very small neutron width and its magnitude is determined by the fit of the fission and capture channels. Although there is a large amount of measured data for the fission reaction channel as shown in Fig. 56, the capture channel has been particularly difficult to estimate due to the very limited amount of experimental data below 1 eV.

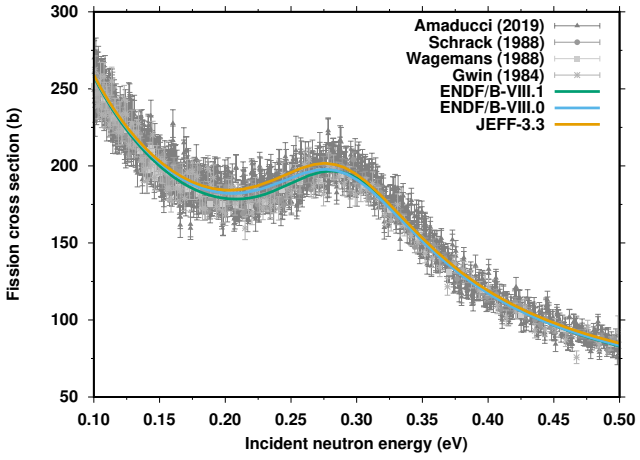


FIG. 56. n+^{235}U fission neutron cross section calculated for three nuclear data libraries together with selected measured data below 0.5 eV of neutron incident energy [75, 76, 244, 245].

Since the evaluation of the capture reaction channel has a straightforward impact on the criticality of a fissile nuclear system, the increase of the capture cross section, as shown in Fig. 57 for the ENDF/B-VIII.0 release (cyan curve in (b) panel), was suggested by updates in the PFNS [44, 246, 247] that featured a softer PFNS with lower average neutron energy than in the previous ENDF/B-VII.1 nuclear data library. By keeping the thermal values consistent with the thermal neutron constants recommended by the Standards group [1], the recent measured data induced a reduction of both fission and capture yields for the 0.3 eV level (green curve in the top and bottom panels). The energy region below 0.5 eV was fitted with particular emphasis in evaluating the interference effect at the minimum-yield neutron energy of 0.2 eV that was not very well reproduced in ENDF/B-VIII.0 or JEFF-3.3 evaluations as shown in the figure. This has the consequence of slightly underestimating the peak of the 0.3 eV level for the capture channel although still within the lower limit of the experimental uncertainty. The fission and capture yields measured at

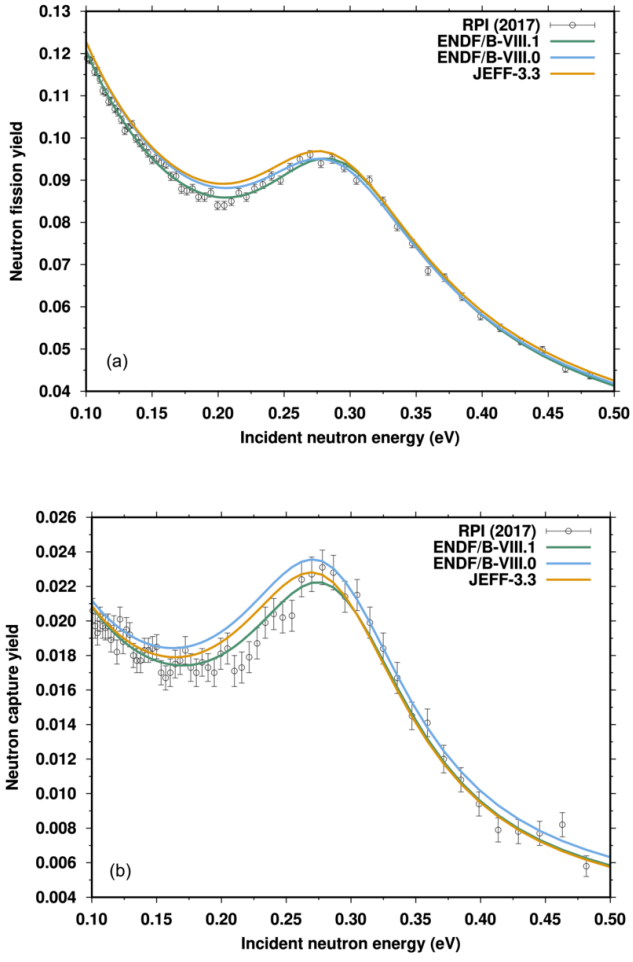


FIG. 57. n+^{235}U fission and capture neutron yield data calculated for three nuclear data libraries are compared with the RPI measured data [243] below 0.5 eV.

RPI [243] were compared to ENDF/B-VII.1 evaluation [162], ENDF/B-VIII.0 and the new resonance evaluation (note: labelled IAEA 2020) by Danon *et al.* [9] as shown

[9] see Danon presentation at the INDEN meeting at https:

in the Table XII. Systematic uncertainties are estimated to be 2% for fission and 3% for measured capture yields. It is observed that the capture yield of the 8.76 eV resonance [243] was overestimated by 10% in the ENDF/B-VIII.0 evaluation; the capture yield was 5% higher than the RPI measured already above the 0.6 eV valley. The new ENDF/B-VIII.1 resonance evaluation agrees within quoted uncertainty with the measured RPI data [243] below 250 eV. Small differences between the ENDF/B-VIII.1 evaluation and measured data remain from 250 up to 350 eV and from 850 up to 950 eV for the capture yield.

TABLE XII. C/E of energy-grouped fission and capture yields for both RPI experiments compared to ENDF/B-VII.1 (B7.1), ENDF/B-VIII.0 (B8.0) and the ENDF/B-VIII.1 (B8.1) ^{235}U resonance evaluation. Values highlighted in red show evaluated deviations in the capture yield larger than the estimated experimental uncertainty of 3%.

From Thermal experiment:							
E1	E2	Fission yield			Capture yield		
(eV)	(eV)	B7.1	B8.0	B8.1	B7.1	B8.0	B8.1
0.01	0.0206	1.01	1.00	1.00	1.02	1.01	1.01
0.02	0.03	1.00	1.00	1.00	0.99	0.99	0.99
0.0206	0.0623	1.00	1.00	1.00	0.98	0.99	0.99
0.0623	0.6	0.99	1.01	1.01	0.99	1.05	1.03
0.6	7.8	0.97	0.99	1.00	0.99	1.05	1.02
0.0253	9.4	0.98	0.99	1.01	0.99	1.06	1.02
7.8	11.	0.98	0.98	1.01	1.00	1.10	1.02
From Epithermal experiment:							
E1	E2	Fission yield			Capture yield		
(eV)	(eV)	B7.1	B8.0	B8.1	B7.1	B8.0	B8.1
9.4	150	1.02	1.01	1.01	1.04	1.03	1.03
150	250	1.02	1.00	1.00	1.07	1.03	1.03
250	350	1.04	1.02	1.02	1.06	0.96	0.96
350	450	1.03	1.04	1.04	1.12	0.99	0.99
450	550	1.02	1.02	1.02	1.17	1.00	1.00
550	650	1.03	1.01	1.01	1.18	1.00	1.00
650	750	1.03	1.02	1.02	1.17	1.02	1.02
750	850	1.03	1.03	1.03	1.17	1.03	1.03
850	950	1.00	1.01	1.01	1.17	1.07	1.07
950	1500	1.02	1.00	1.00	1.25	1.02	1.02

It was independently tested at ORNL that the current resonance-parameter updates implemented in the ENDF/B-VIII.1 had negligible impact on the loss of reactivity of the ENDF/B-VIII.0 library in depletion calculations as a function of the burnup. This has been an indication of the little correlation between the loss of reactivity in depletion calculations and the excellent performance of the ^{235}U ENDF/B-VIII.0 library in criticality benchmarks particularly for HEU configurations. In fact, additional tests demonstrated that the impact of ^{238}U and ^{239,240,241}Pu was directly responsible for the loss of reactivity in depletion calculations [39].

//www-nds.iaea.org/index-meeting-crp/CM-INDEN-2020-res/docs/Danon-INDEN-RR-III.pdf

In Table XIII, the thermal constants for scattering, fission, and capture cross sections are reported for three nuclear data libraries showing very consistent values; values for the new ENDF/B-VIII.1 evaluation agree with the recommended standard Thermal Neutron Constants [1] as well as with thermal cross sections recommended by Duran *et al.* [82, 83]. An excellent agreement of evaluated α_{therm} with Lounsbury *et al.* measurement [84–86] is observed for all libraries well within quoted uncertainties.

TABLE XIII. n+^{235}U 2200 m/s thermal cross sections for three nuclear data libraries compared with the Thermal Neutron Constants derived by the Standard group [1] and Duran *et al.* [82, 83] estimates. Available experimental data by Adamchuk *et al.* [248] and Lounsbury *et al.* [84–86] are also listed.

Source	α_{therm} (b)	σ_{el} (b)	σ_f (b)	σ_c (b)
ENDF/B-VIII.1	0.1696(8)	14.07(35)	586.2(29)	99.4(2)
relat. uncert.	0.5%	2.5%	0.5%	0.2%
ENDF/B-VIII.0	0.1694(10)	14.11(37)	586.7(37)	99.4(2)
relat. uncert.	0.6%	2.6%	0.6%	0.2%
ENDF/B-VII.1	0.1687(27)	15.11(77)	585.0(20)	98.7(16)
relat. uncert.	1.6%	5.1%	0.3%	1.6%
Standards [1]	0.1694(22)	14.1(2)	587.3(14)	99.5(13)
relat. uncert.	1.3%	1.4%	0.2%	1.3%
Duran [82, 83]	0.1711(43)	14.3(5)	586.1(26)	100.3(25)
relat. uncert.	2.5%	3.5%	0.4%	2.5%
Lounsbury [84–86]	0.1697(29)	–	–	–
relat. uncert.	1.7%	–	–	–
Adamchuk [248]	0.1690(35)	–	–	–
relat. uncert.	2.1%	–	–	–

b. (n,f) Prompt Fission Neutron Spectrum

The ^{235}U PFNS at thermal neutron energies was carried over from ENDF/B-VIII.0. This PFNS evaluation by the IAEA [44, 246, 247] was obtained as part of the IAEA standard effort by a least-squares analysis of experimental data and their covariances and adjusting the high-energy tail above 10 MeV to reproduce the evaluated ^{90}Zr(n,2n) spectrum averaged cross section in the standard ^{235}U(n_{th},f) neutron field. The physical origin of the PFNS high-energy neutrons above 10 MeV is still being clarified. It seems very unlikely that those neutrons are emitted during the deexcitation of fission fragments. An excellent agreement was found between evaluated PFNS and measured spectrum averaged cross section data of very high threshold dosimetry reactions [249], which explicitly supports the IAEA PFNS thermal evaluation. Further investigations are warranted.

PFNS at all other energies were reevaluated as described in Ref. [250]. This evaluation builds on PFNS work included in ENDF/B-VIII.0 and documented in detail in Ref. [70]. The main difference is the inclusion of final high-precision ^{235}U PFNS measured by the Chi-Nu team of LANL and LLNL [251]. For ENDF/B-VIII.0, preliminary Chi-Nu PFNS were included for PFNS above incident neutron energies, $E_{\rm inc}$, of 5 MeV; these prelim-

inary data were only going up to outgoing neutron energies, E_{out}, of 2 MeV. Now, the final Chi-Nu data are included for E_{inc} = 2–10 MeV and up to E_{out} of 10 MeV. Previously available data sets were measured at a limited incident neutron energy range or had larger uncertainties.

The newly evaluated PFNS shown in Fig. 58(a) follow closely ENDF/B-VIII.0 for $E_{inc} < 6$ MeV except for a small decrease of the PFNS for $E_{out} > 7$ MeV which reflects Chi-Nu data's shape. This decrease leads to a modest criticality reduction of Godiva, Flattop and BigTen k_{eff} values by 52(11), 40(13) and 31(13) pcm [250].

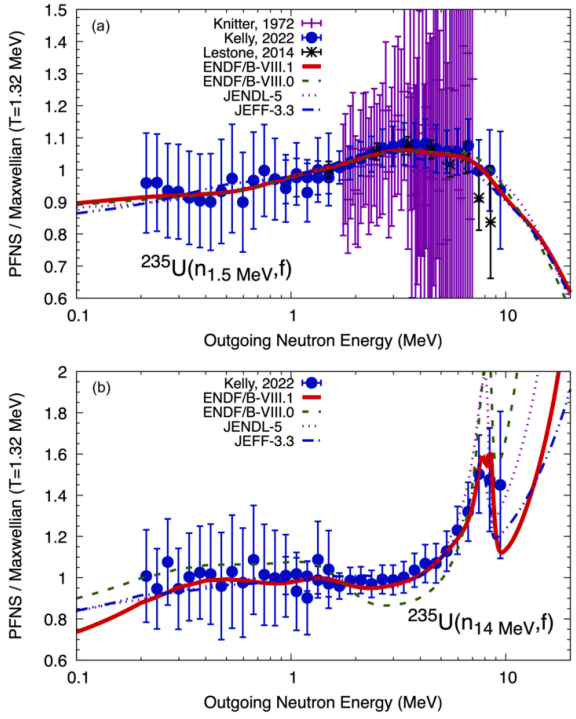


FIG. 58. Experimental data [65, 251, 252] and evaluated ^{235}U PFNS for E_{inc}=1.5 (a) and 14 MeV (b).

The changes from ENDF/B-VIII.0 at higher E_{inc} are more pronounced as can be seen in the mean energy of the PFNS (Fig. 59) and individual PFNS (Fig. 58(b)). The distinct change around E_{inc} of 14 MeV led to improvements in predicting ^{235}U LLNL 14-MeV pulsed sphere neutron leakage spectra in the valley after the peak, in Ref. [250, Figs. 10 and 11], and shown later in Fig. 226.

Evaluated PFNS covariances are provided for five E_{inc} bins. Their mean energy uncertainties, $\delta\langle E\rangle$, are lowest in Table XIV at thermal and from 0.5–5 MeV, where most experimental data are available. In the E_{inc} bin spanning 0.5–5 MeV, the low uncertainties are driven by Chi-Nu (K.J. Kelly) and Lestone data at 1.5 MeV [65, 251]. In fact, the too-low uncertainties resulting from an evaluation with the Los Alamos model were increased to match Lestone uncertainties from E_{out} = 5–8 MeV, which have the lowest ^{235}U PFNS uncertainties (Fig. 60).

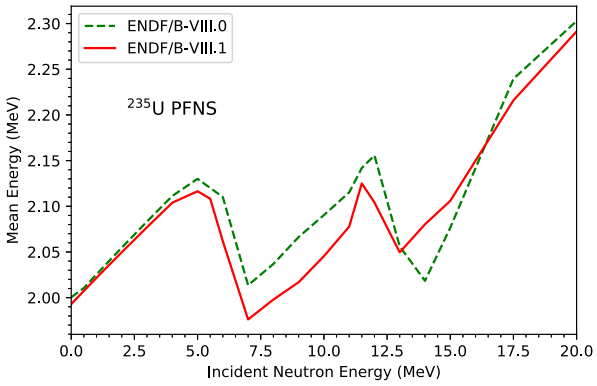


FIG. 59. Evaluated ^{235}U PFNS mean energy.

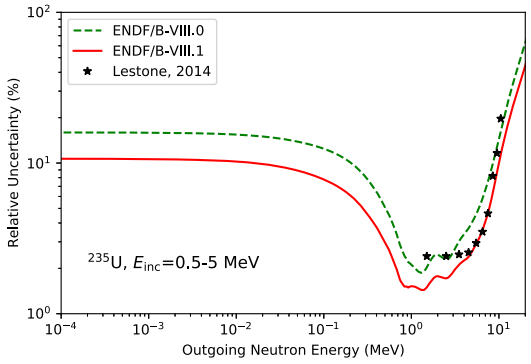


FIG. 60. Evaluated ^{235}U PFNS uncertainties for E_{inc}=0.5–5 MeV compared to experimental data of Ref. [65].

c. *(n,f) Fission $\overline{\nu}$*

The thermal $\overline{\nu}_{tot}$ in the new evaluation was slightly reduced to 2.42685, which is 0.13% lower than the ENDF/B-VIII.0 value. The newly adopted value is in agreement with the thermal neutron constant value of 2.425(0.011) within uncertainties [1]. Following the ENDF/B-VIII.0 evaluation, the Reed experimental data [253, 254] renormalized to the above-discussed thermal value is used to define the $\overline{\nu}$ energy dependence below 20 eV. ENDF/B-VIII.0 nubar fluctuations from about 20 eV up to 500 eV were replaced by linear interpolation as shown in Fig. 61. The tweak used in ENDF/B-VIII.0

TABLE XIV. The mean energy uncertainties, $\delta\langle E\rangle$, for the ^{235}U PFNS are listed per incident-neutron energy, E_{inc}.

E_{inc} (MeV)	$\delta\langle E\rangle$ (keV)
Thermal	10
0.5–5	24
5–7	57
7–12	39
12–30	43

evaluation for the negative resonance at 2 eV was eliminated.

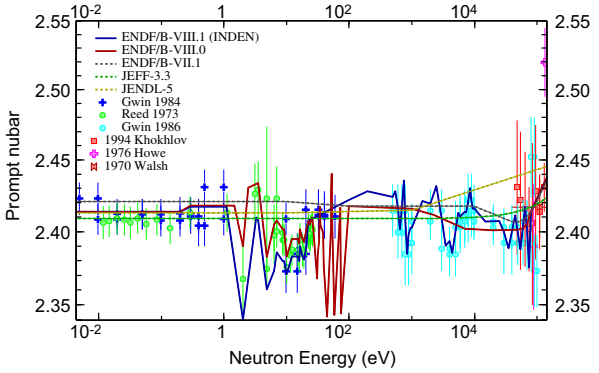


FIG. 61. Reed [253, 254] and Gwin *et al.* [40] experimental data versus evaluated ^{235}U $\overline{\nu}$ below 100 keV.

Gwin nubar data [40] were directly used from 500 eV up to 80 keV, leading to a significant reduction of the nubar uncertainty to values from 0.6% up to 0.8% in that region in the new evaluation (from about 2% in ENDF/B-VIII.0 to roughly the uncertainty of Gwin's experiment) as shown in Fig. 62. Overall, the evaluated ^{235}U $\overline{\nu}$ uncertainty was reduced compared to ENDF/B-VIII.0 except for the fast neutron range above 80 keV. The ENDF/B-VIII.1 evaluated $\overline{\nu}$ uncertainties in Fig. 62 are distinctly larger above 80 keV due to the increased $\overline{\nu}(^{252}\text{Cf(sf)})$ standard uncertainties (0.42%). The correlation matrix is strongly correlated due to the full correlation stemming from the dominant ^{252}Cf(sf) standard uncertainties.

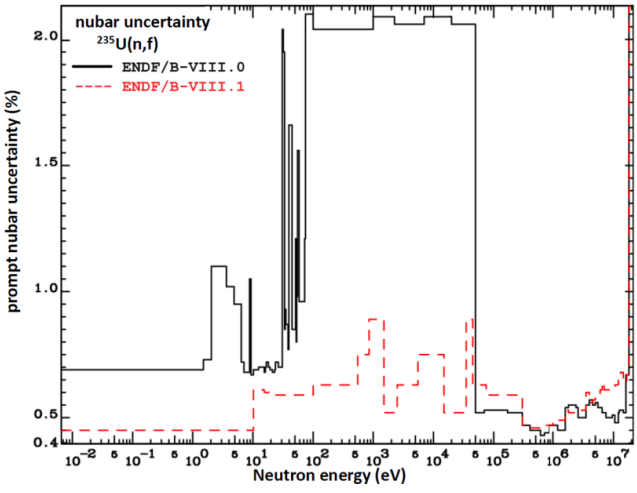


FIG. 62. Evaluated ^{235}U $\overline{\nu}$ uncertainty.

The neutron-induced average prompt fission neutron multiplicity, $\overline{\nu}$, for ^{235}U was reevaluated from scratch for ENDF/B-VIII.1 [48, 255]. Uncertainties for all experimental data were reevaluated in detail using the literature of data sets as well as templates of expected $\overline{\nu}$ measurement uncertainties [49]. It was unclear what data were used for the previous ENDF/B-VII.1 evaluation, but all data currently in EXFOR were re-visited [45]. Also, similar to the ^{239}Pu $\overline{\nu}$ evaluation, the `CGMF` fission-event generator [50] was used as model to evaluate the $\overline{\nu}$. Including that model into the evaluation made it possible to employ evaluated model parameters to compute other fission quantities, such as yields as a function of mass, the average total kinetic energy of fission fragments, etc. It was shown in Ref. [255] that most of these predicted fission quantities agree well with experimental data except for the PFNS – a known model deficiency that is being investigated. This combined new information led to changes from ENDF/B-VIII.0 (Fig. 63)—on the order of 0.5% up to 5 MeV. The changed $\overline{\nu}$ resulted originally in an increase in Godiva k_{eff} by 114(10) pcm. However, $\overline{\nu}$ was tweaked from 2.5–5.5 MeV where the model stiffness led to a departure from the evaluation with only experimental data [255]. The tweaked $\overline{\nu}$ changes Godiva k_{eff} by 31(10) pcm. The finally adopted $\overline{\nu}$ was further reduced at the IAEA by about 0.1% from 2.5–3 MeV to reduce Godiva k_{eff} by 30 pcm to 1.00009(10).

12. ^{238}U

A focused international effort on the evaluation of neutron induced reactions on ^{238}U target adopted for the ENDF/B-VIII.0 library was coordinated by the IAEA within the CIELO project [242]. The IAEA CIELO evaluation was described by Capote *et al.* [67] and Chadwick *et al.* [189]. ^{238}U cross section evaluation in the fast neutron range remains unchanged for ENDF/B-VIII.1. PFNS and $\overline{\nu}$ were revisited as described below. Changes were also undertaken in the resonance region driven by identified deficiencies in ENDF/B-VIII.0 evaluations for depletion in power reactors [39].

a. Thermal and Resonance regions

One of the identified deficiencies of the ^{238}U CIELO evaluation was the -500 pcm criticality swing at high burnup (exposures higher than 60 MWd/kgU) relative to the ENDF/B-VII.1 reference value [39]. It was clearly stated by Kim *et al.* that such swing precluded the use of the ENDF/B-VIII.0 library for power reactor calculations [39]. A solution of the *burnup* problem became a high priority for next generation nuclear data libraries, and special attention was paid to this problem within the INDEN collaboration with inputs from both JEFF and ENDF research groups. The -500 pcm reactivity swing was partially tracked down to the insufficient ^{239}Pu production via neutron capture on the ^{238}U. This reduced ^{239}Pu production was due to the reduced capture from 100 eV up to 20 keV in the CIELO evaluation of n+^{238}U resonance parameters. Two solutions were discussed within the INDEN collaboration: changing the resonance gamma widths or changing the resonance parameters above the 100 eV.

For the ENDF/B-VIII.1 library, the n+^{238}U resonance parameters proposed by our Japanese colleagues for the

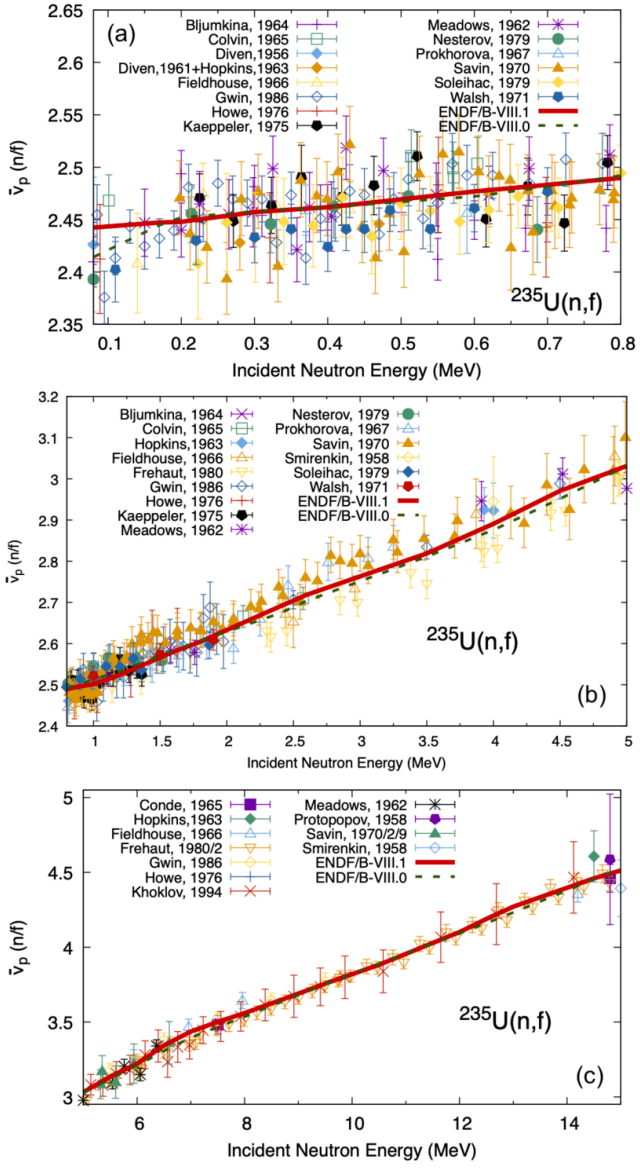


FIG. 63. Experimental and evaluated ^{235}U $\overline{\nu}$ shown for three relevant incident neutron energy ranges: ∼100 keV to 800 keV in panel (a); ∼1 MeV to 5 MeV in panel (b); and ∼5 MeV to ∼15 MeV in panel (c). Experimental data from Refs. [234, 235, 238, 240, 256–272]

JENDL-5 library [16] were adopted. Reconstructed ^{238}U capture cross sections of the JENDL-5 evaluation are shown in Fig. 64 as a ratio to the ENDF/B-VIII.0 CIELO cross sections. No changes were made to resonance parameters below 100 eV, and reconstructed cross sections are practically identical to ENDF/B-VIII.0 below 100 eV preserving the criticality at zero power (BOL). However, a 1% to 3% increase in the average capture cross sections is observed in the figure from 100 eV up to 20 keV, which increases significantly the ^{239}Pu production in reactors via neutron capture on the ^{238}U. This change of capture cross sections (resonance parameters), combined with additional changes in the ^{239,240,241}Pu cross sections, flattens the calculated depletion (e.g., see Figs. 203 and 207 in Section XIV D), largely eliminating the *burnup* problem.

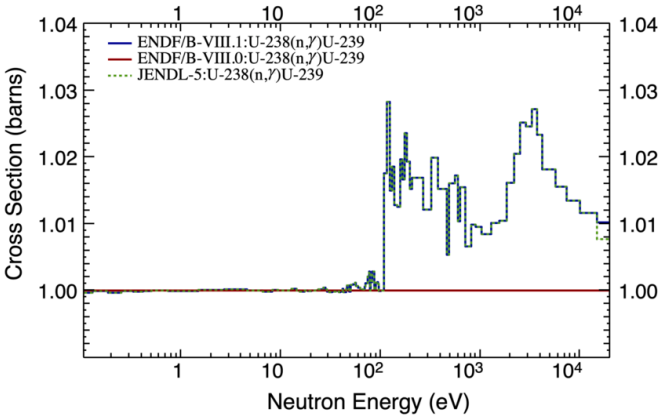


FIG. 64. Group averaged capture cross sections of the JENDL-5 library [16] and the ENDF/B-VIII.1 new library in the resolved resonance region of ^{238}U as a ratio to the ENDF/B-VIII.0 cross sections.

b. Fission cross section

^{238}U neutron induced fission cross section is an standard reaction [1]. Three new time-of-flight measurements of the ^{238}U(n,f)/^{235}U(n,f) fission cross-section ratio in three different laboratories have been published since the ENDF/B-VIII.0 release: a measurement using a newly developed TPC detector by Casperson *et al.* [273] at WNR neutron source in LANL, USA; a measurement by Ren *et al.* [274] using the Back_n neutron flight path at the China Spallation Neutron Source; and a measurement by Vorobyev *et al.* [275] at the GNEIS neutron complex based on the 1 GeV proton synchrocyclotron in Russia. The three measured ^{238}U(n,f) cross sections have been derived by multiplying the measured ratio by the standard ^{235}U(n,f) cross section and are compared with the ^{238}U(n,f) ENDF/B-VIII.0 cross section in Fig. 65 from 0.5 MeV up to 30 MeV. An excellent agreement is observed inspiring confidence in the neutron standard evaluation [1]. Note that the ^{238}U(n,f) cross section is standard above 2 MeV [1]. ENDF/B-VIII.1 evaluated cross sections are identical to the ENDF/B-VIII.0. Only the neutron multiplicity changed as described below.

c. (n,f) Prompt Fission Neutron Spectrum

New Chi-Nu PFNS experimental data measured at LANL in collaboration with LLNL were recently published [276]. A new LANL evaluation [277] was finalized in spring 2024 and will be reviewed for inclusion into ENDF/B-IX.0. For ENDF/B-VIII.1, the ^{238}U PFNS evaluation was carried over from ENDF/B-VIII.0 with the exception of adopting the JENDL-5 PFNS evaluation [16] from 5 MeV up to 8 MeV to consistently follow the JENDL-4 (JENDL-5) evaluation above the first chance fission. Note that the JENDL-4 (JENDL-5) PFNS was

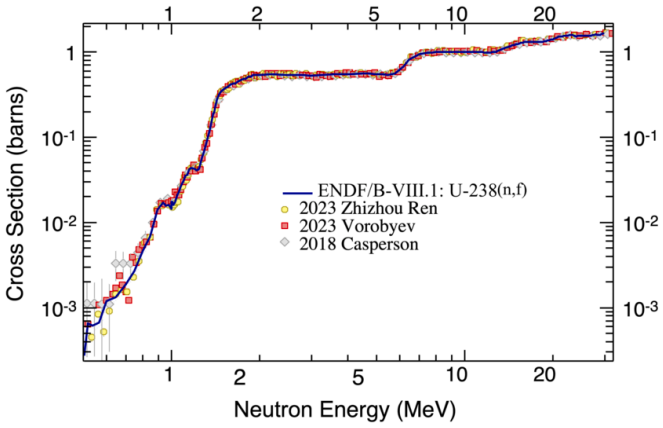


FIG. 65. New experimental data since 2018 [273–275] are compared to the ENDF/B-VIII.1 ^{238}U(n,f) cross section, which is identical to the evaluated ENDF/B-VIII.0 and includes the standard energy range from 2 MeV up to 200 MeV.

already adopted in ENDF/B-VIII.0 above 8 MeV. This change improves the agreement with measured Livermore Pulsed Sphere response.

d. (n,f) fission $\overline{\nu}$

Three different evaluations were considered for ENDF/B-VIII.1 ^{238}U $\overline{\nu}$ in the fast range: ENDF/B-VIII.0, JENDL-5 and a new LANL evaluation [278]. Open questions remain; namely, there is a large spread in trustworthy experimental data below 5 MeV, and no new experimental data are available. ENDF/B-VIII.0 follows Frehaut *et al.* data around 2 MeV as can be seen in Fig. 66.

The new LANL evaluation [278] based on the experimental data shown (including Frehaut data but also the 2% higher data by Nurpeisov *et al.* and Vorobyeva *et al.*) would indicate a significantly (2%) higher $\overline{\nu}$ value around 2 MeV as does JENDL-5 data in Fig. 67. LANL evaluators took the cautious approach of not recommending their new evaluation as long as we have no new experimental data. Simulation studies by the IAEA indicated that a change in ^{238}U $\overline{\nu}$ would be beneficial for benchmark performance, especially considering the criticality decrease associated with the new ^{234}U evaluation. So, a pragmatic approach was adopted by the IAEA team that used trends seen across all three evaluations for different energy regions. This approach is described below.

The LANL evaluation [48, 255, 278] was done from scratch; uncertainties for all experimental data were re-evaluated in detail using the literature of data sets as well as templates of expected $\overline{\nu}$ measurement uncertainties [49]. All data currently in EXFOR were re-visited. Despite discussions with experimenters, no clear conclusion could be reached on the spread in data below 5 MeV. Similar to the ^{239}Pu $\overline{\nu}$ evaluation, the CGMF fission-event generator [50] was used as a model to evaluate $\overline{\nu}$. The model information combined with experimental data led to significant changes from the ENDF/B-VIII.0 evaluation as shown in Fig. 67 – over 2% at 3 MeV. As can be

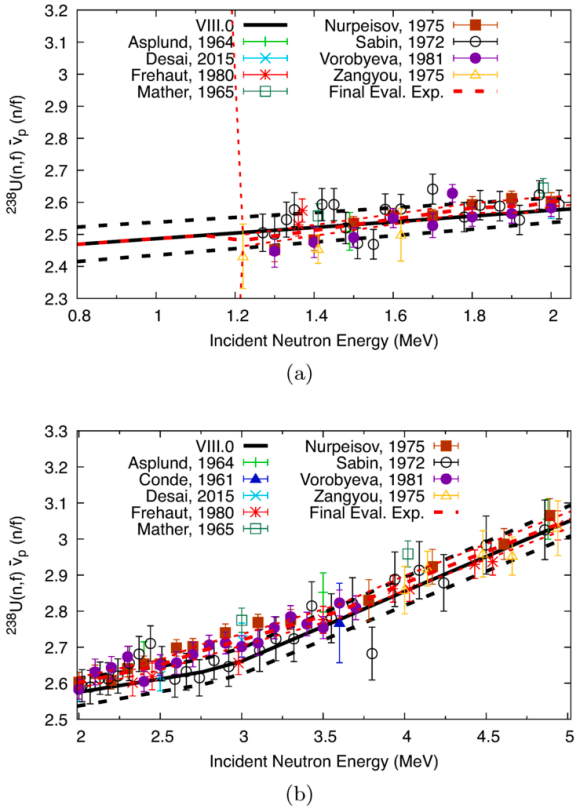


FIG. 66. Selected experimental data [261, 279–287] are compared to ENDF/B-VIII.0 and a LANL ^{238}U $\overline{\nu}$ evaluation based on only experimental data shown. Panel (a) spans from 0.8 MeV to 2.5 MeV and (b) from 2 MeV to 5 MeV. Plots were taken from Ref. [278].

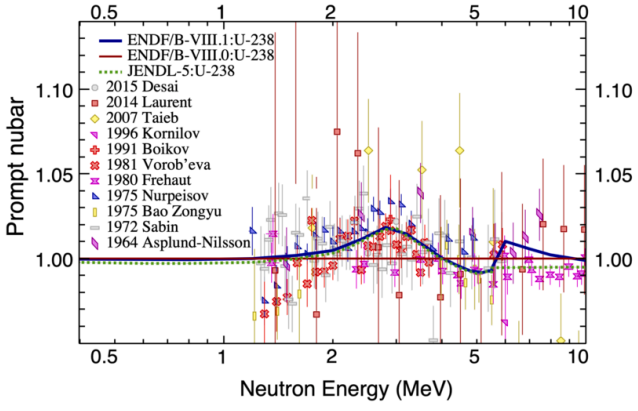


FIG. 67. Selected experimental data [261, 279–291] and evaluated ^{238}U $\overline{\nu}$ as a ratio to the ENDF/B-VIII.0 ^{238}U $\overline{\nu}$ evaluation.

seen from Fig. 66, this large change is mostly driven by experimental data. A sudden increase of the evaluated neutron multiplicity is observed relative to the ENDF/B-VIII.0 evaluation going from -1% at 5 MeV to +1% at 6 MeV – a 2% increase. The observed increase washes out around 9 MeV.

The $\overline{\nu}$ was tweaked by the IAEA team. The changed values are well within evaluated uncertainties. The goal of this modification was to improve the BigTen C/E (calculation/experiment ratio) benchmark performance whilst keeping the good ENDF/B-VIII.0 performance for Jemima benchmarks. We checked that the region below 1.5 MeV of neutron incident energy has no impact on BigTen criticality as the ^{238}U(n,f) cross section is too small. Therefore, we adopted ENDF/B-VIII.0 $\overline{\nu}$ evaluation below 1.4 MeV, which is consistent with the new LANL evaluation. Above, we started from the JENDL-5 evaluation [16] as its performance was closer to our target. Tweaked values are within 0.1% of the JENDL-5 evaluation from 1.4 MeV up to 5 MeV. At 5 MeV, the JENDL-5 evaluation is almost 1% lower than the ENDF/B-VIII.0 evaluation as shown in Fig. 67. Following the LANL evaluation and theoretical insights, we have increased $\overline{\nu}$ above 5 MeV to about 0.3% larger than ENDF/B-VIII.0 (almost 1% higher than the JENDL-5 at 6 MeV). There is an increase in the LANL evaluation around the second chance fission threshold in Fig. 67 that, while lying within the spread of shown data, would benefit from additional (future) experimental information.

Summarizing, the tweaked $\overline{\nu}$ agrees with ENDF/B-VIII.0 below 1.4 MeV, and it is within 0.1% of the JENDL-5 evaluation from 1.4 MeV up to 5 MeV, also following a trend seen in the LANL evaluation. The ENDF/B-VIII.1 evaluation is similar in shape to the increase observed in the LANL evaluation above 5 MeV but with a lower amplitude at 6 MeV and slightly larger value above 8 MeV.

The 2% increase of the ^{238}U $\overline{\nu}$ at 3 MeV was partially compensated in fast assemblies' criticality by the significant increase in newly evaluated ^{234}U capture in the fast region. The ^{238}U $\overline{\nu}$ increase also played a positive role in the reactivity increase of critical lattices (LCT benchmarks) by about 70 pcm compared to the ENDF/B-VIII.0 performance. Lattice criticality will be discussed in the validation section.

13. ^{240,241}Pu

Deficiencies found in the resonance region evaluation of ^{240,241}Pu isotopes led to changes described below. These changes were proposed for the JEFF-4 library and were also adopted here. From the application's point of view, the changes were important to increase criticality of Pu thermal systems at high burnup.

a. Resolved resonance range of ^{240}Pu

An update to the ^{240}Pu resonance parameters up to 5.7 keV was a necessity for reducing the calculated reactivity of some thermal critical benchmarks, such as PST018 from the ICSBEP database, and improving the prediction of ^{244}Cm buildup in spent nuclear fuel inventory. The resonance analysis was performed with the CONRAD code using data available in the EXFOR database [45]. For the first resonance of ^{240}Pu, close to 1.06 eV, we have used ^{239}Pu transmission data measured by Spencer (L=18 m, 1987) [292] and two sets measured by Harvey (L=18 m, 1985 and 1988) [73] in which ^{240}Pu is an impurity (Fig. 68). Two transmission data from Kolar (L= 100 m, 1968) [293] and a fission cross section from Weston (1984) [294] were also included in the fitting procedure. Prior resonance parameters were taken from the JEFF-3.3 library [64]. The results leads to a thermal capture cross section σ_γ of 285.6 barns. The capture resonance integral (I_γ=8829 barns) increases by +4.1% compared to ENDF/B-VIII.0 value.

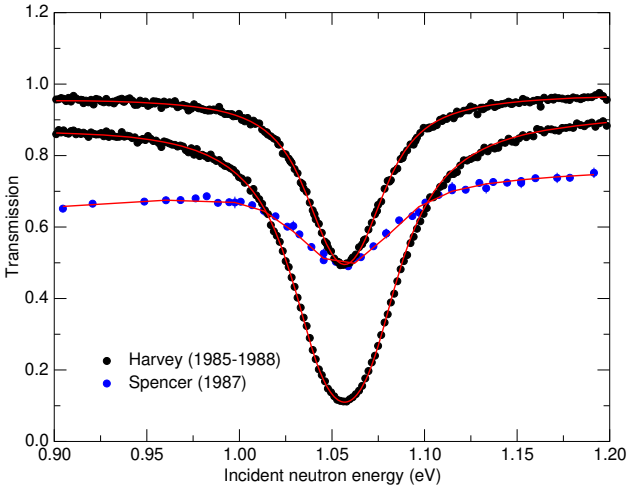


FIG. 68. CONRAD analysis of three ^{240}Pu transmission experiments (1st resonance at 1.06 eV) taken from the EXFOR database.

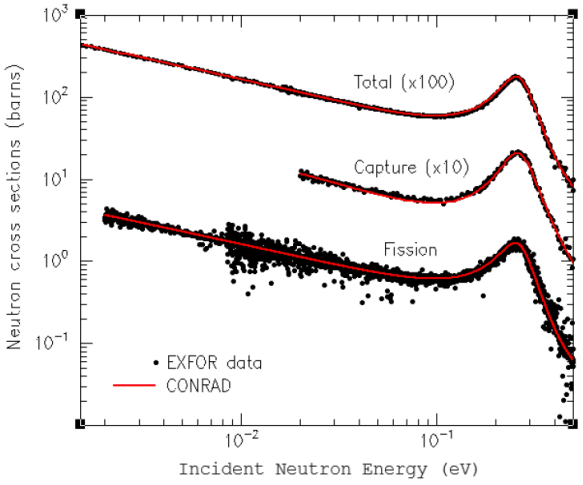


FIG. 69. Comparison of the CONRAD results with experimental data available in the EXFOR database for total, fission and capture neutron cross sections of ^{241}Pu.

b. Resolved resonance range of ^{241}Pu

The need for revisiting the ^{241}Pu resonance range up to 300 eV emerged mainly from the underestimation of the calculated reactivity in power reactors at high burn up.

At the same time, the Thermal Neutron Constants were updated according to works done in the framework of the neutron Standard group of the IAEA [1, 82]. Most of the EXFOR data reported since the 1950s were included in the CONRAD analysis. The transmission data come from Harvey (1972), Kolar (1971), Pattenden (1963) and Simpson (1961). A few total cross sections from Smith (1970), Young (1968) and Craig (1964) were also included for the 1^{st} resonance. For fission, we used data sets from Wagemans (1976, 1991), Weston (1978), Blons (1971), Migneco (1970), James (1965), Watanabe (1964), Raffle (1959), Leonard (1959), Seppi (1958), Richmond (1956) and Adamchuk (1955). In contrast, a single capture data set was reported by Weston (1978).

TABLE XV. n+^{241}Pu 2200 m/s thermal cross sections for three nuclear data libraries compared with the Thermal Neutron Constants derived by the Standard group [1] and Duran *et al.* estimates [82, 83]. Note that the ENDF/B-VIII.0 evaluation was adopted from ENDF/B-VII.1.

Source	α_{therm} (b)	σ_{el} (b)	σ_f (b)	σ_c (b)
ENDF/B-VIII.1	0.3554	12.0	1023.7	363.8
relat. uncert.	2.5%	10%	1.5%	2.0%
ENDF/B-VIII.0	0.3586	11.23	1012.3	363.0
relat. uncert.	2.5%	10%	1.5%	2.0%
JEFF-3.3	0.3586	11.26	1012.3	363.0
relat. uncert.	–	5%	2.0%	–
Standards [1]	0.3539(79)	11.9(26)	1023.6(108)	362.3(61)
Duran [82, 83]	0.3550(36)	11.5(15)	1018.9(25)	361.7(36)

Evaluated cross section for all libraries show good agreement with standard values [1] as well as with thermal cross sections recommended by Duran *et al.* [82, 83] as shown in Table XV. For the resonance integrals, the one for fission (I_f = 588.8 barns) increases by +3.3% compared to the ENDF/B-VIII.0 evaluation, while the one for capture (I_γ = 176 barns) decreases by −2.3%, accordingly. Such changes increase significantly the resonance α value, and therefore, the reactivity in reactors at high-burnup.

C. Non-INDEN evaluations

1. ^3He

An updated evaluation for the n+^{3}He reactions was submitted for ENDF/B-VIII.1. The primary purpose of the update was to add angular distributions for the reactions for which only integrated cross sections had been given in ENDF/B-VIII.0. However, in the process, small changes were made in the integrated cross section for the ^{3}He$(n,p)^3$H reaction above about 8 MeV and in the ^{3}He$(n,d)^2$H reaction above about 12 MeV neutron energy. This occurred because we adopted the evaluated differential cross sections of Drosg and Otuka [295] for those reactions in the MeV region, including the integrated cross sections. No changes were made in the ^{3}He$(n,p)^3$H cross section in the region where it is a standard ($E_n \leq 50$ keV).

In addition, we calculated angular distributions for the ^{3}He$(n,\gamma)^4$He reaction from the parameters of the ^{4}He R-matrix analysis that had been used to fit the capture cross section data. The mass of the ^{3}He target was changed to the nuclear mass, and the energy of the outgoing gamma-ray at zero incident neutron energy was adjusted accordingly. These changes made the evaluation more useful for tracking charged particles that are produced by neutrons incident on ^{3}He.

2. ^6Li

The new evaluation for n+^{6}Li reactions is based on an R-matrix analysis of reactions in the ^{7}Li system at excitation energies up to E_x = 14.1 MeV, which corresponds to E_n = 8 MeV. The analysis included six arrangement channels, as shown in the top part of Table XVI. The lower part of the table summarizes the data analyzed for each of the nine reactions included. The fit to more than 6300 data points has a χ^2 per datum of 1.39, or χ^2 per degree-of-freedom is 1.43 for 170 parameters.

TABLE XVI. Channel configuration (top) and data summary (bottom) for each reaction in the ^{7}Li system R-matrix analysis. The projectile energy E_{proj} range given in the second column of the lower panel corresponds to the laboratory bombarding energy of the projectile corresponding to either trition E_t or the neutron E_n energies.

Channel	$l_{\max}$	a_c (fm)
t+^{4}He	5	4.0
n+^{6}Li	3	5.0
d+^{5}He	1	7.5
n+^{6}Li*	1	5.0
p+^{6}He	1	5.0
n+^{6}Li**	1	5.5

Reaction	E_{proj} (MeV)	Observables	# data	χ^2/pt.
^{4}He$(t,t)^4$He	3 − 17	$\sigma(\theta), A_y(\theta)$	1689	1.03
^{4}He$(t,n_0)^6$Li	8.75 − 14.4	$\sigma(\theta)$	39	1.14
^{4}He$(t,n_1)^6$Li*	8.75 − 14.4	$\sigma(\theta)$	3	0.42
^{6}Li$(n,t)^4$He	0 − 8	$\sigma_{\rm int}, \sigma(\theta)$	2840	1.44
^{6}Li$(n,n_0)^6$Li	0 − 8	$\sigma_{\rm int}$, $\sigma_{\rm T}, \sigma(\theta), P_y(\theta)$	1451	1.36
^{6}Li$(n,d)^5$He	3.4 − 8	$\sigma_{\rm int}, \sigma(\theta)$	28	11.9
^{6}Li$(n,n_1)^6$Li*	3.4 − 8	$\sigma_{\rm int}, \sigma(\theta)$	175	2.11
^{6}Li$(n,p)^6$He	3.2 − 9	$\sigma_{\rm int}, \sigma(\theta)$	92	1.58
^{6}Li$(n,n_2)^6$Li**	4.2 − 7	$\sigma_{\rm int}$	41	0.30
Totals	2268	17	6358	1.39

We show in the following only the integrated neutron cross sections that changed significantly in ENDF/B-VIII.1. However, it should be noted that a very good fit was maintained to the high-precision $t+\alpha$ elastic scattering data included, except at the highest energies (∼ 17

MeV). Generally speaking, the fits to the angular distributions for the neutron-induced reactions were also quite good, especially for the ^{6}Li$(n,t)^4$He reaction measured by Bai *et al.* [296] in the energy range $0 < E_n \leq 3$ MeV. Some measurements of the neutron angular distributions at higher energies were in significant disagreement, however.

The ^{6}Li$(n,t)^4$He cross section is shown in Fig. 70 at energies up to 20 MeV. Below 1 MeV, it is unchanged from the standards cross section determined for ENDF/B-VIII.0 [297]. It becomes substantially different above 1 MeV, especially in the 4–8 MeV region, which is above the range of the previous R-matrix analysis. This is illustrated in Fig. 71, where it can be seen that a prominent peak in the ENDF/B-VIII.0 cross section at around 6 MeV is no longer present. This makes the new evaluation consistent with older ENDF/B evaluations and with the IRDFF-II evaluation [2] (see Ref. [2, Fig.75]). The level structure of the decreasing cross section in the MeV region is rather subtle and not clearly defined because of disagreements among the different data sets. The shoulder at around 2 MeV and the broad rise at around 4.5 MeV come from $J^\pi = 3/2^-$ levels that are more evident in other cross sections.

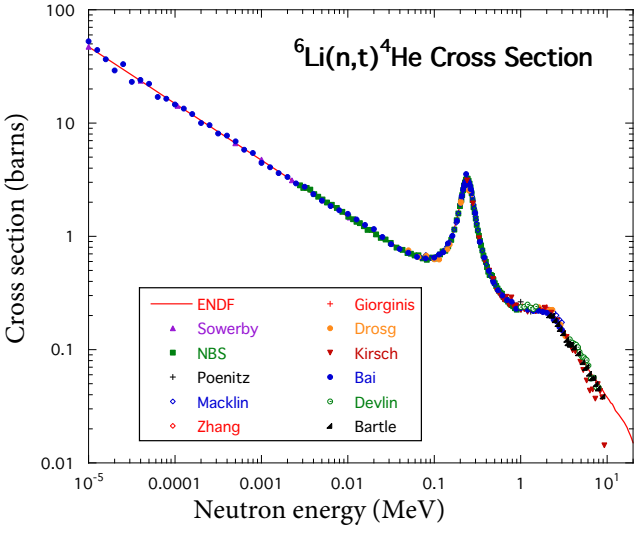


FIG. 70. Measurements of the ^{6}Li$(n,t)^4$He cross section compared to the ENDF/B-VIII.1 evaluation at incident neutron energies between 10 eV and 20 MeV. The experimental data are from Refs. [153, 296, 298–306].

Figs. 72 and 73 show the cross sections for the ^{6}Li$(n,p)^6$He and ^{6}Li$(n,n_2)^6$Li** reactions in which the effects of the higher-energy $3/2^-$ levels in the 4–5 MeV region are clearly seen. The double-peak structure of the interfering $3/2^-$ levels does not show up in the (n,n_2) reaction because its threshold is too high.

Finally, we show in Fig. 74 the three-body breakup cross section, ^{6}Li$(n,n')d\alpha$, which in this evaluation is represented by the sum of a continuum contribution from the $d+^5$He channel and one from the $n+^6$Li* channel in the

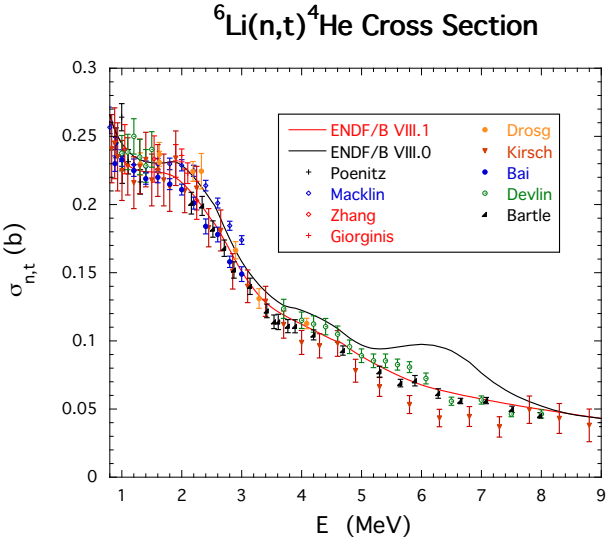


FIG. 71. Comparison of measurements of the ^{6}Li$(n,t)^4$He cross section to the ENDF/B-VIII.1 evaluation and to ENDF/B-VIII.0 at incident neutron energies between 1 and 9 MeV.

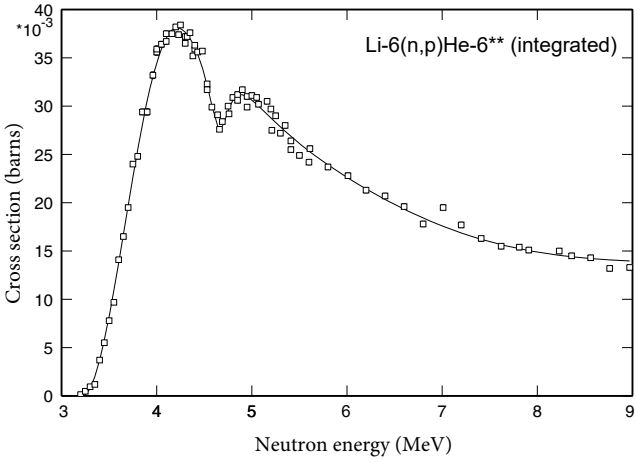


FIG. 72. Measurements of the ^{6}Li$(n,p)^6$He cross section compared to the ENDF/B-VIII.1 evaluation at incident neutron energies between 3 and 9 MeV. The experimental data are from Presser *et al.* [307].

$n+d+\alpha$ final state. The cross section is somewhat lower than before (blue dashed curve) and shows the double-peak structure of the interfering $3/2^-$ levels in the 4–6 MeV region.

Covariances were not updated from those in ENDF/B-VIII.0 library.

3. ^{9}Be

The current ENDF/B-VIII.1 file is identical to the previous ENDF/B-VIII.0 with two exceptions: *i)* the neu-

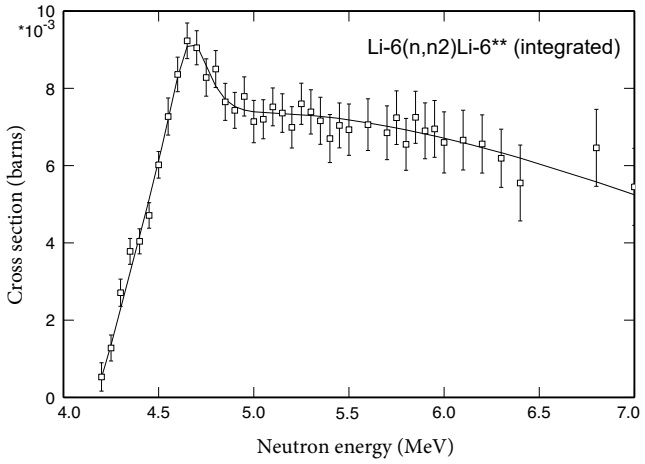


FIG. 73. Measurements of the ^{6}Li$(n,n_2)^{6}$Li** cross section compared to the ENDF/B-VIII.1 evaluation at incident neutron energies between 4 and 7 MeV. The experimental data are from Presser *et al.* [307].

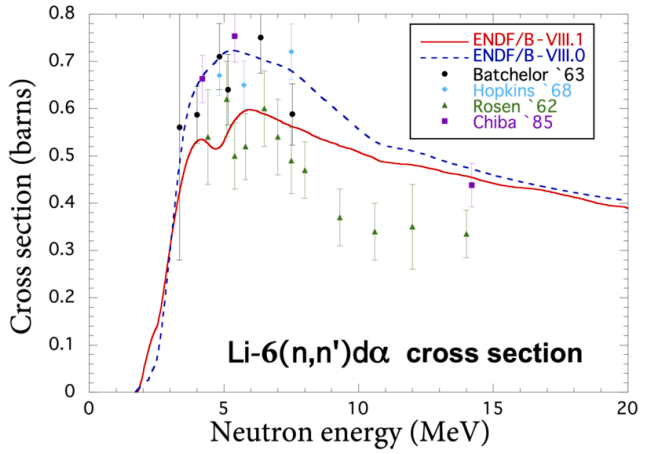


FIG. 74. Measurements of the ^{6}Li(n,n′)dα cross section compared to the ENDF/B-VIII.1 and ENDF/B-VIII.0 evaluations at incident neutron energies between 0 and 20 MeV. The experimental data are from Refs. [308–311].

tron capture cross section (MF=3, MT=102) has been updated to include more recent data in the resonance region; this has resulted in a smaller cross section in the thermal-capture, $1/v$-region, with energies $E \lesssim 10^{-2}$ MeV, than the previous evaluation; and *ii)* the total cross section (MF=3, MT=1) has been updated in accordance with the changes to (n,γ) capture, which are small relative to the total for most of the energy region.

The current evaluation is based on the previous R-matrix evaluation, to which the γ+^{10}Be partition was added, with channels sufficient to cover multipole transitions E_ℓ and M_ℓ with $\ell = 1, 2, 3$. This single added channel treats the γ production as an inclusive (or "lumped") channel, as the sum over all possible ^{10}Be excited-state transitions. Observed data has been included in the evaluation from Refs. [312–316]. The data point labeled 25 keV MACS is from Ref. [315], with its energy transformed from the center of mass value of 25 keV to the laboratory frame value of 27.78 keV, as shown in Table XVII.

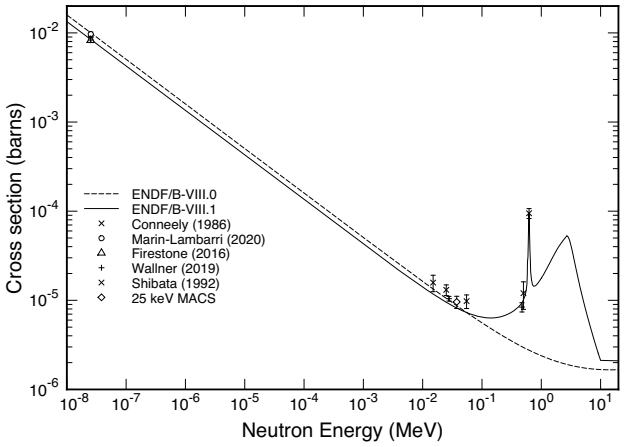


FIG. 75. Comparison of the integrated capture cross section (in barns), ^{9}Be$(n,\gamma)^{10}$Be of the updated evaluation for ENDF/B-VIII.1 to that of ENDF/B-VIII.0 as a function of incident neutron energy E in MeV, compared to the available data. The observed data points in the legend are marked by references given in the text; the legend marked "25 keV MACS" is from Ref. [315].

TABLE XVII. Observed ^{9}Be$(n,\gamma)^{10}$Be capture cross section $\sigma_{(n,\gamma)}$ (in mb and μb) and uncertainty $\delta\sigma_{(n,\gamma)}$. The 30.0 keV data point from the original document of Ref. [313] differs from that given in Ref. [315].

E		$\sigma_{(n,\gamma)}$		$\delta\sigma_{(n,\gamma)}$		Ref.
0.0253	eV	8.49	mb	0.34	mb	[312]
0.0253	eV	9.70	mb	0.53	mb	[316]
0.0253	eV	8.27	mb	0.13	mb	[314]
0.0253	eV	8.31	mb	0.52	mb	[315]
15.0	keV	15.81	μb	3.3	μb	[313]
30.0	keV	13.00	μb	1.8	μb	[313]
55.0	keV	9.79	μb	1.7	μb	[313]
27.8	keV	10.44	μb	0.63	μb	[315]
473	keV	8.4	μb	1.0	μb	[315]
500	keV	12.02	μb	4.1	μb	[313]
622	keV	94.80	μb	12.1	μb	[313]

4. ^{51}V

A ^{51}V resolved resonance evaluation was carried out up to 200 keV based on the reduced R-matrix RM formalism. The ^{51}V resonance evaluation included in the ENDF/B-VIII.0 is listed up to 100 keV. The new evaluation represents an extension of the RRR of 100 keV.

The evaluation uses the $LRF = 7$ resonance parameter format, referred to as the R-matrix Limited (RML) format. ^{51}V is an isotope with ground-state spin and parity of $I^\pi = 7/2^-$ which leads to channel spins and parities, $s^\pi = 3^-$ and $s^\pi = 4^-$, respectively. Below 200 keV, neutron penetration factor shows that angular momentum $l = 0$ and $l = 1$; that is, $s-$, and $p-$ waves contribute the most. The normalized neutron penetration factor for $l = 0$, $l = 1$, and $l = 2$; that is, $s-$, $p-$, and $d-$ waves, at 200 keV are 1, 0.21, and 7.23×10^{-3}, respectively. Clearly, $d-$wave contributions are negligible below 200 keV. For $p-$wave, the total angular momentum; that is, the resonance spin J^π, shows identical values for the spin channels $s^\pi = 3^-$ and $s^\pi = 4^-$ which are $J^\pi = 3^+$, and $J^\pi = 4^+$, respectively. In the ENDF format, this characteristic can only be described by using the format option LRF=7 of the resolved resonance parameters. The evaluation includes resonance parameters covariance using the LCOMP=2 (compact format). Above 200 keV, covariance information was taken from the TENDL library [222].

a. Resonance evaluation

The ^{51}V resolved resonance parameter evaluation was done in the energy range from 10^{-5} eV to 200 keV with the RM methodology included in the code SAMMY [317]. The experimental data used in the evaluation were those carried out at the Geel Electron LINear Accelerator Facility (GELINA) LINAC [318] by Guber *et al.* [319]. They are capture and transmission measurements for which detailed information is available in Ref. [319]. In the energy range below 0.1 eV, measurements covering thermal energy, 0.0253 eV, cross-section data available in the EXFOR [45, 320–322] database were used in the evaluation. The GELINA measurements consisted of two transmissions and two capture yields for natural vanadium. The transmissions data were taken at a flight-path length of 47.64 meters with thickness of 0.016032 at/b and 0.002468 at/b, respectively. Capture yield measurements were performed on a 58.586 meter flight-path with sample thicknesses as mentioned previously. The SAMMY fitting, solid dark line, to the GELINA transmission and capture cross section data, in red, is displayed in Fig. 76 up to 20 keV.

Capture yield data show some structures around the energies 3 keV and 6–7 keV that are not resonances, since they are not shown in the transmission data, but rather are artifacts due to the presence of background filters in the beam and background effects due to sample scattered neutrons which are capture events in the detectors environment. Multiple scattering effects in the capture data are reflected in the SAMMY fit of the data, as can be seen around energy 4.5 keV. Fitting of the transmission and capture yield data in the energy range 50 keV to 150 keV is shown in Fig. 77. In the energy range 90 keV to 110 keV, anomalies are also observed for the 0.002468 at/b capture yield data. This is due to the sulphur background filter.

The ^{51}V resonance parameters obtained in this work were used to calculate some quantities of interest. Thermal capture, scattering and total cross section and resonance integral with uncertainties in connection to the Resonance Parameter Covariance (RPC) derived in this work are presented in Table XVIII.

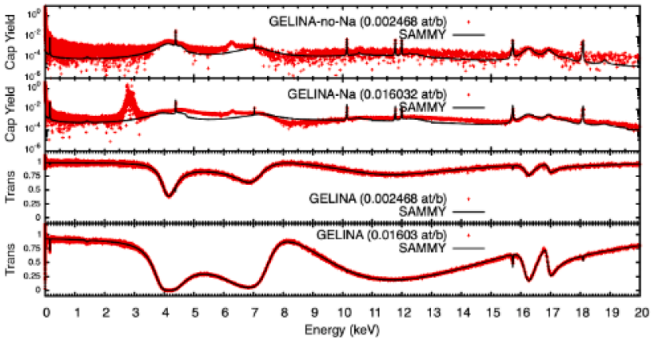


FIG. 76. GELINA transmission and capture yield data up to 20 keV.

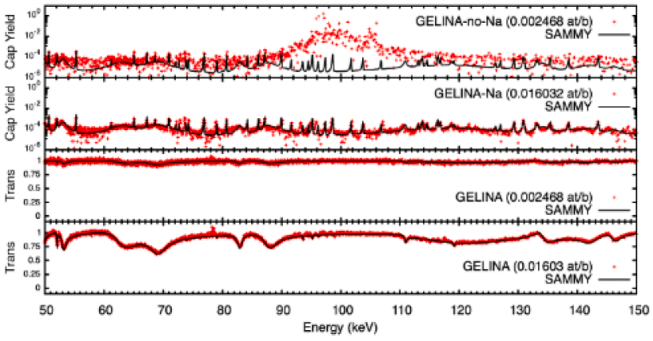


FIG. 77. GELINA transmission and capture yield data from 50 keV to 150 keV.

b. Benchmark results

Very few experiments for which k_{eff} is sensitive to the cross sections of ^{51}V are available in the literature. However, a benchmark evaluation with five different experimental cases from the ICSBEP Handbook (**HMF-025**) [158] shows k_{eff} sensitive to the cross sections of ^{51}V in the fast energy range of neutrons. As a result, various evaluations of ^{51}V cross sections were tested on this benchmark evaluation, using the JEFF-3.3 evaluation as a reference. The calculations were performed with the MORET 5 code

TABLE XVIII. Cross section at thermal (0.0253 eV) and resonance integral for ^{51}V in ENDF/B-VIII.1.

Cross Section (b)	ENDF/B-VIII.1	Atlas [323]
σ_t	9.80(21)	–
σ_γ	4.88(21)	4.94(4)
σ_s	4.92(6)	4.90(6)
I_γ	2.57(23)	–

TABLE XIX. k_{eff} values of the **HEU-MET-FAST-025** benchmark for various evaluations of ^{51}V.

Case	Benchmark	k_{eff}
	Benchmark ± Uncertainty	0.99870 ± 0.00140
	JEFF-3.3	1.00322
1	JEFF-3.3 with ^{51}V from JEFF-4T3	0.99918
	JEFF-3.3 with ^{51}V from ENDF/B-VIII.0	0.99913
	JEFF-3.3 with ^{51}V from ENDF/B-VIII.1	0.99909
	Benchmark ± Uncertainty	0.99900 ± 0.00160
	JEFF-3.3	1.00739
2	JEFF-3.3 with ^{51}V from JEFF-4T3	1.00106
	JEFF-3.3 with ^{51}V from ENDF/B-VIII.0	1.00128
	JEFF-3.3 with ^{51}V from ENDF/B-VIII.1	1.00129
	Benchmark ± Uncertainty	0.99910 ± 0.00160
	JEFF-3.3	1.01184
3	JEFF-3.3 with ^{51}V from JEFF-4T3	1.00237
	JEFF-3.3 with ^{51}V from ENDF/B-VIII.0	1.00371
	JEFF-3.3 with ^{51}V from ENDF/B-VIII.1	1.00386
	Benchmark ± Uncertainty	0.99950 ± 0.00160
	JEFF-3.3	1.01285
4	JEFF-3.3 with ^{51}V from JEFF-4T3	1.00250
	JEFF-3.3 with ^{51}V from ENDF/B-VIII.0	1.00497
	JEFF-3.3 with ^{51}V from ENDF/B-VIII.1	1.00558
	Benchmark ± Uncertainty	0.99910 ± 0.00160
	JEFF-3.3	1.01329
5	JEFF-3.3 with ^{51}V from JEFF-4T3	1.00279
	JEFF-3.3 with ^{51}V from ENDF/B-VIII.0	1.00549
	JEFF-3.3 with ^{51}V from ENDF/B-VIII.1	1.00553

(Monte Carlo standard deviation of 0.00010) [324] using cross sections processed with the `NJOY` code [325]. The results of the testing together with the benchmark k_{eff} and uncertainties are gathered in Table XIX.

It can be concluded from the table that the JEFF-4T3, ENDF/B-VIII.0, and the new ^{51}V evaluation contribute to improve quite significantly the k_{eff} results leading to a good agreement (within experimental uncertainties at 3-σ level) between the calculated k_{eff} and the benchmark k_{eff} at least for cases 1 to 3 and with the three libraries. The agreement is still good for cases 4 and 5 with the JEFF-4T3 library. However, it is a little worse with the ENDF/B-VIII.0 and the new ^{51}V evaluation. The reason for this difference remains unclear since the neutron spectrum and the Energy corresponding to the Average Lethargy of neutrons causing Fission (EALF) values are quite the same for the five benchmark cases. Finally, it can be pointed out that the JEFF-4T3, ENDF/B-VIII.0 and the new evaluation of ^{51}V perform quite similarly.

c. Conclusions

A resonance region evaluation of ^{51}V in the energy range 10^{-5} eV to 200 keV was performed using the computer code `SAMMY`. Measurements taken at the GELINA LINAC were included in the evaluation. Uncertainty and covariance were generated. Issues with the GELINA capture yield measurements below 20 keV precluded a complete analysis and evaluation of the ^{51}V cross sections leading to a higher uncertainty on the capture cross section. However, the use of a more complete representation of the ENDF resonance parameters based on the LRF=7 option makes the evaluation more attractive. It is recommended that new capture cross section data below 20 keV be re-measured with very thin target samples. Above the resonance region, the new evaluation borrow information from the TENDL library. Benchmark results show improvement with the evaluation.

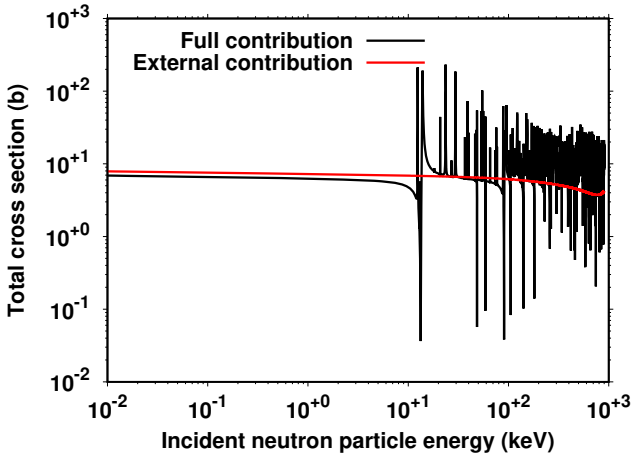


FIG. 78. ^{88}Sr(n,tot) cross sections up to 950 keV, including both resonance and external parameters (in black). The energy dependent contribution to the total cross sections from the R external parameterization is shown in red. Figure taken from Ref. [328].

5. ^{88}Sr

The resonance parameter evaluation of ^{88}Sr for incident neutron energy up to 950 keV was compiled from a publicly available set of resonance parameters [326, 327] and used to generate an Evaluated Nuclear Data File (ENDF) submitted for inclusion to the Evaluated Nuclear Data File ENDF/B-VIII.1 release. Details of the evaluation work are discussed in the letter report [328] and only key features of the evaluation work are briefly described in this journal paper. The novelty of this evaluation work is an external function representation defined by pole strengths and R^{∞} parameters over the entire RRR extended thrice with respect to the current ENDF/B-VIII.0 resolved resonance evaluation. As an example, the external function is shown in red for the total cross section in Fig. 78. Moreover, the RM formalism used for the newly assembled ENDF file represents an improvement over the multi-level Breit-Wigner approximation.

Selected experimental data measured at the ORELA facility [326, 327] were chosen to test the quality of the resonance parameters as plotted in Figs. 79–81 showing the overall good agreement between calculated and experimental (cross section and transmission) data. This also resulted in generating `SAMMY` inputs, including exper-

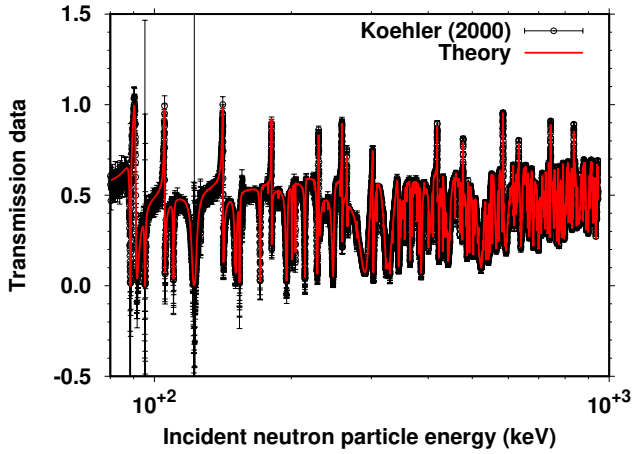


FIG. 79. n+^{88}Sr transmission data measured at 200 m flight path (FP) from 80 keV up to 1 MeV at the ORELA facility (black dots) compared to theoretical data (solid red line). The obtained χ^2/dof value is 0.72 over the specified energy range. Figure taken from Ref. [328].

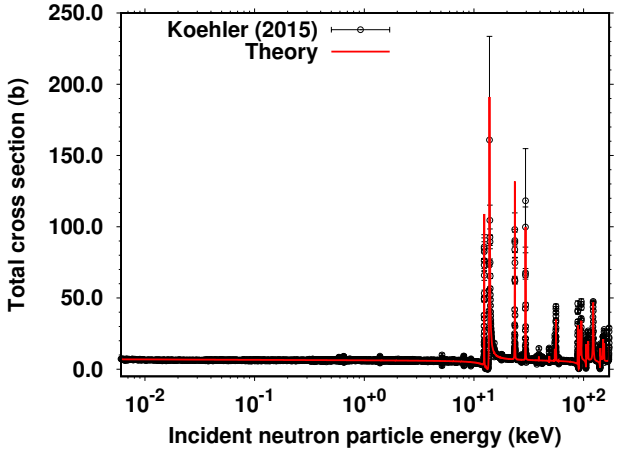


FIG. 80. n+^{88}Sr total cross-section data measured at 80 m flight path (FP) from 6 up to 170 keV at the ORELA facility (black dots) compared to theoretical data (solid red line). The obtained χ^2/dof value is 3.34 over the specified energy range. Figure taken from Ref. [328].

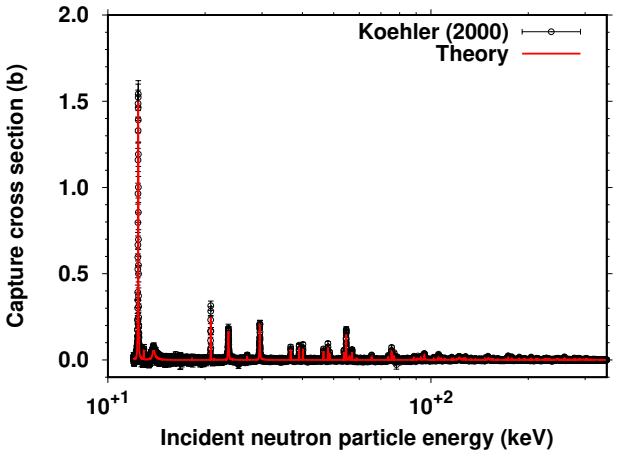


FIG. 81. n+^{88}Sr capture data measured at 40 m flight path (FP) from 12 up to 350 keV at the ORELA facility (black dots) compared to theoretical data (solid red line). The obtained χ^2/dof value is 0.57 over the specified energy range. Figure taken from Ref. [328].

TABLE XX. n+^{88}Sr thermal cross sections (in barns) calculated at T=0 K.

Isotope	Source*	Total	Scattering	Capture**
^{88}Sr	ENDF/B-VIII.0	7.30710	7.29841	0.00869
	ENDF/B-VIII.1	7.71347	7.70983	0.00364

* Cross section uncertainties are missing in the ENDF/B-VIII.0 library as well as in the ENDF/B-VIII.1 release as the contribution of the external function uncertainty is not yet implemented in processing codes.

** Calculated from resonance parameters only. The estimated contribution of the direct capture cross section is 0.45 mb, which added to the value above gives about 41 mb.

imental configurations for those selected measurements.

In the thermal energy region, the present evaluation work features an increased elastic cross section of about 5% and a reduction of about 60% in the capture cross section; recent activation measurements [329] support these changes in the capture channel. In view of this reduction, the *s*-wave direct capture contribution at the thermal energy was reduced to 0.45 mb and considered negligible at 5 keV. Table XX shows the thermal cross sections for both ENDF/B-VIII.1 and ENDF/B-VIII.0. Despite the thermal scattering cross section of 6.4(1) b reported by the National Institute of Standards and Technology that is based on the coherent scattering lengths measured by Koester [330], the value of 7.7 b was adopted in this work since it is preserving the quality of the ORELA 80 m data. In this regard, new measurements may be needed to evaluate accurately the thermal scattering cross section. Furthermore, the set of resonance parameters was merged in the existing n+^{88}Sr evaluation of the ENDF/B-VIII.0 library by replacing the MF=2 section (resonance parameter) and consistently adjusting the beginning of the MF=3 section (cross section) at 950 keV. The ENDF section related to MF=3, MT=102 was also updated to account for *s*-wave contribution of the direct capture cross section up to 5 keV. Moreover, due to the incompatibility with Koester's measured data, new measurements may be needed to evaluate accurately the thermal scattering cross section. This work was one of the milestones of the NCSP (Appendix B), and future work will consist of measuring and evaluating minor Sr isotopes and related uncertainty quantification. No covariance information was added in this release as the contribution of the external function uncertainty is not yet implemented in processing codes.

6. ^{103}Rh

A ^{103}Rh resolved resonance evaluation was carried out up to 8000 eV based on the reduced R-matrix RM formalism in the energy range from 10^{-5} eV to 8000 eV. The ^{103}Rh resonance evaluation included in ENDF/B-VIII.0 is listed up to 4170 eV. The new evaluation represents an extension of the RRR of $\sim$ 4000 eV. The evaluation uses the LRF=7 resonance parameter format, referred to as the RML format. ^{103}Rh is an isotope with ground-state spin and parity of $I^\pi = 1/2^-$ which leads to channel spins and parities, $s^\pi = 0^-$ and $s^\pi = 1^-$, respectively. Below 8000 eV, neutron penetration factor shows that angular momentum $l = 0$ and $l = 1$, that is, s-, and p-waves contribute the most. For p-wave, the resonance spin J^π, shows identical values for the spin channels $s^\pi = 0^-$ and $s^\pi = 1^-$ which is $J^\pi = 1^+$. In the ENDF format, this characteristic can only be described by using the format option LRF=7 of the resolved resonance parameters. The evaluation includes resonance parameters covariance using the LCOMP=2 (compact format).

a. Resonance evaluation

Resonance parameters and resonance parameter covariance for ^{103}Rh were determined by a self-consistent analysis of relevant experimental data; namely, high-resolution transmission and capture yield data. The multi-level R-matrix code SAMMY [317] was used for the analysis. In addition to existing experimental data available in the EXFOR [45] system, neutron transmission and capture yield measurements performed at the GELINA [318] of the Institute for Reference Materials and Measurements (IRMM) of the Joint Research Centre (JRC) Belgium and from the Gaerttner LINAC Center at RPI [331] were used to extend the upper energy range to 8000 eV. Three energy bound levels (negative energies) and three energy levels above 8000 eV were used to mock up the interference effects of external levels in the energy range 10^{-5} eV to 8000 eV. The GELINA experimental data used in the evaluation are displayed in Table XXI. The SAMMY analysis of the experimental data identified 549 resonances; namely 197 s-wave and 352 p-wave. Excellent fit of the experimental data with the SAMMY code were obtained for all experimental data up to 8000 eV. As an example, a fit of Mihailescu [332] transmission data from 1.85 eV to 8000 eV is displayed in Fig. 82 together with residues. Likewise, Fig. 83 and Fig. 84 display the fit of the RPI transmission and capture cross section and respective residues in the energy range 100 eV to 500 eV. Values of the thermal capture cross section compared with the experimental data for Brusegan [333] is listed in Table XXII. Additionally, listed in Table XXII are the resonance integral values calculated with the evaluated resonance parameters and the values listed in the Atlas of Neutron Resonances [323]. The uncertainty in the calculated values are from the resonance parameter covariance derived in the evaluation.

b. Unresolved resonance evaluation

A new ^{103}Rh URR evaluation was performed concurrently with the aforementioned RRR evaluation. The URR evaluation procedure and corresponding results were previously published [336]. The SAMMY code [317] was used to simultaneously fit experimental total and capture cross section data and extract energy dependent average URR parameters in the energy region from 8 keV up to the first inelastic threshold at 40.146 keV. The SAMMY code was also used to generate covariance information for the URR parameters.

c. Benchmark results

Benchmark calculations were performed using the present evaluation. The resonance parameters, converted to ENDF format, were used instead of those

TABLE XXI. GELINA experimental data

Reference	Energy Range (eV)	Data
	Transmission	
Brusegan [333]	0.4 – 1000	49.3 m, 0.002207 at/b
Brusegan [333]	0.4 – 1000	49.3 m, 0.000337 at/b
Ribon [334]	18.0 – 95.0	53.7 m, 0.00608 at/b
Ribon [334]	84.0 – 503.0	53.7 m, 0.0001487 at/b
Ribon [334]	178.0 – 757.0	53.7 m, 0.05 at/b
Ribon [334]	600.0 – 4000.0	103.7 m, 0.02435 at/b
Mihailescu [332]	1.85 – 8000.0	49.343 m, 0.0458 at/b
	Capture	
Brusegan [333]	0.01 – 1000	14.3624 m, 0.00187 at/b
Mihailescu [332]	1.72 – 8000.0	28.814 m, 0.000337 at/b
Mihailescu [332]	1.72 – 8000.0	28.814 m, 0.00187 at/b

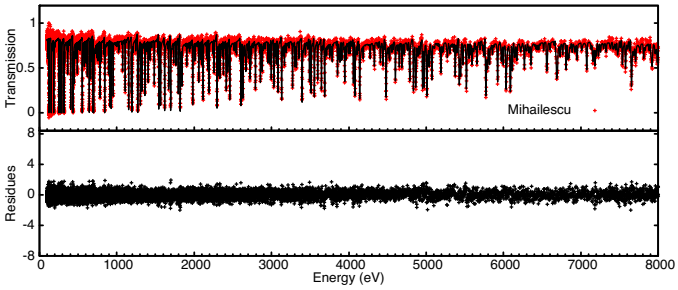


FIG. 82. SAMMY fitting of Mihailescu [332] ^{103}Rh transmission data and residues.

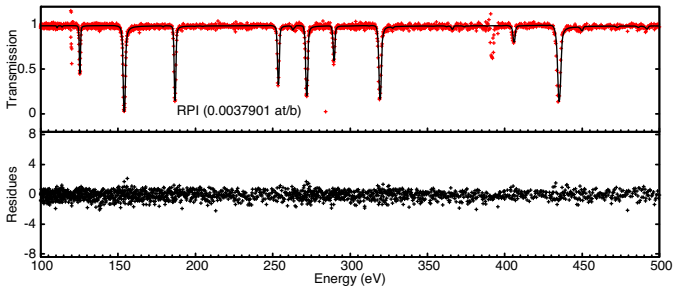


FIG. 83. SAMMY fitting of RPI ^{103}Rh transmission data and residues.

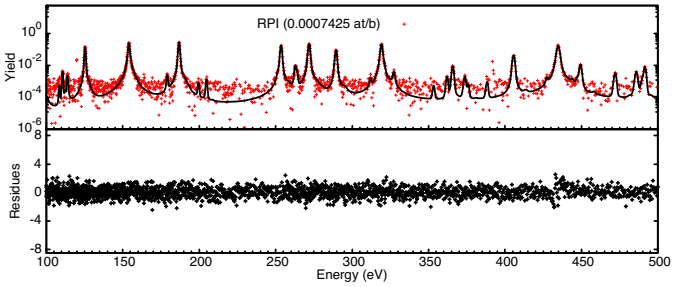


FIG. 84. SAMMY fitting of RPI ^{103}Rh capture yield data and residues.

TABLE XXII. Capture cross section at thermal energy (0.0253 eV) and resonance integral for ^{103}Rh.

Cross Section (b)	This Work	Atlas [323, 335]	Brusegam [333]
σ_γ	142.8(23)	143.5(15)	142.5(15)
I_γ	1007(41)	1012(50)	–

from ENDF/B-VIII.0. The evaluation is referred to as ENDF/B-VIII.0mod. The Institute for Radiological Protection and Nuclear Safety from the French name "Institut de Radioprotection et de Sûreté Nucléaire (IRSN)" participated on critical experiments aimed at nuclear data measurements for code and data validations, in particular for testing the ^{103}Rh cross section data and uncertainties. The critical benchmark program named "Matériaux Interaction Réflexion Toutes Epaisseurs" (MIRTE) was designed by IRSN and carried out at the "Commissariat à l'Energie Atomique (CEA)" Valduc Center in the Apparatus B assembly. The benchmark is listed in the ICSBEP handbook [158] as LEU-COMP-THERM-106. Benchmark calculations were performed with the MORET 5 code (Monte Carlo standard deviation of 0.00010) [324] using cross sections processed with the NJOY code [325]. The results of the testing together with the benchmark k_{eff} and uncertainties are gathered in Table XXIII.

Comparisons of the ENDF/B-VIII.0 results with calculations using the ENDF/B-VIII.0mod library indicates a decrease on Δk corresponding to about 80 pcm. The new evaluation provides a good indication that the criticality safety prediction for thermal system including ^{103}Rh has improved.

TABLE XXIII. Comparisons of k_{eff} results for the LEU-COMP-THERM-106 [158] benchmark.

Evaluation	k_{eff} results
Benchmark	1.00040(64)
ENDF/B-VIII.0	1.00296
ENDF/B-VIII.0mod	1.00216

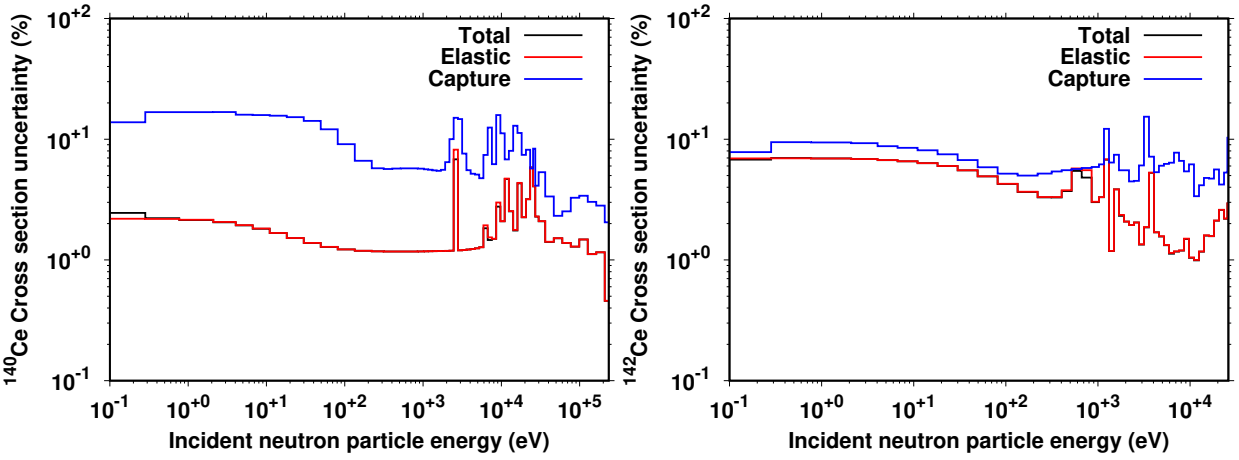
Resolved resonance evaluation of the ^{103}Rh cross sections included several experimental data sets. Resonance parameter covariance and uncertainties have been generated together with the resonance parameters evaluation. The new ^{103}Rh resonance evaluation extends the upper energy limit of existing evaluation of about 4000 eV. Thermal benchmark results indicate that the new ^{103}Rh resolved resonance evaluation is as good as those of existing evaluations or even potentially slightly better. Presently, no benchmark in the epithermal energy region exists to test the efficiency of the new evaluation.

7. $^{140,142}Ce$

Details of the evaluation work in the RRR on even-A cerium isotopes ^{140,142}Ce are reported in Ref. [337]. Constrained by measured thermal constants available from the EXFOR database, these evaluations are based on recent high-resolution transmission and capture measurements performed on $^{\text{nat}}$Ce and highly enriched ^{142}Ce samples at the JRC-GELINA facility. Due to their poor quality and documentation, other available transmission data were disregarded and not included in the evaluation work. Improved with the RM R-matrix approximation over the Multi-level Breit Wigner approximation, the resonance parameterization performed in this work also resolves the long standing issue of the cerium evaluations of the ENDF/B nuclear data releases reporting incorrect resonance widths, particularly, for the 1.3 keV energy level. The updated and corrected set of resonance parameters included their uncertainty quantification. The uncertainty quantification was performed with a retroactive methodology to generate covariance matrices compatible with experimental uncertainty guidelines, although these can be questionable particularly for theoretical observables, such as resonance parameters. The generated uncertainty and related correlations for both isotopes and all available reaction channel in the RRR are reported in Fig. 85 for a defined 80-group energy-averaged representation. Following the resonance structure of the reconstructed cross sections, the related fluctuating uncertainty of the total reaction channel is ranging between 1 and 7%. Uncertainty between 7 and 14% in the thermal energy region for the capture reaction channel seems consistent with the small magnitude of the cross sections for both isotopes. For this reason, the contribution of the capture channels to the total uncertainty is small, and the total and elastic reaction channel are comparable in both magnitude and structure.

8. $^{156,158,160,161,162,163,164}Dy$

In support of the NCSP, the evaluation work in the RRR for the set of seven Dy isotopes, $^{156,158,160-164}$Dy, is described in detail in Ref. [338]. This is a brief summary of the evaluation work about the generated res-



(a)^{140}Ce cross section uncertainties. (b)^{142}Ce cross section uncertainties.

FIG. 85. 80-group representation of ^{140,142}Ce cross section uncertainties for total, elastic, and capture reaction channels.

onance parameters (File MF=2) and related covariance information (File MF=32). By adopting the RM approximation implemented in the *R*-matrix code SAMMY, the high-resolution capture and transmission measurements performed at the RPI Gaerttner LINAC facility [339, 340] were included in the Bayesian fitting procedure. Additional transmission data measured on enriched samples by Liou [341] at the Columbia University Nevis synchrocyclotron in the mid-seventies were used to gauge the neutron widths above 15 eV. The experimental conditions, such as resolution function, finite size sample, detector efficiencies, and nuclide abundances of sample, multiple scattering, self-shielding, normalization, background, and Doppler broadening, were taken into account as implemented in the SAMMY input files reported in Ref. [338]. Thermal constants, such as absorption and (in)coherent scattering cross sections and corresponding scattering lengths, were calibrated to the National Institute of Standards and Technology's compilation [87] except for ^{161,164}Dy isotopes. The guidance provided by Sears' (or NIST) compilation [87] for the thermal constants was augmented by high-resolution capture yields and transmission data [339] due to their extension to thermal energies. In the thermal region, the evaluated thermal scattering and capture constant for the ^{164}Dy isotope shows differences with the NIST compilation up to 8%. Also, for ^{161}Dy isotope, this work reports a value of the scattering cross section 10% higher than the NIST's reported value. Particular emphasis should be devoted in future experimental campaigns to measuring scattering lengths for these two isotopes, particularly for the most abundant isotope, ^{164}Dy, with the largest total thermal cross section among the seven Dy isotopes. In this regard, the capability to include scattering lengths in the fitting procedure, among other possible measured quantities and as an additional constraint, should be developed. This work included uncertainty quantification of the total, elastic scattering and capture cross section for all isotopes. The uncertainty in the thermal energy region were about 1% constrained by the transmission, and capture measurements on natural samples [339] were reported to have a similar uncertainty. In the energy region above 15 eV, although high-resolution capture yield data measured by Shin [340] are available, high-resolution transmission data are still needed for isotopically enriched samples. The currently available Liou's transmission data [341] are poorly documented in the uncertainty quantification analysis, and it is very likely that the reported data communicated to the EXFOR database are not measured data but total cross section data reconstructed from resonance parameters fitted to the measured transmission data. Moreover, Liou's measurements campaign included capture measurements that are not available in the EXFOR library. The lack of modern transmission data measured on isotopically enriched samples in the neutron energy above 15 eV also precludes any attempt to extend the RRR to the currently reported upper energy ranges.

In the specific case of Dy isotopes, there is a very limited number of modern benchmarks that can be used to perform a conclusive validation over a comprehensive suite of cases. Therefore, no particular validation test was performed on the evaluated data, although Block's transmission and Shin's capture data represents a perfect example of nuclear data ready for validation purposes due to their extension to thermal energies.

Finally, this work represents one of the first attempts to generate a fully reproducible evaluation in the RRR as this is the primary goal of the Working Party on International Nuclear Data Evaluation Co-operation Subgroup 49 [342].

9. ^{181}Ta

a. Resonance range

The previous ^{181}Ta evaluation was identified as one of the oldest evaluations within ENDF/B-VIII.0 [343], containing some resonance parameters that appear to have originated in ENDF/B-IV. The ^{181}Ta ENDF/B-VIII.0 evaluation uses a currently outdated multi-level Breit-Wigner (MLBW) formalism to represent the RRR and no covariance data are provided. The previous RRR energy range only extends to 330 eV. The URR in ENDF/B-VIII.0 extended from 330 eV to 5 keV. The energy region from 5 keV and above contained no resonance self-shielding, causing major discrepancies with experimental data. There was no evaluated uncertainty or covariance data reported with the URR cross sections.

The new ^{181}Ta RRR parameters are a result of fitting several experimental transmission and capture yield data sets using the modern `SAMMY` code [317]. The `SAMMY` fitting process used a RM approximation to the R-matrix formalism. The starting RRR parameters were based on JEFF-3.3 [64]. Spin assignments were adopted from the neutron ATLAS [344]. For spins not given in the ATLAS, the values were randomly generated using a Monte Carlo process. This Monte Carlo process was extended to randomly add small fictitious resonances above $\approx$ 777 eV that improve RRR parameter statistics. All relevant experimental information, such as the resolution function, were included in the `SAMMY` fitting process. The uncertainty on these experimental parameters were propagated into the final RRR parameter uncertainty. The new evaluation extends the RRR region up to 2.554 keV and provides covariance information for all RRR parameters. As part of validation, the new RRR parameters produce thermal coherent and incoherent scattering cross section values that agree with the NIST [87] values. The details of ^{181}Ta RRR evaluation were previously published [345].

The new URR parameters for ^{181}Ta are the posterior values of a `SAMMY` [317] Bayesian evaluation of multiple datasets for total cross section [346–348], capture cross section [349–355], and elastic cross section [356] found in EXFOR [45]. A coordinated inter-institution effort was made to ensure consistency between the RRR, URR, and fast neutron evaluation efforts. To achieve self-consistency for RRR–URR evaluation, a subset of the posterior resonance parameters (in the energy range $<$ 330 eV) from the RRR evaluation were directly used to calculate prior parameters for the URR. The URR evaluation was extended from the end of the RRR (2.554 keV) to 100 keV where the fast neutron evaluation began. The URR and fast neutron evaluators agreed on several high-accuracy datasets (*e.g.*, Poenitz *et al.* [348] and McDermott *et al.* [349]) that would constrain the evaluations to similar final mean values at the 100 keV matching point. The posterior average resonance parameters included a full covariance matrix from the generalized least squares fit. The posterior covariance on the average resonance parameters was used to calculate a full covariance matrix for the total, capture, elastic, and 1st excited state inelastic cross sections to conform to the current ENDF/B format requirements. The new URR evaluation shows better agreement with energy-differential measurements (*e.g.*, Brown *et al.* [357] and Byoun [358]) and integral benchmark experiments. Reasonable covariance estimates are now available to estimate the impact of nuclear data uncertainties on modeled transport applications. Due to an unfortunate clerical error, however, the URR covariances for ^{181}Ta in the final ENDF/B-VIII.1 release were unintentionally overwritten in the process of file assembly with higher values that are incorrect but more conservative. The incorrect covariances were added from 2 keV to 100 keV. The released standard deviations on total cross section ranged from 4-10%, elastic cross section from 4-9%, capture cross section from 2-4%, and inelastic cross section from 20-60%. The correct values will be released in an updated file that will be available from the NNDC. The finer details of the URR evaluation were published by Brown *et al.* [359].

b. Fast neutron range

The new ^{181}Ta evaluation in the fast neutron range has been performed by combining selected differential measurements with modern nuclear reaction physics into a consistent set of nuclear data and at 100 keV merged with the above-described evaluation in the unresolved resonance range.

Tantalum is a nearly mono-isotopic metal with ^{181}Ta being 99.988% of the natural mixture. There is, therefore, an exceptional wealth of experimental data available for total, capture, (n,p), (n,α), (n,t), (n,^{3}He) and (n,2n) cross sections, elastic and inelastic angular distributions, as well as neutron- and γ-spectra (including double-differential cross sections) in the high energy region. The total number of EXFOR datasets is over 340 covering nearly 140 quantities. Because of the space limitation, we do not review here such a vast data set, but Table XXIV lists most trusted and consistent experiments that were considered in the development of the evaluation. We used the EXFOR-interface feature to renormalize old experimental data to the current standards. In spite of this, more than 30% of experimental data were considered incompatible with the consistency condition and dropped out from the analysis.

c. Evaluation concept and model

The overall methodology employed in the current evaluation is based on the concept of limited trust, consistency, and hierarchy. The principal notions of such approach are:

- The limited trust applies to experimental data which can be subjectively adopted, included after renormalization, or ignored. It applies also to the model calculations which, while using default parameters, are usually not capable of reproducing experimental data within the required accuracy. In the extreme cases, model calculations can be tuned by energy dependent factors to reproduce particular shapes of the well-trusted experimental data.

TABLE XXIV. Experiments adopted for guiding ^{181}Ta evaluation.

Reaction/Quantity	Adopted references
Total x-sect.	[348, 360–368]
Elastic x-sect.	[369, 370]
Inelastic x-sect.	[371–374]
Capture x-sect.	[213, 349–351, 375]
(n,p) x-sect.	[376–381]
(n,2n) x-sect.	[382, 383]
(n,3n) x-sect.	[383]
(n,α) x-sect.	[376, 381, 384]
Angular distr.	[369, 374, 385–392]
Neutron energy spectra	[142, 389, 393, 394]
Neutron double-diff. dist.	[142, 373, 374, 389, 394–396]

Such tuning, however, preserves all the constraints imposed by the reaction physics.

- The consistency implies selecting nuclear reaction models (along with their respective parameters) and the experimental data that agree with each other creating a consistent picture for all reaction observables (e.g., cross sections, spectra, angular distributions and isomeric cross sections). To some extent, the same may apply to integral experiments, but this was not the case in the present evaluation.

- The hierarchy concept is applied to adjusting the model parameters. Rather than fitting all model parameters to all selected experimental data, we opt for a step-wise gradual approach, in which a set of model parameters is adjusted to the observables which predominantly depend of this set, e.g., spherical optical model parameters are fitted only to total and elastic cross sections and elastic angular distributions (in case of coupled-channel, calculations experimental database includes also inelastic observables). The idea is to link certain model parameters to a set of physical quantities that predominantly depend on these parameters and are not (or weakly) sensitive to the others. In the following evaluation phases, we are going to keep this subset of parameters fixed.

- The evaluation is entirely given by the model calculations, which are adjusted to the selected set of differential experimental data that are considered reliable. Thus, the evaluation is effectively reduced to the set of model parameters and the exact version of the modeling code and is perfectly reproducible.

The ^{181}Ta calculations were performed with `EMPIRE`-3.2.3 [107, 397] reaction model code. In view of multiple choices for selecting specific models available in `EMPIRE`, various combinations of these models were first explored in an attempt to reproduce the large set of available experimental data, while refraining from adjusting individual model parameters. The adopted models are:

- Coupled-Channels (CC) with dispersive Optical Model potential.

- Quantum-mechanical Multistep Direct [398, 399] (MSD) model for pre-equilibrium neutron emission.

- Heidelberg formulation of the Multistep Compound (MSC) model for pre-equilibrium neutron [400, 401] and gamma emission [402, 403].

- Exciton model with Iwamoto-Harada [404] extension and Kalbach [405] systematics for angular distributions for pre-equilibrium emission of protons and clusters.

- Hauser-Feshbach with Moldauer [406] width fluctuation correction, anisotropy calculated using Blatt-Biedenharn coefficients, full gamma cascade using E1 γ-strength function set to RIPL-3 MLO1 [407].

- Gilbert-Cameron [408] level densities.

Selection of the models and their parameters is discussed briefly below. For more details, we refer readers to the descriptive part of the ENDF file.

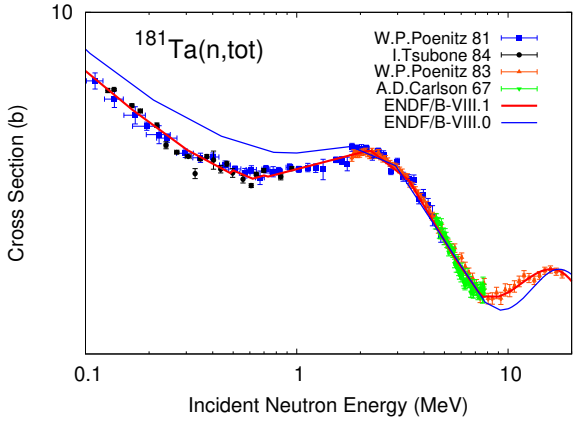


FIG. 86. Evaluated total cross sections compared with the experimental data selected to drive the evaluation.

d. Optical model - total and elastic

Strongly deformed ^{181}Ta requires CC modeling of the incident channel. The RIPL-3 [185] regional CC potential (#610) that covers ^{181}Ta and extends up to 200 MeV was not designed specifically for tantalum and needed adjustments to optimally describe the incident energy region from 50 keV up to 20 MeV. The two very reliable and consistent measurements of total by Poenitz *et al.* [348, 360], which cover entirely this energy range and overlap each other between 2 and 4 MeV, were used to refine the RIPL-3 potential. The fitting has been performed using Kalman filter [151] and resulted in rather minor (a few percent) corrections to the three geometry and two deformation parameters while the third deformation parameter has been reduced by 51%. Fig. 86 shows that experiments by Tsubone [361] and Carlson [366] perfectly agree with

the evaluated total calculated using updated optical potential. Results by Rapp [362] and Smith [363] also agree with the evaluation but were not included in the plot for clarity. Also not shown on the plot are data by Hannaske [364] and Byoun [365] that reveal the same shape as current evaluation and agree after 3% and 4.5% reduction, respectively. Similarly, a 1.5% upscaling brings into agreement Foster [368] data, while Finlay's [367] shape is slightly different but still within 2% of the new evaluation.

The performance of the adjusted potential on semi-elastic[10] cross section data is good considering the wide spread of experimental data. Comparison with elastic angular distributions demonstrate good or excellent agreement with A. Smith [369] data up to 1.5 MeV (see "good" example at 1.465 MeV on Fig. 87). At higher incident energies, abundant and smooth Smith data tend to be higher than the evaluation. The overall shape is very similar, but the difference is forward peaked suggesting that either more inelastics should be added to the semi-elastic or the three added inelastics might be underestimated. On the other hand, other experiments in majority support the current evaluation. An example is shown in Fig. 88.

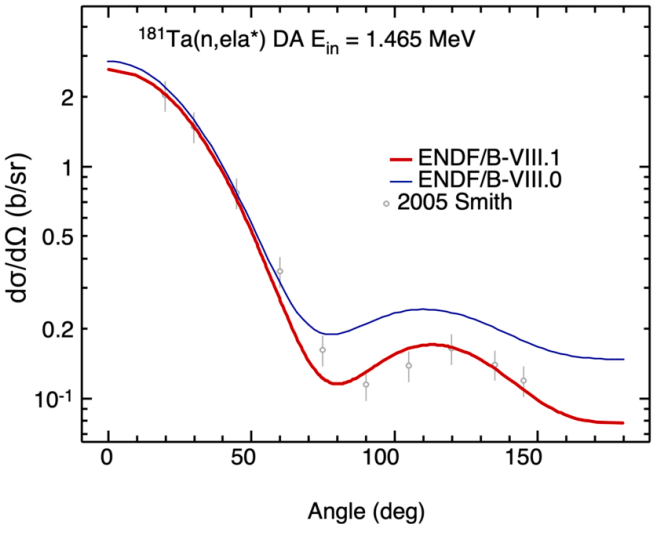


FIG. 87. An example of semi-elastic angular distribution. Agreement between Smith data [369] and the new evaluation is good, but similar comparisons at lower incident energies are often much better. The ENDF/B-VIII.0 overestimates experimental results in the backward hemisphere, but it should be noted that if the first inelastic were the only inelastic supposed to contribute to the semi-elastic, the agreement with the experimental data would be comparable to ENDF/B-VIII.1.

[10] Because of the experimental energy resolution, the 1^{st}, 2^{nd} and eventually also the 3^{rd} inelastics are summed with the elastic.

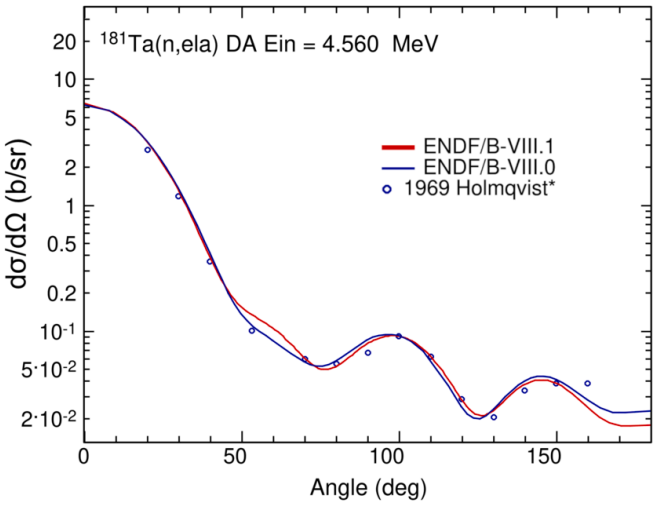


FIG. 88. Semi-elastic angular distribution at 4.56 MeV compared with the current evaluation and ENDF/B-VIII.0. Both evaluations agree very well with the experimental data, and consequently with each other, in spite of very different optical potential employed in the calculations and large differences in total cross sections shown in Fig. 86.

e. Capture evaluation

There are over 30 capture experiments which spread about 20% above and below the average. Default model calculations were well within these limits, but we decided to follow a few, most trusted and statistically consistent sets. These were measured by McDermott [349], Wisshak [350, 351], Voignier [213], and Poenitz [375]. We used manually adjusted energy-dependent scaling factors to reproduce these data up to 2.75 MeV (see Fig. 89). We note that this choice is supported by a number of other experiments which are very close to the evaluation but are either consistently off by a couple of percent, or affected by larger spread of points, or agree with absolute value but cover too small an energy range to provide additional information. For the first time, the preequilibrium emission of γ-rays was analyzed using the MSC mechanism [403]. This mechanism, without any manual intervention, reflects Giant Dipole Resonance (GDR) with a hump between 9 and 15 MeV. However, between 6 and 9 MeV, the MSC contribution to the compound nucleus capture cross sections is relatively small, resulting in a discrepancy with the semi-direct results apparently used in the ENDF/B-VIII.0 evaluation. While applying larger smoothing to the MSC results could potentially alleviate this difference, there is no experimental evidence to support either of the two theoretical approaches. Furthermore, the capture cross sections in this energy range lack practical significance. Therefore, we have decided to retain the original MSC results without any artificial modifications.

f. Preequilibrium emission

The Multistep Direct (MSD) model provides an excel-

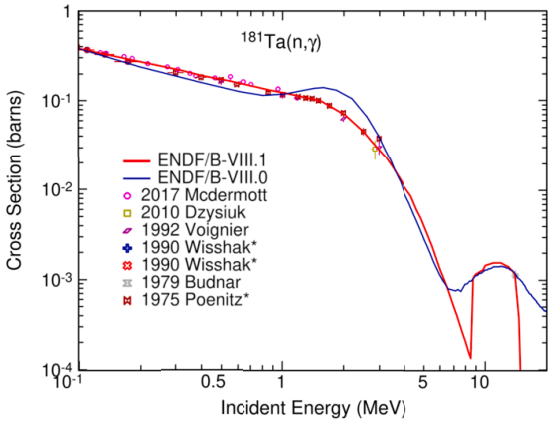


FIG. 89. Selected set of experimental data compared with the new and previous evaluation. The GDR bump at high energies comes in the new evaluation from the γ emission through the MSC mechanism.

lent tool for description of the high energy tail of neutron spectra, which is impossible for the classical exciton model. Only one parameter, l=0 transfer response function, was slightly tuned to improve neutron spectra (see Fig. 90) and at the same time ameliorate agreement for (n,2n) and (n,p) reactions. According to the hierarchical concept, this parameter was kept unchanged in the remaining evaluation process.

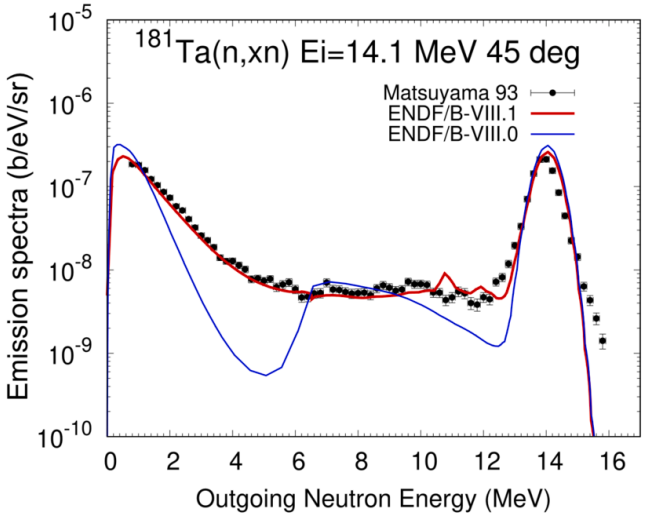


FIG. 90. Double-differential neutron emission spectrum compared with the experimental data by Matsuyama [395] showing essential improvement compared to ENDF/B-VIII.0.

The MSC mechanism is responsible for the middle-energy range of neutron spectra. None of the MSC parameters was adjusted but the gradual absorption concept has been turned off.

Using MSD and MSC for neutron emission leaves more flexibility for reproducing charged particle channels with the exciton model. The mean free path in the model has been set at 81% of the theoretical value (default is 150%) to reproduce experimental proton and cluster emission data.

g. Compound Nucleus

Three components are critical for the compound nucleus calculations: level densities, discrete levels and their decay schemes, and transmission coefficients.

Level densities affect cross sections and have strong impact on the spectra. Gilbert-Cameron (GC) level densities were chosen over Enhanced Generalized Superfluid Model (EGSM) and microscopic Hartree-Fock-Bogolyubov because GC produce better capture cross sections between 1 and 3 MeV and slightly better γ-spectra. The effect on the neutron spectra is mixed with GC working better at incident energies around 14 MeV while EGSM has an advantage at 20 MeV. Following standard routine, level density parameters and numbers of discrete levels were adjusted to ensure smooth transition between discrete levels and continuum. Level density 'a'-parameters were globally adjusted with the Kalman filter to improve overall agreement with reaction cross sections.

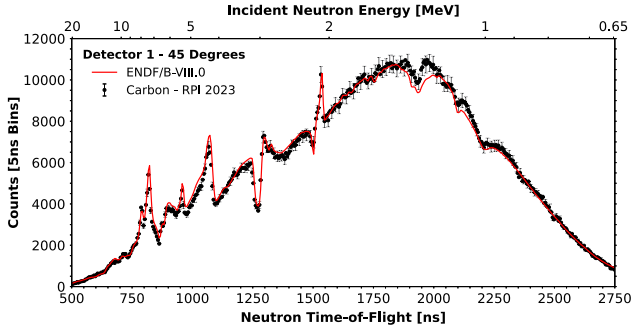
Discrete levels decay schemes are often incomplete. For the purpose of evaluating isomeric cross sections, the non-decaying levels were assigned transition(s) to the lowest energy level of the same parity and closest spin. Isomeric cross sections are provided for ^{181}Ta(n,2n)^{g,m}, ^{181}Ta(n,nα)^{g,m}, ^{181}Ta(n,2nα)^{m}, ^{181}Ta(n,γ)^{g,m}, and ^{181}Ta(n,α)^{g,m}.

A spherical optical model is used to calculate transmission coefficients for the outgoing particles. Usually these coefficients are not adjusted, but we realized that increasing real potential depth and radius by 2% for the second neutron in (n,2n) is an efficient way of lowering cross sections just above the threshold.

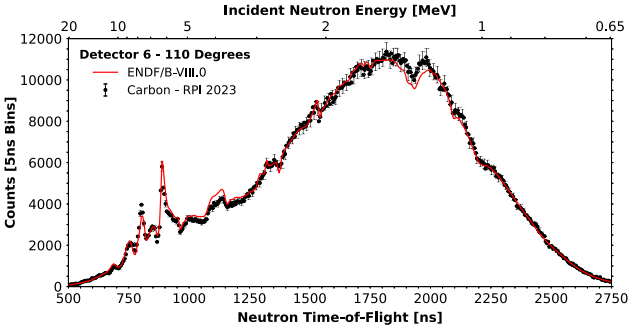
The essential difference between current evaluation and ENDF/B-VIII.0 (as well as JENDL-4.0) is the inelastic cross section to the first excited level in ^{181}Ta. We adopted model calculations that are up to 300 mb lower than EXFOR values by Rogers [371]. Other evaluations follow Rogers' experimental data. However, the Rogers' values for the first inelastic of 6.237 keV are actually not an experimental result. Due to its low excitation energy, the first inelastic is practically impossible to separate from the elastic, and Rogers' values are actually coming out of their calculations. This is explicitly stated in Ref. [371], but it was inadvertently overlooked in the EXFOR compilation process, resulting in its listing as experimental and causing confusion in previous evaluations.

h. Covariances

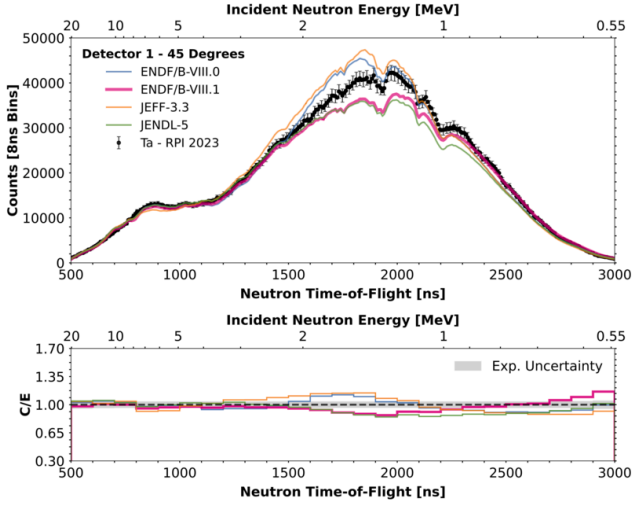
Covariances were calculated with the Kalman filter using cross section sensitivities to 53 model parameters (mostly level density and optical model parameters involved in the incident and major outgoing channels). Experimental data sets used in covariance calculations were additionally curated in order to: eliminate outliers, thin overly abundant data sets, smooth statistical fluctuations, and correct missing or statistical only uncertain-



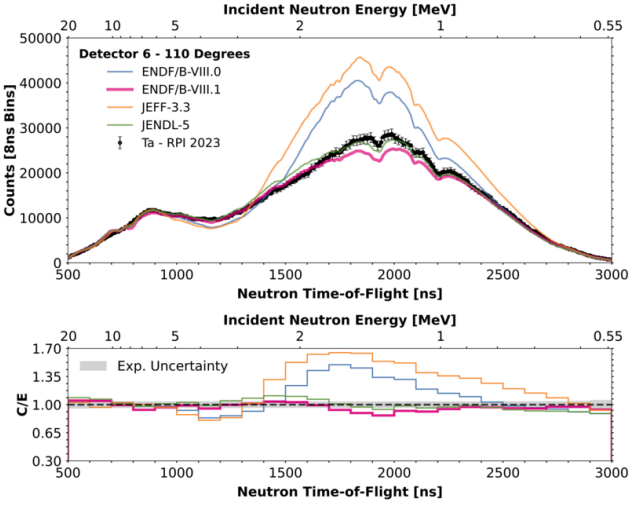
(a) Carbon measured and simulated quasi-differential neutron scattering at 45 degrees.



(b) Carbon measured and simulated quasi-differential neutron scattering at 110 degrees.



(c) Ta measured (E) and simulated (C) quasi-differential neutron scattering at 45 degrees.



(d) Ta measured (E) and simulated (C) quasi-differential neutron scattering at 110 degrees.

FIG. 91. Results from the elemental tantalum quasi-differential neutron scattering experiment at RPI [409] in the incident neutron energy range of 0.55 to 20 MeV. Carbon neutron scattering yields, measured during the Ta experiment, at a forward and backward detector compared to MCNP simulations of the ENDF/B-VIII.0 carbon evaluation are presented in Fig. 91(a) and Fig. 91(b), respectively. Measured tantalum neutron scattering yields at corresponding forward and backward detectors compared to MCNP simulations of the ENDF/B-VIII.0, JEFF-3.3, JENDL-5.0, and ENDF/B-VIII.1 evaluations are presented in Fig. 91(c) and Fig. 91(d), respectively. C/E ratios are provided to compare the experimental and simulated results along with the experimental uncertainty band.

ties.

The Kalman filter has a tendency to yield uncertainties that decrease with the total number of experimental points reaching unacceptably small values. To counteract this undesirable feature, we applied, in addition to thinning big datasets, an $1/\sqrt{n}$ weight to each experiment (n being the number of points in the experiment). This procedure allows to keep uncertainties within acceptable limits.

Relative covariances, including cross-reaction terms, were put into the ENDF-6 format using `EMPIRE`'s IO modules.

i. Validation

Robust validation of the ^{181}Ta evaluation is provided by a recent quasi-differential measurement of the scattered neutron yield from a tantalum sample, undertaken by Siemers and colleagues at RPI [409]. Neutron scattering and emissions were measured by time-of-flight from a 2.165" thick 3" diameter right metallic cylinder of tantalum with an estimated 6% systematic uncertainty in the incident neutron energies range of 0.55 MeV to 20 MeV. A 2.75" thick 3" diameter right cylindrical sample of carbon was also measured as part of the Ta experiment to validate the experimental findings. MCNP6 was used to perform the radiation transport calculations of the experiment to compare evaluated nuclear data with the experimental data. The methodology describing the carbon validation was previously described in the ^{19}F validation

section. The carbon results for a typical forward scattering angle (45 degrees) are shown in Fig. 91(a) and for a typical perpendicular to backward scattering angle (110 degrees) in Fig. 91(b).

Similarly to the Teflon® carbon validation measurement, excellent agreement between the measured scattering yield and the MCNP6 simulated scattering yield is observed in most of the experimental energy region. Minor disagreements are noted around 1.3 MeV and 5 MeV at both the forward and backward neutron scattering angles. Carbon results from this measurement and the Teflon® carbon measurement suggest deficiencies may exist in evaluated carbon nuclear data, especially at backward angles. Note that the carbon elastic angular distributions is the only standard angular distribution up to 1.8 MeV of neutron incident energy [1].

Evaluated ^{181}Ta nuclear data from the ENDF/B-VIII.1, ENDF/B-VIII.0, JEFF-3.3, and JENDL-5 libraries were used to reproduce the measured tantalum neutron scattering yield in simulation and compared with the measured data. Results for a typical forward scattering angle (45 degrees) are shown in Fig. 91(c) and for a perpendicular to backward scattering angle (110 degrees) in Fig. 91(d). Note that these scattering angles correspond to the angles of the aforementioned carbon validation measurement. At forward angles from 1.5 MeV up to 3 MeV, ENDF/B-VIII.0 and JEFF-3.3 slightly overestimate the RPI data, whilst JENDL-5 and ENDF/B-VIII.1 slightly underestimate the data. At perpendicular to backward angles (110 degrees), the JENDL-5 evaluation shows the best agreement while the new ENDF/B-VIII.1 evaluation remains low from 1 MeV up to 2 MeV. ENDF/B-VIII.0 and JEFF-3.3 significantly overestimate the measured RPI data. The JENDL-5 and ENDF/B-VIII.1 evaluations were observed to best reproduce the experimental data. Although the ENDF/B-VIII.1 evaluation shows large improvements over ENDF/B-VIII.0, especially at 110 degrees, an underestimation of the measured scattered neutron yield remains between 1.2 and 2 MeV at both detection angles. This underestimation suggests that some deficiencies in the elastic and inelastic cross sections and angular distributions still remain between 1 MeV and 2 MeV in the current evaluation. Despite this, the results from this experiment demonstrate that we have advanced our understanding of high energy incident neutron interactions with ^{181}Ta.

10. $^{190,191,192,193,194,195,196,197,198}Pt$

ENDF/B-VIII.0 contains nine Pt isotopes adopted from TENDL-15 – a large scale evaluation project using the TALYS code [221]. It is safe to assume that all these evaluations are at least nine years old and, therefore, a more focused and more up-to-date approach would be beneficial. There are 22 isomers in the residues of neutron interaction with Pt isotopes. Some of them might be of practical interest but are not included in the current evaluations. The new evaluation is trying to fix these gaps by providing cross sections for isomeric or unstable ground states if the cross sections are of a measurable size.

A fair amount of experimental data, mostly for abundant isotopes and natural element, are available. They are not enough, however, to fully pinpoint evaluations, especially as many of the available experiments are not very useful. Thus, the evaluation procedure must, to a large extent, rely on the model calculations.

a. Evaluation in the fast neutron energy range

The chain of isotopes must be evaluated in parallel in order to make use of experimental data taken on the natural element, which often are the most reliable source of information. In the case of Pt, the evaluation methodology was the same as the one used for ^{181}Ta detailed in the previous section. Dealing with a chain of several isotopes implies, however, that the consistency requirement must be extended. We need to ensure that the same model parameters are used when a given isotope appears in different calculations. Technically, this condition was imposed by defining the common input file containing all input parameters, except those pertinent to the particular target, such as target A and Z, or CC coupling scheme. This file was included while reading input files for the individual isotopes. In contrast to ^{181}Ta, we employed the Hofmann, Richert, Tepel, and Weidenmüller (HRTW) [410] width fluctuation correction and EGSM level densities. The consistency was compromised only for ^{198}Pt, where GC level densities were utilized. This deviation from the rule was attributed to the fact that GC level densities provided a more accurate representation of the experimental data, and we prioritized agreement with data over consistency of the models. From a physics perspective, the ability to reproduce data with a consistent set of parameters enhances our confidence in the accuracy of our reaction modeling. However, the necessity to compromise consistency for one of the nine isotopes suggests that our understanding, likely of level densities, may not be comprehensive.

Soukhovitskii-Capote CC potential (RIPL #1483 [185]) was adopted for all Pt isotopes with their respective level-scheme couplings. This potential, originally developed for gold, turns out to work so well on platinum that we labeled it the "Jewels Potential." It calculates total cross sections for elemental Pt much better than the potential used in TENDL evaluations (see Fig. 92). The same is confirmed also for ^{194}Pt. Elastic cross sections on the natural Pt are very good as well. Excellent agreement is obtained for elastic angular distributions on ^{194}Pt at 2.5 MeV and 4.55 MeV. Inelastic cross sections for ^{194,196,198}Pt are considerably higher than those in ENDF/B-VIII.0 although still slightly below the experimental values. The agreement for the inelastic angular distributions is fair, which is quite typical for these quantities.

The shape of the calculated capture cross sections is very similar to the Koehler [422] measurements (see 3rd

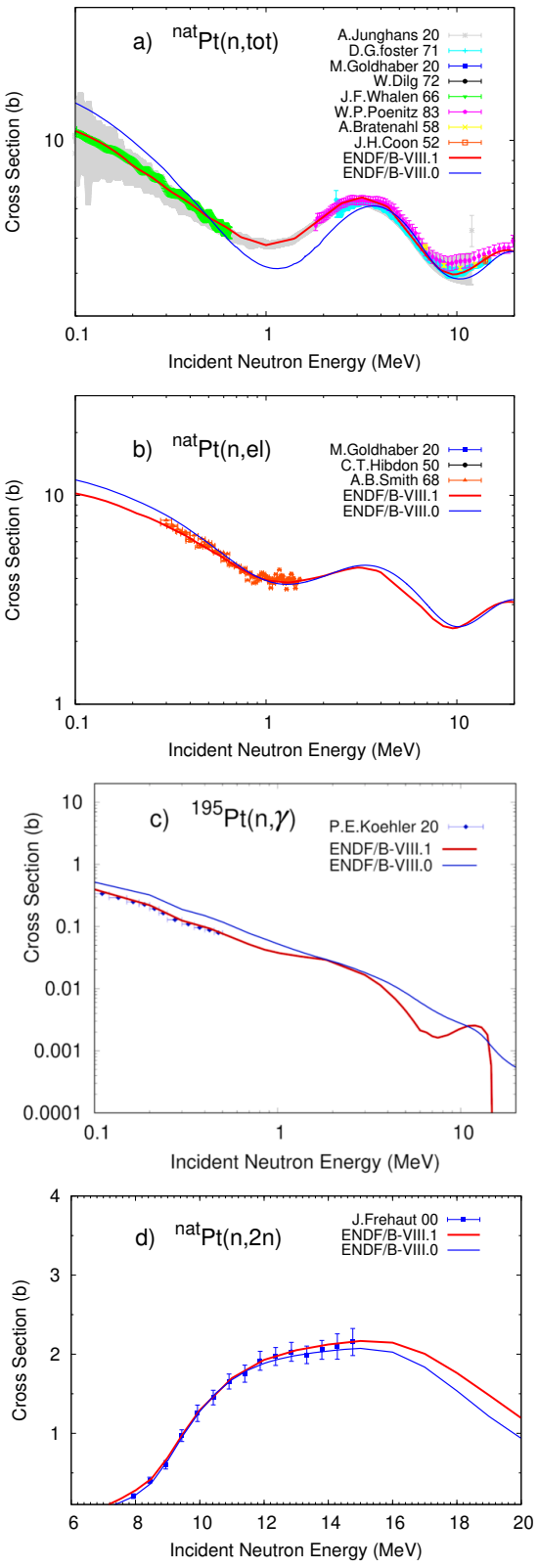


FIG. 92. Evaluated cross sections for total, elastic, capture and (n,2n) compared with the experimental data and ENDF/B-VIII.0. Except capture, all reactions are for the natural target and their cross sections are weighted sum over all stable isotopes. Data taken from Refs.[411–423].

plot of Fig. 92). We only scaled down calculated cross sections with a single, energy-independent factor per each isotope. These factors, which multiply the original MLO1 γ-strength, are closer to 1 than the default factors resulting from normalization to the thermal γ width. Choosing to follow isotopic measurements by Koehler, we underestimate by about 5% the respectable experiments on the natural platinum that were very well reproduced with the default (thermal normalization) calculations. There is a disagreement between these experiments and those by Koehler, and we hope that the new LANSCE results will help to make a final decision.

Elemental (n,2n) cross sections by Frehaut [424], corrected by a factor of 1.078 as suggested by Vonach [425], are well reproduced by the new evaluation. The ENDF/B-VIII.0 evaluation is a bit lower but equally good. The two evaluations differ mostly in the high energy tail where no experimental data exist, as shown in the bottom plot of Fig. 92.

In the case of (n,p) and (n,α) reactions, we followed primarily data by Filatenkov [376]. Ground-state cross sections agree with ENDF/B-VIII.0 within uncertainties. No isomeric meta state cross sections are given in the current ENDF/B-VIII.0 evaluations. Our (n,p) isomeric and ground-state cross sections reproduce measurements but at the price of modifying particle-hole spin distribution in the preequilibrium emission of protons. Typically, this distribution is assumed to be $\sigma^2 = f \times n \times A^{1/3}$ where n is a number of excitons (in this case $n = 2$) and A stands for the isotope mass number. Factor f is commonly set to 0.24. We had to reduce this factor to 0.12 for ^{194}Pt(n,p), 0.14 for ^{195}Pt(n,p), and 0.04 for ^{196}Pt(n,p). This rather significant reduction is likely related to the fact that Multistep Direct mechanism, that is here simulated by the exciton model, favors low angular momentum transfer populating states with the spin close to the ground state.

Fast neutron evaluations for nine Pt isotopes were merged with ENDF/B-VIII.0 resonance regions.

b. Covariances

The covariances were calculated using a Kalman filter that combined the above model calculations with available experimental data on all of the Pt isotopes. Each experimental data set was weighted by $1/n$, where n is the number of data points in each data set to eliminate the need for a posteriori scaling on any channel uncertainty. For each isotope, the same set of 53 model parameters were varied. We note that the optical model parameters included not only the incident channel but also outgoing neutrons, protons, αs, deuterons, tritons, and ^{3}He. The level density parameters for 11 residuals, and four parameters in the preequilibrium emission model were varied. Using the Kalman filter, the prior parameter uncertainties will be reduced where constraining experimental data are available. For the unstable isotopes, Kalman propagates the default parameter variations, unless the parameters are constrained by other targets. These additional constraints are one benefit of performing such a simulta-

neous evaluation, as they provide realistic cross sections and uncertainties even though no experimental data are available.

In addition to providing the correlations between incident energies in each channel, we also provide cross correlations between different reaction channels. As expected, the cross correlations between elastic and total cross sections show similar structure to their in-channel correlations (which are similar in structure to one another). There are also significant correlations between the total cross section and the inelastic and capture channels. On the other hand, the correlations between the total cross section and both (n,p) and (n,α) cross sections are close to zero.

One additional benefit of performing this type of simultaneous evaluation is that cross-isotope covariances could be provided between the various Pt isotopes. These are currently not included in ENDF/B-VIII.1 but could be constructed and formatted if they were of interest.

11. $^{206,207,208}Pb$

The major isotopes of lead, ^{206,207,208}Pb, constitute 98.6% of the natural element. Full reevaluation of these isotopes was undertaken as part of the US's Nuclear Energy University Program (DOE-NEUP) endeavors [426] towards lead fast reactors and accompanying technologies [427]. A comprehensive examination of all benchmark experiments containing lead were used to prioritize reactions channels and isotopes for the evaluation [428–431]. Across the board, ^{208}Pb elastic scattering has the largest impact to system performance as ^{208}Pb comprises over 52% of natural lead and has an uncharacteristically high inelastic threshold for its mass. This characteristic derives from the fact that ^{208}Pb is a double magic nucleus. Other outcomes of the double magic nucleus are a large level spacing and resonances that can be resolved well past 1 MeV. Similarly, as ^{206}Pb and ^{207}Pb are near the closed shell, these isotopes also have sufficiently large level spacing to resolve resonances higher than 0.5 MeV. Since the evaluation focused on cross sections relevant for fast spectra systems, neutron energies above 100 keV were prioritized. However, the RM formalism of R-matrix used in the evaluation exhibits strong dependency on the channel radius, distant, and bound levels. This means it was then necessary to perform evaluations down to 10^{-5} eV for consistency within the RRR. The RRR evaluations were performed using the R-matrix code `SAMMY` [317] and the fast region evaluations were modeled with the Hauser-Feshbach code CoH3 [432].

Comparison of the ^{208}Pb resonance parameters from ENDF/B-VIII.0 to the ORELA transmission measurement by Carlton [433] yields good agreement. Little was done in terms of adjustments to neutron widths (Γ_n) below 1 MeV as the total (and by extension the elastic) cross sections are well constrained. Time was spent on the capture cross section of ^{208}Pb around 30 keV, relevant for the 30 keV MACS. Here, the capture cross section is dominated by compound reactions of two p-wave resonances near 40 keV. However, several measurements make note of evidence of direct capture in the region below 40 keV where no resonances have been reported [434, 435]. An energy-dependent background was provided in MF-3 to account for this direct capture component which adds an order of magnitude to the capture cross section in between resonances, Fig. 93. The thermal capture cross section is constrained by Blackmon [436] with $\sigma_\gamma = 230$ μb. The evaluator acknowledges conflicting accounts of this value from D.J. Hughes [437] and J.F. Emery [438] who both claim $\sigma_\gamma = 470$ μb; however, documentation for either of these values cannot be obtained. Extension of the RRR from 1.0 to 1.5 MeV was deemed necessary to account for scattering anisotropy observed in RPI quasi-differential high energy scattering experiments [439] that was attributed solely to ^{208}Pb. A novel methodology of employing quasi-differential scattering data simulations in MCNPv6.2 [440], `NJOY2016` [325], and `SAMMY` to validate (ℓ, J) states of resonances was developed in order to provide additional information of doublets observed while fitting transmission data. The new RRR evaluation of ^{208}Pb was joined with a LANL evaluation above 1.5 MeV, resulting in new cross sections from 10^{-5} to 20 MeV.

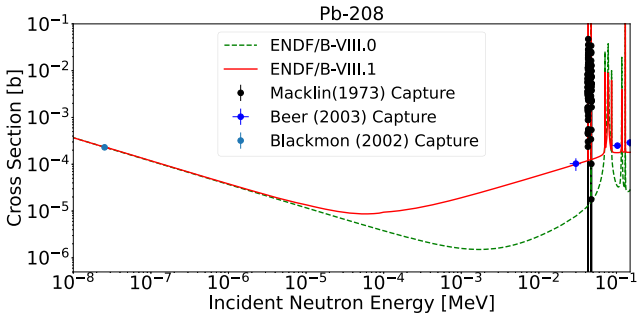


FIG. 93. New capture cross section of ^{208}Pb compared to ENDF/B-VIII.0 [68] and data from Macklin [435], Blackmon [436], and Beer [434].

The ^{206}Pb RRR evaluation focused on updating the radiation widths, Γ_γ, from two differential capture yields by Domingo-Pardo [441] and Borella [442]. These capture yield data provide the basis for adding 50 minor p- and d-wave resonances below 900 keV. However, the effects of these resonance are only observable in statistical plots as they contribute little to overall system performance. The fast region evaluation was undertaken to fit inelastic gamma production data from Negret [443]. The purpose of this step is to add resonance structure to both the elastic and inelastic channels where previous evaluations had resonance structure only in the elastic channel. Post model fitting, the computed inelastic and elastic cross sections from CoH3 were normalized by the calculated total cross section and multiplied by total cross section measurements [444]. The overall outcome is that now the

ENDF/B-VIII.1 inelastic cross section is larger than that of the ENDF/B-VIII.0.

Much like ^{206}Pb, the ^{207}Pb evaluation encompassed updates to the inelastic scattering and (n,2n) cross sections from measurements by Mihailescu [445] as well as Frehaut (2016 version [424] including Vonach 1.078 normalization correction [425]), as seen in Fig. 94. In addition, updates to Γ_γ were performed using Domingo-Pardo [446] data and resonance parameters adopted from JENDL-4.0 [447] as the library supports a higher upper energy of the RRR. Besides refitting to Domingo-Pardo capture yield data and Horen transmission [448], special care was taken in the bound levels for this isotope. Thermal scattering lengths and thermal capture ratios calculated from resonance parameters in the previous evaluation pointed to less than ideal prediction of incoherent scattering [87] and the capture from the $(\ell = 0, J = 1)$ state which dominates thermal capture. Changes to the energies and strengths of the bound s-wave resonances have since fixed this issue, giving thermal capture cross sections that are consistent with the corresponding measured gamma spectra.

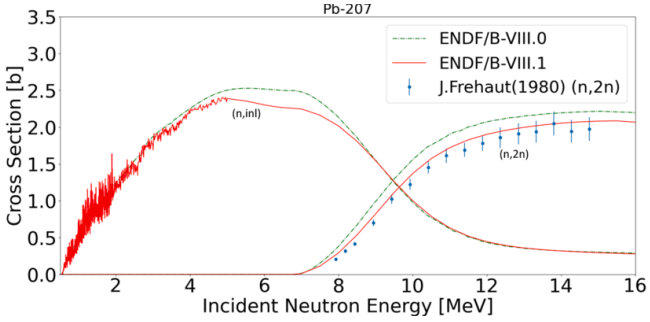


FIG. 94. New ^{207}Pb inelastic and (n,2n) cross sections compared to ENDF/B-VIII.0 and Frehaut [424].

New elastic scattering angular distributions were calculated for all isotopes within their respective RRR using the Blatt-Biedenharn formalism in NJOY2016. Fast region scattering distributions are likewise updated from the CoH3 calculations. Nuclear data covariance for total, elastic, inelastic, capture, and (n,2n) are provided for all isotopes in the evaluation, the representations of which are split between MF-32 and MF-33. For MF-32, SAMMY generated covariance in addition to scattering radii uncertainty provide sufficient quantification of uncertainties. In the fast region, a CoH3-KALMAN approach [449] was undertaken in Python. Uncertainties for elastic scattering angular distributions, MF-34, are provided for ^{208}Pb as this is the only isotope able to be quantified in natural quasi-differential scattering data. Validation of the lead isotopes was done with critical, shielding, and scattering benchmarks. There is great improvement over ENDF/B-VIII.0 for fast critical benchmarks and scattering experiments resulting largely from ^{208}Pb scattering updates observable in scattering data, Fig. 95.

Specifically, fast critical benchmarks go from an average bias of -350 pcm with ENDF/B-VIII.0 to +70

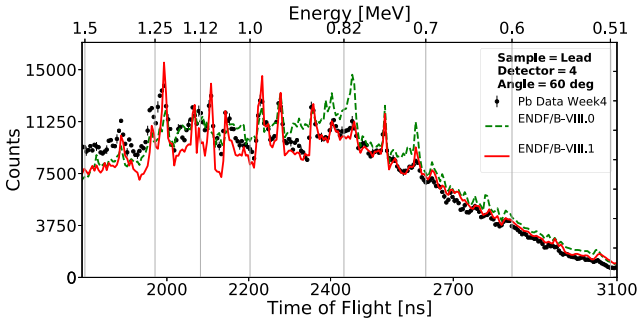


FIG. 95. Comparison of simulation and experiment of high energy quasi-differential scattering experiment of natural lead [439] from ENDF/B-VIII.0 and ENDF/B-VIII.1.

pcm with ENDF/B-VIII.1. These benchmarks include PU-MET-INTER-004 [450], HEU-MET-FAST-064 [431], HEU-MET-FAST-027 [429], PU-MET-FAST-035 [430], and MIXED-MET-FAST-006 [451]. Shielding benchmarks prove to be rather insensitive to the lead library chosen except for rather thick cases, 40 cm or more of lead [428, 452]. The effect of improving the fast assemblies resulted in a higher bias on thermal benchmarks when compared to ENDF/B-VIII.0. While a portion of the "worsening deviation" from C/E = 1 is expected and supported from changes in the high energy scattering distributions, an equal portion was a result from the RRR analysis. Upon consensus of the CSEWG committee, a small increase in the ^{207}Pb capture cross section at thermal energies was included as well as lowering the thermal elastic scattering cross sections of all three isotopes. Both adjustments are supported by quantities from NIST [87] and integral measurements. Still, lead-reflected water moderated LEU assemblies trend high, and effort should be expended to verify the benchmark geometries. The evaluator points to high energy capture measurements on ^{207}Pb and quasi-differential scattering of enriched samples for new measurements to be performed. In addition, the current ensemble of fast critical benchmarks [158] are not sufficient in terms of uncertainty analysis and geometry description to be considered adequate for nuclear data validation. New sub-critical lead-reflected plutonium experiments have been proposed as a remedy for this lack of well-validated integral experiments [453].

12. ^{234}U

In this update, we have performed a new GLS fit of the fission cross section data, including the newest Tovesson data [454], which were not considered in the previous evaluations and have smaller reported uncertainties. The energy range in which the fit was performed was 0.8 MeV to 30 MeV. Below 0.8 MeV, we have kept the previous evaluation. As can be seen from Fig. 96, the largest changes are between 9 MeV and 17 MeV, where the fit was strongly influenced by the new Tovesson data due to

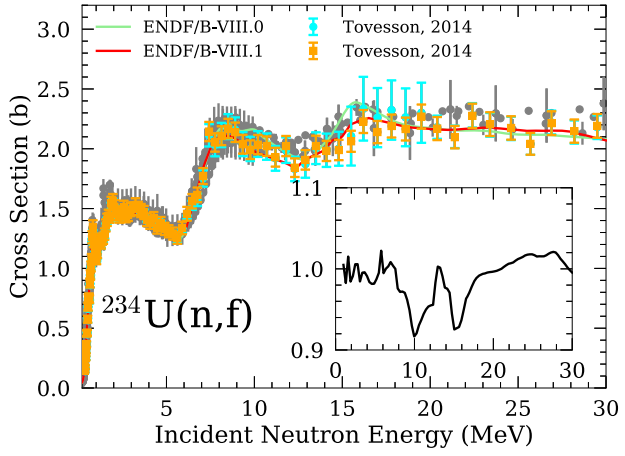


FIG. 96. Cross section for the ^{234}U(n,f) reaction. In the insert we show the ratio of the ENDF/B-VIII.1 fission cross section to ENDF/B-VIII.0. The gray data points are other available experiments except for Tovesson *et al.* [454].

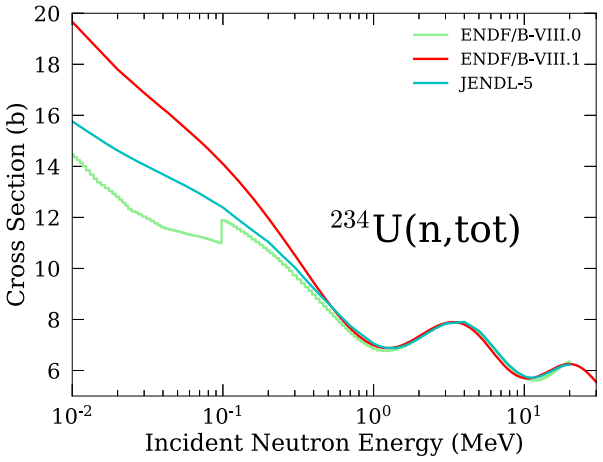


FIG. 97. Cross section for the ^{234}U(n,tot) reaction.

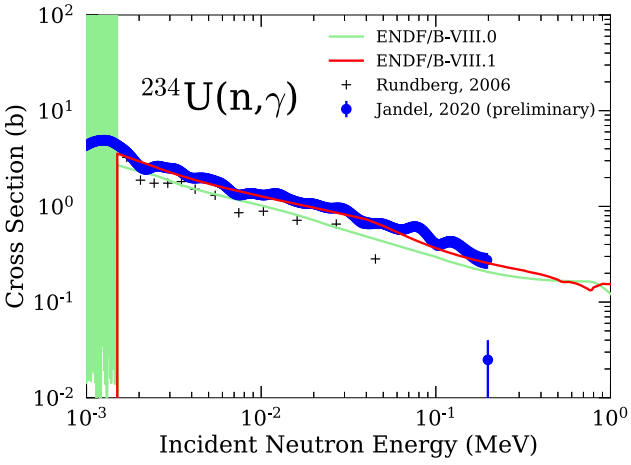


FIG. 98. Cross section for the ^{234}U(n,γ) reaction.

their smaller uncertainties.

The main theoretical tool was the code CoH_3, which was used to generate the total cross section and the individual channel cross sections. Since the model is not flexible enough for the fission channel, we have used an energy-dependent adjustment of the transmission in the fission channel, so that the calculated fission cross section reproduces exactly the evaluation based on a direct fit to the data.

For the total cross section plotted in Fig. 97, we have employed the Soukhovitskiĭ 2005 optical model potential [149]. The calculated total cross sections on ^{234}U target below 500 keV is much larger than in ENDF/B-VIII.0 and JENDL-5 libraries despite the same optical model potential being used. This points to inconsistencies in the undertaken CC calculations as well as used deformation parameters ($\beta_2 = 0.215$, $\beta_4 = 0.109$ and $\beta_6 = 0.00039$). Optical model calculations will have to be carefully revisited in a future reevaluation effort. Observed total cross section differences have a negative impact on calculated neutron strength functions at 1 keV, which is a well-defined quantity [185]. The main impact of the new evaluation on criticality benchmarks is due to the changed capture and fission cross sections in the fast range. However, the elastic cross section is also increased by the too-high total cross section below 500 keV.

The capture cross section is shown in Fig. 98, and it is based on CoH_3 calculations with enhanced $M1$ transitions. As can be observed in Fig. 98, the new evaluation is in good agreement with the preliminary data from an earlier DANCE measurement and higher than in ENDF/B-VIII.0. The ^{234}U intentionally matches the new Los Alamos Jandel data and not the old Los Alamos (unpublished) Rundberg 2006 data. Note, however, that a final analysis of the DANCE data is not available yet.

All the other channels, except elastic, were taken from CoH_3 calculations. The elastic cross section was calculated as the difference between total and non-elastic. Significant deviations from the previous evaluations can be observed for (n,n'), (n,2n), and (n,3n), but there is no data to invalidate the newest evaluation. However, we note that the peak of the (n,2n) cross section follows an expected trend when looking at ^{236}U (new evaluation) and ^{238}U evaluation in ENDF/B-VIII.0. The newest (n,3n) peak is in better agreement with the JENDL-5.

The correlation matrices in all channels have been updated using a Kalman filter, including available experimental data in all channels with sensitivities calculated to CoH_3 parameters. For fission, the shape of the uncertainties from Kalman was used below 300 keV and matched to the magnitude of the ENDF/B-VIII.0 uncertainties, and above 300 keV they have been adjusted to match the Tovesson data. The capture uncertainties follow the shape and magnitude of ENDF/B-VIII.0 uncertainties. For the total cross section, the uncertainties come from Kalman below 10 keV; above 10 keV, the uncertainties

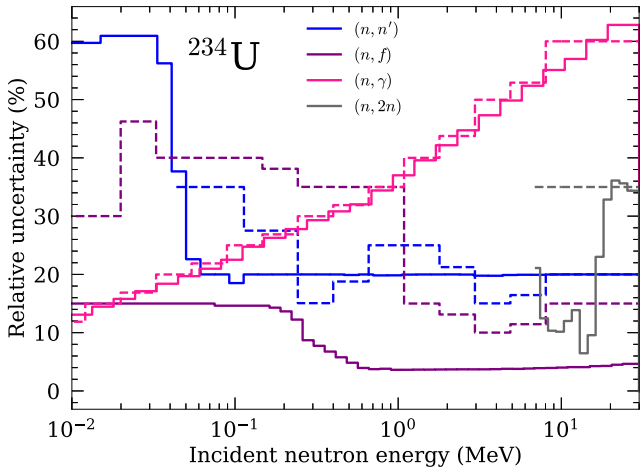


FIG. 99. Comparison between the relative uncertainties for ^{234}U from ENDF/B-VIII.0 (dashed) and ENDF/B-VIII.1 (solid) for (n,n'), (n,f), (n,γ), and $(n,2n)$.

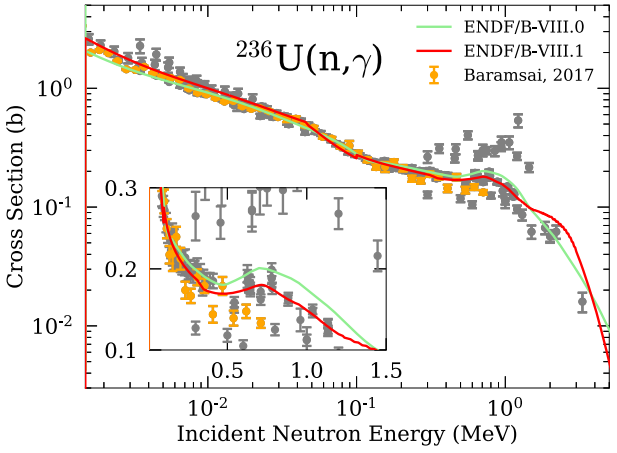


FIG. 100. Cross section for the ^{236}U(n,γ) reaction. In the insert we show the same quantity in linear scale up to 1.5 MeV incident energy. The gray data points are other available experiments except for Baramsai *et al.* [456].

remain at the value at 10 keV (about 3.5%). For the inelastic channel, the shape of the Kalman uncertainties were scaled so that we reproduce the average magnitude from ENDF/B-VIII.0 with a minimum set to 20%, as recommended by templates of expected uncertainties [455]. For all other channels, the uncertainties from Kalman were scaled so that the maximum values were close to the ENDF/B-VIII.0 values at about 30%, while keeping the shape of the energy-dependence extracted from Kalman. Fig. 99 shows the comparison between the relative uncertainties of ENDF/B-VIII.0 and ENDF/B-VIII.1 for the inelastic, fission, capture, and $(n,2n)$ channels.

13. ^{236}U

We have used a very similar methodology to update the evaluation of neutron-induced reactions on ^{236}U with the one for neutron-induced reactions on ^{234}U targets presented in Section III C 12. The only change in methodology versus ^{234}U was that we have used Kalman to refit the capture cross section above 100 keV to the available data. The CoH_3 calculation reproduce well some of the data points from LANSCE [456], but it tends to be low with respect to other data sets in this region. Hence, we have performed a parametric Kalman fit in which we also increased the uncertainties of the LANSCE measurement. This brought the evaluation of the capture cross section in better agreement with the available measurements and lowered it with respect to the ENDF/B-VIII.0 evaluation, as showed in Fig. 100.

We have also updated the total cross section and the fission cross section in the fast region. In both cases, the change from the ENDF/B-VIII.0 evaluation is of a few percent, with a maximum of about 5% change. This relatively small change is unlikely to impact any benchmark that includes ^{236}U. An example is shown in Fig. 101(a), where we show the reaction rates in the Flattop 25 critical assembly.

^{236}U capture reaction rates now in ENDF/B-VIII.1 are lower than for ENDF/B-VIII.0, as shown in the upper panel of Fig. 101, and are below the measurements (but are generally within or just outside the σ uncertainties). This reflects our intentional decision to lower the capture cross section based on our analysis of the cross section data.

The correlation matrices in all channels have been updated using a similar procedure as for ^{234}U. The capture uncertainties have been evaluated based on DANCE data below 1 MeV, and above we use a logarithmic function that follows the ENDF/B-VIII.0 uncertainties. For fission, the ENDF/B-VIII.0 uncertainties have been used below 300 keV, and above 800 keV they have been adjusted to match Tovesson. Between 300 and 800 keV, the uncertainties linearly decrease. Inelastic uncertainties have been set to 20%, as recommended by templates of expected uncertainties [455]. For all other channels, the uncertainties from Kalman were scaled so that the maximum values were close to the ENDF/B-VIII.0 values at about 17%, while keeping the shape of the energy-dependence extracted from Kalman. Figure 102 shows the comparison between the relative uncertainties of ENDF/B-VIII.0 and ENDF/B-VIII.1 for the inelastic, fission, capture, and $(n,2n)$ channels.

14. Adoption of IRDFF-II neutron dosimetry evaluations

The IRDFF-II library [2] contains 119 reaction entries and addresses incident neutron energies from 0 to 60 MeV. IRDFF evaluations include consistent mean val-

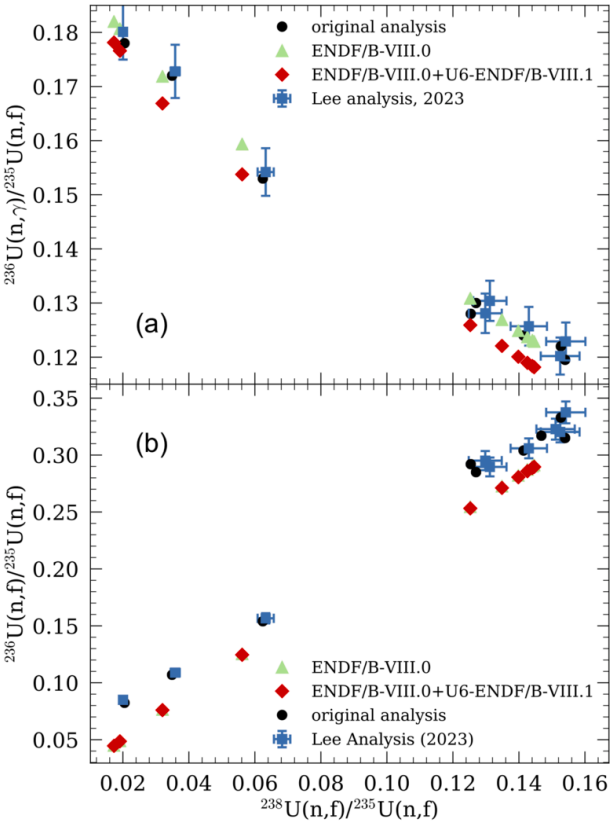


FIG. 101. Comparison of the measured and experimental values of the ratio of the ^{236}U capture rates to ^{235}U fission rates (a) as a function of spectral index at different locations in the Flattop-25 critical assembly, and the ratio of the ^{236}U fission rates to the ^{235}U fission rates (b) as a function of the same spectral index.

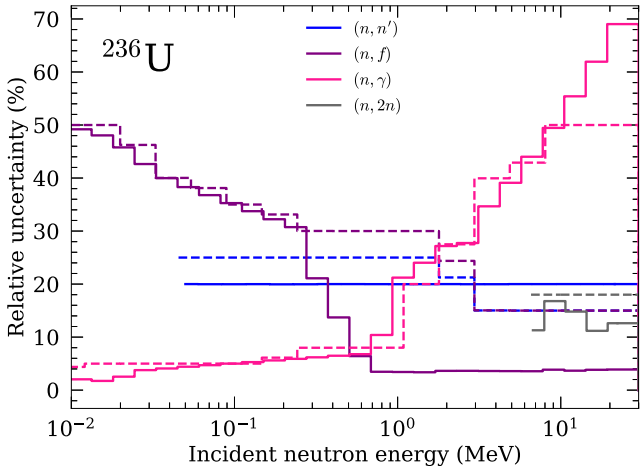


FIG. 102. Comparison between the relative uncertainties for ^{236}U from ENDF/B-VIII.0 (dashed) and ENDF/B-VIII.1 (solid) for (n,n'), (n,f), (n,γ), and $(n,2n)$.

TABLE XXV. $C/E-1$ of measured SACS averaged in LR-0 reactor spectrum [457] compared with SACS calculations using IRDFF-II or ENDF/B-VIII.0 evaluations with MCNP-6.2(R) code. Reactions with C/E outside the 1-sigma experimental uncertainty are highlighted in red. Cd denotes measurements with Cd cover.

Dosimeters Reaction	Exp.unc.	C/E-1 IRDFF-II	C/E-1 ENDF/B-VIII.0
^{58}Fe(n,γ)	4.2%	2.9%	3.2%
^{59}Co(n,γ)	4.1%	4.6%	4.6%
Cd ^{23}Na(n,γ)	3.3%	5.0%	5.4%
Cd ^{58}Fe(n,γ)	3.5%	4.4%	6.1%
^{47}Ti(n,p)	2.0%	1.6%	7.3%
^{64}Zn(n,p)	5.3%	-0.1%	-9.5%
^{58}Ni(n,p)	2.2%	0.1%	-1.0%
^{54}Fe(n,p)	2.4%	-1.9%	-1.9%
^{46}Ti(n,p)	2.2%	2.3%	-6.2%
^{60}Ni(n,p)	8.5%	-0.1%	-7.1%
^{63}Cu(n,α)	2.9%	1.6%	45.4%
^{54}Fe(n,α)	10.5%	5.7%	-16.2%
^{56}Fe(n,p)	2.6%	-0.3%	-0.3%
^{48}Ti(n,p)	2.6%	-0.2%	17.1%
^{24}Mg(n,p)	4.6%	1.6%	10.6%
^{27}Al(n,α)	2.3%	0.4%	2.3%
^{51}V(n,α)	3.5%	1.4%	8.7%
^{197}Au(n,2n)	4.0%	-2.9%	-7.6%
^{127}I(n,2n)	4.0%	0.1%	1.5%
^{55}Mn(n,2n)	4.5%	6.7%	4.5%
^{75}As(n,2n)	4.3%	0.6%	3.5%
^{89}Y(n,2n)	3.2%	2.1%	3.2%
^{19}F(n,2n)	4.0%	5.6%	26.6%
^{90}Zr(n,2n)	4.0%	0.9%	2.9%
^{23}Na(n,2n)	4.8%	-1.5%	55.2%

ues and covariances [2] which were adopted where possible in the ENDF/B-VIII.1 library. Only the reactions on isotopic materials were considered to update the ENDF/B-VIII.1 library. The IRDFF evaluations have been extremely well-validated and generally show at least equal or better performance than the corresponding ENDF/B-VIII.0 evaluations. This is illustrated in Table XXV with a comparison of measured SACS in the LR-0 reactor near Prague [457] versus calculated SACS. Note that capture cross sections cannot be replaced as the IRDFF-II library contains point-wise evaluations without resonance parameters, making the replacement impossible. However, we can see in Table XXV that the agreement of calculated SACS capture cross sections from both evaluations (ENDF/B-VIII.0 and IRDFF-II) with experimental data is pretty good for the thermal and epithermal regions.

Only for the ^{55}Mn(n,2n) reaction, the C/E of the IRDFF-II SACS is slightly worse than the ENDF/B-VIII.0: 6.7% for the IRDFF-II evaluation versus 4.5% for the ENDF/B-VIII.0 with experimental uncertainty of 4.5%. However, there are 12 dosimetry reactions (highlighted in red in Table XXV) where the C/E of the IRDFF-II SACS is much better than the one calcu-

lated using ENDF/B-VIII.0. Worse C/E cases beyond 2-sigma experimental uncertainty are ^{46}Ti(n,p), ^{47}Ti(n,p), ^{63}Cu(n,α), ^{48}Ti(n,p), ^{24}Mg(n,p), ^{51}V(n,α), ^{19}F(n,2n), and ^{23}Na(n,2n).

Threshold dosimetry reaction cross sections and associated covariances in the ENDF/B-VIII.1 library were replaced by those enumerated in Table XXVI from the IRDFF-II library as described by Trkov and Capote in Ref. [183], and noted in Comment's column in the Table. All discrepant reactions discussed above were replaced, which resulted in a significant improvement in ENDF/B-VIII.1 neutron dosimetry performance compared to ENDF/B-VIII.0.

After the cross-section and covariance replacements by IRDFF, consistency fixes were implemented, such as reconstruction of the elastic cross section to preserve unitarity with the total cross section and rescaling of partial threshold reactions so their sum corresponds to the adopted IRDFF cross section, whenever appropriate.

Also noteworthy is that other partial or complete evaluations included in the ENDF/B-VIII.1 release and discussed in the present paper may have already chosen to include IRDFF dosimetry cross sections and associated covariances (e.g., ^{19}F(n,2n), ^{63}Cu(n,2n), etc.). These cases are discussed in their corresponding sections but are also listed here.

The differences seen in the C/E listed in Table XXV are also shown in Figs. 103 and 104. For example, the ^{24}Mg(n,p), ^{51}V(n,α), ^{63}Cu(n,α), ^{19}F(n,2n), and ^{23}Na(n,2n) plots show that the ENDF/B-VIII.0 evaluations clearly overestimate measured differential cross-section data leading to the large positive C/E shown in Table XXV. Light-element evaluations generally show IRDFF-II evaluations to be in better agreement with experimental data than ENDF/B-VIII.0. Several cases like ^{89}Y(n,2n) and ^{169}Tm(n,xn) show very good agreement of IRDFF-II evaluations with the ENDF/B-VIII.0, especially within the first few MeV above the reaction threshold which is the most important region for neutron dosimetry.

TABLE XXVI: IRDFF-II reaction list and evaluation sources [2] adopted for the ENDF/B-VIII.1 library. Major sources of data were K.I. Zolotarev and IPPE colleagues evaluations [458–467]. Selected energy regions and/or evaluations were also adopted from IRDF-2002 [468], IRDF-2005 [220, 469], EAF-2010 [470], JENDL-4 [447], ENDF/B-VIII.0 [68], and JEFF-3.3 [64] libraries. All IRDFF-II evaluations were cut to comply with the energy limit of the corresponding ENDF/B-VIII.1 neutron-transport evaluations. That means IRDFF-II extensions beyond 20 MeV that were mostly based on TENDL evaluations [471, 472] were not used. In the "Energy Interval" column, $E_{\text{thr.}}$ corresponds to the energy threshold of that particular reaction. The "Reaction ID" column identifies the corresponding reaction in the IRDFF-II evaluation [2, Table I] that was adopted in ENDF/B-VIII.1.

No.	Reaction	Reaction ID	MAT	Energy Interval	Evaluation source	Comments
6	^{7}Li(n,X)^{4}He	Li7He4	328	0 – 20 MeV 0 – 20 MeV 0 – 20 MeV 0 – 20 MeV	IRDFF-II Li7t MT25 – ENDF/B-VIII.0 MT33=ENDF/B-VIII.0 (n,n') MT102 – ENDF/B-VIII.0	adopted unchanged unchanged unchanged
7	^{7}Li(n,X)^{3}H	Li7H3	328	0 – 20 MeV	MT33 – ENDF/B-VIII.0 (n,n')	adopted
15	^{19}F(n,2n)^{18}F	F192	925	$E_{\text{thr.}}$ – 20 MeV	RRDF-2002	adopted
16	^{23}Na(n,2n)^{22}Na	Na232	1125	$E_{\text{thr.}}$ – 20 MeV	INDC(NDS)-0705	adopted
19	^{24}Mg(n,p)^{24}Na	Mg24p	1225	$E_{\text{thr.}}$ – 20 MeV	INDC(NDS)-0526	adopted
20	^{27}Al(n,p)^{27}Mg	Al27p	1325	$E_{\text{thr.}}$ – 20 MeV	INDC(CCP)-0438	adopted
21	^{27}Al(n,α)^{24}Na	Al27a	1325	$E_{\text{thr.}}$ – 20 MeV	INDC(NDS)-0546	adopted
23	^{27}Al(n,2n)^{26g}Al	Al272g	1325	$E_{\text{thr.}}$ – 20 MeV	INDC(NDS)-0705	adopted
24	^{28}Si(n,p)^{28}Al	Si28p	1425	$E_{\text{thr.}}$ – 20 MeV	INDC(NDS)-0668	adopted
25	^{29}Si(n,X)^{28}Al	Si29Al28	1428	$E_{\text{thr.}}$ – 60 MeV	IRDFF-II Si29p	adopted (MF10)
27	^{31}P(n,p)^{31}Si	P31p	1525	$E_{\text{thr.}}$ – 20 MeV	INDC(NDS)-0668	adopted
29	^{32}S(n,p)^{32}P	S32p	1625	$E_{\text{thr.}}$ – 20 MeV	INDC(NDS)-0526	adopted
31	^{46}Ti(n,2n)^{45}Ti	Ti462	2225	$E_{\text{thr.}}$ – 20 MeV	INDC(CCP)-0360	adopted
32	^{46}Ti(n,p)^{46}Sc	Ti46p	2225	$E_{\text{thr.}}$ – 20 MeV	IRDF-2002	adopted
33	^{47}Ti(n,p)^{47}Sc	Ti47p	2228	$E_{\text{thr.}}$ – 20 MeV	RRDF-2002	adopted
34	^{48}Ti(n,p)^{48}Sc	Ti48p	2231	$E_{\text{thr.}}$ – 20 MeV	IRDF-2002	adopted
39	^{51}V(n,α)^{48}Sc	V51a	2328	$E_{\text{thr.}}$ – 20 MeV	IRDF-2002	adopted
42	^{55}Mn(n,2n)^{54}Mn	Mn552	2525	$E_{\text{thr.}}$ – 60 MeV	K.I.Zolotarev	adopted

Continued on next page

TABLE XXVI: (continued). IRDFF-II reaction list and evaluation sources [2] adopted for the ENDF/B-VIII.1 library.

No.	Reaction	Reaction ID	MAT	Energy Interval	Evaluation source	Comments
43	^{55}Mn(n,γ)^{56}Mn	Mn55g	2525	$E_{\text{thr.}}$ – 60 MeV	ENDF/B-VII.1 [108, 162]	unchanged
48	^{54}Fe(n,2n)^{53}Fe	Fe542	2625	$E_{\text{thr.}}$ – 20 MeV	INDC(CCP)-0360	adopted
51	^{56}Fe(n,p)^{56}Mn	Fe56p	2631	$E_{\text{thr.}}$ – 20 MeV	INDC(CCP)-0438	unchanged
53	^{59}Co(n,2n)^{58}Co	Co592	2725	$E_{\text{thr.}}$ – 20 MeV	INDC(NDS)-0546	adopted
54	^{59}Co(n,3n)^{57}Co	Co593	2725	$E_{\text{thr.}}$ – 20 MeV	INDC(NDS)-0584	adopted
55	^{59}Co(n,γ)^{60}Co	Co59g	2725	$E_{\text{thr.}}$ – 20 MeV	IRDF-2002	unchanged
56	^{59}Co(n,p)^{59}Fe	Co59p	2725	$E_{\text{thr.}}$ – 20 MeV	INDC(NDS)-0546	adopted
57	^{59}Co(n,α)^{56}Mn	Co59a	2725	$E_{\text{thr.}}$ – 20 MeV	IRDF-2002	adopted
62	^{58}Ni(n,2n)^{57}Ni	Ni582	2825	$E_{\text{thr.}}$ – 20 MeV	INDC(NDS)-0657	adopted
63	^{58}Ni(n,p)^{58}Co	Ni58p	2825	0 – 20 MeV	K.I.Zolotarev (RRDF-2002)	adopted
64	^{60}Ni(n,p)^{60}Co	Ni60p	2831	$E_{\text{thr.}}$ – 20 MeV	INDC(NDS)-0526	adopted
68	^{63}Cu(n,2n)^{62}Cu	Cu632	2925	$E_{\text{thr.}}$ – 20 MeV	INDC(NDS)-0526	adopted
70	^{63}Cu(n,α)^{60}Co	Cu63a	2925	$E_{\text{thr.}}$ – 20 MeV	IRDF-2002	adopted
71	^{65}Cu(n,2n)^{64}Cu	Cu652	2931	$E_{\text{thr.}}$ – 20 MeV	INDC(NDS)-0526	adopted
74	^{64}Zn(n,p)^{64}Cu	Zn64p	3025	0 – 20 MeV	INDC(NDS)-0526	adopted
75	^{67}Zn(n,p)^{67}Cu	Zn67p	3034	$E_{\text{thr.}}$ – 20 MeV	INDC(NDS)-0526	adopted
76	^{68}Zn(n,X)^{67}Cu	Zn68Cu67	3034	$E_{\text{thr.}}$ – 20 MeV	INDC(NDS)-0796	adopted (MF10)
77	^{75}As(n,2n)^{74}As	As752	3325	$E_{\text{thr.}}$ – 20 MeV	IRDF-2002	adopted
78	^{89}Y(n,2n)^{88}Y	Y892	3925	$E_{\text{thr.}}$ – 20 MeV	INDC(NDS)-0584	adopted
80	^{90}Zr(n,2n)^{89}Zr	Zr902	4025	$E_{\text{thr.}}$ – 20 MeV	INDC(NDS)-0546	adopted
86	^{92}Mo(n,p)^{92m}Nb	Mo92pm	4225	$E_{\text{thr.}}$ – 20 MeV	INDC(NDS)-0657	adopted
87	^{103}Rh(n,n')^{103m}Rh	Rh103nm	4525	$E_{\text{thr.}}$ – 20 MeV	IRDF-2002	adopted (MF10)
88	^{109}Ag(n,γ)^{110m}Ag	Ag109gm	4731	0 – 60 MeV	JENDL-3.2	adopted (MF10)
91	^{113}In(n,n')^{113m}In	In113nm	4925	$E_{\text{thr.}}$ – 20 MeV	INDC(NDS)-0657	adopted (MF10)
92	^{115}In(n,2n)^{114m}In	In1152m	4931	$E_{\text{thr.}}$ – 20 MeV	INDC(NDS)-0526	adopted (MF10)
93	^{115}In(n,n')^{115m}In	In115nm	4931	$E_{\text{thr.}}$ – 20 MeV	IRDF-2002	adopted (MF10)
95	^{127}I(n,2n)^{126}I	I1272	5325	$E_{\text{thr.}}$ – 20 MeV	INDC(NDS)-0526	adopted
97	^{141}Pr(n,2n)^{140}Pr	Pr1412	5925	$E_{\text{thr.}}$ – 20 MeV	IRDF-2002	adopted
98	^{169}Tm(n,2n)^{168}Tm	Tm1692	6925	$E_{\text{thr.}}$ – 20 MeV	INDC(NDS)-0584	adopted
99	^{169}Tm(n,3n)^{167}Tm	Tm1693	6925	$E_{\text{thr.}}$ – 20 MeV	INDC(NDS)-0657	adopted
101	^{186}W(n,γ)^{187}W	W186g	7443	0 – 20 MeV	ENDF/B-VII.1 [108, 162]	unchanged
102	^{197}Au(n,2n)^{196}Au	Au1972	7925	$E_{\text{thr.}}$ – 20 MeV	INDC(NDS)-0526	adopted
103	^{197}Au(n,γ)^{198}Au	Au197g	7925	0 – 20 MeV	IAEA STD 2017 [1]	unchanged
104	^{199}Hg(n,n')^{199m}Hg	Hg199nm	8034	$E_{\text{thr.}}$ – 20 MeV	INDC(NDS)-0526	adopted (MF10)
105	^{204}Pb(n,n')^{204m}Pb	Pb204nm	8225	$E_{\text{thr.}}$ – 20 MeV	INDC(CCP)-0431	adopted (MF10)
106	^{209}Bi(n,2n)^{208}Bi	Bi2092	8325	$E_{\text{thr.}}$ – 20MeV	V.G.Pronyaev	adopted
107	^{209}Bi(n,3n)^{207}Bi	Bi2093	8325	$E_{\text{thr.}}$ – 20MeV	V.G.Pronyaev	adopted
113	^{235}U(n,f)	U235f	9228	0 – 20 MeV	ENDF/B-VIII.0,CIELO [67, 189, 473]	unchanged
114	^{238}U(n,2n)^{237}U	U2382	9237	$E_{\text{thr.}}$ – 20 MeV	ENDF/B-VIII.0,CIELO [67, 189, 473]	unchanged
115	^{238}U(n,f)	U238f	9237	0 – 20 MeV	ENDF/B-VIII.0,CIELO [67, 189, 473]	unchanged
116	^{238}U(n,γ)^{239}U	U238g	9237	0 – 20 MeV	ENDF/B-VIII.0,CIELO [67, 189, 473]	unchanged

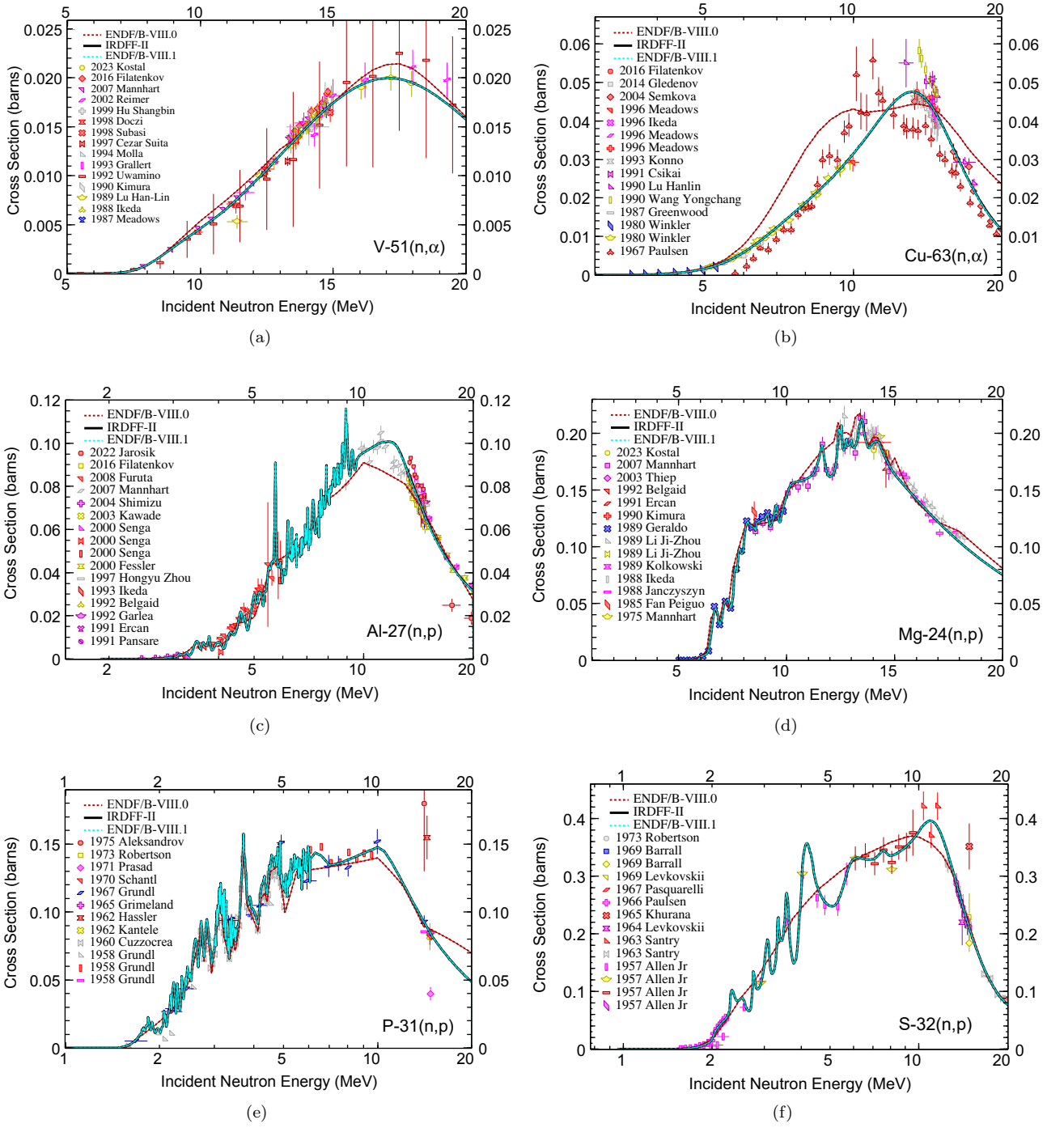


FIG. 103. (Color online) Selected IRDFF-II [2] (n,α) and (n,p) dosimetry evaluations adopted for ENDF/B-VIII.1 are compared with selected data from EXFOR [45] and ENDF/B-VIII.0. On the plots, ENDF/B-VIII.1 (cyan dashed lines) curves are exactly on top of IRDFF-II (solid black lines).

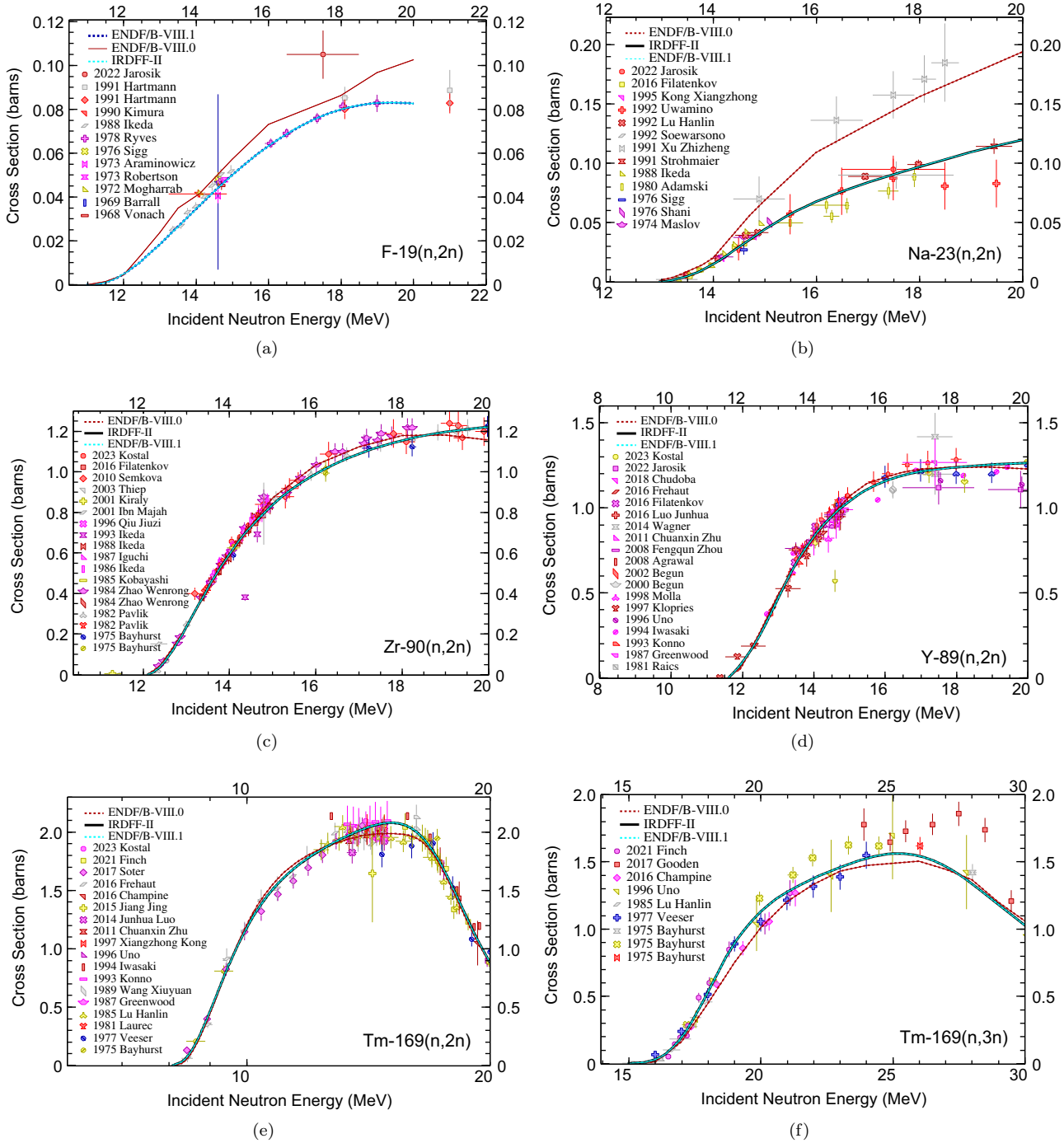


FIG. 104. (Color online) Selected IRDFF-II [2] (n,2n) and (n,3n) dosimetry evaluations adopted for ENDF/B-VIII.1 are compared with selected data from EXFOR [45] and ENDF/B-VIII.0. On the plots, ENDF/B-VIII.1 (cyan dashed lines) curves are exactly on top of IRDFF-II (solid black lines).

D. Fixes or improvements to existing evaluations

1. $^{106,108,110,111,112,114,116}Cd$

The cadmium isotopes ^{106,108,110,111,112,114,116}Cd had one fix implemented related to the scattering radius, AP in the ENDF-6 format. The ENDF-6 format manual [474] states that if the ℓ-dependent scattering radius APL is provided for all ℓ-values NLS levels, a value of AP is still required. For the definitions of the aforementioned parameters, refer to the ENDF-6 format manual [474].

2. *Gamma-spectra fixes*

To improve the accuracy and utility of the gamma-ray production data library, the GRIN project [187] has performed systematic improvements in the evaluations of capture and inelastic gamma-ray production for neutron interactions. The isotopes ^{13}C, ^{16}O, ^{19}F, ^{28}Si have revised data in the MT=102 reaction channel where missing emissions were included, and the proper flagging primary gammas now ensures the representation of incident neutron energy dependence. Additionally, the dataset for inelastic gamma-ray production for these isotopes (and ^{32,34}S) have been updated to fill in missing entries and to update energies and branching ratios, in accordance with the latest values from RIPL [185, 475]. These changes not only resolve previous discrepancies but help to reconcile the structure and reaction information of these files.

3. *Previously missing outgoing-particle distributions*

There were several missing exit distributions in many of the neutron evaluations in ENDF/B-VIII.0. Not only there were no distributions given for outgoing charged particles, but about half of these evaluations were missing energy distributions for gamma production after capture, which made it difficult for transport codes.

a. Distributions adopted from TENDL

A first round of patched exit distributions for charged particle and gamma production were, therefore, imported from TENDL2019 [476]. The imported reactions and exit products are described in Table XXVII. A second round of improvements are described in the next subsection, so this list excludes those nuclides with additional proton and alpha distributions supplied by LANL also for this release.

TABLE XXVII: Patched exit distributions for missing gammas and charged particles by importing energy and angular distributions from TENDL2019. Labels give MT number and the exit particle which now has an exit distribution.

Nuclide	MT : outgoing particle
^{22}Na	28:^{1}H, 22:^{4}He, 103:^{1}H, 104:^{2}H, 107:^{4}He, 108:^{4}He, 102:photon
^{23}Na	103:^{1}H, 107:^{4}He
^{24}Mg	28:^{1}H, 22:^{4}He, 103:^{1}H, 107:^{4}He
^{25}Mg	28:^{1}H, 22:^{4}He, 103:^{1}H, 107:^{4}He
^{26}Mg	28:^{1}H, 22:^{4}He, 103:^{1}H, 107:^{4}He
^{28}Si	104:^{2}H
^{31}P	28:^{1}H, 103:^{1}H, 107:^{4}He
^{32}S	28:^{1}H, 22:^{4}He, 103:^{1}H, 107:^{4}He
^{33}S	28:^{1}H, 22:^{4}He, 103:^{1}H, 107:^{4}He
^{34}S	28:^{1}H, 22:^{4}He, 103:^{1}H, 107:^{4}He
^{36}S	28:^{1}H, 22:^{4}He, 103:^{1}H, 107:^{4}He
^{36}Ar	28:^{1}H, 22:^{4}He, 103:^{1}H, 104:^{2}H, 107:^{4}He, 108:^{4}He, 102:photon
^{38}Ar	28:^{1}H, 22:^{4}He, 103:^{1}H, 104:^{2}H, 107:^{4}He, 108:^{4}He, 102:photon
^{45}Sc	28:^{1}H, 22:^{4}He, 103:^{1}H, 104:^{2}H, 105:^{3}H, 106:^{3}He, 107:^{4}He
^{58m1}Co	28:^{1}H, 22:^{4}He, 103:^{1}H, 104:^{2}H, 107:^{4}He, 102:photon
^{69}Ga	28:^{1}H, 32:^{2}H, 22:^{4}He, 103:^{1}H, 111:^{1}H, 104:^{2}H, 105:^{3}H, 106:^{3}He, 107:^{4}He, 102:photon
^{71}Ga	28:^{1}H, 22:^{4}He, 103:^{1}H, 111:^{1}H, 104:^{2}H, 105:^{3}H, 106:^{3}He, 107:^{4}He, 102:photon
^{70}Ge	112:^{1}H, 112:^{4}He
^{72}Ge	112:^{1}H, 112:^{4}He
^{73}Ge	112:^{1}H, 112:^{4}He
^{74}Ge	112:^{1}H, 112:^{4}He
^{76}Ge	112:^{1}H, 112:^{4}He
^{74}Se	28:^{1}H, 22:^{4}He, 103:^{1}H, 111:^{1}H, 104:^{2}H, 105:^{3}H, 106:^{3}He, 107:^{4}He, 102:photon
^{76}Se	28:^{1}H, 22:^{4}He, 103:^{1}H, 111:^{1}H, 104:^{2}H, 105:^{3}H, 106:^{3}He, 107:^{4}He, 102:photon
^{77}Se	28:^{1}H, 32:^{2}H, 22:^{4}He, 103:^{1}H, 111:^{1}H, 104:^{2}H, 105:^{3}H, 106:^{3}He, 107:^{4}He, 102:photon
^{78}Se	28:^{1}H, 22:^{4}He, 103:^{1}H, 104:^{2}H, 105:^{3}H, 106:^{3}He, 107:^{4}He, 102:photon
^{79}Se	28:^{1}H, 32:^{2}H, 22:^{4}He, 103:^{1}H, 104:^{2}H, 105:^{3}H, 106:^{3}He, 107:^{4}He, 102:photon
^{80}Se	28:^{1}H, 22:^{4}He, 103:^{1}H, 104:^{2}H, 105:^{3}H, 107:^{4}He, 102:photon
^{82}Se	28:^{1}H, 22:^{4}He, 103:^{1}H, 104:^{2}H, 105:^{3}H, 107:^{4}He, 102:photon

Continued on next page

TABLE XXVII – continued from previous page

Nuclide	MT : outgoing particle
^{79}Br	28:^{1}H, 32:^{2}H, 33:^{3}H, 22:^{4}He, 103:^{1}H, 111:^{1}H, 104:^{2}H, 105:^{3}H, 106:^{3}He, 107:^{4}He, 102:photon
^{81}Br	28:^{1}H, 32:^{2}H, 33:^{3}H, 22:^{4}He, 103:^{1}H, 104:^{2}H, 105:^{3}H, 107:^{4}He, 102:photon
^{80}Kr	28:^{1}H, 22:^{4}He, 103:^{1}H, 111:^{1}H, 104:^{2}H, 105:^{3}H, 106:^{3}He, 107:^{4}He, 102:photon
^{82}Kr	28:^{1}H, 22:^{4}He, 103:^{1}H, 104:^{2}H, 105:^{3}H, 107:^{4}He, 102:photon
^{83}Kr	28:^{1}H, 22:^{4}He, 103:^{1}H, 111:^{1}H, 104:^{2}H, 105:^{3}H, 106:^{3}He, 107:^{4}He, 102:photon
^{84}Kr	28:^{1}H, 22:^{4}He, 103:^{1}H, 104:^{2}H, 105:^{3}H, 106:^{3}He, 107:^{4}He, 102:photon
^{85}Rb	28:^{1}H, 32:^{2}H, 22:^{4}He, 103:^{1}H, 104:^{2}H, 105:^{3}H, 106:^{3}He, 107:^{4}He, 102:photon
^{87}Rb	28:^{1}H, 32:^{2}H, 22:^{4}He, 103:^{1}H, 104:^{2}H, 105:^{3}H, 107:^{4}He, 102:photon
^{86}Sr	28:^{1}H, 22:^{4}He, 103:^{1}H, 111:^{1}H, 104:^{2}H, 105:^{3}H, 107:^{4}He, 102:photon
^{87}Sr	28:^{1}H, 32:^{2}H, 22:^{4}He, 103:^{1}H, 104:^{2}H, 105:^{3}H, 106:^{3}He, 107:^{4}He, 102:photon
^{88}Sr	28:^{1}H, 22:^{4}He, 103:^{1}H, 104:^{2}H, 105:^{3}H, 106:^{3}He, 107:^{4}He, 102:photon
^{89}Sr	28:^{1}H, 22:^{4}He, 103:^{1}H, 104:^{2}H, 105:^{3}H, 106:^{3}He, 107:^{4}He, 102:photon
^{90}Sr	28:^{1}H, 32:^{2}H, 22:^{4}He, 103:^{1}H, 104:^{2}H, 105:^{3}H, 107:^{4}He, 102:photon
^{91}Y	28:^{1}H, 32:^{2}H, 33:^{3}H, 22:^{4}He, 103:^{1}H, 104:^{2}H, 105:^{3}H, 107:^{4}He, 102:photon
^{93}Nb	28:^{1}H, 32:^{2}H, 33:^{3}H, 22:^{4}He, 103:^{1}H, 104:^{2}H, 105:^{3}H, 107:^{4}He
^{94}Nb	28:^{1}H, 32:^{2}H, 33:^{3}H, 22:^{4}He, 103:^{1}H, 104:^{2}H, 105:^{3}H, 106:^{3}He, 107:^{4}He, 102:photon
^{95}Nb	28:^{1}H, 32:^{2}H, 33:^{3}H, 22:^{4}He, 103:^{1}H, 104:^{2}H, 105:^{3}H, 106:^{3}He, 107:^{4}He, 102:photon
^{92}Mo	28:^{1}H, 22:^{4}He, 103:^{1}H, 111:^{1}H, 104:^{2}H, 105:^{3}H, 106:^{3}He, 107:^{4}He
^{94}Mo	28:^{1}H, 22:^{4}He, 103:^{1}H, 111:^{1}H, 104:^{2}H, 105:^{3}H, 106:^{3}He, 107:^{4}He
^{95}Mo	107:^{4}He
^{96}Mo	28:^{1}H, 22:^{4}He, 103:^{1}H, 104:^{2}H, 105:^{3}H, 107:^{4}He
^{97}Mo	28:^{1}H, 22:^{4}He, 103:^{1}H, 104:^{2}H, 105:^{3}H, 106:^{3}He, 107:^{4}He
^{98}Mo	28:^{1}H, 22:^{4}He, 103:^{1}H, 104:^{2}H, 105:^{3}H, 107:^{4}He
^{99}Mo	28:^{1}H, 32:^{2}H, 33:^{3}H, 22:^{4}He, 103:^{1}H, 104:^{2}H, 105:^{3}H, 107:^{4}He, 102:photon
^{100}Mo	28:^{1}H, 22:^{4}He, 103:^{1}H, 104:^{2}H, 105:^{3}H, 107:^{4}He, 102:photon
^{96}Ru	28:^{1}H, 32:^{2}H, 22:^{4}He, 103:^{1}H, 111:^{1}H, 104:^{2}H, 105:^{3}H, 106:^{3}He, 107:^{4}He, 102:photon
^{98}Ru	28:^{1}H, 32:^{2}H, 22:^{4}He, 103:^{1}H, 111:^{1}H, 104:^{2}H, 105:^{3}H, 106:^{3}He, 107:^{4}He, 102:photon
^{99}Ru	28:^{1}H, 32:^{2}H, 22:^{4}He, 103:^{1}H, 104:^{2}H, 105:^{3}H, 106:^{3}He, 107:^{4}He, 102:photon
^{100}Ru	28:^{1}H, 32:^{2}H, 22:^{4}He, 103:^{1}H, 104:^{2}H, 105:^{3}H, 107:^{4}He, 102:photon
^{102}Ru	28:^{1}H, 22:^{4}He, 103:^{1}H, 104:^{2}H, 105:^{3}H, 106:^{3}He, 107:^{4}He, 102:photon
^{103}Ru	28:^{1}H, 22:^{4}He, 103:^{1}H, 104:^{2}H, 105:^{3}H, 107:^{4}He, 102:photon
^{104}Ru	28:^{1}H, 22:^{4}He, 103:^{1}H, 104:^{2}H, 105:^{3}H, 107:^{4}He, 102:photon
^{105}Ru	28:^{1}H, 22:^{4}He, 103:^{1}H, 104:^{2}H, 105:^{3}H, 107:^{4}He, 102:photon
^{106}Ru	28:^{1}H, 22:^{4}He, 103:^{1}H, 104:^{2}H, 105:^{3}H, 107:^{4}He, 102:photon
^{103}Rh	107:^{4}He
^{105}Rh	28:^{1}H, 32:^{2}H, 33:^{3}H, 22:^{4}He, 103:^{1}H, 104:^{2}H, 105:^{3}H, 107:^{4}He, 102:photon
^{107}Pd	28:^{1}H, 32:^{2}H, 22:^{4}He, 103:^{1}H, 104:^{2}H, 105:^{3}H, 107:^{4}He, 102:photon
^{110m1}Ag	28:^{1}H, 32:^{2}H, 33:^{3}H, 22:^{4}He, 103:^{1}H, 104:^{2}H, 105:^{3}H, 106:^{3}He, 107:^{4}He, 102:photon
^{106}Cd	28:^{1}H, 32:^{2}H, 22:^{4}He, 103:^{1}H, 111:^{1}H, 104:^{2}H, 105:^{3}H, 106:^{3}He, 107:^{4}He
^{108}Cd	28:^{1}H, 32:^{2}H, 33:^{3}H, 22:^{4}He, 103:^{1}H, 104:^{2}H, 105:^{3}H, 106:^{3}He, 107:^{4}He, 102:photon
^{110}Cd	28:^{1}H, 32:^{2}H, 33:^{3}H, 22:^{4}He, 103:^{1}H, 104:^{2}H, 105:^{3}H, 106:^{3}He, 107:^{4}He, 102:photon
^{111}Cd	28:^{1}H, 32:^{2}H, 22:^{4}He, 103:^{1}H, 104:^{2}H, 105:^{3}H, 107:^{4}He
^{112}Cd	28:^{1}H, 32:^{2}H, 33:^{3}H, 22:^{4}He, 103:^{1}H, 104:^{2}H, 105:^{3}H, 106:^{3}He, 107:^{4}He, 102:photon
^{113}Cd	28:^{1}H, 22:^{4}He, 103:^{1}H, 104:^{2}H, 105:^{3}H, 107:^{4}He, 102:photon
^{114}Cd	28:^{1}H, 32:^{2}H, 33:^{3}H, 22:^{4}He, 103:^{1}H, 104:^{2}H, 105:^{3}H, 106:^{3}He, 107:^{4}He, 102:photon
^{116}Cd	28:^{1}H, 32:^{2}H, 33:^{3}H, 22:^{4}He, 103:^{1}H, 104:^{2}H, 105:^{3}H, 106:^{3}He, 107:^{4}He, 102:photon
^{113}In	28:^{1}H, 32:^{2}H, 22:^{4}He, 103:^{1}H, 104:^{2}H, 105:^{3}H, 106:^{3}He, 107:^{4}He, 102:photon
^{115}In	28:^{1}H, 32:^{2}H, 33:^{3}H, 22:^{4}He, 103:^{1}H, 104:^{2}H, 105:^{3}H, 107:^{4}He, 102:photon
^{112}Sn	28:^{1}H, 22:^{4}He, 103:^{1}H, 111:^{1}H, 104:^{2}H, 105:^{3}H, 106:^{3}He, 107:^{4}He, 102:photon
^{114}Sn	28:^{1}H, 22:^{4}He, 103:^{1}H, 104:^{2}H, 105:^{3}H, 106:^{3}He, 107:^{4}He, 102:photon
^{115}Sn	28:^{1}H, 32:^{2}H, 22:^{4}He, 103:^{1}H, 104:^{2}H, 105:^{3}H, 106:^{3}He, 107:^{4}He, 102:photon
^{116}Sn	28:^{1}H, 22:^{4}He, 103:^{1}H, 104:^{2}H, 105:^{3}H, 107:^{4}He, 102:photon
^{117}Sn	28:^{1}H, 32:^{2}H, 22:^{4}He, 103:^{1}H, 104:^{2}H, 105:^{3}H, 107:^{4}He, 102:photon
^{118}Sn	28:^{1}H, 22:^{4}He, 103:^{1}H, 104:^{2}H, 105:^{3}H, 107:^{4}He, 102:photon
^{119}Sn	103:^{1}H, 104:^{2}H, 105:^{3}H, 106:^{3}He, 107:^{4}He
^{122}Sn	28:^{1}H, 22:^{4}He, 103:^{1}H, 104:^{2}H, 105:^{3}H, 107:^{4}He, 102:photon
^{123}Sn	28:^{1}H, 22:^{4}He, 103:^{1}H, 104:^{2}H, 105:^{3}H, 107:^{4}He, 102:photon

Continued on next page

TABLE XXVII – continued from previous page

Nuclide	MT : outgoing particle
^{124}Sn	28:^{1}H, 22:^{4}He, 103:^{1}H, 104:^{2}H, 105:^{3}H, 107:^{4}He, 102:photon
^{126}Sn	28:^{1}H, 22:^{4}He, 103:^{1}H, 104:^{2}H, 105:^{3}H, 107:^{4}He, 102:photon
^{121}Sb	28:^{1}H, 22:^{4}He, 103:^{1}H, 104:^{2}H, 105:^{3}H, 107:^{4}He, 102:photon
^{123}Sb	28:^{1}H, 22:^{4}He, 103:^{1}H, 104:^{2}H, 105:^{3}H, 107:^{4}He, 102:photon
^{124}Sb	28:^{1}H, 32:^{2}H, 33:^{3}H, 22:^{4}He, 103:^{1}H, 104:^{2}H, 105:^{3}H, 107:^{4}He, 102:photon
^{125}Sb	28:^{1}H, 32:^{2}H, 33:^{3}H, 22:^{4}He, 103:^{1}H, 104:^{2}H, 105:^{3}H, 107:^{4}He, 102:photon
^{120}Te	28:^{1}H, 32:^{2}H, 22:^{4}He, 103:^{1}H, 104:^{2}H, 105:^{3}H, 106:^{3}He, 107:^{4}He, 102:photon
^{122}Te	28:^{1}H, 22:^{4}He, 103:^{1}H, 104:^{2}H, 105:^{3}H, 106:^{3}He, 107:^{4}He, 102:photon
^{123}Te	28:^{1}H, 32:^{2}H, 22:^{4}He, 103:^{1}H, 104:^{2}H, 105:^{3}H, 106:^{3}He, 107:^{4}He, 102:photon
^{124}Te	28:^{1}H, 22:^{4}He, 103:^{1}H, 104:^{2}H, 105:^{3}H, 107:^{4}He, 102:photon
^{125}Te	28:^{1}H, 32:^{2}H, 22:^{4}He, 103:^{1}H, 104:^{2}H, 105:^{3}H, 107:^{4}He, 102:photon
^{126}Te	28:^{1}H, 22:^{4}He, 103:^{1}H, 104:^{2}H, 105:^{3}H, 107:^{4}He, 102:photon
^{127m1}Te	28:^{1}H, 32:^{2}H, 22:^{4}He, 103:^{1}H, 104:^{2}H, 105:^{3}H, 107:^{4}He, 102:photon
^{128}Te	28:^{1}H, 22:^{4}He, 103:^{1}H, 104:^{2}H, 105:^{3}H, 107:^{4}He, 102:photon
^{129m1}Te	28:^{1}H, 32:^{2}H, 22:^{4}He, 103:^{1}H, 104:^{2}H, 105:^{3}H, 107:^{4}He, 102:photon
^{130}Te	28:^{1}H, 22:^{4}He, 103:^{1}H, 104:^{2}H, 105:^{3}H, 107:^{4}He, 102:photon
^{129}I	28:^{1}H, 32:^{2}H, 33:^{3}H, 22:^{4}He, 103:^{1}H, 104:^{2}H, 105:^{3}H, 107:^{4}He, 102:photon
^{131}I	28:^{1}H, 32:^{2}H, 33:^{3}H, 22:^{4}He, 103:^{1}H, 104:^{2}H, 105:^{3}H, 107:^{4}He, 102:photon
^{135}I	28:^{1}H, 22:^{4}He, 103:^{1}H, 104:^{2}H, 105:^{3}H, 107:^{4}He, 102:photon
^{126}Xe	28:^{1}H, 22:^{4}He, 103:^{1}H, 104:^{2}H, 105:^{3}H, 106:^{3}He, 107:^{4}He, 102:photon
^{128}Xe	28:^{1}H, 22:^{4}He, 103:^{1}H, 104:^{2}H, 105:^{3}H, 107:^{4}He, 102:photon
^{129}Xe	28:^{1}H, 32:^{2}H, 22:^{4}He, 103:^{1}H, 104:^{2}H, 105:^{3}H, 106:^{3}He, 107:^{4}He, 102:photon
^{130}Xe	103:^{1}H, 104:^{2}H, 105:^{3}H, 107:^{4}He, 102:photon
^{132}Xe	28:^{1}H, 22:^{4}He, 103:^{1}H, 104:^{2}H, 105:^{3}H, 107:^{4}He, 102:photon
^{133}Xe	28:^{1}H, 32:^{2}H, 22:^{4}He, 103:^{1}H, 104:^{2}H, 105:^{3}H, 107:^{4}He, 102:photon
^{134}Xe	28:^{1}H, 22:^{4}He, 103:^{1}H, 104:^{2}H, 105:^{3}H, 107:^{4}He, 102:photon
^{135}Xe	28:^{1}H, 32:^{2}H, 22:^{4}He, 103:^{1}H, 104:^{2}H, 105:^{3}H, 107:^{4}He, 102:photon
^{136}Xe	28:^{1}H, 22:^{4}He, 103:^{1}H, 104:^{2}H, 105:^{3}H, 107:^{4}He, 102:photon
^{134}Cs	115:^{1}H, 115:^{2}H, 116:^{1}H, 116:^{3}H, 112:^{1}H, 112:^{4}He, 103:^{1}H, 111:^{1}H, 117:^{2}H, 117:^{4}He, 104:^{2}H, 105:^{3}H, 106:^{3}He, 107:^{4}He, 108:^{4}He
^{135}Cs	28:^{1}H, 32:^{2}H, 33:^{3}H, 22:^{4}He, 103:^{1}H, 104:^{2}H, 105:^{3}H, 107:^{4}He, 102:photon
^{136}Cs	28:^{1}H, 32:^{2}H, 33:^{3}H, 22:^{4}He, 103:^{1}H, 104:^{2}H, 105:^{3}H, 107:^{4}He, 102:photon
^{137}Cs	28:^{1}H, 32:^{2}H, 33:^{3}H, 22:^{4}He, 103:^{1}H, 104:^{2}H, 105:^{3}H, 107:^{4}He, 102:photon
^{130}Ba	28:^{1}H, 32:^{2}H, 22:^{4}He, 103:^{1}H, 111:^{1}H, 104:^{2}H, 105:^{3}H, 106:^{3}He, 107:^{4}He, 102:photon
^{132}Ba	28:^{1}H, 22:^{4}He, 103:^{1}H, 104:^{2}H, 105:^{3}H, 106:^{3}He, 107:^{4}He, 102:photon
^{134}Ba	28:^{1}H, 22:^{4}He, 103:^{1}H, 104:^{2}H, 105:^{3}H, 107:^{4}He, 102:photon
^{135}Ba	28:^{1}H, 32:^{2}H, 22:^{4}He, 103:^{1}H, 104:^{2}H, 105:^{3}H, 106:^{3}He, 107:^{4}He, 102:photon
^{136}Ba	28:^{1}H, 22:^{4}He, 103:^{1}H, 104:^{2}H, 105:^{3}H, 107:^{4}He, 102:photon
^{137}Ba	28:^{1}H, 32:^{2}H, 22:^{4}He, 103:^{1}H, 104:^{2}H, 105:^{3}H, 107:^{4}He, 102:photon
^{138}Ba	28:^{1}H, 22:^{4}He, 103:^{1}H, 104:^{2}H, 105:^{3}H, 106:^{3}He, 107:^{4}He, 102:photon
^{140}Ba	103:^{1}H, 111:^{1}H, 104:^{2}H, 105:^{3}H, 106:^{3}He, 107:^{4}He, 102:photon
^{138}La	28:^{1}H, 32:^{2}H, 33:^{3}H, 22:^{4}He, 103:^{1}H, 104:^{2}H, 105:^{3}H, 106:^{3}He, 107:^{4}He, 102:photon
^{140}Ce	28:^{1}H, 32:^{2}H, 22:^{4}He, 103:^{1}H, 104:^{2}H, 105:^{3}H, 107:^{4}He, 102:photon
^{141}Ce	28:^{1}H, 22:^{4}He, 103:^{1}H, 104:^{2}H, 105:^{3}H, 106:^{3}He, 107:^{4}He, 102:photon
^{142}Ce	28:^{1}H, 32:^{2}H, 33:^{3}H, 22:^{4}He, 103:^{1}H, 104:^{2}H, 105:^{3}H, 107:^{4}He, 102:photon
^{144}Ce	28:^{1}H, 32:^{2}H, 33:^{3}H, 22:^{4}He, 103:^{1}H, 104:^{2}H, 105:^{3}H, 107:^{4}He, 102:photon
^{143}Pr	28:^{1}H, 32:^{2}H, 33:^{3}H, 22:^{4}He, 103:^{1}H, 104:^{2}H, 105:^{3}H, 106:^{3}He, 107:^{4}He, 102:photon
^{143}Nd	107:^{4}He
^{145}Nd	107:^{4}He
^{147}Pm	103:^{1}H, 104:^{2}H, 105:^{3}H, 106:^{3}He, 107:^{4}He
^{148}Pm	28:^{1}H, 32:^{2}H, 33:^{3}H, 22:^{4}He, 103:^{1}H, 104:^{2}H, 105:^{3}H, 106:^{3}He, 107:^{4}He, 102:photon
^{148m1}Pm	28:^{1}H, 22:^{4}He, 103:^{1}H, 104:^{2}H, 105:^{3}H, 107:^{4}He, 102:photon
^{149}Pm	28:^{1}H, 32:^{2}H, 33:^{3}H, 22:^{4}He, 103:^{1}H, 104:^{2}H, 105:^{3}H, 107:^{4}He, 102:photon
^{147}Sm	107:^{4}He
^{149}Sm	107:^{4}He
^{153}Sm	103:^{1}H, 104:^{2}H, 105:^{3}H, 106:^{3}He, 107:^{4}He
^{151}Eu	28:^{1}H, 22:^{4}He, 103:^{1}H, 104:^{2}H, 105:^{3}H, 106:^{3}He, 107:^{4}He, 102:photon

Continued on next page

TABLE XXVII – continued from previous page

Nuclide	MT : outgoing particle
^{152}Eu	28:^{1}H, 32:^{2}H, 33:^{3}H, 22:^{4}He, 103:^{1}H, 104:^{2}H, 105:^{3}H, 106:^{3}He, 107:^{4}He, 102:photon
^{153}Eu	112:^{1}H, 112:^{4}He, 103:^{1}H, 104:^{2}H, 105:^{3}H, 106:^{3}He, 107:^{4}He
^{154}Eu	28:^{1}H, 22:^{4}He, 103:^{1}H, 104:^{2}H, 105:^{3}H, 107:^{4}He, 102:photon
^{155}Eu	103:^{1}H, 104:^{2}H, 105:^{3}H, 106:^{3}He, 107:^{4}He
^{156}Eu	28:^{1}H, 32:^{2}H, 33:^{3}H, 22:^{4}He, 103:^{1}H, 104:^{2}H, 105:^{3}H, 107:^{4}He, 102:photon
^{152}Gd	107:^{4}He
^{153}Gd	107:^{4}He
^{155}Gd	107:^{4}He
^{157}Gd	107:^{4}He
^{159}Tb	28:^{1}H, 32:^{2}H, 33:^{3}H, 22:^{4}He, 103:^{1}H, 104:^{2}H, 105:^{3}H, 107:^{4}He, 102:photon
^{154}Dy	112:^{1}H, 112:^{4}He, 103:^{1}H, 111:^{1}H, 117:^{2}H, 117:^{4}He, 104:^{2}H, 105:^{3}H, 106:^{3}He, 107:^{4}He, 108:^{4}He
^{159}Dy	103:^{1}H, 104:^{2}H, 105:^{3}H, 106:^{3}He, 107:^{4}He
^{162}Er	28:^{1}H, 22:^{4}He, 103:^{1}H, 104:^{2}H, 105:^{3}H, 107:^{4}He
^{164}Er	28:^{1}H, 22:^{4}He, 103:^{1}H, 104:^{2}H, 105:^{3}H, 107:^{4}He
^{166}Er	28:^{1}H, 32:^{2}H, 22:^{4}He, 103:^{1}H, 104:^{2}H, 105:^{3}H, 107:^{4}He
^{167}Er	28:^{1}H, 32:^{2}H, 22:^{4}He, 103:^{1}H, 104:^{2}H, 105:^{3}H, 107:^{4}He
^{168}Er	28:^{1}H, 32:^{2}H, 22:^{4}He, 103:^{1}H, 104:^{2}H, 105:^{3}H, 107:^{4}He
^{170}Er	28:^{1}H, 32:^{2}H, 22:^{4}He, 103:^{1}H, 104:^{2}H, 105:^{3}H, 107:^{4}He
^{168}Yb	28:^{1}H, 32:^{2}H, 22:^{4}He, 103:^{1}H, 104:^{2}H, 105:^{3}H, 106:^{3}He, 107:^{4}He, 102:photon
^{170}Yb	28:^{1}H, 32:^{2}H, 22:^{4}He, 103:^{1}H, 104:^{2}H, 105:^{3}H, 106:^{3}He, 107:^{4}He, 102:photon
^{171}Yb	28:^{1}H, 32:^{2}H, 22:^{4}He, 103:^{1}H, 104:^{2}H, 105:^{3}H, 106:^{3}He, 107:^{4}He, 102:photon
^{172}Yb	28:^{1}H, 32:^{2}H, 22:^{4}He, 103:^{1}H, 104:^{2}H, 105:^{3}H, 106:^{3}He, 107:^{4}He, 102:photon
^{173}Yb	28:^{1}H, 32:^{2}H, 22:^{4}He, 103:^{1}H, 104:^{2}H, 105:^{3}H, 106:^{3}He, 107:^{4}He, 102:photon
^{174}Yb	28:^{1}H, 32:^{2}H, 22:^{4}He, 103:^{1}H, 104:^{2}H, 105:^{3}H, 106:^{3}He, 107:^{4}He, 102:photon
^{176}Yb	28:^{1}H, 32:^{2}H, 22:^{4}He, 103:^{1}H, 104:^{2}H, 105:^{3}H, 106:^{3}He, 107:^{4}He, 102:photon
^{175}Lu	103:^{1}H, 107:^{4}He, 102:photon
^{176}Lu	103:^{1}H, 107:^{4}He, 102:photon
^{174}Hf	28:^{1}H, 32:^{2}H, 22:^{4}He, 103:^{1}H, 104:^{2}H, 105:^{3}H, 106:^{3}He, 107:^{4}He, 102:photon
^{176}Hf	28:^{1}H, 32:^{2}H, 22:^{4}He, 103:^{1}H, 104:^{2}H, 105:^{3}H, 106:^{3}He, 107:^{4}He, 102:photon
^{178}Hf	28:^{1}H, 32:^{2}H, 22:^{4}He, 103:^{1}H, 104:^{2}H, 105:^{3}H, 106:^{3}He, 107:^{4}He, 102:photon
^{179}Hf	28:^{1}H, 32:^{2}H, 22:^{4}He, 103:^{1}H, 104:^{2}H, 105:^{3}H, 106:^{3}He, 107:^{4}He, 102:photon
^{180}Hf	28:^{1}H, 32:^{2}H, 22:^{4}He, 103:^{1}H, 104:^{2}H, 105:^{3}H, 106:^{3}He, 107:^{4}He, 102:photon
^{181}Hf	28:^{1}H, 32:^{2}H, 22:^{4}He, 103:^{1}H, 104:^{2}H, 105:^{3}H, 106:^{3}He, 107:^{4}He, 102:photon
^{182}Hf	28:^{1}H, 32:^{2}H, 22:^{4}He, 103:^{1}H, 104:^{2}H, 105:^{3}H, 106:^{3}He, 107:^{4}He, 102:photon
^{182}Ta	107:^{4}He, 102:photon
^{184}Os	103:^{1}H, 104:^{2}H, 105:^{3}H, 106:^{3}He, 107:^{4}He
^{186}Os	103:^{1}H, 104:^{2}H, 105:^{3}H, 106:^{3}He, 107:^{4}He
^{187}Os	103:^{1}H, 104:^{2}H, 105:^{3}H, 106:^{3}He, 107:^{4}He
^{188}Os	103:^{1}H, 104:^{2}H, 105:^{3}H, 106:^{3}He, 107:^{4}He
^{189}Os	103:^{1}H, 104:^{2}H, 105:^{3}H, 106:^{3}He, 107:^{4}He
^{190}Os	103:^{1}H, 104:^{2}H, 105:^{3}H, 106:^{3}He, 107:^{4}He
^{192}Os	103:^{1}H, 104:^{2}H, 105:^{3}H, 106:^{3}He, 107:^{4}He
^{196}Hg	28:^{1}H, 22:^{4}He, 103:^{1}H, 104:^{2}H, 107:^{4}He
^{198}Hg	28:^{1}H, 22:^{4}He, 103:^{1}H, 104:^{2}H, 107:^{4}He
^{199}Hg	28:^{1}H, 22:^{4}He, 103:^{1}H, 104:^{2}H, 107:^{4}He
^{200}Hg	28:^{1}H, 22:^{4}He, 103:^{1}H, 104:^{2}H, 107:^{4}He
^{201}Hg	28:^{1}H, 22:^{4}He, 103:^{1}H, 104:^{2}H, 107:^{4}He
^{202}Hg	28:^{1}H, 22:^{4}He, 103:^{1}H, 104:^{2}H, 107:^{4}He
^{204}Hg	28:^{1}H, 22:^{4}He, 103:^{1}H, 104:^{2}H, 107:^{4}He
^{209}Bi	28:^{1}H, 32:^{2}H, 33:^{3}H, 22:^{4}He, 103:^{1}H, 104:^{2}H, 105:^{3}H, 106:^{3}He, 107:^{4}He
^{223}Ra	102:photon
^{224}Ra	102:photon
^{225}Ra	102:photon
^{226}Ra	102:photon
^{235}U	800-835:^{4}He
^{238}Pu	102:photon
^{242}Am	102:photon

Continued on next page

TABLE XXVII – continued from previous page

Nuclide	MT : outgoing particle
^{242m1}Am	102:photon
^{244}Am	102:photon
^{244m1}Am	102:photon

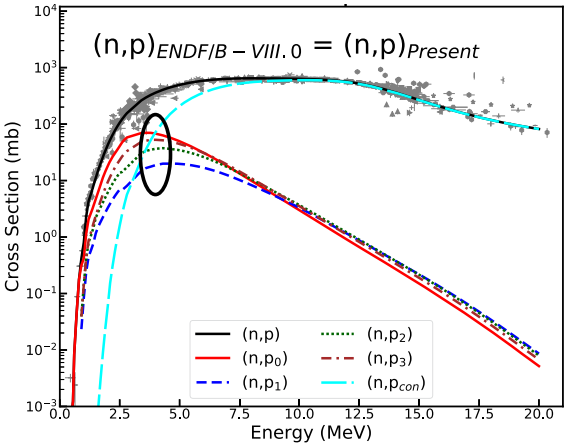
b. Missing distributions adopted from reaction models

To complete missing angular distributions and energy spectra of secondary particles in the ENDF/B-VIII.0 library, a statistical Hauser-Feshbach code, CoH_3 [94], was used for calculating angular distributions for neutron-induced charged particle reactions including (n,p), (n,α), (n,d), (n,t) and (n,^{3}He).

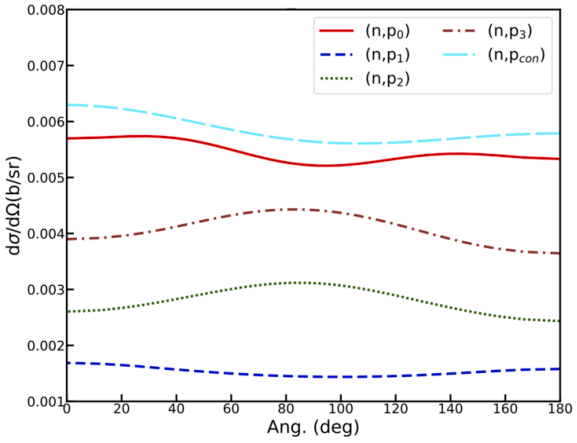
In the CoH_3 calculations, we employ the OMP parameters by Koning and Delaroche [477] for proton and neutron, Avrigeanu *et al.* [478] for α-particle, Bojowald *et al.* [479] for deuteron, and Becchetti *el al.* [480] for triton and ^{3}He. The Gilbert-Cameron level density [408] is adopted for all nuclei. Q-values are updated using the mass data in Audi's 2012 mass table [481] and FRDM2012 [482]. Isotropic angular distributions in ENDF/B-VIII.0 are replaced with explicit angular distributions from CoH_3-calculated results. Energy distributions of the emitted particles are described in terms of the preequilibrium process and the compound nuclear reaction. In the preequilibrium process, the two-component exciton model [483] is employed with the angular distribution described by Kalbach's systematics [405].

Depending on the reaction in ENDF/B-VIII.0, differential cross sections are presented in two ways: (1) only the total (n,X) reaction cross section is given, where X=p, d, α, and so on, or (2) the (n,X) cross section is divided into the discrete level population σ_0, σ_1, ..., σ_i and the continuum part $\sigma_{\rm cont}$. For the case of (1), missing discrete level cross sections were newly calculated and renormalized to make the total cross section ($\sum_i \sigma_i + \sigma_{\rm cont}$) equal to the cross section given in ENDF/B-VIII.0. For example, ^{58}Ni in the ENDF/B-VIII.0 library has no partial (n,p) cross sections for discrete levels. We included 10 discrete levels of these residual nuclei to calculate cross sections as well as angular distributions of those levels.

Fig. 105(a) shows that the total (n,p) cross section is exactly the same as that given in ENDF/B-VIII.0, along with four newly decomposed cross sections of the discrete levels and the continuum part. The additional angular distributions for these levels in the laboratory system are calculated and shown Fig. 105(b) at the neutron incident energy of 4.0 MeV, which corresponds to the black circle in the top panel. For the case of (2), we simply adopted partial and continuum cross sections as given in ENDF/B-VIII.0 and replaced the isotropic angular distributions in ENDF/B-VIII.0 with the new calculations by CoH_3 for discrete levels of charged particle emissions. Fig. 106 shows the angular distributions for discrete levels of proton (Fig. 106(a)) and alpha (Fig. 106(b)) emissions induced by 10 MeV neutrons for ^{90}Zr.



(a)^{58}Ni(n,p) cross sections.

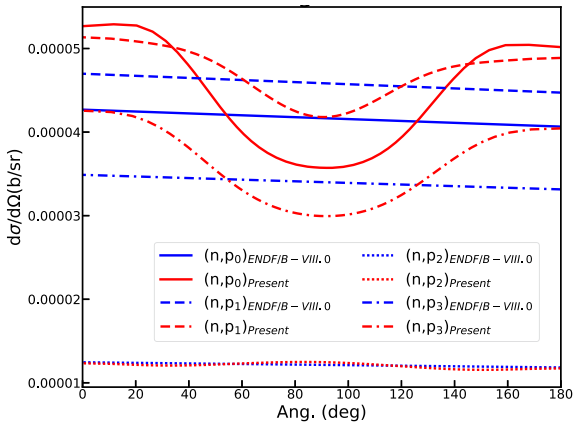


(b)^{58}Ni(n,p) angular distributions at neutron incident energy of 4.0MeV.

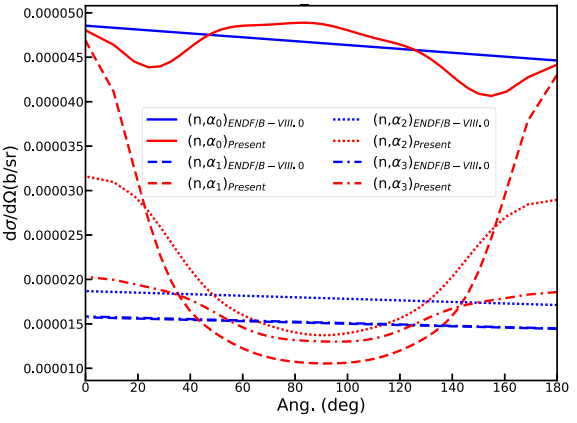
FIG. 105. Evaluated ^{58}Ni(n,p) cross sections are exactly the same as those of ENDF/B-VIII.0. The total (n,p) cross sections, along with those to the ground state, the first three excited states and to the continuum, are shown in the panel (a). Angular distributions of emitted protons induced by 4.0 MeV neutrons (black ellipse in the top plot) are shown in the panel (b) after converting calculations to the Lab system.

Numbers of discrete levels to calculate the (n,p), (n,α), (n,d), (n,t) and (n,^{3}He) reaction cross sections are listed in Table XXVIII for 53 nuclides [484].

The numbers in parenthesis are those given in ENDF/B-VIII.0, which show that many evaluations in ENDF/B-VIII.0 do not contain any information on discrete-level productions. As a consistent approach, we calculated discrete-level cross sections up to the maxi-



(a)^{90}Zr(n,p) angular distributions.



(b)^{90}Zr(n,α) angular distributions.

FIG. 106. Angular distributions at neutron incident energy of 10 MeV for discrete levels of (n,p) and (n,α) in reactions in panels (a) and (b), respectively, in the Lab system are compared to those for ^{90}Zr. Most of the distributions of new evaluations are 90-degree symmetric in the CM system while those of ENDF/B-VIII.0 are isotropic.

mum ten discrete levels for these. Photon productions both in discrete transitions and in the continuum are also replaced by CoH_3 results to preserve proper energy balance. Details of this work can be found in Ref. [484].

4. Fission-product updates in the URR

The capture, elastic and total cross sections in the URR were revised and updated for many fission products. Experimental data and other evaluations, in particular ENDF/B-VIII.0 and JENDL-4.0 [447], were considered when revising outdated values. Table XXIX summarizes all these updates implemented in ENDF/B-VIII.1. Fig. 107 shows a couple of illustrative and representative examples of the changes made in the files described in this section, in this case for ^{99}Tc (Fig. 107(a)) and ^{137}Ba (Fig. 107(b)) in the URR.

TABLE XXVIII. Numbers of discrete levels in the residual nuclei included to calculate (n,p), (n,α), (n,d), (n,t) and (n,^{3}He) reaction cross sections. The numbers in parenthesis present the number of discrete levels given in ENDF/B-VIII.0, where "0" stands for no partial cross section given in the evaluation.

Target	p	α	d	t	^{3}He
^{27}Al	20 (20)	20 (20)	20 (20)	11 (11)	-
^{29}Si	16 (16)	20 (20)	-	-	-
^{30}Si	6 (6)	12 (12)	-	-	-
^{31}Si	1 (1)	15 (15)	-	-	-
^{32}Si	1 (1)	1 (1)	-	-	-
^{35}Cl	30 (30)	21 (21)	31 (31)	31 (31)	-
^{36}Cl	16 (16)	32 (32)	16 (16)	32 (32)	-
^{37}Cl	10 (0)	6 (6)	12 (12)	16 (16)	-
^{39}K	10 (0)	10 (0)	-	-	-
^{40}K	10 (0)	10 (0)	-	-	-
^{41}K	10 (0)	10 (0)	-	-	-
^{46}Ti	10 (0)	10 (0)	10 (0)	10 (0)	10 (0)
^{47}Ti	10 (0)	10 (0)	10 (0)	10 (0)	10 (0)
^{48}Ti	10 (0)	10 (0)	10 (0)	10 (0)	10 (0)
^{49}Ti	10 (0)	10 (0)	10 (0)	10 (0)	10 (0)
^{50}Ti	9 (0)	10 (0)	10 (0)	10 (0)	10 (0)
^{49}V	40 (40)	40 (40)	-	-	-
^{50}V	10 (0)	10 (0)	10 (0)	10 (0)	10 (0)
^{51}V	10 (0)	10 (0)	10 (0)	10 (0)	10 (0)
^{51}Cr	10 (0)	10 (0)	10 (0)	10 (0)	10 (0)
^{58}Co	40 (40)	40 (40)	10 (0)	10 (0)	-
^{59}Co	10 (0)	10 (0)	10 (0)	10 (0)	10 (0)
^{58}Ni	10 (0)	10 (0)	10 (0)	10 (0)	-
^{59}Ni	10 (0)	10 (0)	10 (0)	10 (0)	10 (0)
^{60}Ni	10 (0)	10 (0)	10 (0)	10 (0)	-
^{61}Ni	10 (0)	10 (0)	10 (0)	10 (0)	-
^{62}Ni	10 (0)	10 (0)	10 (0)	10 (0)	-
^{63}Ni	26 (26)	28 (28)	-	-	-
^{64}Ni	10 (0)	1 (0)	10 (0)	10 (0)	-
^{63}Cu	10 (0)	10 (0)	10 (0)	10 (0)	-
^{64}Cu	40 (40)	40 (40)	-	-	-
^{65}Cu	10 (0)	10 (0)	10 (0)	10 (0)	-
^{64}Zn	10 (0)	10 (0)	10 (0)	10 (0)	10 (0)
^{65}Zn	10 (0)	10 (0)	10 (0)	10 (0)	10 (0)
^{66}Zn	10 (0)	10 (0)	10 (0)	10 (0)	10 (0)
^{67}Zn	10 (0)	10 (0)	10 (0)	10 (0)	10 (0)
^{68}Zn	8 (0)	10 (0)	10 (0)	10 (0)	10 (0)
^{69}Zn	17 (17)	18 (18)	-	-	-
^{70}Zn	1 (0)	1 (0)	10 (0)	10 (0)	-
^{73}As	10 (0)	10 (0)	-	-	-
^{74}As	10 (0)	10 (0)	-	-	-
^{90}Zr	12 (12)	9 (9)	10 (0)	10 (0)	-
^{91}Zr	6 (6)	40 (40)	10 (0)	10 (0)	-
^{92}Zr	1 (1)	40 (40)	10 (0)	10 (0)	-
^{93}Zr	17 (17)	27 (27)	9 (0)	10 (0)	-
^{94}Zr	10 (10)	40 (40)	10 (0)	9 (0)	-
^{95}Zr	16 (16)	9 (9)	10 (0)	10 (0)	-
^{96}Zr	3 (3)	10 (10)	10 (0)	10 (0)	-
^{107}Ag	10 (0)	10 (0)	-	-	-
^{109}Ag	31 (31)	2 (2)	-	-	-
^{180}Ta	10 (0)	10 (0)	10 (0)	10 (0)	-
^{181}Ta	10 (0)	10 (0)	-	-	10 (0)
^{197}Au	10 (0)	10 (0)	-	-	-

TABLE XXIX: Description of the URR updates for fission products. They were based in either ENDF/B-VIII.0 and/or JENDL-4.0 [447] with revisions made to the specified reactions and energy ranges.

Isotope	Description
^{78}Se	Total, elastic, and capture were revised between 12 to 600 keV. Adopted JENDL-4 evaluation above 600 keV.
^{84}Kr	URR parameters from JENDL-4 from 20 to 500 keV. Elastic and capture cross sections were revised between 20 to 100 keV; above 100 keV is unchanged from JENDL-4.
^{85}Rb	URR is from 8.468 to 100 keV. Elastic and total are revised between 8.468 to 100 keV. Revised capture is in good agreement with Beer & Macklin data [485].
^{97}Mo	URR parameters from JENDL-4 from 2 to 100 keV. Total, elastic, and capture revised between 2 to 300 keV. Same as ENDF/B-VIII.0 between 0.30 to 20 MeV.
^{99}Tc	Adopted initially ENDF/B-VIII.0 URR, which is defined from 6.38 to 140.34 keV. Elastic and capture were revised from 6.38 to 450 keV. Cross sections above 450 keV were maintained from ENDF/B-VIII.0.
^{102}Pd	In ENDF/B-VIII.0, resolved parameters are up to 820 eV, without URR. Elastic and capture revised from 820 eV to 4 MeV. Same as ENDF/B-VIII.0 above 4 MeV.
^{109}Ag	URR parameters taken from JENDL-4 for the energy range 7.0095 to 88.915 keV. Total, elastic, and capture are revised for 7.0095 to 100 keV. Capture is lower than ENDF/B-VIII.0 by 3.6 – 21.8% from 10 to 80 keV.
^{113}In	Capture and elastic were revised from JENDL-4 between 0.83 and 250 keV. Capture is 13% higher from 0.83 to 100 keV.
^{115}In	Total, elastic and capture changed from ENDF/B-VIII.0 between 2 – 300 keV. Revised capture is in good agreement with Kononov *et al.* [354, 486].
^{115}Sn	Elastic and total are changed from ENDF/B-VIII.0 between 0.9 – 300 keV. Revised capture is in good agreement with Wisshak *et al.* [487].
^{119}Sn	Adopted JENDL-4 with elastic and capture revised between 1.3 – 100 keV. Revised capture is in good agreement with Timokhov *et al.* [488].
^{127}I	Adopted URR from JENDL-4, with cross section (total, elastic, and capture) revisions between 5.2 to 200 keV. Capture is in very close agreement with Macklin [489] between 10 to 100 keV.
^{122}Te	Adopted JENDL-4 with elastic and total changed between 11 - 200 keV. Revised capture is in good agreement with Wisshak *et al.* [490].
^{124}Te	Elastic and total cross sections changed between 15.0 - 150 keV. Revised capture is in good agreement with Wisshak *et al.* [490].
^{133}Cs	Adopted unresolved parameters from ENDF/B-VII.0 between 4 and 81.607 keV. Revised elastic and capture cross sections were revised from 4 to 100 keV. Capture is excellent agreement with Bokhovko *et al.* [491].
^{134}Cs	Adopted JENDL-4, which has URR defined from 270 eV to 100 keV. Elastic and capture were revised between 270 eV and 170 keV, resulting in capture being 15% higher than JENDL-4 between 4 and 100 keV.
^{130}Ba	URR from ENDF/B-VIII.0 (2.8 keV - 100 keV), with revised capture and elastic cross sections from 2.8 to 200 keV.
^{134}Ba	Adopted JENDL-4, which has URR defined from 10.575 to 200 keV. Capture and elastic cross sections revised between 10.575 keV and 1 MeV, leading to a good capture agreement with Voss *et al.* [492].
^{137}Ba	Adopted JENDL-4, which has URR from 11.885 to 100 keV, with revised capture and elastic cross sections between 11.885 and 250 keV. Revised capture is in good agreement with Voss *et al.* [492].
^{138}La	Revised capture, total, and elastic cross sections from ENDF/B-VIII.0 from 330 eV to 150 keV, leading to capture being 15% higher than ENDF/B-VIII.0 between 330 eV and 80 keV.

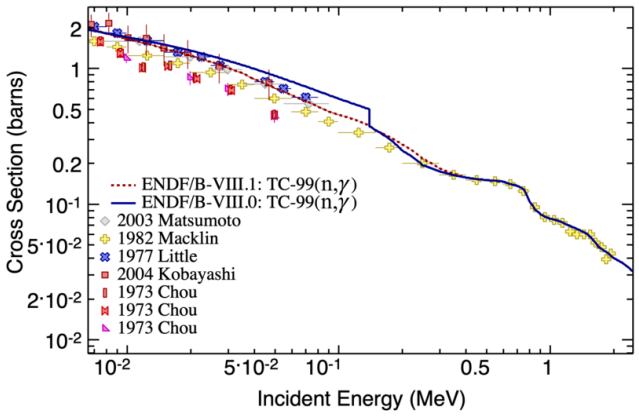
Continued on next page

TABLE XXIX – continued from previous page

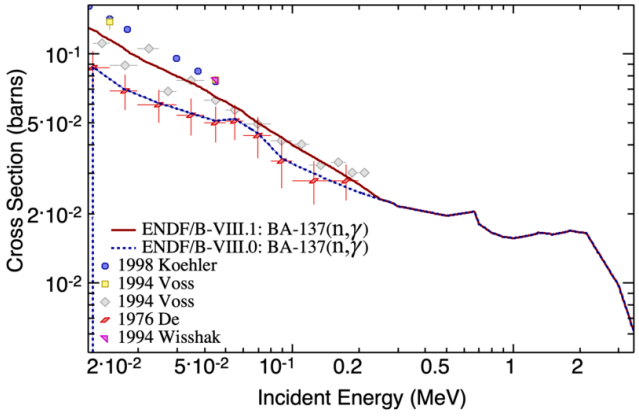
Isotope	Description
^{147}Pm	Adopted JENDL-4 (URR from 102 eV to 100 keV) without changes. The half-life of ^{147}Pm is 2.62 years.
^{148}Nd	Revised capture and elastic cross sections from ENDF/B-VIII.0 between 8.15 and 200 keV. URR is now defined between 8.15 and 300 keV.
^{150}Nd	Revised capture and elastic cross sections from ENDF/B-VIII.0 between 13.85 and 200 keV. URR defined from 13.85 to 130.97 keV.
^{153}Sm	Resolved parameters adopted from ENDF/B-VIII.0 up to 25 eV. Adopted JENDL-4 evaluation above 25 eV.
^{155}Eu	Adopted revised JENDL-4 for elastic and capture from 1 to 200 keV, leading to capture being 15% higher than JENDL-4 between 4 and 80 keV. Same as JENDL-4 above 200 keV.
^{160}Gd	Adopted ENDF/B-VIII.0 resolved parameters up to 9.7 keV. Adopted URR from 9.7 to 100 keV from JENDL-4, with revisions made to total, elastic, and capture cross sections from 9.7 to 200 keV. In the range between 0.2 and 20 MeV, cross sections were kept from ENDF/B-VIII.0.
^{159}Tb	URR parameters taken from JENDL-4 (1.2 to 100 keV). Total, elastic, and capture cross sections were revised between 1.2 and 200 keV.
^{166}Er	URR parameters taken fom JENDL-4. Elastic and capture cross sections were revised between 5 and 200 keV, leading to good capture agreement with Kononov *et al.* [486, 493].
^{168}Er	URR parameters were initially adopted from JENDL-4. Capture and elastic cross sections were revised from 9.96 to 100 keV.
^{170}Er	URR parameters adopted from JENDL-4 (5.0 to 79.147 keV). Capture and elastic cross sections were revised from 5 to 110 keV.
^{175}Lu	Capture and elastic cross sections from ENDF/B-VIII.0 were revised between 10 and 200 keV. Revised capture is in good agreement with Wisshak *et al.* [494].
^{176}Lu	URR initially adopted from ENDF/B-VIII.0 (102 eV to 10 keV). Total, capture, and elastic cross sections were revised from 102 eV to 150 keV.
^{168}Yb	URR initially adopted from ENDF/B-VIII.0 (190 eV to 250 keV). Capture and elastic cross sections were revised from 0.19 to 100 keV.
^{176}Yb	URR initially adopted from ENDF/B-VIII.0 (5 to 250 keV). Capture and elastic cross sections were revised from 5 to 100 keV.
^{174}Hf	Adopted JENDL-4 without changes in the URR.
^{176}Hf	Adopted JENDL-4 without changes in the URR.
^{177}Hf	URR parameters initially adopted from JENDL-4. Capture cross section was revised from 60 to 600 keV based on the measurements of Beer *et al.* [495] and Bokhovko *et al.* [353]. Non-elastic channel consistently recalculated.
^{178}Hf	URR parameters initially adopted from JENDL-4. The first three positive resonances were then revised based on Trbovich *et al.* [496]. Bound level (-49.1 eV), total and elastic cross section between 0.1 to 4.5 MeV, and capture cross section between 0.1 to 2.0 MeV, were also revised.
^{179}Hf	URR parameters initially adopted from JENDL-4. Total and elastic cross section between 0.1 to 4.5 MeV and capture cross section between 0.1 to 2.0 MeV were then revised.
^{180}Hf	URR parameters initially adopted from JENDL-4. Total and elastic cross section between 0.1 to 4.5 MeV and capture cross section between 0.1 to 2.0 MeV were then revised.

5. Prompt nubar evaluations of minor actinides

Values of prompt nubar for 18 minor actinide ground state files, plus one isomeric state file, were updated based on previous nubar evaluation efforts by Maslov *et al.*



(a)n+^{99}Tc(n,γ). Data taken from Refs. [497–501].



(b)n+^{137}Ba(n,γ). Data taken from Refs. [502–504].

FIG. 107. Comparison of the capture cross sections in the URR between ENDF/B-VIII.1 and ENDF/B-VIII.0. Selected experimental data retrieved from EXFOR [45].

found in a series of reports [505–508] and model calculations. Table XXX shows the nuclei for which prompt nubar were updated in ENDF/B-VIII.1 and the corresponding source of nubar values. Total nubar was modified to account for the changes in prompt nubar.

E. File updates due to only minor fixes

In addition to all the major updates from ENDF/B-VIII.0 to evaluated files in the neutron sublibrary described in the previous sections, there were also updates to more than 200 files due solely to minor to small fixes. Those correspond mostly to minor format, processing or cosmetic fixes. Due to their large number and limited importance, we chose not to list and describe them individually. More details about each individual update can be found in the library change logs (`CHANGELOG.md` files) distributed within each ENDF/B-VIII.1 released sublibrary [19–34], as well as with the whole ENDF/B-VIII.1 release package [19]), or through contact with corresponding author.

TABLE XXX. Files with prompt nubar updated in ENDF/B-VIII.1 and their respective source.

Nuclide	Prompt nubar source
^{230}Pa	Ref. [507]
^{232}Pa	Ref. [508]
^{230}U	Ref. [507]
^{231}U	Ref. [507]
^{232}U	Ref. [507]
^{237}Pu	Madland-Nix calculations
^{240}Am	Ref. [507]
^{244}Am	Ref. [506]
^{240}Cm	Ref. [505]
^{246}Cf	Madland-Nix calculations
^{248}Cf	Madland-Nix calculations
^{249}Cf	Madland-Nix calculations
^{250}Cf	Madland-Nix calculations
^{251}Cf	Madland-Nix calculations
^{252}Cf	Madland-Nix calculations
^{253}Cf	Madland-Nix calculations
^{254}Cf	Madland-Nix calculations
^{254m1}Es	Same as ^{254}Es

IV. NEUTRON REACTION COVARIANCES

The covariance session ran three big, distinctive initiatives for this library release cycle. Since the last release of the library:

- A concerted effort was made to deliver covariances for ENDF/B-VIII.1 earlier in the β-release phase than previously to allow for more stringent verification and validation. Also, CSEWG member institutions developed new codes for better testing of covariances.
- Templates of expected measurement uncertainties were developed to aid evaluators and experimenters in estimating or providing more complete experimental uncertainties.
- A discussion and vote was held on whether CSEWG wants to provide a library of formally adjusted nuclear data mean values and covariances.

A. Improved Testing of Nuclear Data Covariances

It was discussed at WANDA 2020 [509] that some issues were found by the community and users in ENDF/B-VIII.0 covariances after their release. One issue that was raised regarding testing ENDF/B-VIII.0 covariances was that evaluators provided covariances too late in the β-release phases, resulting in insufficient time for thorough testing. Therefore, the executive committee requested that preliminary nuclear data covariances should already be delivered for ENDF/B-VIII.1β1 in February

2023 – about half a year earlier than was the case for ENDF/B-VIII.0. This additional time allowed for more stringent testing with LANL's ENDFtk [510] and CovVal codes [511] and ORNL's `AMPX` code [512] during the release phases. The LLNL covariance testing employed a combination of `NJOY` [325], `empy` tools from `EMPIRE` [107], and `x4i` [513].

The following verification and validation tests were performed on covariances:

1. It was tested whether the covariance formatting was correct by processing ENDF-6 formatted files with codes, such as `NJOY` and `AMPX` [325, 512]. This test requires processing dedicated specifically to covariances which is sometimes omitted when processing mean values for quick testing of beta libraries.

2. Are mathematical properties satisfied?

3. Are physics properties satisfied?

Below examples are given of succesfully identifying and correcting issues given increased testing. For instance, ^{50,52,53}Cr covariances in ENDF/B-VIII.1β3 could not be processed because of an inconsistency in mean values and covariances. ^{50,52,53}Cr mean values were updated for ENDF/B-VIII.1 and no longer supplied MT=22, but ENDF/B-VIII.0 covariances were carried over, including those for MT=22. This processing issue was resolved by removing MF=33, MT=22. Covariances obtained from the same evaluation as the mean values will be supplied for ENDF/B-IX.0 as mentioned in Section III B 5.

On item 2., we tested for symmetry, positive semi-definiteness, if correlations were within $\pm$ 1, and if all covariance constraints were satisfied. The checks for semi-definiteness and correlations often implicitly test for the same thing–negative eigenvalues. Differences between the checks arise since different energy ranges are emphasized in each of the tests (absolute covariances versus relative covariances, and correlations). For example, a negative eigenvalue found in the relative covariances at energies where the associated cross section is very small will not be very significant in the absolute covariances. The covariance constraint tests check whether the zero-sum rule for MF=35 data is enforced [514]. A related constraint (though not explicitly documented in Ref. [514]) is whether the total MF=33 covariances are a sum of the partials covariances. For instance, MF=31, MT=456 (covariances for the average prompt fission neutron multiplicity, $\overline{\nu}$) for ^{239}Pu for ENDF/B-VIII.1β1 failed the test for positive definiteness. This covariance matrix was assembled from several pieces from three different institutes, and a mistake had happened in the non-trivial assembly. This issue was found through testing for positive semi-definiteness as it led to medium-sized negative eigenvalues. It was corrected for ENDF/B-VIII.1β2.

On item 3, we test for several issues. One test is whether uncertainties are within reasonable limits (e.g., no >100% uncertainties for mubar). Another important test is whether the evaluated uncertainties are larger than those of the Neutron Standard data, which are frequently used as monitor for experiments supporting the evaluated uncertainties. For example, the ^{237}Np(n,f) cross section uncertainties are expected to be larger than those of ^{235}U(n,f) Standards cross sections, as ^{237}Np(n,f) cross section measurement use in most cases the ^{235}U(n,f) cross sections as a monitor. Finally, the uncertainties are counter-checked with those of templates [49, 96, 97, 455, 515–521] to verify if uncertainties are realistic. Also, the previous covariance session chair, D.L. Smith, provided in Ref. [516, Table 1] (repeated in Ref. [515, Table I]) reasonable lower bounds for evaluated uncertainties of specific nuclear data observables. Another test was employing upper and lower bounds obtained from the "Physical Uncertainty Bounds" [522] method for fission cross-section; PFNS and $\overline{\nu}$ uncertainties to cross-check whether evaluated uncertainties are realistic. While testing mathematical properties is often unambiguous in that the mathematical property is either satisfied or not, the tests of item 3. are less clear-cut but aim to provide some clues that uncertainties are either over or underestimated. It is then the job of the evaluator to judge, after being pointed to potential issues by these clues, whether uncertainties are indeed unrealistic given the evaluation input. One example is given with Fig. 108 that drew attention to the fact that ENDF/B-VIII.1β1 ^{235}U(n,f) $\overline{\nu}$ uncertainties were smaller than the current standard, ^{252}Cf(sf) $\overline{\nu}_{\rm tot}$, uncertainties from approximately 1–100 keV. This uncertainty lower than the standard is implausible as many $\overline{\nu}$ experimental data are measured relative to ^{252}Cf(sf) $\overline{\nu}_{\rm tot}$ and few data sets are available in that energy range. In fact, ^{235}U(n,f) $\overline{\nu}$ covariances were updated for thermal, resonance, and fast ranges but were carried over unchanged from ENDF/B-VIII.0 for 1–100 keV. However, the previous, much lower, ^{252}Cf(sf) $\overline{\nu}_{\rm tot}$ were applied for ENDF/B-VIII.0 ^{235}U(n,f) $\overline{\nu}$ covariances and it was missed to update the 1–100 keV range for ENDF/B-VIII.1β1 with the new standard uncertainties. This issue was succesfully resolved for ENDF/B-VIII.1β4 by Capote and Trkov. The updated covariance matrix is described in Section III B 11.

For ENDF/B-VIII.1, all those covariances were tested with the CovVal code [511] where at least a single digit changed in the covariance file. Due to that, on some cases, covariances were checked that were not new in ENDF/B-VIII.1 and could not be corrected as no one was working on them. Below we note covariance issues that could not be resolved in ENDF/B-VIII.1 and will be addressed in later releases:

- Covariances are missing in the RRR for ^{51}Cr, ^{58}Ni, ^{54}Fe, ^{86}Kr, and ^{236}U(n,γ) cross section.

- Covariances are missing in the fast range for ^{35,36}Cl, ^{39}K, ^{51}Cr, $^{156,158,160-164}$Dy,^{170}Tm, ^{35,36}Cl, ^{63,65}Cu, ^{140}Ce, and ^{169}Er.

- Some covariances in the RRR for ^{181}Ta, ^{182,183}W and ^{206,207,208}Pb were flagged as unrealistically low

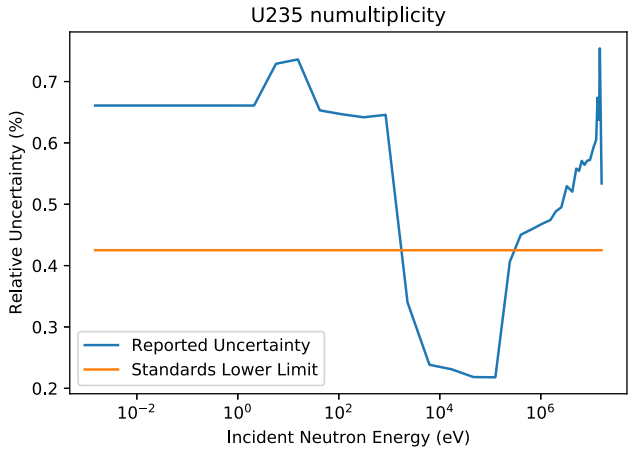


FIG. 108. ^{235}U(n,f) $\overline{\nu}$ uncertainties for ENDF/B-VIII.1β1 are compared to standard, ^{252}Cf(sf) $\overline{\nu}_{\rm tot}$, uncertainties.

despite the best efforts of the evaluators to provide realistic uncertainties. These low uncertainties might be the result of an ENDF-6 format formalism that does not allow to store all relevant RRR uncertainties; namely, those coming from combined experiment information. This problem might affect several RRR evaluation. Solving it will require detailed discussions on potentially missed uncertainties in the evaluation and required extensions to the RRR format.

- ^{234}U, and ^{242}Pu PFNS ENDF/B-VIII.1 covariances have lower experimental uncertainties than the standard (^{252}Cf(sf) PFNS) without supporting experiments. These covariances are underestimated and need to be updated.

- Fast ^{240}Pu $\overline{\nu}$ and (n,f) cross section uncertainties were not updated with the newest standard covariances (^{252}Cf(sf) $\overline{\nu}$ and ^{235}U(n,f) cross sections) and are now below standard uncertainties. The same is true for fast ^{233}U(n,f) cross section covariances. These ^{233}U and ^{240}Pu covariances are underestimated and need to be updated.

To mention another example of a successful fix: Updated ^{233}U PFNS covariances in the 0–5 MeV incident-neutron energy range were identified as needed, as new PFNS from Ref. [44] at thermal and from Ref. [523] from 0.5–5 MeV were adopted. One covariance matrix was supplied for ENDF/B-VIII.1 covering 0–5 MeV based on work of Ref. [523].

It should be emphasized that the CovVal testing focused on covariances that were new in ENDF/B-VIII.1. Issues in covariances that did not change might exist and need to be studied for the next release now that the code was developed.

Additionally, visual comparisons were made between cross section confidence bands and EXFOR-data uncertainties [45], primarily looking for unjustifiably small or large uncertainties. For instance, ^{234}U(n,f) cross-section uncertainties improved significantly from ENDF/B-VIII.0 to ENDF/B-VIII.1β1: the evaluated uncertainties at 2 MeV incident neutron energy represent better now the existing experimental data. ^{234}U(n,n') cross-section uncertainties, on the other hand, were found to have a smaller uncertainty at 4 MeV than any of the major actinides despite an absence of data as can be seen from Fig. 109. Fig. 110 shows a comparison of ^{234}U cross section uncertainties for ENDF/B-VIII.0 and ENDF/B-VIII.1β1.

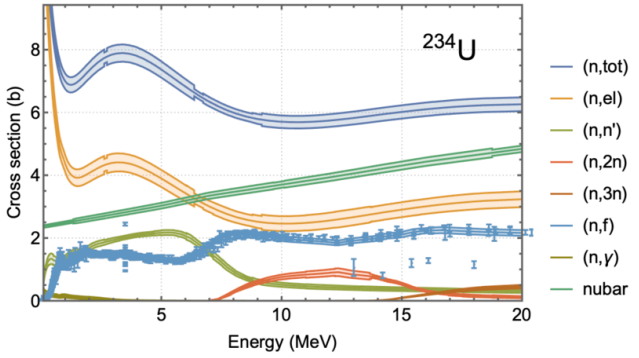


FIG. 109. ^{234}U cross-section uncertainties for ENDF/B-VIII.1β1 are compared to EXFOR data to assess whether the uncertainties are reasonable given the spread in the experimental data.

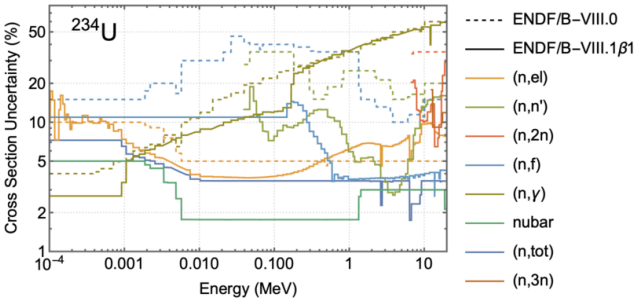


FIG. 110. ^{234}U cross-section uncertainties for ENDF/B-VIII.0 and ENDF/B-VIII.1β1.

Also, the covariances provided in ENDF/B-VIII.1β1 were processed through `AMPX` and combined with the `SCALE` 6.2 covariance library for any nuclides with no covariance data to generate a complete library for testing. This combined library was used to determine the estimated uncertainty in $k_{\rm eff}$ propagated from the nuclear data covariances for benchmarks in the VALID library maintained at ORNL [524] and for spent fuel in a hypothetical storage cask [525]. The majority of the data-induced uncertainty in these systems comes from the major actinides, but the spent fuel system allows for testing the covariance data changes in major fission product nuclides typically credited in spent nuclear fuel (SNF) stor-

TABLE XXXI. Average simulated uncertainties, σ, on k_{eff} values of ICSBEP due to ENDF/B-VIII.0 and ENDF/B-VIII.1 covariances. All values except for # cases are in pcm. δE are average experiment uncertainties and Σ the standard devaiation of C/E.

	# Cases	$\langle C/E \rangle$	δE	$\Sigma_{\text{VIII.0}}$	σ	$\sigma_{\text{VIII.1}}$
HMF	50	1.00002	193	467	979	950
HST	52	0.999	494	615	652	792
IMF	13	1.00132	269	362	1027	1003
LCT	140	0.99874	195	162	603	737
LST	19	0.9992	318	283	824	944
MCT	49	0.99244	400	313	973	758
MST	10	0.99177	452	384	1323	1019
PMF	12	0.99902	207	133	1022	1038
PST	81	0.99927	497	429	1344	937

TABLE XXXII. Impact of various ^{235}U ENDF/B-VIII.0 and ENDF/B-VIII.1 covariances on simulated HMF-001 ("Godiva" simple sphere) k_{eff} uncertainties. All values are in pcm.

	ENDF/B-VIII.0	ENDF/B-VIII.1
(n,f) cs	787	787
$\overline{\nu}$	399	382
PFNS	124	33
(n,el) cs	224	224
(n,inl) cs	239	239
(n,γ) cs	277	277
Sum	982	975
Exp. Unc.	100	100
$C-E$	14	0

age and transportation applications licensed by the US Nuclear Regulatory Commission [526].

The results of the data-induced uncertainty for the benchmarks are summarized below in Table XXXI. The standard deviation of the C/E values within each benchmark category is compared to the average data-induced uncertainty using the `SCALE` covariance library based on ENDF/B-VIII.0 and the equivalent library based on ENDF/B-VIII.1 covariance data. In all nine categories, including different uranium enrichments, plutonium, fast spectrum benchmarks, and thermal spectrum systems, the observed variability is significantly lower than the predicted variation based on the nuclear data covariance. The ENDF/B-VIII.1-based data has significantly lower overpredictions compared to the ENDF/B-VIII.0 data for thermal spectrum Pu-fueled systems. The overall uncertainty in these systems is reduced by 20–30%, with the change being driven by significant reductions in the ^{239}Pu PFNS, fission, and (n,γ) cross sections. The (n,γ) uncertainty dropped approximately 95%, which may require further evaluation in future releases. Unfortunately, the data-induced uncertainty increased for thermal spectrum U-fueled systems. This change was driven by increased uncertainty in ^{235}U $\overline{\nu}$.

The reduction in ^{239}Pu uncertainty and increase in ^{235}U uncertainty for thermal systems will induce a shift in similarity metrics, such as c_k for thermal SNF storage systems. c_k values will be increased for LEU experiments and reduced for mixed systems. Most major fission product evaluations remained unchanged, though ^{103}Rh uncertainty increased almost 30%. This represents the k_{eff} uncertainty from ^{103}Rh increasing from 21 pcm to 27 pcm in pressurized water reactor (PWR) fuel with a burnup of 40 GWd/MTU, so it is only a minor impact.

In Tables XXXII and XXXIII, it is shown that Godiva and Jezebel k_{eff} uncertainties due to PFNS covariances dropped significantly from ENDF/B-VIII.0 to ENDF/B-VIII.1. This drop was expected and is supported by inclusion of high-precision experimental data that were recently released. Jezebel k_{eff} uncertainties due to ^{239}Pu $\overline{\nu}$ increased due to inclusion of somewhat larger standard

TABLE XXXIII. Impact of various ^{239}Pu ENDF/B-VIII.0 and ENDF/B-VIII.1 covariances on simulated PMF-001 ("Jezebel" simple sphere) k_{eff} uncertainties. All values are in pcm. The asterisk (*) highlights that the adjustment for the cross correlation between elastic and inelastic scattering is larger than the inelastic scattering contribution. The total scattering uncertainty (elastic and inelastic) is 469 pcm with ENDF/B-VIII.1β1 covariances compared to 396 pcm with ENDF/B-VIII.0 covariances.

	ENDF/B-VIII.0	ENDF/B-VIII.1
(n,f) cs	877	920
$\overline{\nu}$	317	416
PFNS	179	37
(n,el) cs	484	360
(n,inl) cs	-119*	165
(n,γ) cs	64	19
Sum	1061	1085
Exp. Unc.	130	130
$C-E$	-28	-116

uncertainties, while Godiva k_{eff} uncertainties due to ^{235}U $\overline{\nu}$ are fairly similar. A significant drop in Jezebel k_{eff} uncertainties was observed due to ^{239}Pu capture uncertainties.

Finally, O. Cabellos processed ENDF/B-VIII.0, ENDF/B-VIII.1β2 and ENDF/B-VIII.1β4 covariances with `NJOY2016.74` [325]. Then, covariances were sandwiched with ICSBEP benchmark sensitivities using the NDaST tool (www.oecd-nea.org/ndast) using the BOXER format. Average simulated k_{eff} uncertainties for Pu, HEU and ^{233}U due to the processed covariances are tabulated in Tables XXXIV–XXXVI. As mentioned before, PFNS uncertainties for Pu assemblies dropped due to the inclusion of Chi-nu, CEA and Lestone experimental data, while $\overline{\nu}$ uncertainties increased because of considering the new standard uncertainties (^{252}Cf(sf)) in the evaluation process. The lower cross section uncertainties in the RRR triggered some discussions as mentioned above and is an active field of investigation.

TABLE XXXIV. Average simulated uncertainties on k_{eff} values of Pu ICSBEP assemblies due to ENDF/B-VIII.0 and ENDF/B-VIII.1 covariances for specific observables. All values except for # cases are in pcm. δE are average experiment uncertainties. Cross-section uncertainties consider cross correlations. ENDF/B-VIII.1β4 was used.

Spectrum	FAST	INTER	MIXED	THERM
# benchmarks	152	4	9	624
δE	334	710	587	427
Total VIII.1	931	551	536	645
Total VIII.0	921	1403	1055	1099
Cross sections VIII.1	841	360	224	106
Cross sections VIII.0	857	1368	983	998
P1-elastic VIII.1	66	-	-	-
P1-elastic VIII.0	66	-	-	-
$\overline{\nu}$ VIII.1	390	389	479	632
$\overline{\nu}$ VIII.0	300	271	275	308
PFNS VIII.1	27	25	53	59
PFNS VIII.0	117	106	265	297

TABLE XXXV. Average simulated uncertainties on k_{eff} values of HEU ICSBEP assemblies due to ENDF/B-VIII.0 and ENDF/B-VIII.1 covariances for specific observables. All values except for # cases are in pcm. δE are average experiment uncertainties. Cross-section uncertainties consider cross correlations. ENDF/B-VIII.1β2 was used.

Spectrum	FAST	INTER	MIXED	THERM
# benchmarks	477	21	78	798
δE	225	310	415	473
Total VIII.1	883	649	588	667
Total VIII.0	911	758	649	497
Cross sections VIII.1	811	514	442	143
Cross sections VIII.0	816	545	470	155
P1-elastic VIII.1	-	-	-	-
P1-elastic VIII.0	-	-	-	-
$\overline{\nu}$ VIII.1	346	333	364	640
$\overline{\nu}$ VIII.0	402	501	435	457
PFNS VIII.1	29	60	61	98
PFNS VIII.0	29	60	61	98

TABLE XXXVI. Average simulated uncertainties on k_{eff} values of ^{233}U ICSBEP assemblies due to ENDF/B-VIII.0 and ENDF/B-VIII.1 covariances for specific observables. All values except for # cases are in pcm. δE are average experiment uncertainties. Cross-section uncertainties consider cross correlations. ENDF/B-VIII.1β4 was used.

Spectrum	FAST	INTER	MIXED	THERM
# benchmarks	8	29	8	194
δE	174	670	601	600
Total VIII.1	810	1001	1026	1018
Total VIII.0	810	1132	1155	1131
Cross sections VIII.1	640	145	161	347
Cross sections VIII.0	640	315	329	514
P1-elastic VIII.1	-	-	-	-
P1-elastic VIII.0	-	-	-	-
$\overline{\nu}$ VIII.1	475	479	490	539
$\overline{\nu}$ VIII.0	484	496	501	508
PFNS VIII.1	137	867	887	758
PFNS VIII.0	95	967	987	837

B. Templates of Expected Measurement Uncertainties

Templates of expected measurement uncertainties were established in Refs. [49, 455, 517–521, 527]. This effort was started after fission cross section templates [96, 97] and initial versions of total and capture templates were discussed at the fall CSEWG meeting of 2018. In spring 2019, a mini-CSEWG on that topic was held, and the scope was extended to encompass prompt fission neutron spectra, average prompt and total fission neutron multiplicities, charged-particle cross sections, (n,xn) cross sections, and fission yield.

These provide listings of expected uncertainties for a specific measurement type related to one nuclear-data observables; for instance, transmission for total cross sections or absolute liquid-scintillator measurements for the average prompt fission neutron multiplicity. These listings can be used by experimenters as a check-list before the release of their data, or by evaluators to counter-check whether all pertinent uncertainties were provided for experiments chosen for their evaluation input database. Also, recommended values of many uncertainty sources are provided based on literature, EXFOR entries [45], and expert judgment from experimenters. These uncertainty values can be used as a last resort if they are not provided for past experiments. These uncertainty values should only be used for evaluations in the absence of other information to estimate the uncertainty source. Estimates of correlation coefficient between uncertainties of the same and different experiments for evaluation purposes are also given. The long-term goal of these templates is to provide better experimental uncertainties for evaluation purposes, be it either that experimenters use them as check-lists to provide data, or by evaluators to fill in missing uncertainties for their evaluation database. Ultimately, having better quantified experimental uncertainties for evaluation purpose will lead to more realistic evaluated uncertainties for nuclear data libraries.

Most of the templates were published in 2023, at the end of the library release cycle. Despite that, they were already applied for some evaluations: The fission cross section template was applied in Ref. [97] for the experimental uncertainty quantification of the fast ENDF/B-VIII.1 ^{239}Pu(n,f) cross section, while the templates for

$\overline{\nu}_p$ [49] were applied to inform part of ENDF/B-VIII.1 ^{235,238}U and ^{239}Pu $\overline{\nu}_p$ evaluations. The experimental uncertainty quantification for fast ENDF/B-VIII.1 ^{235}U and ^{239}Pu PFNS evaluations also made use of PFNS template uncertainties [520], where individual uncertainty sources were not provided by the author. Finally, information from all the templates described above were used for covariances testing with the CovVal codes [511] as described above.

C. Decision Process of CSEWG to not Provide Mathematically Adjusted Libraries for ENDF/B-VIII.1

Meeting records as far back as the eighties of the last century show that CSEWG regularly had discussions on whether evaluated mean values and covariances should be formally adjusted by the CSEWG community to trusted integral data. Formally adjusted means in this context that nuclear data mean values and covariances are updated with integral mean values and uncertainties via a mathematical algorithm, such as generalized least squares. So far, this step has not been undertaken but been left for the application user to do with integral experiments of their choice. However, ENDF/B nuclear data libraries do use information coming from integral data.

For instance, ENDF/B-VIII.0 nuclear data mean values were partially tweaked by hand or favorably selected to reproduce k_{eff} values of selected ICBSEP critical assemblies [158], LLNL pulsed spheres [141], reaction rates, etc. [68]. Such changes were undertaken by computing integral data first with nuclear data obtained without integral information. Then, a limited set of nuclear data, usually one or two observables, were changed by hand until one reached the desired agreement with integral data. Examples of such changes were documented for the thermal ^{239}Pu prompt fission neutron spectrum or for the ^{235}U average prompt fission neutron multiplicity in the resonance range [68]. Such changes are usually undertaken within the bounds of differential experimental data. In formal adjustment procedures, on the contrary, usually all nuclear data that are sensitive to the particular integral data are adjusted simultaneously.

Another important difference between by-hand tweaking and formal adjustment is that in the former case ENDF/B covariances remain unchanged. This leads to seemingly over predicted k_{eff} uncertainties when one forward-propagates nuclear data covariances to simulated k_{eff} bounds and compares them to the spread in calculated over experimental k_{eff} values C/E [509]. As a consequence, some users do not use ENDF/B covariances because this tweaking renders covariances inconsistent with mean values. Some users have expressed concerns about this approach and the lack of documentation of it, because many of these changes and choices on nuclear data are not fully documented and neither are the benchmarks used for this by-hand tweaking and the reasoning for the choices. This lack of documentation also constitutes a problem for some user communities as it is unclear which k_{eff} benchmarks can be used for formal adjustment [509] while others are already incorporated in ENDF/B data. Of course, many of these tweaks are built into ENDF/B libraries through the work of generations of scientists. Removing them means re-doing major parts of ENDF/B. On the other hand, a formal adjustment may lead to producing a library which will be only valid to describe specific assemblies, geometries, etc., which may not be acceptable for a general purpose library.

Given this situation and frequent criticism by users [509], discussions on whether CSEWG should provide one true general-purpose library (i.e., without by-hand tweaking), and additional adjusted nuclear data libraries using formal mathematical algorithms came up regularly at CSEWG meetings. To reach a decision for what to do for ENDF/B-VIII.1, a detailed discussion was held on the topic of adjustment as part of a mini-CSEWG covariance session on August 19, 2021 culminating in a vote whether adjustment should be undertaken for ENDF/B-VIIII.1. This vote came out with more than two-thirds of attendees preferring not to adjust, reflecting the reality that there are no tools applicable to all integral responses catering to many subject areas, and that CSEWG is not yet ready to distribute and vet several adjusted libraries.

However, many people showed interest in learning about potential weaknesses in the library through adjustment results. Also, the following recommendations were given for the future:

- Results from adjustment and tool development should be discussed in the covariance session. The aim is to give recommendations to user how adjustment could be done and warn them about potential caveats. Also, evaluators could learn from adjustment results where nuclear data could be improved.
- If possible, evaluators should document some of their by-hand tweaks in ENDF/B-VIII.1 nuclear data along with the integral experiments used,
- Work should be undertaken in the future with the validation session to agree on what benchmarks/integral responses we use for tweaking. Integral responses used for tweaking should be carefully vetted.

V. THERMAL NEUTRON SCATTERING SUBLIBRARY

Accurate description of thermal neutron scattering on different materials is required in modeling neutron transport in many different circumstances, from nuclear power reactors to cryogenic setups at neutron beam facilities. Nuclear data files (File 7), which allow the double differential scattering cross sections in the thermal energy

region (and up to E ~1–5 eV) to be constructed for the specified materials, are distributed in a special sublibrary called the thermal neutron scattering law (TSL) sublibrary, or $S(\alpha, \beta)$ data. Materials are classified as moderators, fuel, or special purpose – usage restrictions defined below.

The TSL sublibrary of ENDF/B-VIII.1 contains 114 evaluations for 69 materials. Nine materials (light water, beryllium oxide, beryllium-metal, yttrium hydride, silicon carbide, silicon dioxide, Lucite, liquid hydrogen, and liquid deuterium) were reevaluated, and 18 new materials were added (calcium hydride, uranium hydride, lithium-7 hydride, lithium-7 deuteride, paraffinic oil, polystyrene, Teflon, FLiBe, hydrogen fluoride, sapphire, uranium-metal, plutonium dioxide, magnesium oxide, beryllium fluoride, magnesium fluoride, beryllium carbide, uranium carbide, and zirconium carbide). Two materials were evaluated with added physics (crystalline-graphite+$S_d$and beryllium-metal+S_d). Four material evaluation sets were expanded to include new phases, material conditions, or enrichments (zirconium hydride, 20% porous graphite, uranium dioxide, and uranium nitride). The remaining evaluations were imported from the ENDF/B-VIII.0 TSL sublibrary. Due to the increase in the number of materials in the current release, a new database of MAT numbers for File 7 has been established.

New File 7 evaluations and reevaluations for ENDF/B-VIII.1 were generated in ENDF-6 format [474] by Naval Nuclear Laboratory (NNL), the Low Energy Interaction Physics (LEIP) group from Texas A&M University (TAMU) and North Carolina State University (NCSU), ORNL, and European Spallation Source ERIC (ESS). The efforts were coordinated through NEA/WPEC subgroups 42 and 48 [528]. The new evaluations and reevaluations were performed using the `FLASSH` [529], `NJOY` [325], and `NJOY`+`NCrystal` [530] code systems. The evaluations were developed with the use of computational material science methods (density functional theory, lattice dynamics, and molecular dynamics). Most evaluations were developed in the incoherent approximation with semi-empirical force-field molecular dynamics (MD) or *ab initio* lattice dynamics (AILD) techniques [531, 532] introduced in ENDF/B-VIII.0. However, several physics and methodology advances are introduced in this release. An *ab initio* molecular dynamics (AIMD) methodology [533, 534] has been introduced to treat temperature effects on vibration in ZrH_x and ZrH_2. A technique to adjust computed molecular vibration spectra with inelastic neutron measurements [535, 536] has been introduced for polystyrene and Lucite. Coherent inelastic 1-phonon corrections have been introduced to Be-metal+$S_d$and crystalline-graphite+$S_d$as a relaxation of the incoherent and cubic approximations used in other evaluations. The ENDF-6 format was extended to support thermal scattering evaluations for materials, which include of both coherent and incoherent elastic scattering effects [537].

Unlike prior ENDF/B releases, uranium compounds (UC, UN, UO_2, U-metal) included in this release are evaluated for several enrichments of ^{235}U: natural, 5%, 10%, High-Assay Low-Enriched Uranium (HALEU) (19.75%), HEU (93%), and 100%. Although it is the same material for each value of enrichment, each evaluation (e.g., U(UO_2-HEU) and O(UO_2-HEU)) is assigned a unique MAT numbers. The UN and UO_2 reevaluations use the same material models as ENDF/B-VIII.0 with updated lattice parameter; whereas UC and U-metal are considered new evaluations.

Several materials (BeO, SiC, SiO_2, Be-metal, graphite, UO_2, UN) were reevaluated to use room temperature experimental data rather than computational ones for the crystal lattice parameters. The material models and evaluation methodologies of these material evaluations are otherwise the same as or highly similar to ENDF/B-VIII.0.

Details of the evaluation and validation methodologies for each new and updated material in this release are given below in three subsections: moderators, fuels, and special purpose. Moderator and fuel evaluations support criticality analyses. Fuel evaluations can also aid fundamental investigations of chemical binding effects on Doppler broadening. Special purpose evaluations, such as liquid H_2 and D_2, sapphire single-crystal, etc., are optimized for neutron beamline applications and are **not suitable** for use in nuclear reactor design and criticality safety applications.

As the ENDF-6/GNDS formats for the TSL covariances (File 37) are not finalized yet, and additional research is needed on methods to generate consistent covariances, the TSL evaluations in ENDF/B-VIII.1 are given without estimations of their uncertainties. The consistent evaluations of the TSL data with their covariances are left for the future releases of the ENDF/B family of nuclear data libraries.

A. Moderators

1. *Light water (H_2O)*

Similarly to ENDF/B-VIII.0, the proposed evaluation for light water is based on the CAB Model for neutron scattering on water [538]. This model reproduces very well the properties of water and the evolution of the total cross section with temperature [539]. Nevertheless, the discrete nature of the MD simulations used in this model made it a collection of evaluations for different temperatures instead of a single continuous evaluation.

To overcome this deficiency, the evaluation was updated to include a continuous temperature behavior. In this new methodology, the computed vibrational spectra for all temperatures is decomposed as a sum of Gaussian contributions, following the work by Esch [540], Lisichkin [541] and Maul [542]. In Fig. 111, we show the Gaussian decomposition of the frequency spectrum at $T = 293.6$ K. The parameters for the Gaussian distributions and the

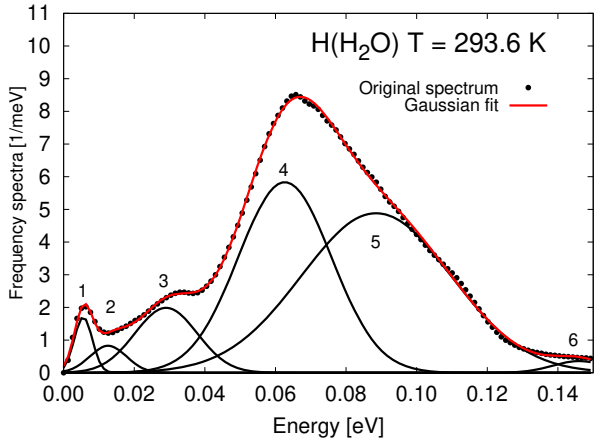


FIG. 111. (Color online) Frequency spectrum of hydrogen in light water at $T = 293.6$ K and its decomposition in Gaussian distributions, which are numbered from low to high energy. Although this description is purely mathematical, there are certain features that can be associated with each distribution: 1, 2 and 3 roughly correspond to stretching and bending of the hydrogen bond network, and 4, 5 and 6 correspond to hindered molecular rotations (librations) [541].

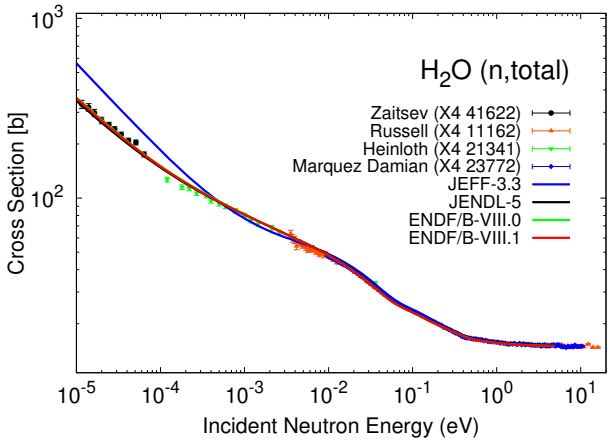


FIG. 112. (Color online) Total cross section for the interaction of neutrons with light water at room temperature as a function of energy.

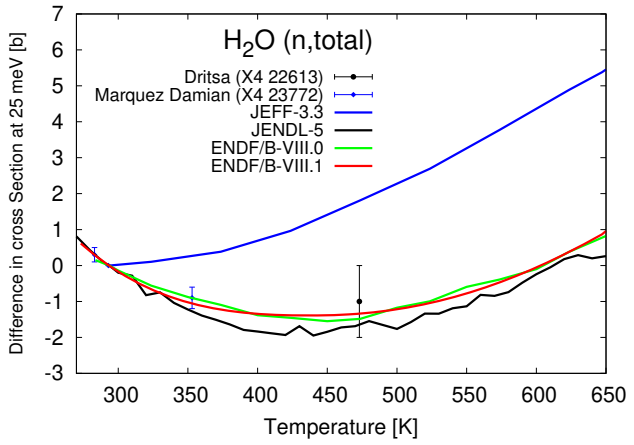


FIG. 113. (Color online) Difference in total cross section for the interaction of neutrons with light water at $E = 0.0253$ eV as a function of water temperature against the reference value at $T = 293.6$ K.

translational weight are then fitted using a fourth-order polynomial in inverse temperature, using the values at $T_0 = 293.6$ K as anchor points. The diffusion coefficient is interpolated using a logarithmic fifth-order polynomial in inverse temperature, following the work by Yoshida [543] but modified to reproduce the value of the diffusion coefficient used in ENDF/B-VIII.0 at room temperature. The data from the CAB Model was complemented with a new MD simulation at $T = 275$ K to improve the performance below room temperature. Further details on the analysis, and the source code used to perform it, can be found in Ref. [544].

Using this methodology, the thermal scattering library for hydrogen in light water was computed on a 5 K grid from 273.15 K to 647.1 K, and a extrapolated 50 K grid above the critical temperature from 650 K to 1000 K. As in previous evaluations, oxygen in light water should be included using a free gas model.

Overall, the good agreement found in the ENDF/B-VIII.0 evaluation at room temperature is preserved in the updated evaluation of H_2O in ENDF/B-VIII.1 (Fig. 112). In addition, the temperature dependence of the neutron scattering cross section is now smoother (see Fig. 113). Compared with the JENDL-5 [16] evaluation, a general agreement is observed, which might be caused from both evaluations being derived from MD simulations using the TIP4P/2005f model. However, the JENDL-5 evaluation shows oscillations similar to the ones observed in the ENDF/B-VIII.0 evaluation. These oscillations were suppressed in update-16 (January 2025) of JENDL-5 $S(\alpha, \beta)$ for H in H_2O and O in H_2O [545] by smoothing the temperature-dependent vibrational density of states (frequency spectra) based on multiple MD simulations of liquid H_2O at a given temperature [546]. Bigger differences are seen when the computed cross sections are compared with the JEFF-3.3 [64] light water evaluation, which is based on the model by Keinert and Mattes [547].

2. *Beryllium (Be-metal)*

This contribution updates the Be-metal evaluation of ENDF/B-VIII.0 with average experimental lattice parameters [548, 549] in the calculation of the coherent elastic data instead of *ab initio* values as well as additional temperatures for potential utilization as a cold neutron moderator/reflector.

Be-metal was evaluated using modern AILD methods [531, 532] for its hexagonal close-packed crystal structure [533]. This *ab initio* model is the same as that used

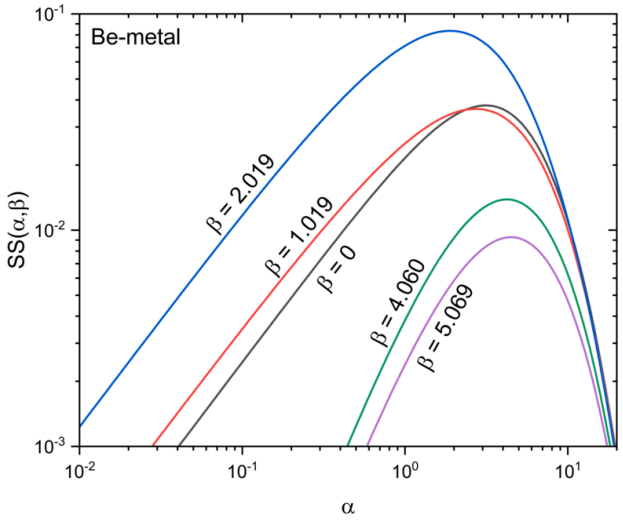


FIG. 114. (Color online) The symmetric TSL of Be-metal as a function of momentum transfer, α, for various values of β at 296 K. $SS(\alpha, \beta)$ for each β is labeled with the corresponding line.

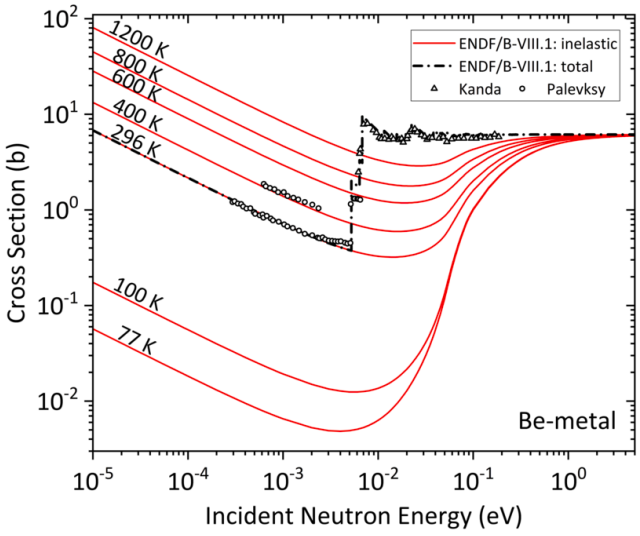


FIG. 115. (Color online) The inelastic scattering cross section of Be-metal shown at selected temperatures. The total cross section of Be-metal, experimental measurements at room temperature [555, 556] and measurements at 440 K [555] are shown.

in the ENDF/B-VIII.0 evaluation. Electronic and bulk structure minimization was conducted using density functional theory (DFT) to validate thermophysical properties predicted in the `VASP` code [550–552]. Subsequently, Hellmann-Feynman forces were calculated using the finite displacement method and used in PHONON [553] for predicting phonon dispersion relations and sampling phonon density of states (PDOS). Computed dispersion relations map phonon wave vectors to energy along high-symmetry lattice directions and demonstrate good agreement with experimental inelastic neutron scattering measurements as shown in Ref. [533, Fig. 3].

The ENDF TSL for Be-metal (File 7, MAT26) was generated using the AILD density of states (DOS) in the Full Law Analysis Scattering System Hub (`FLASSH`) [529] for cryogenic and standard temperatures of 77, 100, 293.6, 296, 400, 500, 600, 700, 800, 1000, and 1200 K. Mass and free atom cross sections [68] for ^{9}Be are used as input. The symmetric TSL, *i.e.*, $S_s(\alpha,\beta)$, is tabulated as ENDF File 7 (MAT26), MT4 in the incoherent approximation [514, 554] and is illustrated at 296 K versus α for select β in Fig. 114. Coherent elastic scattering is evaluated in `FLASSH` within the cubic approximation and stored as ENDF File 7, MT2.

The ENDF/B-VIII.1 total cross section of Be-metal is shown in Fig. 115 [555, 556]. Experimental cross sections have been used for validation at room temperature and higher temperatures and show excellent agreement with the ENDF/B-VIII.1 data. Lower temperature cross section measurements have been discarded for validation as competing effects from absorption dominate the total cross section. The inelastic scattering cross sections are also shown at select temperatures including the extension to cryogenic temperatures.

3. *Beryllium-Metal with Distinct Effects (Be+S_d)*

Beryllium-metal was evaluated using AILD techniques [531, 532] to generate the phonon dispersion relationships and resulting PDOS. The validated ENDF/B-VIII.0 material model [533] was used as the primary input to generate a novel evaluation which removes traditional approximations. The incoherent, cubic, and atom-site approximations to the TSL evaluation are removed; instead, this evaluation provides a non-cubic formulation of the TSL with additional distinct effects (S_d), which include coherent interactions in the inelastic cross section [557]. The S_d libraries were generated in a consistent fashion with the standard Be-metal evaluation. The same inputs and codes are used for both evaluations. Therefore, users would be able to recognize directly the impact of the isolated S_d effect on their calculations. Consequently, including the ENDF/B-VIII.1 S_d evaluations as presented here is highly informative to the community.

The dispersion relations, which were developed in this model, demonstrated reasonable agreement with the measurement [533]. The corresponding phonon DOS is fundamental input for the generation of the TSL with mass and free atom cross sections [68] for ^{9}Be. Using the `FLASSH` code's advanced physics modules, the TSL for beryllium-metal with S_d effects (File 7, MAT204) was evaluated at temperatures of 77, 100, 296, 400, 500, 600, 700, 800, 1000, and 1200 K without the incoherent approximation and using the non-cubic formulation [529]. The symmetric TSL at 296 K tabulated in File 7, MT4 of the ENDF file is illustrated in Fig. 116 and compared with experimental measurements [558].

Coherent elastic scattering was evaluated using the generalized non-cubic routine in FLASSH with a Debye-Waller matrix capturing asymmetric lattice effects [529] with average experimental lattice parameters [548, 549]. This allows a consistent evaluation method between the TSL and resulting inelastic cross sections and the coherent elastic cross sections. The resulting total integrated scattering cross section for the ENDF/B-VIII.1 Be-metal with S_d effects, corrected for absorption, is shown in Fig. 117. The comparison with experimental data shows excellent agreement of the S_d data.

This addition of distinct (S_d) effects provides the ability to directly benchmark the TSL evaluation against experimentally measured TSL data for beryllium-metal and improves the agreement with experimentally measured cross sections [555, 556]. The beryllium-metal with S_d evaluation represents a new TSL that is included for the first time in the ENDF/B database.

4. *Beryllium Oxide (BeO)*

This contribution updates the BeO evaluation of ENDF/B-VIII.0 with the atomic mass and cross sections [68] of natural oxygen [87], as opposed to ^{16}O, and uses experimental lattice parameters [559] in the calculation of the coherent elastic data instead of *ab initio* values.

BeO was evaluated using AILD methods [531, 532]. BeO has a Wurtzite crystal structure. The VASP code [550–552] was used to generate the Hellmann-Feynman forces for this structure, and the PHONON code [553] was used to calculate the phonon dispersion curves and DOS for each element from the Hellmann-Feynman forces using the dynamical matrix method. This DOS was used in both the ENDF/B-VIII.0 and current evaluation. The phonon dispersions calculated using this method reasonably agree with experiment as shown in Fig. 118 [560–562].

The TSL (File 7) was calculated from the partial PDOS for Be(BeO) (MAT27) and O(BeO) (MAT46) at 293.6, 400, 500, 600, 700, 800, 1000, and 1200 K using FLASSH [529]. The incoherent approximation was applied in the evaluation of the TSL; Fig. 119 shows the symmetric TSL of Be(BeO) and O(BeO) at 293.6 K.

The cubic approximation was used to calculate the coherent elastic scattering cross section of the compound, which is split evenly between the File 7 for each of Be(BeO) and O(BeO) (MT2). The ENDF/B-VIII.1 total scattering cross section of BeO is shown in Fig. 120 and found to be in good agreement with measured total cross sections [563]. The inelastic scattering cross sections are also compared at select temperatures.

5. *Calcium Hydride (CaH_2)*

Calcium hydride (CaH_2) was evaluated using standard AILD methods [531, 532]. CaH_2 has an orthorhombic crystal structure belonging to the *Pnma* space group. An optimized structure with lattice parameters close to experimental values [564] was created using MedeA-VASP [550–552, 565]. The Hellmann-Feynman forces were calculated using VASP [550–552] and used in PHONON [553] to calculate the phonon dispersion curves and DOS using the dynamical matrix method [566]. The generated partial DOS for each nonequivalent atom site matches experimental data well, as shown in Ref. [566, Fig. 2].

The TSL (File 7) was calculated from the partial phonon DOS for Ca(CaH_2) (MAT3011) and both non-equivalent hydrogen atom site locations $H_1(CaH_2)$ (MAT3013) and $H_2(CaH_2)$ (MAT3014) at 293.6, 400,

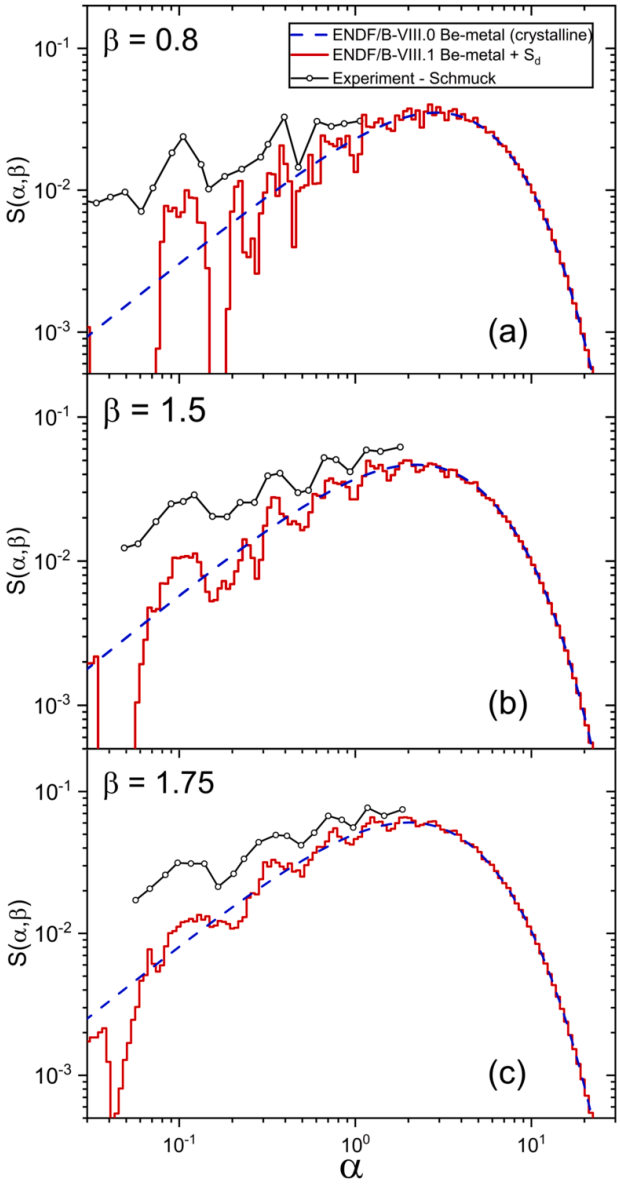


FIG. 116. (Color online)The symmetric TSL for beryllium metal with S_d effects at 296 K as a function of momentum transfer α compared to experimental data [558].

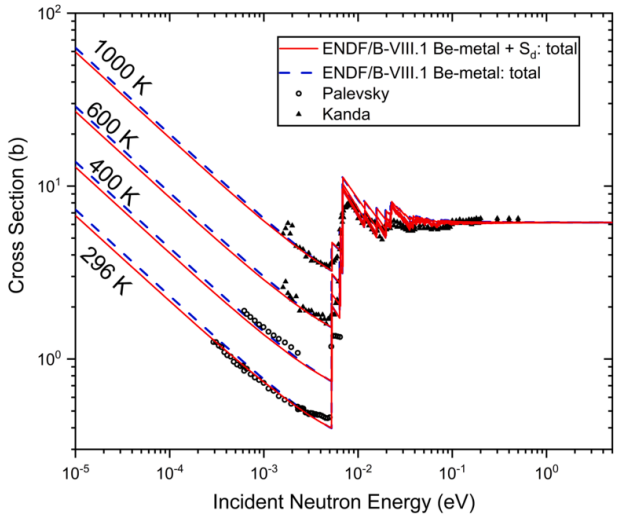


FIG. 117. (Color online) Total cross sections of beryllium-metal with and without S_d effects at select temperatures are compared to experimental data at 300 [555], 440 [555], 573 [556], and 973 K [556].

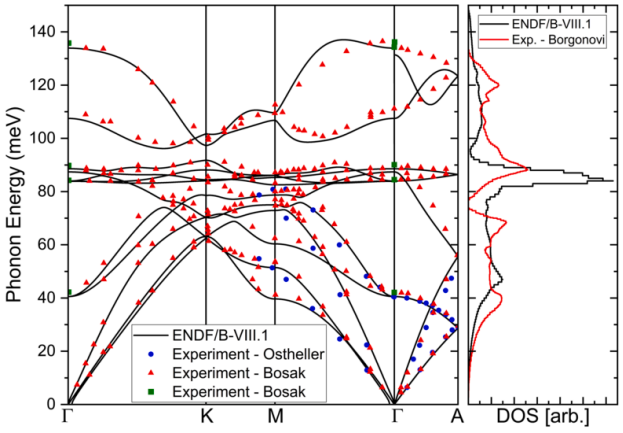


FIG. 118. (Color online) The phonon spectrum of BeO used as input for the TSL evaluation compared with experimental data [560–562].

500, 600, 700, 800, 1000, and 1200 K using the FLASSH code [529]. Mass and total isotopic free atom cross sections were derived from the ENDF/B-VIII.0 nuclide evaluations [68] at 1.0E-05 eV for all isotopes except ^{46}Ca. For the ^{46}Ca isotope, the total free atom cross section was obtained from the NIST database [87]. The incoherent free atom cross sections for all isotopes were likewise obtained from the NIST database [87]. For calcium, natural isotopic abundances were assumed [87], and ^{1}H was used as opposed to naturally weighted hydrogen. The incoherent approximation was applied in the evaluation of the TSL; Fig. 121 shows the symmetric TSL of Ca(CaH_2), H_1(CaH_2), and H_2(CaH_2) at 293.6 K.

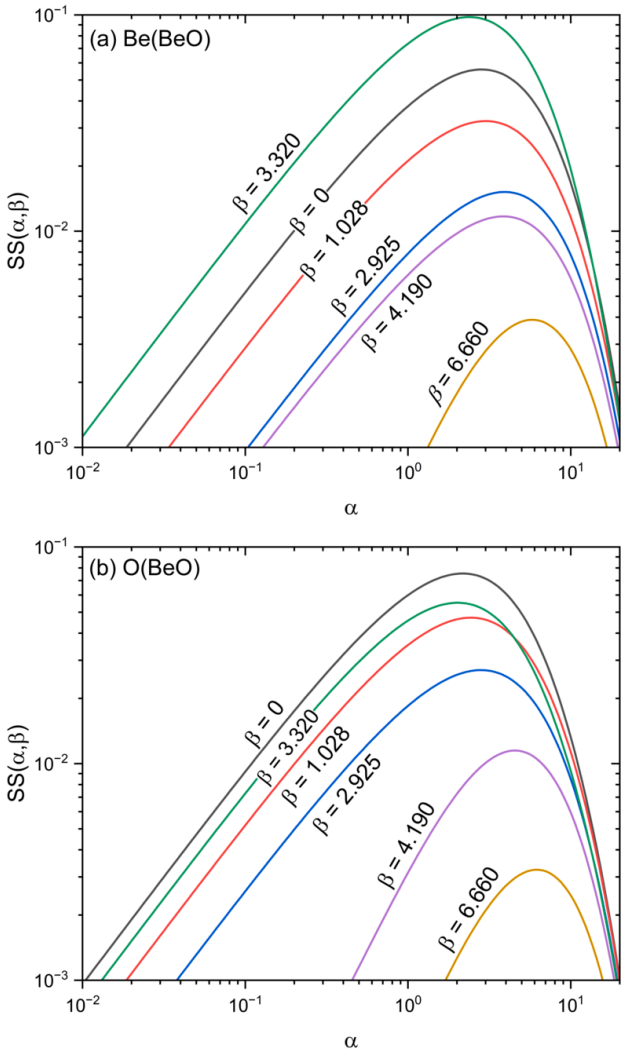


FIG. 119. (Color online) The symmetric TSL of (a) Be(BeO) and (b) O(BeO) as a function of momentum transfer, α, for various values of β at 293.6 K. $SS(\alpha, \beta)$ for each β is labeled with the corresponding line.

The cubic approximation was used to calculate the coherent elastic scattering cross section of the full compound, which is stored on the Ca(CaH_2) File 7 (MT2). The coherent elastic cross sections are calculated to account for the negative scattering length of hydrogen. Hydrogen has a large incoherent scattering length, so the incoherent elastic scattering cross section is stored on the File 7 for each of H_1(CaH_2) and H_2(CaH_2) (MT2). Fig. 122 compares the ENDF/B-VIII.1 total scattering cross section of CaH_2 with JEFF-3.3 [64, 567] at select temperatures. The robust ability of FLASSH to process the coherent scattering behavior of any crystal structure enabled the inclusion of both the coherent elastic scattering of the full compound and the inelastic scattering of the distinct H sites.

Fig. 123 compares the total H cross sections of this

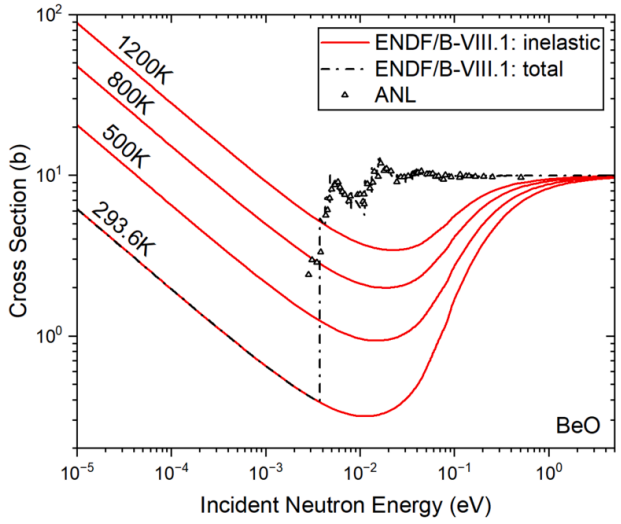


FIG. 120. (Color online) The total scattering cross section of BeO for ENDF/B-VIII.1 at 293.6 K; measurement is at room temperature from Argonne National Laboratory (ANL) [563]. The inelastic scattering cross section of BeO is also shown at selected temperatures.

evaluation with the behavior of neutrons in a hydrogenous substance as predicted by Fermi [568]. The Fermi data has been digitized and scaled such that the start of the first oscillation aligns with those of the calculated H_1 and H_2 data. The behavior predicted by Fermi can be seen in the calculated cross sections for H_1 and H_2 albeit with discrepancy in the magnitudes of individual oscillations likely due to the difference between Ca's finite mass and Fermi's assumed infinite binding mass.

6. *FLiBe Molten Salt*

To support design and operational analysis of FLiBe molten salt reactors, the TSL for FLiBe molten salt was evaluated using fundamental data generated using classical MD simulations [569, 570]. The LAMMPS MD code [571] was used to construct an atomistic supercell of FLiBe molecules assuming a Born-Mayer type force field [569]. As described in Ref. [570], FLiBe density, viscosity, diffusion coefficients, heat capacity, and thermal conductivity are compared with experimental data and used to benchmark the FLiBe MD model which was used to generate the inputs for the ENDF/B-VIII.1 TSL evaluations. Using this model, the velocity auto-correlation function of F, Li, and Be was calculated and converted by Fourier transform into the excitation DOS of each species.

Subsequently, the DOS of each species was used in the `FLASSH` [529] code to generate the TSL (File 7, MAT4001, MAT4002, and MAT4003), under the incoherent approximation, and assuming the convolution of the solid component of the TSL with the diffusive component, to produce the total TSL. Fig. 124 shows the symmetric TSL for F,

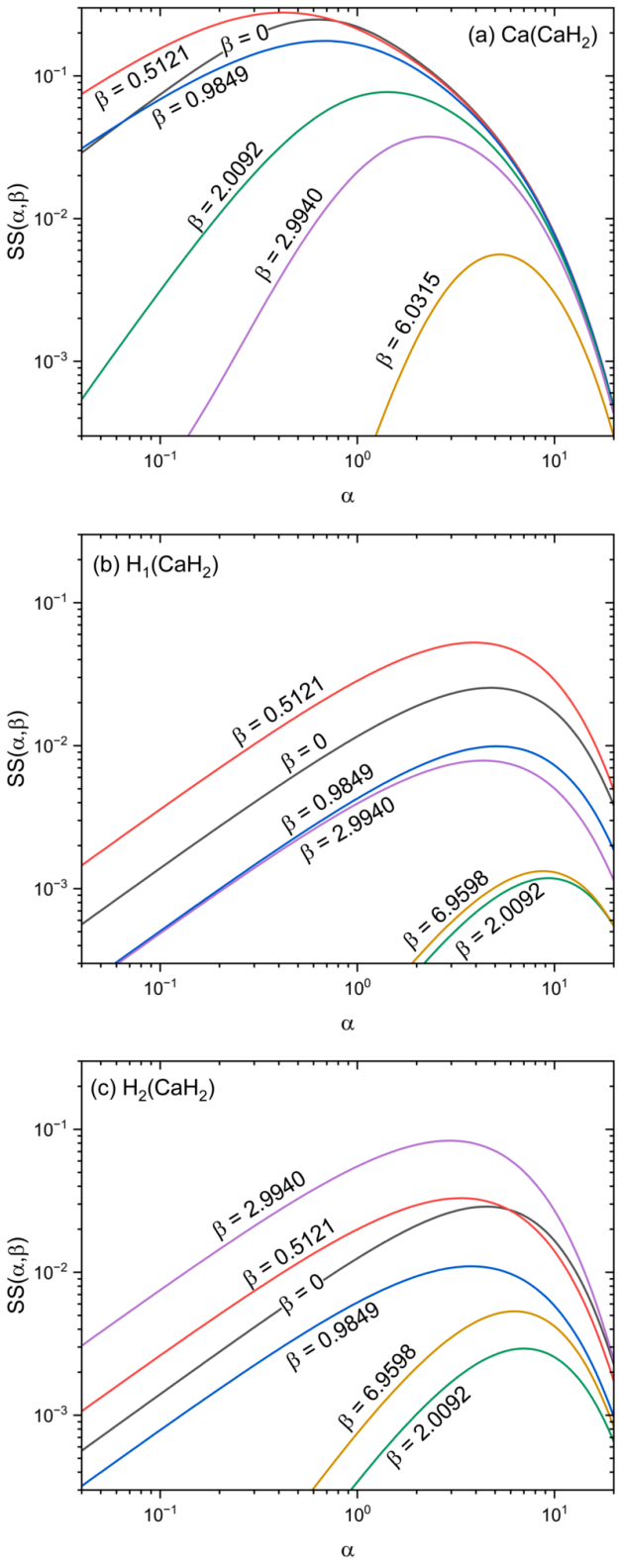


FIG. 121. (Color online) The symmetric TSL of (a) $Ca(CaH_2)$, (b) $H_1(CaH_2)$, and (c) $H_2(CaH_2)$ as a function of momentum transfer, α, for various values of β at 293.6 K. $SS(\alpha, \beta)$ for each β is labeled with the corresponding line.

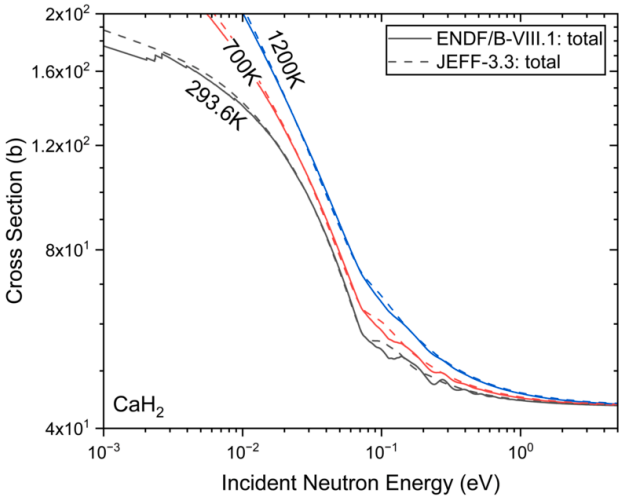


FIG. 122. (Color online) The total scattering cross section of CaH_2 shown at select temperatures. The total cross sections of CaH_2 for 296, 700, and 1200 K from the JEFF-3.3 library are also shown for comparison [64, 567]. The energy range is limited to highlight the differences in the coherent elastic and inelastic behavior of the cross sections.

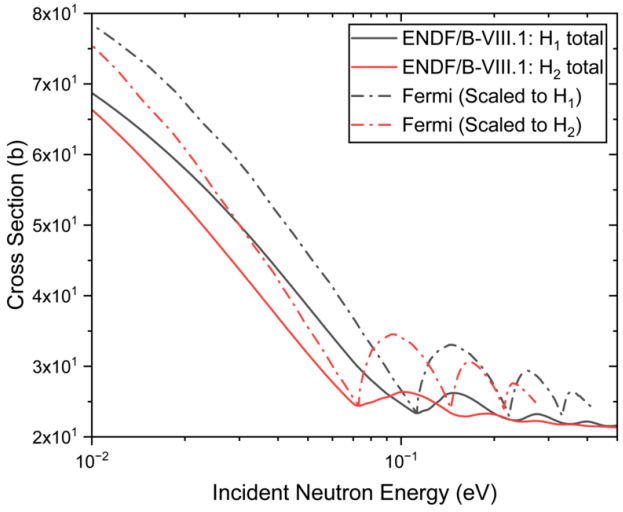


FIG. 123. (Color online) The ENDF/B-VIII.1 total cross sections of H_1 and H_2 in CaH_2 compared to the scattering cross section of a neutron in a hydrogenous substance as predicted by Fermi [568], scaled to the ENDF/B-VIII.1 data. The predicted behavior can be seen in the ENDF/B-VIII.1 cross sections, with diminished magnitudes due to the finite mass of Ca in CaH_2.

Li, and Be in FLiBe. The total thermal neutron scattering cross section of FLiBe is shown in Fig. 125. The evaluation was completed at 773, 873, 923, 973, 1073, 1173, 1273, 1473, and 1673 K, which corresponds to relevant operation and potential safety conditions of molten salt reactors. Mass and free atom cross sections [68] for ^{19}F, ^{7}Li, and ^{9}Be are used for the evaluations. The FLiBe evaluations represent new TSL contributions that are included for the first time in the ENDF/B database.

7. *Nuclear/Reactor Graphite (20%)*

Nuclear/reactor graphite with 20% porosity (reactor-graphite-20P) was evaluated using a PDOS that is constructed using the systematics observed based in the classical MD models of 10% and 30% porous graphite. Nuclear graphite is a multi-phase material whose microstructure differs from that of ideal, crystalline graphite. Specifically, localized graphite microcrystals are located in a carbon binder matrix, which impacts characteristic lattice vibrations and distinguishes its thermal scattering cross sections from crystalline graphite. Initially, a MD model for crystalline graphite was validated in LAMMPS [571] against experimental thermophysical properties. Next, porosity was introduced by stochastically removing atoms from the crystalline structure. For the 20% porous nuclear graphite, the porosity would correspond to a graphite density of approximately 1.7 g/cm^3. Time-dependent atomic velocities are calculated and used to generate the PDOS as the Fourier transform of the velocity auto-correlation function [572]. The DOS used for the evaluation is shown in Fig. 126.

The ENDF TSL for reactor-graphite-20P (File 7, MAT320) was generated in `FLASSH` [529] with mass and free atom cross sections for natural carbon [162] at standard temperatures of 296, 400, 500, 600, 700, 800, 1000, 1200, 1600, and 2000 K. In the incoherent approximation [514, 554], the symmetric TSL is stored as ENDF File 7, MT4 and presented in Fig. 127 at 296 K versus α for select β. Coherent elastic scattering describes zero-phonon interactions, is evaluated with the cubic approximation in `FLASSH`, and tabulated in File 7, MT2. In this case, crystalline graphite's coherent elastic behavior is assumed to be representative of nuclear/reactor graphite as well. Thermal scattering cross sections generated in `FLASSH` are depicted in Fig. 128. This is a novel TSL evaluation to be included for the first time in the ENDF/B-VIII.1 database. These cross sections have additionally been benchmarked against thermal scattering benchmarks, including the graphite slowing-down-time spectroscopy experiment that was performed at the ORELA facility [573]. As seen in Ref. [574], the use of the nuclear/reactor graphite with 20% porosity reduces the discrepancy between the measured and calculated thermal slowing-down-time spectrum (mean absolute deviation) from 4.14% with crystalline graphite to 2.13% with 20% porosity.

8. *Crystalline Graphite with Distinct Effects (graph+S_d)*

Crystalline graphite was evaluated as part of the ENDF/B-VIII.0 database using AILD techniques [531, 532] to generate the phonon dispersion relationships and

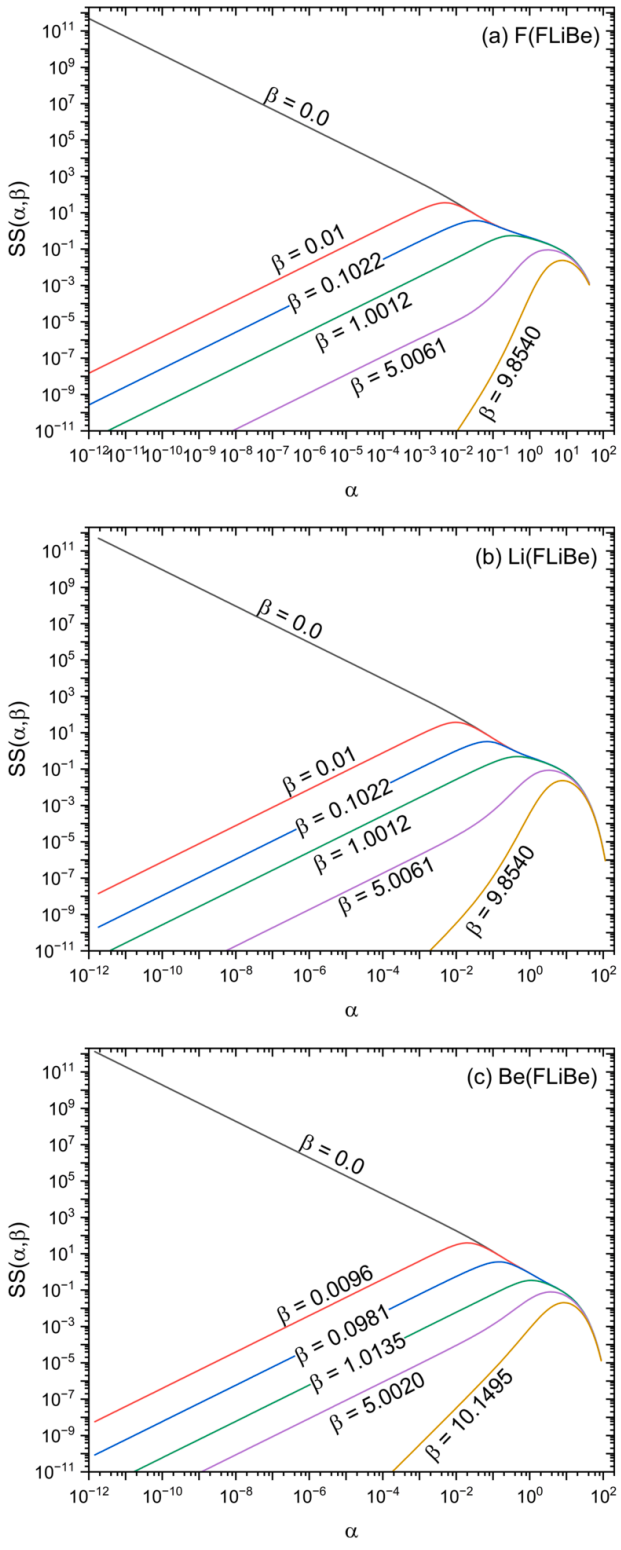


FIG. 124. (Color online) The symmetric TSL of (a) F(FLiBe), (b) Li(FLiBe), and (c) Be(FLiBe) as a function of momentum transfer, α, for various values of β at 773 K. $SS(\alpha, \beta)$ for each β is labeled with the corresponding line.

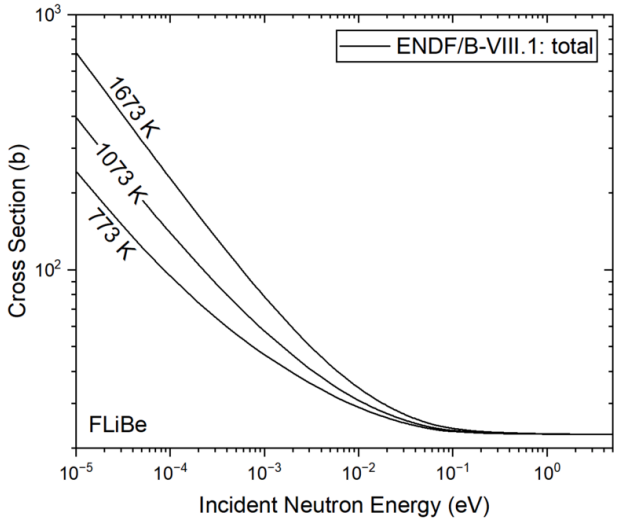


FIG. 125. Total thermal neutron scattering cross section of liquid FLiBe at select temperatures.

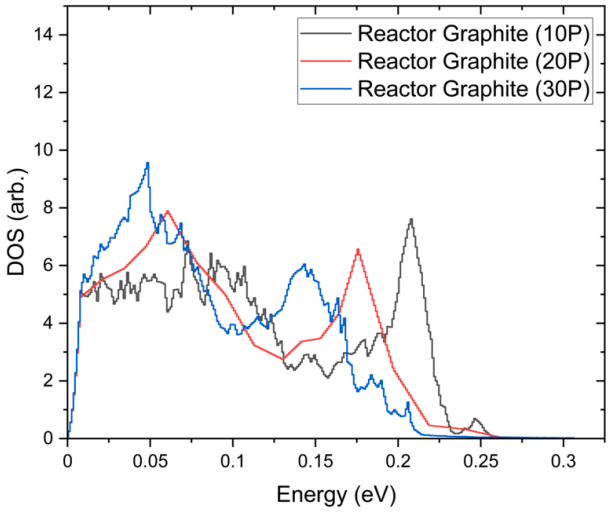


FIG. 126. (Color online) The DOS used for reactor graphite (20% porosity) as compared with 10% and 30%.

PDOS. Graphite is a crystalline material with tightly bound basal planes separated by Van der Waals forces. Its asymmetric crystalline structure results in directionally dependent thermal scattering effects. Using the validated ENDF/B-VIII.0 crystalline model of graphite [533], a novel evaluation was created, which accounts for the directional dependence of the graphite structure and removes traditional incoherent, cubic, and atom-site approximations to the TSL [575]. This evaluation utilizes a non-cubic formulation of the TSL with additional distinct effects (S_d) which include coherent interactions in the inelastic cross section [557]. The dispersion relations, which were developed in the AILD model demonstrated reasonable agreement with measurement [533]. These relation-

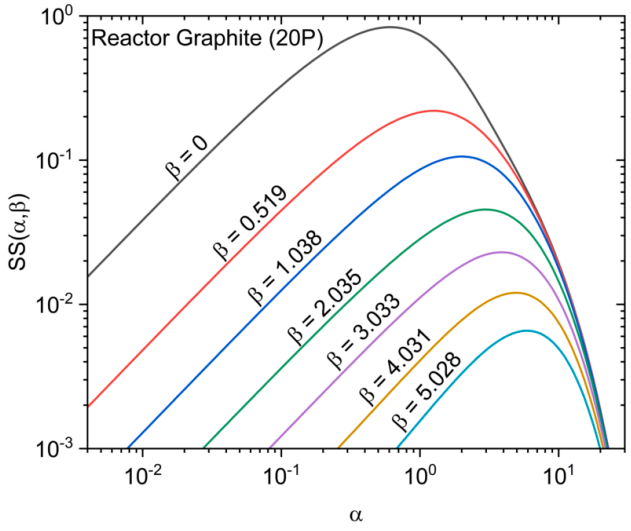


FIG. 127. (Color online) The symmetric TSL of reactor graphite (20% porosity) as a function of momentum transfer, α, for various values of β at 296 K. $SS(\alpha, \beta)$ for each β is labeled with the corresponding line.

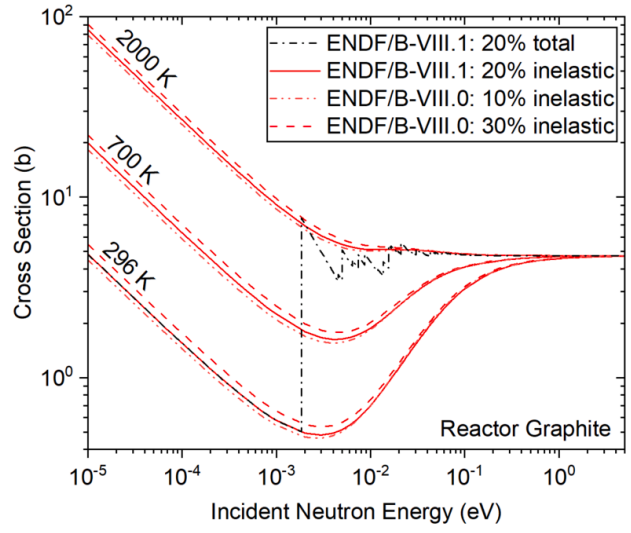


FIG. 128. (Color online) The inelastic scattering cross section of 20% porosity reactor graphite (ENDF/B-VIII.1) compared with 10% and 30% reactor graphite from ENDF/B-VIII.0 at selected temperatures. The total scattering cross section of 20% reactor graphite at 296 K is also shown.

ships then form the fundamental input for the generation of the TSL with mass and free atom cross section for natural carbon [162]. Using the FLASSH code and the advanced physics modules, the TSL for crystalline graphite with S_d effects (File 7, MAT301) was evaluated at temperatures of 296, 400, 500, 600, 700, 800, 1000, and 1200 K without the incoherent approximation and using the non-cubic formulation [529]. The symmetric TSL at 296 K tabulated in File 7, MT4 of the ENDF file is illustrated

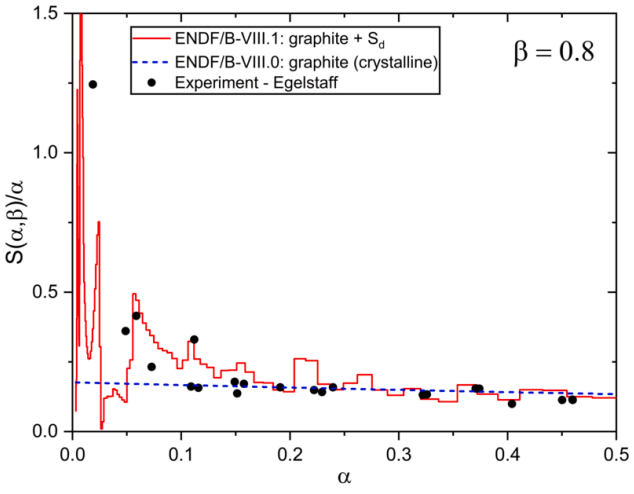


FIG. 129. (Color online) The symmetric TSL for graphite with S_d effects at 296 K as a function of momentum transfer α compared to experimental data [576, 577].

in Fig. 129, and an example comparison with experimental measurements is shown [576, 577]. Additional TSL and experimental data comparisons of this data can be found in Ref. [575].

Coherent elastic scattering was evaluated using the generalized non-cubic routine in FLASSH through the use of the directionally dependent Debye-Waller matrix that explicitly treats asymmetric vibrational behavior in different crystallographic directions [529]. This allows a consistent evaluation method between the TSL and resulting inelastic cross sections and the coherent elastic cross sections. The resulting total integrated scattering cross section for the ENDF/B-VIII.1 crystalline graphite with S_d effects is shown in Fig. 130. The comparison with experimental data shows improved agreement over the similar evaluation in ENDF/B-VIII.0 without S_d effects.

This addition of distinct (S_d) effects provides the ability to directly benchmark the TSL evaluation against experimentally measured TSL data [575] for crystalline graphite and improves the agreement with experimentally measured inelastic cross sections [563, 578, 579]. The crystalline graphite with S_d evaluation represents a new TSL evaluation that is included for the first time in the ENDF/B database.

The users of the crystalline graphite of ENDF/B-VIII.0 are encouraged to try the graphite with S_d of ENDF/B-VIII.1 and provide feedback to the authors if feasible. Similarly, the authors encourage the users of the crystalline graphite to test the porosity effect in the systems with "real" graphite by changing the ideal graphite $S(\alpha, \beta)$ to one of the porous graphite $S(\alpha, \beta)$ available in ENDF/B-VIII.1 and provide feedback to the authors.

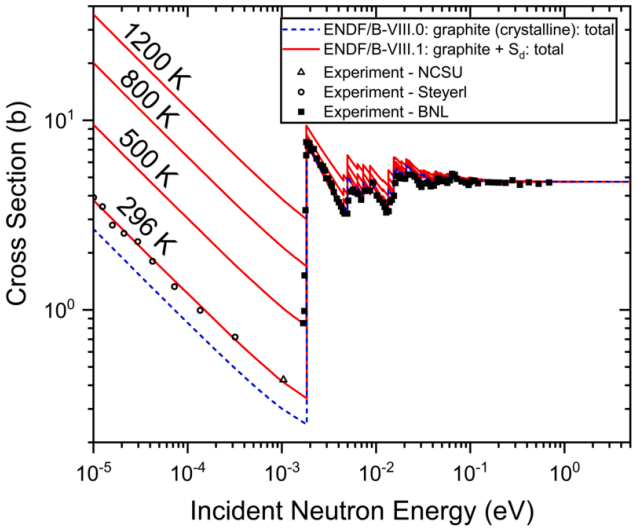


FIG. 130. (Color online) Total thermal neutron scattering cross section of crystalline graphite with S_d effects at 296 K compared to experimental data [563, 578, 579]. The total cross section with S_d effects is also shown at select temperatures.

9. *Anhydrous Hydrogen Fluoride (HF)*

Hydrogen Fluoride (HF) is a liquid material which is used at elevated temperatures and pressures to process and manufacture nuclear fuel. It is comprised of long chains of bonded hydrogen and fluorine molecules. The evaluation was based on a classical MD model composed of a supercell of 1000 HF molecules [580]. The model was executed using the GROMACS code [581] to produce temperature-dependent DOS of intra- and intermolecular excitations as the power spectrum of relevant atomic trajectory autocorrelation functions for thermodynamic state-points between 343 K (3 atmospheres) and 383 K (17 atmospheres). The MD model validated using density, diffusion coefficients, potential energy, and bond length experimental data, and the resulting DOS is shown in Ref. [580, Fig. 9].

The TSLs of H(HF) (File 7, MAT3048) and F(HF) (File 7, MAT3047) were generated in `FLASSH` [529] under the incoherent approximation with a Schofield diffusional model [582]. Diffusional parameters were derived from the MD model based on the model's effective cluster size of eight molecules. The TSL was generated for temperatures of 343, 348, 353, 363, 373, and 383 K with mass and free atom cross sections [68] for ^{1}H and ^{19}F. Fig. 131 shows the scattering law at various α and β values. Fig. 132 shows the total scattering cross sections for H and F in HF.

These evaluations represent new additions to the ENDF/B database. Benchmark testing of these evaluations in ICSBEP HEU-SOL-THERM-039 [583] have been completed and showed improvement on the order of 1000 pcm in the criticality calculations in comparison to experimental data [580]. The HF evaluations represent new TSL contributions that are included for the first time in the ENDF/B database.

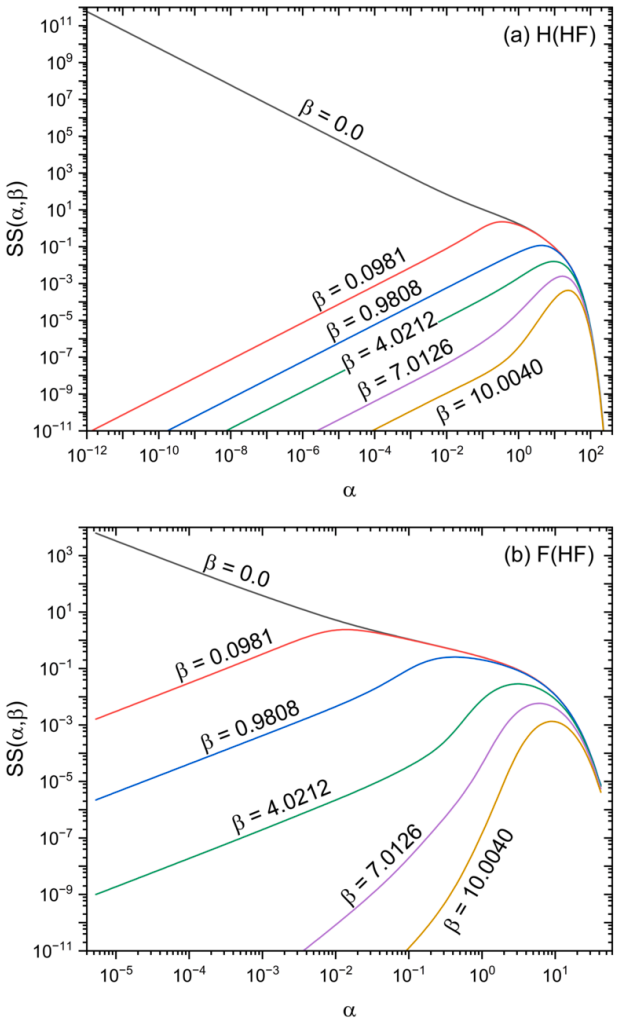


FIG. 131. (Color online) The symmetric TSL for (a) H(HF) and (b) F(HF) 343 K as a function of momentum transfer α, for a range of neutron energy transfers, β. $S_s(\alpha,\beta)$ for each β is labeled with the corresponding line.

10. *Heavy Paraffinic Oil*

Paraffinic-based oils (a hydrocarbon material) appear in various industrial applications, including those involving nuclear reactor and neutronic systems. In such cases, the description of neutron interactions and thermalization in paraffinic oil environments requires the use of TSL data and related cross sections. Therefore, to evaluate the TSL of paraffinic oil, classical MD methods, with the COMPASS force field, were used to establish the atomistic models for generating the velocity auto-correlation function and DOS of hydrogen in oil [584]. The MD mod-

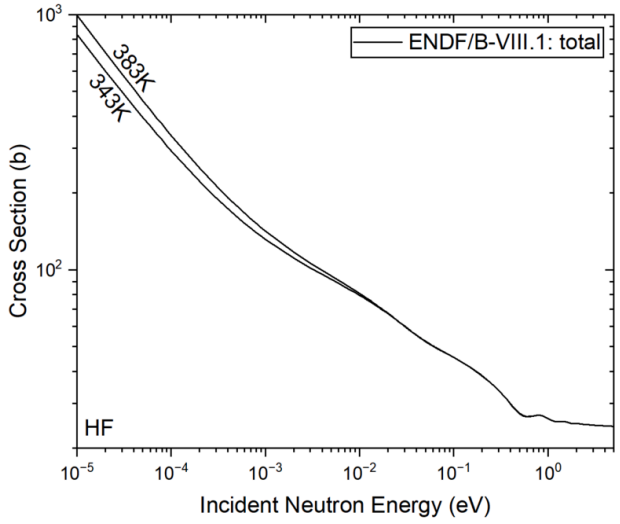


FIG. 132. Total thermal neutron scattering cross section of HF at select temperatures.

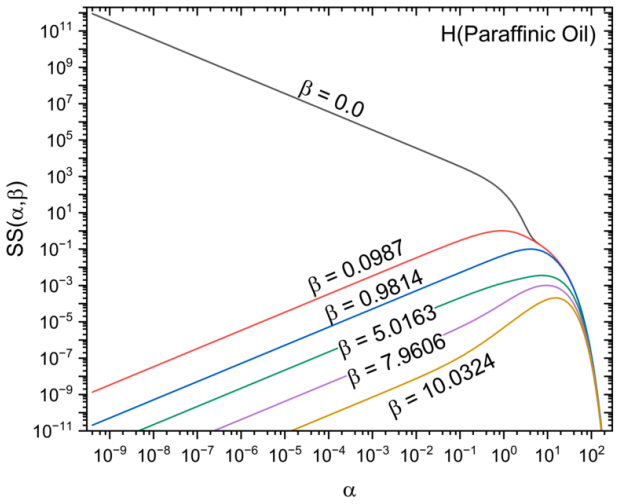


FIG. 133. (Color online) The symmetric TSL of H(ParaffinicOil) as a function of momentum transfer, α, for various values of β at 293.6 K. $SS(\alpha, \beta)$ for each β is labeled with the corresponding line.

els were designed to capture a highly viscous oil and are described in Ref. [584].

The `FLASSH` [529] code was used to perform the TSL evaluation and produce the H(ParaffinicOil) data in the ENDF File 7 format (MAT41). The total TSL, SS(α,β), was calculated assuming the incoherent approximation and the convolution of the solid TSL component with a diffusive component based on a Langevin model with mass and free atom cross sections [68] for ^{1}H. Fig. 133 shows the symmetric TSL of hydrogen in paraffinic oil as a function of α for various values of β. The total thermal scattering cross section of hydrogen is shown in Fig. 134. Benchmark comparison of this evaluation against transmission data shows excellent agreement [585]. The evaluation was performed for 293.6, 300, 325, 350, 375, 400 K. The paraffinic oil evaluation represents a new TSL contribution that is included for the first time in the ENDF/B database.

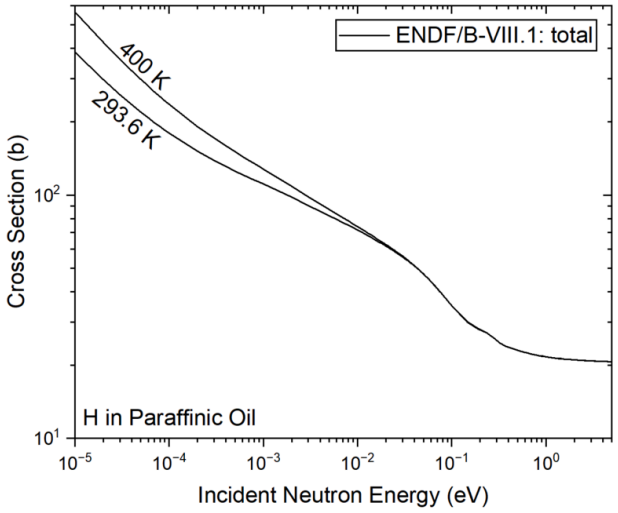


FIG. 134. Total thermal neutron scattering cross section of H in paraffinic oil at select temperatures.

11. Silicon Carbide (SiC)

The evaluation for 3C-SiC (SiC) is based on the previous ENDF/B-VIII.0 evaluation with key updates to improve the TSL and resulting cross section. The ENDF/B-VIII.0 AILD simulations of the lattice structure were maintained [586, 587]; however, updates to the evaluation of the PDOS were performed to provide needed energy resolution. In addition, this contribution updates the evaluation to use the natural abundances [87] of the atomic mass and cross sections of C and Si [68], as opposed to ^{12}C and ^{28}Si, and to use experimental lattice parameters [588] in the calculation of the coherent elastic data instead of *ab initio* values.

3C-SiC was evaluated using typical AILD methods [531, 532]. *Ab initio* simulations of 3C-SiC were performed using the `VASP` code [550–552], and the resultant Hellmann-Feynman forces were used in the PHONON code [553] to calculate the phonon dispersion relations and PDOS for each element using the dynamical matrix method [587]. Ref. [587, Fig. 9] shows a comparison of the calculated and experimental phonon dispersion curves.

The partial PDOS for Si and C in SiC were used to calculate the TSL (File 7) at 296, 300, 400, 500, 600, 700, 800, 1000, and 1200 K under the incoherent approximation for Si(3C-SiC) (MAT43) and C(3C-SiC) (MAT44) using `FLASSH` [529]. The symmetric TSL of Si(3C-SiC) and C(3C-SiC) at 296 K are shown in Fig. 135.

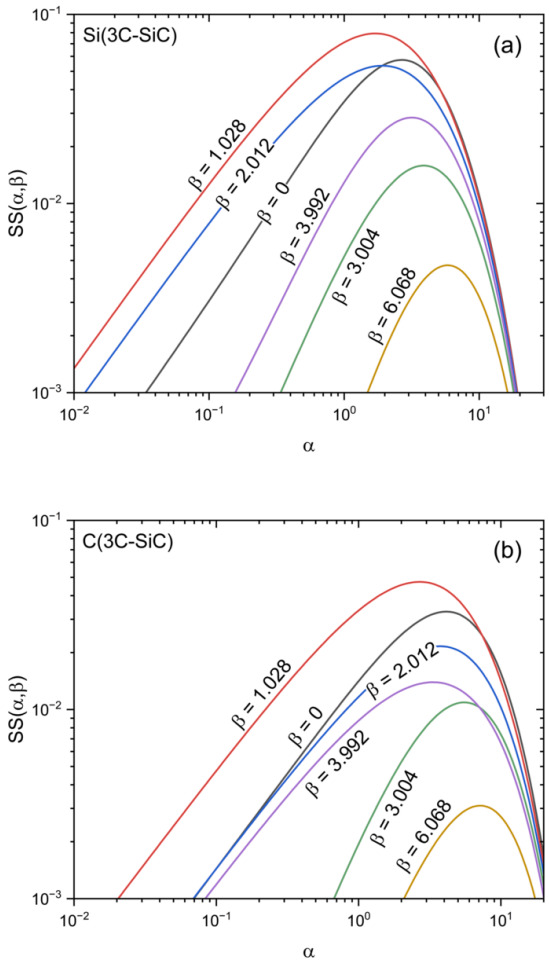


FIG. 135. (Color online) The symmetric TSL of (a) Si(3C-SiC), and (b) C(3C-SiC) as a function of momentum transfer, α, for various values of β at 296 K. $SS(\alpha,\beta)$ for each β is labeled with the corresponding line.

The coherent elastic scattering cross section of 3C-SiC was generated using the cubic approximation in FLASSH and is split evenly between the File 7 for each of Si(3C-SiC) and C(3C-SiC) (MT2). The ENDF/B-VIII.1 total scattering cross section of SiC at 296 K is shown in Fig. 136, along with the inelastic scattering cross section at select temperatures.

12. Silicon Dioxide (SiO_2, α Phase)

SiO_2-α was reevaluated using standard AILD methods [531, 532]. Also called α-quartz, SiO_2-α is a common material and a major component of rock and earth. The α-phase is the low-temperature phase, existing in this form until temperatures exceed 836 K, at which point it transitions to β-quartz. SiO_2-α has a trigonal crystal structure belonging to the $P3_221$ (#154) or $P3_121$ (#152) space

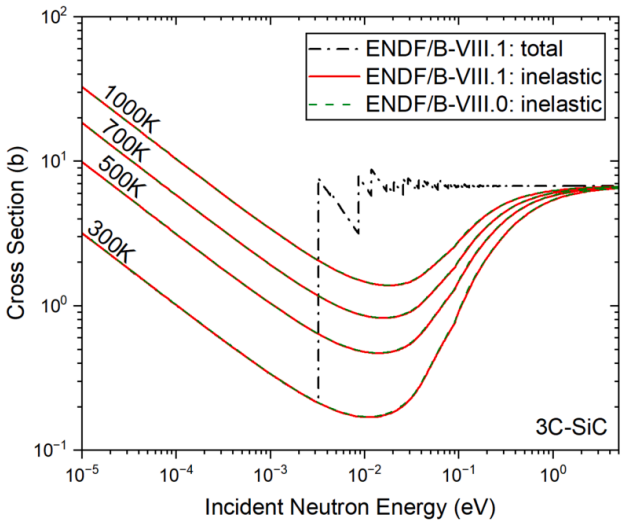


FIG. 136. (Color online) The inelastic scattering cross section of 3C-SiC shown at selected temperatures. The total scattering cross section of 3C-SiC at 300 K is also shown. The inelastic scattering cross section from ENDF/B-VIII.0 is shown for comparison.

group depending on chirality. The VASP code [550–552] was used to perform the *ab initio* modeling and calculate the Hellmann-Feynman forces of the crystal. These were used by the PHONON code [553] to calculate the phonon dispersion relations and PDOS via the dynamical matrix method.

The SiO_2-α evaluation has been improved for ENDF/B-VIII.1 through the use of a new PDOS for Si and O in SiO_2-α and the separation of the single SiO_2-α evaluation from ENDF/B-VIII.0 into distinct evaluations of Si(SiO_2-α) and O(SiO_2-α). A comparison of the ENDF/B-VIII.0 and ENDF/B-VIII.1 DOSs are shown in Fig. 137. The calculation of the coherent elastic scattering cross section was updated to use synthesized experimental lattice parameters and atomic positions [589–591], and naturally weighted [87] atomic masses and cross sections [68] were used throughout the evaluation.

The partial PDOS were used to calculate the TSL (File 7) for Si(SiO_2-α) (MAT3016) and O(SiO_2-α) (MAT3017) at 293.6, 350, 400, 500, 650, 800, and 846 K. The calculation of the TSL and thermal neutron scattering cross sections were performed using FLASSH [529], using the incoherent approximation for the former. Fig. 138 presents the symmetric TSL of Si(SiO_2-α) and O(SiO_2-α) at 293.6 K.

The cubic approximation was invoked in the calculation of the coherent elastic scattering contribution of the lattice, and the coherent elastic data is split between the File 7 of Si(SiO_2-α) and O(SiO_2-α) according to stoichiometry, with a weighting factor of 1/3. Fig. 139 shows the ENDF/B-VIII.1 total scattering cross section of SiO_2-α at 293.6 K, as well as the inelastic scattering cross section of the compound at selected temperatures. The total

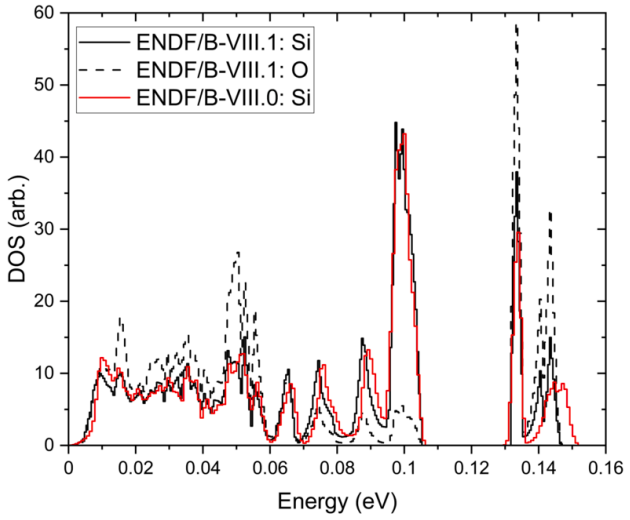


FIG. 137. (Color online) The Si(SiO_2-α) and O(SiO_2-α) DOSs used in the ENDF/B-VIII.0 and ENDF/B-VIII.1 evaluations.

and inelastic cross sections are compared to experimental data at room temperature [592, 593], where the experimental data for inelastic scattering has been corrected for absorption.

13. Polystyrene ($(C_8H_8)_n$)

The neutronic interest in polystyrene stemmed from a question surrounding several benchmarks in the ICSBEP benchmark suite. Specifically, MCT-002 and PCM-034 both contain appreciable quantities of polystyrene. Historically, the TSL file for polyethylene was used as a surrogate for calculating integral eigenvalue. This file was created to try and quantify the accuracy of this assumption.

The PDOS for hydrogen and carbon in polystyrene was calculated using CASTEP [594]. The starting structure was taken from Ref. [595], with a unit cell containing 48 carbon and hydrogen atoms. The structure was first relaxed using the Broyden-Fletcher-Goldfarb-Shanno (BFGS) minimization algorithm to identify an energetically stable atomic configuration and unit cell shape. A 750 eV energy cutoff was used in the Perdew-Burke-Ernzerhof formulation of the generalized gradient approximation. The system was relaxed until a tolerance of 5e-9 eV/atom for the ground state energy and 5e-4 Å for the geometric displacement of each atom was met. This relaxed unit cell was then used to calculate phonon properties using CASTEP's built-in density functional perturbation theory (DFPT) method. The advantage of CASTEP's DFPT implementation is that the calculations can be performed on the unit cell instead of the (often much larger) supercell. Because of the large size of the unit cell, a k-point grid of 1 × 1 × 3 was

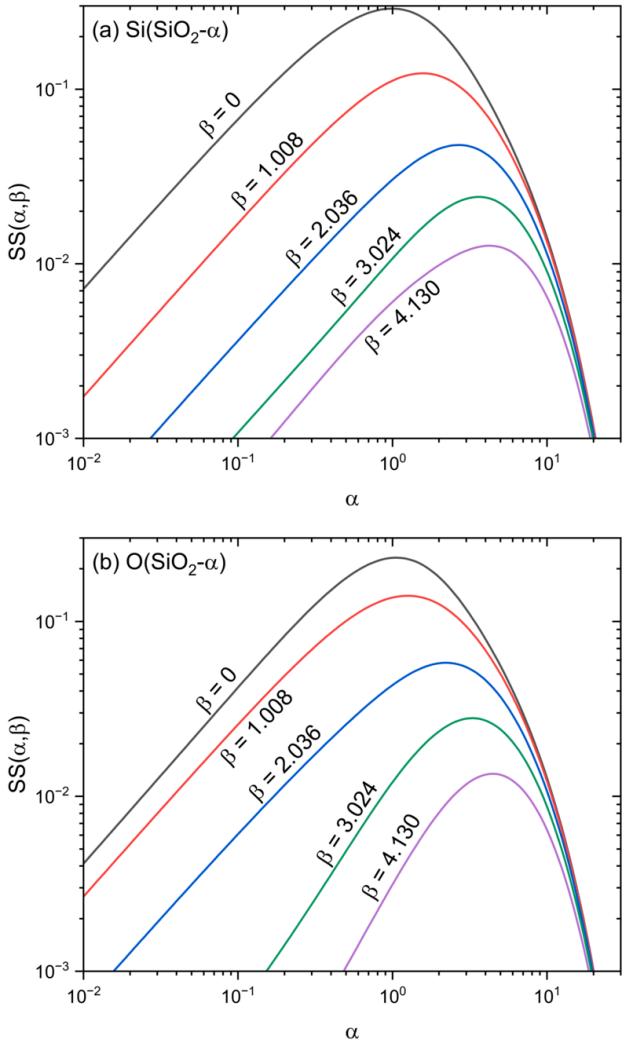


FIG. 138. (Color online) The symmetric TSL of (a) Si(SiO_2-α) and (b) O(SiO_2-α) as a function of momentum transfer, α, for various values of β at 293.6 K. $SS(\alpha,\beta)$ for each β is labeled with the corresponding line.

found to be sufficient for calculating the phonon properties. The resulting phonon file was then fed into OCLIMAX [596, 597], which was used to calculate the partial PDOS for carbon and hydrogen. Phonon spectra were then used to calculate the resulting ENDF TSL files using `NJOY2016` [325]. A plot of the constituent phonon spectra is shown in Fig.. 140.

The basis of ORNL-developed TSLs are inelastic neutron scattering (INS) and transmission (i.e., total scattering) measurements. INS measurements are performed using the VISION instrument [598] at the Spallation Neutron Source at ORNL to measure $S(Q,\omega)$, which is directly comparable to $S(\alpha,\beta)$: $S(\alpha,\beta,T) = k_BT\ exp\left(\frac{-\hbar\omega}{2k_BT}\right) S(Q,\omega,T)$, where T is the temperature, and k_B is the Boltzmann constant; $S(\alpha,\beta)$ is the quantity

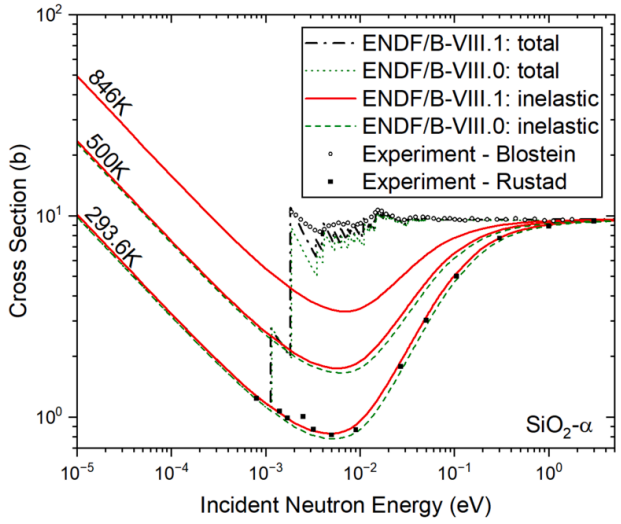


FIG. 139. (Color online) The inelastic scattering cross section of SiO_2-α shown at selected temperatures. The total scattering cross section of SiO_2-α at 293.6 K is also shown. The total and inelastic cross sections are compared to experimental data at room temperature [592, 593]. The ENDF/B-VIII.0 SiO_2-α inelastic scattering cross sections below 500 K are shown for comparison.

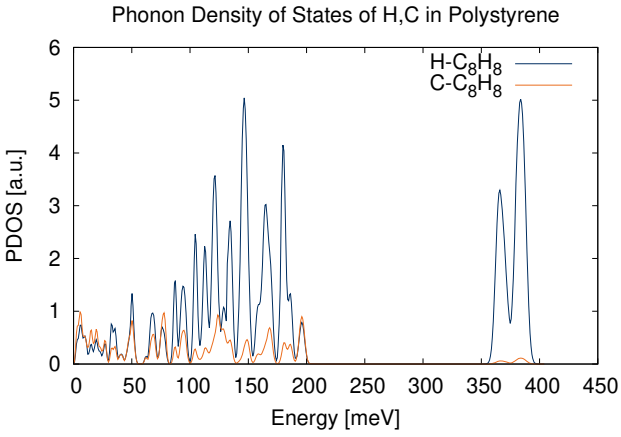


FIG. 140. Phonon density of states for H & C in polystyrene.

stored in ENDF File 7, MT4 of the TSL file. This means that INS measurements are explicit tools for validation of TSLs. Transmission measurements were performed at the Gaerttner LINAC at RPI [599].

For polystyrene, two samples were measured using the VISION instrument: one with a molecular weight of 223200 g/mol and the other with a molecular weight of 6400 g/mol. The difference in the molecular weight implies that the samples were different structurally, where a higher molecular weight polymer tends to have a more complex and larger structure compared to a polymer with a lower molecular weight. To compare with the VISION measurement, we converted $S(\alpha, \beta)$ from an ENDF file to $S(Q,\omega)$, extracted the values along the same Q and ω trajectory as in the VISION experiment, and applied the VISION instrumental resolution. The comparison with the experimentally measured $S(Q,\omega)$ is shown in Fig. 141, where the agreement between measured and calculated spectra is excellent. Most of the vibrational modes can be observed, although some small inconsistencies were seen at lower energies.

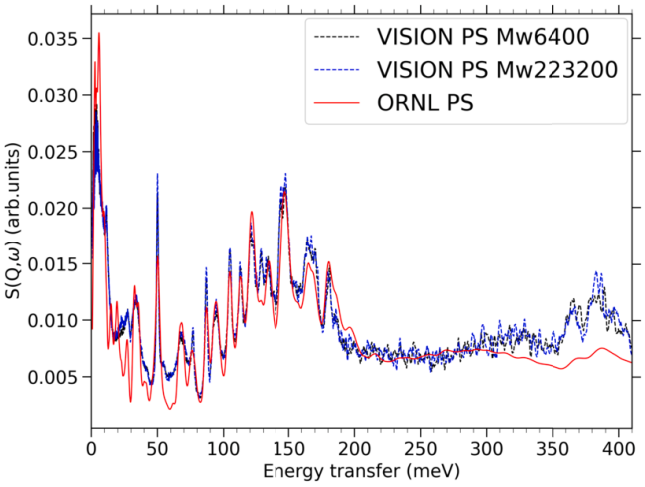


FIG. 141. Comparison of calculated S(Q,ω) spectra versus measured for PS.

Note that the TSL evaluation used an optimization method developed at ORNL. The basis for any TSL evaluation is the phonon spectrum, and from it, the whole scattering kernel—that is, $S(\alpha, \beta)$—as well as the total cross section can be calculated. Thus, because the phonon spectra have distinct vibrational modes (i.e., peaks), the developed method assigns weights to each peak and uses an optimization procedure using Dakota [600] to change the weights while minimizing the χ^2 square value between the calculated and measured $S(Q,\omega)$, as well as the calculated and measured total cross section, as measured at the RPI LINAC. The detailed optimization procedure details will be provided in a companion article. The comparison between measured and calculated total cross section is shown in Fig. 142, as well as the C/E plot. More information about this fitting procedure can be found in [601]. Fig. 142 shows that the agreement between the measured and calculated total cross section is excellent. This is in part because the evaluation was optimized using our methodology to match the RPI experimental transmission data. Ideally, for validation purposes, additional polystyrene transmission data are necessary.

For both carbon and hydrogen in polystyrene, TSLs were calculated using `NJOY2016` in the incoherent approximation, and the symmetric $S(\alpha, \beta)$ is stored as ENDF File 7, MT 4, with incoherent elastic stored in ENDF File 7, MT 2.

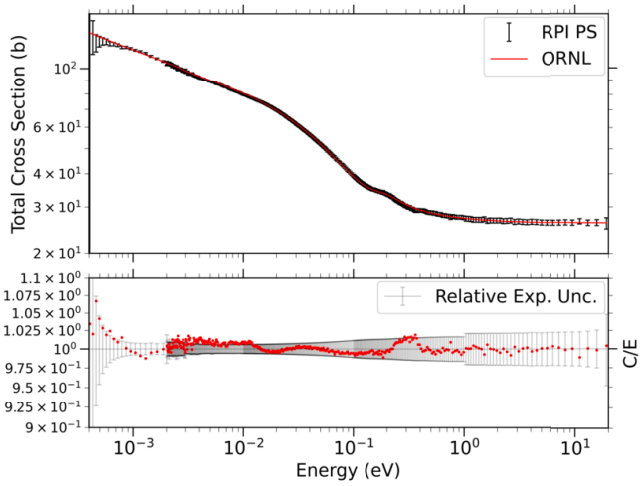


FIG. 142. Comparison of calculated total cross section versus that measured for PS (top) and C/E plot (bottom).

14. *Poly(methyl methacrylate) ($(C_5O_2H_8)_n$)*

Polymethyl methacrylate ($(C_5O_2H_8)_n$, or PMMA), also known as Lucite or Plexiglass, was evaluated using LAMMPS [571]. Phonon spectra for all atoms in lucite (i.e., hydrogen, carbon, and oxygen) were calculated. Lucite is a polymer with an amorphous structure. The initial structure for MD calculations was obtained using Polymer Builder [602], as implemented in CHARMM-GUI [603]. The structure created by the Polymer Builder consisted of 55 chains and 20 monomers of lucite at each chain. The specific computational details will be provided in the follow-up article to this paper. The partial DOS for each atom were calculated using velocity auto-correlation function, as implemented in MDANSE [604]. A plot of the constituent phonon spectra is shown in Fig.. 143.

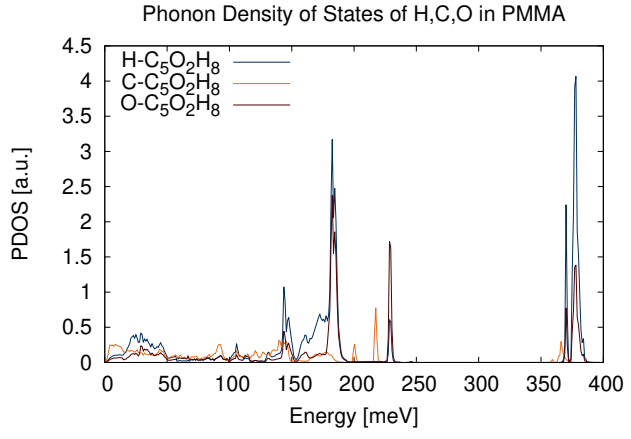


FIG. 143. Phonon density of states for H, C, & O in Poly(methyl methacrylate).

Five different samples of lucite were measured with the VISION instrument: two lucite powders (with a molecular weight of 15,000 g/mol and 120,000 g/mol), a sheet of regular store-bought lucite, a clear scratch and UV-resistant sheet of lucite, and a clear high-strength UV-resistant sheet of lucite. The main difference between all these samples was in the additives used to achieve different properties; lucite powders had no additives. Additionally, samples were of different thicknesses. The comparison of different TSLs with the experimentally measured $S(Q,\omega)$ can be seen in Fig. 144. Very little variation in the shape of the measured spectra was observed even though the samples were of significantly different compositions. The variations in the intensity of the spectra are due to differences in the thickness due to multiple neutron scattering. Additionally, it is noticeable that none of the TSLs do a great job of reproducing the measured spectra, but the ORNL (ENDF/B-VIII.1) TSL reproduces the shape better than ENDF/B-VIII.0 TSL. This can be seen in the calculated χ^2 values for each TSL in Table XXXVII.

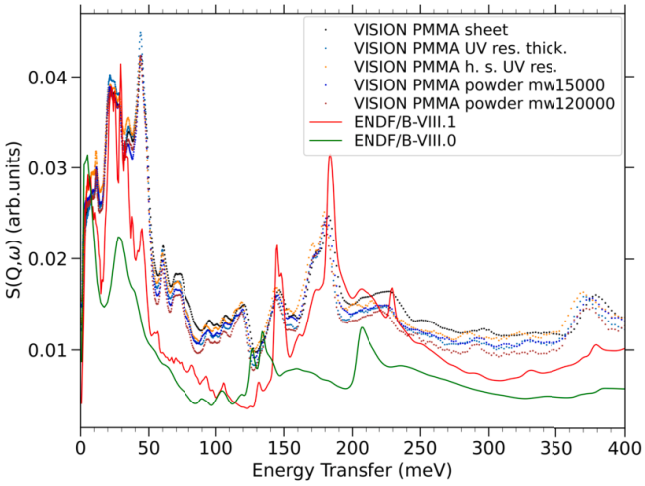


FIG. 144. Comparison of calculated S(Q,ω) spectra from different TSLs versus that measured for PMMA.

TABLE XXXVII. Calculated χ^2 values for ENDF/B-VIII.0 and ENDF/B-VIII.1 TSLs with respect to $S(Q,\omega)$ measurements with the VISION instrument.

TSL	χ^2
ENDF/B-VIII.0	1.24E+6
ENDF/B-VIII.1	4.94E+5

The comparison between measured and calculated total cross sections is given in Fig. 145, as well as the C/E plot. The ENDF/B-VIII.0 TSL overpredicts the total cross section below 3 meV, whereas ENDF/B-VIII.1 TSLs does significantly better. Both TSLs overcalculate the total cross section between 5 meV and 10 meV. Looking at the χ^2 values for each TSL in Table XXXVIII, we can see that ORNL TSL has slightly lower value.

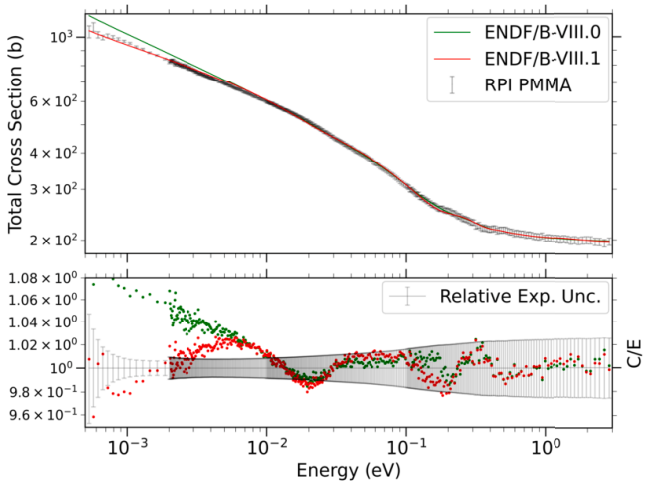


FIG. 145. Comparison of calculated total cross sections versus those measured for PMMA (top) and C/E plot (bottom).

TABLE XXXVIII. Calculated χ^2 values for ENDF/B-VIII.0 and ENDF/B-VIII.1 TSLs with respect to total cross section measurements at RPI.

TSL	χ^2
ENDF/B-VIII.0	294.4
ENDF/B-VIII.1	293.1

The TSLs for PMMA were compared against the new pulsed-neutron die-away (PNDA) measurements from LLNL [605]. The comparison between the calculated and measured decay constant eigenvalue, α, is shown in Fig. 146. As shown in comparison with the measured total cross section, the ENDF/B-VIII.0 TSL overpredicts the measured decay constant eigenvalues, whereas the ORNL TSL performs significantly better. The calculated cumulative χ^2 values for each TSL can be seen in Table XXXIX.

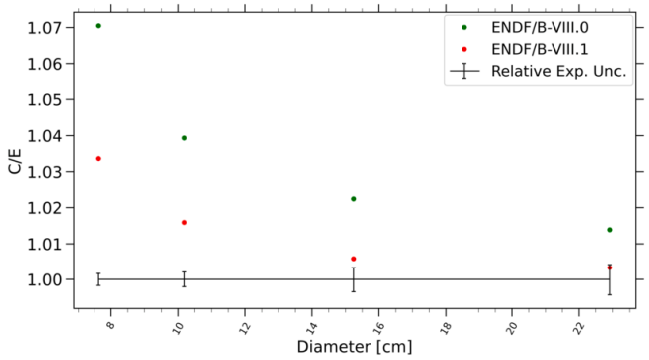


FIG. 146. Comparison of calculated decay constant eigenvalues from ENDF/B-VIII.0 and ENDF/B-VIII.1 TSLs versus measured for PMMA.

The available PMMA TSLs were compared against most of the thermal benchmarks that contain PMMA in the ICSBEP Handbook, 2021 edition. The comparison of calculated k_{eff} C/E values versus various benchmarks can be seen in Fig. 147. Similar to what was observed in the PNDA and total cross section comparisons, the ENDF/B-VIII.0 TSL overpredicts k_{eff} values, whereas the ORNL TSL performs better, including new HMT-004 benchmarks from LLNL. The calculated cumulative χ^2 values for each TSL can be seen in Table XL.

TABLE XXXIX. Calculated cumulative χ^2 values for ENDF/B-VIII.0 and ENDF/B-VIII.1 TSLs with respect to PNDA measurements.

TSL	χ^2
ENDF/B-VIII.0	2.24E+3
ENDF/B-VIII.1	4.77E+2

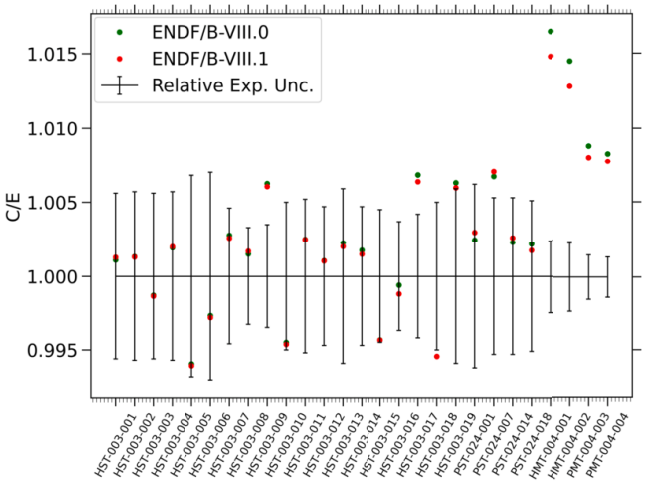


FIG. 147. Comparison of calculated k_{eff} values from ENDF/B-VIII.0 and ENDF/B-VIII.1 TSLs versus those measured for different thermal criticality benchmarks, taken from the ICSBEP 2021 Handbook.

TABLE XL. Calculated cumulative χ^2 values for ENDF/B-VIII.0 and ENDF/B-VIII.1 TSLs with respect to k_{eff} measurements.

TSL	χ^2
ENDF/B-VIII.0	1.33E+2
ENDF/B-VIII.1	9.34E+1

Hydrogen, carbon, and oxygen in PMMA TSLs were calculated using NJOY2016 in the incoherent approximation, and the symmetric $S(\alpha, \beta)$ is stored as ENDF File 7, MT 4, with incoherent elastic stored in ENDF File 7, MT 2.

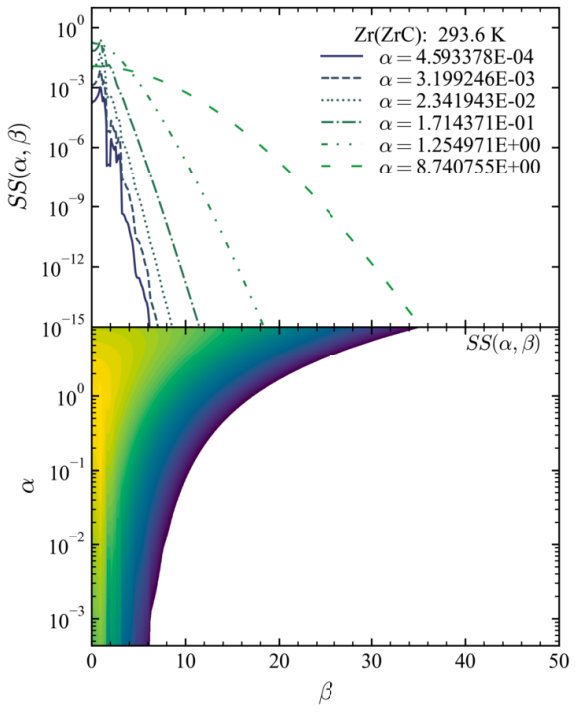
15. Zirconium Carbide (ZrC)

The TSL for C and Zr bound in ZrC have been evaluated by AILD techniques with `FLASSH` [529] and constitute a new material evaluation, included in the ENDF/B database for the first time. ZrC has a rock-salt crystal structure. Partial PDOS for Zr(ZrC) and C(ZrC) were generated with density functional theory and lattice dynamics; the calculations are detailed in Ref. [606]. Lattice parameters, phonon dispersion relations and Debye-Waller coefficients are found to be in good agreement with experiment [606].

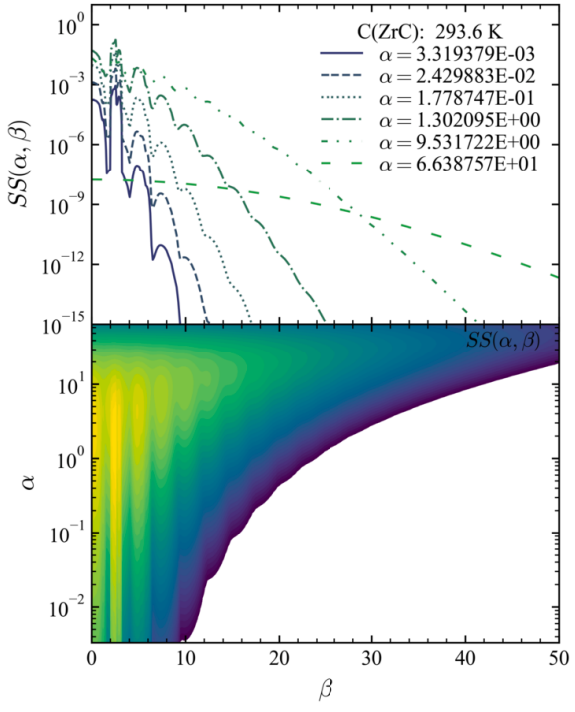
TSL File 7 evaluations are available for Zr(ZrC) and C(ZrC) at temperatures of 77, 293.6, 400, 500, 600, 700, 800, 1000, 1200, 1400, 1600, 1800, and 2000 K. This temperature range supports cryogenic through high temperature simulations. Each element was evaluated as the natural isotopic composition recommended by NIST [607] with total scattering cross sections and atomic weight ratios (AWR) extracted from the ENDF/B-VIII.1 nuclide evaluations; NIST cross sections were used to supplement incoherent elastic [87]. The ^{12}C AWR is set to exactly 12 amu. The mixed elastic scattering format [474, 537] was used to capture both coherent and incoherent contributions to elastic scattering (MT2). Coherent elastic scattering was treated with random alloy theory to account for isotopic variation in neutron scattering lengths of each element [606, 608], although, the natural C scattering length differs slightly from Ref. [606] due to the updated definition of ^{12}C mass. Inelastic scattering (MT4) was evaluated in the incoherent approximation with the phonon expansion method and automatic (α, β) gridding in `FLASSH`.

The symmetric TSL at 293.6 K tabulated in File 7, MT4 is illustrated in Fig. 148 for Zr(ZrC) and C(ZrC). Quantum oscillations in the C(ZrC) TSL, like those of metal hydrides, occur at fixed β intervals corresponding to localization of the partial phonon spectra around 0.065 eV, which is accompanied by a phonon band gap between acoustic and optical phonon modes. Monte Carlo transport simulations indicate that the quantized energy exchange can influence reactivity and shape the thermal neutron spectra from ambient to high temperatures [606]. Further, the gapped, optical phonon spectrum imparts quantum driven neutron thermalization behaviors similar to metal hydrides with analogs to electronic semiconductor physics, as described in Ref. [606].

The ZrC integrated inelastic and total scattering cross sections computed with the NDEX nuclear data processing code [609, 610] are illustrated in Fig. 149. Inelastic scattering for C(ZrC) has an apparent discontinuity in slope near 0.065 eV due to the localized optical phonon peak.



(a) Zr(ZrC).



(b) C(ZrC).

FIG. 148. (Color online) Zr(ZrC) and C(ZrC) symmetric TSL, $SS(\alpha, \beta)$, at 293.6 K. The (α, β) grid is referenced to $k_B T = 0.0253$ eV. The contour plot illustrates only $SS(\alpha, \beta) > 10^{-15}$; other non-zero values are not shown. Quantized oscillations in the C(ZrC) occur at integer values of $k_B T\beta \approx 0.065$ eV.

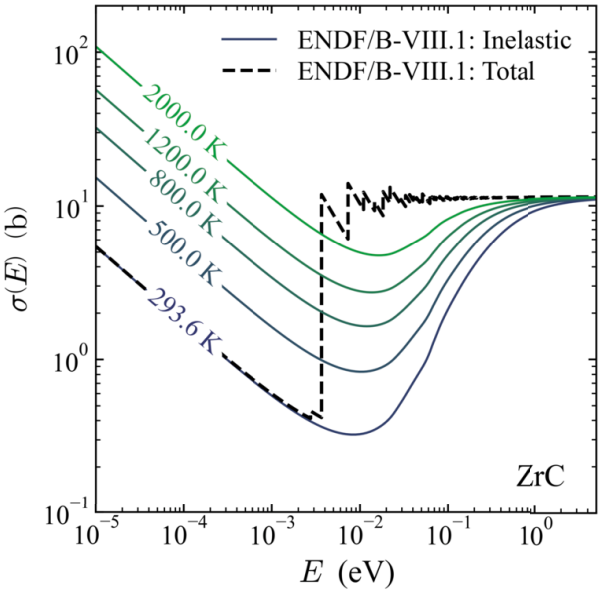


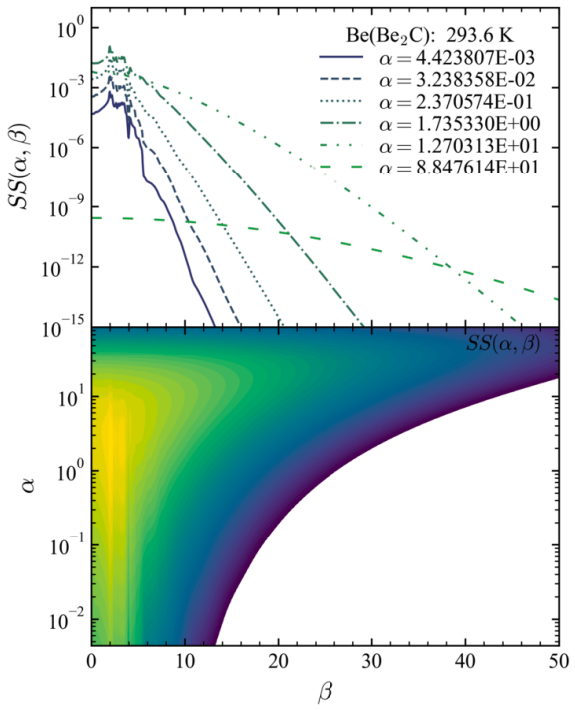
FIG. 149. (Color online) Total scattering cross section of ZrC at 293.6 K. The inelastic cross section between 293.6 K and 2000 K is also shown. The abrupt change in slope of the inelastic cross section near 0.065 eV is due to the gapped phonon spectra.

16. Beryllium Carbide (Be_2C)

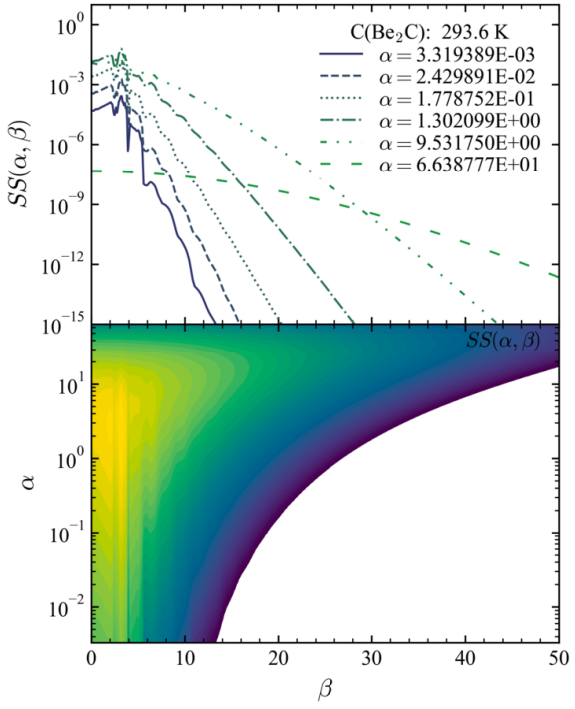
TSL evaluations Be and C bound in Be_2C were generated with `FLASSH` [529] and AILD techniques as a new material evaluation to the ENDF/B database. Be_2C has an anti-fluorite crystal structure. The partial phonon spectra were generated with density functional theory and lattice dynamics. The AILD methodology is similar to Ref. [611] and the PDOS demonstrate reasonable agreement with heat capacity measurements [612].

TSL File 7 evaluations are available for Be(Be_2C) and C(Be_2C) at 293.6, 400, 500, 600, 700, 800, 1000, 1200, 1600, and 2000 K. The material TSL evaluation considers ^{9}Be but uses an elemental composition for C from NIST [607]. For both elements, the total scattering cross sections and AWR were extracted from the ENDF/B-VIII.1 nuclide evaluation. Coherent elastic scattering (MT2) treatment was selected and evaluated using the experimental lattice parameter at room temperature [613]. Inelastic scattering was evaluated in the incoherent approximation with the phonon expansion and automatic (α, β) gridding in `FLASSH`.

Symmetric TSLs at 293.6 K tabulated in File 7, MT4, are illustrated for Be(Be_2C) and C(Be_2C) in Fig. 150, respectively. The TSL for both elements lack significant structure as a function of β beyond two phonon orders (≈ 0.16 eV). The integrated inelastic and total cross sections computed with NDEX nuclear data processing code [609, 610] is illustrated in Fig. 151.



(a) Be(Be_2C).



(b) C(Be_2C).

FIG. 150. (Color online) Be(Be_2C) and C(Be_2C) symmetric TSL, $SS(\alpha, \beta)$, at 293.6 K. The (α, β) grid is referenced to $k_BT = 0.0253$ eV. The contour plot illustrates only $SS(\alpha, \beta) > 10^{-15}$; other non-zero values are not shown.

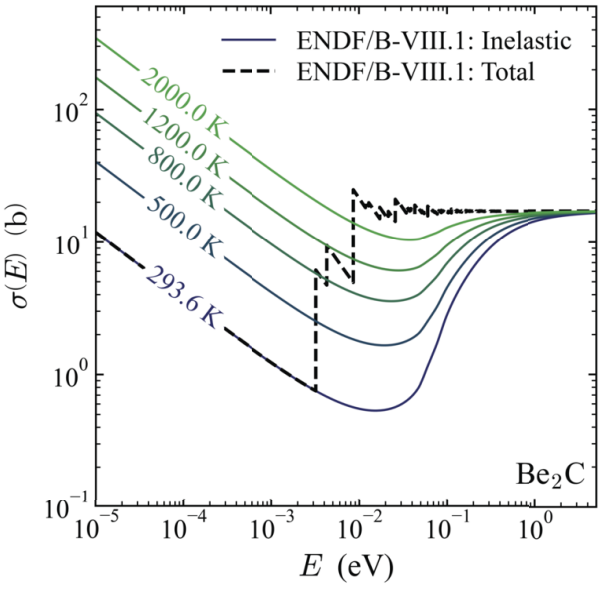


FIG. 151. (Color online) Total scattering cross section of Be_2C at 293.6 K. The inelastic cross section between 293.6 K and 2000 K is also shown.

17. *Zirconium Hydride (ZrH_x and ZrH_2)*

Zirconium hydride exists in two stable phases: the cubic δ-ZrH_x (Fluorite structure) and tetragonal ϵ-ZrH_2 (distorted-Fluorite structure). TSL evaluations were generated with `FLASSH` [529] using a combination of AILD and AIMD techniques for H and Zr for each phase [614]. The inclusion of both phases is an expansion of the ENDF database, where up through ENDF/B-VIII.0 a single evaluation was used to approximate both material phases.

The partial phonon spectra for $Zr(ZrH_x)$ and $Zr(ZrH_2)$ were generated with AILD methods, whereas $H(ZrH_x)$ and $H(ZrH_2)$ were generated with AIMD methods to capture anharmonicity [614]. The hydrogen phonon spectra capture experimentally observed differences in phases and have improved agreement with experiment when compared to the General Atomics (GA) spectrum used in prior ENDF evaluations [615]. TSL evaluations are likewise demonstrated to be in reasonable agreement with neutron scattering measurements [614].

TSL File 7 evaluations are available for $H(ZrH_x)$, $Zr(ZrH_x)$, $H(ZrH_2)$, and $Zr(ZrH_2)$ at temperatures of 77, 293.6, 400, 500, 600, 700, 800, 1000, and 1200 K. Hydrogen was evaluated as ^{1}H and Zr with the natural isotopic abundances recommended by NIST [607]. For both elements, the total scattering cross sections and AWR were extracted from the ENDF/B-VIII.1 nuclide evaluations. Coherent elastic scattering (MT2), which was omitted in prior ENDF releases, has been added for the zirconium sublattice of both material phases and is treated with random alloy theory [608] to account for the variation in zirconium nuclide scattering lengths. In this case, the zirconium scattering lengths and cross sections are the same those used in ZrC [606]. For completeness, mixed elastic scattering is used to add incoherent elastic for $Zr(ZrH_x)$ and $Zr(ZrH_2)$. $H(ZrH_x)$ and $H(ZrH_2)$ are evaluated with incoherent elastic scattering only such that the evaluations can be used with variable H stoichiometry defined by the phase diagram (e.g., the Zr-H system proposed by Zuzek *et al.* [616]). Inelastic scattering (MT4) contributions were evaluated in the incoherent approximation with the phonon expansion method and automatic (α, β) gridding in `FLASSH`.

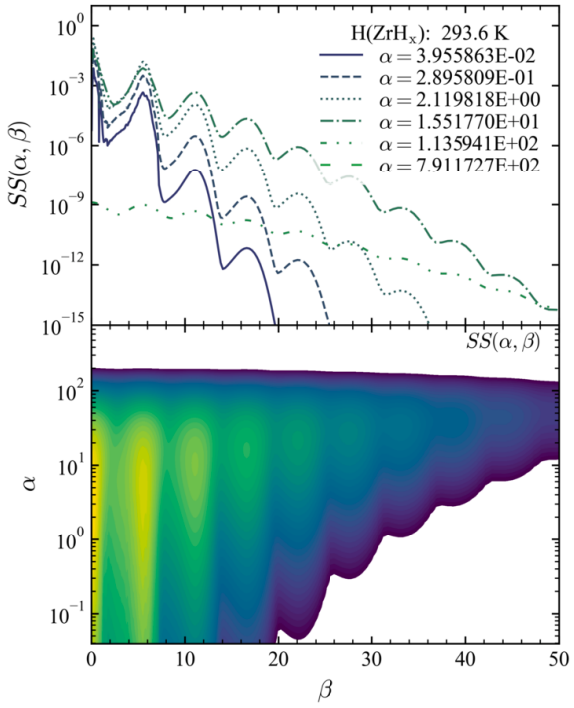
Symmetric TSLs at 293.6 K tabulated in File 7, MT4, are illustrated in Fig. 152 for $H(ZrH_x)$ and $H(ZrH_2)$. Quantized oscillations in each hydrogen TSL are present at fixed intervals of $k_BT\beta \approx 0.13$ eV. The integrated inelastic and total cross sections for ZrH_x and ZrH_2 computed with NDEX nuclear data processing code [609, 610] are illustrated in Fig. 153. Notably, the adaptive energy meshing in NDEX is necessary to fully capture the oscillator behavior in the cross section. The ENDF/B-VIII.1 evaluations are found to capture the Bragg edge features observed in neutron transmission measurements [617] that are neglected from the ENDF/B-VIII.0 ZrH material evaluation; however, oscillations in the inelastic cross section at higher energies are similar between ENDF/B-VIII.0 and ENDF/B-VIII.1 evaluations.

Initial testing of ZrH_x in the ICT-003 ICSBEP model of the Jožef Stefan Institute (JSI) TRIGA [158] using NDEX/MC21 [618] indicate a 300 pcm bias in k_{eff} between ZrH_x and the historic ZrH, which is well within the 1120 pcm benchmark uncertainty that results from fuel enrichment and hydrogen content. Additional TSL testing at JSI indicates a small variation in k_{eff} (< 100 pcm) between the ZrH_x evaluation and the historic ZrH evaluations [619]. A variation in k_{eff} between ZrH_x, ZrH_2, and ZrH evaluations of near or less than 150 pcm is observed more generally [619]. These findings are supported by critical mass calculations that illustrate small variations in critical mass for ^{235}U loadings historically used in U-ZrH_x fuel systems [620].

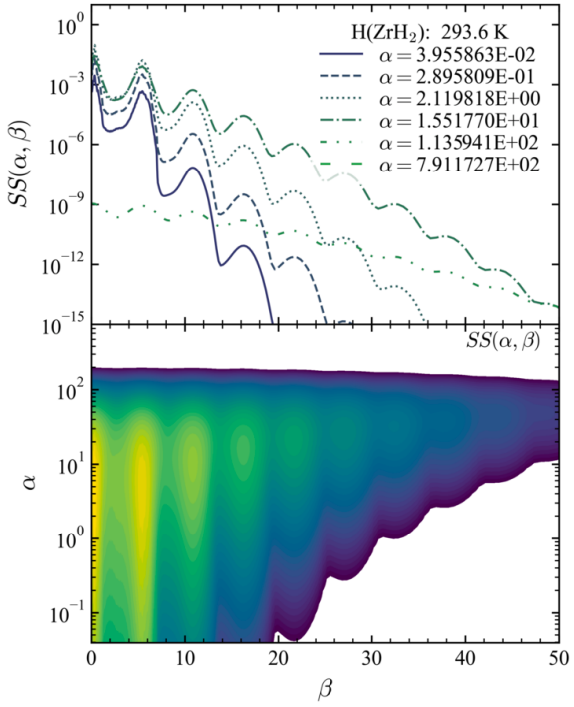
18. *Yttrium Hydride (YH_2)*

TSL evaluations H and Y bound in YH_2 were generated with `FLASSH` [529] and AILD techniques as reevaluations of the ENDF/B-VIII.0 TSL File 7. Yttrium hydride (YH_2) has a Fluorite crystal structure. Partial phonon spectra were generated from density functional theory and lattice dynamics, described in Refs. [621] and [622], and are the same as those used for the ENDF/B-VIII.0 evaluations. The $H(YH_2)$ spectrum has been demonstrated to be in good agreement with the experiment documented in Ref. [622].

TSL File 7 evaluations are available for $H(YH_2)$ and $Y(YH_2)$ at 293.6, 400, 500, 600, 700, 800, 1000, 1200, and 1600 K. The material TSL evaluation considers only ^{1}H and ^{89}Y. Both elements in the total scattering cross sec-

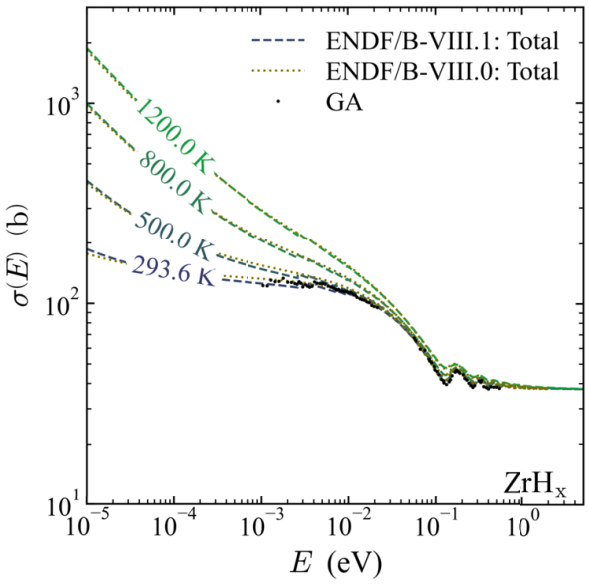


(a) H(ZrH_x).

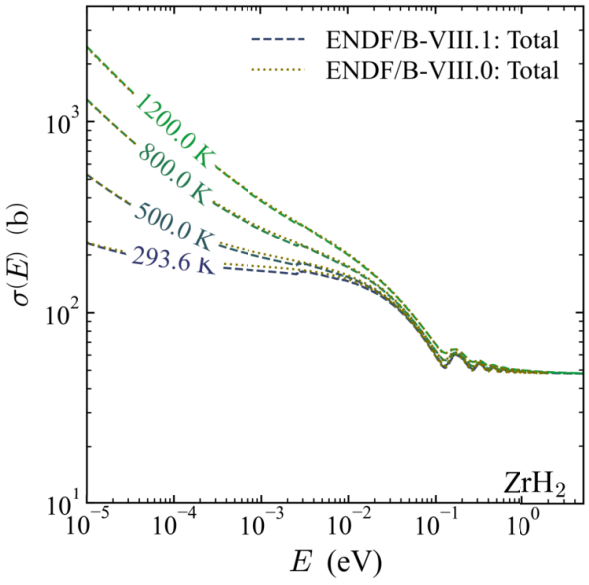


(b) H(ZrH_2).

FIG. 152. (Color online) H(ZrH_x) and H(ZrH_2) symmetric TSL, $SS(\alpha,\beta)$, at 293.6 K. The (α,β) grid is referenced to $k_BT = 0.0253$ eV. The contour plot illustrates only $SS(\alpha,\beta) > 10^{-15}$; other non-zero values are not shown. Quantized oscillations in each TSL occur at integer values of $k_BT\beta \approx 0.13$ eV.



(a) H(ZrH_x).



(b) H(ZrH_2).

FIG. 153. (Color online) Total scattering cross section of ZrH_x ($x = 1.5$) and ZrH_2 ($x = 2$) between 293.6–1200 K as compared to the ENDF/B-VIII.0 ZrH material evaluation. Oscillations in the cross section correspond to the H oscillator energy of ≈ 0.13 eV. Neutron transmission measurements from GA [617] at room temperature are also compared to the ZrH_x material evaluation. GA cross sections have been adjusted by the ENDF/B-VIII.1 elemental zirconium free atom scattering cross section above 0.004 eV per Ref. [617]. The ENDF/B-VIII.1 ZrH_x material evaluation captures the Bragg edges neglected in the ENDF/B-VIII.0 ZrH material evaluation.

tion and AWR were validated or updated to be consistent with the ENDF/B-VIII.1 nuclide evaluations. Coherent elastic scattering (MT2) for the yttrium sublattice, omitted in ENDF/B-VIII.0, has been added to the $Y(YH_2)$ evaluation using the experimental lattice parameter [622]. The restriction of coherent elastic scattering to yttrium permits the present evaluation to be used with variable H stoichiometry defined by the phase diagram (e.g., Y-H system proposed by Fu *et al.* [623]). Inelastic scattering (MT4) in all cases was reevaluated in the incoherent approximation with the phonon expansion and the automatic `FLASSH` (α, β) gridding.

The symmetric TSL for $H(YH_2)$ at 293.6 K tabulated in File 7, MT4, is illustrated in Fig. 154. Quantized oscillations are present at fixed intervals of $k_BT\beta \approx 0.125$ eV. The integrated total cross section for YH_2 computed with NDEX [609, 610] is illustrated in Fig. 155 and compared to neutron transmission measurements at the RPI LINAC facility [624] as well as the ENDF/B-VIII.0 YH_2 material evalution. The adaptive energy meshing in NDEX fully captures the oscillator behavior in the cross section. The revised ENDF/B-VIII.1 values are found to have good agreement with experiment and appropriately reproduce the Bragg edges. Oscillatory behavior above 0.1 eV due to inelastic contributions from $H(YH_2)$ are also consistent with experimental trends.

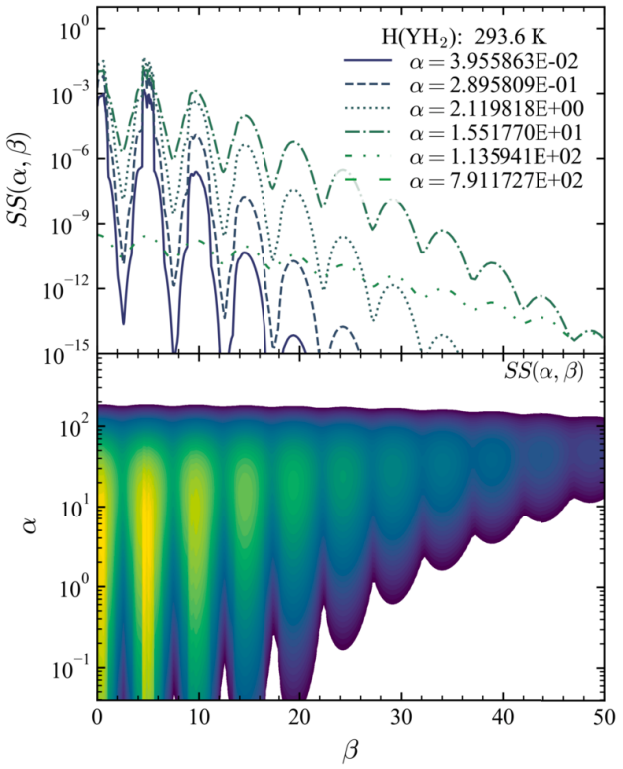


FIG. 154. (Color online) $H(YH_2)$ symmetric TSL, $SS(\alpha, \beta)$, at 293.6 K. The (α, β) grid is referenced to $k_BT = 0.0253$ eV. The contour plot illustrates only $SS(\alpha, \beta) > 10^{-15}$; other non-zero values are not shown. Quantized oscillations in the TSL occur at integer values of $k_BT\beta \approx 0.125$ eV.

19. *Lithium-7 Hydride (^{7}LiH) and Deuteride (^{7}LiD)*

TSL evaluations for H and ^{7}Li bound in lithium-7-enriched LiH as well as ^{7}Li and D in lithium-7-enriched LiD have been generated with `FLASSH` [529] and AILD methods as new material evaluations in the ENDF/B database. LiH and LiD have a rock-salt crystal structure. The partial phonon spectra were generated in each case with density functional theory and lattice dynamics. In the AILD approach, the *ab initio* force-field was the same for LiH and LiD; however, the mass of H and D differ in the lattice dynamics calculation.

TSL File 7 evaluations are available for H(^{7}LiH), ^{7}Li(^{7}LiH), D(^{7}LiD), and ^{7}Li(^{7}LiD) at 293.6, 400, 500, 600, 700 and 800 K. For both elements, the total scattering cross sections and AWR were extracted from the ENDF/B-VIII.1 nuclide evaluation; NIST cross sections were used to supplement incoherent elastic [87]. The mixed elastic scattering format [474, 537] was used to capture both coherent and incoherent contributions to elastic scattering (MT2). Coherent elastic scattering was evaluated using the experimental lattice parameter at room temperature [625]. Inelastic scattering (MT4) was evaluated in the incoherent approximation with the phonon expansion and automatic (α, β) gridding in `FLASSH`.

Symmetric TSLs for H(^{7}LiH) and D(^{7}LiD) at 293.6 K tabulated in File 7, MT4, are illustrated in Fig. 156. A limited number of quantized oscillations are present at fixed intervals of $k_BT\beta \approx 0.1$ eV and $k_BT\beta \approx 0.07$ eV for H(^{7}LiH) and D(^{7}LiD), respectively. The integrated scattering cross section for ^{7}LiH and ^{7}LiD computed with NDEX [609, 610] is illustrated in Fig. 157, respectively.

B. Fuels

1. *Plutonium Dioxide (PuO_2)*

PuO_2 was evaluated using modern AILD techniques [531, 532] for its fluorite-type crystal structure. The minimized electronic structure was predicted with `VASP` [550–552] DFT and accounts for spin-orbit coupling, semi-itinerant 5f electrons, Pu-5f / O-2p hybridization and AFM-1K magnetic ordering [626]. Hellmann-Feynman forces were used in PHONON [553] to construct and solve the dynamical matrix for sampling partial PDOS of $Pu(PuO_2)$ and $O(PuO_2)$. The AILD lattice constant and predicted electronic DOS demonstrate good agreement with experimental data. Furthermore, the Lorentzian broadening of partial DOS using the resolution of the HERIX instrument compares well with inelastic X-ray scattering (IXS) measurements [627].

The TSLs for $Pu(PuO_2)$ (File 7, MAT7200) and $O(PuO_2)$ (File 7, MAT7250) were evaluated in `FLASSH`

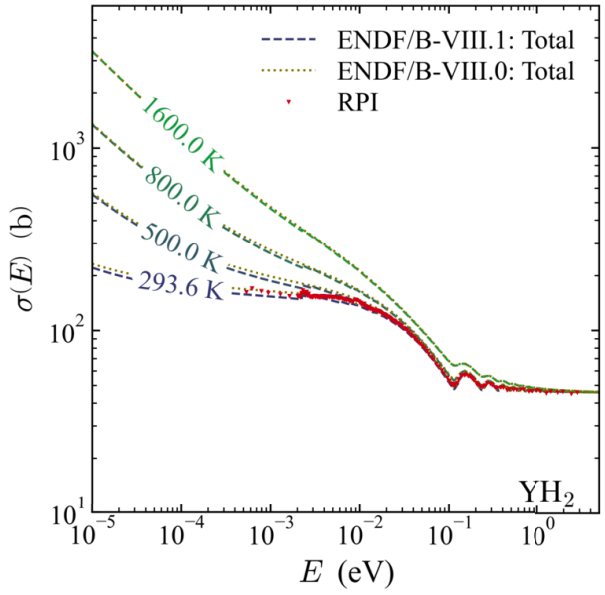


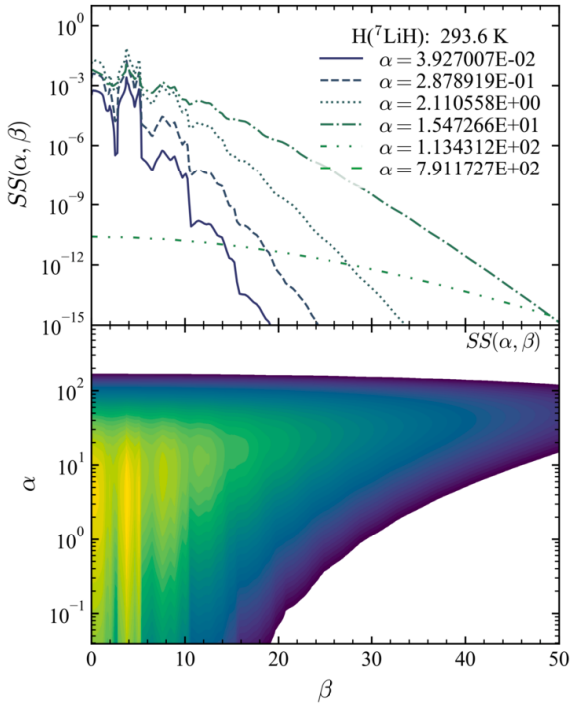
FIG. 155. (Color online) Total scattering cross section of YH_2 ($x = 1.85$) between 293.6–1200 K as compared to the ENDF/B-VIII.0 YH_2 material evaluation. Oscillations in the cross section correspond to the H oscillator energy of ≈ 0.125 eV. Room temperature neutron transmission measurements at the RPI LINAC [624] are also shown. LINAC cross sections have been adjusted for neutron capture using the ENDF/B-VIII.1 nuclide evaluations. The ENDF/B-VIII.1 YH_2 material evaluation captures the Bragg edges neglected in the ENDF/B-VIII.0 YH_2 material evaluation.

[529] with mass and free atom cross sections [68] reflecting 100% ^{239}Pu and a natural abundance [87] of oxygen at temperatures of 296, 400, 500, 600, 700, 800, 1000, 1200, 1600, 2000, 2400, 2800 K. $S_s(\alpha,\beta)$ (MT4) at 296 K for Pu(PuO_2) and O(PuO_2) are shown in Fig. 158.

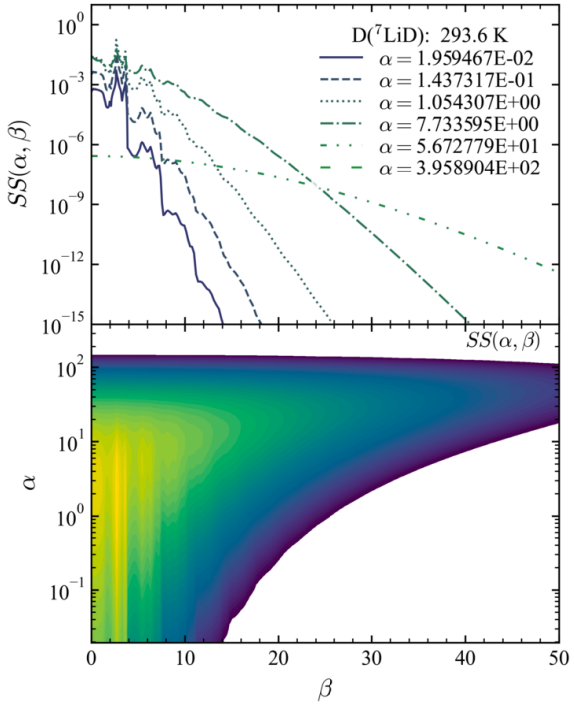
The *ab initio* thermal scattering cross sections, with incoherent inelastic and coherent elastic data calculated in `FLASSH` are shown in Fig. 159. These plutonium dioxide TSL evaluations are novel contributions to the ENDF/B-VIII.1 database.

2. *Uranium Carbide (UC)*

UC was evaluated using modern AILD techniques [531, 532] for varying ^{235}U enrichment of its rock-salt crystal structure [628]. The minimized crystalline and electronic structures predicted within the `VASP` [550–552] DFT framework account for spin-orbit-coupling, localized 5f interactions and approximate the paramagnetic ground state [629]. Averaged Hellmann-Feynman forces for AFM-1K orientations parallel and perpendicular to atomic displacements were used in PHONON [553] to construct the dynamical matrix, relate phonon wave vectors to energy, and sample partial PDOS for U(UC) and

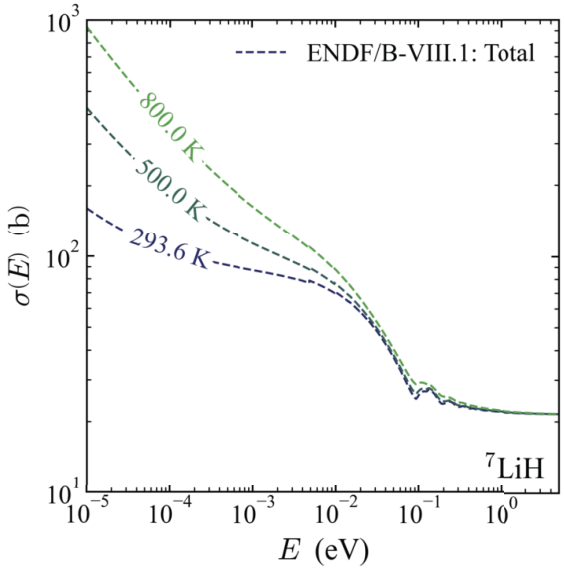


(a) H(^{7}LiH).

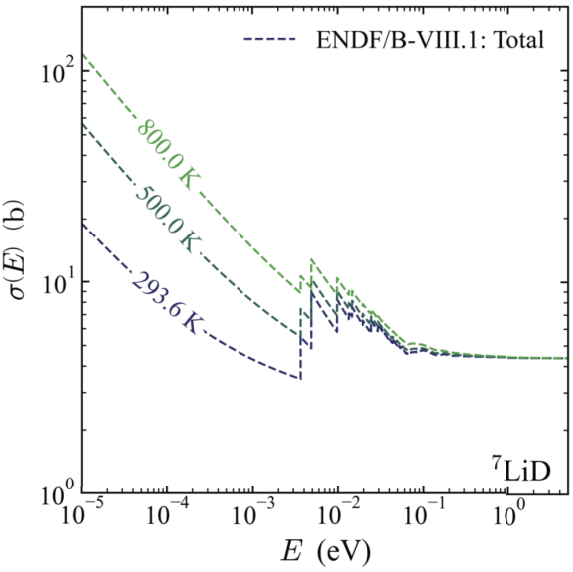


(b) D(^{7}LiD).

FIG. 156. (Color online) H(^{7}LiH) and D(^{7}LiD) symmetric TSL, $SS(\alpha,\beta)$, at 293.6 K. The (α,β) grid is referenced to $k_BT = 0.0253$ eV. The contour plot illustrates only $SS(\alpha,\beta) > 10^{-15}$: other non-zero values are not shown. Quantized oscillations occur at integer values of $k_BT\beta \approx 0.1$ eV in H(^{7}LiH) and $k_BT\beta \approx 0.07$ eV in D(^{7}LiD).



(a) H(^{7}LiH).



(b) D(^{7}LiD).

FIG. 157. (Color online) Total scattering cross section of H(^{7}LiH) and D(^{7}LiD) between 293.6–800 K. Limited oscillations in the cross section H(^{7}LiH) correspond to the H oscillator energy of ≈ 0.1 eV, whereas similar cross section behavior in D(^{7}LiD) correspond to the D oscillator energy of ≈ 0.07 eV.

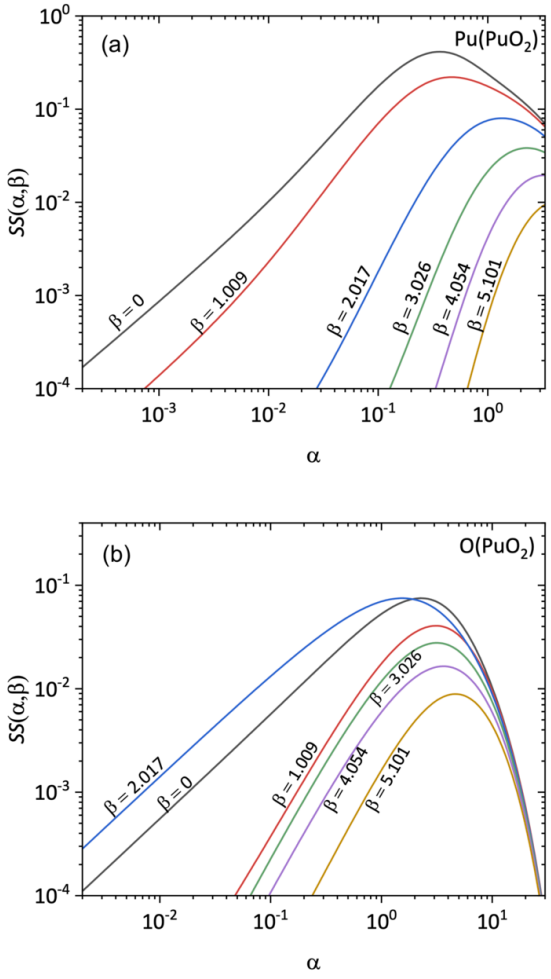


FIG. 158. (Color online) The symmetric TSL of (a) Pu(PuO$_2$), and (b) O(PuO$_2$) as a function of momentum transfer, α, for various values of β at 296 K. $SS(\alpha,\beta)$ for each β is labeled with the corresponding line.

C(UC). The predicted lattice parameter, electronic DOS, phonon dispersion relations, and total neutron-weighted PDOS demonstrate good agreement with measured data [628].

With partial PDOS as fundamental input, the TSLs for U(UC) and C(UC) were evaluated at temperatures of 293.6, 400, 500, 600, 700, 800, 1000, 1200, 1600 and 2000 K. $S_s(\alpha,\beta)$ (MT4) at 293.6 K for natural U(UC) and C(UC) are shown in Fig. 160. Enriched TSLs were evaluated using the characteristic AILD partial PDOS detailed above, and account for the impact of varying isotope dependent free-atom cross sections and masses [68]. These evaluations reflect natural (≈ 0.72%) [87], 5%, 10%, 19.75% (HALEU), 93% (HEU), and 100% ^{235}U enrichments and capture the impact of isotope abundance on the total cross section. Evaluations were completed using the `FLASSH` code for U(UC) for naturally enriched, 5%, 10%, 19.75% (HALEU), 93% (HEU), and 100% ^{235}U (File 7, MAT76, MAT8105, MAT8110, MAT8148, MAT8149, MAT8147, respectively) and for natural [630] C(UC) paired with each ^{235}U enrichment (File 7, MAT8150, MAT8155, MAT8160, MAT8198, MAT8199, MAT8197, respectively). Two files are required for each enrichment (a uranium and a carbon evaluation) because the tabulated compound coherent elastic will be impacted by the changing inputs associated with the uranium; MT4 for

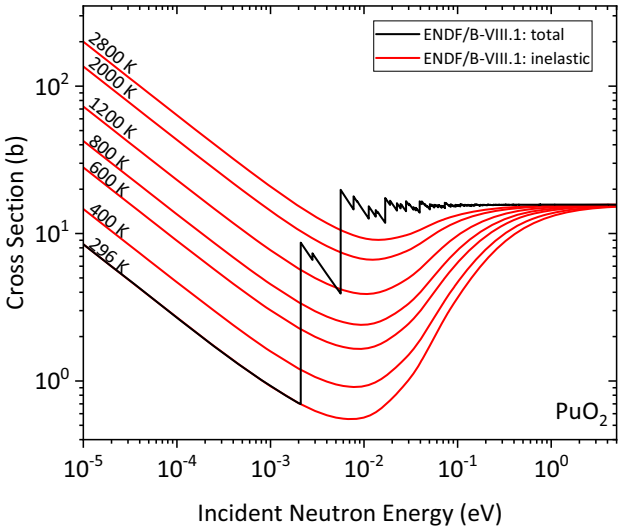


FIG. 159. (Color online) The inelastic scattering cross section of PuO_2 shown at selected temperatures. The total scattering cross sections of PuO_2 is also shown at 296 K.

C(UC) remains the same for each enrichment while MT2 varies.

The integrated total scattering cross sections containing incoherent inelastic (MT4) and coherent elastic (MT2) contributions are shown in Fig. 161 for varying temperatures and enrichments. When accounting for neutron absorption effects, the ENDF/B-VIII.1 natural UC cross sections demonstrate good agreement with neutron transmission measurements [631]. These UC TSL evaluations are novel contributions to the ENDF/B database.

3. *Uranium Metal (U-metal)*

The thermal scattering law for U-metal was evaluated using modern molecular dynamics/ lattice dynamics (MDLD) techniques to capture the combined temperature and lattice effects [575]. The α-phase of U-metal, which exists at room temperature, is a highly temperature-dependent structure and requires the use of MD techniques to capture the resulting temperature effects on the dynamical matrix. The MD model was composed of 8,000 atoms with a temperature of 296 K and zero pressure [575]. Perturbing the MD model, the resulting forces were used in the dynamical matrix method in phonopy [632] to calculate the PDOS. The resulting phonon dispersion relations and DOS were found to be in good agreement with experimental data [575].

Using the PDOS as the fundamental input, the `FLASSH` code [529] was used to evaluate the TSL for a natural enrichment U-metal (File 7, MAT8000) at temperatures of 293.6, 400, 500, 600, 700, 800, and 900 K, which correspond to the stable temperature region for U-metal. The

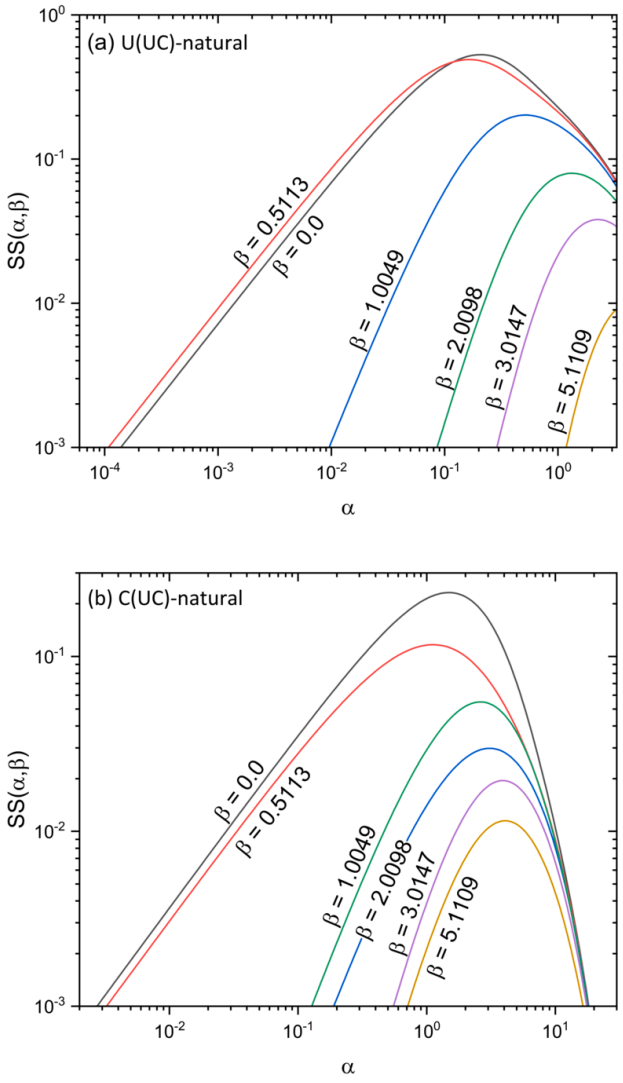


FIG. 160. (Color online) The symmetric TSL of natural abundance (a) U(UC) and (b) C(UC) as a function of momentum transfer, α, for various values of β at 293.6 K. $SS(\alpha,\beta)$ for each β is labeled with the corresponding line.

symmetric TSL (MT4) at 293.6 K is shown in Fig. 162.

Various enrichments of U-metal were evaluated using the PDOS described above. This DOS, which supports the structure of U-metal, was then combined with various mass and free atom cross sections [68] to represent a natural [630], 5%, 10%, 19.75% (HALEU), 93% (HEU), and 100% enrichment of ^{235}U. This then captures the impact of various compositions on the total scattering cross section. These evaluations were completed using the `FLASSH` code for naturally enriched, 5%, 10%, 19.75%, 93%, and 100% ^{235}U (File 7, MAT8000, MAT8005, MAT8010, MAT8048, MAT8099, and MAT8047, respectively). The integrated scattering cross sections as evaluated by `FLASSH` are shown in Fig. 163.

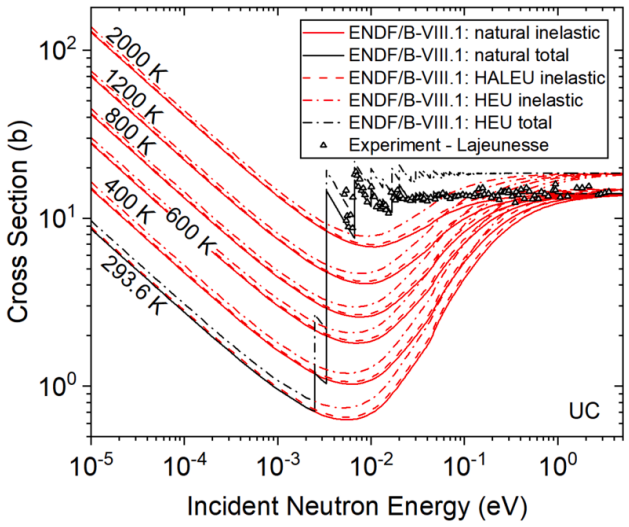


FIG. 161. (Color online) The inelastic scattering cross section of UC shown at selected temperatures and enrichments. The natural total scattering cross sections of UC at 293.6 K and measurement [631] are also shown.

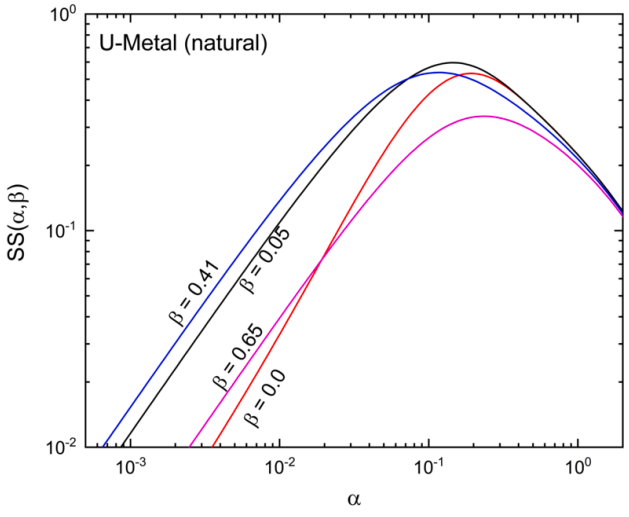


FIG. 162. (Color online) The symmetric TSL for natural uranium metal at 293.6 K as a function of momentum transfer α, for a range of neutron energy transfers, β. $S_s(\alpha,\beta)$ for each β is labeled with the corresponding line.

The use of enrichment-dependent evaluations provides cross sections which can be directly compared to experimental data. These evaluations have been preliminarily tested in criticality benchmarks which show impact due to the enrichment effects. U-metal and all the various enrichment-dependent evaluations represent new TSLs that are included for the first time in the ENDF/B database.

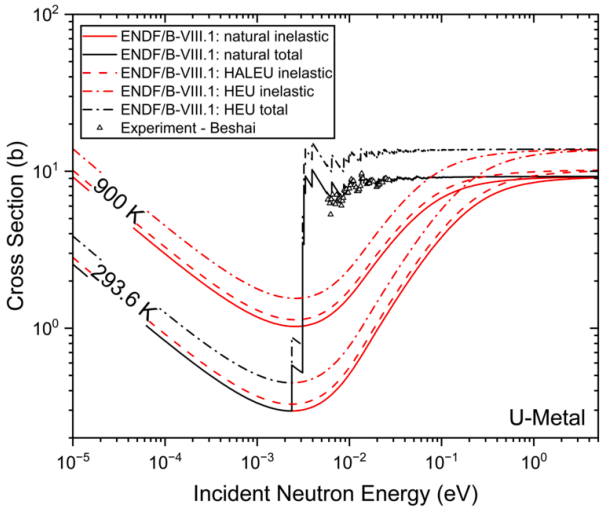


FIG. 163. (Color online) The inelastic scattering cross section of U-metal shown at selected temperatures and enrichments. The natural and high enriched total scattering cross sections for U-metal at 293.6 K are also shown and compared to experimental data [633].

4. *Uranium Nitride (UN)*

The evaluation for UN is based on the previous ENDF/B-VIII.0 evaluation with key updates to improve the TSL and resulting cross section. The original AILD simulations of the lattice structure and resulting PDOS were maintained [634]. The DOS was used as the primary input to the `FLASSH` code [529] to evaluate both the TSL (MT4) as shown in Fig. 164 and the incoherent and coherent elastic scattering (MT2) at 296, 400, 500, 600, 700, 800, 1000, and 1200 K.

Because of the significant contribution from both coherent and incoherent elastic effects, coherent elastic effects were tabulated for the compound UN. Half the coherent elastic is stored with the U(UN) evaluation with the other half stored using the mixed elastic ENDF formatting [474] in the N(UN) evaluation. The incoherent elastic contributions, which arise solely from the nitrogen, are tabulated in MT2 of N(UN) using the mixed elastic formatting. The resulting total cross sections are shown in Fig. 165. Various enrichments of uranium within UN were evaluated using the PDOS described above. This DOS, which supports the structure of UN, was combined with various mass and free atom cross section [68] to represent natural [630], 5%, 10%, 19.75% (HALEU), 93% (HEU), and 100% enrichment of ^{235}U with natural [87] nitrogen.

Evaluations were completed using the `FLASSH` code for U(UN) for naturally enriched, 5%, 10%, 19.75% (HALEU), 93% (HEU), and 100% ^{235}U (File 7, MAT72, MAT8305, MAT8310, MAT8348, MAT8349, and MAT8347, respectively) and for N(UN) paired with each ^{235}U enrichment (File 7, MAT71, MAT8355,

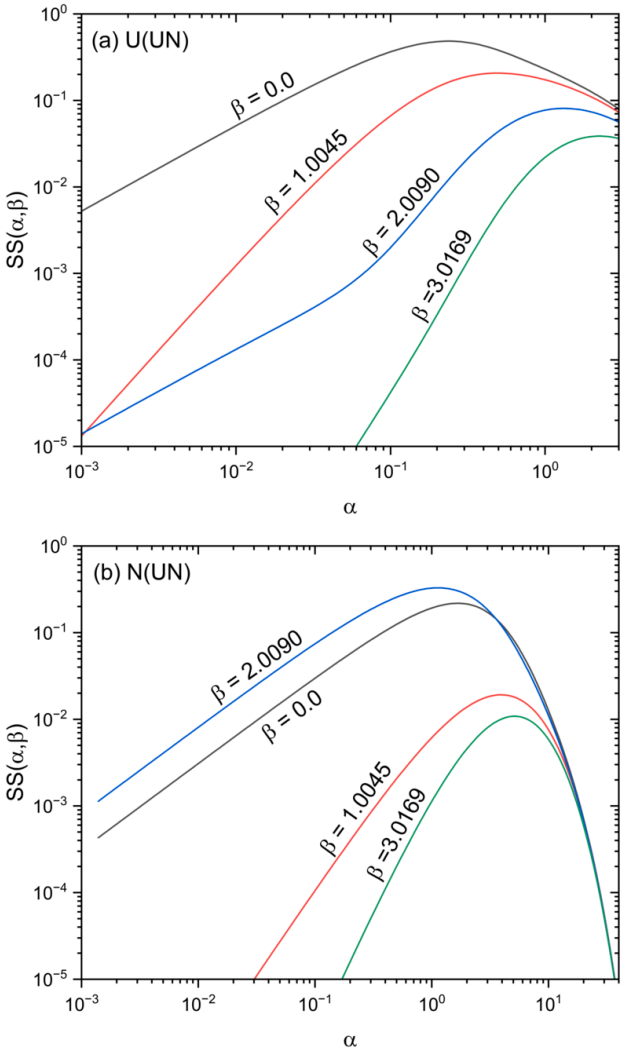


FIG. 164. (Color online) The symmetric TSL for (a) U(UN)-natural and (b) N(UN)-natural at 296 K as a function of momentum transfer α, for a range of neutron energy transfers, β. $S_s(\alpha,\beta)$ for each β is labeled with the corresponding line.

MAT8360, MAT8398, MAT8399, and MAT8397, respectively). Two files are required for each enrichment (a uranium and a nitrogen evaluation) because the tabulated compound coherent elastic will be impacted by the changing inputs associated with the uranium; MT4 for N(UN) remains the same for each enrichment while MT2 varies. The integrated scattering cross section as evaluated by FLASSH are shown in Fig. 165.

The use of enrichment-dependent evaluations provides cross sections, which can be directly compared to experimental data. The enrichment-dependent UN evaluations represent novel TSLs that are included for the first time in the ENDF/B database.

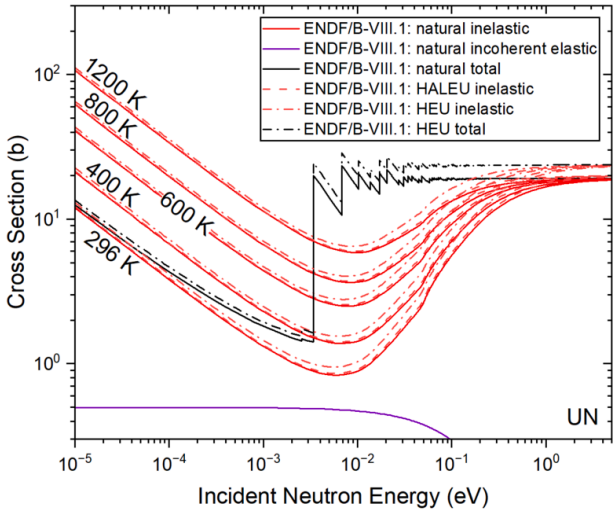


FIG. 165. (Color online) The inelastic scattering cross section of UN shown at selected temperatures and enrichments. The natural and high enriched total scattering cross sections for UN at 296 K are also shown, in addition to the natural incoherent elastic scattering cross section.

5. *Uranium Dioxide (UO_2)*

The evaluation for UO_2 is based on the previous ENDF/B-VIII.0 evaluation with key updates to improve the TSL and resulting cross section. The original AILD simulations of the lattice structure and resulting PDOS were maintained [629]. The DOS was used as the primary input to the FLASSH code [529] to evaluate both the TSL (MT4) as shown in Fig. 166 and the coherent elastic scattering (MT2) at 296, 400, 500, 600, 700, 800, 1000, and 1200 K.

The coherent elastic was evaluated using the cubic approximation updated to reference experimental lattice parameters [635] with a third of the compound's elastic tabulated in MT2 in each of the U and O evaluations [629]. The resulting total scattering cross sections are shown in Fig. 167. Various enrichments of UO_2 were evaluated using the PDOS described above. This DOS, which supports the structure of UO_2, was combined with different masses and free atom cross sections [68] to represent ^{235}U enrichments varying from natural [630] to 100% to capture the impact of enrichment on the total scattering cross section. Evaluations were completed using the FLASSH code for U(UO_2) for naturally enriched, 5%, 10%, 19.75% (HALEU), 93% (HEU), and 100% ^{235}U (File 7, MAT75, MAT8205, MAT8210, MAT8248, MAT8249, and MAT8247, respectively) and for O(UO_2) paired with each ^{235}U enrichment (File 7, MAT45, MAT8255, MAT8260, MAT8298, MAT8299, and MAT8297, respectively). Two files are required for each enrichment (a uranium and an oxygen evaluation) because the tabulated compound coherent elastic will be impacted by the changing inputs associated with the ura-

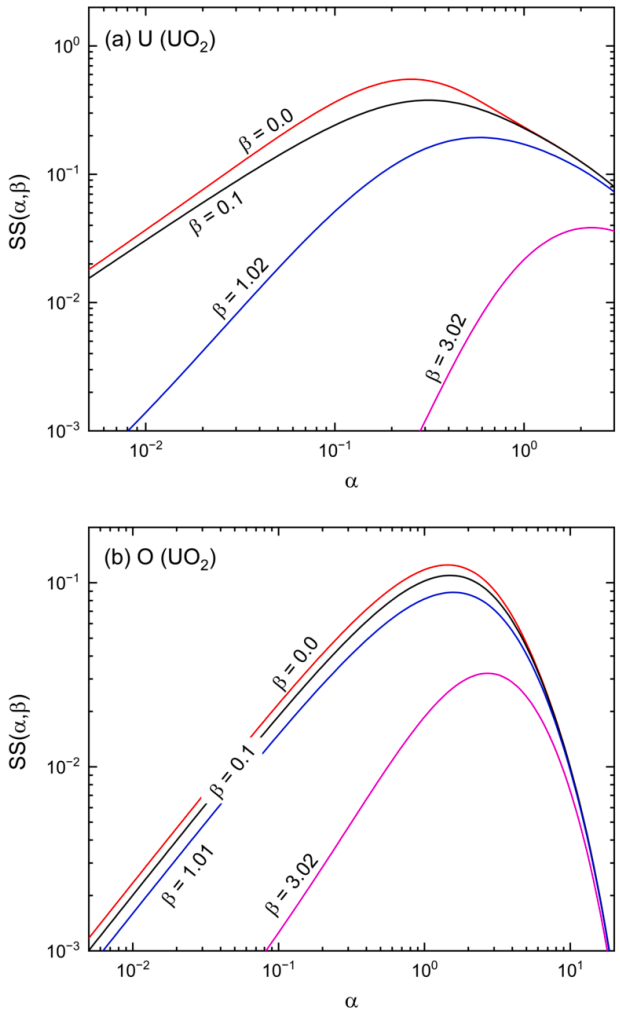


FIG. 166. (Color online) The symmetric TSL for $U(UO_2)$-natural and (b) $O(UO_2)$-natural at 296 K as a function of momentum transfer α, for a range of neutron energy transfers, β. $S_s(\alpha,\beta)$ for each β is labeled with the corresponding line.

nium; MT4 for $O(UO_2)$ remains the same for each enrichment while MT2 varies. The integrated scattering cross section as evaluated by `FLASSH` are shown in Fig. 167 and compared to experimental data, which have been corrected for neutron absorption [633].

The use of enrichment-dependent evaluations provides cross sections which can be directly compared to experimental data. The enrichment-dependent UO_2 evaluations represent novel TSLs that are included for the first time in the ENDF/B database.

6. *Uranium Hydride (UH_3)*

The TSL evaluation for H bound in UH_3 has been generated with `NJOY2012` [636] and AILD as a new contribution to the ENDF/B database. The partial phonon

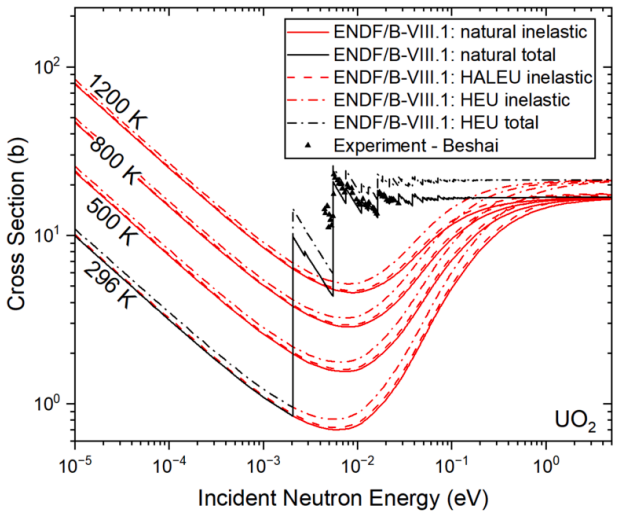


FIG. 167. (Color online) The inelastic scattering cross section of UO_2 shown at selected temperatures and enrichments. The natural and high enriched total scattering cross sections for UO_2 at 296 K are also shown, with the former compared to experimental data [633].

spectrum of $H(UH_3)$ was generated with Hubbard model corrected density functional theory and lattice dynamics described in Ref. [637]. The $H(UH_3)$ phonon spectrum is found to be in reasonable agreement with the experiment described in Ref. [637].

A TSL File 7 evaluation is available for $H(UH_3)$ at 293.6 K. Only ^1H was considered in the evaluation. When using the $H(UH_3)$ evaluation, the uranium isotopes should be modeled with the free gas approximation. The total scattering cross sections and AWR were extracted from the ENDF/B-VIII.1 nuclide evaluation. Elastic scattering (MT2) was evaluated as incoherent. Inelastic scattering (MT4) was evaluated in the incoherent approximation with the phonon expansion method on a custom (α, β) grid.

The symmetric TSL for $H(UH_3)$ at 293.6 K tabulated in File 7, MT4, is illustrated in Fig. 168. A limited number of quantized oscillations are present at fixed intervals of $k_BT\beta \approx 0.12$ eV. The integrated inelastic and total cross sections computed with the NDEX nuclear data processing code [609, 610] is illustrated in Fig. 169. The adaptive energy meshing in NDEX is necessary to fully capture the oscillator behavior in the cross section.

C. Special Purpose

1. *Liquid hydrogen and deuterium (l-H_2, l-D_2)*

Compared to ENDF/B-VIII.0, the evaluations for liquid hydrogen and deuterium are now available at temperatures of 14, 15, 16, 17, 18, 19, and 20 K for para/ortho hydrogen and 19, 20, 21, 22, and 23 K for para/ortho

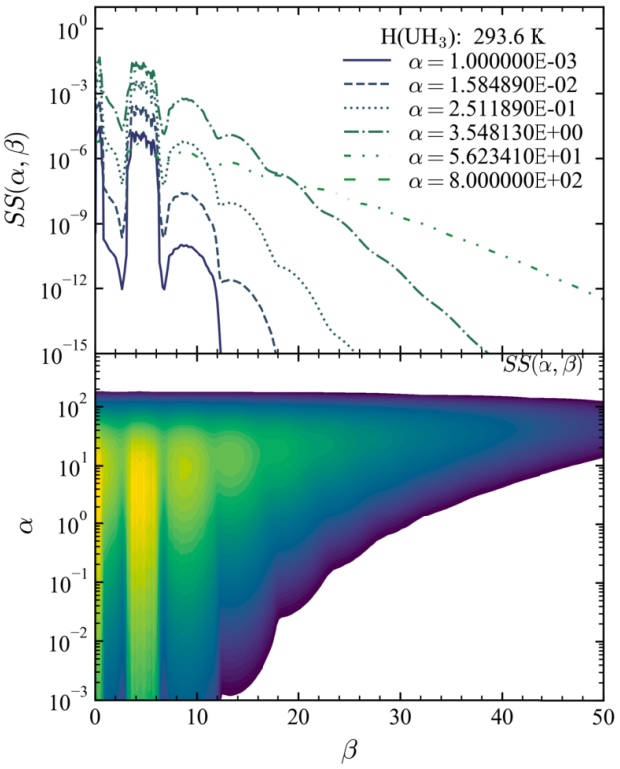


FIG. 168. (Color online) $H(UH_3)$ symmetric TSL, $SS(\alpha,\beta)$, at 293.6 K. The (α,β) grid is referenced to $k_BT = 0.0253$ eV. The contour plot illustrates only $SS(\alpha,\beta) > 10^{-15}$; other non-zero values are not shown. Quantized oscillations in the TSL occur at integer values of $k_BT\beta \approx 0.12$ eV.

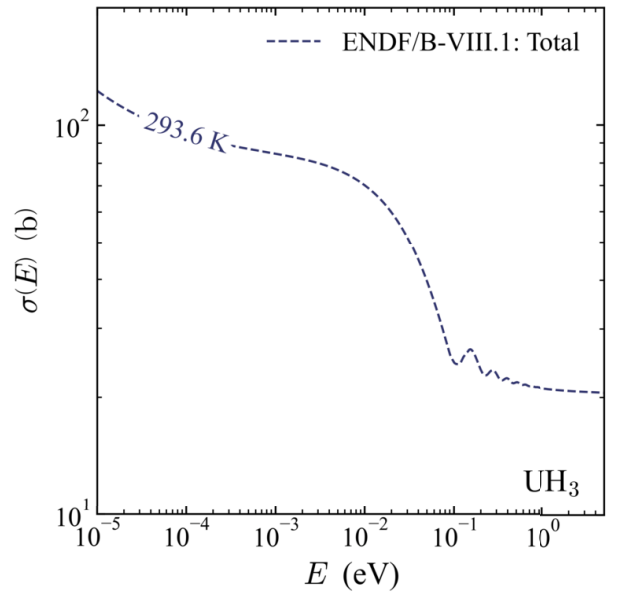


FIG. 169. (Color online) Total scattering cross section of UH_3 between 293.6 K as compared to the ENDF/B-VIII.0 YH_2 material evaluation. Oscillations in the cross section correspond to the H oscillator energy of ≈ 0.12 eV.

deuterium. The evaluations are based on the approach described in Ref. [638], where path-integral molecular dynamics (PIMD) techniques have been used to produce input data for the neutron scattering models in a modified `LEAPR` module of `NJOY` called `NJOY-H2D2` [528]. The main ingredients are the static structure factors and the frequency spectra, which have been generated from the radial distribution and velocity autocorrelation functions computed from the MD simulations, respectively. An example of the frequency spectrum for liquid hydrogen from the PIMD calculations at 14 K, compared to previous experimentally derived and simulated data, is shown in Fig. 170. For input into `LEAPR`, the frequency spectra were decomposed into solid-like and diffusive parts, and the rotational and vibrational components were included using previously existing methods [639, 640]. The solid-like part and the static structure factor at 14 K for liquid hydrogen are compared to data used for ENDF/B-VIII.0 and JEFF-3.3 evaluations in Figs. 171 and 172, respectively. In the ENDF/B-VIII.0 evaluations, the coherent scattering contributions were computed using the Vineyard approximation [641]. In the ENDF/B-VIII.1 evaluations, the coherent scattering was instead computed using the Sköld approximation [642], which is included in `NJOY-H2D2`.

Figs. 173 and 174 show a selection of the total scattering cross sections for the ENDF/B-VIII.1 evaluations for liquid para-hydrogen and ortho-deuterium at the indicated temperatures compared to available experimental data, the ENDF/B-VIII.0 evaluations, and also the evaluations from JEFF-3.3 [64]. For para-hydrogen, the ENDF/B-VIII.1 evaluation shows good agreement with the more recent measurements of Ref. [643] in the range of about 2–12 meV, which is also supported by a separate earlier study based also on path-integral MD techniques [644]. In the case of ortho-deuterium, the ENDF/B-VIII.1 evaluation shows improved agreement with experimental data compared to the ENDF/B-VIII.0 evaluation.

2. *Sapphire Single-Crystal Neutron Filter (Al_2O_3)*

Sapphire (Al_2O_3) was evaluated using modern AILD techniques [531, 532]. Sapphire filters are single crystal materials, which consist of highly ordered structure to allow neutrons of select energies to pass through. As a filter material, sapphire is used in research reactors, which require the neutron beam to be filtered to transmit specific neutron energies and remove others [652]. The structure of sapphire was modeled using the `VASP` code [550–552] to predict the Hellmann-Feynman forces. The resulting forces were used in the dynamical matrix approach within the PHONON code [553] to calculate the phonon dispersion relations which were found to be in good agreement with experimental data [653, 654].

Using the PDOS as the fundamental input, the `FLASSH` code [529] was used to evaluate the TSL for both $Al(Al_2O_3)$ (File 7, MAT3052) and $O(Al_2O_3)$ (File 7,

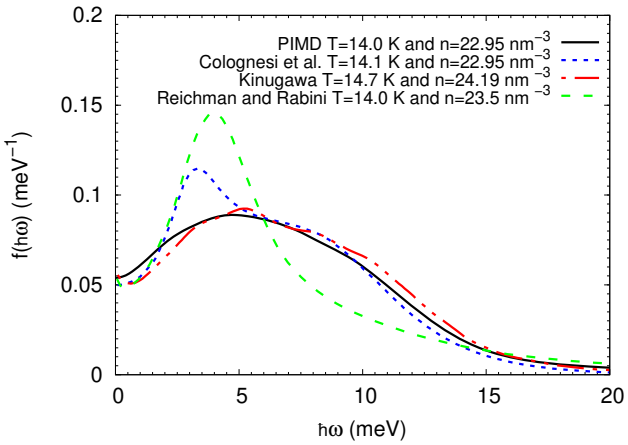


FIG. 170. (Color online) Simulated frequency spectrum for liquid hydrogen at 14 K from the PIMD calculations compared to experimentally derived data from Colognesi *et al.* [645] and simulations from Kinugawa [646] and from Reichman and Rabini [647]. Data is digitized from Ref. [645].

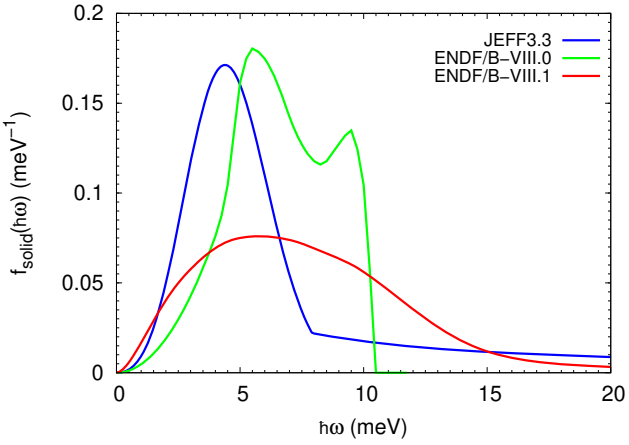


FIG. 171. (Color online) Comparison of the solid-like frequency spectrum for liquid hydrogen at 14 K used in the ENDF/B-VIII.1 evaluation to the solid-like frequency spectra used in the ENDF/B-VIII.0 and JEFF-3.3 evaluations.

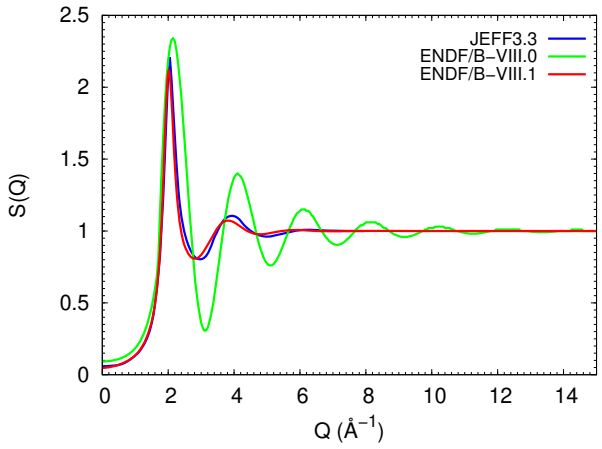


FIG. 172. (Color online) Comparison of the static structure factor for liquid hydrogen at 14 K used in the ENDF/B-VIII.1 evaluation to the static-structure factors used in the ENDF/B-VIII.0 and JEFF-3.3 evaluations.

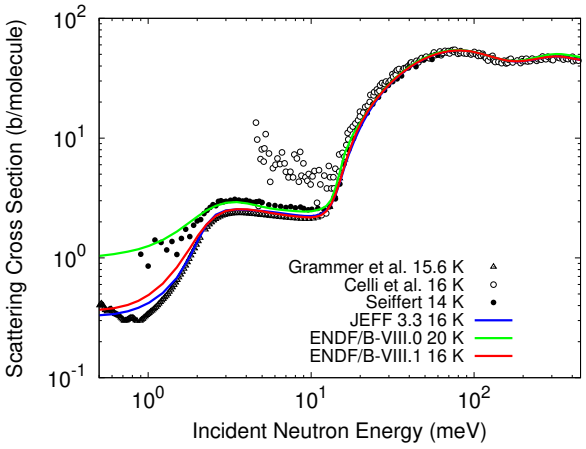


FIG. 173. (Color online) Total scattering cross sections for liquid para-hydrogen at the indicated temperature from ENDF/B-VIII.0 and ENDF/B-VIII.1 compared to experimental data from Refs. [643, 648, 649] and JEFF-3.3 [64].

MAT3053) with mass and free atom cross sections [68] for ^{27}Al and ^{16}O at temperatures of 77, 80, 100, 200, 293.6, 296, and 300 K. This temperature grid supports common single crystal filter applications. The symmetric TSL (MT4) at 296 K is shown in Fig. 175.

In order to serve as a filter material, the coherent elastic impacts must be removed from the evaluation. As such, both the Al(Al_2O_3) and O(Al_2O_3) TSL evaluations provide information only with respect to inelastic scattering (MT4), and the MT2 card has been removed. The inelastic cross sections integrated from the MT4 TSL were processed using the `FLASSH` [529] cross section routines and are shown in Fig. 176 in comparison to experimental data [655, 656].

3. Magnesium Oxide Neutron Filter (MgO)

The objective of this evaluation is to utilize MgO as a neutron filter, a critical component for selectively transmitting thermal neutrons while attenuating higher-order neutrons and gamma rays, thereby reducing radiation background. The vibrational properties of MgO were calculated utilizing density functional perturbation theory employing linear response calculations with the ABINIT code [657]. This approach efficiently determines phonon excitations at any wavevectors by examining the system's response to perturbations, including atomic displacements and constant electric fields. These perturbations facilitate the computation of interatomic force constants, dielectric constants, and Born effective charges,

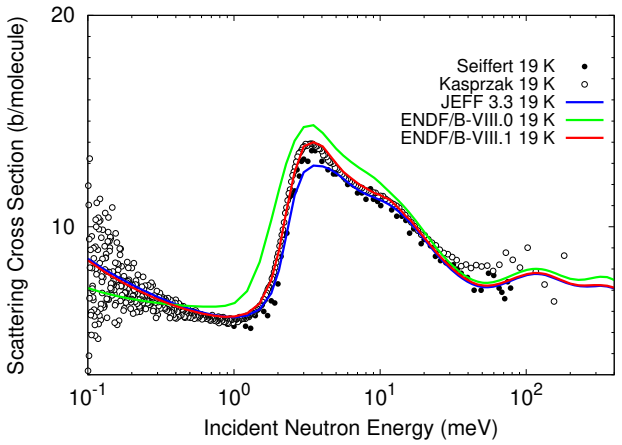


FIG. 174. (Color online) Total scattering cross-sections for liquid ortho-deuterium at the indicated temperature from ENDF/B-VIII.0 and ENDF/B-VIII.1 compared to experimental data from Refs. [648, 650, 651] and JEFF-3.3 [64].

crucial for accurately describing phenomena like the longitudinal optical-transverse optical (LO-TO) splitting in polar materials, such as MgO.

MgO has a cubic symmetry and crystallizes in the rock-salt structure. It has two atoms per primitive unit cell. The calculated phonon dispersion relations exhibit excellent agreement with experimental data, validating the accuracy of the calculated PDOS. The partial PDOSs are then employed to calculate the TSL (File 7) for Mg(MAT3146) and O(MAT3147) in MgO, utilizing the incoherent approximation at 293.6 K as well as the incoherent elastic scattering cross section utilizing the `LEAPR` module of `NJOY` [325] code. The free atom cross sections and AWR for both oxygen (O) and magnesium (Mg) were obtained from the nuclide evaluations in ENDF/B-VIII.0 [68]. Furthermore, the incoherent bound scattering cross sections and the natural abundances of isotopes were defined according to the recommendations of the NIST database [87]. For more details about the first-principles calculations and thermal neutron scattering analysis of MgO as a neutron filter, refer to Ref [658]. Fig. 177 shows the room temperature incoherent inelastic and incoherent elastic scattering cross sections of Mg and O in MgO.

4. Magnesium Fluoride Neutron Filter (MgF_2)

Neutron transmission through a single crystal of MgF_2 at liquid-nitrogen and room temperatures was first measured by Barker *et al.* [659] to explore its potential as a neutron filter. In this work, the lattice vibrations of MgF_2 were computed using first-principles calculations. The calculated phonon dispersion relations showed excellent agreement with available experimental data, confirming the accuracy and reliability of the calculated PDOS.

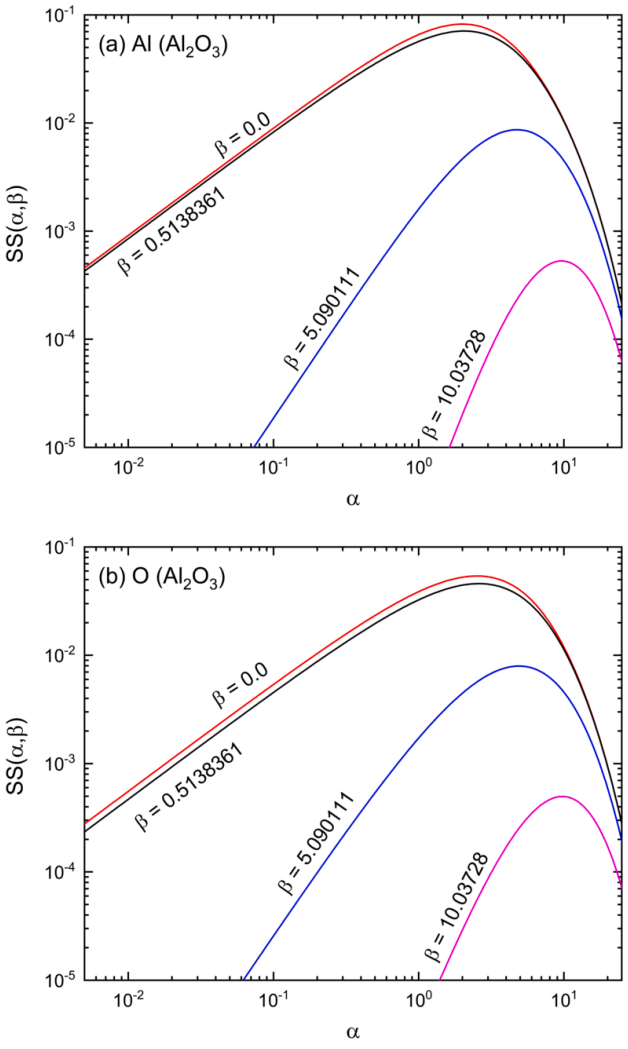


FIG. 175. (Color online) The symmetric TSL for (a) Al(Al_2O_3) and (b) O(Al_2O_3) at 296 K as a function of momentum transfer α, for a range of neutron energy transfers, β. $S_s(\alpha,\beta)$ for each β is labeled with the corresponding line.

This was further verified by investigating the heat capacity and comparing it with experimental data. The obtained PDOS was then used to calculate the incoherent inelastic and incoherent elastic thermal neutron scattering cross sections at room temperature, resulting in excellent agreement between the calculated total cross section and the measured transmission data.

At ambient pressure and temperature, MgF_2 crystallizes into the rutile structure. It possesses a body-centered tetragonal symmetry and belongs to the $P4_2/mnm$ space group. The hexagonal primitive unit cell of MgF_2 contains six atoms. The structural and vibrational characteristics of MgF_2 were investigated through a density functional perturbation theory as implemented in the ABINIT code [657], utilizing the local density approximation (LDA) for the exchange-correlation poten-

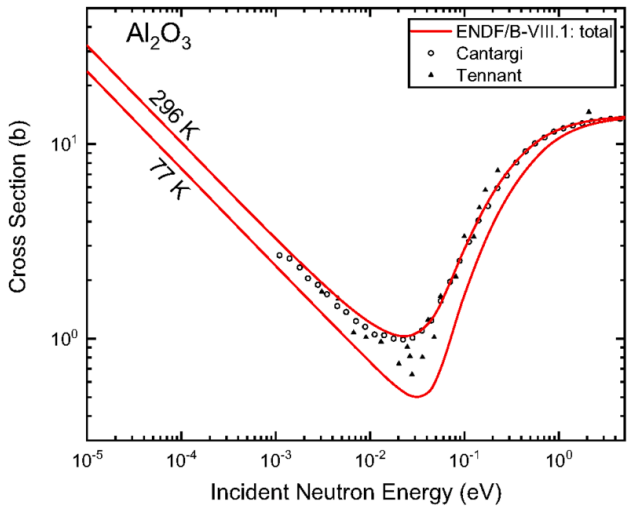


FIG. 176. (Color online) Total cross section for ENDF/B-VIII.1 sapphire (Al_2O_3) compared to measured data at room temperature [655, 656]. No elastic components are included in the evaluation.

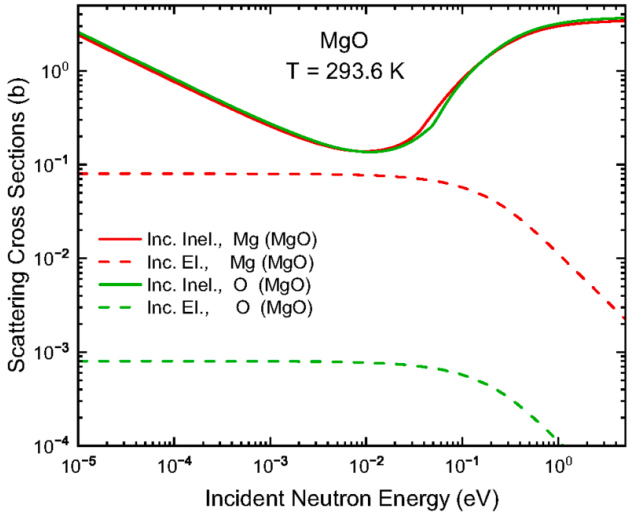


FIG. 177. (Color online) Calculated scattering cross section (solid curves) Incoherent inelastic of Mg (red) and O (green) in MgO, and (dashed curves) incoherent elastic of Mg (red) and O (green) in MgO.

tial. The pseudopotentials for Mg and F were generated using the Troullier & Martins [660] optimization scheme with the FHI98PP code [661].

The TSL for Mg (MAT3142) and F (MAT3141) in MgF_2 were computed using partial PDOSs of Mg and F. This calculation was conducted at 293.6 K, employing the incoherent approximation as implemented in the `LEAPR` module of `NJOY` code [325]. Additionally, incoherent elastic scattering cross section was determined. The cross sections for free atoms and AWR for Mg and F were ob-

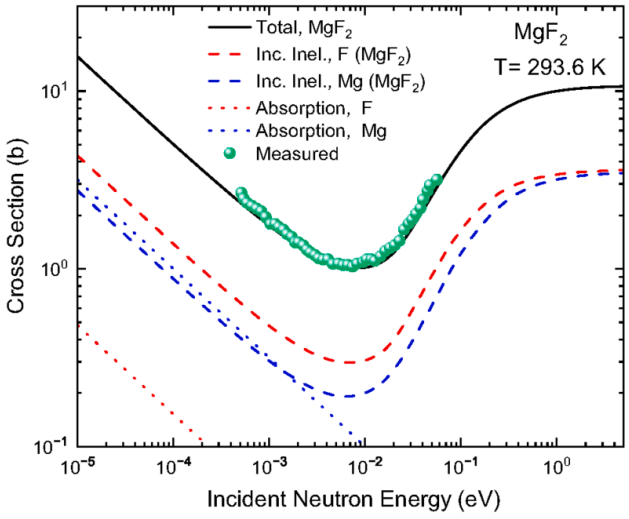


FIG. 178. (Color online) MgF_2 Calculated (black solid curve) total cross section, (dashed curves) incoherent inelastic scattering cross sections, (dotted lines) absorption cross sections, and (spheres) measured total cross section [659].

tained from nuclide evaluations in ENDF/B-VIII.0 [68]. Moreover, incoherent bound scattering cross sections for MF=7 and MT=2, as well as natural abundances of isotopes, were extracted from the NIST database [87]. For further insights into the first-principles calculations and thermal neutron scattering analysis of MgF_2 as a neutron filter, readers are encouraged to refer to Ref. [662]. Fig. 178 compares the calculated total cross section at room temperature with measured data [659]. It also displays the incoherent inelastic scattering cross sections of Mg and F in MgF_2 as well as their absorption cross sections. The incoherent elastic cross sections are excluded for clarity, as they are several orders of magnitude smaller than the incoherent inelastic cross sections.

5. *Beryllium Fluoride Neutron Filter (BeF_2)*

The Be nucleus has a smaller absorption and higher bound scattering cross section than that of Mg, which suggests that BeF_2 is also a promising neutron filter. The BeF_2 crystal structure has a trigonal symmetry and $P3_121$ space group. It has a tetrahedral network where each Be atom is bonded to four F atoms, and each F atom is bonded to two Be atoms. The hexagonal primitive unit cell has nine atoms. A 2 x 2 x 2 supercell containing 72 atoms was constructed to determine the vibrational properties using the direct method. First-principles projector augmented wave method as implemented in the `VASP` [550–552] was used to calculate the Hellmann-Feynman forces. The calculations were conducted at the GGA level, employing the PBE functional [663]. The Phonopy software [632] was utilized to calculate the interatomic force constants and obtain the partial

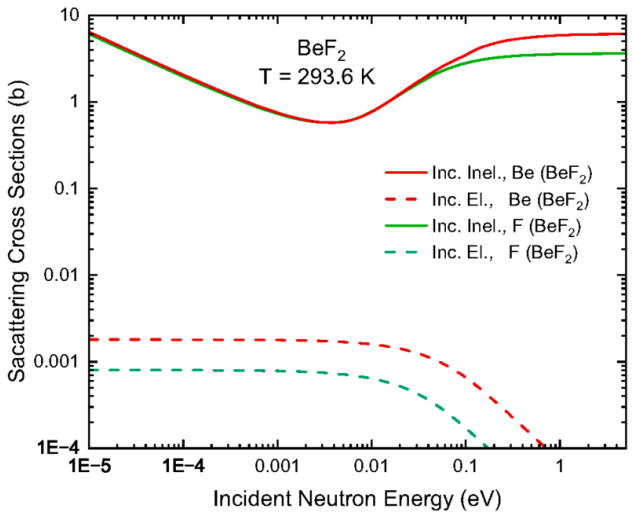


FIG. 179. (Color online) Calculated scattering cross sections (solid curves) Incoherent inelastic of Be (red) and F (green) in BeF_2 and (dashed curves) incoherent elastic of Be (red) and F (green) in BeF_2.

PDOSs for Be and F in BeF_2.

The `LEAPR` module of the `NJOY` code [325] was used to compute the TSL for Be (MAT3137) and F (MAT3136) in BeF_2 utilizing the partial PDOSs for Be and F at 293.6 K under the incoherent approximation. Additionally, the incoherent elastic scattering cross section was calculated. Cross sections for free atoms and AWR for Be and F were taken from nuclide evaluations in ENDF/B-VIII.0 [68]. Incoherent bound scattering cross sections for MT=2 and MF=7, along with natural isotope abundances, were sourced from the NIST database [87]. For more details of the first-principles calculations and thermal neutron scattering analysis of BeF_2 as a neutron filter, readers are directed to Ref [662]. Fig. 179 shows the room temperature incoherent inelastic and incoherent elastic scattering cross sections of Be and F in BeF_2.

VI. PHOTONUCLEAR SUBLIBRARY

In the late 1990s, the first IAEA CRP on photonuclear data was chaired by Chadwick [15]. During this period, LANL developed evaluations for various isotopes of hydrogen (D), carbon, nitrogen, oxygen, aluminum, silicon, calcium, copper, tantalum, tungsten, lead, uranium, plutonium, neptunium, and americium. The actinides were developed through a LANL-Saclay (CEA) collaboration. Some of these evaluations were incorporated into the IAEA database. The results of the LANL-CEA collaboration were documented in three Nuclear Science and Engineering journal papers [664–666] and the comprehensive ENDF/B-VII.0 publication in 2007. These evaluations were also released alongside over 100 others in the IAEA's 1999 library – IAEA1999 [15].

To meet the increasing demand for precise and dependable photonuclear data, the IAEA conducted a new CRP entitled "Updating the IAEA Photonuclear Data Library and generating a Reference Database for Photon Strength Functions" from 2016 to 2019 [14, 667]. The component dedicated to updating the IAEA1999 photonuclear data library was chaired by Kawano. This project resulted in the creation of the IAEA2019 Photonuclear Data Library, detailed in Ref. [14], available on the IAEA website at `https://www-nds.iaea.org/photonuclear`. The library encompasses photon absorption data, total and partial photoneutron reaction cross-sections, and neutron spectra for 220 isotopes. The 220 isotopes included in the IAEA2019 Photonuclear Data Library [14] fall into five categories:

- Structural, shielding, and bremsstrahlung target materials: Be, Al, Si, Ti, V, Cr, Fe, Co, Ni, Cu, Zn, Zr, Mo, Sn, Ta, W, and Pb;
- Biological materials: C, N, O, Na, S, P, Cl, and Ca;
- Fissionable materials: Th, U, Np, and Pu;
- Other materials: H, K, Ge, Sr, Nb, Pd, Ag, Cd, Sb, Te, I, Cs, Sm, and Tb;
- Potential diagnostic and therapeutic radionuclides.

With the emergence of new facilities generating intense photon beams, the photo-production of certain significant radionuclides could emerge as a competitive alternative to traditional methods, utilizing neutrons from highly enriched Uranium reactors or charged-particle beams [668–671]. The identified radionuclides for potential diagnostic and therapeutic applications in nuclear medicine suitable for production via photonuclear reactions include:^{168,170}Er for the production of ^{167,169}Er, ^{187}Re for the production of ^{186}Re,^{226}Ra for the production of ^{225}Ra which further decays to ^{225}Ac, ^{98}Ru for the production of ^{97}Ru, ^{194}Pt for the production of ^{193}Pt, ^{132}Xe for the production of ^{131}I, ^{162}Dy for the production of ^{161}Tb, and ^{178}Hf for the production of ^{177}Lu.

In brief, the 164 isotopes from the IAEA1999 library [15] underwent comprehensive reevaluation, incorporating new data when available, results from experimental-based assessments by Varlamov, updated GDR parameters from the recently revised Atlas of GDR parameters [672], and enhanced reaction models. Additionally, evaluations were conducted for 37 isotopes, not included in IAEA1999, with available experimental data, along with the nine isotopes identified for medical applications. Where experimental data was lacking, model predictions were provided for evaluation. A total of 220 isotopes were assessed, encompassing all available experimental data on photo-absorption cross sections, photo-neutron production cross sections and yields, as well as partial photo-neutron and photo-charged-particle cross sections from the EXFOR database [45] up to April 2019.

Particular attention was given to re-assessing the partial photoneutron cross sections from multiplicity sorting

measurements performed at LLNL and Saclay between 1960 and 1990. By applying a new approach using physical criteria, as detailed in Ref. [14], Varlamov identified issues in the $1n$, $2n$, and $3n$ partial photoneutron cross sections of several Livermore and Saclay measurements. These criteria were consistent with the new measurements obtained using the neutron-multiplicity sorting technique [673]. In total, photonuclear data for 34 nuclides were assessed, and new recommendations were made within the CRP. While many of these recommendations were adopted by the CRP evaluators, they were not implemented in the JENDL and JAEA evaluations included in IAEA2019. Lastly, all the new measurements obtained through the direct neutron-multiplicity sorting technique [673], which were fully developed and implemented for the CRP, were incorporated into the evaluations. The assessments were extended to energies of 200 MeV to support accelerator-driven transmutation technologies, complementing the ongoing development of high-energy neutron and proton libraries for radiation transport simulation codes.

To summarize, significant progress was made in this CRP, benefiting from many new photonuclear measurements conducted since the first CRP. However, no new evaluations authored by the US were included in the resulting IAEA2019 file. For our new ENDF-VIII.1 evaluation of photon-induced reactions, we have adopted the majority of the new IAEA CRP evaluations. However, we have retained almost all the previous US (LANL) ENDF evaluations, only replacing them when new experimental data support the new IAEA work over our previous US evaluations. The previous ENDF-VIII.0=ENDF-VII.0 library is widely used in DOE photonuclear applications today, and these applications depend on high-quality photonuclear data. While the IAEA2019 documentation presents comparison plots against IAEA1999 data, these are not particularly useful for ENDF evaluations, as IAEA1999 does not equate to ENDF-VIII.0=ENDF-VII.0 in many cases. Therefore, comparisons should focus on ENDF versus IAEA2019 [14], and indeed it was such comparisons that guided our evaluation decisions for ENDF-B/VIII.1. Our detailed principles for the choices we made were discussed in Sec. I.

Photonuclear measurement discrepancies have long posed challenges, particularly regarding cross section magnitudes and multiplicity sorting assessments (e.g., LLNL versus Saclay versus Russian data). Resolving these discrepancies requires care and study. Conclusions drawn in 1999, such as normalization techniques for LLNL 1980 (Caldwell-Berman) data [674–679] versus Saclay (Veyssiere) [680, 681] and Russian bremsstrahlung (Gurevich) data [682], are provisional and need continuous scrutiny. To date, we are not aware of peer-reviewed papers that have contested the 1999 reasoning by Varlamov concerning the magnitude of ^{235}U photonuclear data [15, 683], as adopted by ENDF/B-VIII.0=ENDF/B-VII.0, IAEA1999, and Obninsk. Varlamov analysis was based on a least-square fit of available data as discussed in EXFOR entry M030 [683] and recently reviewed in Ref. [684]. New ratio data from the collaboration between the Triangle Universities Nuclear Laboratory (TUNL) and LLNL [685] do not support the latest IAEA evaluation adopted from JAEA evaluations (JENDL/PD-2016 and JENDL(u)) over the earlier ENDF data for the ^{235}U/^{239}Pu ratio.

A. Evaluation choices

For ^{239}Pu, the existing ENDF evaluation appears superior versus the new IAEA evaluation. ENDF/B-VIII.0 provides a better fit to the LLNL Berman data. In the range of 7-17 MeV, the integrated ENDF/measured-data ratio is 1.01, while IAEA2019/measured-data is 1.025. Both evaluations aimed to model the LLNL Berman data, but ENDF/B-VIII.0 shows a superior fit for (γ,F), (γ,1n), (γ,2n), and (γ,xn). Hence, ENDF/B-VIII.0=ENDF/B-VII.0 is retained for ENDF-VIII.1.

Regarding ^{235}U, many of the various measured data sets are discrepant, and ENDF and IAEA2019 (JAEA) made different evaluation decisions. New ratio data from TUNL/LLNL at the Duke University Higgs facility [685] do not support IAEA2019's evaluations of the ^{235}U/^{239}Pu ratio. As noted earlier, the original ENDF normalization choice was based on Varlamov analysis [683]; we are not aware of a peer-reviewed paper that challenges Varlamov logic [683, 684], so for now ENDF-VIII.0=ENDF-VII.0 is retained for ENDF-VIII.1. It is prudent to await new measurements before making changes to ENDF here.

For many of the other LANL photonuclear evaluations in ENDF/B-VIII.0=ENDF/B-VII.0, no new accurate photonuclear measurements have been made. Consequently, the LANL ENDF/B-VIII.0=ENDF/B-VII.0 evaluations will be retained for ENDF/B-VIII.1 for these cases, as are listed below. For ^{181}Ta, new IAEA2019 evaluation for ^{181}Ta follows new NewSUBARU measured data, which appear reasonable; therefore, we adopt IAEA2019 evaluation for this isotope.

Below we list the sources of the evaluations used in ENDF/B-VIII.1:

- Nuclei with evaluated files taken from the IAEA CRP (IAEA-PD2019) [14] without any changes: ^{3}He, ^{6}Li, ^{7}Li, ^{9}Be, ^{13}C, ^{14}C, ^{15}N, ^{17}O, ^{18}O, ^{19}F, ^{23}Na, ^{24}Mg, ^{25}Mg, ^{26}Mg, ^{27}Si, ^{29}Si, ^{30}Si, ^{32}S, ^{33}S, ^{34}S, ^{36}S, ^{35}Cl, ^{37}Cl, ^{36}Ar, ^{38}Ar, ^{40}Ar, ^{39}K, ^{40}K, ^{41}K, ^{42}Ca, ^{43}Ca, ^{44}Ca, ^{46}Ca, ^{48}Ca, ^{45}Sc, ^{46}Ti, ^{47}Ti, ^{48}Ti, ^{49}Ti, ^{50}Ti, ^{50}V, ^{51}V, ^{50}Cr, ^{52}Cr, ^{53}Cr, ^{54}Cr, ^{55}Mn, ^{56}Fe, ^{57}Fe, ^{58}Fe, ^{59}Co, ^{58}Ni, ^{60}Ni, ^{61}Ni, ^{62}Ni, ^{64}Ni, ^{65}Cu, ^{64}Zn, ^{66}Zn, ^{67}Zn, ^{68}Zn, ^{70}Zn, ^{70}Ge, ^{72}Ge, ^{73}Ge, ^{74}Ge, ^{76}Ge, ^{75}As, ^{76}Se, ^{78}Se, ^{80}Se, ^{82}Se, ^{84}Sr, ^{86}Sr, ^{87}Sr, ^{88}Sr, ^{90}Sr, ^{89}Y, ^{90}Zr, ^{91}Zr, ^{92}Zr, ^{93}Zr, ^{94}Zr, ^{96}Zr, ^{93}Nb, ^{94}Nb, ^{92}Mo, ^{94}Mo, ^{95}Mo, ^{96}Mo, ^{97}Mo, ^{98}Mo, ^{100}Mo, ^{98}Ru, ^{102}Pd, ^{104}Pd, ^{105}Pd, ^{106}Pd, ^{107}Pd, ^{108}Pd, ^{110}Pd, ^{107}Ag, ^{108}Ag, ^{109}Ag, ^{106}Cd, ^{108}Cd, ^{110}Cd, ^{111}Cd, ^{112}Cd, ^{113}Cd, ^{114}Cd, ^{116}Cd, ^{115}In, ^{112}Sn, ^{114}Sn, ^{115}Sn, ^{116}Sn,

^{117}Sn, ^{118}Sn, ^{119}Sn, ^{120}Sn, ^{122}Sn, ^{124}Sn, ^{121}Sb, ^{123}Sb, ^{120}Te, ^{122}Te, ^{123}Te, ^{124}Te, ^{125}Te, ^{126}Te, ^{128}Te, ^{130}Te, ^{127}I, ^{129}I, ^{132}Xe, ^{133}Cs, ^{135}Cs, ^{137}Cs, ^{138}Ba, ^{139}La, ^{140}Ce, ^{142}Ce, ^{141}Pr, ^{142}Nd, ^{143}Nd, ^{144}Nd, ^{145}Nd, ^{146}Nd, ^{148}Nd, ^{150}Nd, ^{144}Sm, ^{147}Sm, ^{148}Sm, ^{149}Sm, ^{150}Sm, ^{151}Sm, ^{152}Sm, ^{154}Sm, ^{153}Eu, ^{156}Gd, ^{160}Gd, ^{158}Tb, ^{162}Dy, ^{163}Dy, ^{166}Er, ^{170}Er, ^{169}Tm, ^{175}Lu, ^{174}Hf, ^{176}Hf, ^{177}Hf, ^{178}Hf, ^{179}Hf, ^{180}Hf, ^{186}Os, ^{188}Os, ^{189}Os, ^{190}Os, ^{192}Os, ^{209}Bi.

- Nuclei with evaluated files taken from the IAEA CRP (IAEA-PD2019) [14] after fixes to level index on isomeric production were implemented: ^{103}Rh, ^{159}Tb, ^{165}Ho, ^{181}Ta.

- Nuclei with evaluated files adopted from the IAEA CRP (IAEA-PD2019) [14] after minor fixes were implemented: ^{185}Re, ^{187}Re, ^{194}Pt, ^{197}Au, ^{226}Ra, ^{232}Th, ^{233}U, ^{234}U, ^{236}U, ^{238}Pu, ^{241}Pu.

- Nuclei with evaluated files kept from ENDF/B-VIII.0 without changes: ^{2}H, ^{12}C, ^{14}N, ^{16}O, ^{27}Al, ^{28}Si, ^{40}Ca, ^{63}Cu, ^{180}W, ^{182}W, ^{183}W, ^{184}W, ^{186}W, ^{206}Pb, ^{207}Pb, ^{208}Pb, ^{235}U, ^{238}U, ^{237}Np, ^{239}Pu.

- Nuclei with evaluated files adopted from ENDF/B-VIII.0 after fixes were implemented: ^{40}Ca (Fix to discrepant masses), ^{14}N (added missing photon distributions to MT=102 with energies and branching ratios taken from ENSDF).

- Nuclei with evaluated files kept from ENDF/B-VIII.0 after minor fixes were implemented: ^{240}Pu, ^{241}Am.

- New evaluated file adopted from JENDL-5 [16]: ^{242}Pu.

VII. CHARGED PARTICLE REACTION SUBLIBRARIES

The changes from ENDF/B-VIII.1 relative to ENDF/B-VIII.0 for the charged particle sublibraries are described in the following sections.

A. Alphas sublibrary

The incident alpha-particle sublibrary expanded in the ENDF/B-VIII.1 release to include a ^{6}Li evalution from the LLNL ECPL as well as new evaluations for ^{9}Be, ^{17}O and ^{18}O produced by NNL.

- ^{4}He: The evaluation is nearly identical to ENDF/B-VIII.0. Minor changes were made to the target mass (adding the electron mass), and an invalid interpolation flag was fixed for Coulomb elastic outgoing product distributions.

- ^{6}Li: The evaluation from the LLNL ECPL [17] is adopted. In addition to elastic scattering, the evaluation includes (α, p) and (α, d) reactions.

- ^{9}Be: The NNL adopted the JENDL/AN-2005 evaluation but made additional modifications to improve modeling of neutron spectra produced by Am-Be neutron sources. The ENDF/B-VIII.1 evaluation produces a better match to the experimental neutron spectrum, especially for outgoing neutron energies below 1.5 MeV.

- ^{17,18}O: The NNL produced a modified version of the JENDL/AN-2005 evaluations for two Oxygen isotopes. The modifications focused on improving modeling of outgoing neutron spectra from (α, n) reactions in actinide oxide fuels.

1. ^{9}Be

For incident α particles above a threshold near 4.5 MeV, the measured low-energy neutron yield cannot be adequately explained by the ^{9}Be(α,n)^{12}C reaction alone, as the ^{9}Be$(\alpha, \alpha')^{9}$Be* $\rightarrow$ ^{8}Be+n "breakup" reaction becomes significant [686–688]. Cross sections for the ^{9}Be$(\alpha, n)^{12}$C and breakup reaction are given by MT=4 and MT=22, respectively.

Am-Be sources are an application where the neutron yield and energy spectrum resulting from (α, n)-type reactions with ^{9}Be are of interest. In this case, ^{241}Am is the primary source for α particles, with α decay energies of about 5.5 MeV. At this maximum α energy, the breakup reaction accounts for about 30% of total neutron yield [689], with almost all below 1.5 MeV [687, 688]. A similar situation exists for Pu-Be sources, where ^{239}Pu has α decay energies of about 5.15 MeV [690]. The NNL Monte Carlo radiation transport code MC21 was used to simulate the neutron energy spectrum for an Am–Be source using the JENDL/AN-2005 (NMOD=2) evaluation for ^{9}Be. A continuous-slowing-down model is used for α particles in MC21 without transport or use of MT=2 elastic cross sections [691]. Fission neutrons were accounted for but were statistically insignificant. The results generally compared well to experimental data, except for neutron energies below about 1.5 MeV. In this low-energy region, results were substantially low compared with Marsh *et al.* [692], one of the few publications reporting high-quality Am–Be neutron energy spectrum measurements including energies from near-zero to 1.5 MeV.

The JENDL/AN-2005 evaluation (NMOD=2) uses experimental data from Gibbons *et al.* [693] in the evaluation of the MT=201 total cross sections. MT=22 cross sections are based on experimental data from Obst *et al.* [687]. As a result, above the breakup threshold, the MT=4 cross sections (MT4 = MT201 – MT22) depend on the difference between two separately normalized components derived from completely independent experiments.

MT=50-52 were informed by measurements from Van Der Zwan *et al.* [694], and the MT=50-52,91 partials were set to maintain consistency with MT=4.

Geiger *et al.* [689] measured the MT=50-53 partial cross sections (physically comprising all of MT=4 for the α energies studied) and MT=201 total cross sections, allowing MT=22/MT=201 ratios to be determined directly in a single experiment. Based on Ref. [689], the JENDL/AN-2005 (NMOD=2) breakup reaction fraction appears to be highly underestimated for α energies from the minimum threshold for MT=22 up to about 6.0 MeV. Above about 7.0 MeV, the JENDL fraction is generally consistent with Ref. [689].

The following modifications were made to ^{9}Be MF=3 data by NNL. Within the α energy range 4.64 MeV (the JENDL/AN-2005 minimum threshold for MT=22) to 7.90 MeV (the maximum energy studied in Ref. [689]), MT=4 and MT=22 were adjusted to match the experimentally observed MT=4/MT=22 ratios from Ref. [689]. The MT=201 total cross sections were unchanged, and the sum of MT=4 + MT=22 remains equal to the original MT=201 total cross sections. The internal ratios for MT=50-52,91 were also unchanged. However, MT=50-52,91 were rescaled to be consistent with the modified MT=4. The original energy grids were retained in all cases. No changes were made to MF=6 data by NNL. IAEA added elastic scattering MT=2 data from TENDL-2019 to MF=3 and MF=6 to complete the evaluation.

The modified NNL evaluation for ^{9}Be was retested in MC21. The resulting Am–Be neutron energy spectrum agreed well with Ref. [692] and showed reasonable agreement in the low-energy region below 1.5 MeV, as shown in Ref. [691, Fig. 8]. The MC21 results and improvement in the predicted neutron energy spectrum are consistent with those of Shores *et al.* [695], where the SOURCES-4C code is specifically modified, based on Ref. [689], to better account for the ^{9}Be breakup reaction.

2. $^{17,18}O$

The original JENDL/AN-2005 evaluations (NMOD=2) use Kalbach-Mann systematics (LAW=1, LANG=2) for MF=6 neutron energy/angle distributions for MT=4,22 for ^{17}O (MT=4,16,22 for ^{18}O). No neutron energy/angle distributions are given for the MT=50-53,91 partial cross sections for ^{17}O (MT=50-54,91 for ^{18}O), and the MF=6 Kalbach-Mann distributions for MT=4 are decoupled from the constituent partial cross sections and associated residual energy states.

The NNL Monte Carlo radiation transport code MC21 was used to simulate the neutron energy spectrum for thick $^{238}UO_2$ and $^{238}PuO_2$ using the original JENDL/AN-2005 (NMOD=2) evaluations for ^{17}O and ^{18}O. A continuous-slowing-down model is used for α particles in MC21 without transport or use of MT=2 elastic cross sections [691]. Fission neutrons were accounted for but were of lesser significance. While neutron yields were predicted very well, the resulting neutron energy spectrum compared very poorly to published experimental measurements [696–699].

Kalbach-Mann systematics may provide a reasonable approximation for (α, n) neutron energy/angle distributions for high-incident-energy α particles in the tens to hundreds of MeV range, where higher-level residual excitations dominate or where a continuum excitation approximation may be appropriate. Kalbach-Mann systematics may also be an acceptable option for (α, n)-type reactions with multiple particle emission or when no partial cross section information is available for discrete residual states.

For the incident α energy spectrum ranging from actinide decay energies (4-8 MeV) down to below the minimum threshold for (α, n) reactions, the total (α, n) neutron yield will be largely due to reactions where the residual is left in the ground state or in low-level excited states. These low-energy residual states have widely separated energy levels that strongly influence the resulting neutron energy spectrum. Therefore, the use of Kalbach-Mann systematics is inappropriate for characterizing (α, n) neutron energy/angle distributions for applications dependent on α particle emission via actinide decay.

The following modifications were made to ^{17}O and ^{18}O MF=6 data by NNL. MT=4 was removed and replaced with MT=50-53,91 for ^{17}O (MT=50-54,91 for ^{18}O). MT=50-54 use LAW=3 (isotropic two-body kinematics) for neutron emission based on AWR, AWP, and QI from the respective MF=3 MT=50-54 sections. MT=91 uses the same Kalbach-Mann systematics neutron distribution data previously used for MT=4. No changes were made to MF=3 data by NNL. IAEA added elastic scattering MT=2 data from TENDL-2019 to MF=3 and MF=6 to complete the evaluation.

The modified NNL evaluations for ^{17}O and ^{18}O were retested in MC21. The resulting neutron energy spectra for thick $^{238}UO_2$ and $^{238}PuO_2$ compared well to Refs. [691, 696–699], as shown in Ref. [691, Fig. 3] and Fig. 180, respectively. Below 1.5 MeV in Fig. 180 results could be improved further by explicit inclusion of MT=53 with two-body kinematics instead of including it as part of MT=91 with Kalbach-Mann systematics.

B. Helions sublibrary

For the incident ^{3}He sublibrary, the ^{3}He + ^{3}He evaluated file from ENDF/B-VIII.0 was kept.

For ^{3}He + ^{4}He, a new evaluation from the INDEN light elements collaboration was adopted. The new evaluation is based on an R-Matrix fit using the Brune parameterization, including experimental data from multiple experiments that populated the same Be7 system. Some data renormalization was required, including revising estimated uncertainties to take discretization error into account. The fit included 14 resonances including some broad 3/2+ and 5/2+ poles contributing to the back-

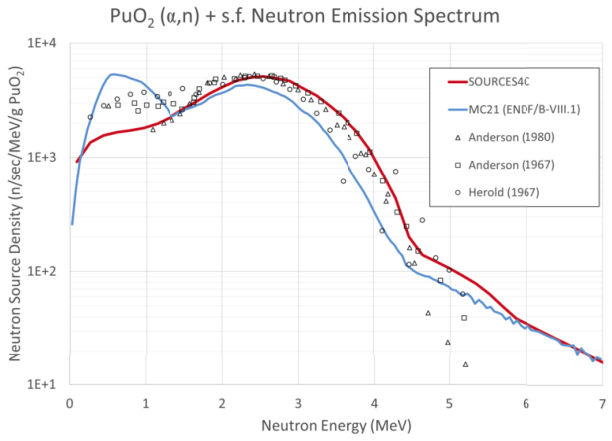


FIG. 180. Comparison of MC21 neutron emission energy spectra for PuO_2 using ENDF/B-VIII.1 to SOURCES-4C and to experimental data Refs. [691, 698, 699].

ground. Details about the evaluation were presented as part of the 2022 CSEWG meeting [700]. The R-Matrix resonance parameters are included in the evaluation, but since resonance reconstruction for incident charged particles has not been fully tested in processing codes, the reconstructed cross sections are also provided for MTs 2 and 600, and the LRP=2 flag is set to indicate that resonance reconstruction is not needed.

The ^{6}Li ENDF/B-VIII.1 evaluation replaced the (h,2n) and (h,p) cross sections and distributions from ENDF/B-VIII.0 with values from the LLNL ECPL, while keeping the Coulomb elastic scattering from ENDF/B-VIII.0.

A new evaluation of ^{7}Li was adopted from the LLNL ECPL. This evaluation includes (h,p), (h,d), (h,t), (h,n+p) reactions as well as (h,a) reactions to both the ground state and second excited state in ^{6}Li.

C. Deuterons sublibrary

Updates to the deuteron sublibrary are being provided for target materials ^{3}H, ^{3}He, and ^{6}Li. Minor modifications and corrections were made for tritium, which is based on an R-matrix evaluation [701] and described for the ENDF/B-VII.0 library [702]. Significant revisions to the d+^{3}He reaction were made on the basis of an updated R-matrix evaluation for the ^{5}Li system [703] (which also results in an updated p+^{4}He described below in Section VII D 1).

1. ^3H

The previous evaluation of the d+t reactions is summarized in Section VII.B.1 of the paper describing ENDF/B-VII.0 [702, Section VII.B.1]. A few additions and corrections were made to this evaluation for ENDF/B-VIII.1. The evaluation is based fundamentally on a LANL R-matrix analysis of reactions in the ^{5}He system at deuteron energies up to 10 MeV, which includes data for all the reactions possible between $d+t$ and n+^{4}He channels, as well as branching-ratio measurements for $\mathrm{T}(d,\gamma)^5\mathrm{He}/\mathrm{T}(d,n)^4\mathrm{He}$. The addition of the branching-ratio data allowed us to include gamma-production cross sections from the first and second excited states of ^{5}He for the $\mathrm{T}(d,\gamma)^5\mathrm{He}$ reaction in MF=3, MT=91. Also, the integrated cross section for the inelastic process to the first excited state of ^{4}He, $\mathrm{T}(d,n_1)^4\mathrm{He}^*$ (MT=51), was extended to 20 MeV in MF=3 and MF=6 using extrapolations calculated from the ^{5}He R-matrix analysis. The LR flag for this reaction was changed to LR=0 to reflect that it is a two-body reaction, with subsequent decay of the $^4\mathrm{He}^*$ to $p+t$. The Q-values for the $\mathrm{T}(d,n_0)$ and $\mathrm{T}(d,n_1)$ reactions (MT=50,51) were corrected in MF=3. And finally, the integrated cross sections and angular distributions for the $\mathrm{T}(d,n_0)^4\mathrm{He}$ reaction (MF=3,6 for MT=50) were extended to 40 MeV, using newer results from the experimentally determined coefficients provided by M. Drosg (U. Vienna) [295].

2. ^3He

The evaluation update for d+^{3}He is derived from the multichannel unitary R-matrix evaluation of the ^{5}Li compound system described in some detail in Ref. [703]. The top portion of Table XLI shows the channels along with the channel-radius parameters a_c of the R-matrix parametrization and the maximum value of the orbital angular momentum $\ell_{\max}$ for the channel. The scattering and reaction processes (collectively "Reactions") of the ^{5}Li compound system are shown in the left column of the lower portion of the table. Energy ranges, numbers of data points and types of observables are shown in the remaining columns of the lower portion.

The column labeled "Observables" indicates the following data types: $\sigma(E)$, integrated cross section; $\sigma(\theta)$, unpolarized angular distributions (energy-dependence suppressed); A, initial-state analyzing power; P, final-state polarization; C, spin correlation coefficients; K, polarization transfer coefficients. (We have suppressed the indices $i,j,\ldots$ which take on values x,y,z for spins/polarization directions in configuration space.) All polarization and spin distributions are angular distributions, which depend on the angle of the outgoing particle. The χ-squared per degree of freedom for the analysis is $\chi^2/\mathrm{dof} \simeq 2.7$ over 7,178 data points.

In the current evaluation, the differential cross section angular distributions in the center-of-mass frame and the experimentally observed data for $^3\mathrm{He}(d,d)^3\mathrm{He}$ elastic scattering are fit to data up to $E_d \simeq 10$ MeV. (A previous, unpublished, LANL-internal evaluation, "CP2011" covered deuteron incident laboratory energies from $0 \le E_d \le 1.4$ MeV.) New data has been added to both the existing region from Refs. [704–708]. The evaluated data has been

TABLE XLI. Channel configuration (top) and data summary (bottom) for the ^{5}Li system analysis.

Channel	a_c (fm)	$\ell_{\max}$
d +^{3}He($\frac{1}{2}^+$)	4.8	4
p +^{4}He(0^+)	2.9	4
p +^{4}He*(0^+; 20.2 MeV)	3.4	2
d_0+^{3}He($\frac{1}{2}^+$)	5.1	0

Reaction	$E_{\rm proj}$ range (MeV)	# Data Points	Observables
^{3}He$(d,d)^3$He	0.32 – 10.0	2,229	$\sigma(\theta), A_i, A_{ii}, C_{i,j}, C_{ij,k}, K_{i,j'k'}, K_{ij,k'l'}$
^{3}He$(d,p)^4$He	0.13 – 10.0	3,839	$\sigma(E), \sigma(\theta), A_i, A_{ii}, C_{i,j}, K_{ij,k'}$
^{3}He$(d,p)^4$He*	3.70 – 6.70	28	$\sigma(\theta)$
^{4}He$(p,p)^4$He	0.92 – 34.3	867	$\sigma(E), \sigma(\theta), A_y, P_y$
Total:		6963	

encoded in the following files and sections: MF=3 and MF=6, MT=600 for ^{3}He$(d,p)^4$He and MF=6 for MT=2, ^{3}He$(d,d)^3$He.

3. ^{6}Li

The evaluation of ^{6}Li is based on an R-matrix analysis of reactions in the ^{8}Be system done at LANL in 2004 at incident deuteron energies up to 5 MeV. It includes data for d+^{6}Li elastic scattering in the 3 - 5 MeV range, for ^{6}Li$(d,n)^7$Be in the 0.1 - 3.7 MeV range, for ^{6}Li$(d,p)^7$Li in the 0.1 - 5.0 MeV range, and for ^{6}Li$(d,\alpha)^4$He in the 0.0 - 5 MeV range. Smooth extensions of these cross sections to 20 MeV based on experimental data were added in 2020.

The analysis treats p+^{7}Li and n+^{7}Be as charge-conjugate channels, which imposes isospin (T) constraints on the reduced widths in the $T = 0$ and $T = 1$ levels and relates the cross sections for reactions involving those channels. Therefore, the cross sections for ^{6}Li$(d,n)^7$Be and ^{6}Li$(d,p)^7$Li, for example, are expected to be similar. This is illustrated in Figs. 181 and 182, in which the evaluation is compared with some of the experimental data, and with an evaluation done at LLNL. One sees that the LLNL evaluation is same as LANL's for the ^{6}Li$(d,p)^7$Li cross section at energies below 5 MeV but has a different extension to 20 MeV. For the ^{6}Li$(d,n)^7$Be reaction, however, the LLNL evaluation is substantially different from the LANL one at energies above 200 keV, following the higher data of Ruby [709] and Guzhovskij [710]. The LANL evaluation is more consistent with the data of McClenahan [711], which are roughly comparable in magnitude for the two reactions, in agreement with the charge-conjugate R-matrix calculation. The reason for this difference is that the measurements of Ruby and of Guzhovskij on which the LLNL evaluation is based

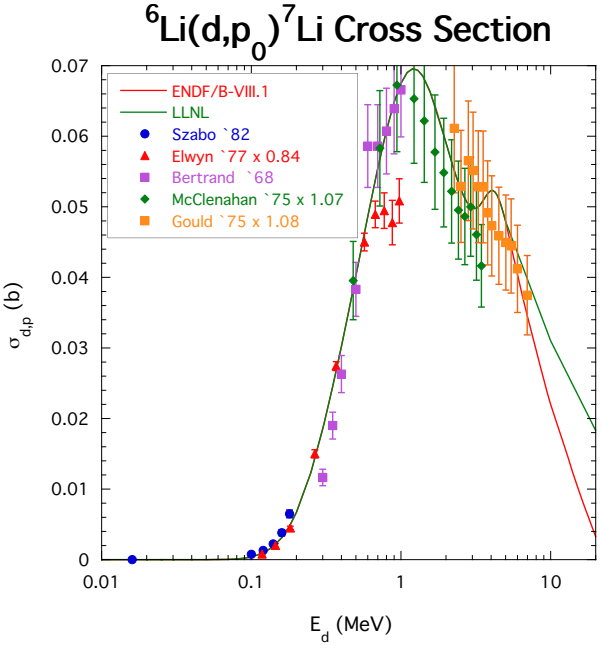


FIG. 181. Measurements of the ^{6}Li(d,p)^{7}Li cross section compared to the (LANL) ENDF/B-VIII.1 and LLNL evaluations at incident neutron energies between 0.01 and 20 MeV. The experimental data are from Refs. [711, 714–717].

include neutrons recoiling from the ground- and first-excited states of ^{7}Be, whereas the McClenahan measurement separates the two neutron groups, and only the ground-state cross section is shown in Fig. 182. Presumably, the difference between the two evaluated curves represents the contribution from the ^{6}Li$(d,n_1)^7$Be* reaction.

Work is continuing on the ^{8}Be system R-matrix analysis, in collaboration with S. Paneru, who is using the AZURE-2 R-matrix code to cross-check the results of the LANL code EDA, and extend the results to higher energies [712]. This involves adding excited-state channels of n+^{7}Be* and p+^{7}Li*, and of course, more experimental data at higher energies [713]. We expect improved evaluations will result from this combined effort, not only for the d+^{6}Li reactions, but also for n+^{7}Be, p+^{7}Li, and α+^{4}He.

D. Protons sublibrary

The proton sublibrary has been updated to include the proton-^{4}He elastic scattering angular distributions. This evaluation has been derived from an update of a previous LANL EDA-code based evaluation, not previously published, and is described in the following section.

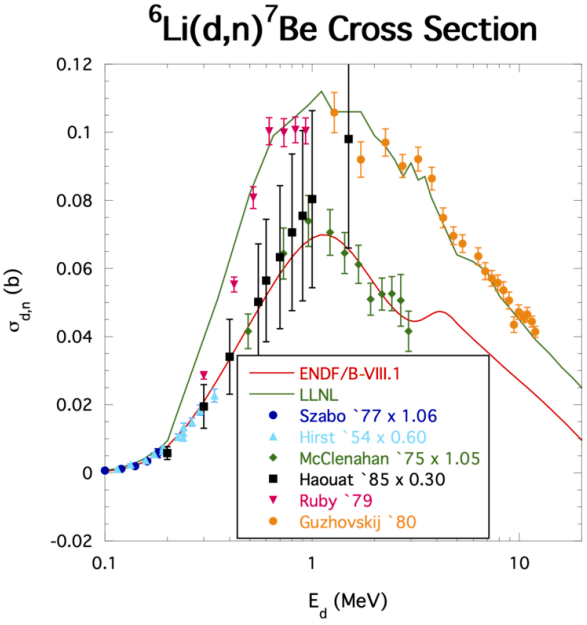


FIG. 182. Measurements of the ^{6}Li(d,n)^{7}Be cross section compared to the (LANL) ENDF/B-VIII.1 and LLNL evaluations at incident neutron energies between 0.1 and 20 MeV. The experimental data are from Refs. [709, 711, 718–720], and [710]. The data of Ruby, Guzhovskij, and possibly those of Haouat, contain contributions from excited-state neutrons, which are included in the LLNL curve.

1. ^{4}*He*

The present evaluation for ENDF/B-VIII.1 subsumes the previous ENDF/B-VIII.0 file, which was derived from the evaluations of Refs. [17, 721]. The present evaluation is preferred since it is based on the multichannel unitary R-matrix evaluation of ^{5}Li discussed in Section VII C 2.

The current evaluation includes reaction data up to $E_d < 10$ MeV, to just above the three-body break-up threshold at $E_d \simeq 8.9$ MeV. The resulting extension of the elastic p-induced data on ^{4}He, part of the same ^{5}Li compound system, to $E_p \lesssim 34.3$ MeV, permits application codes testing between the ENDF/B-VIII.0 and the present libraries to determine requirements on upper energy limits for charged particles, which is a point of increasing concern that is not completely or consistently discussed in the ENDF-6 format manual.

E. Tritons sublibrary

The triton sublibrary has been updated for ^{4}He. The new evaluation is based on the ^{7}Li evaluation, which couples to t+^{4}He, which was described in Section III C 2.

1. ^{4}*He*

The t+^{4}He entrance channel for the ^{7}Li compound system has been significantly updated since the previous evaluation [722, 723]. The R-matrix analysis, described in detail in the Section III C 2, includes elastic ^{4}He$(t,t)^{4}$He differential scattering cross sections and analyzing powers (A_y) for $E_t \leq 17$ MeV. These data extend beyond the three-body break-up threshold at $E_t \approx 11$ MeV, the ^{4}He$(t,n)^{6}$Li reaction data, for 8.5 MeV $< E_t <$ 14.4MeV and ^{4}He$(t,n_1)^{6}$Li$(3^{+};0)$ for $E_t = 12.9$ MeV.

This information has been encoded in the file `t-002_He_004.endf` in files MF=3, MF=4 and MF=6. The MT=50 section corresponds to observations of neutron groups recoiling against the ground state nucleus ^{6}Li that give the ^{4}He(t,n)^{6}Li reaction cross section. The observed data for this reaction is mainly from the inverse reaction, ^{6}Li$(n,t)^{4}$He (as in Table XVI), including the measurements of integrated and differential cross sections at neutron energies up to incident neutron energy of $E_n = 8.0$ MeV. The MT=51, ^{4}He$(t,n)^{6}$Li* reaction cross section has been determined primarily by the t-alpha total reaction cross section, plus a direct measurement at one energy of the differential cross section. The MT=52, 600, and 650 sections for ^{4}He$(t,n)^{6}$Li**, ^{4}He$(t,p)^{6}$He, and ^{4}He$(t,d)^{5}$He reaction cross sections predicted from the ^{7}Li R-matrix analysis of Section III C 2.

The MT=2 sections encode the nuclear cross sections for t+α elastic scattering. The data set included measurements of the differential cross section and triton analyzing power, including precise measurements from LANL [724]. Legendre coefficients are calculated from the R-matrix fit using the exact (LAW=5) nuclear amplitude representation. Nuclear partial waves through H-waves were allowed in the analysis giving Legendre orders $L = 0$ to 10 in the nuclear cross section and $L = 0$ to 5 in the complex nuclear amplitude that interferes with the Coulomb amplitude.

The MT=50, ^{4}He$(t,n)^{6}$Li reaction, is represented by Legendre coefficients (for MF=4) through $L = 6$, which are given for the calculated angular distributions. Data included differential cross section measurements for both the forward and reverse reactions at triton energies up to 14 MeV and at neutron energies up to 8.0 MeV.

The MT=51, ^{4}He$(t,n)^{6}$Li* reaction is given in terms of Legendre coefficients through $L = 2$ for the calculated angular distributions. Only one measurement exists, at $E_t = 12.888$ MeV.

VIII. FISSION YIELDS SUBLIBRARIES

In this updated release of the fission product yields sublibraries, we address an issue related to anomalously large uncertainties of nuclides close to stability, as well as a nonphysical discontinuity in the thermal neutron-induced fission yields of ^{241}Pu, which has affected the ENDF/B library since the release VI.2.

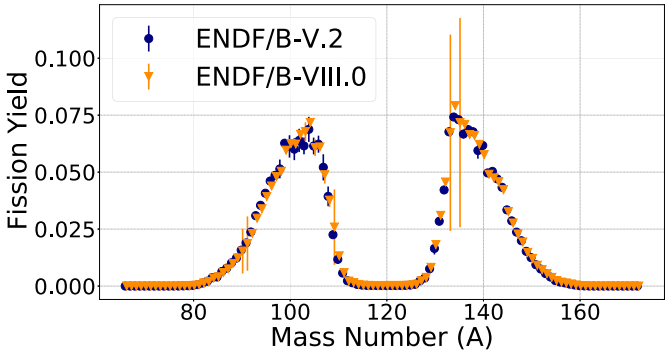


FIG. 183. Chain yields for thermal-neutron induced fission of ^{241}Pu for ENDF/B-V.2 (blue circles) and ENDF/B-VIII.0 (orange triangles).

A. Correction to the uncertainties of cumulative yields near stability

The update of the uncertainties affects the cumulative fission yields (MT=459) of 17 nuclides: ^{90g}Y, ^{90g}Zr, ^{91g}Y, ^{91m}Y, ^{93g}Y, ^{93m}Y, ^{109g}Ru, ^{109g}Rh, ^{109g}Pd, ^{109g}Ag, ^{109m}Ag, ^{132g}I, ^{133g}I, ^{133g}Xe, ^{135g}Cs, ^{135g}Ba, ^{148g}Pr.

In addition, 4 independent yields (MT=454) were modified to account for the fact that isomers for ^{109}Ru and ^{109}Rh have not been confirmed.

A brief description of the changes and the methodology will follow. For more details and a complete list of the updated values, the reader is referred to Ref. [725]. The changes have been applied to all NFY and SFY files, except for the cumulative yields of ^{135g}Ba in the neutron-induced fission of ^{239}Pu at 500 keV, 2 MeV and 14 MeV incident energies, which were recently revised contextually with the release of ENDF/B-VII.1 [162] and were not modified further.

The yields included in the ENDF/B-VIII.1 NFY (31 materials) and SFY sublibraries (9 materials) are based on the seminal work of T. R. England and B. F. Rider [726], published for the first time in the ENDF/B-VI.1 release and subsequently updated for ENDF/B-VI.3. Yields were then inherited from one minor release of ENDF/B-VI to the next, and finally incorporated in ENDF/B-VII and -VIII. The only documented change to the yields was introduced in ENDF/B-VII.1, where NFYs of ^{239}Pu at 500 keV, 2 MeV and 14 MeV incident energies were revised [162, 727].

Upon careful analysis of ENDF/B-VIII.0, we noticed abnormally high uncertainties of the cumulative yields of nuclides in proximity to the valley of stability. The chain yields for thermal-neutron-induced fission of ^{241}Pu from ENDF/B-VIII.0 are compared to those of an earlier evaluation (ENDF/B-V.2) in Fig. 183, revealing unusually large error bars for masses 133 and 135. These anomalous uncertainties appear to have been introduced with the ENDF/B-VI.1 release, and they are not consistent with the expected trends of the uncertainties of cumulative yields for end-of-chain fission products nor are they supported by any other experimental evidence.

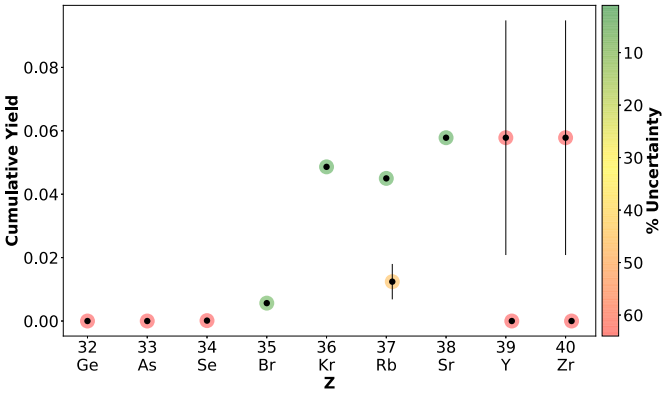


FIG. 184. Cumulative yields and relative uncertainties of fission products with mass A=90 for thermal-neutron-induced fission of ^{235}U. The large uncertainties for ^{90}Y and ^{90}Zr are not consistent with the expected trends of cumulative yields for end-of-chain fission products and are not supported by experimental evidence.

As an example, one can look at the cumulative yields of the A=90 mass chain, shown in Fig. 184. Here the anomalously large uncertainties are evident for ^{90g}Y and ^{90g}Zr. As an example, the uncertainty of ^{90g}Y was recalculated as:

$$\Delta^2 CY(^{90g}\mathrm{Y}) = \Delta^2 CY(^{90g}\mathrm{Sr}) + \Delta^2 IY(^{90m}\mathrm{Y}) + \Delta^2 IY(^{90g}\mathrm{Y})$$

These corrections lead to a reduction of the uncertainty that, depending on the fissioning system, can be up to two orders of magnitude.

In addition to corrections such as the one discussed above for ^{90g}Y, which were applied to 17 fission products in all NFY and SFY materials (with the exception noted for ^{239}Pu), two isomers were removed from the decay chain in mass A=109. Long-lived isomers for ^{109}Ru and ^{109}Rh are assumed in the ENDF/B decay data sublibrary but have not been confirmed by nuclear structure or FY measurements [728].

For these two isotopes, the independent yield of the isomer was set to 0, and the independent yield of the ground state was defined as:

$$IY'(g.s.) = IY(g.s.) + IY(m.s.),$$

where IY'(g.s.) is the new value for the ground state yield, and IY(g.s.) (IY(m.s.)) is the yield of the ground (isomeric) state included in ENDF/B-VIII.0.

B. Corrections to the thermal-neutron-induced fission yields of ^{241}Pu

Another long-standing issue addressed in this release affected the thermal-neutron-induced fission yields of

^{241}Pu showing a nonphysical discontinuity in the yields of fission products in 13 mass chains. The anomalous yields appeared after the ENDF/B-VI.2 release and was left unchanged in all releases since, as shown in Fig. 185. For a detailed list of all the changes, the reader is referred to Ref. [729].

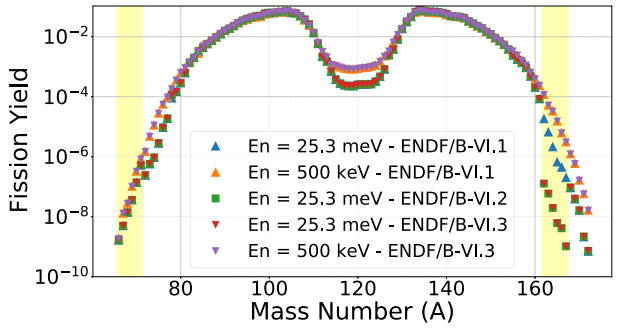


FIG. 185. Mass-chain yields for thermal- and fast-neutron-induced fission of ^{241}Pu in the releases from ENDF/B-VI.1 to ENDF/B-VI.3. Notice that ENDF/B-VI.2 mistakenly omitted the fast fission energy point. The FYs included in ENDF/B-VIII.0 have been substantially inherited from ENDF/B-VI.3. FYs in the shaded regions are those for which the yields were changed in the current ENDF/B-VIII.1 release.

The extensive documentation that accompanies the evaluation work of England and Rider in Ref. [726] allowed us to take a close look at the possible origin of the anomalous yields. For mass chains between 162 and 168, no experimental data are available, and the cumulative yields of the end-of-chain isotopes are obtained from Ref. [730, Table VIII], where the chain yields of every fissioning system included in the evaluation are estimated and tabulated. Comparing the values in the table with those included in Ref. [726], it seems that the data used for the evaluation were mistakenly obtained from the chain yields of ^{233}U(n_{th},f). With a deeper dive into the England and Rider documentation in Ref. [726], we found additional mass chains at the edge of the distribution (A=66-71), where no experimental data are available, that are also affected by this very same issue.

In order to address the anomaly, we introduced correction factors (CF) for the independent yields of masses 66 to 71 and 162 to 168 (reported in Table XLII), based on the ratio between the current mass chain yields and the ones tabulated in Ref. [730].

Despite the fact that the affected yields only represent a small fraction of the entire mass distribution, all independent FYs had to be corrected to normalize the sum to 200%.

The CF was obtained as:

$$CF = \frac{200\%}{\sum_i IY_i'} = 0.99998, \quad (1)$$

where IY_i' are the independent FYs after the factors in Table XLII were applied to masses 66-71 and 162-168 and are summed over the full mass distribution. CF was uniformly applied to all independent FYs and, in all cases,

TABLE XLII. Correction factors proposed for masses 66-71 and 162-168, based on the ratio between the mass chain yields from ENDF/B-VI.3 and those tabulated in Ref. [730]. All other masses were corrected with a CF=0.99998 defined in Eq. 1.

Light Fragments		Heavy Fragments	
A	Correction Factor	A	Correction Factor
		162	2.057×10^{2}
66	8.02×10^{-1}	163	1.597×10^{2}
67	4.93×10^{-1}	164	1.533×10^{2}
68	4.08×10^{-1}	165	1.535×10^{2}
69	3.43×10^{-1}	166	1.529×10^{2}
70	3.21×10^{-1}	167	2.750×10^{2}
71	1.28×10^{-1}	168	1.379

represents only a fraction of the uncertainty on the mass yield, that – for ^{241}Pu – are estimated to be known at best at 1.4% accuracy even for fission products in the peaks of the distribution [730].

Cumulative FYs could have been recalculated from independent yields using the decay data sublibrary, but to ensure consistency with the remaining body of FYs, we decided to apply the same correction factors to the cumulative FYs. This is possible since there is no transfer of yields via β-delayed neutron decay between two mass chains with different correction factors, and with this method, we introduce only negligible changes to those mass chains not affected by the anomaly.

Uncertainties of both independent and cumulative yields were also rescaled by the same factor, to preserve the percentage uncertainty estimated by England and Rider in their original work.

A number of tests were made on the corrected FY data, in terms of atom, neutron, proton balances; total sum of chain yields in the heavy and mass peaks, and over the entire distribution. Results are summarized in Tables XLIII and XLIV, expressed as total sum of independent yields, as well as residuals, i.e., difference between 1 (2) and the sum of the yields of the light/heavy peaks (full distribution). Despite a slight worsening of the sum of the light/heavy peaks, the difference (0.0023%) is still an order of magnitude lower than the accepted differences for a number of other nuclides.

Additional tests included calculating the average mass of the heavy and light fission products, the average number of emitted neutrons ($\bar{\nu}$), and the sum of the yield-weighted atomic number (Z). Also in this case, the values after the implemented corrections are comparable with those in the original ENDF/B-VIII.0 evaluation, and always within the errors accepted for other fissioning systems in the library.

TABLE XLIII. Comparison of the sum of independent yields between ENDF/B-VIII.0 and ENDF/B-VIII.1. The sum was performed in the light/heavy peaks, in the full mass distribution. The residuals, defined as the difference between 1 (2) and the sum of the yields of the light/heavy peaks (full distribution), are also shown.

ENDF/B-VIII.0			
	Light	Heavy	Full Dist.
Sum	0.99999741	1.00000278	2.00000019
Residual	2.587e-06	-2.776e-06	-1.882e-07
	Zlow	Zhigh	Full Dist.
Sum	1.00015263	0.99984756	2.00000019
ENDF/B-VIII.1			
	Light	Heavy	Full Dist.
Sum	0.99997721	1.00002336	2.00000057
Residual	2.279e-05	-2.336e-05	-5.740e-07
	Zlow	Zhigh	Full Dist.
Sum	1.00013243	0.99986814	2.00000057

IX. DECAY SUBLIBRARY

Although some preliminary decay evaluations were developed since ENDF/B-VIII.0, they did not reach the stage of maturity necessary to be incorporated into the final ENDF/B-VIII.1. Therefore, there were no significant updates or major evaluations incorporated into the ENDF/B-VIII.1 decay sublibrary. For the following library release, expected to be ENDF/B-IX.0, we anticipate a major evaluation effort for the decay sublibrary.

Compared to ENDF/B-VIII.0, only 10 decay files were updated; namely, ^{91,92}Rb, ^{97}Y, ^{101}Nb, ^{105}Mo, $^{104-107}$Tc, and ^{135}Sb. The reason for these updates was simply to accommodate updates from their corresponding ENSDF evaluations from May/June 2012 [731] and improved neutrino spectra, and they are not expected to have any significant impact in applications. Although in some cases there is an improvement, compared to ENDF/B-VIII.0, in accounting for missing energy (^{92}Rb, ^{97}Y), or the missing energy is preserved (^{135}Sb), in most cases an increase in missing energy is observed. This indicates that these nuclides should also be considered for reevaluation for a future release.

X. ATOMIC SUBLIBRARIES

For the atomic sublibraries in ENDF/B-VIII.1, we adopted the updated files from the Electron-Photon Interaction Cross Sections, 2023 version (EPICS2023), described in Ref. [732]. The nomenclature correspondence between ENDF/B-VIII.1 and EPICS is as follows: the EADL, EEDL, and EPDL in EPICS correspond to the atomic relaxation, electrons, and photo-atomic sublibraries in ENDF/B, respectively. More information about EPICS can be found in the EPICS website [733].

As stated in Ref. [732], EPICS2023 includes elemental, cold, neutral, isolated atomic data, in the absence of electrical or magnetic fields. EPICS is designed to handle ENDF applications involving photons and electrons in the keV and MeV energy ranges, which can accurately be described by simple elemental data with atomic number ranging from 1 to 100. However, EPICS is not designed to handle density or molecular and other binding effects that are important at low energies. Nor is it designed to handle nuclear effects that are important at higher energy. The atomic sublibraries in ENDF/B-VIII.1 inherit from EPICS its atomic self-consistency as all elements were obtaining simultaneously using the same methods, preserving important atomic number dependencies, such as sub-shell binding energies. Additionally, for the same reason, all three atomic sublibraries use the same subshell binding energies, in order to conserve energy when performing coupled electron-photon calculations.

The changes in ENDF/B-VIII.1 from ENDF/B-VIII.0 for the atomic sublibraries are thus the same as the changes in EPICS2023 compared to its earlier version (EPICS2017), that is:

- Corrected electrons (EEDL) bremsstrahlung ZAP (particle emitted), to 0 (photons), which in earlier versions was incorrectly defined as 11 (electrons); this caused the bremsstrahlung to appear to emit only electrons and no photons.
- Deleted extraneous repeated energies in earlier versions of the photo-atomic data (EPDL).
- Ensured that all thresholds start with a zero cross section, e.g., all photoionization sub-shells); earlier versions potentially confused users regarding interpolating or extrapolating data.

XI. NEUTRON DATA STANDARDS

There were no changes made in the standards for ENDF/B-VIII.1. A new evaluation of the standards leads to a new version of ENDF/B. It is understood that the standards should not change within a given version of ENDF/B. The energy ranges of validity of neutron cross section standards including the Thermal Neutron Constants, high energy reference cross sections, prompt γ-ray reference cross sections, and prompt fission fission spectra are given in Table XLV. The Thermal Neutron Constants included in the Standards are reviewed in Section XI A and listed in Table XLVI below.

We would like to remark on two important points regarding the dissemination of Neutron Data Standards:

1. In the IAEA Neutron Data Standards webpage (https://nds.iaea.org/standards/), the ^{239}Pu(n,f) and the ^{238}U(n,γ) cross sections are listed as additional cross sections used within the standard GMA fit. This is due to the fact that

TABLE XLIV. Comparison of the average atomic and mass numbers, and apparent average neutron multiplicity for ENDF/B-VIII.0 and ENDF/B-VIII.1.

	Sum of Z*Yields	Atomic Number	Avg. Light Mass	Avg. Heavy Mass	Apparent $\bar{\nu}$
ENDF/B-VIII.0	94.00	94	100.2828	138.7657	2.95
ENDF/B-VIII.1	94.00	94	100.2808	138.7695	2.95

those cross sections were fitted within the Neutron Standard cross sections, but the quality and consistency of available data was not enough to declare them standard cross sections.

2. The ENDF/B-VIII.0 neutron standards sublibrary (NSUB-19) includes evaluated data both inside and outside the energy range of the standards as well as non-standard reactions, without distinction. The correct energy range for the neutron data standards reactions is shown in Table XLV.

A. Thermal Neutron Constants (TNC)

These data historically have been evaluated using least-square techniques by the Standards community since the 60's. The fission, capture and elastic thermal cross sections at the thermal point (2200 m/s of neutron velocity) play an especially important role for the normalization of time-of-flight measurements for R-matrix evaluations.

These data are particularly important in the determination of the neutron economy in thermal reactors. Since thermal data are included in the Standards' evaluation, the thermal constants will have an impact on the results of the evaluation [734]. It should be noted, however, that most of the TNC were never directly used in the evaluated data files, mainly due to constraints in the R-matrix evaluations used in the RRR of heavy actinides. The TNC in Standards 2017 [1] are listed in Table XLVI and compared with values used in ENDF/B-VIII.0 (in *italics*) and ENDF/B-VIII.1 evaluations (in **bold**). It is strongly suggested that any changes in the thermal constants by evaluators be within the uncertainties shown here. The consistency for ^{235}U evaluated cross sections and $\bar{\nu}_{\text{total}}$ with TNC is excellent. However, the situation is different for other fissile actinides. For example, the ^{233}U thermal-capture cross section of 42.3 barn used in ENDF/B-VIII.0 was almost three sigmas lower than the recommended TNC value of 44.9(9) barn. Similarly, the ^{239}Pu thermal fission cross section of 747.4 barn used in ENDF/B-VIII.0 was much lower than the recommended TNC value of 752.4(22) barn.

Evaluated values used in the ENDF/B-VIII.1 evaluations are fully consistent with the TNC, a clear progress from the ENDF/B-VIII.0 situation.

TABLE XLV. Neutron Data Standards.

Neutron cross section standards	
Reaction	Standards incident neutron energy range
H(n,n)	1 keV to 20 MeV
^{3}He(n,p)	0.0253 eV to 50 keV
^{6}Li(n,t)	0.0253 eV to 1.0 MeV
^{10}B(n,α)	0.0253 eV to 1 MeV
^{10}B(n,$\alpha_1\gamma$)	0.0253 eV to 1 MeV
C(n,n)	10 eV to 1.8 MeV[a]
Au(n,γ)	0.0253 eV, 0.2 to 2.5 MeV, 30 keV MACS
^{235}U(n,f)	8–11eV (integral)
	0.15 to 200 MeV
^{238}U(n,f)	2 MeV to 200 MeV
High energy reference fission cross sections	
Reaction	Reference incident neutron energy range
$^{\text{Nat}}$Pb(n,f)	$\approx$ 34 MeV up to 1 GeV
^{209}Bi(n,f)	$\approx$ 34 MeV up to 1 GeV
^{235}U(n,f)	200 MeV to 1 GeV
^{238}U(n,f)	200 MeV to 1 GeV
^{239}Pu(n,f)	200 MeV to 1 GeV
Prompt γ-ray production reference cross sections	
Reaction	Reference incident neutron energy range
^{10}B(n,$\alpha_1\gamma$)	0.0253 eV to 1 MeV
^{7}Li(n,n$'\gamma$)	0.9 MeV to 8 MeV
^{48}Ti(n,n$'\gamma$)	2.8 MeV to 16 MeV
Thermal neutron constants at E=0.0253 eV (2200 m/s)	
Prompt fission neutron spectra (PFNS)	
Reaction	Reference outgoing neutron energy range
^{235}U(n_{th},f)	0.00001 eV to 30 MeV
^{252}Cf(sf)	0.00001 eV to 30 MeV

[a] The angular distributions at these incident energies are declared standard

XII. SUMMARY OF FORMAT CHANGES SINCE ENDF/B-VIII.0

In the early stage of work on the ENDF/B-VII.1 library release, CSEWG made the practical and important decision to use the same ENDF-6 format [514] for the next few ENDF releases. This decision was adopted even though it was argued that it would be timely to modernize the formats as the Generalised Nuclear Database Structure (GNDS) was now available. After careful de-

TABLE XLVI. The thermal neutron constants in Standards 2017 [1]. The constants in *italics* are those obtained from the ENDF/B-VIII.0 evaluations, while those in **bold** are the values in the ENDF/B-VIII.1 neutron sublibrary files.

Quantity	^{233}U	^{235}U	^{239}Pu	^{241}Pu
$\sigma_{(n,f)}$(b)	533.0(2.2)	587.3(1.4)	752.4(2.2)	1024(11)
	533.4	**586.1**	**751.1**	**1024**
	534.1	*586.7*	*747.4*	*1012*
$\sigma_{(n,\gamma)}$(b)	44.9(9)	99.5(1.3)	269.8(2.5)	362.3(6.1)
	44.1	**99.4**	**270.4**	**363.8**
	42.3	*99.4*	*270.1*	*363.1*
$\sigma_{(n,n)}$(b)	12.2(7)	14.09(22)	7.8(1.0)	11.9(2.6)
	12.1	**14.07**	**8.1**	**12.0**
	12.2	*14.11*	*8.1*	*11.3*
$\bar{\nu}_{total}$	2.487(11)	2.425(11)	2.878(13)	2.940(13)
	2.4869	**2.4299**	**2.8614**	**2.9453**
	2.4852	*2.4298*	*2.8769*	*2.9453*

liberation, CSEWG concluded that actual GNDS implementation requires considerable resources to modify processing codes and to guarantee high quality of the files processed by these codes. As the transition to GNDS is now underway, CSEWG determined that both ENDF/B-VIII libraries will be released in both the ENDF-6 format and in the GNDS format.

For both ENDF/B-VIII.0 and ENDF/B-VIII.1 releases, CSEWG adopted minor format changes to correct the ENDF-6 format and deal with emerging needs. ENDF-6 format changes for ENDF/B-VIII.0 are described in the 2018 ENDF-102 report [735]. ENDF-6 changes for the current ENDF/B-VIII.1 are summarized here and detailed in the 2024 ENDF-102 report [474]. The GNDS-2.0 format changes are summarized here as well and are detailed in the GNDS specifications [736].

A. ENDF-6 Format Changes

For the ENDF/B-VIII.1 release, significant changes were made to both the TSL data and to the covariance data. In addition, there are a number of important changes made to resonance, decay data and gamma data formats. Finally, there were a number of minor and sometimes cosmetic changes.

Significant changes to the thermal-neutron scattering formats include:

- Adding a generalized information file for MF7 (thermal-neutron scattering) files. This format allows the evaluator to explicitly state the isotopic distribution of atoms used to generate the MF7 data. This, in turn, enables the linkage to corresponding neutron sublibrary evaluations during the processing step (Chapter 7).
- Added a mixed elastic scattering format to File 7 to improve thermal scattering physics for nuclides with substantial coherent and incoherent scattering cross sections (Chapter 7).
- As the number of new thermal-neutron scattering evaluations submitted to ENDF/B-VIII.1 far exceeded the previous MAT number availablility, CSEWG adopted an entirely different scheme for thermal-neutron scattering evaluation MAT (Appendix C).

Significant changes to covariance formats include:

- Clarifying the procedure for collapsing File 35 covariance data to match those in Files 31 and 33 (Chapter 35).
- Changing one of the LTY=0 sub-subsection rules to disallow overlapping NI-type subsections (Chapter 33). The previous rule potentially allowed for recursive definitions of covariance matrices. Although this never occurred in practice, processing codes have no easy way to determine whether covariance matrices were recursively defined. Therefore, it was decided that allowing for overlapping NI-type subsections was unsafe.

Other significant changes:

- In order to be both consistent with resonance physics and to meet evaluator needs, various background R-matrix options were adopted (Chapter 2).
- Added an option to denote fission as a "decay product" in MF=10 (Chapter 10).
- Equations describing the energies of primary gammas were adjusted to include nuclear recoil (Chapters 12 and 13). This change improves energy balance for capture reactions when primary gammas are given.

Other less important changes:

- Various references to the ^{3}He nuclide were replaced with the word "helion" or the abbreviation "h".
- The IAEA Photonuclear Data Library was assigned a library identifier (NLIB).
- ENDF-6 sum rules are now illustrated with graphics (Sections 0.4.3.11 and 23.2).
- Various other clarifications and minor revisions.

B. GNDS Format Changes

The GNDS underwent two sizeable revisions (GNDS 1.9 [737] and GNDS 2.0 [736]) since the previous ENDF release. As of the 2.0 release, GNDS supports all ENDF-6 formats and meets all of the requirements laid out by

WPEC Subgroup 38. It should be mentioned that GNDS, unlike the ENDF-6 format, is managed by the WPEC Expert Group (EG) on the Generalised Nuclear Database Structure (EG-GNDS). In all, EG-GNDS made 149 formal merge requests and 29 of the merge requests were substantive format proposal requiring peer review from the EG and domain experts from the larger nuclear data community. The changes made to GNDS centered on nine themes, summarized below:

1. **Atomic data:**
   - Support for electron sub-shells as given in the ENDF-6 format.
2. **Covariances:**
   - Support for "sandwich product" covariance, allowing for storage of sensitivity matrices;
   - Add support for multi-dimensional covariances, such as encountered in TSL covariance data;
   - Simplify the covariance section naming.
3. **Documentation:**
   - Change the GNDS date formats to comply with international standards;
   - Improve documentation markup, bringing it into compliance with the requirements document;
   - Align the GNDS `documentation` node and decedants with DataCite.org's schema [738];
   - Make many small corrections, clarifications, simplifications and renamings to improve the usability of the documentation markups.
4. **File management:**
   - Add an `externalFiles` markup to denote external resources that may need to be read before processing interaction;
   - Add support for file checksums;
   - Add support for `map` files, the GNDS analog of `MCNP`'s `xsdir` file [440].
5. **Gamma data:**
   - Add a `finalState` attribute to primary gamma data markup so that enough information is available to perform a gamma cascade initiated by a primary gamma transition.
6. **Resonances:**
   - Consolidate the ENDF-6 "scattering radius" and "hard sphere radius" concepts into one R-matrix radius;
   - Expand options for the boundary condition of the R-matrix;
   - Add support for the various background R-matrix treatments recently added to the ENDF-6 format as noted above;
   - Add URR probability tables.
7. **SG-38 Compliance:**
   - Improve multi-group data styles;
   - Consolidate and clean up fission data support;
   - Add appendices, including a change log and mapping between ENDF and GNDS.
8. **Thermal neutron scattering:**
   - Improve thermal-neutron scattering markup by bring it into compliance with the requirements document, including:
     - Added a mixed elastic scattering format to improve thermal scattering physics for nuclides with substantial coherent and incoherent scattering cross sections;
     - Reorganize the TNSL transport data to mimic the organization of other transport data;
     - Add support for storing isotopic abundances (approved for GNDS-2.1). This section is equivalent to the new MF7 MT451 general information section in the ENDF-6 format;
   - TNSL erroneously required a special `interaction` attribute in the main `map` container.
9. **Usability:**
   - Resolve possible discrepancy between branchings and PoPs;
   - Denote what kind of reaction evaluation is being considered using the `interaction` tag;
   - Fix inconsistency in orphan product organization;
   - Add functional container organization to low-level containers;
   - Rename 'value' attribute for clarity in multi-dimensional containers;
   - Add `uncertainty` as allowed child node of `shell` in the PoPs database;
   - Improve element names, making them comply with conventions elsewhere in the specifications.

XIII. PROCESSING UPDATES

Evaluated nuclear data files are formatted in a compact way that is not the most suitable for transport calculations. Therefore, the files in ENDF/B-VIII.1 should be

properly processed to ensure the users will access the data in a more standardized way. Also, processing codes are stringent test of the proper formatting of the evaluated files.

The ENDF-6 files in this ENDF/B-VIII.1 release were successfully processed using NJOY-16.76 and FUDGE-6.7 for all sublibraries and AMPX (SCALE-7.0b08) for neutrons and photoatomic sublibraries. AMPX processing for the thermal-neutron scattering sublibrary used features to be made available in a future SCALE-7.0 beta. The sections below describe the updates done in those three processing codes to process correctly ENDF/B-VIII.1.

A. NJOY

Each release of the ENDF/B nuclear data library pushes the limits of the processing codes through the introduction of new data and new data formats. Processing codes must be adapted to ensure that they are capable of using these new formats, or at the very least understand them. NJOY [325], the nuclear data processing code developed at LANL is no exception to this. As NJOY2016 is still the main production code for nuclear data libraries at LANL, we will continue to make the necessary changes in this version of NJOY to ensure full compatibility with the ENDF/B-VIII.1 nuclear data library.

The ENDF/B-VIII.1 nuclear data library added the following capabilities to the ENDF-6 format:

- The addition of the mixed elastic scattering option (LTHR = 2) for elastic thermal scattering (found in MF7 MT2).
- The addition of general information concerning moderator materials in thermal scattering (found in MF7 MT451).
- The correction of the background R-matrix elements for resonance parameters (found in MF2 MT151).

The addition of the mixed elastic scattering option (LTHR = 2) for elastic thermal scattering is one of the most anticipated changes for the ENDF/B-VIII.1 nuclear data library since it lifts the limitation of using either coherent or incoherent elastic scattering for moderators. For NJOY2016, this new format has required changes in various modules, the most important ones being THERMR (which processes the thermal scattering data) and ACER (which formats the data into an ACE file for use in application codes like the MCNP code [739]). Fig. 186 gives an example of what this mixed mode data looks like for D in 7LiD after processing through ACER in NJOY2016. To enable the use of this new type of thermal scattering data, NJOY users have to use NJOY2016.65 or above.

Because the coherent and incoherent data needs to be treated separately by MCNP6, the mixed mode scattering also necessitated an update to the ACE format itself by

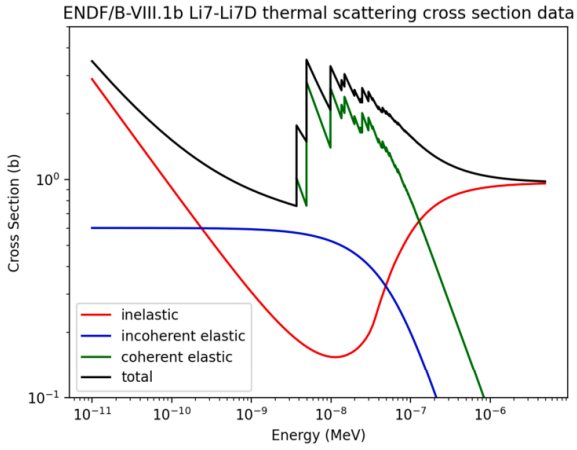


FIG. 186. Mixed mode thermal scattering in D-7LiD at 400 K processed by NJOY2016.65.

adding an additional elastic scattering data block [740], and a subsequent modification to MCNP so that the mixed mode elastic data can be used during a Monte Carlo simulation. This new format is fully supported in MCNP, Version 6.3.0 and above [739].

The second change to thermal scattering that was introduced in the ENDF/B-VIII.1 library is the general information concerning moderator materials in thermal scattering (found in MF7 MT451). This section was added to the ENDF-6 format to have a machine-readable description of some of the moderator characteristics (such as the uranium enrichment for the U in UO2 thermal scattering law). None of this information is required for processing the thermal scattering data. As a result, only MODER in NJOY2016 had to be modified to account for the presence of the MF7 MT451 general information section in the ENDF-6 format.

The third ENDF format change that impacts the processing of ENDF/B-VIII.1 is the addition of R-matrix background elements for resonance channels in the R-matrix limited format (LRF = 7, see Section 2.2.1.6 and D.1.7.5 of the ENDF-6 format manual [474]). The ENDF-6 format has had the option for R-matrix background elements for quite some time, but the formats that were laid out in the format manual were broken and the use of this format option would have led to a malformatted ENDF file. These format issues were corrected in 2021 and were subsequently used in the ENDF/B-VIII.1 evaluation for ^{88}Sr. This evaluation is the only evaluation in the ENDF/B-VIII.1 nuclear data library that uses these options.

The background R-matrix elements modify the diagonal of the R-matrix for a particular spin group through an external function (the background elements are, therefore, defined per channel). The corrected ENDF-6 format for the background R-matrix elements allow for four different options:

- no background element (the R-matrix for the spin group is thus not modified),
- a tabulated complex function of energy (this would be the most general case possible),
- a real statistical parameterization of the form available in SAMMY [317],
- a complex statistical parameterization of the forms described by Frohner [741, 742].

The new ^{88}Sr evaluation in ENDF/B-VIII.1 uses the SAMMY parametrization option.

Contrary to the mixed mode elastic scattering where changes to the ACE format and, therefore, MCNP were required, only the data processing itself is impacted by these new options. The changes in NJOY2016 have, therefore, been limited to MODER (to account for the change in the ENDF-6 format in MF2 MT151), RECONR and ERRORR. Although only the SAMMY parametrization has been used in the ENDF/B-VIII.1 ^{88}Sr evaluation, RECONR was modified to be able to use all background options. The SAMMY parametrization option was tested against the ^{88}Sr evaluation in collaboration with ORNL. ERRORR was also updated to allow for covariance data with respect to these background R-matrix options, although currently only the SAMMY parametrization is supported. Since the new ^{88}Sr evaluation does not include covariance data for the resonance parameters (in MF32), these updates could not be validated. NJOY2016.73 or higher is required to process evaluations that use these background R-matrix element options.

In addition to these format changes that have had an impact on the nuclear data processing software, some processing limitations in NJOY2016 that were identified in the past also have been lifted to process ENDF/B-VIII.1 evaluations. Examples here would be MF34 covariance processing with multiple subsections in ERRORR or improved photonuclear data processing. For a detailed overview of all changes to NJOY2016, we refer to the release notes on the NJOY2016 repository on GitHub[11].

B. FUDGE

LLNL maintains a nuclear data infrastructure code called FUDGE (For Updating Data and Generating Evaluations) [743]. FUDGE is written primarily in Python, with computationally intensive tasks implemented in C and C++. FUDGE supports interacting with GNDS-formatted nuclear data via the Python interpreter, including visualizing, checking, modifying and processing GNDS nuclear data. It is designed primarily as a toolkit to enable users to write their own workflow for handling nuclear data, but it also includes many useful Python scripts for common workflows, such as visualization, checking and processing. FUDGE is an open source code and is available for download at https://github.com/LLNL/fudge.

FUDGE does not directly process a file in the ENDF-6 format, but it includes tools for translating an evaluated ENDF-6 file into the GNDS/XML format and then processing the resulting GNDS data. The ENDF-6 to GNDS translator strictly interprets the ENDF/B format manual [474] and raises warnings or errors when data and/or format issues are encountered, making the translator a useful tool for uncovering problems in an ENDF-6 evaluation. The translator was used to detect and resolve many issues before the release of several recent ENDF/B library releases, starting with the ENDF/B-VII.1 release in 2011 [162]. The same translator was also used to prepare the GNDS-2.0 version of the final ENDF/B-VIII.1 library, available from the NNDC at https://www.nndc.bnl.gov/endf-library/B-VIII.1/GNDS/. FUDGE also comes packaged with a physics checking tool called 'checkGNDS.py' that was used to help uncover a variety of problems in ENDF/B-VIII.1 candidate evaluations and beta releases.

Several recent improvements have been made to processing and physics checking capabilities in FUDGE, including:

- support for external R-Matrix contributions as seen in the new n + Sr-88 evaluation,
- improved support for generating cross-section probability tables in the URR,
- improvements in processing thermal-neutron scattering evaluations, to better support the many new TNSL evaluations introduced in ENDF/B-VIII.1,
- many enhancements to the physics checking capabilities in 'checkGNDS.py', including better options for filtering out minor issues to focus on the most important problems, and
- improved capabilities for exporting continuous-energy processed libraries to ACE format [740] to support transport codes that depend on ACE-formatted data.

Using FUDGE, LLNL processed each ENDF/B-VIII.1 beta release into both multi-group and continuous-energy libraries. The resulting processed libraries are also stored in the GNDS format, using a hybrid combination of XML and HDF5 files to reduce disk space and improve data load times. Processed libraries were then tested with the LLNL Metis Validation and Verification platform [744] against a wide range of benchmarks, including critical assemblies, pulsed spheres, and reaction ratios. Results were compared to those obtained with the ENDF/B-VIII.0 library in GNDS format. Metis supports running several radiation transport codes, including the LLNL Monte Carlo code Mercury [745] and deterministic code Ardra [746]. Both Mercury and Ardra use the

[11] See https://github.com/njoy/NJOY2016/releases

C++ GIDI+ API (also developed at LLNL) to access the GNDS data [747]. Additionally, Mercury uses the GPU-enabled GIDI+/MCGIDI API for cross-section lookup and to sample product distributions. GIDI+ is available for download from https://github.com/LLNL/gidiplus.

C. AMPX

The AMPX code system [512] is the nuclear data processing code for the SCALE code system [748]. AMPX is developed and distributed with the SCALE code system. Additionally, an open source version of AMPX is now available [749]. Modernization and development efforts in AMPX are funded through the US NCSP.

Key processing capabilities of AMPX include:

- generation of temperature-dependent continuous-energy cross-section data;
- resonance self-shielding for resolved and unresolved resonance ranges;
- generation of energy and angle distributions for secondary particles;
- processing of thermal scattering law data, $S(\alpha, \beta)$, for thermal moderators;
- processing of particle-yield and decay data;
- production of cross-section covariance data files for sensitivity/uncertainty analyses;
- performance of multi-group averaging operations; and
- generation of continuous-energy weighting spectra.

The detailed thermal moderator evaluations present in the ENDF/B-VIII.1, especially those with large numbers of Bragg edges, spurred development in AMPX and SCALE in order to prepare for the library's release. AMPX and the SCALE transport codes have historically adopted the philosophy to represent continuous energy data uniformly, with all reactions represented as fully double-differential cross-section cumulative probability distributions. While that approach facilitates sampling in the transport codes, it comes with the cost of very large CE libraries. The ENDF/B-VIII.0 CE library, for example, is 28 GB; the ENDF/B-VIII.1 CE library in double-differential representation would more than double that size. Some of the thermal moderator files proved to be too prohibitive in run-time memory to process in double-differential representation.

This issue is being addressed by ongoing development in AMPX and SCALE to update the CE library format to accommodate a simplified representation for Bragg edge data. This development is targeting testing and release with SCALE 7.0.0.

Another improvement to the processing of thermal moderator materials has been developed in the XSPROC problem-specific cross-section processing module of SCALE [750]. In particular, it proved necessary to improve the interpolation within the pointwise slowing down calculations for materials that have bound thermal scattering data with high forward peaks, such as the light water evaluation in ENDF/B-VIII.0.

Another significant development for AMPX is the capability to process the photonuclear sublibrary [751], funded by a collaboration between National Nuclear Security Administration (NNSA) and industry partnerships. The photonuclear sublibrary processing is available in the open source version of AMPX, and will be released generally with the corresponding transport capabilities in SCALE 7.0.0.

The ENDF/B-VIII.1 library was processed into multi-group and continuous-energy libraries. The library was subsequently tested with a suite derived from multiple applications of interest: criticality safety benchmarks (VALID), reactor physics benchmarks, and nuclide inventory benchmarks.

XIV. INTEGRAL DATA TESTING SUMMARY

The new nuclear data evaluations in the ENDF/B-VIII.1 nuclear data library were validated with experimentally measured values of the neutron multiplication factor in criticality benchmark experiments, delayed neutron benchmark experiments, reaction rate ratios in criticality benchmark experiments, reactor depletion benchmarks, and neutron leakage spectra in LLNL 14–MeV pulsed-sphere experiments. An emphasis is placed on the validation of the neutron multiplication factor with measured values from recently performed criticality safety benchmark experiments. The "modern criticality benchmark experiment suite" has been organized to showcase this validation. The significant effort to support new criticality safety experiments and reevaluation of important nuclides has successfully led to the production of reduced nuclear data uncertainties and more accurate nuclear data mean values. Information about thermal-neutron cross sections, Westcott factors, resonance integrals, MACS, astrophysical reaction rates, and solar system r-process abundances obtained through calculations using the ENDF/B-VIII.1 data can be found in Ref. [752].

Additionally, for the first time ever, the new ENDF/B-VIII.1 library has been validated in depletion prediction and reactivity calculations in power reactors, which is crucial for economics of operating commercial reactors. This validation addresses deficiencies found in the ENDF/B-VIII.0 library.

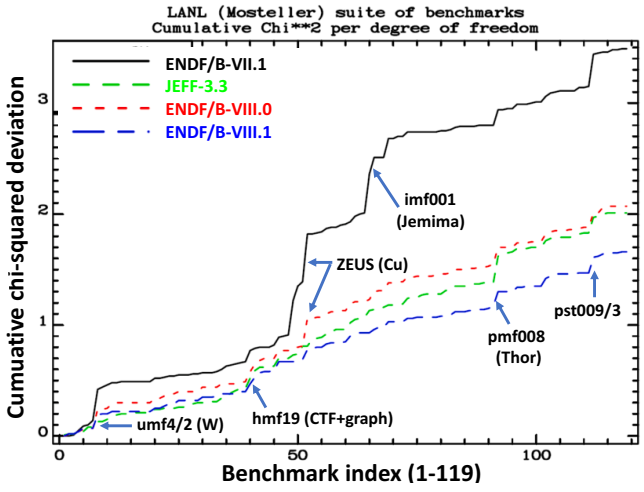


FIG. 187. The cumulative chi-squared deviation for the new ENDF/B-VIII.1 evaluation, versus ENDF/B-VII.1, ENDF/B-VIII.0, and JEFF-3.3 libraries for a suite of 119 assemblies defined by Mosteller *et al.* [753].

A. Criticality Benchmark Experiment Results

1. The Mosteller Suite

An example of the progress made by the current ENDF/BVIII.1 is shown in Fig. 187, from the analysis by A. Trkov. Over the Mosteller suite of 119 benchmarks that have been systematically modeled by LANL for many decades [753], and compared with reference (measured) k_{eff} values, the cumulative Chi-squared per degree of freedom value is seen to have been reduced compared to both JEFF-3.3 and ENDF/B-VIII.0 values. A more detailed investigation is still needed for discrepant benchmarks bearing ^{233}U with a tungsten reflector (umf4/2), ^{235}U with a graphite or a copper reflector (hmf19, ZEUS), ^{239}Pu with a ^{232}Th reflector (Thor) and ^{239}Pu nitrate solutions (pst900). Some of the discrepancies could be caused by materials other than the primary actinides. We note that the Chi-squared per degree of freedom values shown in Fig. 187 follow the usual definition where the squared (C-E) differences are divided by the squared experimental uncertainty in k_{eff} for each critical assembly. This differs from the definition shown in the next subsection.

2. Complete Criticality Testing

The criticality benchmark experiments used for validation in this work are documented in the ICSBEP Handbook [158]. The categories of criticality benchmark experiments used in this work include HEU-MET-FAST, HEU-MET-INTER, HEU-MET-MIXED, HEU-MET-THERM, HEU-SOL-THERM, LEU-COMP-THERM, LEU-SOL-THERM, MIX-MET-FAST, MIX-MET-INTER, MIX-MET-MIXED, PU-MET-FAST, PU-MET-INTER, PU-SOL-THERM, U233-COMP-THERM, U233-MET-FAST, U233-SOL-INTER, and U233-SOL-THERM. The categories have three abbreviations which denote the (1) fissile material, (2) physical form of the fissile material, and (3) energy range of a majority of neutrons causing fission. All benchmark input files were run with the radiation transport code, Monte Carlo N-Particle® Code Version 6.3[12] (MCNP). Two metrics, χ^2 and mean absolute bias, were used to compare the ENDF/B-VIII.1 nuclear data library to the previously released ENDF/B-VIII.0 nuclear data library. The χ^2 metric can be written mathematically as

$$\chi^2 = \sum_i^N \frac{(C_i - E_i)^2}{E_i}, \tag{2}$$

where N is the number of criticality benchmark experiments, C is the calculated neutron multiplication factor, and E is the experimentally measured neutron multiplication factor. This definition of chi-squared in the above equation differs from that used in the previous subsection and does not include experimental uncertainties in the denominator; hence, the y-values in Fig. 188 are very different in scale from those in Fig. 187. Additionally, mean absolute bias can be calculated using

$$\frac{\sum_i^N |C_i - E_i|}{N}, \tag{3}$$

where N, C, and E have the same definition as in Equation 2. The mean absolute bias is reported in units of pcm (percent mille, 10^{-5} k_{eff}). Two figures were produced for all benchmarks to compare ENDF/B-VIII.0 and ENDF/B-VIII.1. The first figure, Fig. 188, shows the cumulative χ^2 value as a function of criticality benchmark experiment number for both nuclear data libraries. The solid black vertical lines in this figure represent a division of benchmark categories. From this figure, it can be deduced that the calculated values of criticality using the ENDF/B-VIII.1 nuclear data library are closer to experimentally measured values than those calculated using the ENDF/B-VIII.0 nuclear data library as evident by the lower calculated cumulative χ^2 value. Although the final cumulative χ^2 value for ENDF/B-VIII.1 is lower than ENDF/B-VIII.0, the χ^2 value for individual benchmarks for ENDF/B-VIII.1 is not always lower than ENDF/B-VIII.0.

[12] MCNP® and Monte Carlo N-Particle® are registered trademarks owned by Triad National Security, LLC, manager and operator of Los Alamos National Laboratory. Any third party use of such registered marks should be properly attributed to Triad National Security, LLC, including the use of the designation as appropriate. For the purposes of visual clarity, the registered trademark symbol is assumed for all references to MCNP within the remainder of this paper.

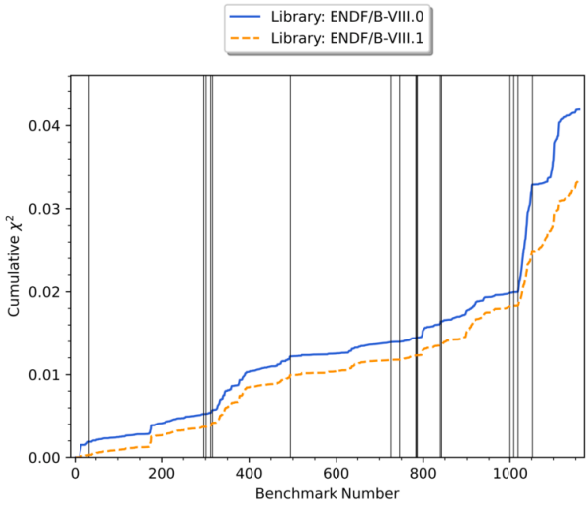


FIG. 188. The value of χ^2 plotted cumulatively as a function of criticality benchmark experiment number. Each benchmark category is separated with solid black vertical lines.

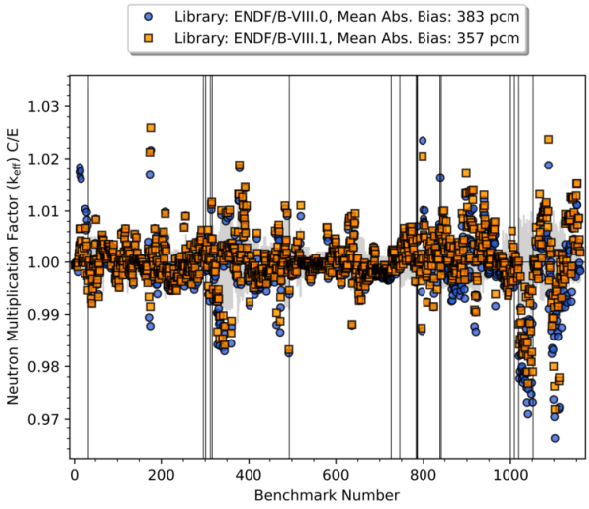


FIG. 189. The value of the neutron multiplication factor (k_{eff}) plotted as a function of criticality benchmark experiment number. The grey shaded region outlines the experimental one-σ uncertainty.

The second figure, Fig. 189, shows how well the calculated values of the neutron multiplication factor match experimentally measured values on a benchmark-by-benchmark basis. Each benchmark was run for a sufficient amount of time such that the calculation uncertainty is negligible; therefore, the grey shading outlines the experimental uncertainty. The mean absolute bias calculated for results using ENDF/B-VIII.1 is lower than the mean absolute bias calculated for results using ENDF/B-VIII.0. An improvement in C/E values is especially evident in the last benchmark categories, which contain ^{233}U fissile material. This figure gives a brief overview of the entire library as a whole; however, it is important to investigate each category of benchmarks. After analyzing legacy and modern suites of criticality experiment benchmarks, Fig. 189 will be divided by fissile material into plots to provide more insightful analysis.

The legacy criticality experiment benchmark suite has been used for many years to provide validation of intermediate (i.e., 1 eV–100 keV) and fast (i.e., > 100 keV) energy cross-section values for ^{235,238}U, ^{239}Pu, ^{233}U, and ^{232}Th. The benchmarks and associated ICSBEP Handbook designations included in the legacy suite: (1) Lady Godiva, HEU-MET-FAST-001 Revision 2, (2) Flattop with HEU core (Flattop-25), HEU-MET-FAST-028 Revision 2 (3) Jemima, IEU-MET-FAST-001 Revision 0, (4) Bigten, IEU-MET-FAST-007 Revision 1, (5) Jezebel, PU-MET-FAST-001 Revision 5, (6) ^{240}Pu Jezebel (Jezebel-Pu), PU-MET-FAST-002 Revision 1, (7) Flattop with Pu core (Flattop-Pu), PU-MET-FAST-006 Revision 1, (8) Thor Core, PU-MET-FAST-008, (9) U-233 Jezebel (Jezebel-23), U233-MET-FAST-001 Revision 3, and (10) Flattop with U-233 core (Flattop-23), U233-MET-FAST-006 Revision 1. As shown in Fig. 190 by the calculated results for plutonium benchmarks Jezebel, Jezebel-Pu, and Flattop-Pu, the updated evaluation for ^{239}Pu has contributed to a much better agreement of calculated results with ENDF/B-VIII.1 to experimentally measured values compared to the calculated results of ENDF/B-VIII.0. Evaluation changes for ^{238}U and ^{233}U have also contributed to substantial improvements in calculating k_{eff} for Jemima Case 3, Big Ten, and Jezebel-23. Overall, there is very good agreement between calculated and experimental values for fast plutonium and uranium bare systems (i.e., critical assemblies without reflectors). The results for the legacy criticality experiment benchmark suite are supplemented by results in the modern criticality experiment benchmark suite. As stated earlier, in Fig. 190, for Jezebel, ENDF/B-VIII.1 matches the data better than ENDF/B-VIII.0 simply because CSEWG made a decision to adopt the recently reassessed (Jeff Favorite) rev-5 measured benchmark value, and calibrated ENDF/B-VIII.1 to that value.

The modern criticality experiment benchmark suite was put together to showcase recently performed criticality safety experiments. The benchmark evaluations for these criticality safety experiments are extremely well documented. The benchmarks and associated ICSBEP Handbook designations included in the modern suite: (1) Kilowatt Reactor Using Stirling Technology (KRUSTY), HEU-MET-FAST-101 (Detailed Cases 1-5), (2) Measurement of Uranium Subcritical and Critical (MUSiC), HEU-MET-FAST-104 (Detailed Cases 1-2), (3) ZEUS-Graphite, HEU-MET-INTER-006 (Detailed Cases 1-4), (4) ZEUS-Teflon, also known as Critical Unresolved Region Integral Experiment (CURIE), HEU-MET-INTER-011 (Detailed Cases 1-5), (5) Jezebel Revision 5, PU-MET-FAST-001 (Detailed Cases 1-4), (6) Beryllium-reflected Plutonium (BeRP) Ball, PU-MET-FAST-038 (Detailed Case 1), (7) Jupiter, PU-MET-FAST-047 (Detailed Cases 1-3), (8) Plutonium Thermal/Epithermal eXperiments (TEX), PU-MET-MIXED-002 (Detailed Cases 1-5), and (9) Tantalum TEX, PU-

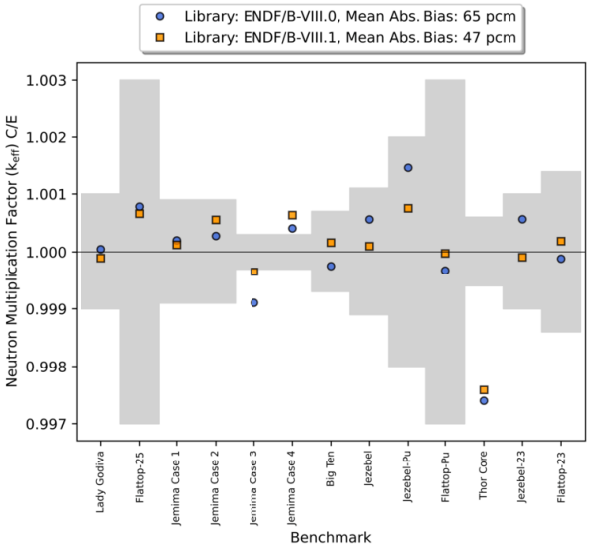


FIG. 190. The value of the neutron multiplication factor (k_{eff}) plotted as a function of criticality benchmark experiment for the legacy criticality experiment benchmark suite. The grey shaded region outlines the experimental one-σ uncertainty.

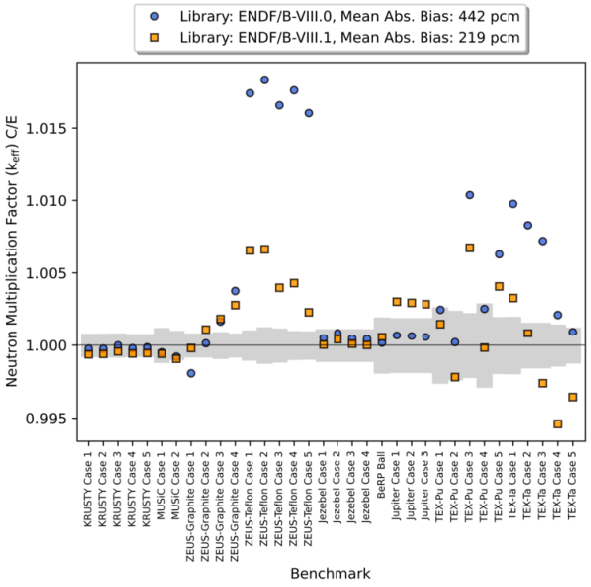


FIG. 191. The value of the neutron multiplication factor (k_{eff}) plotted as a function of criticality benchmark experiment for the modern criticality experiment benchmark suite. The grey shaded region outlines the experimental one-σ uncertainty.

MET-MIXED-003 (Detailed Cases 1-5). This suite of criticality experiment benchmarks provides validation for thermal (i.e., < 1 eV), intermediate, and fast cross sections of various fissile materials, moderator materials, and reflector materials. Fig. 191 shows the calculated over experimental values of k_{eff} for all benchmarks in this suite. A significant reduction in bias can be seen for many benchmarks in Fig. 191. The significant reduction in bias for ZEUS-Teflon and specific cases of TEX-Ta are directly related to evaluation updates made to ^{19}F and ^{181}Ta. An important note: the reduction of bias in Jezebel was mainly due to the model being updated from Revision 4 to Revision 5. In the future, it will be important to investigate evaluations of ^{9}Be, Pb isotopes, and ^{181}Ta to better understand the undesired calculated value changes to KRUSTY, BeRP Ball, Jupiter, and cases of TEX-Ta with higher percentages of thermal neutrons causing fission. One of the major evaluation changes of this new nuclear data library for actinides was ^{239}Pu.

The benchmarks containing ^{239}Pu fissile material are shown in Fig. 192. In this figure, benchmarks with a majority of fissions being caused by higher energy neutrons have similar calculated values using both ENDF/B-VIII.0 and ENDF/B-VIII.1. The ^{239}Pu evaluation was specifically adjusted such that the calculated value of k_{eff} for the latest revision of the Jezebel benchmark (Revision 5) exactly matched the experimental value[13]. Therefore, calculated values of plutonium benchmarks with higher energy neutron spectra using ENDF/B-VIII.1 are slightly closer to experimentally measured values than those calculated with ENDF/B-VIII.0. The opposite is true for most plutonium solution benchmarks that have thermal-energy neutron spectra. The exception to this statement includes the case of plutonium solution benchmarks with gadolinium (PU-SOL-THERM-034) C/E values that are now closer to unity. The average energy of the thermal PFNS for the latest ^{239}Pu evaluation is 30 keV lower than the one used in the ENDF/B-VIII.0 library, which has resulted in increased criticality of high-leakage critical assemblies. The increase in criticality breaks the nearly flat trend for PST benchmark C/E values as a function of above-thermal leakage fraction (ATLF) observed for the ENDF/B-VIII.0 library. The new positively sloped trend line for C/E values as a function of ATLF for the ENDF/B-VIII.1 library is plotted in Fig. 193. Due to the updated changes in thermal PFNS, the ^{239}Pu cross sections and $\overline{\nu}$ need to be adjusted to reduce criticality. Unfortunately, such reduction is in contradiction with the required criticality increase to satisfy depletion metrics and reactivity temperature coefficients (e.g., the CEA MISTRAL benchmark). The success of the ENDF/B-VIII.0 ^{239}Pu evaluation to reduce the magnitude of the trend line as a function of the ATLF should be revisited in future releases considering the recommended ^{239}Pu thermal PFNS. Measurements of PFNS at the thermal point and fluctuations of neutron multiplicity below 5 eV need to be prioritized to improve the PST performance. Uranium isotope RRR evaluations did not have as significant of performance changes as the updated ^{239}Pu evaluation showing the challenge of this reevaluation.

The changes in ^{235}U and ^{238}U did not have a significant effect on the calculated k_{eff} values of HEU systems as shown in Fig. 194. The calculated values for

[13] A similar adjustment was made for the ENDF/B-VIII.0 library using Revision 4 of the Jezebel model.

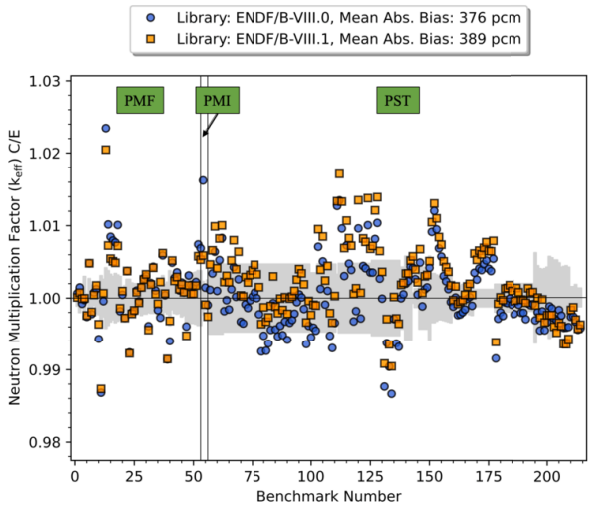


FIG. 192. The value of the neutron multiplication factor (k_{eff}) plotted as a function of criticality benchmark experiment for the plutonium criticality experiment benchmark suite. The grey shaded region outlines the experimental one-σ uncertainty.

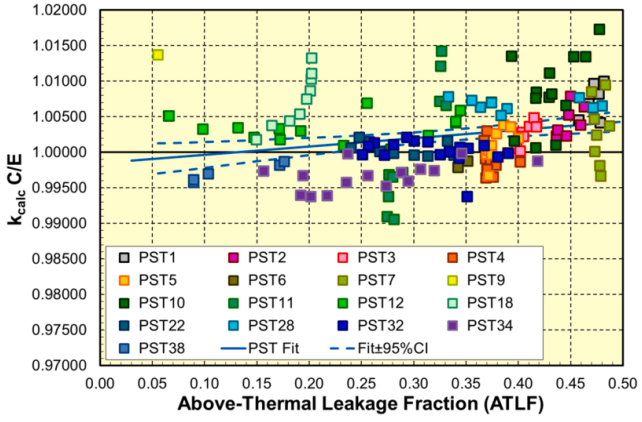


FIG. 193. The calculated over experimental value of the neutron multiplication factor (k_{eff}) plotted as a function of above-thermal leakage fraction (ATLF) for PU-SOL-THERM (PST) benchmarks. A regression fit is shown for ENDF/B-VIII.1. The ideal regression fit would have an intercept of 1 and slope of zero.

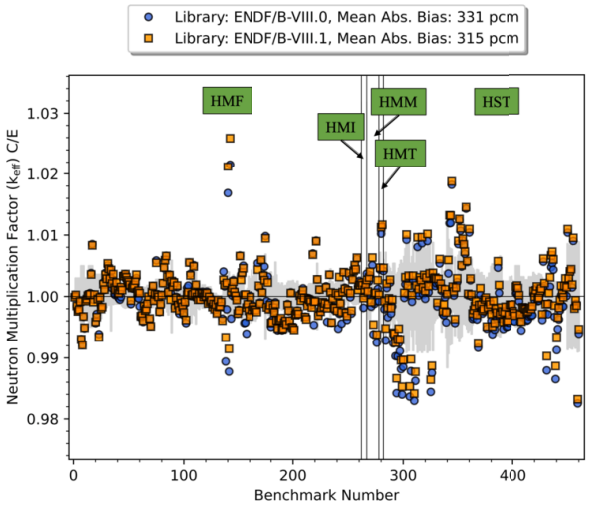


FIG. 194. The value of the neutron multiplication factor (k_{eff}) plotted as a function of criticality benchmark experiment for the highly enriched uranium (HEU) criticality experiment benchmark suite. The grey shaded region outlines the experimental one-σ uncertainty.

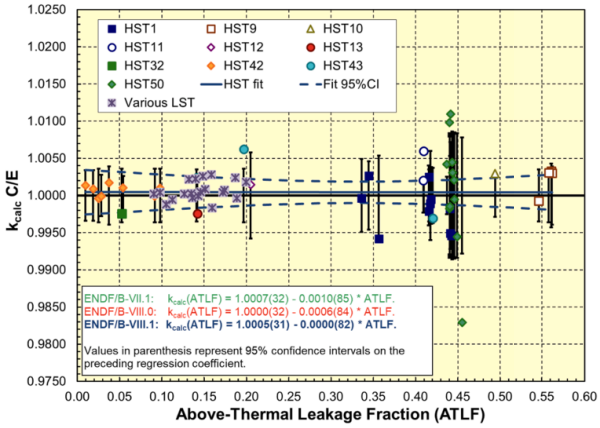


FIG. 195. The calculated over experimental value of the neutron multiplication factor (k_{eff}) plotted as a function of above-thermal leakage fraction (ATLF) for HEU-SOL-THERM (HST) and LEU-SOL-THERM (LST) benchmarks. A regression fit is shown for ENDF/B-VII.1, ENDF/B-VIII.0, and ENDF/B-VIII.1. The ideal regression fit would have an intercept of 1 and slope of zero.

the HEU benchmark series are in excellent agreement with experimentally measured values. Even with more benchmarks, the mean absolute bias shown calculated for ENDF/B-VIII.1 in Fig. 194 is lower than that calculated for ENDF/B-VIII.1 in Fig. 192. Normally, the HEU solution benchmarks from Fig. 194 are isolated to test thermal ^{235}U nuclear data. The dependence of k_{eff} as a function of ATLF is calculated for ENDF/B-VII.1, ENDF/B-VIII.0, and ENDF/B-VIII.1 in Fig. 195. The LEU-SOL-THERM (LST) benchmarks included in Fig. 195 were not considered in the calculation but rather are plotted for comparison. The regression fit for ENDF/B-VIII.1 has an intercept slightly higher than unity, which is undesired, but has a very small slope, which is desired. The results are very consistent with ENDF/B-VIII.0 and do not require considerable attention. The calculated results for benchmarks containing LEU instead of HEU are also comparable for both nuclear data libraries, with an slight +70 pcm increase in LEU-COMP-THERM (LCT) criticality of the ENDF/B-VIII.1 results compared to ENDF/B-VIII.0, which makes the new ENDF/B-VIII.1 evaluation looks much closer to the reference ENDF/B-VII.1 LCT criticality, which is important for reactor applications.

Calculated results for benchmarks containing LEU are shown in Fig. 196. Conclusive statements about the results shown in this figure are very similar to those pre-

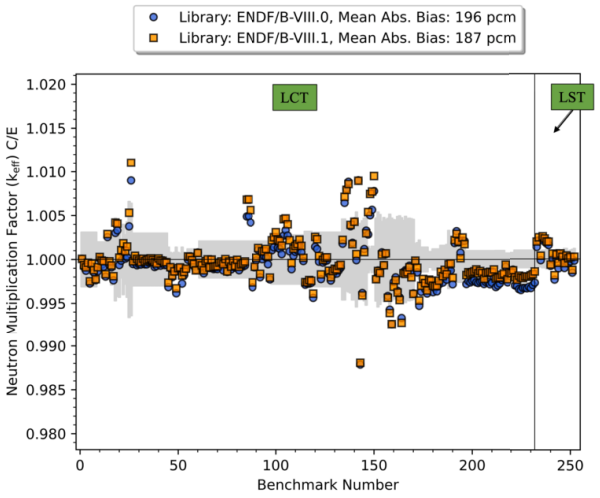


FIG. 196. The value of the neutron multiplication factor (k_{eff}) plotted as a function of criticality benchmark experiment for the low enriched uranium (LEU) criticality experiment benchmark suite. The grey shaded region outlines the experimental one-σ uncertainty.

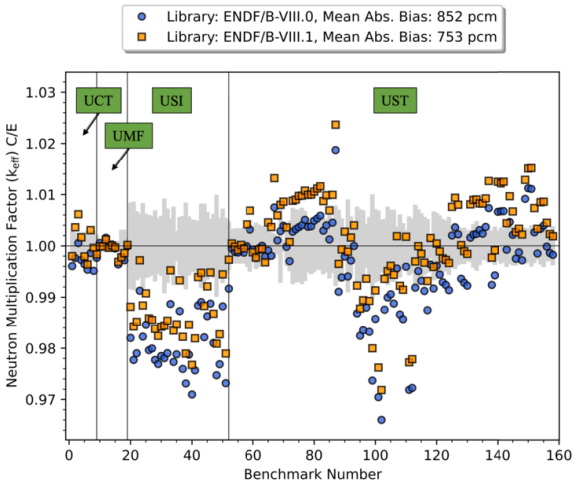


FIG. 197. The value of the neutron multiplication factor (k_{eff}) plotted as a function of criticality benchmark experiment for the ^{233}U criticality experiment benchmark suite. The grey shaded region outlines the experimental one-σ uncertainty.

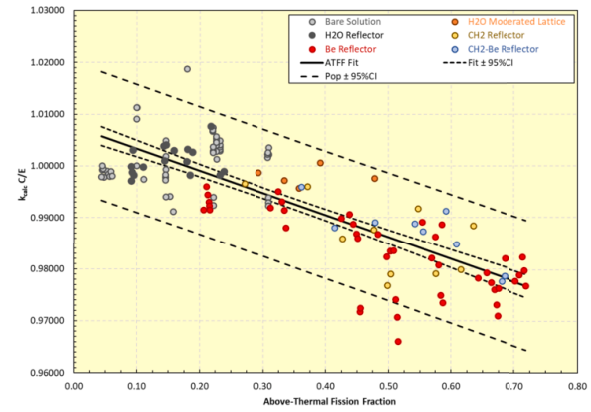
viously stated for benchmarks containing HEU. One important trend to take note of in Fig. 196 is the slight increase in reactivity calculated for almost all criticality benchmark experiments using ENDF/B-VIII.1. The LCT set of benchmarks is important for reactor lattice calculations. The low mean absolute bias calculated for LCT using ENDF/B-VIII.1 is a great sign that these reactor validation benchmarks are well characterized and useful for future validation.

The last set of benchmarks used for validation contained ^{233}U. The changes of the ^{233}U evaluation in the resonance region created significant performance changes in calculated values of k_{eff} using ENDF/B-VIII.1 compared to ENDF/B-VIII.0 as shown in Fig. 197. The mean absolute bias calculated for benchmarks using ENDF/B-VIII.1 was substantially reduced compared to the mean absolute bias calculated for benchmarks using ENDF/B-VIII.0. Although there was a significant reduction in mean absolute bias with the new ^{233}U evaluation changes, the calculated over experimental values for many U233-SOL-INTER and U233-SOL-THERM are far from unity. A more detailed analysis of the calculated over experimental value trend for U233-SOL-THERM benchmarks is presented in Fig. 198. Eigenvalue calculations for ^{233}U thermal and intermediate energy benchmarks have exhibited a strong, negative trend with increasing energy for decades. It is shown in Fig. 198(b) that the trend for ENDF/B-VIII.1 is very much the same as previously calculated. At higher energies, beryllium and Be-CH2 reflected systems are now calculated about 1000 pcm higher, which is a better result compared to ENDF/B-VIII.0. However, the average calculated k_{eff} is still low. At lower energies (i.e., above-thermal fission fraction 0.1–0.3), calculated k_{eff} values for bare solution and water-reflected systems are now too large and show a positive trend compared to ENDF/B-VIII.0, which is bad. Overall, the trend line for ^{233}U criticality benchmark experiments is flattening, but careful attention will be needed for bare solutions and water-reflected systems. An in-depth analysis of ^{233}U benchmark quality is long due, especially for benchmarks having above-thermal fission fraction larger than 0.35. In summary, the evaluation of ^{233}U in the resonance region is still challenging; additional efforts will be needed in future libraries.

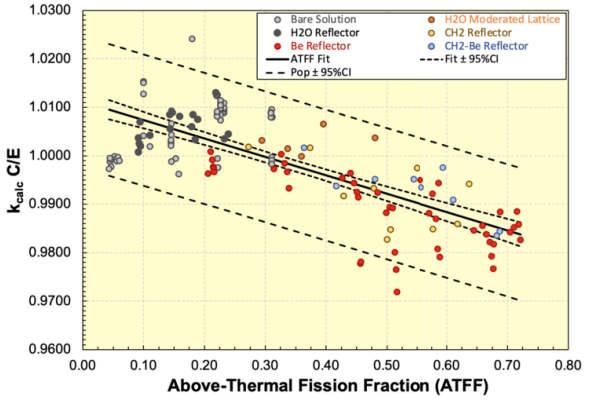
B. Delayed Neutron Experiment Results

Although the delayed neutron data have not been changed from their ENDF/B-VIII.0 values, they were tested against measurements of effective delayed neutron fraction β_{eff} in critical configurations. Unlike the situation for k_{eff}, only a handful of measurements of β_{eff} have been reported in open literature with sufficiently detailed information. Twenty-one measurements originally used in Ref. [754] were supplemented with two ORSphere measurements. We avoid the term "benchmark" for these cases, because good benchmark descriptions, comparable to those given in the ICSBEP Handbook, are generally not available.

The delayed neutron experiment measurement data were tested using the MC21 correlated sampling method [755]. The β_{eff} measurement data include assemblies with ^{233}U, ^{235}U, ^{238}U, and ^{239}Pu. There is one thermal spectrum assembly fueled by low enriched ^{235}U (TCA). The majority of the measurement data is for fast spectrum assemblies, including ^{233}U-driven assemblies (Skidoo and 23 Flattop), ^{235}U-driven assemblies (Big Ten, Topsy, Godiva, Masurca, FCA, SNEAK, ZPR, ORSphere), ^{239}Pu-driven assemblies (Popsy, Jezebel, Masurca, FCA, SNEAK, ZPR) and some mixed assemblies



(a)ENDF/B-VIII.0



(b)ENDF/B-VIII.1

FIG. 198. The calculated over experimental value of k_{eff} plotted as a function of above-thermal fission fraction for (a) ENDF/B-VIII.0 and (b) ENDF/B-VIII.1. The regression fit and confidence intervals are plotted with the bare and reflected criticality benchmark experiments.

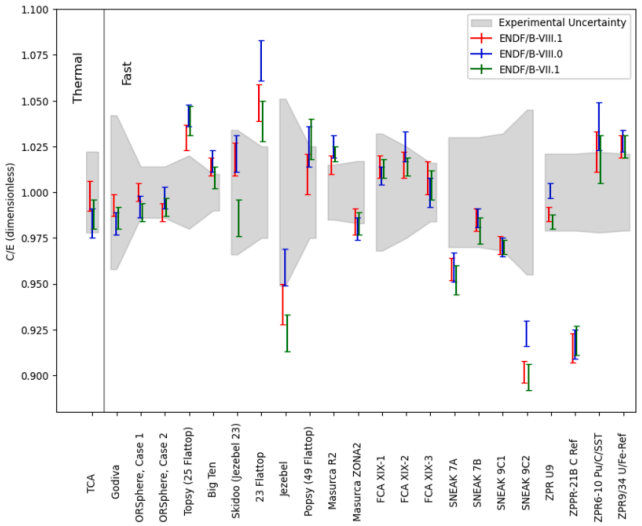


FIG. 199. C/E values for delayed neutron tests. The systems are roughly ordered by spectrum and fissile nuclide driving the assembly, thermal (left) and fast (right) then ^{235}U-driven, ^{233}U-driven, ^{239}Pu-driven, and fast reactor mockup assemblies. The grey shaded region outlines the experimental one-σ uncertainty.

(Masurca, FCA, SNEAK, ZPPR). Table XLVII provides the MC21 C/E values for the β_{eff} experiments, which are also plotted in Fig. 199. C/E values are provided for ENDF/B-VIII.1, ENDF/B-VIII.0, and ENDF/B-VII.1 along with the standard deviation of the experimental uncertainty of the β_{eff} measurements. Good agreement with the delayed neutron experiments is observed. One should note that the tests performed are only sensitive to the total delayed neutron yields. The delayed neutron yields per group are not tested, nor are the values for the decay constant per group.

C. Reaction Rate Ratio Results

Reaction rate ratios were measured in the legacy criticality benchmark experiments. Typically, foils made of certain materials were placed inside a central cavity or glory hole, irradiated, and then subsequently placed near/inside a detection system. The radiation detection system would count radiation emitted from the foils to measure the activity. Later, the measurement of activity would be used to calculate a reaction rate ratio. The measurement of these ratios was well established; however, the procedure for measuring reaction rate ratios is less common today. Reaction rate ratios were calculated using ENDF/B-VIII.0 and ENDF/B-VIII.1 for legacy criticality benchmark experiments in Table XLVIII. The naming convention used in Section 5.1 for these legacy criticality benchmark experiments is replicated here. Calculation of these reaction rate ratios was performed in MCNP by applying a detector tally in the center of the fissile material of each benchmark. The neutron flux was calculated in a sphere with radius equal to 1.3335 cm (0.525 inches), which is the typical size of a foil measured for reaction rate ratios. The values calculated using ENDF/B-VIII.0 and ENDF/B-VIII.1 are very consistent. There are no significant differences that need to be highlighted, addressed, or investigated.

We show graphically the variation of various reaction rate spectral indexes at different locations in LANL's fast critical assemblies, and for a variety of assemblies, that cover a range of neutron spectra. These plots represent updates of previous similar plots we have shown in publications documenting earlier versions of the ENDF libraries, such as in Ref. [68].

Fig. 200 shows the ^{238}U fission and (n,2n) reaction rates (divided by ^{235}U(n,f)) as a function of the radial distance in the Flattop-25 assembly. As expected, the spectral indices decrease with increasing distance from the center of the assembly. For larger radial locations (larger x-axis values), the neutron spectrum becomes softer and, therefore, threshold reactions (both ^{238}U(n,f) and (n,2n))

TABLE XLVII. MC21 C/E values for the β_{eff} calculations. The uncertainties quoted for the C/E values include only the statistical uncertainty of the calculation. All cases are fast spectrum except TCA.

	Experiment β_{eff} (pcm)	ENDF/B-VIII.1 C/E	ENDF/B-VIII.0 C/E	ENDF/B-VII.1 C/E
TCA	771 (2.2%)	0.998±0.008	0.983±0.008	0.988±0.008
Big Ten	720 (1.0%)	1.014±0.005	1.017±0.006	1.008±0.006
Topsy (25 Flattop)	665 (2.0%)	1.030±0.007	1.042±0.006	1.039±0.008
Godiva	659 (4.2%)	0.993±0.006	0.983±0.006	0.986±0.006
23 Flattop	360 (2.5%)	1.049±0.010	1.072±0.011	1.039±0.011
Skidoo (Jezebel 23)	290 (3.4%)	1.018±0.009	1.021±0.010	0.986±0.010
Popsy (49 Flattop)	276 (2.5%)	1.010±0.011	1.025±0.011	1.029±0.011
Jezebel	195 (5.1%)	0.939±0.011	0.959±0.010	0.923±0.010
Masurca R2	721 (1.5%)	1.015±0.005	1.025±0.006	1.021±0.004
Masurca ZONA2	349 (1.7%)	0.984±0.007	0.980±0.006	0.983±0.006
FCA XIX-1	742 (3.2%)	1.014±0.006	1.009±0.005	1.013±0.005
FCA XIX-2	364 (2.5%)	1.015±0.007	1.025±0.008	1.014±0.005
FCA XIX-3	251 (1.6%)	1.008±0.009	1.000±0.008	1.004±0.008
SNEAK 7A	395 (3.0%)	0.958±0.006	0.959±0.008	0.952±0.008
SNEAK 7B	429 (3.0%)	0.985±0.006	0.986±0.005	0.979±0.007
SNEAK 9C1	758 (3.2%)	0.971±0.005	0.970±0.005	0.970±0.004
SNEAK 9C2	426 (4.5%)	0.902±0.006	0.923±0.007	0.899±0.007
ZPR U9	731 (2.1%)	0.988±0.004	1.001±0.004	0.984±0.004
ZPPR-21B C Ref	384 (2.1%)	0.915±0.008	0.917±0.008	0.919±0.008
ZPR6-10 Pu/C/SST	223 (2.2%)	1.022±0.011	1.036±0.013	1.018±0.013
ZPR9/34 U/Fe-Ref	671 (2.1%)	1.025±0.006	1.028±0.006	1.025±0.006
ORSphere, Case 1	657 (1.4%)	1.000±0.005	0.992±0.006	0.989±0.005
ORSphere, Case 2	657 (1.4%)	0.989±0.005	0.997±0.006	0.992±0.005

become relatively smaller compared to ^{235}U(n,f), so the ratio decreases. Agreement between calculation and measurement is good, similar to the previous ENDF/B-VIII.0 evaluation.

Fig. 201 shows the ^{238}U(n,g)/^{235}U(n,f) rate as a function of the ^{238}U(n,f)/^{235}U(n,f) spectral index measured at the same location, allowing us to plot many critical assembly measurements on the same plot. Again, agreement between calculation and measurement is fairly good, similar to the previous ENDF/B-VIII.0 evaluation. In some assemblies, the trend of the calculation is below the measured data; this reflects the fact that the evaluation for ^{238}U(n,g) was based on fundamental lab cross section-measurements and not on these integral data.

Fig. 202 is similar to the previous plot, but this time for ^{241}Am(n,g) (relative to ^{239}Pu(n,f)). Agreement between calculation and measurement is fairly good, similar to the previous ENDF/B-VIII.0 evaluation.

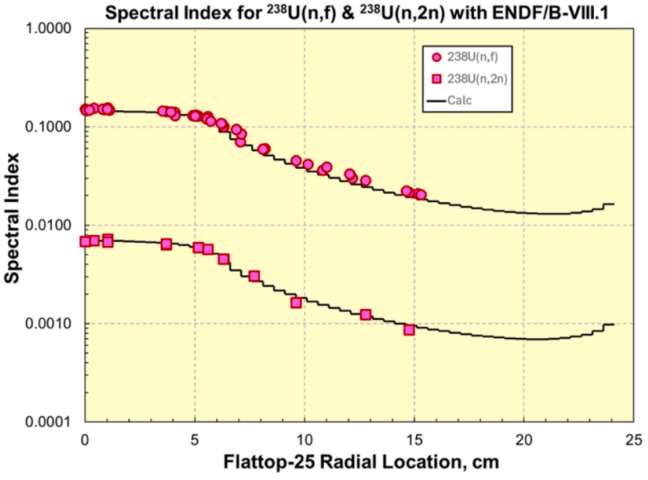


FIG. 200. MCNP-calculated and measured spectral indices for ^{238}U(n,f)/^{235}U(n,f) and ^{238}U(n,2n)/^{235}U(n,f), as a function of the radial location, in the Flattop-25 critical assembly.

D. Reactor Depletion

The accuracy of predicting the depletion and subsequent loss of reactivity in power reactors is crucial for fuel management and particularly for the determination of the cycle length in operating commercial reactors, which has significant economic implications. The industry was reasonably happy with the performance of the ENDF/B-VII.1 library[14] in this respect. Although the ENDF/B-VIII.0 library contained better physics, it was clearly pointed out by ORNL (Kim and Wieselquist) [39] that the loss of reactivity with burnup is considerably larger

[14] and similarly with the JEFF-3.1.1 library performance in Europe.

TABLE XLVIII. Reaction rate ratio values for legacy criticality benchmark experiments. The calculated ratios were rounded to the same significant figures as the measured values. The four ratios that do not have associated measured values are included for historical comparison. These LANL-calculated values can be compared to LLNL GNDS/Mercury calculated values in Table LXI. They are similar.

		Calculated Value	
Experiment, Ratio	Measured Value	ENDF/B-VIII.0	ENDF/B-VIII.1
Lady Godiva, $\frac{^{233}\mathrm{U(n,f)}}{^{235}\mathrm{U(n,f)}}$	1.59(3)	1.58	1.58
Lady Godiva, $\frac{^{237}\mathrm{Np(n,f)}}{^{235}\mathrm{U(n,f)}}$	0.8516(120)	0.8311	0.8307
Lady Godiva, $\frac{^{238}\mathrm{U(n,f)}}{^{235}\mathrm{U(n,f)}}$	0.1643(18)	0.1582	0.1580
Lady Godiva, $\frac{^{239}\mathrm{Pu(n,f)}}{^{235}\mathrm{U(n,f)}}$	1.4152(140)	1.3844	1.3832
Big Ten, $\frac{^{238}\mathrm{U(n,f)}}{^{235}\mathrm{U(n,f)}}$	0.0375(9)	0.0357	0.0362
Big Ten, $\frac{^{239}\mathrm{Pu(n,f)}}{^{235}\mathrm{U(n,f)}}$	1.198(28)	1.170	1.170
Jezebel, $\frac{^{233}\mathrm{U(n,f)}}{^{235}\mathrm{U(n,f)}}$	1.578(27)	1.566	1.566
Jezebel, $\frac{^{237}\mathrm{Np(n,f)}}{^{235}\mathrm{U(n,f)}}$	0.9835(14)	0.9768	0.9710
Jezebel, $\frac{^{238}\mathrm{U(n,f)}}{^{235}\mathrm{U(n,f)}}$	0.2133(23)	0.2119	0.2106
Jezebel, $\frac{^{239}\mathrm{Pu(n,f)}}{^{235}\mathrm{U(n,f)}}$	1.4609(130)	1.4273	1.4242
Jezebel, $\frac{^{239}\mathrm{Pu(n,2n)}}{^{239}\mathrm{Pu(n,f)}}$	None	0.0023	0.0022
Jezebel, $\frac{^{239}\mathrm{Pu(n,\gamma)}}{^{239}\mathrm{Pu(n,f)}}$	None	0.0345	0.0359
Jezebel-23, $\frac{^{237}\mathrm{Np(n,f)}}{^{235}\mathrm{U(n,f)}}$	0.997(15)	0.984	0.984
Jezebel-23, $\frac{^{238}\mathrm{U(n,f)}}{^{235}\mathrm{U(n,f)}}$	0.2131(26)	0.2116	0.2110
Flattop-Pu, $\frac{^{237}\mathrm{Np(n,f)}}{^{235}\mathrm{U(n,f)}}$	0.8561(120)	0.8569	0.8513
Flattop-Pu, $\frac{^{238}\mathrm{U(n,f)}}{^{235}\mathrm{U(n,f)}}$	0.1799(20)	0.1793	0.1779
Flattop-Pu, $\frac{^{239}\mathrm{Pu(n,2n)}}{^{239}\mathrm{Pu(n,f)}}$	None	0.0020	0.0019
Flattop-Pu, $\frac{^{239}\mathrm{Pu(n,\gamma)}}{^{239}\mathrm{Pu(n,f)}}$	None	0.0458	0.0468
Flattop-23, $\frac{^{237}\mathrm{Np(n,f)}}{^{235}\mathrm{U(n,f)}}$	0.910(13)	0.900	0.898
Flattop-23, $\frac{^{238}\mathrm{U(n,f)}}{^{235}\mathrm{U(n,f)}}$	0.1916(21)	0.1882	0.1869
Flattop-25, $\frac{^{233}\mathrm{U(n,f)}}{^{235}\mathrm{U(n,f)}}$	1.608(30)	1.578	1.578
Flattop-25, $\frac{^{237}\mathrm{Np(n,f)}}{^{235}\mathrm{U(n,f)}}$	0.7804(100)	0.7716	0.7712
Flattop-25, $\frac{^{238}\mathrm{U(n,f)}}{^{235}\mathrm{U(n,f)}}$	0.1492(16)	0.1445	0.1444
Flattop-25, $\frac{^{239}\mathrm{Pu(n,f)}}{^{235}\mathrm{U(n,f)}}$	1.3847(120)	1.3615	1.3602

with the ENDF/B-VIII.0 cross-section data (a swing of about -500 pcm compared to ENDF/B-VII.1), which means that the industry could not accept the ENDF/B-VIII.0 library for nuclear power applications without expensive data adjustment. It is also worth to point out that an even larger problem at high burnup was identified in the JEFF-3.3 library. This led to several studies, both at CSEWG and JEFF committees, made to pin down the root cause of the unfavorable loss of reactivity with burnup in ENDF/B-VIII.0 and JEFF-3.3 evaluations and to restore the ENDF/B-VII.1 performance in the new ENDF/B-VIII.1 and JEFF-4 libraries. The relevant ENDF/B-VIII.0 changes will be summarized below. Achieved consistent performance for the new ENDF/B-VIII.1 will be reviewed with calculations presented by four groups using different depletion benchmarks.

1. *Depletion calculations using* `Serpent`

The calculations carried out to test the performance of the ENDF/B-VIII.1 library during depletion calculations are divided in two main parts. In the first part, a code-to-code comparison is carried out while in the second step, the Duke1 benchmark from IRPhE is analyzed.

a. Three Mile Island Pincell depletion calculations

The pincell configuration utilized for testing the performance of the ENDF/B-VIII.1 library with respect to its older declinations (ENDF/B-VII.1 [162] and ENDF/B-

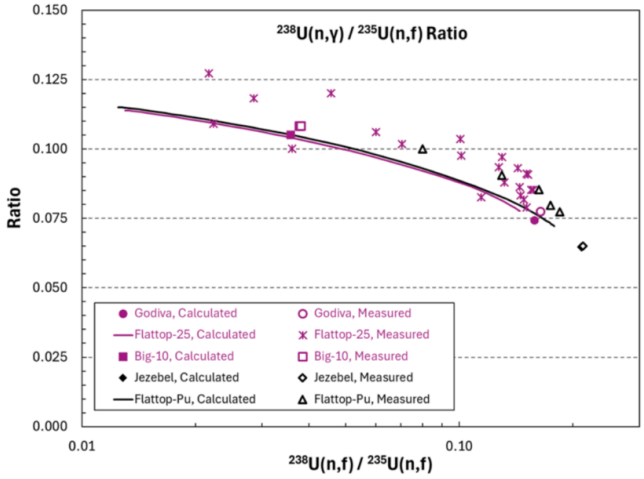


FIG. 201. MCNP-calculated and measured rates for ^{238}U(n,γ)/^{235}U(n,f), as a function of the hardness of the neutron energy spectrum (as characterized by the spectral index ^{238}U(n,f)/^{235}U(n,f)), in a variety of fast Los Alamos critical assemblies.

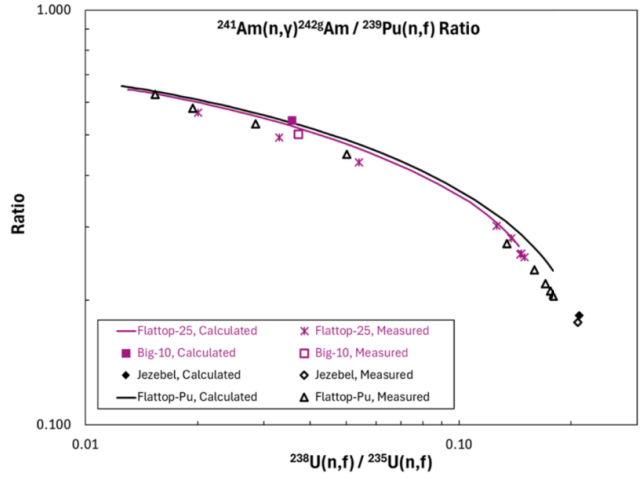


FIG. 202. MCNP-calculated and measured rates for ^{241}Am(n,γ)/^{239}Pu(n,f), as a function of the hardness of the neutron energy spectrum (as characterized by the spectral index ^{238}U(n,f)/^{235}U(n,f)), in a variety of fast Los Alamos critical assemblies.

VIII.0 [68]) is modeled after the TMI-1 PWR unit cell setup specified in the OECD/NEA Uncertainty Analysis in Modeling (UAM) benchmark, Exercise I-1b [756]. The fuel is made of 4.85 wt.% enriched uranium with a boron free moderator density of 0.7484 g/cm^3.

The `Serpent2` code [757] (Version 2.2.0) is used with ACE-formatted libraries based on ENDF/B-VII.1, ENDF/B-VIII.0, ENDF/B-VIII.1 distributed by LANL. Consistent fission yield and decay data information is used as well. The number of neutron histories considered is 25×10^6 (500 active batches of 10^4 neutrons each). The closest temperature available in the library is used for the $S(\alpha, \beta)$ tables (consistent temperatures are used for all libraries). The energy released per fission model takes into account the facts that the neutrons deposit energy along their history in various reactions; the energy deposition due to reactions other than fission is calculated using KERMA coefficients [758]. The resonance upscattering – Doppler broadened rejection correction (DBRC) treatment [759] – is considered only for one special case as described below. A standard predictor/corrector approach is used.

The depletion benchmark results are plotted in Fig. 203. Each library was used to calculate the effective multiplication coefficient of the reactor, k_{eff}, which was compared to the ENDF/B-VII.1 reference as a function of burnup. In the figure, the black solid line at 0 pcm defines the ENDF/B-VII.1 performance, and the blue and red dots represent the difference in k_{eff}, Δk_{eff}, for ENDF/B-VIII.0 and ENDF/B-VIII.1, respectively. Also shown by the yellow markers is the depletion calculation with ENDF/B-VIII.1 using the DBRC. ENDF/B-VII.1 is the reference as it is used in the industry for routine reactor applications with good performance [760].

For this computational benchmark, the ENDF/B-VIII.0 library shows decreased criticality of about -500 pcm relative to ENDF/B-VII.1. The Δk_{eff} is fairly constant with exposure within 200 pcm. The ENDF/B-VIII.1 library shows a lower criticality (about -300 pcm) at BOL compared to the ENDF/B-VII.1. However, the ENDF/B-VIII.1 criticality already at 30 MWd/kg exposure becomes quite similar to the ENDF/B-VII.1 showing a significant improvement compared to the ENDF/B-VIII.0 performance. The DBRC correction reduces the criticality at the BOL by 200 pcm; a reduction which decreases in magnitude with exposure.

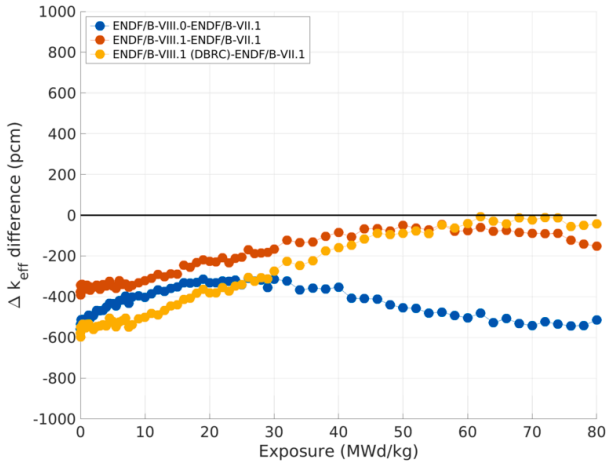


FIG. 203. The k_{eff} obtained with the ENDF/B-VIII.0 and ENDF/B-VIII.1 libraries (red and blue curves) is compared to ENDF/B-VII.1 by subtracting the VII.1 k_{eff} value. The yellow curve represents the reactivity loss change due to the resonance upscattering model (DBRC) obtained with ENDF/B-VIII.1.

In power reactor operation, the cycle length depends on the loss of reactivity $\Delta\rho(t)$ and not on Δk_{eff}. The reactivity loss $\Delta\rho^{XY}(t)$ with exposure t for a given nuclear data library labelled XY is defined in Eq. (4):

$$\Delta\rho^{XY}(t) = \left[\frac{1}{k_{eff}^{XY}(t)} - \frac{1}{k_{eff}^{XY}(0)}\right] \times 10^5 \text{ pcm} \qquad (4)$$

The reactivity loss with exposure difference $\Delta\rho^{XY}(t)$ between the various libraries labeled XY relative to the one calculated for the ENDF/B-VII.1 library $\Delta\rho^{B71}(t)$ is shown in Fig. 204. A clear negative swing of reactivity of about -500 pcm is observable when using the ENDF/B-VIII.0 library. This issue is fixed when using ENDF/B-VIII.1 as the reactivity difference with exposure is now fairly constant. The DBRC correction induces a reactivity gain of about 200 pcm at the EOL for the ENDF/B-VIII.1 library. Further research on the impact of the DBRC on reactivity is needed.

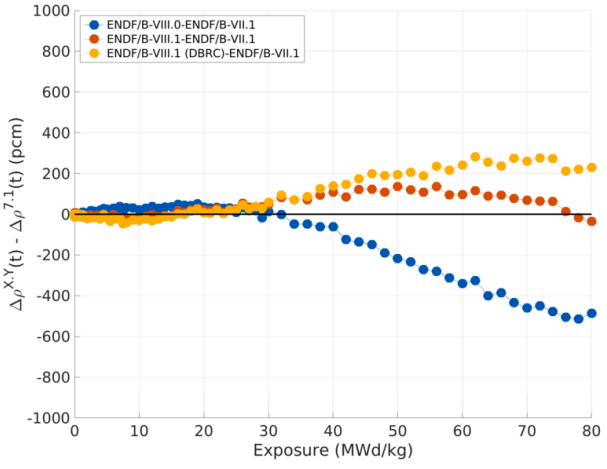


FIG. 204. The reactivity loss difference $\Delta\rho^{XY}(t)$ obtained with the ENDF/B-VIII.0 and ENDF/B-VIII.1 libraries (red and blue curves) is compared to ENDF/B-VII.1 by subtracting the $\Delta\rho^{B71}(t)$ value. The yellow curve represents the reactivity loss change due to the resonance upscattering model (DBRC) obtained with ENDF/B-VIII.1.

b. Modeling of the IRPhE/DUKE benchmark

The IRPhE/DUKE [761] experimental benchmark provides valuable information on the integral prediction of the reactivity decrement during burnup that can be used to assess the depletion reactivity change in LWRs. This has been inferred from an extensive study of differences between 680 core-wide fission rate distribution measurements and calculated neutron flux during 44 cycles PWR operation at McGuire and Catawba NPPs. This magnitude has been demonstrated to be essentially code independent.

The fuel assembly configuration is a typical PWR 17 × 17. The fuel assembly contains 160 rods UO_2 (4.25 wt%), Zircaloy-4 cladding and water with 990 ppm boron as moderator. There are 104 rods with ZrB_2 coating. The burnup is modeled at constant power level of 104.5 W/cm^3, with an average temperature of 900 K in the fuel, 618.4 K in the cladding and 580 K in the moderator.

The `Serpent2` code (Version 2.2.1) is used with a number of neutron histories of 12.8×10^6 (400 active batches of 32,000 neutrons each), which gives a statistical uncertainty in k_∞ of around 15 pcm. To model the burnup, similar options to TMI pincell were used; except for the time integration method, only predictor method with constant extrapolation is used in this calculation. DBRC treatment for ^{238}U is also included in the calculation to show the impact on the burnup reactivity loss. The Serpent2 calculations are performed with ACE-formatted libraries based on ENDF/B-VII.1 distributed by SERPENT, ENDF/B-VIII.0 distributed by LANL and ENDF/B-VIII.1 processed with `NJOY2016.76`. Consistent fission yield and decay data information is used as well.

For this benchmark, the benchmark depletion criticality difference ($\Delta k_{\text{eff}}^{\text{exp}}$) is defined as the Δk_∞ from the initial fresh fuel assembly condition. The fresh fuel is assumed to be at hot full-power (HFP) conditions with burnable absorbers and no Xe, so depletion criticality difference includes the worth of ^{135}Xe as well as the worth of partially depleted burnable absorbers. The PWR depletion benchmark is for one HFP lattice depletion at six specific burnups: 10, 20, 30, 40, 50, and 60 GWd/MTU. The SERPENT 2 code is used to predict the calculated k_∞ for fresh fuel at HFP and no burnup, and the k_∞ for fuel with the specified burnup at the specified temperature. Then, the calculated depletion criticality difference ($\Delta k_{\text{eff}}^{\text{C}}$) is predicted as the Δk_∞ from fresh to the specified burnup. These values are compared with the $\Delta k_{\text{eff}}^{\text{exp}}$ for that burnup. The depletion criticality difference bias ($\Delta k_{\text{eff}}^{\text{C}} - \Delta k_{\text{eff}}^{\text{exp}}$) is shown in Fig. 205.

The 1-sigma total uncertainty of the benchmark depletion criticality difference ($\Delta k_{\text{eff}}^{\text{exp}}$) as a function of the exposure is shown in the shadow area. The ENDF/B-VII.1 is close to the 1-sigma total uncertainty while ENDFB/B-VIII.0 and ENDF/B-VIII.1 are within 2-sigmas. It can be noted a better performance of ENDF/B-VIII.1 at high burnup.

The DBRC correction increases the criticality at the largest calculated 60 MWd/kgU burnup by about 200 pcm for this benchmark.

2. *Depletion calculations using* `Shift`

Shortly after the ENDF/B-VIII.0 release [68], a depletion analysis comparing ENDF/B-VII.1 [162] and ENDF/B-VIII.0 was published by Kim *et al.* [39]; the results showed that reactor criticality using ENDF/B-VIII.0 was underestimated by about -600 pcm at high burnups. A similar method of analysis was performed in this work using the same benchmark problems and the

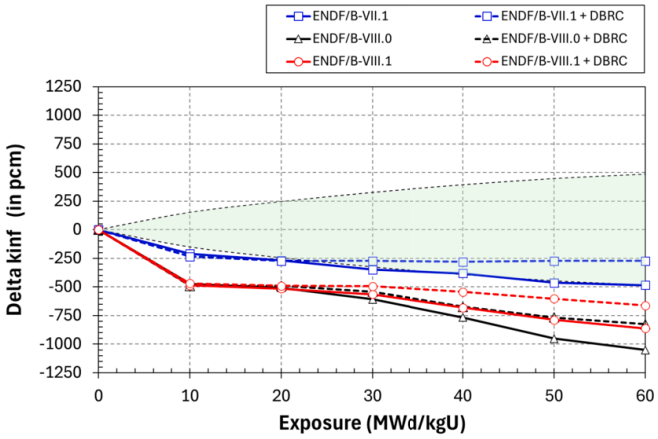


FIG. 205. PWR Fuel Assembly Depletion Criticality Bias (in pcm) of the DUKE-PWR-POWER-001-REAC Benchmark of IRPhE.

ENDF/B-VIII.1 library. This analysis used the new capability in the `Shift` code [762] for massively parallel continuous-energy Monte Carlo calculations with depletion. The total run time for the current analysis was approximately 1.6 CPU-years. The model was a single PWR pin with a reflecting boundary condition based on Virtual Environment for Reactor Applications (VERA) PWR depletion benchmark problem 1C, as described in Kim and Wieselquist [39]. The modeled fuel temperature was 900 K, and all other materials were 600 K. Fresh fuel enrichment was 3.1% ^{235}U. Performance of the full assembly was found to be nearly identical to the single pin problem in Ref. [39], so no full assembly problems were tested. The same fission product yields and decay data as those validated by Ilas *et al.* [763] were used for the present analysis.

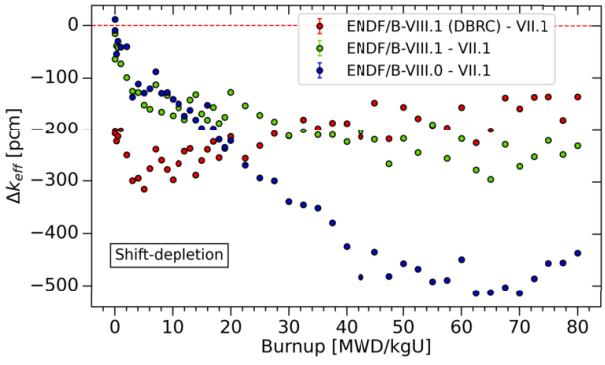


FIG. 206. The depletion calculation for each library is compared to ENDF/B-VII.1 by subtracting the ENDF/B-VII.1 k_{eff} value. The changes made to the neutron sublibrary have a significant impact on reactor criticality as a function of burnup, bringing the performance much closer to the values using ENDF/B-VII.1.

The depletion benchmark results are plotted in Fig. 206. Following the method of Kim *et al.* , each library version used to calculate the effective multiplication of the reactor, k_{eff}, was compared to ENDF/B-VII.1 as a function of burnup. In the figure, the red dashed line at 0 pcm defines the ENDF/B-VII.1 performance, and the blue and green markers represent the difference in k_{eff}, Δk_{eff}, for ENDF/B-VIII.0 and ENDF/B-VIII.1, respectively. Also shown by the red markers is the depletion calculation with ENDF/B-VIII.1 using the DBRC. The DBRC is calculated on-the-fly during transport [764] using the 0 K cross sections from `AMPX` processing (see Section XIII C) and is made available for isotopes of the following elements: Hg, Tl, Pb, Bi, Po, Ra, Ac, Th, Pa, U, Np, Pu, Am, Cm, Bk, Cf, Es, and Fm. The depletion benchmark results indicate that the ENDF/B-VIII.1 library is a significant improvement compared to ENDF/B-VIII.0 and that performance is closer to ENDF/B-VII.1 for high-burnup criticality. The Δk trends shown in Figs. 203 and 206 are slightly different due to the different enrichments and boron concentrations in the two models. The effects of DBRC, however, appear to have a similar magnitude.

3. *Depletion calculations using* `CASMO5`

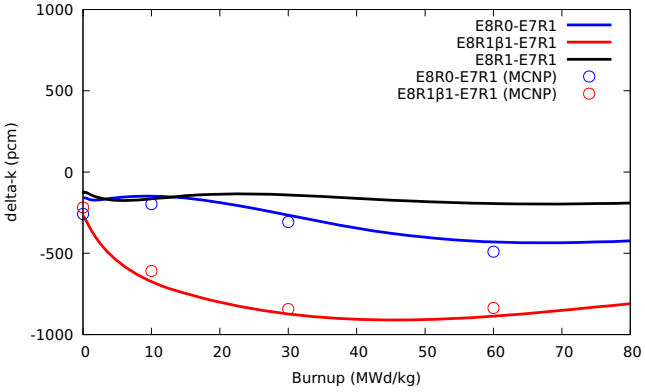


FIG. 207. Comparison of `CASMO5` pincell depletion results for ENDF/B-VIII.0 (E8R0), ENDF/B-VIII.1β1 (E8R1β1), and ENDF/B-VIII.1 (E8R1) with ENDF/B-VII.1 (E7R1).

Initial testing of the ENDF/B-VIII.1β1 and of the final ENDF/B-VIII.1 evaluations was performed by Studsvik using the `CASMO5` advanced lattice physics code [765], which solves fixed-source and eigenvalue problems using the Method of Characteristics (MOC). The burnup calculation uses a predictor-corrector scheme and the Chebyshev Rational Approximation Method (CRAM). Each ENDF/B evaluation has been processed with `NJOY` (`NJOY2016` [325]) and the resulting `CASMO5` multi-group nuclear data library is denoted by the letter "E" followed by the release, revision number and β release if applicable, e.g., the ENDF/B-VIII.1-based `CASMO5` multi-group library is denoted as E8R1. Depletion calculations using `CASMO5` demonstrated a decrease in the ENDF/B-VIII.1β1-predicted k_∞ as a function of burnup relative

to previous libraries [766]. This trend was observed for depletions of a typical single pin cell (Fig. 207), boiling water reactor bundle (Fig. 208), and PWR assembly (Fig. 209), all involving low-enrichment uranium fuel. For instance, the ENDF/B-VIII.1β1-predicted k_∞ was observed to be as much as 600 pcm lower than the ENDF/B-VII.1-based result in the range of 0 to 20 MWd/kg for the PWR assembly depletion case. This trend was verified by performing independent MCNP (MCNPv6.2 [440]) calculations at selected exposure points using the same details as used in the `CASMO5` models. The ^{239}Pu ENDF/B-VIII.1β1 evaluation was identified as the source of most of the discrepancy. The initial ENDF/B-VIII.1β1 had focused mostly on criticality benchmarks and not on depletion results. Although there were many changes between ENDF/B-VIII.1β1 and the final release, the most impactful change was found to be ^{239}Pu [766]. In the end, ENDF/B-VIII.1 was a compromise between optimal performance in criticality and depletion tests, with the latter practically recovering the ENDF/B-VII.1 performance, which is considered here as the reference in reactor applications. Following the release of ENDF/B-VIII.1, which included the revised ^{239}Pu evaluation relative to ENDF/B-VIII.1β1, the `CASMO5` depletions were performed again. Improved agreement was observed between the ENDF/B-VIII.1 results relative to the ENDF/B-VII.1 k_∞ values calculated by `CASMO5` (Figs. 207–209). This agreement is a desirable improvement given that the ENDF/B-VII.1 evaluation, as the basis for the `CASMO5` E7R1 multi-group library, is routinely used for in-core fuel management calculations and found to provide the best agreement with operating power reactor measurements [760].

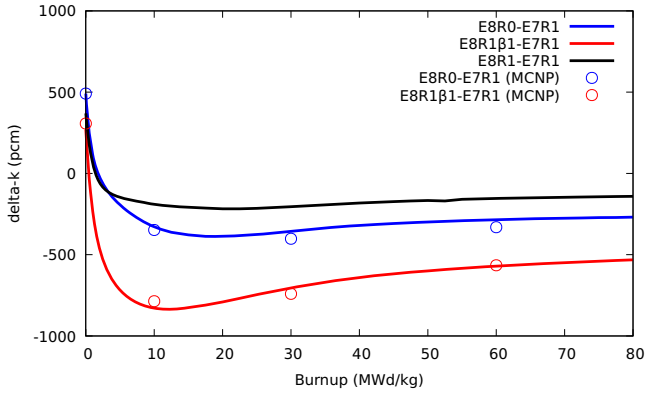


FIG. 208. Comparison of `CASMO5` BWR fuel assembly depletion results for ENDF/B-VIII.0 (E8R0), ENDF/B-VIII.1β1 (E8R1β1), and ENDF/B-VIII.1 (E8R1) with ENDF/B-VII.1 (E7R1).

4. Fuel cycle calculations using CORD-2 and WIMSD-5B

The CORD-2 package [767] is used at the Jožef Stefan Institute in Ljubljana, Slovenia for core design calculations of the Krško NPP. The package uses the WIMSD-5B code [768, 769] for lattice cell calculations. The WIMSD-5B is a 1D reactor lattice transport solver that uses a 69-group library in WIMS-D format [770–772] and features lattice cell homogenization, group condensation and depletion calculations.

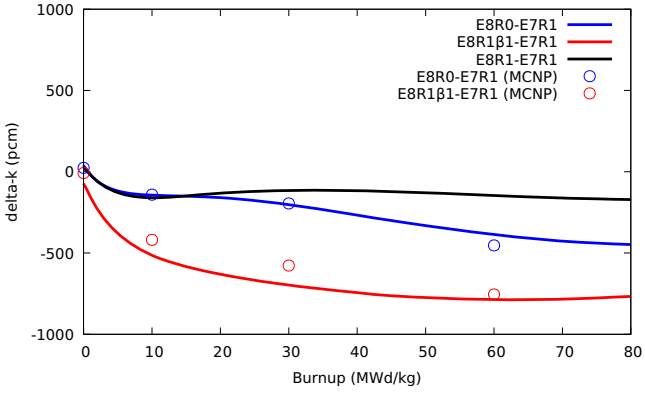


FIG. 209. Comparison of `CASMO5` PWR fuel assembly depletion results for ENDF/B-VIII.0 (E8R0), ENDF/B-VIII.1β1 (E8R1β1), and ENDF/B-VIII.1 (E8R1) with ENDF/B-VII.1 (E7R1).

The WIMSD-5B code was verified by comparing the isotopic composition and reactivity loss with burnup to `Serpent` and `OpenMC` Monte Carlo calculations. The test case was the TMI-1 pin-cell benchmark. For code comparison, the libraries based on ENDF/B-VIII.0 data were used. In the process, the following tests were done:

- The WIMS-D libraries from different evaluated data files were generated with `NJOY2016.75` according to the procedures developed within the WLUP project of the IAEA [771, 772].
- A few explicitly treated fission products were added to the WIMS-D libraries to achieve agreement with `Serpent` and `OpenMC` results. The updated WIMS-D libraries are available from the IAEA web site [770].
- The ^{135}Xe production by the decay of ^{135}I is treated explicitly in WIMS. Small changes (within the uncertainty) of the decay constant of ^{135}I has negligible effect on reactivity as a function of burnup. Changes to the fission yield of ^{135}I (for example, adopting the value from JEFF-3.3) produces a positive shift in reactivity at HFP conditions, but has negligible effect on the reactivity gradient with burnup.
- Taking all fission yield and decay data of the major actinides from JEFF-3.3 increases the reactivity gradient in an unfavourable way.
- The strongest impact on the reactivity gradient comes from the assumptions about the energy released per fission. The option of fixing the energy

released per fission of ^{235}U to $E^* = 202.23$ MeV, defining the ratio $R = E^*/E_{U235}$, where E_{U235} is the fission Q-value in the ENDF file, and normalizing the fission Q-values of all fissile isotopes by this ratio produces a burnup reactivity gradient marginally steeper than predicted by WIMSD-5B. Using a similar assumption in `OpenMC` with $E^* = 205.0$ MeV the same reactivity gradient is reproduced.

Differences in the calculated multiplication factor Δk relative to ENDF/B-VII.1 for short burnups are shown in Fig. 210. As soon as xenon reaches equilibrium, the reactivity is lower by about 300 pcm with ENDF/B-VIII.0 data. About 100 pcm is recovered when ENDF/B-VIII.1 data are used.

The trends for long burnups are shown in Fig. 211. The plot of Δk shows a similar trend like in Fig. 203, but there are some differences, mainly because the absolute k_{eff} calculated with WIMSD-5B has an inherent bias due to the simplified transport model. It has been checked independently that displaying the trends in terms of reactivity loss the agreement is good.

In power reactor operation, the cycle length depends on the loss of reactivity and not on Δk. The reactivity loss as a function of burnup is shown in Fig. 212. To separate out the initial transient when short-lived fission products approach equilibrium, a bias was added to each curve so that reactivities with all libraries coincide at 500 MWd/tU. The plot shows that with ENDF/B-VIII.0 data compared to ENDF/B-VII.1, the reactivity increases by up to 80 pcm below 20 GWd/tU but then decreases sharply, reaching about -600 pcm near 80 GWd/tU. On the contrary, with ENDF/B-VIII.1 data, the increase of reactivity above 500 MWd/tU is smaller, but the total loss of reactivity at 60 GWd/tU compared to ENDF/B-VII.1 stays below 100 pcm.

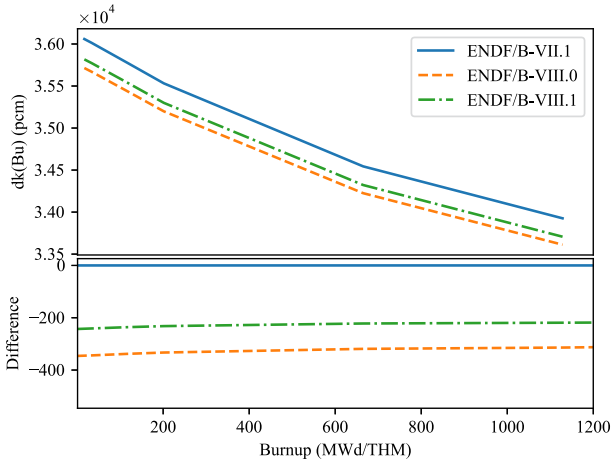


FIG. 210. Differences in the multiplication factor Δk relative to ENDF/B-VII.1 with various version of the ENDF/B libraries at short burnups for the TMI-1 pincell benchmark.

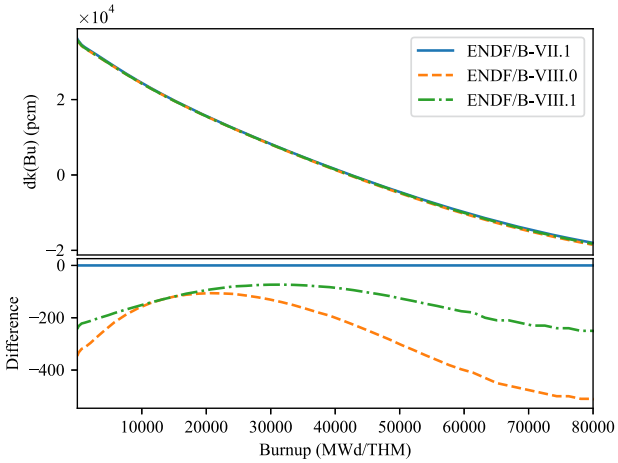


FIG. 211. Differences in the multiplication factor Δk relative to ENDF/B-VII.1 with various version of the ENDF/B libraries at long burnups for the TMI-1 pincell benchmark.

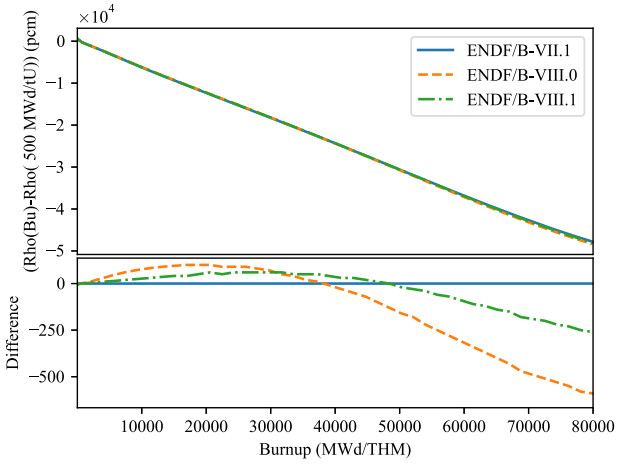


FIG. 212. Reactivity differences relative to ENDF/B-VII.1 with various version of the ENDF/B libraries at long burnups for the TMI-1 pincell benchmark.

Having verified that WIMSD-5B [769] calculations are representative of the detailed Monte Carlo calculations in terms of reactivity, the full core design calculations were launched for 32 cycles of the Krško NPP using WIMS-D 69-group libraries based on the following data:

- ENDF/B-VII.1
- ENDF/B-VIII.0
- ENDF/B-VIII.1

The results were compared against data measured at the plant during startup physics tests and boron concentration monitoring during each cycle.

In Fig. 213, the hot-zero-power (HZP) boron concentrations are compared to measured values. The simple

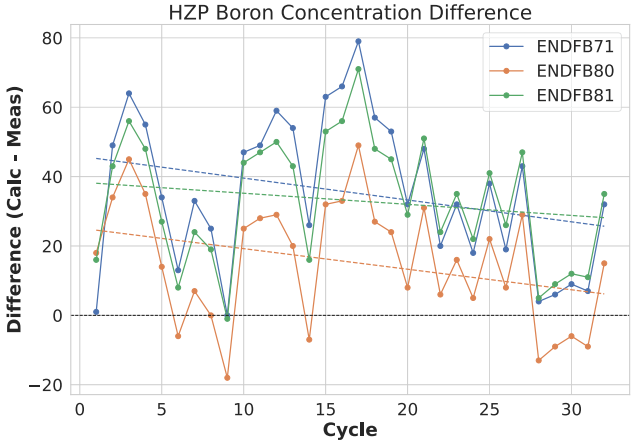


FIG. 213. Critical boron concentration differences with various version of the ENDF/B libraries at HZP conditions of the Krško NPP.

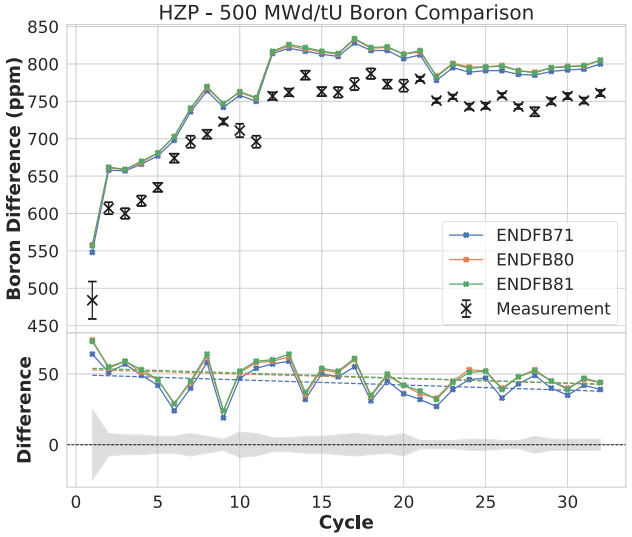


FIG. 214. Differences in the critical boron concentration at HZP and at 500 MWd/tU compared to measured values of the Krško NPP.

1-D transport cell calculations in WIMSD-5B are less accurate than Monte Carlo calculations, so a global bias in terms of a buckling is applied, which normalizes the calculations. In this particular case, a fixed buckling was used so that different libraries could be compared. The scattering is partly due to the simplified computational model, but also partly due to detailed plant specifications, which are not captured in the computational models and can change from cycle to cycle. The review criterion for predicting the critical boron concentration at HZP conditions is 50 ppm.

In spite of the scattering in the calculated values, the relative differences between calculations with different libraries are representative of the differences in the data. We can see that there is some decrease of reactivity with ENDF/B-VIII.0 data, which is partly compensated with ENDF/B-VIII.1 data, which is consistent with the pincell results reported above. There is a slight negative trend with cycle number, but over the last 40 years of operation, the enrichment steadily increased, the low-leakage loading pattern was introduced, burnable absorber rods were replaced by integral fuel burnable absorber rods, and the power rating was increased from 1876 MW to 1994 MW thermal power; thus some differences are not unexpected.

In Fig. 214 the differences in boron concentrations at HZP and at 500 MWd/tU are compared to measured values. This is an indication of the power and xenon defect. We can see that prediction of this defect is too strong. As shown with the testing of the libraries at the cell level, the ^{135}I fission yield in JEFF-3.3 is lower and helps to reduce the power defect. This could be a hint to review the fission yields of ^{135}I, its precursors, and other short-lived fission products in the next library, although a contribution from the simplifications in the thermal hydraulics models are also partly responsible for the differences.

The difference in boron concentration at 500 MWd/tU and at end-of-cycle is closely related to the cycle length. Calculated differences in boron concentration are compared to the measured differences in Fig. 215. From the figure, it is evident that overall the cycle length prediction improves with ENDF/B-VIII.1 data and that the excessive reactivity loss in terms of critical boron concentration is only about 10 ppm on average over 32 cycles of operation.

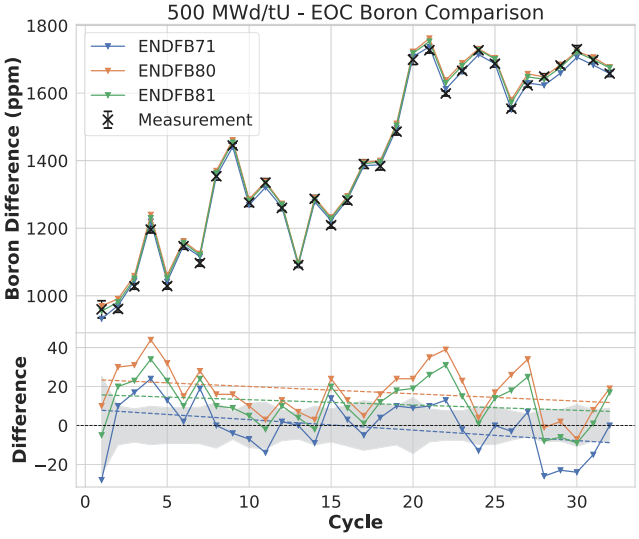


FIG. 215. Differences in the critical boron concentration at 500 MWd/tU and at end-of-cycle compared to measured values of the Krško NPP.

The overall conclusion from the validation exercise with CORD-2 is that the calculations with WIMSD-5B [769] at the cell level are representative of the more accurate Monte Carlo calculations. The full core design calculations show some over-prediction of the power and xenon defect, which could partly be attributed to the fission yield of ^{135}I and its precursors. The cycle length prediction is improved with ENDF/B-VIII.1 data compared to previous versions of the library.

E. Pulsed Spheres Results

LLNL pulsed-spheres measurements provide neutron-leakage spectra over time-of-flight pulsed by a 14-MeV neutron source in the center of the sphere [141]. They allow us to validate nuclear data from 15 MeV down to several MeV dependent on the sphere's thickness and the level scheme of the nuclei at hand [773, 774]. Below, validation results with ENDF/B-VIII.0 and ENDF/B-VIII.1β3 are given. These simulated values are virtually the same as for β4 except for Pb where simulated values for β4 are shown. Also, hints are provided how predictions of neutron-leakage spectra can be improved by nuclear data changes based on sensitivity profiles computed as part of the LANL EUCLID LDRD-DR project [773, 774].

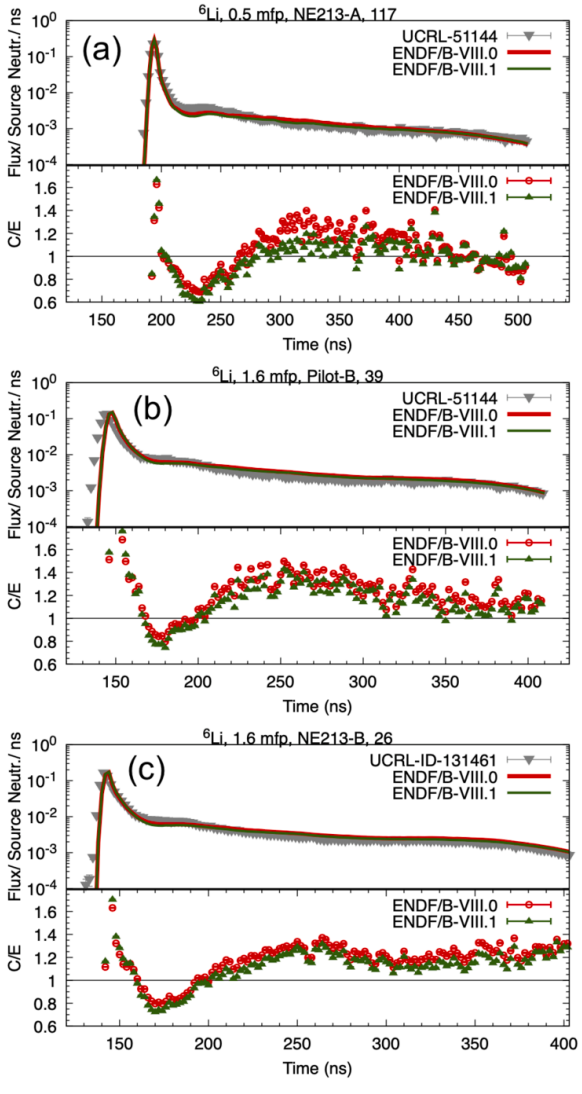


FIG. 216. LLNL pulsed-sphere neutron-leakage spectra simulated with ENDF/B-VIII.0 and ENDF/B-VIII.1 for ^{6}Li compared to experimental data.

^{6}Li LLNL pulsed-sphere neutron-leakage spectra change distinctly in Fig. 216 when simulated with ENDF/B-VIII.0 and ENDF/B-VIII.1. The spheres are thin, with mfp 0.5 and 1.6; little multiple scattering of neutrons will happen and most neutrons will be induced in the sphere by the incident-neutron beam with energies of 12–15 MeV. In this energy range, one major change happened for the ^{6}Li(n,n') cross sections; the reaction was changed from the laboratory to the center-of-mass frame. To be clear, both evaluations are leading to large biases in simulating pulsed-sphere spectra. While the simulations with the new evaluation get closer at later times, it is slightly worse in the peak region and right after. One could study changing MF=$\{3,4\}$ MT=53 for better predicting ^{6}Li LLNL pulsed-sphere neutron-leakage spectra.

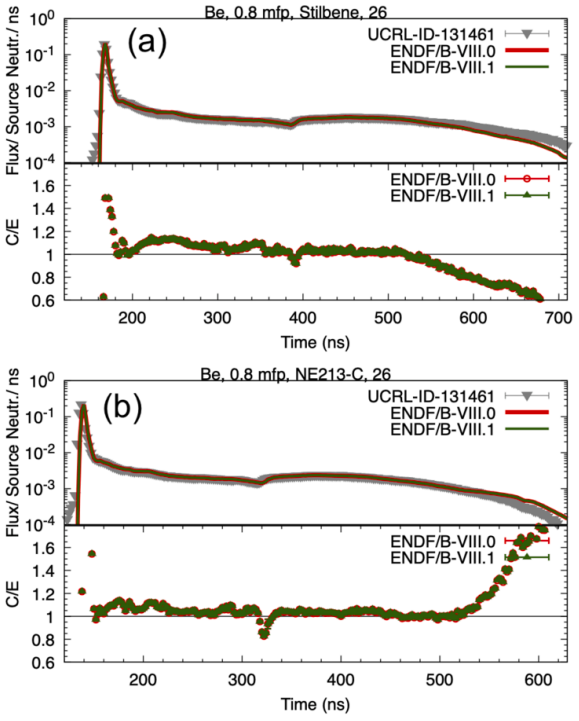


FIG. 217. LLNL pulsed-sphere neutron-leakage spectra simulated with ENDF/B-VIII.0 and ENDF/B-VIII.1 for ^{8}Be compared to experimental data.

The ^{9}Be LLNL pulsed-sphere neutron-leakage spectra in Fig. 217 are described similarly in ENDF/B-VIII.1 to ENDF/B-VIII.0. This similarity was expected given that mostly the capture cross section changed, which would minimally impact the neutron-leakage spectra. In general, the agreement between simulated and experimental data is within the knowledge we have of the pulsed spheres.

There are only small changes observed in the simulations of pulsed spheres containing ^{16}O to a non-negligible amount (light water in Fig. 220, "pure" ^{16}O and heavy water in Fig. 219 and concrete in Fig. 218) if one uses ENDF/B-VIII.0 and ENDF/B-VIII.1 nuclear data. If one would like to improve agreement of simulations right after the peak, one could investigate MF=4, MT=2, and

MF={3, 4}, MT=52, as these ^{16}O observables matter most in the simulations of the spheres shown. Slightly

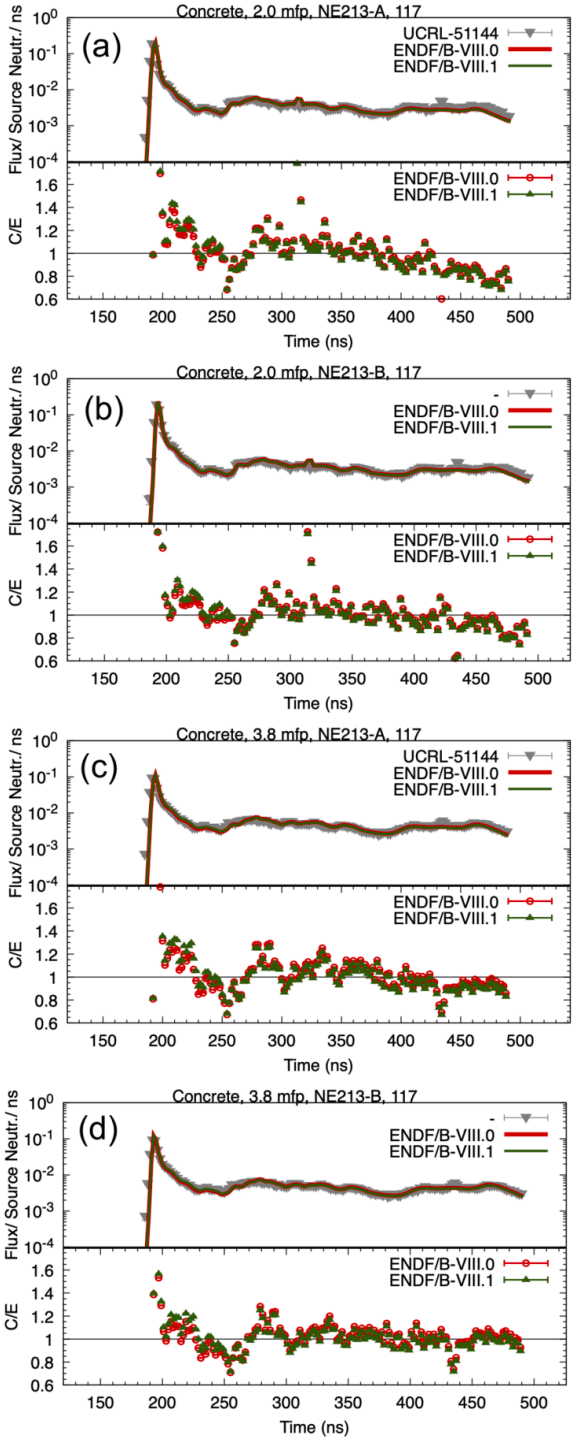


FIG. 218. LLNL pulsed-sphere neutron-leakage spectra simulated with ENDF/B-VIII.0 and ENDF/B-VIII.1 for concrete compared to experimental data.

larger changes are observed between ENDF/B-VIII.0 and ENDF/B-VIII.1 in concrete spheres (Fig. 218) than in the ^{16}O, light and heavy water spheres. The concrete spheres are made up to close to 15% of ^{1}H and Si (mostly

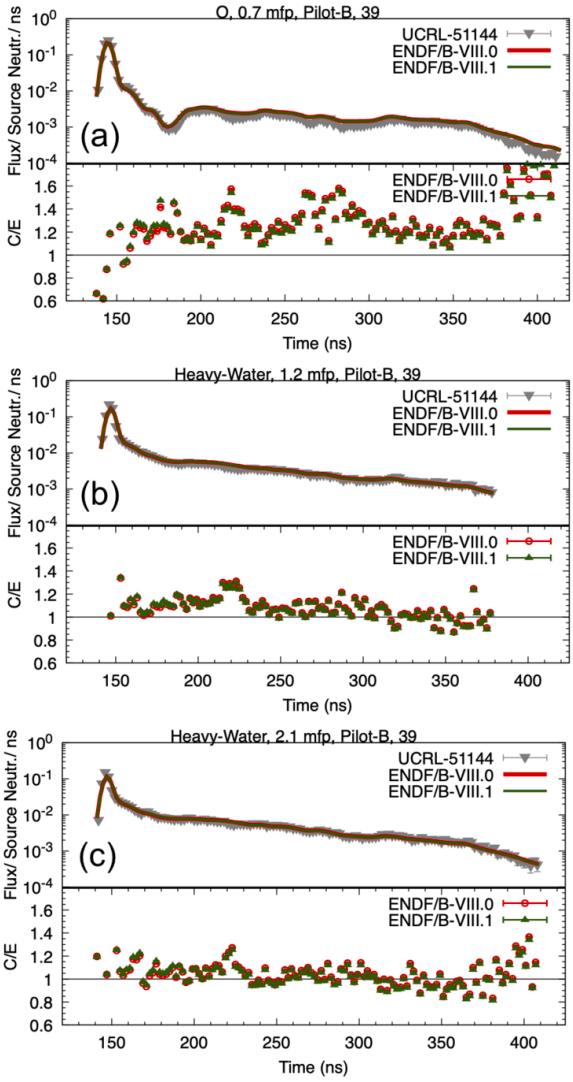


FIG. 219. LLNL pulsed-sphere neutron-leakage spectra simulated with ENDF/B-VIII.0 and ENDF/B-VIII.1 for ^{16}O and heavy water compared to experimental data.

^{28}Si). While ^{1}H nuclear data changed in ENDF/B-VIII.0, the change's impact on light-water spheres is minimal. Hence, the ^{28}Si nuclear data changes can be seen in concrete-sphere spectra but are well within experimental uncertainties. Small improvements can be observed in simulations of Teflon LLNL pulsed-sphere neutron-leakage spectra in Fig. 221 if ENDF/B-VIII.1 nuclear data are used. The overall agreement is poor, which could be either due to carbon or ^{19}F nuclear data given the fact that the predictions of carbon pulsed spheres is also poor. If one would like to try to improve predictions of Teflon pulsed-sphere spectra via ^{19}F nuclear data, one could investigate MF=4, MT=2 and MF={3, 4}, MT=51,55 nuclear data. The updates in Mg ENDF/B-VIII.1 nuclear data compared to ENDF/B-VIII.0 led to only small changes in the simulated Mg LLNL pulsed-sphere neutron-leakage spectra (Fig. 222). These differ-

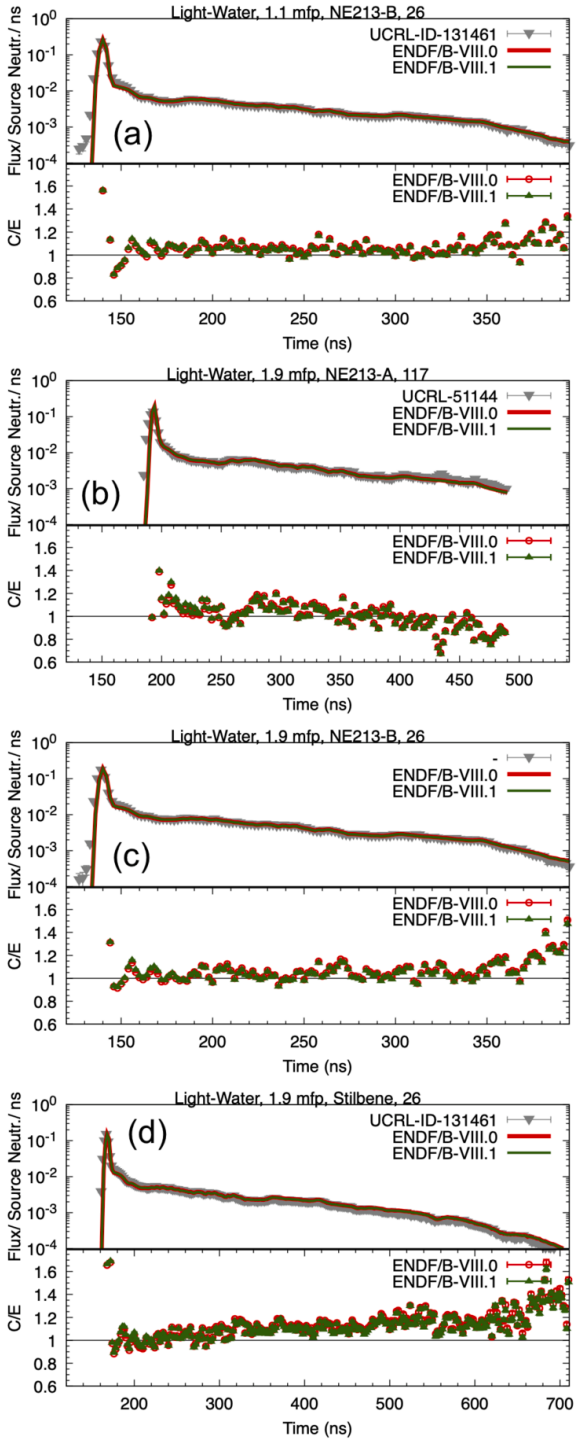


FIG. 220. LLNL pulsed-sphere neutron-leakage spectra simulated with ENDF/B-VIII.0 and ENDF/B-VIII.1 for light water compared to experimental data.

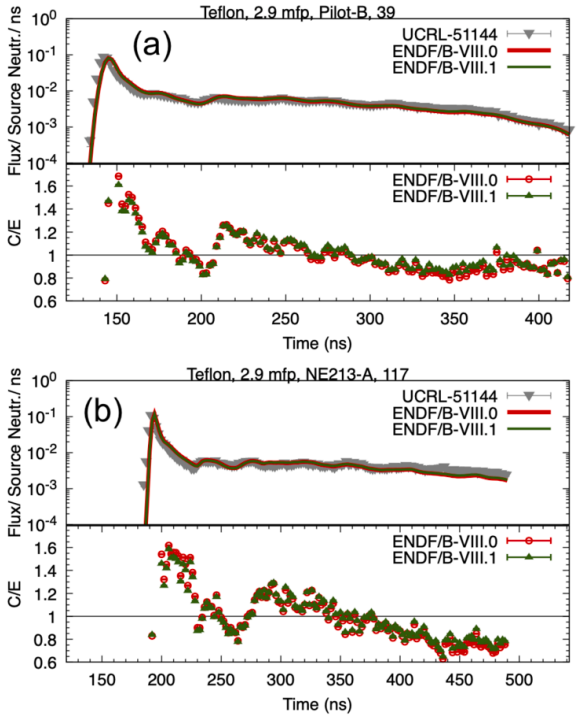


FIG. 221. LLNL pulsed-sphere neutron-leakage spectra simulated with ENDF/B-VIII.0 and ENDF/B-VIII.1 for teflon compared to experimental data.

ences are only at late times and are within experimental uncertainties. In general, the nuclear data describes the spectrum poorly; 79% of the sphere is made up of ^{28}Mg. One could investigate MF=4, MT=2 and MF=$\{3,4,6\}$, MT=$\{2,51,91\}$ nuclear data. The updates for iron nuclear data in ENDF/B-VIII.1 compared to ENDF/B-VIII.0 led to only small changes in the simulated iron LLNL pulsed-sphere neutron-leakage spectra. It can be seen in Fig. 223 that the changes are a bit larger for thicker spheres than thinner ones. The thicker the sphere, the more multiple scattering of neutrons happens, and one uses lower-energy nuclear data (4–10 MeV) for the spectra's simulations. Hence, changes in inelastic data (MF=$\{3,4,6\}$) are likely an important contributor to differences in simulated spectra. If one would like to improve agreement between simulations and experiments at later times, one could investigate at MF=6, MT=91 iron nuclear data. The new ENDF/B-VIII.1 Pb nuclear data led to a distinct change in simulated Pb LLNL pulsed-sphere spectra in Fig. 224 compared to ENDF/B-VIII.0. The agreement is worse from 240–260 ns but better at later times. Future research could study elastic, inelastic and (n,2) for cross sections and angular distributions. Large changes can be observed for ^{239}Pu LLNL pulsed-sphere neutron-leakage spectra in Fig. 225. The main difference between the ENDF/B-VIII.0 and ENDF/B-VIII.1 simulation is caused by (n,inl) and (n,el) cross sections and angular distributions. The ^{235}U LLNL pulsed-sphere neutron-leakage spectra in Fig. 226 are noticeably better described with ENDF/B-VIII.1 data than ENDF/B-VIII.0 in the valley after the elastic peak. This improved agreement was attributed to the new ^{235}U PFNS evalua-

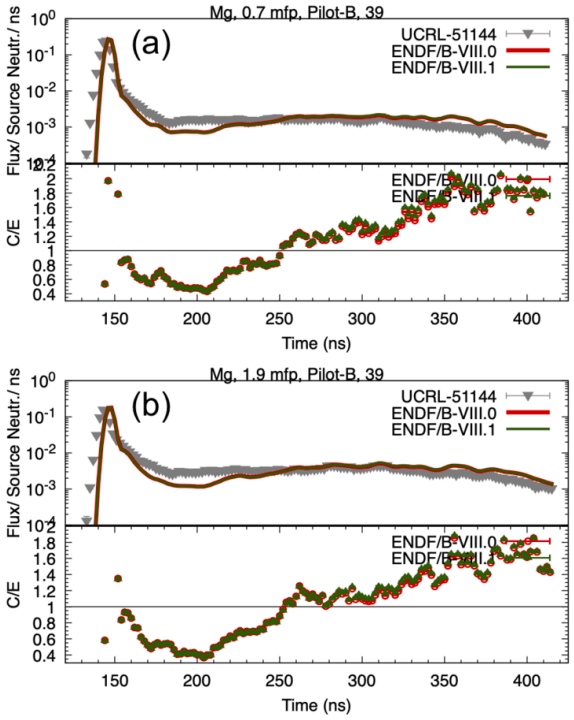


FIG. 222. LLNL pulsed-sphere neutron-leakage spectra simulated with ENDF/B-VIII.0 and ENDF/B-VIII.1 for Mg compared to experimental data.

tion that changed significantly from 12–15 MeV due to inclusion of high-precision Chi-Nu experimental data [250]. Negligible changes were observed between ^{7}Li, ^{12,13}C, ^{27}Al, Ti, and ^{238}U LLNL pulsed-sphere neutron-leakage spectra simulated with ENDF/B-VIII.0 and ENDF/B-VIII.1β1 despite changes in the nuclear data.

XV. CONCLUSIONS & FUTURE WORK

The ENDF/B-VIII.1 library constitutes a substantive advance in the development of evaluated nuclear data, representing an improvement on its predecessor ENDF/B-VIII.0. Through the integration of new evaluations (informed by new experimental data, theory and evaluation methods), adoption of international collaborative efforts, and implementation of improved validation and peer-review protocols, this library provides enhanced fidelity and robustness for applications across the nuclear sciences. Throughout we strove to adhere to these key principles:

- Do no harm
- Be aware of historical and previous evaluation decisions
- Ensure proposed changes are demonstrably better
- Anticipate potential problems and conduct validation testing

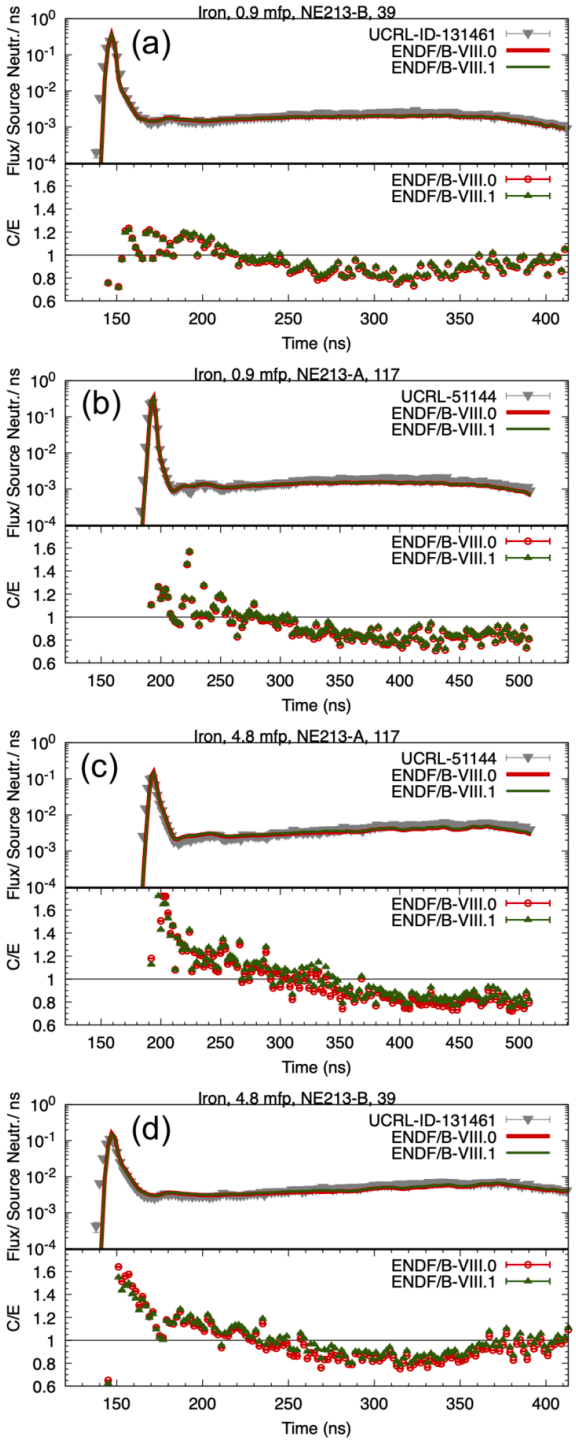


FIG. 223. LLNL pulsed-sphere neutron-leakage spectra simulated with ENDF/B-VIII.0 and ENDF/B-VIII.1 for iron compared to experimental data.

The main achievements of ENDF/B-VIII.1 may be summarized as follows:

- Extensive updates to important actinide and structural material evaluations, notably isotopes of ura-

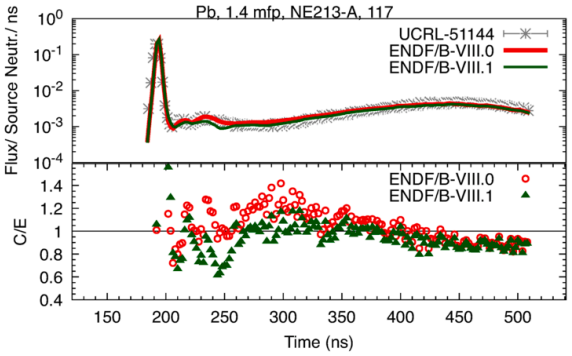


FIG. 224. LLNL pulsed-sphere neutron-leakage spectra simulated with ENDF/B-VIII.0 and ENDF/B-VIII.1 for Pb compared to experimental data.

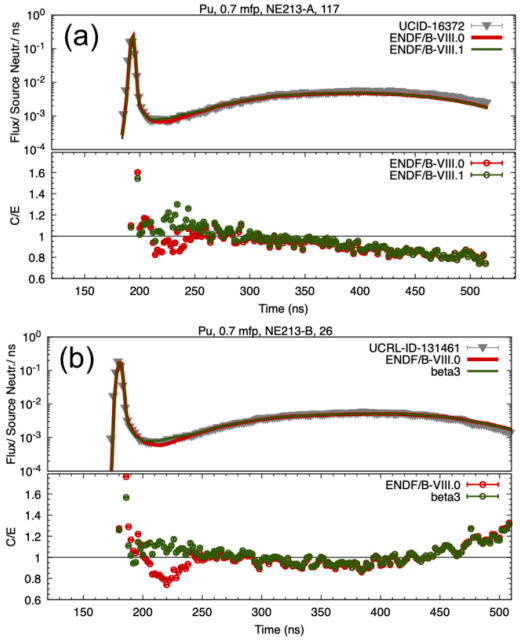


FIG. 225. LLNL pulsed-sphere neutron-leakage spectra simulated with ENDF/B-VIII.0 and ENDF/B-VIII.1 for Pu compared to experimental data.

nium, plutonium, fluorine, silicon, chromium, iron, copper, tantalum, and lead.

- Incorporation of high-quality evaluations from international collaborations, such as INDEN and IRDFF-II, which significantly improve neutron dosimetry standards and reactor benchmark performance.

- Introduction of new and reevaluated thermal-neutron scattering kernels, thereby broadening the coverage and accuracy of low-energy neutron interaction data.

- Resolution of deficiencies in high burnup reactor applications through improved resonance region data for key actinides, thereby enhancing the perfor-

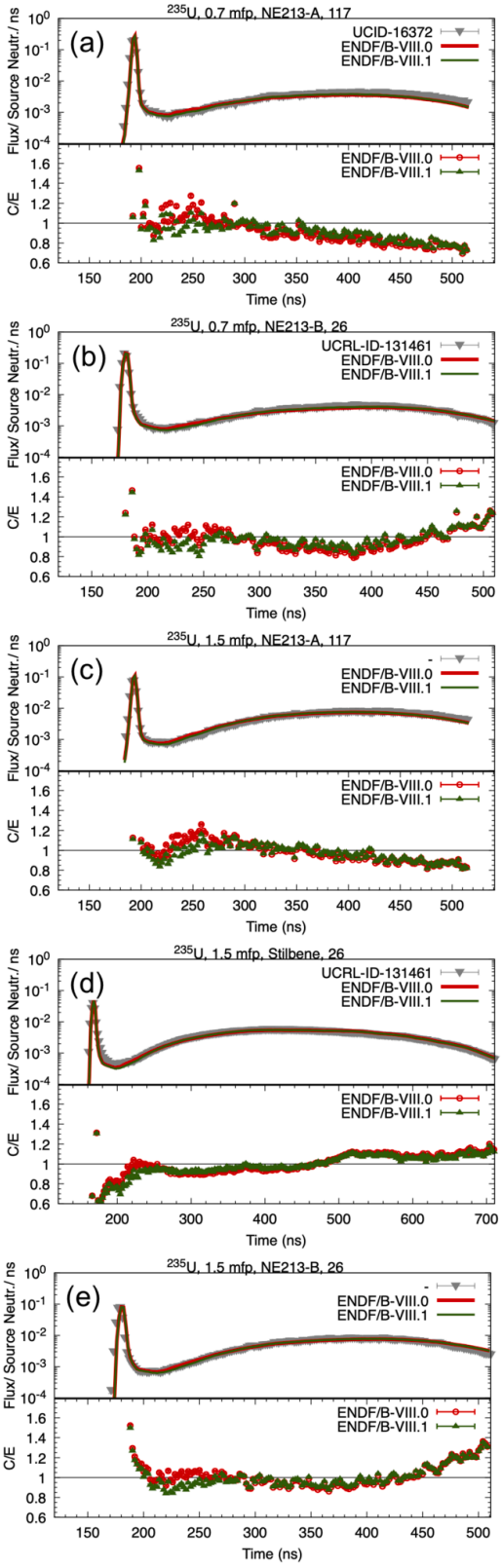


FIG. 226. LLNL pulsed-sphere neutron-leakage spectra simulated with ENDF/B-VIII.0 and ENDF/B-VIII.1 for ^{235}U compared to experimental data.

mance of nuclear data libraries for power reactor simulations.

- Adoption of modern covariance methodologies and improved uncertainty quantification standards, providing more rigorous support for uncertainty propagation in nuclear applications.
- Implementation of a fully online, transparent peer-review and validation workflow, ensuring reproducibility, traceability, and community-wide engagement in the evaluation process.
- Library release in the ENDF-6 and GNDS format.
- Marked improvement in the agreement with fundamental cross-section data, together with demonstrably improved predictive performance for integral critical assembly experimental benchmarks.

Collectively, these advancements underscore the technical maturity and expanded scope of the ENDF/B-VIII.1 release. By improving both differential cross-section fidelity and integral benchmark predictive capability, the library is a cornerstone for modern nuclear data applications. This release not only sustains confidence in current engineering and scientific uses but also establishes a robust foundation for addressing the demands of next-generation applications.

ENDF/B-VIII.1 is most likely the last release of the ENDF/B-VIII series as the next ENDF/B release is expected to contain a new Nuclear Data Standards set of evaluations. ENDF/B-VIII.1 is also expected to be the last ENDF/B library to be released primarily in the legacy ENDF-6 format as ENDF/B-IX.0 is expected to be released in the GNDS format.

In addition to these major changes, we can expect the usual battery of smaller changes, focusing on not just library quality improvements, but on adding features addressing emerging nuclear data needs. These needs often are hard to predict five to six years before another release, but we do expect new generation of nuclear reactors, SMR, fusion and space physics to drive new evaluation efforts. We also hope that the increasing reliance on AI/ML techniques will improve the quality and reach of the library. We also expect these techniques to enable new ways to prioritize evaluations and identify new work that can deliver the greatest impacts to users.

ACKNOWLEDGMENTS

Work at Brookhaven National Laboratory was sponsored by the Office of Nuclear Physics, Office of Science of the U.S. Department of Energy under Contract No. DE-SC0012704 with Brookhaven Science Associates, LLC. Work at Lawrence Livermore National Laboratory was performed under Contract DE-AC52-07NA27344. Work at Los Alamos National Laboratory, operated by Triad National Security, LLC, was carried out under the auspices of the National Nuclear Security Administration of the U.S. Department of Energy under Contract No. 89233218CNA000001. Work at Oak Ridge National Laboratory was authored by UT-Battelle, LLC under Contract No. DE-AC05-00OR22725 with the U.S. Department of Energy. Work at Argonne National Laboratory was supported by the U.S. Department of Energy, Office of Science, under Contract DE-AC02-06CH11357. Work at Naval Nuclear Laboratory, operated by Fluor Marine Propulsion, LLC, was performed under Contract No. 89233018CNR000004 with the U.S. Department of Energy. This work was supported by the Naval Nuclear Propulsion Program and Nuclear Criticality Safety Program, funded and managed by the National Nuclear Security Administration for the U.S. Department of Energy. This work received funding support from the National Nuclear Security Administration, Office of Defense Nuclear Nonproliferation R&D.

The U.S. Government retains right to use the published form of this manuscript, or allow others to do so, for U. S. Government purposes.

[1] A. Carlson, V. Pronyaev, R. Capote, *et al.*, "Evaluation of the Neutron Data Standards," Nucl. Data Sh. **148**, 143 (2018). Special Issue on Nuclear Reaction Data, [Online] Available at https://www.sciencedirect.com/science/article/pii/S0090375218300218.

[2] A. Trkov, P. Griffin, S. Simakov, *et al.*, "IRDFF-II: A new neutron metrology library," Nucl. Data Sh. **163**, 1 (2020). [Online] Available at https://doi.org/10.1016/j.nds.2019.12.001.

[3] M. B. Chadwick, M. W. Paris, G. M. Hale, J. P. Lestone, S. Alhumaidi, J. B. Wilhelmy, and N. A. Gibson, "Early Nuclear Fusion Cross-Section Advances 1934–1952 and Comparison to Today's ENDF Data," Fusion Sci. Techn. **80**, S9 (2024). [Online] Available at https://doi.org/10.1080/15361055.2023.2297128.

[4] M. B. Chadwick and B. C. Reed, "Introduction to special issue on the early history of nuclear fusion," Fusion Sci. Techn. **80**, iii (2024). [Online] Available at https://doi.org/10.1080/15361055.2024.2346868.

[5] M. B. Chadwick, "FST publishes special issue on fusion's early history," Am. Nucl. Soc. Nucl. News **67**, 14 (2024).

[6] M. B. Chadwick, "The Manhattan Project nuclear science and technology developments at Los Alamos: A special issue of Nuclear Technology," Nucl. Techn. **207**, iii (2021). [Online] Available at https://doi.org/10.1080/00295450.2021.1903301.

[7] M. B. Chadwick, "Nuclear science for the Manhattan Project and comparison to today's ENDF data," Nucl. Techn. **207**, S24 (2021). [Online] Available at https://doi.org/10.1080/00295450.2021.1901002.

[8] H. Abu-Shawareb, R. Acree, P. Adams, *et al.* (Indirect Drive ICF Collaboration), "Lawson criterion for ignition exceeded in an inertial fusion experiment," Phys. Rev. Lett. **129**, 075001 (2022). [Online] Available at https://link.aps.org/doi/10.1103/PhysRevLett.129.075001.

[9] B. T. Rearden, "Space reactors," (2021). Presented at WANDA 2021, [Online] Available at https://conferences.lbl.gov/event/504/contributions/4117/attachments/3124/1772/REARDEN_-_WANDA_2021_-_Space_Reactors.pdf.

[10] M. Wall, "NASA, DARPA to launch nuclear rocket to orbit by early 2026," (2023). Retrieved from Space.com 24 Sep. 2024, [Online] Available at https://www.space.com/nasa-darpa-nuclear-thermal-rocket-draco-2026.

[11] M.-L. Mauborgne, F. Allioli, C. Stoller, M. Evans, M. Manclossi, and L. Nicoletti, "Exploring for oil with nuclear physics," EPJ. Web. Conf. **146** (2017). [Online] Available at https://doi.org/10.1051/epjconf/201714609009.

[12] S. McConchie, L. Bernstein, M. Blackston, D. Brown, B. Canion, C. Romano, and J. Verbeke, "Assessment of modeling and nuclear data needs for active neutron interrogation," Tech. Rep. **ORNL/TM-2021/1900**, Oak Ridge National Laboratory (2021). [Online] Available at https://doi.org/10.2172/1778086.

[13] J. Engle, A. Hermanne, A. Nichols, and R. Capote Noy, "Summary Report of the Technical Meeting on Nuclear Data for Medical Applications, 28-31 August 2023, Vienna, Austria," Tech. Rep. **INDC(NDS)-0884**, International Atomic Energy Agency, Vienna, Austria (2024). [Online] Available at https://doi.org/10.61092/iaea.aktc-t5yh.

[14] T. Kawano, Y. Cho, P. Dimitriou, *et al.*, "IAEA photonuclear data library 2019," Nucl. Data Sh. **163**, 109 (2020). [Online] Available at https://www.sciencedirect.com/science/article/pii/S0090375219300699.

[15] IAEA-CRP, "Handbook on photonuclear data for applications, cross-sections and spectra, final report of a co-ordinated research project 1996–1999," Tech. Rep. **IAEA-TECDOC-1178**, International Atomic Energy Agency, Vienna, Austria (2000). [Online] Available at https://www-pub.iaea.org/MTCD/Publications/PDF/te_1178_prn.pdf.

[16] O. Iwamoto, N. Iwamoto, S. Kunieda, *et al.*, "Japanese Evaluated Nuclear Data Library version 5: JENDL-5," J. Nucl. Sci. Technol. (Tokyo) **60**, 1 (2023). [Online] Available at https://doi.org/10.1080/00223131.2022.2141903.

[17] R. M. White, D. A. Resler, and S. I. Warshaw, "Evaluation of charged-particle reactions for fusion applications," in *Nuclear Data for Science and Technology, Juelich, Germany* (S. M. Qaim, ed.), 834, Springer Berlin Heidelberg (1992).

[18] National Nuclear Data Center, "NNDC Gitlab I," (2024). [Online] Available at https://git.nndc.bnl.gov.

[19] "ENDF/B-VIII.1 release." https://doi.org/10.11578/endf/2571019 (2024).

[20] "ENDF/B-VIII.1 release – alphas sublibrary." https://doi.org/10.11578/endf/2571012 (2024).

[21] "ENDF/B-VIII.1 release – atomic relaxation sublibrary." https://doi.org/10.11578/endf/2571013 (2024).

[22] "ENDF/B-VIII.1 release – decay sublibrary." https://doi.org/10.11578/endf/2571014 (2024).

[23] "ENDF/B-VIII.1 release – deuterons sublibrary." https://doi.org/10.11578/endf/2571015 (2024).

[24] "ENDF/B-VIII.1 release – electrons sublibrary." https://doi.org/10.11578/endf/2571016 (2024).

[25] "ENDF/B-VIII.1 release – photonuclear sublibrary." https://doi.org/10.11578/endf/2571020 (2024).

[26] "ENDF/B-VIII.1 release – helions sublibrary." https://doi.org/10.11578/endf/2571021 (2024).

[27] "ENDF/B-VIII.1 release – neutrons sublibrary." https://doi.org/10.11578/endf/2571022 (2024).

[28] "ENDF/B-VIII.1 release – neutron-induced fission product yields sublibrary." https://doi.org/10.11578/endf/2571023 (2024).

[29] "ENDF/B-VIII.1 release – photo-atomic sublibrary." https://doi.org/10.11578/endf/2571024 (2024).

[30] "ENDF/B-VIII.1 release – protons sublibrary." https://doi.org/10.11578/endf/2571025 (2024).

[31] "ENDF/B-VIII.1 release – spontaneous fission product yields sublibrary." https://doi.org/10.11578/endf/2571026 (2024).

[32] "ENDF/B-VIII.1 release – standards sublibrary." https://doi.org/10.11578/endf/2571027 (2024).

[33] "ENDF/B-VIII.1 release – thermal scattering law sublibrary." https://doi.org/10.11578/endf/2571028 (2024).

[34] "ENDF/B-VIII.1 release – tritons sublibrary." https://doi.org/10.11578/endf/2584305 (2024).

[35] K. Kelly, P. Marini, J. Taieb, *et al.*, "Comparison of results from recent NNSA and CEA Measurements of the ^{239}Pu(n,f) prompt fission neutron spectrum," Nucl. Data Sh. **173**, 42 (2021). Special Issue on Nuclear Reaction Data, [Online] Available at https://www.sciencedirect.com/science/article/pii/S0090375221000132.

[36] P. Marini, J. Taieb, B. Laurent, *et al.*, "Prompt-fission-neutron spectra in the ^{239}Pu(n,f) reaction," Phys. Rev. **C101**, 044614 (2020). [Online] Available at https://link.aps.org/doi/10.1103/PhysRevC.101.044614.

[37] K. J. Kelly, M. Devlin, J. M. O'Donnell, *et al.*, "Measurement of the ^{239}Pu(n, f) prompt fission neutron spectrum from 10 keV to 10 MeV induced by neutrons of energy 1–20 MeV," Phys. Rev. **C102**, 034615 (2020). [Online] Available at https://link.aps.org/doi/10.1103/PhysRevC.102.034615.

[38] D. Neudecker, A. E. Lovell, K. J. Kelly, P. Marini, L. Snyder, M. C. White, P. Talou, M. Devlin, J. Taieb, and M. B. Chadwick, "Shedding light on the ^{239}Pu fission source term with new high-precision experiments and advanced fission modeling," Front. Phys. **10** (2023). [Online] Available at https://www.frontiersin.org/articles/10.3389/fphy.2022.1056324.

[39] K.-S. Kim and W. A. Wieselquist, "Neutronic characteristics of ENDF/B-VIII.0 compared to ENDF/B-VII.1 for light-water reactor analysis," J. Nucl. Eng. **2**, 318 (2021). [Online] Available at https://www.mdpi.com/2673-4362/2/4/26.

[40] R. Gwin, R. Spencer, and R. Ingle, "Measurements of the energy dependence of prompt neutron emission from ^{233}U, ^{235}U, ^{239}Pu, and ^{241}Pu for $E_n = 0.005$ to 10 eV relative to emission from spontaneous fission of ^{252}Cf,"

Nucl. Sci. Eng. **87**, 381 (1984).
[41] R. R. S. R. Gwin and R. W. Ingle, "Measurements of the energy dependence of prompt neutron emission from ^{233}U, ^{235}U, and ^{239}Pu for En = 0.0005 to 10 MeV relative to emission from spontaneous fission of ^{252}Cf," Nucl. Sci. Eng. **94**, 365 (1986).
[42] K. Nishio, Y. Nakagome, I. Kanno, and I. Kimura, "Measurement of fragment mass dependent kinetic energy and neutron multiplicity for thermal neutron induced fission of plutonium-239," J. Nucl. Sci. Techn. **32**, 404 (1995). [Online] Available at https://doi.org/10.1080/18811248.1995.9731725.
[43] K. Volodin, V. Kuznetsov, V. Nesterov, B. Nurpeisov, L. Prokhorova, Y. Turchin, and G. Smirenkin, "Average number of prompt neutrons nubar for ^{239}Pu fission by neutrons having an energy up to 1.6 MeV," Sov. Atom. En. **33**, 1045 (1972).
[44] R. Capote, Y.-J. Chen, F.-J. Hambsch, *et al.*, "Prompt fission neutron spectra of actinides," Nucl. Data Sh. **131**, 1 (2016). Special Issue on Nuclear Reaction Data, [Online] Available at https://www.sciencedirect.com/science/article/pii/S0090375215000678.
[45] N. Otuka, E. Dupont, V. Semkova, *et al.*, "Towards a more complete and accurate experimental nuclear reaction data library (EXFOR): International collaboration between nuclear reaction data centres (NRDC)," Nucl. Data Sh. **120**, 272 (2014). [Online] Available at https://www.sciencedirect.com/science/article/pii/S0090375214005171.
[46] P. Marini, J. Taieb, D. Neudecker, *et al.*, "Energy dependence of prompt fission neutron multiplicity in the ^{239}Pu(n, f) reaction," (2021). [Online] Available at https://arxiv.org/abs/2109.14330.
[47] Marini, P., Taieb, J., Neudecker, D., *et al.*, "Multiplicity of prompt fission neutron in the ^{239}Pu(n,f) reaction and its energy dependence," EPJ. Web. Conf. **294**, 02002 (2024). [Online] Available at https://doi.org/10.1051/epjconf/202429402002.
[48] D. Neudecker, A. Lovell, T. Kawano, and P. Talou, "Evaluated ^{238}U(n,f) average prompt fission neutron multiplicities including the CGMF Model," Tech. Rep. **LA-UR-21-29906**, Los Alamos National Laboratory, NM, USA (2022). [Online] Available at https://www.osti.gov/servlets/purl/1889944.
[49] D. Neudecker, A. D. Carlson, S. Croft, M. Devlin, K. J. Kelly, A. E. Lovell, P. Marini, and J. Taieb, "Templates of expected measurement uncertainties for average prompt and total fission neutron multiplicities," EPJ. Nucl. Sci. Techn. **9**, 30 (2023). [Online] Available at https://doi.org/10.1051/epjn/2023016.
[50] P. Talou, I. Stetcu, P. Jaffke, M. Rising, A. Lovell, and T. Kawano, "Fission fragment decay simulations with the CGMF code," Comput. Phys. Commun. **269**, 108087 (2021). [Online] Available at https://doi.org/10.1016%2Fj.cpc.2021.108087.
[51] B. C. Diven, H. C. Martin, R. F. Taschek, and J. Terrell, "Multiplicities of Fission Neutrons," Phys. Rev. **101**, 1012 (1956). EXFOR entry: 12337.004, [Online] Available at https://link.aps.org/doi/10.1103/PhysRev.101.1012.
[52] J. Hopkins and B. Diven, "Prompt neutrons from fission," Nucl. Phys. **48**, 433 (1963). ERXFOR entry: 40148.005, [Online] Available at https://www.sciencedirect.com/science/article/pii/0029558263901822.
[53] R. Gwin, R. Spencer, and R. Ingle, "Measurements of the Energy Dependence of Prompt Neutron Emission from ^{233}U, ^{235}U, and 239Pu for E_n = 0.0005 to 10 MeV Relative to Emission from Spontaneous Fission of ^{252}Cf," Nucl. Sci. Eng. **94**, 365 (1986). EXFOR entry: 13101.004, [Online] Available at https://doi.org/10.13182/NSE86-A18347.
[54] P. Marini, J. Taieb, D. Neudecker, *et al.*, "Energy dependence of prompt fissions neutron multiplicity in the 239pu(n,f) reaction," Phys. Lett. B **835**, 137513 (2022). [Online] Available at https://www.sciencedirect.com/science/article/pii/S0370269322006475.
[55] D. Mather, P. Fieldhouse, and A. Moat, "Measurement of prompt ν for the neutron-induced fission of Th^{232}, U^{233}, U^{234}, U^{238} and Pu^{239}," Nucl. Phys. **66**, 149 (1965). EXFOR entry: 21135.007 & 008, 20453.002 & 003, [Online] Available at https://www.sciencedirect.com/science/article/pii/0029558265901392.
[56] B. Nurpeisov, K. Volodin, L. P. V.G. Nesterov, G. Smirenkin, and Y. Turchin, "Dependence of $\overline{\nu}$ on neutron energies up to 5 MeV for ^{233}U, ^{238}U, and ^{239}Pu," Sov. Atom. En. **39**, 807 (1975). EXFOR entry: 40429.004.
[57] K. Bolodin, V. Kuznetsov, V. Nesterov, B. Nurpeisov, L. Prokhorova, Y. Turchin, and G. Smirenkin, "Average Number of Prompt Neutrons in Pu^{239} Fission," Sov. Atom. En. **33**, 1045 (1972). ERXFOR entry: 40148.003 & 005.
[58] M. Savin, Y. Khokhlov, Y. Zamjatnin, and I. Paramonova, "The average number of prompt neutrons in fast neutron induced fission of ^{235}U and ^{239}Pu," in *Nuclear Data for Reactors Conf., Helsinki*, **2, IAEA-CN-26/40**, 157 (1970). EXFOR entry: 40058.003, [Online] Available at https://www-nds.iaea.org/publications/proceedings/sti-pub-259-Vol2.pdf.
[59] M. Soleilhac, J. Fréhaut, J. Gauriau, and G. Mosinski, "Average Number Of Prompt Neutrons And Relative Fission Cross-Sections Of U-235 And Pu-239 In The 0.3 To 1.4 MeV Range," in *Nuclear Data for Reactors Conf., Helsinki*, **2, IAEA-CN-26/67**, 145 (1970). EXFOR entry: 20568.004, [Online] Available at https://www-nds.iaea.org/publications/proceedings/sti-pub-259-Vol2.pdf.
[60] R. Walsh and J. Boldeman, "The energy dependence of ν_p for ^{233}U, ^{235}U and ^{239}Pu below 5·0 MeV," J. Nucl. En. **25**, 321 (1971). EXFOR entry: 30006.004, [Online] Available at https://www.sciencedirect.com/science/article/pii/0022310771900645.
[61] H. Condé, J. Hansén, and M. Holmberg, "Prompt ν in neutron-induced fission of ^{239}Pu and ^{241}Pu," J. Nucl. En. **22**, 53 (1968). EXFOR entry: 20052.002, [Online] Available at https://www.sciencedirect.com/science/article/pii/0022310768900646.
[62] J. Fréhaut, G. Mosinski, and M. Soleilhac, "Recent results in $\overline{\nu}_p$ measurements between 1.5 and 15 MeV," in $\overline{\nu}_p$ *The average Number of Emitted Neutrons in Fission, Contributions to the EANDC Topical Conference held on Novembre 29, 1972*, **EANDC(E)-154"U"**, 67 (1973). EXFOR entry: 20490.003.
[63] M. Savin, Y. Khokhlov, A. Savelév, and I. Paramonova, "Energy Dependence of $\overline{\nu}$ in the Fission of U^{235} by Fast Neutrons," Sov. J. Nucl. Phys. **16**, 638 (1973). EXFOR entry: 40523.002.

[64] A. J. Plompen, O. Cabellos, C. D. S. Jean, *et al.*, "The Joint Evaluated Fission and Fusion Nuclear Data Library, JEFF-3.3," Eur. Phys. J. **A56**, 181 (2020). [Online] Available at https://doi.org/10.1140/epja/s10050-020-00141-9.

[65] J. Lestone and E. Shores, "Uranium and Plutonium Average Prompt-fission Neutron Energy Spectra (PFNS) from the Analysis of NTS NUEX Data," Nucl. Data Sh. **119**, 213 (2014). [Online] Available at https://www.sciencedirect.com/science/article/pii/S0090375214005936.

[66] A. Chatillon, G. Bélier, T. Granier, *et al.*, "Measurement of prompt neutron spectra from the ^{239}pu(n,f) fission reaction for incident neutron energies from 1 to 200 mev," Phys. Rev. C **89**, 014611 (2014). [Online] Available at https://link.aps.org/doi/10.1103/PhysRevC.89.014611.

[67] R. Capote, A. Trkov, M. Sin, *et al.*, "IAEA CIELO evaluation of neutron-induced reactions on ^{235}U and ^{238}U targets," Nucl. Data Sh. **148**, 254 (2018). Special Issue on Nuclear Reaction Data, [Online] Available at https://www.sciencedirect.com/science/article/pii/S0090375218300243.

[68] D. Brown, M. Chadwick, R. Capote, *et al.*, "ENDF/B-VIII.0: The 8th major release of the nuclear reaction data library with CIELO-project cross sections, new standards and thermal scattering data," Nucl. Data Sh. **148**, 1 (2018).

[69] D. Neudecker, K. Kelly, and P. Marini, "Release of Evaluated ^{239}Pu(n,f) Prompt Fission Neutron Spectra Including the CEA and Chi-Nu High-precision Experimental Data," Tech. Rep. **LA-UR-22-23754**, Los Alamos National Laboratory, NM, USA (2022).

[70] D. Neudecker, P. Talou, T. Kawano, *et al.*, "Evaluations of energy spectra of neutrons emitted promptly in neutron-induced fission of ^{235}U and ^{239}Pu," Nucl. Data Sh. **148**, 293 (2018). Special Issue on Nuclear Reaction Data, [Online] Available at https://www.sciencedirect.com/science/article/pii/S0090375218300255.

[71] K. J. Kelly, T. Kawano, J. M. O'Donnell, *et al.*, "Prequilibrium Asymmetries in the ^{239}Pu(n,f) Prompt Fission Neutron Spectrum," Phys. Rev. Lett. **122**, 072503 (2019). [Online] Available at https://link.aps.org/doi/10.1103/PhysRevLett.122.072503.

[72] M. Pigni, R. Capote, and A. Trkov, "INDEN - International Nuclear Data Evaluation Network Network managed by the International Atomic Energy Agency." https://www-nds.iaea.org/INDEN/.

[73] J. A. Harvey, N. W. Hill, F. G. Perey, G. L. Tweed, and L. Leal, "High-Resolution Neutron Transmission Measurements on ^{235}U, ^{239}Pu, and ^{238}U," in *International Conference on Nuclear Data for Science and Technology, May 30-June 3 1988, Mito, Japan* (S. Igarasi, ed.), 115, Japan Atomic Energy Research Institute, Tokai-mura, Ibaraki, Japan (1988).

[74] L. W. Weston and J. H. Todd, "High-resolution fission cross-section measurements of ^{235}U and ^{239}Pu," Nucl. Sci. Eng. **111**, 415 (1992). [Online] Available at https://doi.org/10.13182/NSE92-A15488.

[75] C. Wagemans, "Subthermal fission cross-section measurements for ^{233}U, ^{235}U and ^{239}Pu," in *International Conference on Nuclear Data for Science and Technology, May 30-June 3 1988, Mito, Japan* (S. Igarasi, ed.), 91, Japan Atomic Energy Research Institute, Tokai-mura, Ibaraki, Japan (1988).

[76] R. Gwin, R. R. Spencer, R. W. Ingle, J. H. Todd, and S. W. Scoles, "Measurements of the Neutron Fission Cross Sections of ^{235}U (E_n = 0.01 eV to 30 keV) and ^{239}Pu (E_n = 0.01 to 60 eV)," Nucl. Sci. Eng. **88**, 37 (1984). [Online] Available at https://doi.org/10.13182/NSE84-A17138.

[77] B. L. Jr and a. W. F. E.J. Seppi, "The relative variation in eta for ^{239}Pu with incident neutron energy," Tech. Rep. **44525**, Hanford Atomic Products, Richland, WA, USA (1956).

[78] N. Pattenden, "The slow neutron total cross section of plutonium," J. Nucl. En. (1954) **2**, 187 (1956). [Online] Available at https://www.sciencedirect.com/science/article/pii/0891391955900334.

[79] L. Bollinger, R. Cote, and G. Thomas, "The slow neutron cross sections of ^{239}Pu," in *International Conference on the Peaceful Uses of Atomic Energy, August 1955, Geneva, Switzerland* (H. Hurwitz, ed.), **15**, 127, United Nations, New York (1958).

[80] L. W. Weston, J. H. Todd, and H. Derrien, "Normalization and minimum values of the ^{239}Pu fission cross section," Nucl. Sci. Eng. **115**, 164 (1993). [Online] Available at https://doi.org/10.13182/NSE93-A28526.

[81] R. Gwin, L. W. Weston, G. de Saussure, R. W. Ingle, J. H. Todd, F. E. Gillespie, R. W. Hockenbury, and R. C. Block, "Simultaneous Measurement of the Neutron Fission and Absorption Cross Sections of ^{239}Pu Over the Energy Region 0.02 eV to 30 keV," Nucl. Sci. Eng. **45**, 25 (1971). [Online] Available at https://doi.org/10.13182/NSE71-A20342.

[82] I. Durán, R. Capote, and P. Cabanelas, "Normalization of ToF (n,f) measurements in fissile targets: Microscopic cross-section integrals," Nucl. Data Sh. **193**, 95 (2024). Special Issue on Nuclear Reaction Data, [Online] Available at https://doi.org/10.1016/j.nds.2024.01.004.

[83] I. Duran, "New Integral references for neutron-induced fission reactions in the RRR." Presentation at the IAEA Technical Meeting on nuclear data evaluation of fissile actinides, 20-23 November 2023 (2023). [Online] Available at https://www-nds.iaea.org/index-meeting-crp/TM%20INDEN%20ACT%202023/docs/Duran-REF-INT--INDEN-ACT-Nov23.pdf.

[84] M. Lounsbury, R. W. Durham, and G. C. Hanna, "Measurements of alpha and fission ratios for ^{233}U, ^{235}U, and ^{239}Pu at thermal energies," in *Nuclear Data for Reactors Conference, Report STI/PUB/259, Helsinki 15-19 June 1970*, **2**, 287 (1970). Lounsbury *et al.* data (1970) were corrected by Beer *et al.* [85, 86] as quoted by Divadeenam and Stehn [775]: ^{233}U α: 0.0861 (.0021); ^{235}U α: 0.1697 (.0029); ^{239}Pu α: 0.3555 (.0057).

[85] M. Beer, M. Kalos, H. Liechtenstein, H. Steinberg, E. Troubetzkoy, N. Chikov, N. Yaneva, and Y. Shchepkin, "Monte Carlo analysis of 2200 m/sec alpha values of fissile nuclides," Trans. Am. Nucl. Soc. **23**, 509 (1972).

[86] M. Beer, M. Kalos, H. Liechtenstein, H. Steinberg, and E. Troubetzkoy, "A Monte Carlo analysis of a Chalk River experiment on cross sections of fissile nuclides," Technical report **EPRI-NP-163**, Electric Power Research Institute (1975).

[87] V. F. Sears, "Neutron scattering lengths and cross sections," Neutron News **3**, 26 (1992). [Online] Available at

https://doi.org/10.1080/10448639208218770.

[88] S. Mosby, T. Bredeweg, A. Couture, M. Jandel, T. Kawano, J. Ullmann, R. Henderson, and C. Wu, "^{239}Pu(n,γ) from 10 eV to 1.3 MeV," Nucl. Data Sh. **148**, 312 (2018). Special Issue on Nuclear Reaction Data, [Online] Available at https://www.sciencedirect.com/science/article/pii/S0090375218300267.

[89] L. A. Snyder, "Preliminary ^{235}U(n,f)/^{6}Li(n,t)α Cross Section Ratio Data and Update on the ^{239}Pu(n,f)/^{235}U(n,f) Cross Section Ratio (FissionTPC FY2019 Report)," Tech. Rep. **LLNL-TR-788566**, Lawrence Livermore National Laboratory, CA, USA (2019). [Online] Available at https://doi.org/10.2172/1560975.

[90] V. Méot, O. Roig, B. Laurent, P. Morel, J. Aupiais, O. Delaune, G. Haouat, and O. Bouland, "^{239}Pu$(n, 2n)$ ^{238}Pu cross section measurement using a recoil method," Phys. Rev. **C103**, 054609 (2021). [Online] Available at https://link.aps.org/doi/10.1103/PhysRevC.103.054609.

[91] M. R. Mumpower, D. Neudecker, T. Kawano, M. Herman, N. Kleedtke, A. E. Lovell, I. Stetcu, and P. Talou, "The Los Alamos evaluation of ^{239}Pu neutron-induced reactions in the fast energy range," (2023). [Online] Available at https://arxiv.org/abs/2302.03129.

[92] T. Kawano, "Unified coupled-channels and Hauser-Feshbach model calculation for nuclear data evaluation," (2019). [Online] Available at https://arxiv.org/abs/1901.05641.

[93] T. Kawano, "Unified description of the coupled-channels and statistical Hauser-Feshbach nuclear reaction theories for low energy neutron incident reactions," Eur. Phys. J. **A57**, 16 (2021). [Online] Available at https://doi.org/10.1140/epja/s10050-020-00311-9.

[94] T. Kawano, "CoH3: The Coupled-Channels and Hauser-Feshbach Code," in *Compound-Nuclear Reactions* (J. Escher, Y. Alhassid, L. A. Bernstein, D. Brown, C. Fröhlich, P. Talou, and W. Younes, eds.), **254**, 27, Cham: Springer International Publishing (2021). Series Title: Springer Proceedings in Physics.

[95] R. Capote, S. Badikov, A. Carlson, *et al.*, "Unrecognized Sources of Uncertainties (USU) in experimental nuclear data," Nucl. Data Sh. **163**, 191 (2020). [Online] Available at https://www.sciencedirect.com/science/article/pii/S0090375219300717.

[96] D. Neudecker, D. Smith, F. Tovesson, *et al.*, "Applying a Template of Expected Uncertainties to Updating ^{239}Pu(n,f) Cross-section Covariances in the Neutron Data Standards Database," Nucl. Data Sh. **163**, 228 (2020). [Online] Available at https://www.sciencedirect.com/science/article/pii/S0090375219300729.

[97] D. Neudecker, B. Hejnal, F. Tovesson, M. C. White, D. L. Smith, D. Vaughan, and R. Capote, "Template for estimating uncertainties of measured neutron-induced fission cross-sections," EPJ. Nucl. Sci. Techn. **4**, 21 (2018). [Online] Available at https://doi.org/10.1051/epjn/2018026.

[98] L. Snyder, M. Anastasiou, N. Bowden, *et al.*, "Measurement of the ^{239}Pu(n,f)/^{235}U(n,f) cross-section ratio with the NIFFTE fission time projection chamber," Nucl. Data Sh. **178**, 1 (2021). [Online] Available at https://www.sciencedirect.com/science/article/pii/S0090375221000612.

[99] D. Neudecker, V. G. Pronyaev, and L. Snyder, "Including ^{238}U(n,f)/^{235}U(n,f) and ^{239}Pu(n,f)/^{235}U(n,f) NIFFTE fission TPC cross-sections into the Neutron Data Standards database," Tech. Rep. **LA-UR-21-24093**, Los Alamos National Laboratory, NM, USA (2021). [Online] Available at https://www.osti.gov/biblio/1788383.

[100] F. Tovesson and T. S. Hill, "Cross sections for 239pu(n, f) and 241pu(n, f) in the range en = 0.01 ev to 200 mev," Nucl. Sci. Eng. **165**, 224 (2010). [Online] Available at https://doi.org/10.13182/NSE09-41.

[101] P. Staples and K. Morley, "Neutron-induced fission cross-section ratios for 239pu, 240pu, 242pu, and 244pu relative to 235u from 0.5 to 400 mev," Nucl. Sci. Eng. **129**, 149 (1998). [Online] Available at https://doi.org/10.13182/NSE98-A1969.

[102] P. Lisowski, A. Gavron, W. Parker, J. Ullmann, S.J.Balestrini, A. Carlson, O. Wasson, and N. Hill, "Neutron-induced fission cross-section ratios for 232th, 235,238u, 237np, and 239pu from 1 to 400 mev," in *International Conference on Nuclear Data for Science and Technology, May 30-June 3 1988, Mito, Japan* (S. Igarasi, ed.), 97, Japan Atomic Energy Research Institute, Tokai-mura, Ibaraki, Japan (1988).

[103] B. I. Fursov, V. M. Kupriyanov, V. I. Ivanov, and G. N. Smirenkin, "Measurement of the ratio of the 239pu and 235u fission cross sections for 0.024-7.4-mev neutrons," Sov. Atom. En. **43**, 894 (1977). [Online] Available at https://doi.org//10.1007/BF01117993.

[104] O. Shcherbakov, A. Donets, A. Evdokimov, *et al.*, "Neutron-induced fission of 233u, 238u, 232th, 239pu, 237np, natpb and 209bi relative to 235u in the energy range 1-200 mev," J. Nucl. Sci. Techn. **39**, 230 (2002). [Online] Available at https://doi.org/10.1080/00223131.2002.10875081.

[105] R. Capote, G. Schnabel, A. Carlson, V. Pronyaev, G. Noguere, and D. Neudecker, "Experimental spectrum averaged cross sections (SACS) in ^{252}Cf(sf) neutron field and its impact on the evaluation of neutron standards," EPJ. Web. Conf. **281**, 00027 (2023). [Online] Available at https://doi.org/10.1051/epjconf/202328100027.

[106] D. W. Muir, A. Trkov, I. Kodeli, R. Capote, and V. Zerkin, "The Global Assessment of Nuclear Data, GANDR," Int. Conf. on Nucl. Data for Sci. Techn. Nice, France, 717 (2007). Code and GUI available online at http://nds.iaea.org/gandr/.

[107] M. Herman, R. Capote, B. Carlson, P. Obložinský, M. Sin, A. Trkov, H. Wienke, and V. Zerkin, "EMPIRE: Nuclear reaction model code system for data evaluation," Nucl. Data Sh. **108**, 2655 (2007). [Online] Available at https://doi.org/10.1016/j.nds.2007.11.003.

[108] A. Trkov, R. Capote, E. S. Soukhovitskii, L. C. Leal, M. Sin, I. Kodeli, and D. W. Muir, "Covariances of evaluated nuclear cross section data for ^{232}Th, ^{182,183,184,186}W and ^{55}Mn," Nucl. Data Sh. **112**, 3098 (2011). Special Issue on ENDF/B-VII.1 Library, [Online] Available at http://www.sciencedirect.com/science/article/pii/S0090375211001189.

[109] F. Belyaev, K. Ignat'ev, S. Sukhoruchkin, S. Borovlev, V. Pavlov, M. Polozov, and A. Soldatov, "Ratio of the capture and fission cross-sections of ^{239}Pu in the energy range 100 eV to 30 keV.," pp 339–344 of IAEA Technical report STI/PUB/259 – Nuclear

Data for Reactors. Vol. I. International Atomic Energy Agency, Vienna, Austria (1970). [Online] Available at https://www-nds.iaea.org/publications/proceedings/sti-pub-259-Vol1.pdf.

[110] J. C. Hopkins and B. C. Diven, "Neutron capture to fission ratios in U-233, U-235, Pu-239," Nucl. Sci. Eng. **12**, 169 (1962). [Online] Available at https://doi.org/10.13182/NSE62-A26055.

[111] V. Andreev, "Measurements of ν_{eff} and fission + capture for fast neutrons in U-235 and Pu-239," Atom. En. **4**, 185 (1958).

[112] P. Spivak, B. Erozolimskij, G. Dorofeev, V. Lavrenchik, I.E.Kutikov, and J. Dobrynin, "Average number of neutrons ν_{eff} emitted by the isotopes U-233, U-235 and Pu-239 on capture of neutrons with energies from 30 to 900 keV," Atom. En. **1**, 21 (1956).

[113] V. Bolotskii, M. Polozov, A. Soldatov, and S. Sukhoruchkin, "Measurement of the ratio between the capture and fission cross sections of ^{239}Pu," Atom. En. **42**, 218 (1977).

[114] Y. V. Ryabov, "Measurement of $\alpha(e) = \sigma_c(e)/\sigma_f(e)$ of Pu-239 for the 0.007 eV–12 keV neutrons," Atom. En. **41**, 45 (1976).

[115] Y. V. Ryabov, "Measurement of $\alpha(e) = \sigma_c(e)/\sigma_f(e)$ of Pu-239 for the 0.007 eV–12 keV neutrons," Tech. Rep. **INDC(CCP)-95**, International Atomic Energy Agency, Vienna, Austria (1976). [Online] Available at https://www-nds.iaea.org/publications/indc/indc-ccp-0095/.

[116] R. Gwin, E. G. Silver, R. W. Ingle, and H. Weaver, "Measurement of the neutron capture and fission cross sections of ^{239}Pu and ^{235}U, 0.02 eV to 200 keV, the neutron capture cross sections of ^{197}Au, 10 to 50 keV, and neutron fission cross sections of ^{233}U, 5 to 200 keV," Nucl. Sci. Eng. **59**, 79 (1976). [Online] Available at https://doi.org/10.13182/NSE76-A15682.

[117] V. Kononov, E. Poletayev, and B. Yurlov, "The measurement of alpha, neutron fission and capture cross sections for Uranium-235 and Plutonium-239 for neutron energies from 10 to 80 keV.," Atom. En. **38**, 82 (1975).

[118] H. M. R. E. Bandl and F. H. Fröhner, "A measurement of the capture-to-fission cross section ratios of Uranium-235 and Plutonium-239 with a new technique," Nucl. Sci. Eng. **48**, 324 (1972). [Online] Available at https://doi.org/10.13182/NSE72-A22490.

[119] M. Kurov, Y. Ryabov, S. D. Sik, and N. Chikov, "Measurement of the ratios of radiative-capture and fission α cross sections for ^{235}U and ^{239}Pu in the neutrons energy range below 30 keV," Tech. Rep. **INDC(CCP)-31**, International Atomic Energy Agency, Vienna, Austria (1972). [Online] Available at https://www-nds.iaea.org/publications/indc/indc-ccp-0031/.

[120] L. W. Weston and J. H. Todd, "Neutron fission and absorption cross section measurement for ^{239}Pu and ^{241}Pu," Trans. Am. Nucl. Soc. **15**, 480 (1972).

[121] J. A. Farrell, G. F. Auchampaugh, M. S. Moore, and P. A. Seeger, "Simultaneous measurement of the fission, capture, scattering, and total cross-sections of ^{239}Pu.," pp 543–50 of IAEA Technical report STI/PUB/259 – Nuclear Data for Reactors. Vol. I. International Atomic Energy Agency, Vienna, Austria (1970). [Online] Available at https://www-nds.iaea.org/publications/proceedings/sti-pub-259-Vol1.pdf.

[122] M. G. Schomberg, M. G. Sowerby, D. A. Boyce, K. J. Murray, and D. L. Sutton, "Ratio of the capture and fission cross-sections of ^{239}Pu in the energy range 100 ev to 30 keV.," pp 315–330 of IAEA Technical report STI/PUB/259 – Nuclear Data for Reactors. Vol. I. International Atomic Energy Agency, Vienna, Austria (1970). [Online] Available at https://www-nds.iaea.org/publications/proceedings/sti-pub-259-Vol1.pdf.

[123] G. D. Saussure, L. Weston, R. Gwin, R. Ingle, J. Todd, R. Hockenbury, R. Fullwood, and A. Lottin, "Measurement of the neutron capture and fission cross sections and of their ratio, alpha, for U-233, U-235, and Pu-239," pp 233–250 of IAEA Technical report STI/PUB/140 – Nuclear Data for Reactors. Vol. II. International Atomic Energy Agency, Vienna, Austria (1967). [Online] Available at https://www-nds.iaea.org/publications/proceedings/66PARIS_2_1967.pdf.

[124] D. W. Muir, A. Mengoni, and I. Kodeli, "Integration of International Standards Evaluation into a Global Data Assessment," Nucl. Data Sh. **109**, 2874 (2008).

[125] D. McNabb, J. Anderson, R. Bauer, J. Becker, F. Dietrich, P. Navratil, M. Chadwick, and P. Young, "Evaluation of the ^{239}Pu(n,2n) integrated cross section," Technical report **UCRL-ID-143328**, Lawrence Livermore National Laboratory, CA, USA (2001).

[126] L. A. Bernstein, J. A. Becker, P. E. Garrett, *et al.*, "^{239}Pu$(n, 2n)^{238}$Pu cross section deduced using a combination of experiment and theory," Phys. Rev. **C65**, 021601 (2002). [Online] Available at https://link.aps.org/doi/10.1103/PhysRevC.65.021601.

[127] D. S. Mather, P. F. Bampton, R. E. Coles, G. James, and P. J. Nind, "Measurement of (n,2n) cross sections for incident energies between 6 and 14 MeV.," Technical report **AWRE-O-72/72, EANDC(UK)142-AL**, A.W.R.E. Aldermaston, United Kingdom (1972). [Online] Available at https://www.osti.gov/biblio/4570888.

[128] J. Fréhaut, A. Bertin, B. Bois, E. Gryntakis, and C. A. Philis, "(n,2n) cross sections of ^{2}H and ^{239}Pu," Radiat. Eff. **96**, 219 (1986). [Online] Available at https://doi.org/10.1080/00337578608211739.

[129] N. Ma, C. Lin, H. Jia, X. Xu, F. Yang, L. Yang, L. Sun, D. Wang, H. Zhang, and Z. Liu, "Measurement of (n,f) and (n,xn) cross sections with surrogate reaction method," EPJ. Web. Conf. **239**, 01007 (2020). [Online] Available at https://doi.org/10.1051/epjconf/202023901007.

[130] R. W. Lougheed, W. Webster, M. N. Namboodiri, *et al.*, "^{239}Pu and ^{241}Am(n,2n) cross-section measurements near En=14 MeV," Radiochimica Acta **90**, 833 (2002). [Online] Available at https://doi.org/10.1524/ract.2002.90.12_2002.833.

[131] C. A. Engelbrecht and H. A. Weidenmüller, "Hauser-Feshbach theory and Ericson fluctuations in the presence of direct reactions," Phys. Rev. **C8**, 859 (1973). [Online] Available at https://link.aps.org/doi/10.1103/PhysRevC.8.859.

[132] A. Smith and P. Guenther, "On neutron inelastic-scattering cross sections of ^{232}Th, ^{233}U, ^{235}U, ^{238}U, ^{239}Pu and ^{240}Pu," Tech. Rep. **ANL-NDM-63**, Argonne National Laboratory, IL, USA (1982). [Online] Available at https://anl.app.box.com/s/p8k43z9sa9pbz7uu9788d84977z0u1ho.

[133] A. Smith and P. Guenther, "On neutron inelastic-

scattering cross sections of ^{232}Th, ^{233}U, ^{235}U, ^{238}U, ^{239}Pu and ^{240}Pu," in *Proceedings of Nuclear Data for Science and Technology, Antwerp, Belgium*, 39 (1982).

[134] T. Kawano, R. Capote, S. Hilaire, and P. Chau Huu-Tai, "Statistical Hauser-Feshbach theory with width-fluctuation correction including direct reaction channels for neutron-induced reactions at low energies," Phys. Rev. **C94**, 014612 (2016). [Online] Available at https://link.aps.org/doi/10.1103/PhysRevC.94.014612.

[135] G. Yue, M. O'Connor, J. Egan, and G. Kegel, "Neutron scattering cross sections for ^{239}Pu at 700 keV," in *Proceedings of Nuclear Data for Science and Technology, Gatlinburg 1994, Vol.1, p.248 (1994), USA*, 248 (1994). USA.

[136] L. Cranberg, "Neutron scattering by U-235, Pu-239, and U-238," Tech. Rep. **LA-2177**, Los Alamos National Laboratory, NM, USA (1959).

[137] H. Knitter and M. Coppola, "Elastic neutron scattering measurements on ^{239}Pu in the energy range between 0.19 and 0.38 MeV," Z. Phys. **228**, 286 (1969). [Online] Available at https://doi.org/10.1007/BF01392133.

[138] M. Coppola and H. Knitter, "Interactions of neutrons with ^{239}Pu in the energy range between 1.5 and 5.5 MeV," Z. Phys. **232**, 286 (1970). [Online] Available at https://doi.org/10.1007/BF01391526.

[139] A. Smith, P. Guenther, and J. Whalen, "Total and elastic scattering neutron cross sections of ^{239}Pu," J. Nucl. En. **27**, 317 (1973). [Online] Available at https://www.osti.gov/biblio/4463473.

[140] J. L. Kammerdiener, "Neutron spectra emitted by ^{239}Pu, ^{238}U, ^{235}U, Pb, Nb, Ni, Al, and C irradiated by 14 MeV neutrons," Tech. Rep. **UCRL-51232**, Lawrence Livermore National Laboratory, Livermore, CA, United States (1972). [Online] Available at https://www.osti.gov/biblio/4669084.

[141] C. Wong, J. Anderson, P. Brown, L. F. Hansen, J. L. Kammerdiener, C. Logan, and B. Pohl, "Livermore Pulsed Sphere Program: Program Summary Through July 1971," Tech. Rep. **LLNL UCRL-51144 Rev.1**, Lawrence Livermore National Laboratory, CA, USA (1972). [Online] Available at https://mcnp.lanl.gov/pdf_files/TechReport_1972_LLNL_UCRL-51144Rev.1_WongAndersonEtAl.pdf.

[142] A. Marcinkowski, J. Rapaport, R. Finlay, C. Brient, M. Herman, and M. Chadwick, "Neutron emission cross sections at low bombarding energies and the novelty in multistep compound reaction model," Nucl. Phys. **A561**, 387 (1993). [Online] Available at https://www.sciencedirect.com/science/article/pii/037594749390018S.

[143] P. G. Young, M. B. Chadwick, R. E. MacFarlane, *et al.*, "Evaluation of neutron reactions for ENDF/B-VII: U-232–241 and Pu-239," Nucl. Data Sh. **108**, 66 (2007). [Online] Available at https://doi.org/10.1016/j.nds.2007.11.002.

[144] H. Wienke, R. Capote, M. Herman, and M. Sin, "Deformation-dependent Tamura-Udagawa-Lenske multistep direct model," Phys. Rev. **C78**, 064611 (2008). [Online] Available at https://doi.org/10.1103/PhysRevC.78.064611.

[145] M. R. Mumpower, D. Neudecker, H. Sasaki, T. Kawano, A. E. Lovell, M. W. Herman, I. Stetcu, and M. Dupuis, "Collective enhancement in the exciton model," Phys. Rev. **C107**, 034606 (2023). [Online] Available at https://link.aps.org/doi/10.1103/PhysRevC.107.034606.

[146] M. Dupuis, R. Capote, T. Kawano, M. Kerveno, P. Dessagne, G. Henning, and S. Hilaire, "Microscopic modeling of direct pre-equilibrium emission: Impact on exclusive and inclusive (n,xn) and fission channels," EPJ. Web. Conf. **292**, 04003 (2024). [Online] Available at https://doi.org/10.1051/epjconf/202429204003.

[147] L. F. Hansen, B. A. Pohl, C. Wong, R. C. Haight, and C. Lagrange, "Measurements and calculations of neutron scattering in the actinide region," Phys. Rev. **C34**, 2075 (1986). [Online] Available at https://link.aps.org/doi/10.1103/PhysRevC.34.2075.

[148] R. Capote, E. S. Soukhovitskii, J. M. Quesada, and S. Chiba, "Is a global coupled-channel dispersive optical model potential for actinides feasible?," Phys. Rev. **C72**, 064610 (2005). [Online] Available at https://link.aps.org/doi/10.1103/PhysRevC.72.064610.

[149] E. S. Soukhovitskii, R. Capote, J. M. Quesada, and S. Chiba, "Dispersive coupled-channel analysis of nucleon scattering from ^{232}Th up to 200 MeV," Phys. Rev. **C72**, 024604 (2005). [Online] Available at https://link.aps.org/doi/10.1103/PhysRevC.72.024604.

[150] R. Capote, S. Chiba, E. S. ı, J. Quesada, and E. Bauge, "A global dispersive coupled-channel optical model potential for actinides," J. Nucl. Sci. Techn. **45**, 333 (2008). [Online] Available at https://doi.org/10.1080/18811248.2008.9711442.

[151] R. E. Kalman, "A new approach to linear filtering and prediction problems," J. Basic Eng. **82**, 35 (1960).

[152] J. K. Bair and F. X. Haas, "Total Neutron Yield from the Reactions ^{13}C$(\alpha,n)^{16}$O and ^{17,18}O$(\alpha,n)^{20,21}$Ne," Phys. Rev. **C7**, 1356 (1973).

[153] Giorginis, G., Khryachkov, V., Corcalciuc, V., and Kievets, M., "The cross section of the ^{16}O$(n,\alpha)^{13}$C reaction in the MeV energy range," Int. Conf. on Nucl. Data for Sci. Techn., 525 (2007).

[154] E. Davis, T. Bonner, D. Worley, and R. Bass, "Disintegration of ^{16}O and ^{12}C by fast neutrons," Nucl. Phys. **48**, 169 (1963).

[155] C. J. Parnell, D. Dandy, and J. L. Wankling, "The Cross-Section for the ^{16}O$(n,\alpha)^{13}$C Reaction," Phys. Med. Biol. **13**, 665 (1968).

[156] S. Simakov and U. Fischer, "ORNL Oxygen Broomstick Experiment: MCNP model and evaluation results for SINBAD entry NEA-1517/59," Technical report **KIT Scientific Working Papers 202**, Institut für Neutronenphysik und Reaktortechnik, KIT, Germany (2022). [Online] Available at https://doi.org/10.5445/IR/1000152418.

[157] R. E. Maerker, "SDT2. oxygen broomstick experiment: an experimental check of neutron total cross sections," Tech. Rep. **ORNL-TM-3868; ENDF-167**, Oak Ridge National Laboratory, Oak Ridge, TN, USA (1972). [Online] Available at https://www.osti.gov/biblio/4639246.

[158] N. E. Agency, "International Handbook of Evaluated Criticality Safety Benchmark Experiments/Nuclear Energy Agency," Tech. Rep. **(NEA 7328)**, Paris: OECD Nuclear Energy Agency, France (2019).

[159] D. Tilley, H. Weller, C. Cheves, and R. Chasteler, "Energy levels of light nuclei $A = 18$–19," Nucl. Phys. A **595**, 1 (1995).

[160] D. L. Broder, A. F. Gamaliy, A. I. Lashuk, B. V. Nesterov, and I. P. Sadokhin, "Cross-sections for gamma-

quanta production in (n,n'gamma) reaction on nuclei of fluorine, cobalt, antimony and tantalum," Technical report **FEI-155**, FEI, Obninsk, Soviet Union (1969).

[161] G. L. Morgan and J. K. Dickens, "Production of low-energy gamma rays by neutron interactions with fluorine for incident neutron energies between 0.1 and 20 MeV," Nucl. Sci. Eng. **60**, 36 (1976).

[162] M. Chadwick, M. Herman, P. Obložinskỳ, *et al.*, "ENDF/B-VII.1 nuclear data for science and technology: cross sections, covariances, fission product yields and decay data," Nucl. Data Sh. **112**, 2887 (2011). [Online] Available at http://linkinghub.elsevier.com/retrieve/pii/S009037521100113X.

[163] D. Neudecker, M. Grosskopf, M. Herman, W. Haeck, P. Grechanuk, S. Vander Wiel, M. Rising, A. Kahler, N. Sly, and P. Talou, "Enhancing nuclear data validation analysis by using machine learning," Nucl. Data Sh. **167**, 36 (2020). [Online] Available at https://www.sciencedirect.com/science/article/pii/S0090375220300247.

[164] M. Kostal, M. Vekarna, F. Cvachovec, *et al.*, "Comparison of fast neutron spectra in graphite and FLINA salt inserted in well-defined core assembled in LR-0 reactor," Ann. Nucl. En. **83**, 216 (2015).

[165] E. Losa, M. Kostal, T. Czakoj, B. Jansky, E. Novak, V. Rypar, J. Powers, N. Brown, and D. Mueller, "Neutronic experiments with fluorine rich compounds at LR-0 reactor," Ann. Nucl. En. **120**, 286 (2018).

[166] G. Siemers, Y. Danon, S. Singh, A. Daskalakis, P. Brain, K. Cook, B. Wang, M. Rapp, and D. Barry, "High Energy Quasi-Differential Neutron Emission Measurements of ^{181}Ta and ^{19}F," (2023). [Online] Available at https://indico.bnl.gov/event/18701/contributions/82698/attachments/51291/87709/SIEMERS_CSWEG_2023_v3.pdf.

[167] G. Siemers, Y. Danon, S. Singh, A. Daskalakis, P. Brain, K. Cook, B. Wang, M. Rapp, and D. Barry, "Quasi-Differential Neutron Scattering Measurements of ^{181}Ta and Teflon from 1.5 to 20 MeV," (2023). [Online] Available at https://indico.cern.ch/event/1201892/contributions/5601237/attachments/2726870/4739224/SIEMERS_WINS_2023_HES_EXPS_FINAL.pdf.

[168] A. J. Elwyn, J. E. Monahan, R. O. Lane, and A. J. Langsdorf, "Neutron scattering from nuclei near A=20 at energies below 2.2 MeV," Nucl. Phys. **59**, 113 (1964).

[169] M. T. Pigni, K. H. Guber, G. Arbanas, D. Wiarda, R. Capote, and A. Trkov, "Evaluation and validation of ^{28,29,30}Si cross sections in the resolved resonance region," Tech. Rep. **ORNL/LTR-2018/1044**, Oak Ridge National Laboratory (2018). [Online] Available at https://www.osti.gov/biblio/1489565.

[170] H. Derrien, L. C. Leal, K. H. Guber, T. Valentine, N. M. Larson, and T. Rauscher, "Evaluation of silicon neutron resonance parameters in the energy range thermal to 1800 keV," Tech. Rep. **ORNL/TM-2001/271**, Oak Ridge National Laboratory, TN, USA (2002).

[171] R. Firestone, K. Abusaleem, M. Basunia, *et al.*, "EGAF: Measurement and analysis of gamma-ray cross sections," Nucl. Data Sh. **119**, 79 (2014). [Online] Available at https://www.sciencedirect.com/science/article/pii/S0090375214005584.

[172] H. Choi, R. Firestone, R. Lindstrom, G. Molnar, S. Mughabghab, R. Paviotti-Corcuera, Z. Revay, A. Trkov, V. Zerkin, and C. Zhou, "Database of Prompt Gamma Rays from Slow Neutron Capture for Elemental Analysis," Tech. Rep. **STI/PUB/1263**, International Atomic Energy Agency, Vienna, Austria (2007). [Online] Available at https://nds.iaea.org/pgaa/data/nglist_a.dat.

[173] R. L. Klueh and D. R. Harries, "High-chromium ferritic and martensitic steels for nuclear applications: (MONO 3)," in *High-Chromium Ferritic and Martensitic Steels for Nuclear Applications: (MONO 3)* (2001). [Online] Available at https://app.knovel.com/hotlink/toc/id:kpHCFMSNA3/high-chromium-ferritic/high-chromium-ferritic.

[174] G. Nobre, M. Pigni, D. Brown, *et al.*, "Newly evaluated neutron reaction data on chromium isotopes," Nucl. Data Sh. **173**, 1 (2021). Special Issue on Nuclear Reaction Data, [Online] Available at https://www.sciencedirect.com/science/article/pii/S0090375221000120.

[175] R. G. Stieglitz, R. W. Hockenbury, and R. C. Block, "keV neutron capture and transmission measurements on ^{50}Cr, ^{52}Cr, ^{53}Cr, ^{54}Cr, ^{60}Ni and V," Nucl. Phys. **A163**, 592 (1971). [Online] Available at http://dx.doi.org/10.1016/0375-9474(71)90512-4.

[176] K. H. Guber, P. E. Koehler, D. Wiarda, and J. A. Harvey, "Neutron cross-section measurements on structural materials at ORELA," J. Korean Phys. Soc. **59**, 1685 (2011). [Online] Available at http://dx.doi.org/10.3938/jkps.59.1685.

[177] R. G. Stieglitz, *keV Neutron Capture and Transmission Measurements on ^{50}Cr, ^{52}Cr, ^{53}Cr, ^{54}Cr, ^{60}Ni and V.* Doctoral Thesis, Rensselaer Polytechnic Institute, Troy, NY (1970). EXFOR 10074.

[178] R. Li, W. Sun, E. Soukhovitskii, J. Quesada, and R. Capote, "Dispersive coupled-channels optical-model potential with soft-rotator couplings for Cr, Fe, and Ni isotopes," Phys. Rev. **C87**, 054611 (2013). [Online] Available at https://link.aps.org/doi/10.1103/PhysRevC.87.054611.

[179] G. P. A. Nobre, D. A. Brown, M. W. Herman, and A. Golas, "Constraining level densities through quantitative correlations with cross-section data," Phys. Rev. **C101**, 034608 (2020). [Online] Available at https://link.aps.org/doi/10.1103/PhysRevC.101.034608.

[180] G. Schnabel, D. L. Aldama, T. Bohm, *et al.*, "FENDL: A library for fusion research and applications," Nucl. Data Sh. **193**, 1 (2024). [Online] Available at https://doi.org/10.1016/j.nds.2024.01.001.

[181] A. Blokhin, E. Gai, A. Ignatyuk, I. Koba, V. Manokhin, and V. Pronyaev, "New version of neutron evaluated data library BROND-3.1," Probl. Atom. Sci. Techn. Series: Nucl. React. Constants, 62 (2016). In Russian.

[182] A. Laureau, V. Lamirand, A. Gruel, P. Frajtag, and A. Pautz, "Dosimetry modeling and experimental validation for the PETALE program in the CROCUS reactor," EPJ. Web. Conf. **247**, 08015 (2021). [Online] Available at https://doi.org/10.1051/epjconf/202124708015.

[183] A. Trkov and R. Capote, "Updating of the ENDF/B-VIII.1b2 candidate evaluations with reaction cross sections from IRDFF-II," Tech. Rep. **INDC(NDS)-0900**, International Atomic Energy Agency, Vienna, Austria (2024). [Online] Available at https://www-nds.iaea.org/publications/indc/indc-nds-0900/.

[184] A. Trkov and R. Capote, "Evaluation of thermal neutron

capture gamma spectra," Tech. Rep. **INDC(NDS)-0810**, International Atomic Energy Agency, Vienna, Austria (2020). [Online] Available at https://www-nds.iaea.org/publications/indc/indc-nds-0810/.

[185] R. Capote, M. Herman, P. Obložinský, *et al.*, "RIPL - Reference Input Parameter Library for Calculation of Nuclear Reactions and Nuclear Data Evaluations," Nucl. Data Sh. **110**, 3107 (2009). [Online] Available at https://doi.org/10.1016/j.nds.2009.10.004.

[186] Y. Danon, K. Cook, A. Golas, S. Singh, and B. Wang, "Overview of nuclear data measurement and analysis at RPI," (2023). [Online] Available at https://indico.bnl.gov/event/18701/contributions/82696/attachments/51290/87708/RPI_CSEWG_2023.pdf.

[187] E. Chimanski, B. Beck, L. Bernstein, *et al.*, "The current status of inelastic and capture gamma-ray production evaluations in translated ENDF-VIII.0 GNDS files and recommended remediation actions," Tech. Rep. **BNL-224447-2023-INRE**, Brookhaven National Laboratory, Upton, NY, United States (2023). [Online] Available at https://www.osti.gov/biblio/1983773.

[188] M. Herman, A. Trkov, R. Capote, *et al.*, "Evaluation of neutron reactions on iron isotopes for CIELO and ENDF/B-VIII.0," Nucl. Data Sh. **148**, 214 (2018).

[189] M. Chadwick, R. Capote, A. Trkov, *et al.*, "CIELO Collaboration Summary Results: International Evaluations of Neutron Reactions on Uranium, Plutonium, Iron, Oxygen and Hydrogen," Nucl. Data Sh. **148**, 189 (2018). Special Issue on Nuclear Reaction Data, [Online] Available at https://www.sciencedirect.com/science/article/pii/S009037521830022X.

[190] A. Trkov, R. Capote, D. Bernard, *et al.*, "Progress in the Evaluation and Validation of n+^{56,57}Fe Cross Sections," EPJ. Web. Conf. **284**, 12002 (2023).

[191] R. Capote, P. Dimitriou, G. Schnabel, and (coordinators), "INDEN - International Nuclear Data Evaluation Network Network managed by the International Atomic Energy Agency." https://www-nds.iaea.org/INDEN/.

[192] C. Perey and F. Perey, "Evaluation of resonance parameters for neutron interaction with iron isotopes for energies up to 400 keV," Technical report **ORNL/TM-6405, ENDF-298**, Oak Ridge National Laboratory, TN, USA (1973). [Online] Available at https://www.nndc.bnl.gov/endfdocs/ENDF-298.pdf.

[193] F. Fröhner and F. Fabbri, "^{56}Fe evaluated nuclear data file, MAT2631 JEF-2.2 library (distr. jan. 1992)," tech. rep., OECD, NEA, Paris, France (1989).

[194] M. Schulc, M. Kostal, T. Czakoj, J. Simon, E. Novak, and Z. Matej, "Comprehensive stainless steel neutron transport libraries validation," Ann. Nucl. En. **179**, 109433 (2022). [Online] Available at https://doi.org/10.1016/j.anucene.2022.109433.

[195] M. Kostal, Z. Matej, M. Schulc, *et al.*, "Benchmarking of stainless steel cube neutron leakage in Research Center Rez," Nucl. Sci. Eng. **198**, 399 (2023). [Online] Available at https://doi.org/10.1080/00295639.2023.2206770.

[196] I. Newsome, M. Bhike, Krishichayan, and W. Tornow, "Neutron radiative capture cross section of ^{63,65}Cu between 0.4 and 7.5 MeV," Phys. Rev. **C97**, 044617 (2018). [Online] Available at https://doi.org/10.1103/PhysRevC.97.044617.

[197] M. Weigand, C. Beinrucker, A. Couture, *et al.*, "^{63}Cu(n,γ) cross section measured via 25 keV activation and time of flight," Phys. Rev. **C95**, 015808 (2017). [Online] Available at https://doi.org/10.1103/PhysRevC.95.015808.

[198] C. J. Prokop, A. Couture, S. Jones, S. Mosby, G. Rusev, J. Ullmann, and M. Krtička, "Measurement of the ^{65}Cu(n,γ) cross section using the Detector for Advanced Neutron Capture Experiments at LANL," Phys. Rev. **C99**, 055809 (2019). [Online] Available at https://doi.org/10.1103/PhysRevC.99.055809.

[199] J. D. McDonnell and M. T. Pigni, "Updates to Improve the Evaluated Nuclear Data of Copper Isotopes in the Resolved and Unresolved Resonance Regions," Tech. Rep. **ORNL/SPR-2021/1957**, Oak Ridge National Laboratory (ORNL), Oak Ridge, TN (United States) (2021). [Online] Available at https://www.osti.gov/biblio/1922326.

[200] V. Sobes, L. Leal, K. Guber, B. Forget, S. Kopecky, P. Schillebeeckx, and P. Siegler, "New resolved resonance region evaluation for ^{63,65}Cu for nuclear criticality safety program," Nucl. Data Sh. **118**, 155 (2014). [Online] Available at https://doi.org/10.1016/j.nds.2014.04.024.

[201] A. B. Popov and G. S. Samosvat, "The neutron integral and differential cross-sections in the energy region below 440 keV at nuclei of Cu, Y, Nb, In, Sb and Nd," Technical report **JINR-P3-86-599**, Joint Institute for Nuclear Research, Dubna, Russia (1986).

[202] A. B. Smith, C. A. Engelbrecht, and D. Reitmann, "Elastic and inelastic scattering of fast neutrons from Co, Cu, and Zn," Phys. Rev. **135**, B76 (1964). [Online] Available at https://doi.org/10.1103/PhysRev.135.B76.

[203] S. Tanaka, K. Tsukada, M. Maruyama, Y. Tomita, and Y. Yamanouti, "Scattering of 1.71 and 2.24 MeV neutrons from zinc and copper," in *Nuclear Data for Reactors Conference, Report STI/PUB/259, Helsinki 15-19 June 1970*, **1**, 305 (1970). EXFOR 20342.002.

[204] R. Becker, W. Guindon, and G. Smith, "Elastic scattering of 3.2 MeV neutrons from many elements," Nucl. Phys. **89**, 154 (1966).

[205] I. Korzh, V. Mishchenko, M. Pasechnik, N. Pravdivyi, I. Sanzhur, and I. Tockii, "Elastic scattering of 1.5 MeV neutrons by medium-atomic-weight nuclei," Ukrainian Phys. J. **12**, 1522 (1968). EXFOR 40042.019.

[206] V. Popov, "Angular distribution of elastically and inelastically scattered 2.9-MeV neutrons," Sov. Atom. En. **3**, 1379 (1957). EXFOR 40367.008, [Online] Available at http://dx.doi.org/10.1007/BF01522503.

[207] E. Blain, Y. Danon, D. P. Barry, B. E. Epping, A. Youmans, M. J. Rapp, A. M. Daskalakis, and R. C. Block, "Measurements of neutron scattering from a copper sample using a quasi-differential method in the region from 2 keV to 20 MeV," Nucl. Sci. Eng. **196**, 121 (2022). [Online] Available at https://doi.org/10.1080/00295639.2021.1961542.

[208] M. S. Pandey, J. B. Garg, and J. A. Harvey, "Neutron total cross sections and resonance parameters of ^{63}Cu and ^{65}Cu. I," Phys. Rev. **C15**, 600 (1977). [Online] Available at https://link.aps.org/doi/10.1103/PhysRevC.15.600.

[209] K. Kauwenberghs, B. Becker, J. C. Drohe, K. Guber, S. Kopecky, P. Schillebeeckx, D. Vendelbo, and R. Wynants, "Results of time-of-flight transmission measurements for ^{63,65}Cu and ^{nat}Cu at a 50 m station of GELINA," Tech. Rep. **26479**, Euratom (2013).

[210] H. Tsuchiya, H. Harada, M. Koizumi, *et al.*, "Impact of systematic effects on results of neutron resonance transmission analysis," Nucl. Inst. Meth. Phys. Res. **A767**, 364 (2014). [Online] Available at http://www.sciencedirect.com/science/article/pii/S0168900214010055.

[211] V. Sobes, L. C. Leal, K. Guber, B. Forget, S. Kopecky, P. Schillebeeckx, and P. Siegler, "New Resolved Resonance Region Evaluation for 63,65Cu for Nuclear Criticality Safety Program," Nucl. Data Sh., 155 (2014). Data from K. Guber shared as private communication within this reference.

[212] R. Firestone, "Renormalization of pile oscillator thermal neutron capture cross section data," Tech. Rep. **INDC(USA)-109**, International Atomic Energy Agency, Vienna, Austria (2021). [Online] Available at https://www-nds.iaea.org/publications/indc/indc-usa-0109.pdf.

[213] S. J. J. Voignier and G. Grenier, "Capture cross sections and gamma-ray spectra from the interaction of 0.5- to 3.0-MeV neutrons with nuclei in the mass range A = 45 to 238," Nucl. Sci. Eng. **112**, 87 (1992). [Online] Available at https://doi.org/10.13182/NSE91-92N.

[214] G. Zaikin, I. Korzh, N. Sklyar, and I. Totskii, "Cross sections for radiative capture of fast neutrons by ^{63}Cu, ^{65}Cu, and ^{186}W," Sov. Atom. En. **25**, 1362 (1968). [Online] Available at https://doi.org/10.1007/BF01162320.

[215] V. Tolstikov, V. Kolesov, A. Dovbenko, and Y. Stavisskii, "Neutron radiative capture in copper and molybdenum," J. Nucl. En. A& B (Reactor Sci. Technol.) **20**, 86 (1966).

[216] A. TAKAHASHI, "Measurements of double differential cross sections at oktavian," J. Nucl. Sci. Techn. **26**, 15 (1989). [Online] Available at https://doi.org/10.1080/18811248.1989.9734264.

[217] K. Amundson *et al.*, "CERBERUS: CEDT Phase-1 Preliminary Design for Cu Critical Experiment," Tech. Rep. **LA-UR-21-24482**, Los Alamos National Laboraty, NM, USA (2021). [Online] Available at https://doi.org/10.2172/1782622.

[218] M. Schulc, M. Košt'ál, E. Novák, and J. Simon, "Copper neutron transport libraries validation by means of a ^{252}Cf standard neutron source," Nucl. Eng. Techn. **53**, 3151 (2021). [Online] Available at https://doi.org/10.1016/j.net.2021.04.029.

[219] M. Schulc, M. Košt'ál, Z. Matej, T. Czakoj, and E. Novák, "Fast neutron spectra measurement in a copper using a ^{252}Cf standard neutron source," Radiat. Phys. Chem. **192**, 109871 (2022). [Online] Available at https://doi.org/10.1016/j.radphyschem.2021.109871.

[220] R. Capote, K. Zolotarev, V. Pronyaev, and A. Trkov, "Updating and extending the IRDF-2002 dosimetry library," J. ASTM Int. **9**, JAI104119 (2012). [Online] Available at https://doi.org/10.1520/JAI104119.

[221] A. Koning, S. Hilaire, and S. Goriely, "TALYS: modeling of nuclear reactions," Eur. Phys. J. **A59**, 131 (2023). [Online] Available at https://doi.org/10.1140/epja/s10050-023-01034-3.

[222] A. J. Koning, D. Rochman, J.-C. Sublet, N. Dzysiuk, M. Fleming, and S. v. d. Marck, "TENDL: Complete nuclear data library for innovative nuclear science and technology," Nucl. Data Sh. **155**, 1 (2019). Special Issue on Nuclear Reaction Data, [Online] Available at https://www.sciencedirect.com/science/article/pii/S009037521930002X.

[223] D. Rochman, A. Koning, and J.-C. Sublet, "A statistical analysis of evaluated neutron resonances with TARES for JEFF-3.3, JENDL-4.0, ENDF/B-VIII.0 and TENDL-2019," Nucl. Data Sh. **163**, 163 (2020). [Online] Available at https://doi.org/10.1016/j.nds.2019.12.003.

[224] A. Koning, "Bayesian Monte Carlo Method for Nuclear Data Evaluation," Nucl. Data Sh. **123**, 207 (2015). [Online] Available at https://doi.org/10.1016/j.nds.2014.12.036.

[225] D. Rochman, E. Bauge, A. Vasiliev, H. Ferroukhi, S. Pelloni, A. J. Koning, and J. C. Sublet, "Monte Carlo nuclear data adjustment via integral information," Eur. Phys. J. Plus **133**, 537 (2018). [Online] Available at https://doi.org/10.1140/epjp/i2018-12361-x.

[226] D. L. Aldama and R. C. Noy, "Processing La-139 in the Unresolved Resonance Region for the FENDL Library," Tech. Rep. **INDC(NDS)-0825**, International Atomic Energy Agency, Vienna, Austria (2021). [Online] Available at https://doi.org/10.61092/iaea.mrpt-xx9q.

[227] E. Leal-Cidoncha, A. Couture, E. M. Bond, *et al.*, "Measurement of the neutron-induced capture-to-fission cross section ratio in ^{233}U at lansce," Phys. Rev. C **108**, 014608 (2023). [Online] Available at https://link.aps.org/doi/10.1103/PhysRevC.108.014608.

[228] K. H. Guber, R. R. Spencer, L. C. Leal, J. A. Harvey, N. W. Hill, G. D. Santos, R. O. Sayer, and D. C. Larson, "New high-resolution fission cross-section measurements of ^{233}U in the 0.4–eV to 700–keV energy range," Nucl. Sci. Eng. **135**, 141 (2000). [Online] Available at https://doi.org/10.13182/NSE00-A2130.

[229] K. H. Guber, R. R. Spencer, L. C. Leal, *et al.*, "High-resolution transmission measurements of ^{233}U using a cooled sample at the temperature T=11 K," Nucl. Sci. Eng. **139**, 111 (2001). [Online] Available at https://doi.org/10.13182/NSE01-A2226.

[230] M. T. Pigni, R. Capote, and A. Trkov, "Progress on the reevaluation and validation of the n+^{233}U neutron cross sections," Ann. Nucl. En. **163**, 108595 (2021). [Online] Available at https://www.sciencedirect.com/science/article/pii/S0306454921004710.

[231] Berthoumieux, E., Abbondanno, U., Aerts, G., *et al.*, "Simultaneous measurement of the neutron capture and fission yields of ^{233}U," Int. Conf. on Nucl. Data for Sci. Techn., 571 (2007). [Online] Available at https://doi.org/10.1051/ndata:07665.

[232] L. W. Weston *et al.*, "Measurement of the Neutron Fission and Capture Cross Sections for ^{233}U in the Energy Region 0.4 to 2000 eV," Nucl. Sci. Eng. **34**, 1 (1968). [Online] Available at https://doi.org/10.13182/NSE68-A19361.

[233] M. Calviani, J. Praena, U. Abbondanno, *et al.* (n_TOF Collaboration), "High-accuracy ^{233}U(n,f) cross-section measurement at the white-neutron source n_tof from near-thermal to 1 MeV neutron energy," Phys. Rev. **C80**, 044604 (2009). [Online] Available at https://link.aps.org/doi/10.1103/PhysRevC.80.044604.

[234] J. Hopkins and B. Diven, "Prompt neutrons from fission," Nucl. Phys. **48**, 433 (1963). [Online] Available at https://www.sciencedirect.com/science/article/pii/0029558263901822.

[235] B. Diven and J. Hopkins, "Numbers of prompt neutrons per fission for U-233, U-235. Pu-239 and Cf-252," in *Proceedings of the Seminar on Physics of Fast and Intermediate Reactors, 3-11 August 1961, STI/PUB-149*, (Vienna, Austria), Vol.1, 149, IAEA (1962). [Online] Available at https://www-nds.iaea.org/publications/proceedings/sti-pub-49-I.pdf.

[236] B. Nurpeisov, V. Nesterov, L. Prokhorova, and G. Smirenkin, "Average yield of prompt neutrons in the fission of U-233 by neutrons with energies from 0 to 1.4 MeV," At. En. **34**, 603 (1973). [Online] Available at https://doi.org/10.1007/BF01117690.

[237] A. Sergachev, N.P.Dyachenko, A. Kovalev, and B. Kuzminov, "Influence of excitation energy on the mass and kinetic energy distribution of U-233 fission fragments," Sov. J. Nucl. Phys. **16**, 266 (1973).

[238] R. Walsh and J. Boldeman, "The energy dependence of ν_p for ^{233}U, ^{235}U and ^{239}Pu below 5.0 MeV," J. Nucl. En. **25**, 321 (1971). [Online] Available at https://www.sciencedirect.com/science/article/pii/0022310771900645.

[239] D. Colvin and M. Sowerby, "Prompt neutron yield determination for U-233 neutron induced fission." EXFOR 22502002, private communication.

[240] G. N. Smirenkin, I. I. Bondarenko, L. S. Kutsaeva, K. D. Mishchenko, L. I. Prokhorova, and B. P. Shemetenko, "Mean number of prompt neutrons in the fission of U233, U235 Pu239 by 4 and 15 MeV neutrons," At. En. **4**, 253 (1958). [Online] Available at https://doi.org/10.1007/BF02207352.

[241] A. N. Protopopov and M. V. Blinov, "Determination of the mean number of neutrons emitted per fission of U233 induced by 14.8-MeV neutrons," The Sov. J. Atom. En. **5**, 885 (1958). [Online] Available at https://doi.org/10.1007/BF01505399.

[242] R. Capote, A. Trkov, and (coordinators), ""IAEA CIELO Data Development Project" within the International Pilot Project of the OECD/NEA [473]." [Online] Available at www-nds.iaea.org/CIELO/.

[243] Y. Danon, D. Williams, R. Bahran, E. Blain, B. McDermott, D. Barry, G. Leinweber, R. Block, and M. Rapp, "Simultaneous Measurement of ^{235}U Fission and Capture Cross Sections From 0.01 eV to 3 keV Using a Gamma Multiplicity Detector," Nucl. Sci. Eng. **187**, 291 (2017). [Online] Available at https://doi.org/10.1080/00295639.2017.1312937.

[244] S. Amaducci, L. Cosentino, M. Barbagallo, *et al.*, "Measurement of the ^{235}U(n,f) cross section relative to the ^{6}Li(n,t) and ^{10}B(n,α) standards from thermal to 170 keV neutron energy range at n_tof," Eur. Phys. J. **A55**, 120 (2019). [Online] Available at https://doi.org/10.1140/epja/i2019-12802-7.

[245] R. A. Shrack, "Measurement of the ^{235}U(n,f) reaction from thermal to 1 keV," in *International Conference on Nuclear Data for Science and Technology, May 30-June 3 1988, Mito, Japan* (S. Igarasi, ed.), 101, Japan Atomic Energy Research Institute, Tokai-mura, Ibaraki, Japan (1988).

[246] A. Trkov, R. Capote, and V. Pronyaev, "Current issues in nuclear data evaluation methodology: ^{235}U prompt fission neutron spectra and multiplicity for thermal neutrons," Nucl. Data Sh. **123**, 8 (2015). [Online] Available at https://doi.org/10.1016/j.nds.2014.12.003.

[247] A. Trkov and R. Capote, "Evaluation of the prompt fission neutron spectrum of thermal-neutron induced fission in ^{235}U," Phys. Procedia **64**, 48 (2015). [Online] Available at https://doi.org/10.1016/j.phpro.2015.04.007.

[248] Y. Adamchuk, M. Voskanyan, G. Georgiev, A. Kovtun, G. Muradyan, N. Stancheva, N. Chikov, N. Yaneva, and Y. Shchepkin, "Measuring the ^{235}U alpha values at a thermal point," Sov. J. Atom. En. **65**, 1022 (1988).

[249] M. Schulc, M. Kostal, R. Capote, J. Simon, E. Novak, and T. Czakoj, "High-energy neutron emission in thermal neutron-induced fission of ^{235}U," Phys. Rev. **C109**, 054616 (2024). [Online] Available at https://link.aps.org/doi/10.1103/PhysRevC.109.054616.

[250] D. Neudecker and K. J. Kelly, "Including Chi-Nu ^{235}U PFNS experimental data into an ENDF/B-VIII.1 release candidate evaluation," Tech. Rep. **LA-UR-22-22220**, Los Alamos National Laboratory, NM, USA (2022).

[251] K. J. Kelly, J. A. Gomez, M. Devlin, *et al.*, "Measurement of the ^{235}U(n,f) prompt fission neutron spectrum from 10 keV to 10 MeV induced by neutrons of energy from 1 MeV to 20 MeV," Phys. Rev. **C105**, 044615 (2022). [Online] Available at https://link.aps.org/doi/10.1103/PhysRevC.105.044615.

[252] H.-H. Knitter, M. Islam, and M. Coppola, "Investigation of Fast Neutron Interaction with ^{235}U," Z. Phy. **257**, 108 (1972).

[253] R. Reed, R. Hockenbury, and R. Block, "Prompt neutron multiplicity measurements for neutron-induced fission of ^{233}U and ^{235}U," Technical report **ORNL/TM-6405, ENDF-298**, Rensselaer Polytechnic Institute, Troy, NY, USA (1973). [Online] Available at https://www.nndc.bnl.gov/endfdocs/ENDF-298.pdf.

[254] R. Reed, *Neutron Multiplicity Measurements for Neutron-Induced Fission of ^{233}U and ^{235}U.* Doctoral Thesis, Rensselaer Polytechnic Institute, Troy, NY, USA (1973).

[255] A. Lovell, D. Neudecker, and P. Talou, "Release of evaluated ^{235}U(n,f) average prompt fission neutron multiplicities including the CGMF model," Tech. Rep. **LA-UR-22-23475**, Los Alamos National Laboratory, NM, USA (2022).

[256] J. Bljumkina, I. Bondarenko, V. Kuznetsov, V. Nesterov, V. Okolovitch, G. Smirenkin, and L. Usachev, "Channel effects in the energy dependence of the number of prompt neutrons and the kinetic energy of fragments in the fission of u235 and u233 by neutrons," Nucl. Phys. **52**, 648 (1964).

[257] D. Colvin and M. Sowerby, "Boron pile nu-bar measurements," in *Proceedings of Nuclear Data for Reactors Conference, Paris*, **1**, 307 (1966).

[258] H. Conde, "Average number of neutrons from the fission of u-235," Arkiv foer Fysik **29**, 293 (1965).

[259] B. Diven, H. Martin, and R. Taschek, "Multiplicities of fission neutrons," Phys. Rev. **101**, 1012 (1956).

[260] D. Mather, M. McTaggart, and A. Moat, "Revision of the harwell 240pu source strength and nu for 235u and 252cf," J. Nucl. En. A&B **20**, 549 (1966).

[261] M. Soleihac, J. Frehaut, and J. Gauriau, "Energy dependence of nu-bar for neutron-induced fission of u235, u238 and pu239 from 1.3 to 15 mev," J. Nucl. En. **23**, 257 (1969).

[262] J. Frehaut, A. Bertin, and R. Bois, "Mesure de nu-bar et e-bar-gamma pour la fission de th232, u235 et np237

induite par des neutrons d'energie comprise entre 1 et 15 mev," Tech. Rep. **2196**, Centre d'Etudes Nucleaires (1981).

[263] R. Gwin, R. Spencer, and R. Ingle, "Measurements of the energy dependence of prompt neutron emission from u233, u235, and pu239," Nucl. Sci. Eng. **94**, 365 (1986).

[264] R. Howe and T. Phillips, "Fission nu-bar measurements," Tech. Rep. **21501**, Brookhaven National Laboratory (1976).

[265] F. Kaeppeler and R. Bandl, "The average number of prompt neutrons from neutron induced fission of u235 between 0.2 and 1.4 mev," in *Proceedings of Conference on Nuclear Cross Sections and Technology, Washington*, **2**, 549 (1975).

[266] J. Meadows and J. Whalen, "Energy dependence of prompt nu-bar for neutron-induced fission of u235," Phys. Rev. **126**, 197 (1962).

[267] L. Prokhorova, R. Bagdasarov, and I. Kotukhov, "Yield of prompt neutrons in the fission of u235 by neutrons with energies up to 1.5 mev," Atomnaya Energiya **30**, 250 (1971).

[268] L. Prokhorova and G. Smirenkin, "Average number of prompt neutrons from u235 and th232 fission induced by neutrons having energies up to 3.3 mev," Yad. Fiz. **7**, 961 (1968).

[269] Y. Khokhlov, I. Ivanin, V. Inkov, Y. Vinogradov, L. Danilin, and B. Polynov, "Measurements results of average neutron multiplicity from neutron induced fission of actinides in 0.5-10 mev energy range," in *Proceedings of Conference on Nuclear Data for Science and Technology, Gatlinburg*, **1**, 272 (1994).

[270] A. Protopopov and M. Blinov, "Mean number of neutrons emitted in u235 fission induced by 14.8 mev neutrons," Atomnaya Energiya **4**, 374 (1958).

[271] M. Savin, Y. Khokhlov, and Y. Zamjatnin, "The average number of prompt neutrons in fast neutron induced fission of u235, pu239 and pu240," Tech. Rep. **IAEA-CN-26/40**, IAEA (1970).

[272] M. Soleihac, J. Frehaut, and J. Gauriau, "Average number of prompt neutrons and relative fission cross-sections of u235 and pu239 in the 0.3 to 1.4 mev range," in *Conference on Nuclear Data for Reactors, Helsinki*, **2**, 145 (1970).

[273] R. J. Casperson, D. M. Asner, J. Baker, *et al.* (NIFFTE Collaboration), "Measurement of the normalized $^{238}\mathrm{U}(n,f)/^{235}\mathrm{U}(n,f)$ cross section ratio from threshold to 30 MeV with the NIFFTE fission Time Projection Chamber," Phys. Rev. **C97**, 034618 (2018). [Online] Available at https://link.aps.org/doi/10.1103/PhysRevC.97.034618.

[274] Z. Ren, Y. Yang, R. Liu, *et al.*, "Measurement of the ^{236,238}U(n,f) cross sections from the threshold to 200 MeV at CSNS Back-n," Eur. Phys. J. **A59**, 5 (2023).

[275] A. Vorobyev, A. Gagarski, O. Shcherbakov, L. Vaishnene, and A. Barabanov, "Measurement of the cross section for the neutron-induced fission of ^{238}U nuclei in the energy range of 0.3-500 MeV," JETP letters (USA) **117**, 557 (2023).

[276] K. J. Kelly, M. Devlin, J. M. O'Donnell, *et al.*, "Measurement of the $^{238}\mathrm{U}(n,f)$ prompt fission neutron spectrum from 10 keV to 10 MeV induced by neutrons with 1.5–20 MeV energy," Phys. Rev. **C108**, 024603 (2023). [Online] Available at https://link.aps.org/doi/10.1103/PhysRevC.108.024603.

[277] D. Neudecker, K. J. Kelly, R. C. Little, A. E. Lovell, and M. J.Devlin, "Evaluating the ^{238}U PFNS including Chi-Nu experimental data," Tech. Rep. **LA-UR-24-25503**, Los Alamos National Laboratory, NM, USA (2024). [Online] Available at https://www.osti.gov/biblio/2372659.

[278] D. Neudecker, A. E. Lovell, T. Kawano, and P. Talou, "Evaluated ^{238}U(n,f) average prompt fission neutron multiplicities including the CGMF model," Tech. Rep. **LA-UR-22-29906**, Los Alamos National Laboratory, NM, USA (2022). [Online] Available at https://www.osti.gov/servlets/purl/1889944.

[279] I. Asplund-Nilsson, H. Conde, and N. Starfelt, "Nu-bar of u238 from 1.5 to 15 mev," Nucl. Sci. Eng. **20**, 527 (1964).

[280] H. Conde and N. Starfelt, "Measurement of nu in fast neutron fission of th232 and u238," Nucl. Sci. Eng. **11**, 397 (1961).

[281] V. Desai, B. Nayak, and A. Saxena, "Prompt fission neutron spectra in fast-neutron-induced fission of u238," Phys. Rev. C **92**, 014609 (2015).

[282] J. Frehaut, G. Mosinski, and M. Soleihac, "Recent results in nu-bar measurements between 1.5 and 15 mev," in *Topical Conference on the Average Number of Neutrons Emitted in Fission* (1973). Report EANDC(E)-15 "U".

[283] D. Mather, P. Fieldhouse, and A. Moat, "Measurement of prompt nu-bar for the neutron-induced fission of th232, u233, u234 and pu239," Nucl. Phys. **66**, 149 (1965).

[284] B. Nurpeisov, K. Volodin, and V. Nesterov, "Dependence of nu-bar on neutron energies up to 5 mev for u233, u238 and pu239," Sov. Atom. En. **39**, 807 (1975).

[285] M. Sabin, Y. Khokhlov, and I. Paramonova, "Energy dependence of average neutron number for fast-neutron fission of u238," Sov. Atom. En. **32**, 474 (1972).

[286] V. Vorobyeva, B. Kuzminov, and V. Malinovskij, "Analysis of the energy dependence of the average number of prompt neutrons for neutron-induced fission of u238," Voprosy Atomnoy Nauki i Tekhniki **1/40**, 62 (1981).

[287] B. Zongyu, "The variation of average prompt neutron number for u238 fission in the fast neutron energy region with incident neutron energy," Atom. En. Sci. Techn. **9**, 362 (1975).

[288] B. Laurent, T. Granier, G. Bélier, *et al.*, "A new neutron counter for fission research," Nucl. Inst. Meth. Phys. Res. Sect. A: Accel. Spectrometers, Detect. Assoc. Equip. **745**, 99 (2014).

[289] J. Taieb, T. Granier, T. Ethvignot, M. Devlin, R. Haight, R. Nelson, J. O'Donnell, and D. Rochman, "Measurement of the average energy and multiplicity of prompt-fission neutrons from ^{238}U(n,f) and ^{237}Np(n,f) from 1 to 200 MeV," in *Conference on Nuclear Data for Science and Technology, Nice 2007*, **1**, 429 (2007). EXFOR 14215, [Online] Available at http://dx.doi.org/10.1051/ndata:07676.

[290] N. Kornilov, V. Baryba, and O.A.Salnikov), "Fission neutron spectra of U-238," Tech. Rep. **INDC(NDS)-169**, International Atomic Energy Agency, Vienna, Austria (1980). EXFOR 40631.

[291] G. Boikov, V. Dmitriev, G. Kudyaev, Y. Ostapenko, M. Svirin, and G. Smirenkin, "Spectrum of neutrons accompanying fission of 232th, 235u, and 238u by 2.9-mev and 14.7-mev neutrons," Sov. J. Nucl. Phys. (English

Transl. **53**, 392–405 (1991).

[292] R. Spencer, J. A. Harvey, N. W. Hill, and L. W. Weston, "Parameters of the 1.056-eV resonance in ^{240}Pu and the 2200 m/s neutron total cross sections of ^{235}U, ^{239}Pu, and ^{240}Pu," Nucl. Sci. Eng. **96**, 318 (1987). [Online] Available at https://doi.org/10.13182/NSE87-A16395.

[293] W. Kolar and K. Böckhoff, "Resonance parameters of ^{240}Pu: Part I—neutron widths," J. Nucl. En. **22**, 299 (1968). [Online] Available at https://doi.org/10.1016/0022-3107(68)90003-8.

[294] L. W. Weston and J. H. Todd, "Subthreshold fission cross section of ^{240}Pu and the fission cross sections of ^{235}U and ^{239}Pu," Nucl. Sci. Eng. **88**, 567 (1984). [Online] Available at https://doi.org/10.13182/NSE84-A18373.

[295] M. Drosg and N. Otuka, "Evaluation of the absolute angle-dependent differential neutron production cross sections by the reactions ^{3}H(p,n)^{3}He, ^{1}H(t,n)^{3}He, ^{2}H(d,n)^{3}He, ^{3}H(d,n)^{4}He, and ^{2}H(t,n)^{4}He and of the cross sections of their time-reversed counterparts up to 30 MeV and beyond," Tech. Rep. **INDC(AUS)-0019**, International Atomic Energy Agency, Vienna, Austria (2015). [Online] Available at https://www-nds.iaea.org/publications/indc/indc-aus-0019.pdf.

[296] H. Bai, R. Fan, H. Jiang, *et al.*, "Measurement of the differential cross sections and angle-integrated cross sections of the ^{6}Li(n, t)^{4}He reaction from 1.0 eV to 3.0 MeV at the CSNS Back-n white neutron source," Chin. Phys. C **44**, 014003 (2020). EXFOR 32800, [Online] Available at http://dx.doi.org/10.1088/1674-1137/44/1/014003.

[297] A. D. Carlson, V. G. Pronyaev, R. Capote, *et al.*, "Recent work leading towards a new evaluation of the Neutron Standards," Nucl. Data Sh. **123**, 27 (2015). [Online] Available at https://doi.org/10.1016/j.nds.2014.12.006.

[298] M. G. Sowerby, B. H. Patrick, C. A. Uttley, and K. M. Diment, "The ratio of the ^{6}Li(n,α) to ^{10}B(n,α) cross-sections from 10 eV to 80 keV and recommended values of the ^{10}B(n,α) cross section," J. Nucl. En. **24**, 323 (1970). EXFOR 20462, [Online] Available at http://dx.doi.org/10.1016/0022-3107(70)90051-1.

[299] R. A. S. G. P. Lamaze and O. A. Wasson, "A New Measurement of the ^{6}Li(n,α)t Cross Section," Nucl. Sci. Eng. **68**, 183 (1978). [Online] Available at https://doi.org/10.13182/NSE78-A27288.

[300] W. P. Poenitz, "Measurements of the ^{6}Li(n,α)t Cross Section in the keV Energy Range," Z. fuer Phys. **268**, 359 (1974). EXFOR 10378, [Online] Available at http://dx.doi.org/10.1007/BF01668910.

[301] R. L. Macklin, R. W. Ingle, and J. Halperin, "^{6}Li(n,α)^{3}H cross section from 70 to 3000-keV from the ^{235}U(n,f) calibration of a thin glass scintillator," Nucl. Sci. Eng. **71**, 205 (1979). EXFOR 10895, [Online] Available at http://dx.doi.org/10.13182/NSE79-A20412.

[302] G. Zhang, J. Chen, G. Tang, Y. M. Gledenov, M. Sedysheva, and G. Khuukhenkhuu, "Measurement of differential and angle-integrated cross sections of the ^{6}Li(n,t)^{4}He reaction in the MeV neutron energy range," Nucl. Instrum. Meth. Phys. Res. **A566**, 615 (2006). EXFOR 32646, [Online] Available at http://dx.doi.org/10.1016/j.nima.2006.06.064.

[303] M. Drosg, D. Drake, and J. Masarik, "Calibration of a Li-glass detector for neutron energies above 50 keV by the ^{1}H(t,n)^{3}He reaction," Nucl. Inst. Meth. Phys. Res. **B94**, 319 (1994). [Online] Available at https://www.sciencedirect.com/science/article/pii/0168583X94953716.

[304] L. E. Kirsch, M. Devlin, S. M. Mosby, and J. A. Gomez, "A new measurement of the ^{6}Li(n,α)t cross section at MeV energies using a ^{252}Cf fission chamber and ^{6}Li scintillators," Nucl. Instrum. Meth. Phys. Res. **A874**, 57 (2017). EXFOR 14483, [Online] Available at http://dx.doi.org/10.1016/j.nima.2017.08.046.

[305] M. Devlin, T. N. Taddeucci, G. M. Hale, and R. C. Haight, "^{6}Li(n,t)α angular distribution measurements for $0.2 < E_n < 10$ MeV at LANSCE/WNR," in *Conferences on Nuclear Data for Science and Technology, Nice 2007*, **2**, 1243 (2007). EXFOR 14159, [Online] Available at http://dx.doi.org/10.1051/ndata:07563.

[306] C. M. Bartle, D. W. Gebbie, and C. L. Hollas, "Total Cross Sections for the ^{6}Li(n,α)^{3}H Reaction between 12 and 18 MeV," Nucl. Phys. **A397**, 21 (1983). EXFOR 30651, [Online] Available at http://dx.doi.org/10.1016/0375-9474(83)90076-3.

[307] G. Presser, R. Bass, and K. Krueger, "The reactions ^{6}Li(n,p)^{6}He(0) and ^{6}Li(n,n')^{6}Li (3.56)," Nucl. Phys. **A131**, 679 (1969). [Online] Available at https://www.osti.gov/biblio/4766476.

[308] L. Rosen and L. Stewart, "Neutron-induced disintegration of ^{6}Li and ^{7}Li," Phys. Rev. **126**, 1150 (1962). [Online] Available at https://doi.org/10.1103/PhysRev.126.1150.

[309] R. Batchelor and J. H. Towle, "The interactions of neutrons with ^{6}Li and ^{7}Li between 1.5 and 7.5 MeV," Nucl. Phys. **47**, 385 (1963). EXFOR 21147, [Online] Available at http://dx.doi.org/10.1016/0029-5582(63)90881-2.

[310] J. C. Hopkins, D. M. Drake, and H. Conde, "Elastic and inelastic scattering of fast neutrons from ^{6}Li and ^{7}Li," Nucl. Phys. **A107**, 139 (1968). EXFOR 11153, [Online] Available at http://dx.doi.org/10.1016/0375-9474(68)90731-8.

[311] S. Chiba, M. Baba, H. Nakashima, M. Ono, N. Yabuta, S. Yukinori, and N. Hirakawa, "Double-differential neutron emission cross sections of ^{6}Li and ^{7}Li at incident neutron energies of 4.2, 5.4, 6.0 and 14.2 MeV," J. Nucl. Sci. Techn. **22**, 771 (1985). EXFOR 21986, [Online] Available at http://dx.doi.org/10.3327/jnst.22.771.

[312] C. Conneely, W. Prestwich, and T. Kennett, "The thermal neutron capture cross section of ^{9}Be," Nucl. Inst. Meth. Phys. Res. **A248**, 416 (1986). [Online] Available at https://doi.org/10.1016/0168-9002(86)91026-0.

[313] S. Shibata (1992). Unpublished; private communication.

[314] R. B. Firestone and Z. Revay, "Thermal neutron radiative cross sections for ^{6,7}Li, ^{9}Be, ^{10,11}B, ^{12,13}C, and ^{14,15}N," Phys. Rev. **C93**, 054306 (2016). [Online] Available at https://doi.org/10.1103/PhysRevC.93.054306.

[315] A. Wallner, M. Bichler, L. Coquard, *et al.*, "Stellar and thermal neutron capture cross section of ^{9}Be," Phys. Rev. **C99**, 015804 (2019). [Online] Available at https://doi.org/10.1103/PhysRevC.99.015804.

[316] D. J. Marín-Lámbarri, J. García-Ramírez, E. Sánchez-Zúñiga, *et al.*, "Measurement of the thermal neutron capture cross section by ^{9}Be using the neutron flux from a nuclear research reactor and the AMS technique,"

Phys. Rev. **C102**, 044601 (2020). [Online] Available at https://doi.org/10.1103/PhysRevC.102.044601.

[317] N. M. Larson, "Updated User's Guide for SAMMY: Multilevel R-Matrix Fits to Neutron Data Using Bayes' Equations," Tech. Rep. **ORNL/TM-9179/R8**, Oak Ridge National Laboratory, TN, USA (2008). [Online] Available at https://doi.org/10.2172/941054.

[318] A. Bensussan and J. M. Salomé, "GELINA: A modern accelerator for high resolution neutron time of flight experiments," Nucl. Inst. Meth. **155**, 11 (1978). [Online] Available at https://api.semanticscholar.org/CorpusID:120998133.

[319] K. Guber, C. Paradela, J. Heyse, S. Kopecky, P. Schillebeeckx, and P. Siegler, "Neutron nuclear data measurements for criticality safety," EPJ. Web. Conf. **146**, 11020 (2017). [Online] Available at http://www.epj-conferences.org/10.1051/epjconf/201714611020.

[320] V. Vertebnyi, M. Vlasov, N. Gnidak, R. Zatserkovskii, A. Ignatenko, A. Kirilyuk, E. Pavlenko, N. Trofimova, and A. Fedorova, "Thermal and epithermal neutron cross sections for vanadium isotopes," Sov. Atom. En. **34**, 441 (1973). [Online] Available at http://dx.doi.org/10.1007/BF01163740.

[321] P. A. Egelstaff, "The thermal neutron cross sections of Hf, Br, V, Se, Mo and Bi," Tech. Rep. **AERE-N/R-1147**, Atomic Energy Research Establishment (AERE), Harwell, United Kingdom (1953).

[322] E. Pavlenko and N. Gnidak, "Measuring neutron absorption cross section," J. Inst. Exp. Tech. **20**, 653 (1977).

[323] S. F. Mughabghab, *Atlas of Neutron Resonances: Thermal Cross Sections and Resonance Parameters*. Amsterdam: Elsevier (2006).

[324] B. Cochet, A. Jinaphanh, L. Heulers, and O. Jacquet, "Capabilities overview of the MORET 5 Monte Carlo code," Ann. Nucl. En. **82**, 74 (2015). [Online] Available at https://doi.org/10.1016/j.anucene.2014.08.022.

[325] R. MacFarlane, D. Muir, R. Boicourt, A. Kahler, J. Conlin, and W. Haeck, "The NJOY Nuclear Data Processing System, Version 2016," Tech. Rep. **LA-UR-17-20093**, Los Alamos National Laboratory, NM, USA (2017).

[326] P. E. Koehler, R. R. Winters, K. H. Guber, *et al.*, "High-resolution neutron capture and transmission measurements, and the stellar neutron-capture cross section of ^{88}Sr," Phys. Rev. **C62**, 055803 (2000). [Online] Available at https://link.aps.org/doi/10.1103/PhysRevC.62.055803.

[327] P. E. Koehler, R. R. Winters, K. H. Guber, *et al.*, "Erratum: High-resolution neutron capture and transmission measurements, and the stellar neutron-capture cross section of ^{88}Sr [Phys. Rev. C 62, 055803 (2000)]," Phys. Rev. **C63**, 049901 (2001). [Online] Available at https://link.aps.org/doi/10.1103/PhysRevC.63.049901.

[328] M. T. Pigni, J. McDonnell, and K. H. Guber, "Resonance parameter evaluation of n+^{88}Sr reactions for ENDF/B-VIII.1 library," Technical report **ORNL/LTR-2023/3004**, Oak Ridge National Laboratory, TN, USA (2023). [Online] Available at https://www.osti.gov/biblio/2205429.

[329] K. S. Krane, "Cross sections and isomer ratios in the Rb(n,γ) and Sr(n,γ) reactions," Eur. Phys. J. **A57**, 18 (2021). [Online] Available at https://doi.org/10.1140/epja/s10050-020-00299-2.

[330] L. Koester, K. Knopf, and W. Waschkowski, "Slow neutron scattering parameters for stable nuclei with nucleon numbers between A=79 and A=96," Z. für Phys. **A301**, 215 (1981). [Online] Available at https://doi.org/10.1007/BF01416296.

[331] E. Gaerttner, M. Yeater, and R. Fullwood, "Rensselaer polytechnic institute linac facility," in *Proceedings of Symposium on Neutron Physics* (M. Yeater, ed.), 263, Academic Press (1962).

[332] L. Mihailescu, A. Borella, R. Capote Noy, *et al.*, "Neutron cross-section measurements on ^{103}Rh and ^{133}Cs for improved nuclear criticality safety," in *NEMEA-3 Neutron Measurements, Evaluations and Applications, Proceedings of the enlargement workshop* (A. Plompen, ed.), 153, Office for Official Publications of the European Communities (2006). [Online] Available at https://publications.jrc.ec.europa.eu/repository/handle/JRC41952.

[333] A. Brusegan, "Neutron capture and transmission measurements on ^{103}Rh down to thermal energies," in *AIP Conference Proceedings*, **769**, (Santa Fe, New Mexico (USA)), 953, AIP (2005). [Online] Available at https://pubs.aip.org/aip/acp/article/769/1/953-956/1014085.

[334] P. Ribon, *Etudes de quelques proprietés des niveaux excités des noyaux composés formés par l'interaction des neutrons lents avec ^{103}Rh, Xe, ^{155}Gd, ^{232}Th.* Doctoral Thesis, CNRS, France (1969). A.0.3560, also CEA Note N-1149.

[335] B. Pritychenko and S. F. Mughabghab, "Neutron Thermal Cross Sections, Westcott Factors, Resonance Integrals, Maxwellian Averaged Cross Sections and Astrophysical Reaction Rates Calculated from the ENDF/B-VII.1, JEFF-3.1.2, JENDL-4.0, ROSFOND-2010, CENDL-3.1 and EAF-2010 Evaluated Data Libraries," Nucl. Data Sh. **113**, 3120 (2012). [Online] Available at https://doi.org/10.1016/j.nds.2012.11.007.

[336] D. Barry, A. Lewis, L. Leal, and J. Brown, "A new ^{103}Rh unresolved resonance region evaluation," Ann. Nucl. En. **188**, 109751 (2023). [Online] Available at https://www.sciencedirect.com/science/article/pii/S0306454923000701.

[337] C. W. Chapman, M. T. Pigni, K. Guber, and G. Arbanas, "R-matrix Resolved Resonance Region Evaluation of ^{140,142}Ce," Tech. Rep. **ORNL/TM-2023/2924**, Oak Ridge National Laboratory (2023). [Online] Available at https://www.osti.gov/biblio/2217725.

[338] M. T. Pigni, "R-matrix analysis and statistical properties of dysprosium isotopes in the neutron energy range up to a few keV," Tech. Rep. **ORNL/TM-2023/2925**, Oak Ridge National Laboratory (2023). [Online] Available at https://www.osti.gov/biblio/1987785.

[339] R. Block, M. Bishop, D. Barry, *et al.*, "Neutron transmission and capture measurements and analysis of Dy from 0.01 to 550 eV," Prog. Nucl. En. **94**, 126 (2017). [Online] Available at https://www.sciencedirect.com/science/article/pii/S0149197016302207.

[340] S. G. Shin, Y. U. Kye, W. Namkung, *et al.*, "Neutron capture measurements and resonance parameters of dysprosium," Eur. Phys. J. **A53**, 203 (2017). [Online] Available at https://doi.org/10.1140/epja/i2017-12402-7.

[341] H. I. Liou, G. Hacken, J. Rainwater, and U. N. Singh,

"Neutron resonance spectroscopy: The separated isotopes of Dy," Phys. Rev. **C11**, 462 (1975). [Online] Available at https://link.aps.org/doi/10.1103/PhysRevC.11.462.

[342] M. Herman, D. Brown, R. Capote, *et al.*, "Infrastructure for the new paradigm of nuclear reaction evaluation," Ann. Nucl. En. **163**, 108494 (2021). [Online] Available at https://www.sciencedirect.com/science/article/pii/S0306454921003704.

[343] A. Chambers, "Five-Year Execution Plan for the Mission and Vision of the United States Department of Energy Nuclear Criticality Safety Program, FY 2023 through FY 2027, Revision 2," tech. rep., US Department of Energy (2022).

[344] S. F. Mughabghab, *Atlas of Neutron Resonances*. Elsevier (2018). [Online] Available at https://linkinghub.elsevier.com/retrieve/pii/C2015000524X.

[345] D. Barry, M. Pigni, J. Brown, A. Lewis, T. Trumbull, K. Guber, B. McDermott, R. Block, and Y. Danon, "A new ^{181}Ta neutron resolved resonance region evaluation," Ann. Nucl. En. **208**, 110778 (2024). [Online] Available at https://www.sciencedirect.com/science/article/pii/S0306454924004419.

[346] J. Harvey, N. Hill, F. Perey, G. Tweed, and L. Leal, "High-resolution neutron transmission measurements on ^{235}U, ^{239}Pu, and ^{238}U," Tech. Rep. **CONF-880546**, ORNL, Oak Ridge, TN, USA (1988).

[347] J. M. Brown, D. P. Barry, R. C. Block, A. Youmans, H. Choun, A. Ney, E. Blain, M. J. Rapp, and Y. Danon, "New measurements to resolve discrepancies in evaluated model parameters of ^{181}Ta," Nucl. **198**, 1 (2024). [Online] Available at https://doi.org/10.1080/00295639.2023.2249786.

[348] W. P. Poenitz, J. F. Whalen, and A. B. Smith, "Total neutron cross sections of heavy nuclei," Nucl. Sci. Eng. **78**, 333 (1981). EXFOR 10935, [Online] Available at https://doi.org/10.13182/NSE81-A21367.

[349] B. J. McDermott *et al.*, "^{181}Ta(n,γ) cross section and average resonance parameter measurements in the unresolved resonance region from 24 to 1180 keV using a filtered-beam technique," Phys. Rev. **C96**, 014607 (2017). [Online] Available at https://link.aps.org/doi/10.1103/PhysRevC.96.014607.

[350] K. Wisshak, F. Voss, F. Käppeler, and G. Reffo, "Measurements of keV neutron capture cross sections with a 4π barium fluoride detector: Examples of ^{93}Nb, ^{103}Rh, and ^{181}Ta," Phys. Rev. **C42**, 1731 (1990). [Online] Available at https://link.aps.org/doi/10.1103/PhysRevC.42.1731.

[351] K. Wisshak, F. Voss, C. Arlandini, F. Käppeler, M. Heil, R. Reifarth, M. Krtička, and F. Bečvář, "Stellar neutron capture on ^{180m}Ta. I. Cross section measurement between 10 keV and 100 keV," Phys. Rev. **C69**, 055801 (2004). [Online] Available at https://doi.org/10.1103/PhysRevC.69.055801.

[352] J. Brzosko, E. Gierlik, A. Soltan Jr, and Z. Wilhelmi, "Effect of the pigmy resonance on the calculations of the neutron capture cross section," Can. J. Phys. **47**, 2849 (1969). [Online] Available at https://doi.org/10.1139/p69-348.

[353] M. Bokhovko, A. Voevodskij, V. Kononov, E. Poletaev, and V. Timokhov, "Neutron radiation capture cross-section and transmission of fast neutrons for isotopes of rare-earth elements ^{181}Ta and ^{187}O," Tech. Rep. **FEI-2169**, IPPE, Obninsk, USSR (1993).

[354] V. Kononov, B. Jurlov, G. Manturov, E. Poletaev, V. Timokhov, and V. Shorin, "Fast neutron radiative capture cross-section for In-115, Ta-181, Au-197 and samarium and europium isotopes," Sov. J. Nucl. Phys. **26**, 500 (1977).

[355] N. Yamamuro, K. Saito, T. Emoto, T. Wadam, Y. Fujita, and K. Kobayashi, "Neutron capture cross section measurements of Nb-93, I-127, Ho-165, Ta-181, and U-238 between 3.2 and 80 keV," J. Nucl. Sci. Techn. **17**, 582 (1980). [Online] Available at https://doi.org/10.1080/18811248.1980.9732628.

[356] I. O. Zo, V. Nikolenko, A. Popov, and G. Samosvat, "The neutron elastic scatterirg differential cross sections in energy range below 440 keV," Tech. Rep. **P3-85-133**, Joint Institute for Nuclear Research, Dubna, Russia (1985). [Online] Available at https://inis.iaea.org/collection/NCLCollectionStore/_Public/16/083/16083652.pdf.

[357] J. M. Brown, R. Block, A. Youmans, H. Choun, A. Ney, E. Blain, D. Barry, M. Rapp, and Y. Danon, "Validation of unresolved neutron resonance parameters using a thick-sample transmission measurement," Nucl. Sci. Eng. **194**, 221 (2020).

[358] T. Y. Byoun, *Experimental Investigation of the Resonance Self-Shielding and Doppler Broadening Effect in Uranium and Tantalum*. Doctoral Thesis, Rensselaer Polytechnic Institute, Troy, NY, USA (1973).

[359] J. M. Brown, D. P. Barry, A. Lewis, T. H. Trumbull, M. T. Pigni, T. Greene, R. C. Block, A. Golas, and Y. Danon, "Unresolved Resonance Parameter Evaluation and Uncertainty Quantification of n+^{181}Ta Reactions," Ann. Nucl. En. **212**, 111013 (2025).

[360] W. P. Poenitz and J. F. Whalen, "Neutron total cross section measurements in the energy region from 47 keV to 20 MeV," Tech. Rep. **ANL-NDM-80**, Argonne National Laboratory, Argonne, IL, USA (1983). EXFOR 10935, [Online] Available at https://www.osti.gov/biblio/5531535.

[361] I. Tsubone, Y. Nakajima, Y. Furuta, and Y. Kanda, "Neutron total cross sections of ^{181}Ta and ^{238}U from 24.3 keV to 1 MeV and average resonance parameters," Nucl. Sci. Eng. **88**, 579 (1984). EXFOR 21813, [Online] Available at http://dx.doi.org/10.13182/NSE84-A18374.

[362] M. J. Rapp, D. P. Barry, G. Leinweber, R. C. Block, B. E. Epping, T. H. Trumbull, and Y. Danon, "Tantalum, titanium, and zirconium neutron total cross-section measurements from 0.4 to 25 MeV," Nucl. Sci. Eng. **193**, 903 (2019). EXFOR 14576, [Online] Available at http://dx.doi.org/10.1080/00295639.2019.1570750.

[363] A. B. Smith, P. T. Guenther, and J. F. Whalen, "Fast-neutron scattering from Ta, Re, and Pt," Phys. Rev. **168**, 1344 (1968). EXFOR 10631, [Online] Available at http://dx.doi.org/10.1103/PhysRev.168.1344.

[364] R. Hannaske, Z. Elekes, R. Beyer, *et al.*, "Neutron total cross section measurements of gold and tantalum at the nELBE photoneutron source," Eur. Phys. J. **A49**, 137 (2013). EXFOR 23199, [Online] Available at http://dx.doi.org/10.1140/epja/i2013-13137-1.

[365] T. Y. Byoun, R. C. Block, and T. Semler, "Average resonance parameters of depleted Uranium and Tantalum in the energy range 10 to 100 keV," Tech. Rep. **Chicago Operations Office, A.E.C., COO-3058-34**, Rensse-

laer Polytechnic Institute, NY, USA (1973). EXFOR 10577.

[366] A. D. Carlson and H. H. Barschall, "Fluctuations in neutron total cross sections," Phys. Rev. **158**, 1142 (1967). EXFOR 11497, [Online] Available at http://dx.doi.org/10.1103/PhysRev.158.1142.

[367] R. W. Finlay, W. P. Abfalterer, G. Fink, E. Montei, T. Adami, P. W. Lisowski, G. L. Morgan, and R. C. Haight, "Neutron total cross sections at intermediate energies," Phys. Rev. **C47**, 237 (1993). EXFOR 13569, [Online] Available at http://dx.doi.org/10.1103/PhysRevC.47.237.

[368] D. G. Foster, J. , and D. W. Glasgow, "Neutron total cross sections, 2.5–15 MeV. I. Experimental," Phys. Rev. **C3**, 576 (1971). EXFOR 10047, [Online] Available at http://dx.doi.org/10.1103/PhysRevC.3.576.

[369] A. B. Smith, "Fast neutrons incident on rotors: Tantalum," Tech. Rep. **ANL-NDM-160**, Argonne National Laboratory, IL, USA (2005). EXFOR 13965, [Online] Available at https://anl.app.box.com/s/9kze0zt38upgrlc27yerfjin3bx9r8ga.

[370] Zo-In-Ok, V. G. Nikolenko, A. B. Popov, and G. S. Samosvat, "The neutron integral and differential cross-sections in the energy region below 440 keV.," Tech. Rep. **JINR-P3-85-133**, Joint Institute for Nuclear Research, Dubna, Russia (1985). EXFOR 40937.

[371] V. C. Rogers, L. E. Beghian, and F. M. Clikeman, "Neutron inelastic scattering cross sections for iron, nickel, niobium, and tantalum from threshold to 1.8 MeV," Nucl. Sci. Eng. **45**, 297 (1971). EXFOR 10146, [Online] Available at http://dx.doi.org/10.13182/NSE71-A19081.

[372] N.P.Glazkov, "Cross sections of the inelastic scattering of neutrons with energies of 0.4–1.2 MeV on medium and light nuclei," Sov. Atom. En. **15**, 1173 (1963). EXFOR 40680.

[373] R. O. Owens and J. H. Towle, "The level density of the deformed rare-earth nuclei," Nucl. Phys. **A112**, 337 (1968). EXFOR 21231, [Online] Available at http://dx.doi.org/10.1016/0375-9474(68)90206-6.

[374] S. Simakov, G. Lovchikova, O. Salnikov, G. Kotelnikova, and A. Trufanov, "Elastic and inelastic scattering of the neutrons with the energies from 5 to 8 MeV on bismuth and tantalum," Tech. Rep. **197**, International Atomic Energy Agency, Vienna, Austria (1982). EXFOR 40603, [Online] Available at https://www-nds.iaea.org/publications/indc/indc-ccp-0197/.

[375] W. P. Poenitz, "Radiative capture of fast neutrons in ^{165}Ho and ^{181}Ta," Tech. Rep. **ANL-NDM-15**, Argonne National Laboratory, IL, USA (1975). EXFOR 10401, [Online] Available at https://anl.app.box.com/s/rpk0qx8zxym28du4cdgxsyvfohby5zps.

[376] A. A. Filatenkov, "Neutron activation cross sections measured at KRI in neutron energy region 13.4–14.9 MeV," Tech. Rep. **INDC(CCP)-0460**, International Atomic Energy Agency, Vienna, Austria (2016). EXFOR 41614, [Online] Available at https://www-nds.iaea.org/publications/indc/indc-ccp-0460/.

[377] Y. Kasugai, M. Asai, A. Tanaka, H. Yamamoto, I. Jun, T. Iida, and K. Kawade, "Measurement of activation cross sections on tantalum and tungsten with 14 MeV neutrons," J. Nucl. Sci. Techn. **31**, 1248 (1994). EXFOR 23011, [Online] Available at http://dx.doi.org/10.3327/jnst.31.1248.

[378] V. Semkova, R. Capote, R. J. Tornin, A. J. Koning, A. Moens, and A. J. M. Plompen, "New cross section measurements for neutron-induced reactions on Cr, Ni, Cu, Ta and W isotopes obtained with the activation technique," in *Conference on Nuclear Data for Science and Technology, Nice 2007*, **1**, 559 (2007). EXFOR 22877, [Online] Available at http://dx.doi.org/10.1051/ndata:07320.

[379] S. Begun, I. Kadenko, V. Maidanyuk, V. Neplyuev, V. Plujko, G. Primenko, and V. Tarakanov, "Determination of the cross sections of (n,x) nuclear reactions on Y, La, Ta, Pb and Bi at the energy of neutrons about 14 MeV," J. Nucl. Sci. Techn. **39**, 425 (2002). [Online] Available at https://doi.org/10.1080/00223131.2002.10875131.

[380] R. Wolfle, A. Mannan, S. M. Qaim, H. Liskien, and R. Widera, "Excitation functions of ^{93}Nb(n,2n)^{92m}Nb, ^{93}Nb(n,α)^{90m,g}Y, ^{139}La(n,α)^{136}Cs and ^{181}Ta(n,p)^{181}Hf reactions in the energy range of 12.5–19.6 MeV," Appl. Radiat. Isot. **39**, 407 (1988). EXFOR 22108, [Online] Available at http://dx.doi.org/10.1016/0883-2889(88)90071-8.

[381] S. K. Mukherjee and H. Bakhru, "Some (n,α) reaction cross-sections and the resulting radio-isotopes.," in *Nuclear and Solid State Physics Symp., Bombay 1963*, 244 (1963). EXFOR 31330.

[382] J. Frehaut and G. Mosinski, "Measurement of the (n,2n) cross-sections for ^{56}Fe, ^{59}Co, ^{89}Y, ^{169}Tm, ^{175}Lu, ^{181}Ta, ^{197}Au, ^{209}Bi, ^{238}U and of the (n,3n) cross-section for ^{238}U from threshold to 15 MeV incident neutron energy," Tech. Rep. **CEA-R-4627**, Centre d'Etudes Nucleaires, Saclay, CEA, France (1974). EXFOR 20416.

[383] L. R. Veeser, E. D. Arthur, and P. G. Young, "Cross sections for (n,2n) and (n,3n) reaction above 14 MeV," Phys. Rev. **C16**, 1792 (1977). EXFOR 10445, [Online] Available at http://dx.doi.org/10.1103/PhysRevC.16.1792.

[384] A. D. Majdeddin, V. Semkova, R. Doczi, C. M. Buczko, and J. Csikai, "Investigations on (n,α) cross sections in the 14 MeV region," Tech. Rep. **INDC(HUN)-031**, International Atomic Energy Agency, Vienna, Austria (1997). EXFOR 31481, [Online] Available at https://www-nds.iaea.org/publications/indc/indc-hun-0031/.

[385] B. Holmqvist, T. Wiedling, V. Benzi, and L. Zuffi, "Analysis of fast neutron elastic scattering from tantalum using a non-spherical optical potential," Nucl. Phys. **A150**, 105 (1970). EXFOR 20019, [Online] Available at http://dx.doi.org/10.1016/0375-9474(70)90460-4.

[386] J. R. Beyster, M. Walt, and E. W. Salmi, "Interaction of 1.0-, 1.77-, 2.5-, 3.25-, and 7.0-MeV neutrons with nuclei," Phys. Rev. **104**, 1319 (1956). EXFOR 11220, [Online] Available at http://dx.doi.org/10.1103/PhysRev.104.1319.

[387] S. C. Buccino, C. E. Hollandsworth, and P. R. Bevington, "Effects of nuclear spin on the elastic scattering of 5 MeV neutrons.," Z. fuer Phys. **196**, 103 (1966). EXFOR 11877, [Online] Available at http://dx.doi.org/10.1007/BF01326420.

[388] J. C. Ferrer, J. D. Carlson, and J. Rapaport, "Neutron elastic scattering at 11 MeV and the isospin dependence of the neutron-nucleus optical potential," Nucl. Phys. **A275**, 325 (1977). EXFOR 10633, [Online] Available at http://dx.doi.org/10.1016/0375-9474(77)90456-0.

[389] A. Takahashi, Y. Sasaki, and H. Sugimoto, "Measurement and analysis of double differential neutron emission cross sections at En=14.1 MeV for ^{93}Nb and ^{181}Ta," Tech. Rep. **OKTAV-A-92-01**, OKTAVIAN, Osaka University, Osaka, Japan (1992). EXFOR 22136.

[390] L. F. Hansen, F. S. Dietrich, B. A. Pohl, C. H. Poppe, and C. Wong, "Test of microscopic optical model potentials for neutron elastic scattering at 14.6 MeV over a wide mass range," Phys. Rev. **C31**, 111 (1985). EXFOR 12935, [Online] Available at http://dx.doi.org/10.1103/PhysRevC.31.111.

[391] W. G. Cross and R. G. Jarvis, "Scattering of 14.6 MeV neutrons by Mg, Ca, Cd, Ta and Bi," Nucl. Phys. **15**, 155 (1960). EXFOR 11465, [Online] Available at http://dx.doi.org/10.1016/0029-5582(60)90294-7.

[392] C. I. Hudson, J. , W. S. Walker, and S. Berko, "Differential elastic scattering of 15.2-MeV Neutrons by Ta, Bi, Th, and U," Phys. Rev. **128**, 1271 (1962). EXFOR 12180, [Online] Available at http://dx.doi.org/10.1103/PhysRev.128.1271.

[393] S. Matsuyama, T. Okubo, M. Baba, T. Ito, T. Akiyama, N. Ito, and N. Hirakawa, "Measurement of double-differential neutron emission cross sections of Mo, Ta and W," Conference Report **JAERI-M-93-046**, Japan Atomic Energy Research Institute, Tokai, Japan (1993). EXFOR 22352.

[394] H. Vonach, A. Chalupka, F. Wenninger, and G. Staffel, "Measurement of the angle-integrated secondary neutron spectra from interaction of 14 MeV neutrons with medium and heavy nuclei," Conference Report **INDC(USA)-84; BNL-NCS-51245 (VOL.1)**, International Atomic Energy Agency, Vienna, Austria (1980). Symposium on neutron cross sections from 10–50 MeV; Upton, NY, USA; 12 - 14 May 1980, EXFOR 21599, [Online] Available at https://www-nds.iaea.org/publications/indc/indc-usa-0084-vol1/.

[395] S. Matsuyama, T. Okubo, M. Baba, T. Ito, T. Akiyama, N. Ito, and N. Hirakawa, "Measurement of double-differential neutron emission cross sections of Mo, Ta and W," Tech. Rep. **JAERI-M-93-046, INDC(JPN)-163**, Japan Atomic Energy Research Institute (1992). EXFOR 22352, [Online] Available at https://www-nds.iaea.org/publications/indc/indc-jpn-0163/.

[396] D. Soda, S. Matsuyama, M. Ibaraki, M. Baba, S. Iwasaki, and N. Hirakawa, "Measurements of double-differential neutron emission cross sections for 18 and 11.5 MeV neutrons," Conference Report **JAERI-C-96-008**, Japan Atomic Energy Research Institute, Tokai, Japan (1996). EXFOR 22343.

[397] M. Herman, R. Capote, M. Sin, *et al.*, "EMPIRE-3.2 Malta modular system for nuclear reaction calculations," Tech. Rep. **INDC(NDS)-0642, BNL-101378-2013**, International Atomic Energy Agency, Vienna, Austria (2013). [Online] Available at https://www-nds.iaea.org/publications/indc/indc-nds-0642/.

[398] T. Tamura, T. Udagawa, and H. Lenske, "Multistep direct reaction analysis of continuum spectra in reactions induced by light ions," Phys. Rev. **C26**, 379 (1982). [Online] Available at https://doi.org/10.1103/PhysRevC.26.379.

[399] H. Lenske and H. H. Wolter, "TRISTAN and ORION codes." private communication to M. Herman.

[400] H. Nishioka, J. J. M. Verbaarschot, H. A. Weidenmüller, and S. Yoshida, "Statistical theory of precompound reactions: The multistep compound process," Ann. Phys. **172**, 67 (1986). [Online] Available at https://doi.org/10.1016/0003-4916(86)90020-5.

[401] M. Herman, G. Reffo, and H. A. Weidenmüller, "Multistep-compound contribution to precompound reaction cross section," Nucl. Phys. **A536**, 124 (1992). [Online] Available at https://doi.org/10.1016/0375-9474(92)90249-J.

[402] A. Höring and H. A. Weidenmüller, "Gamma emission in precompound reactions. I. Statistical model and collective gamma decay," Phys. Rev. **C46**, 2476 (1992). [Online] Available at https://doi.org/10.1103/PhysRevC.46.2476.

[403] M. Herman, A. Höring, and G. Reffo, "Gamma emission in precompound reactions. II. Numerical application," Phys. Rev. **C46**, 2493 (1992). [Online] Available at https://doi.org/10.1103/PhysRevC.46.2493.

[404] A. Iwamoto and K. Harada, "Mechanism of cluster emission in nucleon-induced preequilibrium reactions," Phys. Rev. **C26**, 1821 (1982). [Online] Available at http://dx.doi.org/10.1103/PhysRevC.26.1821.

[405] C. Kalbach, "Systematics of continuum angular distributions: Extensions to higher energies," Phys. Rev. **C37**, 2350 (1988). [Online] Available at https://link.aps.org/doi/10.1103/PhysRevC.37.2350.

[406] P. A. Moldauer, "Evaluation of the fluctuation enhancement factor," Phys. Rev. **C14**, 764 (1976). [Online] Available at http://dx.doi.org/10.1103/PhysRevC.14.764.

[407] T. Belgya, O. Bersillon, R. Capote, *et al.*, "Handbook for Calculations of nuclear reaction data: RIPL-2," Tech. Rep. **IAEA-TECDOC-1506**, International Atomic Energy Agengy, Vienna, Austria (2006). [Online] Available at http://www-nds.iaea.org/RIPL-2/.

[408] A. Gilbert and A. G. W. Cameron, "A composite nuclear-level density formula with shell corrections," Can. J. Phys. **43**, 1446 (1965). [Online] Available at http://www.nrcresearchpress.com/doi/10.1139/p65-139.

[409] G. J. Siemers, Y. Danon, S. Singh, K. C. Keparutis, P. J. Brain, B. H. Wang, A. M. Daskalakis, D. P. Barry, M. J. Rapp, and R. C. Block, "A quasi-differential measurement of neutron scattering from tantalum between 0.65 MeV and 20 MeV," Ann. Nucl. En. **224**, 111676 (2025). [Online] Available at https://www.sciencedirect.com/science/article/pii/S0306454925004931.

[410] H. M. Hofmann, J. Richert, J. W. Tepel, and H. A. Weidenmüller, "Direct reactions and Hauser-Feshbach theory," Ann. Phys. **90**, 403 (1975).

[411] Junghans, Arnd, Beyer, Roland, Claußner, Jürgen, *et al.*, "Neutron transmission measurements at nelbe," EPJ. Web. Conf. **239**, 01006 (2020). [Online] Available at https://doi.org/10.1051/epjconf/202023901006.

[412] D. G. Foster and D. W. Glasgow, "Neutron total cross sections, 2.5-15 mev. i. experimental," Phys. Rev. C **3**, 576 (1971). [Online] Available at https://link.aps.org/doi/10.1103/PhysRevC.3.576.

[413] M. Goldhaber and G. H. Briggs, "Scattering of slow neutrons," Proc. Royal Soc. Lond. A. Math. Phys. Sci. **162**, 127 (1937). [Online] Available at https://doi.org/10.1098/rspa.1937.0172.

[414] W. Dilg and H. Vonach, "Average total neutron cross sections of heavy elements at 2.7 keV," Tech. Rep. **150**,

Report from Euratom-countries + Euratom to EANDC (1972).
[415] J. F. Whalen and J. W. Meadows, "Fast neutron total cross sections using a mono-energetic source and an automated facility," Tech. Rep. **7210**, Argonne National Laboratory (1966).
[416] W. P. Poenitz and J. F. Whalen, "Neutron Total Cross Section Measurements in the Energy Region from 47 keV to 20 MeV," Tech. Rep. **80**, Argonne National Laboratory (1983).
[417] A. Bratenahl, J. M. Peterson, and J. P. Stoering, "Neutron total cross sections in the 7- to 14-mev region," Phys. Rev. **110**, 927 (1958). [Online] Available at https://link.aps.org/doi/10.1103/PhysRev.110.927.
[418] J. H. Coon, E. R. Graves, and H. H. Barschall, "Total cross sections for 14-mev neutrons," Phys. Rev. **88**, 562 (1952). [Online] Available at https://link.aps.org/doi/10.1103/PhysRev.88.562.
[419] C. T. Hibdon, "Neutron cross sections at 120 and 345 ev," Phys. Rev. **79**, 747 (1950). [Online] Available at https://link.aps.org/doi/10.1103/PhysRev.79.747.
[420] A. B. Smith, P. T. Guenther, and J. F. Whalen, "Fast-neutron scattering from ta, re, and pt," Phys. Rev. **168**, 1344 (1968). [Online] Available at https://link.aps.org/doi/10.1103/PhysRev.168.1344.
[421] P. E. Koehler, K. H. Guber, J. A. Harvey, *et al.*, "Recent experiments at orela and lansce, and their impact on compound nuclear models," AIP Conf. Proc. **1005**, 119 (2008). [Online] Available at https://doi.org/10.1063/1.2920713.
[422] P. E. Koehler and K. H. Guber, "Improved ^{192,194,195,196}Pt(n,γ) and ^{192}Ir(n,γ) astrophysical reaction rates," Phys. Rev. **C88**, 035802 (2013). [Online] Available at http://dx.doi.org/10.1103/PhysRevC.88.035802.
[423] J. Frehaut, A. Bertin, R. Bois, J. Jary, and G. Mosinski, "Status of (n,xn) cross section measurements at Bruyeres-le-Chatel," Tech. Rep. **6447**, Centre d'Etudes Nucleaires, Saclay (2016).
[424] J. Frehaut and G. Mosinski, "Measurement of (n,2n) and (n,3n) cross sections at incident energies between 8 and 15 MeV," 5th Int. Symp. on Interact. Fast Neutrons with Nucl., 24 (1975).
[425] H. Vonach, A. Pavlik, and B. Strohmaier, "Accurate determination of (n, 2n) cross sections for heavy nuclei from neutron production spectra," Nucl. Sci. Eng. **106**, 409 (1990).
[426] Y. Danon, D. Brown, *et al.*, "Improvements of Nuclear Data Evaluations for Lead Isotopes in Support of Next Generation Lead-cooled Fast Systems," Tech. Rep. **DOE Technical Narrative 19-16739.**, DOE-NEUP MS-NE-2 (2019).
[427] C. Smith, *Lead-Cooled Fast Reactor (LFR) Design: Safety, Neutronics, Thermal Hydraulics, Structural Mechanics, Fuel, Core, and Plant Design.* Lawrence Livermore National Laboratory, Livermore, CA, USA (2010). **LLNL-BOOK-424323**.
[428] G. Manturov *et al.*, "Neutron and Photon Leakage Spectra from Cf-252 Source at Centers of Three Lead Spheres of Different Diameters: ALARM-CF-PB-SHIELD-001," Int. Handb. Eval. Criticality Saf. Benchmark Exp. **NEA/NSC/DOC(95)03/VIII** (2020). NEA 7329, OECD Nuclear Energy Agency, Paris.
[429] M. Gorbatenko *et al.*, "Spherical Assembly of ^{235}U(90%) with a 3.25-CM Lead Reflector: HEU-MET-FAST-027," Int. Handb. Eval. Criticality Saf. Benchmark Exp. **NEA/NSC/DOC(95)03/II** (2020). NEA 7329, OECD Nuclear Energy Agency, Paris.
[430] M. Gorbatenko *et al.*, "Spherical Assembly of ^{239}Pu(δ, 98%) with a 3.15-CM Lead Reflector : PU-MET-FAST-035," Int. Handb. Eval. Criticality Saf. Benchmark Exp. **NEA/NSC/DOC(95)03/I** (2020). NEA 7329, OECD Nuclear Energy Agency, Paris.
[431] V. D. Lyutov *et al.*, "Three Cylinders of Lead-Reflected Highly Enriched Uranium: HEU-MET-FAST-064," Int. Handb. Eval. Criticality Saf. Benchmark Exp. **NEA/NSC/DOC(95)03/II** (2020). NEA 7329, OECD Nuclear Energy Agency, Paris.
[432] T. Kawano, *Optical and Hauser-Feshbach Statistical Model Code: CoH (ver. 3.5) Manual* (2016).
[433] R. F. Carlton, R. R. Winters, J. A. Harvey, and N. W. Hill, "R-Matrix analysis of an ORELA measurement of n+^{208}Pb total cross section from 78 to 1700 keV," Jour: Bull. Am. Phys. Soc. Ser.II **36**, 1349 J10 (1991).
[434] H. Beer, W. Rochow, F. Käppeler, and T. Rauscher, "The 208Pb(n,γ) cross section," Nucl. Phys. **A718**, 518 (2003). [Online] Available at https://www.sciencedirect.com/science/article/pii/S0375947403008297.
[435] R. L. Macklin and J. H. Gibbons, "^{208}Pb(n,γ) cross sections by Activation between 10 and 200 keV," Phys. Rev. J. **181**, 1639 (1969). [Online] Available at https://doi.org/10.1103/PhysRev.181.1639.
[436] J. C. Blackmon, S. Raman, J. K. Dickens, *et al.*, "Thermal-neutron capture by ^{208}Pb," Phys. Rev. C **65** (2002).
[437] D. J. Hughes (1949). EXFOR 13859001, Private Communication.
[438] J. Emery, "Nuclear properties of radionuclides. thermal-neutron cross sections," Tech. Rep. **ORNL-4343**, Oak Ridge National Laboratory, TN, USA (1971).
[439] A. Youmans, J. Brown, A. Daskalakis, N. Thompson, A. Weltz, Y. Danon, D. Barry, B. Epping, G. Leinweber, and M. Rapp, "Fast neutron scattering measurements with lead," in *12th International Topical Meeting on Nuclear Applications of Accelerators 2015, AccApp 2015*, 12th International Topical Meeting on Nuclear Applications of Accelerators 2015, AccApp 2015, 355, American Nuclear Society (2015).
[440] C. Werner, J. Armstrong, F. Brown, *et al.*, "MCNP Users Manual - Code Version 6.2," Tech. Rep. **LA-UR-17-29981**, Los Alamos National Laboratory, NM, USA (2017). [Online] Available at https://mcnp.lanl.gov/pdf_files/TechReport_2017_LANL_LA-UR-17-29981_WernerArmstrongEtAl.pdf.
[441] C. Domingo-Pardo, U. Abbondanno, G. Aerts, *et al.* (n_TOF Collaboration), "Measurement of the radiative neutron capture cross section of ^{206}Pb and its astrophysical implications," Phys. Rev. **C76**, 045805 (2007). [Online] Available at https://link.aps.org/doi/10.1103/PhysRevC.76.045805.
[442] A. Borella, F. Gunsing, M. Moxon, P. Schillebeeckx, and P. Siegler, "High-resolution neutron transmission and capture measurements of the nucleus ^{206}Pb," Phys. Rev. **C76**, 014605 (2007). [Online] Available at https://link.aps.org/doi/10.1103/PhysRevC.76.014605.
[443] A. Negret, L. C. Mihailescu, C. Borcea, *et al.*, "Cross

section measurements for neutron inelastic scattering and the $(n, 2n\gamma)$ reaction on ^{206}Pb," Phys. Rev. **C91**, 064618 (2015). [Online] Available at https://link.aps.org/doi/10.1103/PhysRevC.91.064618.

[444] D. J. Horen, J. A. Harvey, and N. W. Hill, "^{206}Pb+n resonances for $E = 25 - 600$ keV: s-, p-, and d-wave doorway states and $M1$ ground-state radiative strength in ^{207}Pb," Phys. Rev. **C20**, 478 (1979). [Online] Available at https://link.aps.org/doi/10.1103/PhysRevC.20.478.

[445] L. Mihailescu and A. Plompen, *Neutron (n,xnγ) Cross-Section Measurements for ^{52}Cr, ^{209}Bi and ^{206,207,208}Pb from Threshold up to 20 MeV*. Doctoral Thesis, University of Bucharest, Faculty of Physics, Bucharest (Romania), Luxembourg (Luxembourg) (2006).

[446] C. Domingo-Pardo, U. Abbondanno, G. Aerts, H. Álvarez-Pol, *et al.* (n_TOF Collaboration), "Resonance capture cross section of ^{207}Pb," Phys. Rev. **C74**, 055802 (2006). [Online] Available at https://link.aps.org/doi/10.1103/PhysRevC.74.055802.

[447] K. Shibata, O. Iwamoto, *et al.*, "JENDL-4.0: A new library for nuclear science and engineering," J. Nucl. Sci. Techn. **48**, 1 (2011).

[448] D. J. Horen, J. A. Harvey, and N. W. Hill, "Doorway states in s-, p-, and d-wave entrance channels in ^{207}Pb+n reaction," Phys. Rev. **C18**, 722 (1978). [Online] Available at https://link.aps.org/doi/10.1103/PhysRevC.18.722.

[449] T. Kawano, P. Talou, P. Young, G. Hale, M. B. Chadwick, and R. C. Little, "Covariance evaluation work at lanl," in *Workshop On Neutron Cross Section Covariances, Port Jefferson, NY 2008*, Los Alamos National Laboratory (LANL), Los Alamos, NM (United States) (2008). [Online] Available at https://www.osti.gov/biblio/957817.

[450] R. Lell *et al.*, "ZPR-3 assembly 59: A cylindrical assembly of plutonium metal and graphite with a thick lead reflector: PU-MET-INTER-004," Int. Handb. Eval. Criticality Saf. Benchmark Exp. **NEA/NSC/DOC(95)03/I** (2020). NEA 7329, OECD Nuclear Energy Agency, Paris.

[451] Y. Rozhikhin *et al.*, "BFS-61 Assemblies: Critical Experiments of Mixed Plutonium, Depleted Uranium, Graphite and Lead with Different Reflectors: MIX-MET-FAST-006," Int. Handb. Eval. Criticality Saf. Benchmark Exp. **NEA/NSC/DOC(95)03/VI** (2020). NEA 7329, OECD Nuclear Energy Agency, Paris.

[452] T. Miller *et al.*, "Neutron Activation Foil and Thermoluminescent Dosimeter Responses to a Lead Reflected Pulse of the CEA Valduc SILENE Critical Assembly: ALARM-TRAN-PB-SHIELD-001," Int. Handb. Eval. Criticality Saf. Benchmark Exp. **NEA/NSC/DOC(95)03/VIII** (2020). NEA 7329, OECD Nuclear Energy Agency, Paris.

[453] P. Brain, W. Ji, J. Hutchinson, and A. McSpaden, "Design of Sub-Critical Lead Reflected Experiments for Nuclear Data Validation," Trans. Am. Nucl. Soc. **128**, 454 (2023).

[454] A. L. F. Tovesson and T. S. Hill, "Fast neutron–induced fission cross sections of 233, 234, 236, 238U up to 200 MeV," Nucl. Sci. Eng. **178**, 57 (2014). [Online] Available at https://doi.org/10.13182/NSE13-56.

[455] J. R. Vanhoy, R. C. Haight, S. F. Hicks, M. Devlin, D. Neudecker, M. W. Herman, A. Koning, K. J. Kelly, and I. Thompson, "Templates of expected measurement uncertainties for (n,xn) cross sections," EPJ. Nucl. Sci. Techn. **9**, 31 (2023). [Online] Available at https://doi.org/10.1051/epjn/2023019.

[456] B. Baramsai, M. Jandel, T. A. Bredeweg, *et al.*, "Radiative neutron capture cross section from ^{236}U," Phys. Rev. C **96**, 024619 (2017). [Online] Available at https://link.aps.org/doi/10.1103/PhysRevC.96.024619.

[457] M. Košťál, E. Losa, S. Simakov, *et al.*, "Measurement of spectrum averaged cross sections in LR-0 benchmark reference neutron field," Ann. Nucl. En. **206**, 110616 (2024). [Online] Available at https://www.sciencedirect.com/science/article/pii/S0306454924002792.

[458] S. A. Badikov, A. V. Ignatyuk, A. B. Pashchenko, and K. Zolotarev, "Evaluation of the ^{46}Ti(n,2n)^{45}Ti and ^{54}Fe(n,2n)$^{53m+g}$Fe reaction cross sections for neutron dosimetry in fusion facilities," Tech. Rep. **INDC(NDS)-0360**, International Atomic Energy Agency, Vienna, Austria (1993). [Online] Available at https://www-nds.iaea.org/publications/indc/indc-ccp-0360.pdf.

[459] K. Zolotarev, "Evaluation and Improvement of Cross-Section Accuracy for Most Important Dosimetry Reactions Including Covariance Data (^{139}La(n,γ),^{186}W(n,γ), and ^{204}Pb(n,n')^{204m}Pb)," Tech. Rep. **INDC(CCP)-0431**, International Atomic Energy Agency, Vienna, Austria (2002). [Online] Available at https://www-nds.iaea.org/publications/indc/indc-ccp-0431/.

[460] K. Zolotarev, "Evaluation and improvement of cross section accuracy for most important dosimetry reactions ^{27}Al(n,p), ^{56}Fe(n,p) and ^{237}Np(n,f) including covariance data," Tech. Rep. **INDC(CCP)-0438**, International Atomic Energy Agency, Vienna, Austria (2004). [Online] Available at https://www-nds.iaea.org/publications/indc/indc-ccp-0438/.

[461] K. Zolotarev, "Re-evaluation of microscopic and integral cross-section data for important dosimetry reactions," Tech. Rep. **INDC(NDS)-0526**, International Atomic Energy Agency, Vienna, Austria (2008). [Online] Available at https://www-nds.iaea.org/publications/indc/indc-nds-0526/.

[462] K. Zolotarev, "Evaluation of Cross-section Data from Threshold to 40-60 MeV for Specific Neutron Reactions Important for Neutron Dosimetry Applications. Part 1: Evaluation of the excitation functions for the ^{27}Al(n,α)^{24}Na, ^{55}Mn(n,2n), ^{59}Co(n,p), ^{59}Co(n,2n)$^{58m+g}$Co and ^{90}Zr(n,2n)$^{89m+g}$Zr reactions," Tech. Rep. **INDC(NDS)-0546**, International Atomic Energy Agency, Vienna, Austria (2009). [Online] Available at https://www-nds.iaea.org/publications/indc/indc-nds-0546/.

[463] K. Zolotarev, "Evaluation of cross-section data from threshold to 40 MeV for some neutron reactions important for fusion dosimetry applications, part 2," Tech. Rep. **INDC(NDS)-0584**, International Atomic Energy Agency, Vienna, Austria (2010). [Online] Available at https://www-nds.iaea.org/publications/indc/indc-nds-0584/.

[464] K. Zolotarev and P. Zolotarev, "Evaluation of some (n,n'), (n,γ), (n,p), (n,2n) and (n,3n) reaction excitation functions for fission and fusion reactors dosimetry application," Tech. Rep. **INDC(NDS)-0657**, In-

ternational Atomic Energy Agency, Vienna, Austria (2013). [Online] Available at https://www-nds.iaea.org/publications/indc/indc-nds-0657/.

[465] K. Zolotarev, "Evaluation excitation functions for ^{28}Si(n,p)^{28}Al, ^{31}P(n,p)^{31}Si, and ^{113}In(n,γ)^{114m}In reactions," Tech. Rep. **INDC(NDS)-0668**, International Atomic Energy Agency, Vienna, Austria (2014). [Online] Available at https://www-nds.iaea.org/publications/indc/indc-nds-0668/.

[466] K. Zolotarev, "Evaluation of ^{23}Na(n,γ)^{24}Na, ^{23}Na(n,2n)^{22}Na, and ^{27}Al(n,2n)^{26}Al reaction cross sections for the IRDFF library," Tech. Rep. **INDC(NDS)-0705**, International Atomic Energy Agency, Vienna, Austria (2017). [Online] Available at https://www-nds.iaea.org/publications/indc/indc-nds-0705/.

[467] K. Zolotarev, "Evaluation of ^{50}Cr(n,γ)^{51}Cr, ^{56}Fe(n,x)^{54}Mn, ^{57}Fe(n,x)^{56}Mn, and ^{68}Zn(n,x)^{67}Cu reaction cross sections for the IRDFF library," Tech. Rep. **INDC(NDS)-0796**, International Atomic Energy Agency, Vienna, Austria (2019). [Online] Available at https://www-nds.iaea.org/publications/indc/indc-nds-0796/.

[468] O. Bersillon, L. Greenwood, P. Griffin, W. Mannhart, H. Nolthenius, R. Paviotti-Corcuera, K. Zolotarev, and E. Zsolnay, "International Reactor Dosimetry File 2002 (IRDF-2002)," Tech. Rep. **STI/DOC/010/452, Technical Report Series TRS–0452**, International Atomic Energy Agency, Vienna, Austria (2006). [Online] Available at https://www-nds.iaea.org/publications/tecdocs/sti-doc-010-452/.

[469] E. Zsolnay, R. Capote, H. Nolthenius, and A. Trkov, "Summary description of the new international reactor dosimetry and fusion file (IRDFF release 1.0," Technical report **INDC(NDS)-0616**, International Atomic Energy Agency, Vienna, Austria (2012). [Online] Available at https://www-nds.iaea.org/publications/indc/indc-nds-0616/.

[470] J.-C. Sublet, L. Packer, J. Kopecky, R. Forrest, A. Koning, and D. Rochman, "The European Activation File:EAF-2010 neutron-induced cross section library," Tech. Rep. **CCFE-R (10) 05**, EURATOM/CCFE Fusion Association, Culham Science Centre, Abingdon, Oxfordshire, United Kingdom (2010). [Online] Available at https://fispact.ukaea.uk/wp-content/uploads/2016/07/EAF2010.pdf.

[471] A. J. Koning and D. Rochman, "TENDL-2015: TALYS Evaluated Nuclear Data Library." http://www.talys.eu/tendl-2015/ (2015).

[472] A. J. Koning and D. Rochman, "TENDL-2017: TALYS Evaluated Nuclear Data Library." http://www.talys.eu/tendl-2017/ (2017).

[473] M. Chadwick, E. Dupont, E. Bauge, *et al.*, "The CIELO Collaboration: Neutron Reactions on ^{1}H, ^{16}O, ^{56}Fe, ^{235}U, ^{238}U, and ^{239}Pu," Nucl. Data Sh. **118**, 1 (2014). [Online] Available at https://doi.org/10.1016/j.nds.2014.04.002.

[474] (Cross Section Evaluation Working Group (CSEWG)), "ENDF-6 Formats Manual - Data Formats and Procedures for the Evaluated Nuclear Data Files ENDF/B-VI, ENDF/B-VII and ENDF/B-VIII," Tech. Rep. **BNL-224854-2023-INRE, ENDF Report ENDF-102**, Brookhaven National Laboratory (2023). [Online] Available at https://www.osti.gov/biblio/2007538.

[475] IAEA-CRP, "Reference input parameter library (ripl)," Tech. Rep. **IAEA-TECDOC-1034**, International Atomic Energy Agency, Vienna, Austria (1998). [Online] Available at https://www-nds.iaea.org/ripl/.

[476] A. J. Koning and D. Rochman, "TENDL-2019: TALYS Evaluated Nuclear Data Library." http://www.talys.eu/tendl-2019/ (2019).

[477] A. J. Koning and J. P. Delaroche, "Local and global nucleon optical models from 1 keV to 200 MeV," Nucl. Phys. **A713**, 231 (2003). [Online] Available at https://www.sciencedirect.com/science/article/pii/S0375947402013210.

[478] V. Avrigeanu, P. E. Hodgson, and M. Avrigeanu, "Global optical potentials for emitted alpha particles," Phys. Rev. **C49**, 2136 (1994). [Online] Available at https://link.aps.org/doi/10.1103/PhysRevC.49.2136.

[479] J. Bojowald, H. Machner, H. Nann, W. Oelert, M. Rogge, and P. Turek, "Elastic deuteron scattering and optical model parameters at energies up to 100 MeV," Phys. Rev. **C38**, 1153 (1988). [Online] Available at https://link.aps.org/doi/10.1103/PhysRevC.38.1153.

[480] F. D. Becchetti and G. W. Greenlees, "Nucleon-nucleus optical-model parameters, $A > 40$, $E < 50$ MeV," Phys. Rev. **182**, 1190 (1969). [Online] Available at https://link.aps.org/doi/10.1103/PhysRev.182.1190.

[481] G. Audi, M. Wang, A. H. Wapstra, F. G. Kondev, M. MacCormick, and X. Xu, "The 2012 Atomic Mass Evaluation and the Mass Tables," Nucl. Data Sh. **120**, 1 (2014). [Online] Available at https://www.sciencedirect.com/science/article/pii/S0090375214004438.

[482] P. Möller, A. J. Sierk, T. Ichikawa, and H. Sagawa, "Nuclear ground-state masses and deformations: FRDM(2012)," Atom. Data Nucl. Data Tables **109**, 1 (2016). [Online] Available at http://www.sciencedirect.com/science/article/pii/S0092640X1600005X.

[483] C. Kalbach, "Two-component exciton model: Basic formalism away from shell closures," Phys. Rev. **C33**, 818 (1986). [Online] Available at https://link.aps.org/doi/10.1103/PhysRevC.33.818.

[484] H. Kim, H. Lee, T. Kawano, A. Georgiadou, S. Kuvin, L. Zavorka, and M. Herman, "New evaluation on angular distributions and energy spectra for neutron-induced charged-particle measurements," Nucl. Inst. Meth. Phys. Res. **A963**, 163699 (2020). [Online] Available at https://linkinghub.elsevier.com/retrieve/pii/S0168900220302606.

[485] H. Beer and R. L. Macklin, "Measurement of the 85Rb and 87Rb Capture Cross Sections for s-Process Studies," Astrophys. J. **339**, 962 (1989). [Online] Available at https://doi.org/10.1086/167351.

[486] V. Kononov, B. Yurlov, E. Poletaev, and V. Timokhov, "Fast-Neutron Capture Cross Sections for Indium, Tantalum, Gold, Samarium, and Europium," Yad. Fiz. **26**, 947 (1977).

[487] K. Wisshak, F. Voss, C. Theis, F. Käppeler, K. Guber, L. Kazakov, N. Kornilov, and G. Reffo, "Stellar neutron capture cross sections of the tin isotopes," Phys. Rev. C **54**, 1451 (1996). [Online] Available at https://link.aps.org/doi/10.1103/PhysRevC.54.1451.

[488] V. Timokhov, M. Bokhovko, M. Isakov, L. Kazakov, V. Kononov, G. Manturov, E. Poletaev, and V. Pronyaev, "Average cross-sections for neutron radi-

ation capture, transmission and average resonance parameters for tin isotopes," Tech. Rep. **FEI-1921**, IPPE, Obninsk, USSR (1988).

[489] R. L. Macklin, "Neutron capture cross sections and resonances of iodine-127 and iodine-129," Nucl. Sci. Eng. **85**, 350 (1983). [Online] Available at https://doi.org/10.13182/NSE83-A18382.

[490] K. Wisshak, F. Voss, F. Käppeler, and G. Reffo, "Neutron capture in ^{122,123,124}Te: Critical test for s process studies," Phys. Rev. C **45**, 2470 (1992). [Online] Available at https://link.aps.org/doi/10.1103/PhysRevC.45.2470.

[491] M. Bokhovko, A. Voevodsky, V. Kononov, E. Poletaev, and V. Timokhov, "Radiative capture cross sections, neutron transmissions, and average resonance parameters for several fission product nuclei," Tech. Rep. **FEI-2168**, IPPE, Obninsk, USSR (1991).

[492] F. Voss, K. Wisshak, K. Guber, F. Käppeler, and G. Reffo, "Stellar neutron capture cross sections of the ba isotopes," Phys. Rev. C **50**, 2582 (1994). [Online] Available at https://link.aps.org/doi/10.1103/PhysRevC.50.2582.

[493] V. Kononov, B. Yurlov, G. Manturov, E. Poletaev, V. Timokhov, and V. Shorin, "Fast neutron radiative capture cross-section for In-115, Ta-181, Au-197 and samarium and europium isotopes.," Yad. Fiz. **22**, 29 (1977).

[494] K. Wisshak, F. Voss, F. Käppeler, and L. Kazakov, "Stellar neutron capture cross sections of the lu isotopes," Phys. Rev. C **73**, 015807 (2006). [Online] Available at https://link.aps.org/doi/10.1103/PhysRevC.73.015807.

[495] H. Beer, G. Walter, R. L. Macklin, and P. J. Patchett, "Neutron capture cross sections and solar abundances of ^{160,161}Dy, ^{170,171}Yb, ^{175,176}Lu, and ^{176,177}Hf for the *s*-process analysis of the radionuclide ^{176}Lu," Phys. Rev. C **30**, 464 (1984). [Online] Available at https://link.aps.org/doi/10.1103/PhysRevC.30.464.

[496] M. J. Trbovich, D. P. Barry, R. E. Slovacek, *et al.*, "Hafnium resonance parameter analysis using neutron capture and transmission experiments," Nucl. Sci. Eng. **161**, 303 (2009). [Online] Available at https://doi.org/10.13182/NSE161-303.

[497] J.-C. Chou and H. Werle, "(n,g)-cross-section measurements of 99tc, eu, sm and fe in the energy range 1 ev to 50 kev with a slowing-down time spectrometer," J. Nucl. En. **27**, 811 (1973).

[498] R. Little and R. Block, "Neutron capture cross-section measurements of 99tc up to 80 kev," Trans. Am. Nucl. Soc. **26**, 574 (1977).

[499] R. L. Macklin, "Technetium-99 neutron capture cross section," Nucl. Sci. Eng. **81**, 520 (1982).

[500] T. MATSUMOTO, M. IGASHIRA, and T. OHSAKI, "Measurement of kev-neutron capture cross sections and capture gamma-ray spectra of 99tc," J. Nucl. Sci. Techn. **40**, 61 (2003). [Online] Available at https://doi.org/10.1080/18811248.2003.9715334.

[501] K. Kobayashi, S. Lee, S. Yamamoto, and T. Kawano, "Neutron capture cross-section measurement of 99tc by linac time-of-flight method and the resonance analysis," Nucl. Sci. Eng. **146**, 209 (2004). [Online] Available at https://doi.org/10.13182/NSE04-A2404.

[502] A. L. Musgrove, B. Allen, J. Boldeman, and R. Macklin, "kev neutron capture cross sections of 134ba and 136ba," Nucl. Phys. A **256**, 173 (1976).

[503] F. Voss, K. Wisshak, K. Guber, F. Käppeler, and G. Reffo, "Stellar neutron capture cross sections of the ba isotopes," Phys. Rev. C **50**, 2582 (1994). [Online] Available at https://link.aps.org/doi/10.1103/PhysRevC.50.2582.

[504] P. E. Koehler, R. R. Spencer, K. H. Guber, *et al.*, "High resolution neutron capture and transmission measurements on ^{137}Ba and their impact on the interpretation of meteoric barium anomalies," Phys. Rev. C **57**, R1558 (1998).

[505] V.M. Maslov, E.Sh. Sukhovitskij, Yu.V. Porodzinskij, A.B. Klepatskij, and G.B. Morovogskij, "Evaluation of neutron data for ^{243}Cm isotopes," Tech. Rep. **INDC(BLR)-2**, Joint Institute for Energy and Nuclear Research – Sosny, Belarus (1995). Data files received from the IAEA Nuclear Data Section., [Online] Available at https://www-nds.iaea.org/publications/indc/indc-blr-0002.pdf.

[506] V.M. Maslov, Yu.V. Porodzinskij, E. Sukhovitskij, A.B. Klepatskij, and G.B. Morovogskij, "Evaluation of neutron data for ^{243}Am isotopes," Tech. Rep. **INDC(BLR)-6**, Joint Institute for Energy and Nuclear Research – Sosny, Belarus (1996). Data files received from the IAEA Nuclear Data Section., [Online] Available at https://www-nds.iaea.org/publications/indc/indc-blr-0006.pdf.

[507] V.M. Maslov, Yu.V. Porodzinskij, N.A. Tetereva, A.B. Kagalenko, N.V. Kornilov, M. Baba, and A. Hasegawa, "Neutron Data Evaluation of ^{232}U," Tech. Rep. **INDC(BLR)-15**, Joint Institute for Energy and Nuclear Research – Sosny, Belarus (2003). Data files received from the IAEA Nuclear Data Section., [Online] Available at https://www-nds.iaea.org/publications/indc/indc-blr-0015.pdf.

[508] V.M. Maslov, M. Baba, A. Hasegawa, N.V. Kornilov, A.B. Kagalenko, and N.A. Tetereva, "Neutron Data Evaluation of ^{233}Pa," Tech. Rep. **INDC(BLR)-20**, Joint Institute for Energy and Nuclear Research – Sosny, Belarus (2004). Data files received from the IAEA Nuclear Data Section., [Online] Available at https://www-nds.iaea.org/publications/indc/indc-blr-0020.pdf.

[509] C. Romano, L. Bernstein, T. Bailey, *et al.*, "Proceedings Of The Workshop For Applied Nuclear Data: WANDA2020," Tech. Rep. **ORNL/TM-2020/1617**, Oak Ridge National Laboratory, TN, USA (2020).

[510] W. Haeck, N. Gibson, and P. Talou, "Endftk: A robust tool for reading and writing endf-formatted nuclear data," Comput. Phys. Commun. **303**, 109245 (2024). [Online] Available at https://github.com/njoy/ENDFtk/.

[511] D. Neudecker, "Test results for checking reliability of selected ENDF/B-VIII.0 evaluated uncertainties," Tech. Rep. **LA-UR-22-21551**, Los Alamos National Laboratory, NM, USA (2022).

[512] D. Wiarda *et al.*, "AMPX-6: a modular code system for processing ENDF/B," Tech. Rep. **ORNL/TM-2016/43**, Oak Ridge National Laboratory, TN, USA (2016). Available from Radiation Safety Information Computational Center as **CCC-834**.

[513] D. Brown, "x4i: the EXFOR interface," (2011). [Online] Available at https://github.com/brown170/x4i.

[514] (Cross Section Evaluation Working Group (CSEWG)),

"ENDF-6 formats manual," Tech. Rep. **BNL-90365-2009 Rev. 2, ENDF Report ENDF-102**, Brookhaven National Laboratory, Upton, NY, USA (2012).

[515] D. Neudecker, "Definitions for testing whether evaluated nuclear data relative uncertainties are realistic in size," Tech. Rep. **LA-UR-21-32171**, Los Alamos National Laboratory, NM, USA (2021).

[516] D. Smith, "Guidance on Generating Neutron Reaction Data Covariances for the ENDF/B Library by the CSEWG Covariance Committee," Tech. Rep. **ENDF-378**, Brookhaven National Laboratory, Upton, NY, USA (2021). [Online] Available at https://www.nndc.bnl.gov/endfdocs/ENDF-378.pdf.

[517] D. Neudecker, A. M. Lewis, E. F. Matthews, *et al.*, "Templates of expected measurement uncertainties," EPJ. Nucl. Sci. Techn. **9**, 35 (2023). [Online] Available at https://doi.org/10.1051/epjn/2023014.

[518] A. M. Lewis, D. Neudecker, A. D. Carlson, *et al.*, "Templates of expected measurement uncertainties for neutron-induced capture and charged-particle production cross section observables," EPJ. Nucl. Sci. Techn. **9**, 33 (2023). [Online] Available at https://doi.org/10.1051/epjn/2023015.

[519] A. Lewis, *Uncertainty Analysis Procedures for Neutron-Induced Cross Section Measurements and Evaluations*. Doctoral Thesis, Department of Nuclear Engineering, University of California, Berkeley (2020).

[520] D. Neudecker, M. Devlin, R. C. Haight, K. J. Kelly, P. Marini, A. D. Carlson, J. Taieb, and M. C. White, "Templates of expected measurement uncertainties for prompt fission neutron spectra," EPJ. Nucl. Sci. Techn. **9**, 32 (2023). [Online] Available at https://doi.org/10.1051/epjn/2023013.

[521] E. Matthews, *Advancements in the Nuclear Data of Fission Yields*. Doctoral Thesis, Department of Nuclear Engineering, University of California, Berkeley (2021).

[522] D. Neudecker, M. C. White, D. E. Vaughan, and G. Srinivasan, "Validating nuclear data uncertainties obtained from a statistical analysis of experimental data with the "Physical Uncertainty Bounds" method," EPJ. Nucl. Sci. Techn. **6**, 19 (2020). [Online] Available at https://doi.org/10.1051/epjn/2020007.

[523] M. E. Rising, P. Talou, T. Kawano, and A. K. Prinja, "Evaluation and Uncertainty Quantification of Prompt Fission Neutron Spectra of Uranium and Plutonium Isotopes," Nucl. Sci. Eng. **175**, 81 (2013). [Online] Available at https://doi.org/10.13182/NSE12-34.

[524] W. Marshall and B. Rearden, "The SCALE Verified Archived Library of Inputs and Data - VALID," in *Proceedings of NCSD 2013: Criticality Safety in the Modern Era - Raising the Bar*, (Wilmington, NC, USA), 319 (2013).

[525] J. Wagner, "Computational benchmark for estimation of reactivity margin from fission products and minor acitnides in PWR burnup credit," Tech. Rep. **NUREG/CR-6747**, US Nuclear Regualtory Commission, Washington, DC, USA (2001).

[526] J. Borowski *et al.*, "Standard review plan for transportation packages for spent fuel and radioactive material: Final report," Tech. Rep. **NUREG-2216**, US Nuclear Regulatory Commission, Washington, DC, USA (2020).

[527] A. M. Lewis, A. D. Carlson, D. L. Smith, *et al.*, "Templates of expected measurement uncertainties for total neutron cross-section observables," EPJ. Nucl. Sci. Techn. **9**, 34 (2023). [Online] Available at https://doi.org/10.1051/epjn/202301.

[528] OECD/NEA, "Thermal Scattering Law S(α,β): Measurement, Evaluation and Application," Tech. Rep. **NEA No. 7511**, Nuclear Energy Agency, OECD Publishing, Paris, France (2020). [Online] Available at https://www.oecd-nea.org/upload/docs/application/pdf/2020-03/volume42.pdf.

[529] N. C. Fleming, C. A. Manring, B. K. Laramee, J. P. W. Crozier, E. Lee, and A. I. Hawari, "*FLASSH* 1.0: Thermal scattering law evaluation and cross-section generation for reactor physics applications," Nucl. Sci. Eng. **197**, 1887 (2023). [Online] Available at https://www.tandfonline.com/doi/abs/10.1080/00295639.2023.2194195.

[530] K. Ramić, J. I. Marquez Damian, T. Kittelmann, D. D. Di Julio, D. Campi, M. Bernasconi, G. Gorini, and V. Santoro, "NJOY+NCrystal: An open-source tool for creating thermal neutron scattering libraries with mixed elastic support," Nucl. Inst. Meth. Phys. Res. **A1027**, 166227 (2022). [Online] Available at https://www.sciencedirect.com/science/article/pii/S0168900221010755.

[531] A. I. Hawari *et al.*, "Ab initio generation of thermal neutron scattering cross sections," in *Proceedings of PHYSOR 2004, Chicago, Illinois, USA, April 25-29, 2004*, American Nuclear Society (2004). [Online] Available at https://www.researchgate.net/publication/266357537.

[532] A. I. Hawari, "Modern techniques for inelastic thermal neutron scattering analysis," Nucl. Data Sh. **118**, 172 (2014).

[533] J. L. Wormald and A. I. Hawari, "Thermal neutron scattering law calculations using ab initio molecular dynamics," EPJ. Web. Conf. **146**, 13002 (2017). [Online] Available at https://doi.org/10.1051/epjconf/201714613002.

[534] J. Wormald and A. I. Hawari, "Thermal neutron scattering law calculations using *ab initio* molecular dynamics," EPJ. Web. Conf. **146**, 13002 (2017). [Online] Available at https://doi.org/10.1051/epjconf/201714613002.

[535] A. Ramirez-Cuesta, "aCLIMAX 4.0.1, the new version of the software for analyzing and interpreting INS spectra," Comput. Phys. Commun. **157**, 226 (2004). [Online] Available at https://www.sciencedirect.com/science/article/pii/S0010465503005204.

[536] K. Ramić, C. Wendorff, Y. Cheng, A. I. Kolesnikov, D. L. Abernathy, L. Daemen, G. Arbanas, L. Leal, Y. Danon, and L. E. Liu, "Toward a better thermal scattering law of $(C_5O_2H_8)_n$: Inelastic neutron scattering and oClimax+NJOY2016," Ann. Nucl. En. **133**, 425 (2019). [Online] Available at https://www.sciencedirect.com/science/article/pii/S0306454919302956.

[537] M. L. Zerkle, "TSL mixed elastic scattering format," in *The Annual CSWEG Meeting at Nuclear Data Week 2020*, (Upton, NY), Cross Section Evaluation Working Group (2020). [Online] Available at https://indico.bnl.gov/event/7233/contributions/43822.

[538] J. Marquez Damian, J. Granada, and D. Malaspina, "CAB models for water: A new evaluation of the thermal neutron scattering laws for light and heavy water in ENDF-6 format," Ann. Nucl. En. **65**, 280

(2014). [Online] Available at https://doi.org/10.1016/j.anucene.2013.11.014.

[539] J. Marquez Damian, J. Dawidowski, J. Granada, F. Cantargi, G. Romanelli, C. Helman, M. Krzystyniak, G. Skoro, and D. Roubtsov, "Experimental validation of the temperature behavior of the ENDF/B-VIII.0 thermal scattering kernel for light water," in *EPJ Web of Conferences*, **239**, 14001, EDP Sciences (2020). [Online] Available at https://doi.org/10.1051/epjconf/202023914001.

[540] L. J. Esch, M. Yeater, W. Moore, and K. Seemann, "The temperature dependence of neutron inelastic scattering from water," Nucl. Sci. Eng. **46**, 223 (1971). [Online] Available at https://doi.org/10.13182/NSE71-A22356.

[541] Y. Lisichkin, L. Saharova, J. Marti, and A. Novikov, "Temperature dependence of the generalized frequency distribution of water molecules: comparison of experiments and molecular dynamics simulations," Mol. Simul. **31**, 1019 (2005). [Online] Available at https://doi.org/10.1080/08927020500411930.

[542] L. Maul, J. Marquez Damian, G. Braoudakis, M. Ho, and G. H. Yeoh, "Perturbation scheme for estimating uncertainties in thermal scattering cross sections of water," Ann. Nucl. En. **121**, 232 (2018). [Online] Available at https://doi.org/10.1016/j.anucene.2018.07.020.

[543] K. Yoshida, N. Matubayasi, Y. Uosaki, and M. Nakahara, "Scaled polynomial expression for self-diffusion coefficients for water, benzene, and cyclohexane over a wide range of temperatures and densities," J. Chem. & Eng. Data **55**, 2815 (2010). [Online] Available at https://doi.org/10.1021/je100206s.

[544] J. Marquez Damian, D. DiJulio, and G. Muhrer, "CAB Model Parameter Analysis." ESS Gitlab (2023).

[545] JENDL-5, "Errata of JENDL-5 sublibraries," (2025). Thermal scattering law sublibrary, update-16, [Online] Available at https://wwwndc.jaea.go.jp/jendl/j5/JENDL-5_Errata.html.

[546] K. Tada, "Overview of nuclear data efforts in Japan," (2025). Presented at APRENDE Experimentalists-Evaluators workshop (WP2-WP4), Strasbourg, France, [Online] Available at https://indico.psi.ch/event/16894/timetable/.

[547] M. Mattes and J. Keinert, "Thermal neutron scattering data for the moderator materials H2O, D2O and ZrH x in ENDF-6 format and as ACE library for MCNP (X) codes," Tech. Rep. **INDC(NDS)-0470**, International Atomic Energy Agency, Vienna, Austria (2005). [Online] Available at https://www-nds.iaea.org/publications/indc/indc-nds-0470.pdf.

[548] F. K. Larsen and N. K. Hansen, "Diffraction study of the electron density distribution in beryllium metal," Acta Crystallogr. **B40**, 169 (1984). [Online] Available at https://doi.org/10.1107/S0108768184001932.

[549] P. Gordon, "A high temperature precision X-ray camera: Some measurements of the thermal coefficients of expansion of beryllium," J. Appl. Phys. **20**, 908 (1949). [Online] Available at https://doi.org/10.1063/1.1698252.

[550] G. Kresse and J. Furthmüller, "Efficiency of ab-initio total energy calculations for metals and semiconductors using a plane-wave basis set," Comput. Mater. Sci. **6**, 15 (1996). [Online] Available at https://doi.org/10.1016/0927-0256(96)00008-0.

[551] G. Kresse and J. Furthmüller, "Efficient iterative schemes for ab initio total-energy calculations using a plane-wave basis set," Phys. Rev. **B54**, 11169 (1996). [Online] Available at https://journals.aps.org/prb/abstract/10.1103/PhysRevB.54.11169.

[552] G. Kresse and D. Joubert, "From ultrasoft pseudopotentials to the projector augmented-wave method," Phys. Rev. **B59**, 1758 (1999). [Online] Available at https://journals.aps.org/prb/abstract/10.1103/PhysRevB.59.1758.

[553] K. Parlinski, Z. Q. Li, and Y. Kawazoe, "First-principles determination of the soft mode in cubic ZrO2," Phys. Rev. Lett. **78**, 4063 (1997). [Online] Available at https://journals.aps.org/prl/abstract/10.1103/PhysRevLett.78.4063.

[554] R. E. MacFarlane and D. W. Muir, "The NJOY nuclear data processing system, version 91," Tech. Rep. **LA-12740-M**, Los Alamos National Laboratory, NM, USA (1994).

[555] H. Palevsky and R. R. Smith (1952). private communication, EXFOR 11204.003.

[556] K. Kanda, H. Kadotani, and O. Aizawa, "Effect of temperature on total cross section of beryllium for thermal neutrons," Nucl. Sci. Techn. **12**, 601 (1975). EXFOR subentry 21657.002, [Online] Available at https://doi.org/10.1080/18811248.1975.9733160.

[557] A. I. Hawari *et al.*, "Graphite thermal neutron scattering cross section calculations including coherent 1-phonon effects," in *Proceedings of PHYSOR 2008, Interlaken, Switzerland, September 14-19, 2008*, 347 (2008).

[558] R. E. Schmunk, "Slow-neutron inelastic scattering from beryllium powder," Phys. Rev. **136**, A1303 (1964). [Online] Available at https://doi.org/10.1103/PhysRev.136.A1303.

[559] R. M. Hazen and L. W. Finger, "High-pressure and high-temperature crystal chemistry of beryllium oxide," J. Appl. Phys. **59**, 3728 (1986). [Online] Available at https://doi.org/10.1063/1.336756.

[560] G. Borgonovi, "Lattice dynamics and neutron scattering of BeO," Tech. Rep. **USAEC Report GA-8758**, Gulf General Atomic Incorporated (1968).

[561] G. L. Ostheller, R. E. Schmunk, R. M. Brugger, and R. J. Kearney, "Phonon dispersion relation of beryllium oxide," in *Neutron Inelastic Scattering Vol. I. Proceedings of a Symposium on Neutron Inelastic Scattering, Copenhagen, Denmark, May 20-25, 1968*, 315 (1968). [Online] Available at https://www.osti.gov/etdeweb/biblio/22112007.

[562] A. Bosak, K. Schmalzl, M. Krisch, W. van Beek, and V. Kolobanov, "Lattice dynamics of beryllium oxide: inelastic X-ray scattering and ab initio calculations," Phys. Rev. B **77** (2008). [Online] Available at https://doi.org/10.1103/PhysRevB.77.224303.

[563] D. Hughes and R. Schwartz, "Neutron cross sections," Tech. Rep. **BNL-325**, Brookhaven National Laboratory, Upton, NY, USA (1958). [Online] Available at https://www.osti.gov/biblio/4314386.

[564] H. Wu, W. Zhou, T. J. Udovic, J. J. Rush, and T. Yildirim, "Structure and vibrational spectra of calcium hydride and deuteride," J. Alloy. Compd. **436**, 51 (2007).

[565] MedeA, version 3.0; MedeA is a registered trademark of Materials Design, Inc., San Diego, USA (1998).

[566] B. K. Laramee and A. I. Hawari, "Evaluation of Thermal

Neutron Scattering Law and Cross Sections for Calcium Hydride," EPJ. Web. Conf. **284**, 17014 (2022).

[567] O. Serot, "New results on CaH_2 thermal neutron scattering cross sections," in *AIP Conference Proceedings*, **769**, 1446, AIP (2005). [Online] Available at http://aip.scitation.org/doi/abs/10.1063/1.1945276.

[568] E. Fermi, "On the motion of neutrons in hydrogenous substances," Ricerca Sci. **2** (1936).

[569] Y. Zhu, C. A. Manring, and A. I. Hawari, "Thermal scattering law ENDF libraries for liquid FLiBe," EPJ. Web. Conf. **247**, 09023 (2021). Proceedings of PHYSOR 2020, online, March 29-April 2, 2020, [Online] Available at https://doi.org/10.1051/epjconf/202124709023.

[570] Y. Zhu, *Analysis of Neutron Thermalization in Liquid FLiBe*. Doctoral Thesis, Department of Nuclear Engineering, North Carolina State University (2018).

[571] A. P. Thompson *et al.*, "LAMMPS - a flexible simulation tool for particle-based materials modeling at the atomic, meso, and continuum scales," Comput. Phys. Commun. **271**, 108171 (2022). [Online] Available at https://www.sciencedirect.com/science/article/pii/S0010465521002836.

[572] A. I. Hawari *et al.*, "Inelastic thermal neutron scattering cross sections for reactor-grade graphite," Nucl. Data Sh. **118**, 176 (2014). [Online] Available at https://www.sciencedirect.com/science/article/pii/S009037521400060X.

[573] E. Lee, N. C. Fleming, and A. I. Hawari, "Benchmark of neutron thermalization in graphite using a pulsed slowing-down-time experiment," Nucl. Sci. Eng. **197**, 2007 (2023). [Online] Available at https://doi.org/10.1080/00295639.2022.2162789.

[574] E. Lee and N. C. Fleming, "FUND-ORELA-ACC-GRAPH-PNSDT-001 Benchmark of neutron thermalization in graphite using the slowing-down-time ORELA experiment," in *International Handbook of Evaluated Criticality Safety Benchmark Experiments (ICSBEP)*, Paris: Organization for Economic Co-operation and Development-Nuclear Energy Agency (OECD-NEA) (2022/2023). **NEA/NSC/DOC(95)03**.

[575] N. C. Fleming, *Advanced Methods of Thermal Neutron Scattering Analysis for Reactor Multi-Physics Applications*. Doctoral Thesis, North Carolina State University, NC, USA (2021). [Online] Available at https://repository.lib.ncsu.edu/handle/1840.20/39131.

[576] P. A. Egelstaff, "Practical Analysis of Neutron Scattering Data into Self and Interference Terms," in *Proceedings of the Symposium of Inelastic Scattering of Neutrons in Solids and Liquids, Chalk River, Canada, September 10-14, 1962*, 65, IAEA (1963).

[577] N. F. Wikner, G. D. Joanou, and D. E. Parks, "Neutron thermalization in graphite," Nucl. Sci. Eng. **19** (1964). [Online] Available at https://doi.org/10.13182/NSE64-A19795.

[578] A. I. Hawari, T. Zhou, and P. R. Huffman, "Measurement of the total inelastic scattering cross section of graphite using 9 Angstrom neutrons," Trans. Am. Nucl. Soc. **100**, 591 (2009).

[579] A. Steyerl and W. D. Trustedt, "Experiments with a neutron bottle," Z. Phys. **267**, 379 (1974). [Online] Available at https://doi.org/10.1007/BF01669970.

[580] T. Ahmed, N. Fleming, and A. Hawari, "Evaluation of thermal scattering law and cross sections for liquid hydrogen fluoride," Ann. Nucl. En. **218**, 111403 (2025). [Online] Available at https://www.sciencedirect.com/science/article/pii/S0306454925002208.

[581] M. J. Abraham, T. Murtola, R. Schulz, S. Páll, J. C. Smith, B. Hess, and E. Lindahl, "GROMACS: High performance molecular simulations through multi-level parallelism from laptops to supercomputers," SoftwareX **1–2**, 19 (2015). [Online] Available at https://doi.org/10.1016/j.softx.2015.06.001.

[582] P. A. Egelstaff and P. Schofield, "On the evaluation of the thermal neutron scattering law," Nucl. Sci. Eng. **12**, 260 (1962). [Online] Available at https://doi.org/10.13182/NSE62-A26066.

[583] G. Poullot, "HEU-SOL-THERM-039 Mixture of uranium (93%) hexafluoride and hydrofluoric acid (low H/U ratio) in a hot-water-reflected spherical tank," in *International Handbook of Evaluated Criticality Safety Benchmark Experiments (ICSBEP)*, Paris: Organization for Economic Co-operation and Development-Nuclear Energy Agency (OECD-NEA) (2016). **NEA/NSC/DOC(95)03**.

[584] C. A. Manring and A. I. Hawari, "Assessment of thermal neutron scattering in a heavy paraffinic molecular material," Ann. Nucl. En. **128**, 140 (2019). [Online] Available at https://doi.org/10.1016/j.anucene.2018.12.042.

[585] A. Daskalakis, D. Barry, M. Rapp, *et al.*, "Neutron transmission measurements in support of the validation of the ENDF/B-VIII.1 heavy paraffinic oil TSL," in *Nuclear Criticality Safety Division 2025 Conference (NCSD 2025), Austin, TX, September 14–18, 2025*, 203 (2025).

[586] Y. Zhu, J. L. Wormald, and A. I. Hawari, "Thermal neutron scattering cross sections for silicon carbide," Trans. Am. Nucl. Soc. **108**, 761 (2013).

[587] Y. Zhu, *Thermal Neutron Scattering Cross Sections for Silicon Carbide*. Master of Science Thesis, Department of Nuclear Engineering, North Carolina State University (2014).

[588] O. Madelung, ed., *Physics of Group-IV and III-V Compounds, Vol. 17, Pt. A*. Springer-Verlag Berlin (1982).

[589] M. A. Carpenter, E. K. H. Salje, A. Graeme-Barber, B. Wruck, M. T. Dove, and K. S. Knight, "Calibration of excess thermodynamic properties and elastic constant variations associated with the alpha <–> beta phase transition in quartz," Am. Mineral. **83**, 2 (1998). [Online] Available at https://doi.org/10.2138/am-1998-1-201.

[590] A. J. Cohen and G. G. Sumner, "Relationships among impurity contents, color centers and lattice constants in quartz," Am. Minerol. **43**, 58 (1958).

[591] Y. L. Page and G. Donnay, "Refinement of the crystal structure of low-quartz," Acta Crystallogr. **B32**, 2456 (1976). [Online] Available at https://onlinelibrary.wiley.com/doi/full/10.1107/S0567740876007966.

[592] J. J. Blostein and J. Dawidowski, "Experimental neutron data: σ(E) of vitreous silica (SiO_2) over the thermal energy range," tech. rep., Centro Atomico Bariloche, CNEA, Argentina (1999). EXFOR 31503.001.

[593] B. M. Rustad, E. Melkonian, W. W. Havens, T. I. Taylor, F. T. Gould, and J. A. Moore, "Neutron crystal spectrometer with range extended to subthermal energies," Rev. Sci. Inst. **36**, 887 (1965). [Online] Available at https://doi.org/10.1063/1.1719779.

[594] S. J. Clark, M. D. Segall, C. J. Pickard, P. J. Hasnip,

M. J. Probert, K. Refson, and M. Payne, "First principles methods using CASTEP," Z. Kristall. **220**, 567 (2005).

[595] G. Natta, P. Corradini, and I. Bassi, "Crystal structure of isotactic polystyrene," Nuovo Cimento **15**, 68 (1960).

[596] Y. Q. Cheng, L. L. Daemen, A. I. Kolesnikov, and A. J. Ramirez-Cuesta, "Simulation of inelastic neutron scattering spectra using OCLIMAX," J. Chem. Theory Comput. **15**, 1974 (2019). [Online] Available at https://doi.org/10.1021/acs.jctc.8b01250.

[597] Y. Q. Cheng and A. J. Ramirez-Cuesta, "Calculation of the thermal neutron scattering cross-section of solids using OCLIMAX," J. Chem. Theory Comput. **16**, 5212 (2020).

[598] P. A. Seeger, L. L. Daemen, and J. Z. Larese, "Resolution of VISION, a crystal-analyzer spectrometer," Nucl. Inst. Meth. Phys. Res. Sect. **A604**, 719 (2009). [Online] Available at https://www.sciencedirect.com/science/article/pii/S0168900209006871.

[599] D. Fritz, Y. Danon, K. Ramic, *et al.*, "Total thermal neutron cross section measurements of hydrogen dense polymers from 0.0005–20 eV," Ann. Nucl. En. **183**, 109651 (2023). [Online] Available at https://www.sciencedirect.com/science/article/pii/S0306454922006818.

[600] B. Adams, W. Bohnhoff, K. Dalbey, *et al.*, "Dakota, A Multilevel Parallel Object-Oriented Framework for Design Optimization, Parameter Estimation, Uncertainty Quantification, and Sensitivity Analysis: Version 6.15 User's Manual," Tech. Rep. **SAND2020-12495**, Sandia National Laboratory, NM, USA (2021).

[601] C. W. Chapman, K. Ramic, J. Brown, and G. Arbanas, "Status Report of Joint RPI/ORNL NCSP Task for Thermal Neutron Total Cross Section Measurements," tech. rep., Oak Ridge National Laboratory (ORNL), Oak Ridge, TN (United States) (2023). [Online] Available at https://www.osti.gov/biblio/2217715.

[602] Y. K. Choi, S.-J. Park, S. Park, S. Kim, N. R. Kern, J. Lee, and W. Im, "CHARMM-GUI polymer builder for modeling and simulation of synthetic polymers," J. Chem. Theory Comput. **17**, 2431 (2021). [Online] Available at https://doi.org/10.1021/acs.jctc.1c00169.

[603] S. Jo, T. Kim, V. G. Iyer, and W. Im, "CHARMM-GUI: A web-based graphical user interface for CHARMM," J. Comput. Chem. **29**, 1859 (2008). [Online] Available at https://onlinelibrary.wiley.com/doi/abs/10.1002/jcc.20945.

[604] G. Goret, B. Aoun, and E. Pellegrini, "MDANSE: An interactive analysis environment for molecular dynamics simulations," J. Chem. Inf. Model. **57**, 1 (2017). [Online] Available at https://doi.org/10.1021/acs.jcim.6b00571.

[605] R. Araj, "Pulsed-Neutron Die-Away Response of Polyethylene and Polymethyl Methacrylate Targets to a D-T Neutron Generator Pulse: FUND-LLNL-DT-PE-PNDA-001," Int. Handb. Eval. React. Phys. Benchmark Exp. **NEA 7689** (2024). OECD Nuclear Energy Agency, Pairs.

[606] J. L. Wormald, J. C. Holmes, and M. L. Zerkle, "Influence of quantum oscillations in the thermal scattering law of zirconium carbide on neutron thermalization and criticality," Nucl. Sci. Eng. **197**, 1800 (2023). [Online] Available at https://doi.org/10.1080/00295639.2022.2138063.

[607] J. Coursey, D. Schwab, J. Tsai, and R. Dagoset, "Atomic weights and isotopic compositions (version 4.1)," National Institute of Standards and Technology, 100 Bureau Dr, Gaithersburg, MD 20899, USA (2015), [Online] Available at http://physics.nist.gov/Comp.

[608] W. Schweika, *Disordered Alloys*. Springer-Verlag (2007). [Online] Available at https://doi.org/10.1007/BFb0110656.

[609] J. Wormald, J. Thompson, and T. Trumbull, "Implementation of an adaptive energy grid routine in NDEX for the processing of thermal neutron scattering cross sections," Ann. Nucl. En. **149**, 107773 (2020). [Online] Available at https://www.sciencedirect.com/science/article/pii/S0306454920304710.

[610] T. H. Trumbull, "Computational methods used to process thermal neutron scattering data for use in continuous energy Monte Carlo codes," in *Proceedings of the PHYSOR 2016, Sun Valley, Idaho, USA*, 1, American Nuclear Society (2016).

[611] B. D. Hehr and A. I. Hawari, "Generation of thermal neutron scattering libraries for beryllium carbide," in *2020 1st International & Renewable Energy Conference (INREC), Amman, Jordan*, IEEE (2010). [Online] Available at https://doi.org/10.1109/INREC.2010.5462583.

[612] M. L. Zerkle, "NNL developed TSL evaluations," in *The Annual CSWEG Meeting at Nuclear Data Week 2020*, (Upton, NY), Cross Section Evaluation Working Group (2020). [Online] Available at https://indico.bnl.gov/event/7233/contributions/43575.

[613] E. Staritzky, "Crystallographic data. 120. diberyllium carbide, Be_2C," Anal. Chem. **28**, 915 (1956). [Online] Available at https://doi.org/10.1021/ac60113a044.

[614] J. Wormald, M. Zerkle, and J. Holmes, "Generation of the TSL for zirconium hydrides from ab initio methods," J. Nucl. Eng. **2**, 105 (2021). [Online] Available at https://www.mdpi.com/2673-4362/2/2/11.

[615] E. Slaggie, "Central force lattice dynamical model for zirconium hydride," J. Phys. Chem. Solids **29**, 923 (1968). [Online] Available at https://www.sciencedirect.com/science/article/pii/0022369768902278.

[616] E. Zuzek, J. Abriata, A. San-Martin, *et al.*, "The H-Zr (hydrogen-zirconium) system," Bull. Alloy. Phase Diagrams **11**, 385 (1990). [Online] Available at https://doi.org/10.1007/BF02843318.

[617] W. L. Whittemore, "Neutron interactions in zirconium hydride," Technical report **GA-4490**, General Atomics, San Diego, CA, USA (1986).

[618] Griesheimer, David P., Gill, Daniel F., Nease, Brian R., Pavlou, Andrew, Stedry, Mark H., Thompson, Jason T., Burke, Paul E., and Dobreff, Peter S., "MC21 v.10 – coupled-radiation Monte Carlo transport solver with support for multiphysics simulations," EPJ. Nucl. Sci. Technol. **10**, 23 (2024). [Online] Available at https://doi.org/10.1051/epjn/2024022.

[619] I. Šajger and A. Trkov, "Thermal scattering law data of zirconium hydride," in *The Annual CSWEG Meeting at Nuclear Data Week 2023*, Cross Section Evaluation Working Group, Upton, NY (2023). [Online] Available at https://indico.bnl.gov/event/18701/contributions/82627.

[620] J. L. Wormald, J. C. Holmes, and M. L. Zerkle, "Comparative critical mass calculations for NNL and

ENDF/B-VIII.0 zirconium hydride thermal neutron scattering laws," in *Proceeding of the PHYSOR 2022, Pittsburgh, Pennsylvania, USA, May 15-20, 2022*, 128, American Nuclear Society (2022). [Online] Available at https://www.osti.gov/biblio/1886329.

[621] M. Zerkle and J. Holmes, "A thermal neutron scattering law for yttrium hydride," EPJ. Web. Conf. **146**, 13005 (2017). [Online] Available at https://doi.org/10.1051/epjconf/201714613005.

[622] M. L. Zerkle, J. C. Holmes, and J. L. Wormald, "Re-evaluation of the TSL for yttrium hydride," EPJ. Web. Conf. **247**, 09015 (2021). [Online] Available at https://doi.org/10.1051/epjconf/202124709015.

[623] K. Fu, X. Jiang, Y. Guo, S. Li, J. Zheng, W. Tian, and X. Li, "Experimental investigation and thermodynamic assessment of the yttrium-hydrogen binary system," Prog. Nat. Sci. Mater. Int. **28**, 332 (2018). [Online] Available at https://www.sciencedirect.com/science/article/pii/S1002007117309747.

[624] D. Fritz, Y. Danon, M. Rapp, *et al.*, "Total thermal neutron cross section measurements of yttrium hydride from 0.0005–3 eV," Ann. Nucl. En. **181**, 109475 (2023). [Online] Available at https://www.sciencedirect.com/science/article/pii/S0306454922005059.

[625] E. Staritzky and D. I. Walker, "Crystallographic data. 124. lithium hydride, LiH; 125. lithium deuteride, LiD," Anal. Chem. **28**, 1055 (1956). [Online] Available at https://doi.org/10.1021/ac60114a043.

[626] J. P. W. Crozier and A. I. Hawari, "Ab initio evaluation of plutonium dioxide S(α,β) and thermal neutron cross sections," Trans. Am. Nucl. Soc. **128**, 490 (2023). [Online] Available at https://www.osti.gov/biblio/1994523.

[627] M. E. Manley, J. R. Jeffries, A. H. Said, C. A. Marianetti, H. Cynn, B. M. Leu, and M. A. Wall, "Measurement of the phonon density of states of PuO_2(+2% Ga): A critical test of theory," Phys. Rev. B **85**, 132301 (2012). [Online] Available at https://link.aps.org/doi/10.1103/PhysRevB.85.132301.

[628] J. Crozier and A. Hawari, "Ab Initio Evaluation of Uranium Carbide S(α,β) and Thermal Neutron Cross Sections," EPJ. Web. Conf. **284**, 17005 (2023). [Online] Available at https://doi.org/10.1051/epjconf/202328417005.

[629] J. L. Wormald, N. C. Fleming, A. I. Hawari, and M. L. Zerkle, "Generation of the thermal scattering law of uranium dioxide with ab initio lattice dynamics to capture crystal binding effects on neutron interactions," Nucl. Sci. Eng. **195**, 227 (2021). [Online] Available at https://doi.org/10.1080/00295639.2020.1820826.

[630] M. Berglund and M. E. Wieser, "Isotopic compositions of the elements 2009 (IUPAC technical report)," Pure Appl. Chem. **83**, 397 (2011). [Online] Available at https://doi.org/10.1351/PAC-REP-10-06-02.

[631] C. Lajeunesse, W. Moore, and M. Yeater, "Low energy neutron interactions with uranium carbide," Nucl. Sci. Eng. **47**, 349 (1972).

[632] A. Togo and I. Tanaka, "First principles phonon calculations in materials science," Scripta Materialia **108**, 1 (2015).

[633] S. F. Beshai, "Total cross-sections of U, UO_2 and ThO_2 for thermal and subthermal neutrons," Tech. Rep. **AE-222**, Aktiebolaget Atomenergi, Stockholm, Sweden (1966). EXFOR 20161.

[634] J. L. Wormald, A. I. Hawari, and M. L. Zerkle, "Impact of magnetic structure and thermal effects on vibrational excitations and neutron scattering in uranium mononitride," Ann. Nucl. En. **143**, 107447 (2020). [Online] Available at https://doi.org/10.1016/J.ANUCENE.2020.107447.

[635] G. Leinders, T. Cardinaels, K. Binnemans, and M. Verwerft, "Accurate lattice parameter measurements of stoichiometric uranium dioxide," J. Nucl. Mater. **459**, 135 (2015). [Online] Available at https://www.sciencedirect.com/science/article/pii/S0022311515000331.

[636] R. MacFarlane, D. Muir, R. Boicourt, and A. Kahler, "The NJOY nuclear data processing system, version 2012," Tech. Rep. **LA-UR-12-27079**, Los Alamos National Laboratory, NM, USA (2012).

[637] M. L. Zerkle, "A first look at the thermal neutron scattering law for H-UH_3," Trans. Am. Nucl. Soc. **118**, 531 (2018). [Online] Available at https://www.ans.org/pubs/transactions/article-43694.

[638] D. D. Dijulio, J. I. Marquez Damian, and G. Muhrer, "Generation of thermal neutron scattering libraries for liquid para-hydrogen and ortho-deuterium using ring-polymer molecular dynamics," EPJ. Web. Conf. **284**, 17006 (2023). [Online] Available at https://doi.org/10.1051/epjconf/202328417006.

[639] J. A. Young and J. U. Koppel, "Slow neutron scattering by molecular hydrogen and deuterium," Phys. Rev. **135**, A603 (1964). [Online] Available at https://link.aps.org/doi/10.1103/PhysRev.135.A603.

[640] J. Granada and V. Gillette, "A new thermal neutron scattering kernel for liquid hydrogen," Phys. B: Condens. Matter **348**, 6 (2004). [Online] Available at https://www.sciencedirect.com/science/article/pii/S0921452603006434.

[641] G. H. Vineyard, "Scattering of slow neutrons by a liquid," Phys. Rev. **110**, 999 (1958). [Online] Available at https://link.aps.org/doi/10.1103/PhysRev.110.999.

[642] K. Sköld, "Small energy transfer scattering of cold neutrons from liquid argon," Phys. Rev. Lett. **19**, 1023 (1967). [Online] Available at https://link.aps.org/doi/10.1103/PhysRevLett.19.1023.

[643] K. B. Grammer, R. Alarcon, L. Barrón-Palos, *et al.*, "Measurement of the scattering cross section of slow neutrons on liquid parahydrogen from neutron transmission," Phys. Rev. **B91**, 180301 (2015). [Online] Available at https://link.aps.org/doi/10.1103/PhysRevB.91.180301.

[644] E. Guarini, M. Neumann, U. Bafile, M. Celli, D. Colognesi, E. Farhi, and Y. Calzavara, "Velocity autocorrelation in liquid parahydrogen by quantum simulations for direct parameter-free computations of neutron cross sections," Phys. Rev. **B92**, 104303 (2015). [Online] Available at https://link.aps.org/doi/10.1103/PhysRevB.92.104303.

[645] D. Colognesi, M. Celli, M. Neumann, and M. Zoppi, "Microscopic self-dynamics in liquid hydrogen and in its mixtures with deuterium," Phys. Rev. E-Statistical, Nonlinear, Soft Matter Phys. **70**, 061202 (2004). [Online] Available at https://doi.org/10.1103/PhysRevE.70.061202.

[646] K. Kinugawa, "Path integral centroid molecular dynamics study of the dynamic structure factors of liq-

uid para-hydrogen," Chem. physics letters **292**, 454 (1998). [Online] Available at https://doi.org/10.1016/S0009-2614(98)00703-9.

[647] D. R. Reichman and E. Rabani, "Self-consistent mode-coupling theory for self-diffusion in quantum liquids," Phys. Rev. Lett. **87**, 265702 (2001). [Online] Available at https://doi.org/10.1103/PhysRevLett.87.265702.

[648] W. Seiffert, "Measurements of the scattering cross sections of liquid and solid hydrogen, deuterium hydride for thermal neutrons. (in german)," Tech. Rep. **EUR 4455d**, Euratom (1970).

[649] M. Celli, N. Rhodes, A. K. Soper, and M. Zoppi, "The total neutron cross section of liquid para-hydrogen," J. Physics: Condens. Matter **11**, 10229 (1999). [Online] Available at https://dx.doi.org/10.1088/0953-8984/11/50/315.

[650] F. Atchison, B. van den Brandt, T. Bryś, *et al.*, "Measured total cross sections of slow neutrons scattered by gaseous and liquid $^2H_2$," Phys. Rev. Lett. **94**, 212502 (2005). [Online] Available at https://link.aps.org/doi/10.1103/PhysRevLett.94.212502.

[651] M. Kasprzak, *Ultracold Neutron Converters*. Doctoral Thesis, University of Vienna, Austria (2008).

[652] A. Hawari, I. Al-Qasir, and K. Mishra, "Accurate simulation of thermal neutron filter effects in the design of research reactor beam applications," in *Proceeding of PHYSOR 2006: Advances in Nuclear Analysis and Simulation, Vancouver, BC, Canada, September 10-14, 2006*, A146 (2006).

[653] H. Bialas and H. J. Stolz, "Lattice dynamics of sapphire (corundum)," Z. fur Phys. **B21**, 319 (1975). [Online] Available at https://link.springer.com/article/10.1007/BF01325390.

[654] H. Schober, D. Strauch, and B. Dorner, "Lattice dynamics of sapphire (Al_2O_3)," Z. fur Phys. **B92**, 273 (1993).

[655] D. C. Tennant, "Performance of a cooled sapphire and beryllium assembly for filtering of thermal neutrons," Rev. Sci. Inst. **59**, 380 (1988). [Online] Available at https://doi.org/10.1063/1.1140212.

[656] F. Cantargi, J. R. Granada, and R. E. Mayer, "Thermal neutron scattering kernels for sapphire and silicon single crystals," Ann. Nucl. En. **80**, 43 (2015).

[657] X. Gonze, J.-M. Beuken, R. Caracas, *et al.*, "First-principles computation of material properties: the ABINIT software project," Comput. Mater. Sci. **25**, 478 (2002). [Online] Available at https://www.sciencedirect.com/science/article/pii/S0927025602003257.

[658] I. Al-Qasir, N. Jisrawi, V. Gillette, and A. Qteish, "Thermal neutron scattering cross sections of beryllium and magnesium oxides," Ann. Nucl. En. **87**, 242 (2016). [Online] Available at https://www.sciencedirect.com/science/article/pii/S0306454915004508.

[659] J. G. Barker, D. F. R. Mildner, J. A. Rodriguez, and P. Thiyagarajan, "Neutron transmission of single-crystal magnesium fluoride," J. Appl. Crystallogr. **41**, 1003 (2008). [Online] Available at https://doi.org/10.1107/S0021889808032858.

[660] N. Troullier and J. L. Martins, "Efficient pseudopotentials for plane-wave calculations," Phys. Rev. **B43**, 1993 (1991). [Online] Available at https://link.aps.org/doi/10.1103/PhysRevB.43.1993.

[661] M. Fuchs and M. Scheffler, "Ab initio pseudopotentials for electronic structure calculations of poly-atomic systems using density-functional theory," Comput. Phys. Commun. **119**, 67 (1999). [Online] Available at https://www.sciencedirect.com/science/article/pii/S001046559800201X.

[662] I. Al-Qasir and A. Qteish, "Neutron filter efficiency of beryllium and magnesium fluorides," J. Appl. Crystallogr. **50**, 441 (2017). [Online] Available at https://doi.org/10.1107/S1600576717000851.

[663] J. P. Perdew, K. Burke, and Y. Wang, "Generalized gradient approximation for the exchange-correlation hole of a many-electron system," Phys. Rev. **B54**, 16533 (1996). [Online] Available at https://link.aps.org/doi/10.1103/PhysRevB.54.16533.

[664] M. B. Chadwick, P. G. Young, R. E. MacFarlane, M. C. White, and R. C. Little, "Photonuclear Physics in Radiation Transport – I: Cross Sections and Spectra," Nucl. Sci. Eng. **144**, 157 (2003). [Online] Available at https://doi.org/10.13182/NSE144-157.

[665] M. C. White, R. C. Little, M. B. Chadwick, P. G. Young, and R. E. MacFarlane, "Photonuclear Physics in Radiation Transport – II: Implementation," Nucl. Sci. Eng. **144**, 174 (2003). [Online] Available at https://doi.org/10.13182/NSE144-174.

[666] M.-L. Giacri-Mauborgne, D. Ridikas, M. B. Chadwick, P. G. Young, and W. B. Wilson, "Photonuclear Physics in Radiation Transport – III: Actinide Cross Sections and Spectra," Nucl. Sci. Eng. **153**, 33 (2006). [Online] Available at https://doi.org/10.13182/NSE06-A2592.

[667] S. Goriely, P. Dimitriou, M. Wiedeking, *et al.*, "Reference database for photon strength functions," Eur. Phys. J. **A55**, 172 (2019). [Online] Available at https://doi.org/10.1140/epja/i2019-12840-1.

[668] D. Habs and U. Köster, "Production of medical radioisotopes with high specific activity in photonuclear reactions with γ-beams of high intensity and large brilliance," Appl. Phys. B **103**, 501 (2011). [Online] Available at https://doi.org/10.1007/s00340-010-4278-1.

[669] A. Nichols and R. Capote, "Nuclear data for medical applications - recent developments and future requirements," Nucl. Data Sh. **120**, 239 (2014).

[670] A. Nichols, S. Qaim, and R. Capote, "Summary report of the technical meeting on intermediate-term nuclear data needs for medical applications: Cross sections and decay data," Tech. Rep. **INDC(NDS)-0596**, International Atomic Energy Agency, Vienna, Austria (2011). [Online] Available at https://www-nds.iaea.org/publications/indc/indc-nds-0596.pdf.

[671] A. Nichols, F. Nortier, and R. Capote, "Summary Report from the Third Research Coordination Meeting on nuclear data for charged-particle monitor reactions and medical isotope production, 30 May-3 June 2016, Vienna, Austria," Tech. Rep. **INDC(NDS)-0717**, International Atomic Energy Agency, Vienna, Austria (2016). [Online] Available at https://www-nds.iaea.org/publications/indc/indc-nds-0717/.

[672] V. Plujko, O. Gorbachenko, R. Capote, and P. Dimitriou, "Giant dipole resonance parameters of ground-state photoabsorption: Experimental values with uncertainties," Atom. Data Nucl. Data Tables **123–124**, 1 (2018).

[673] H. Utsunomiya, I. Gheorghe, D. M. Filipescu, *et al.*, "Direct neutron-multiplicity sorting with a flat-efficiency detector," Nucl. Inst. Meth. Phys. Res. **A871**, 135

(2017).
[674] S. C. Fultz, R. L. Bramblett, J. T. Caldwell, N. Hansen, and C. Jupiter, "Photoneutron cross-section measurements on gold using nearly monochromatic photons," Phys. Rev. **128**, 2345 (1962).
[675] R. L. Bramblett, J. T. Caldwell, G. F. Auchampaugh, and S. C. Fultz, "Photoneutron cross sections of ^{181}Ta and ^{165}Ho," Phys. Rev. **129**, 2723 (1963).
[676] R. L. Bramblett, J. T. Caldwell, R. R. Harvey, and S. C. Fultz, "Photoneutron cross sections of ^{159}Tb and ^{16}O," Phys. Rev. **133**, B869 (1964).
[677] B. L. Berman, M. A. Kelly, R. L. Bramblett, J. T. Caldwell, H. S. Davis, and S. C. Fultz, "Giant resonance in deformed nuclei: Photoneutron cross sections for ^{153}Eu,^{160}Gd,^{165}Ho, and ^{186}W," Phys. Rev. **185**, 1576 (1969).
[678] R. A. Alvarez, B. L. Berman, D. D. Faul, F. H. Lewis, and P. Meyer, "Photoneutron cross sections for ^{55}Mn and ^{59}Co," Phys. Rev. **C20**, 128 (1979).
[679] B. Berman, R. Pywell, S. Dietrich, M. Thompson, K. McNeill, and J. Jury, "Absolute photoneutron cross sections for Zr, I, Pr, Au, and Pb," Phys. Rev. **C36**, 1286 (1987).
[680] R. Bergère, H. Beil, and A. Veyssière, "Photoneutron cross sections of La, Tb, Ho and Ta," Nucl. Phys. **A121**, 463 (1968).
[681] A. Veyssiere, H. Beil, R. Bergere, P. carlos, and A. Lepretre, "Photoneutron cross sections of ^{208}Pb and ^{197}Au," Nucl. Phys. **A159**, 561 (1970).
[682] G. Gurevich, L. Lazareva, V. Mazur, G. Solodukhov, and B. Tulupov, "Giant resonance in the total photoabsorption cross section near Z= 90 nuclei," Nucl. Phys. **A273**, 326 (1976). [Online] Available at https://www.sciencedirect.com/science/article/pii/0375947476905947.
[683] V. V. Varlamov, N. G. Efimkin, V. V. Surgutanov, A. A. Khoronenko, and A. P. Chernyaev, "Photonuclear data. photofission of ^{235,238}U," Tech. Rep. **CDFE/FIS2**, Center Photo Nuclear Data, Moscow State University M.V.Lomonosov, Moscow, Russia (1987). EXFOR M030.
[684] V. Varlamov and N. Peskov, "Evaluation of (gamma,xn), (gamma,sn), (gamma,n), (gamma,2n), and (gamma,f) reactions cross sections for actinides nuclei ^{232}Th, ^{238}U, ^{237}Np, and ^{239}Pu: consistency between data obtained using quasimonoenergetic annihilation and bremsstrahlung photons," Tech. Rep. **MSU-INP-2007-8/829**, Moscow State University M.V.Lomonosov, Moscow, Russia (2007).
[685] Krishichayan, S. W. Finch, C. R. Howell, A. P. Tonchev, and W. Tornow, "Monoenergetic photon-induced fission cross-section ratio measurements for ^{235}U, ^{238}U, and ^{239}Pu from 9.0 to 17.0 MeV," Phys. Rev. **C98**, 014608 (2018).
[686] F. A. St. Romain, T. Bonner, R. Bramblett, and J. Hanna, "Low-energy neutrons from the reaction $Be^9(\alpha, n)$ C^{12}," Phys. Rev. **126**, 1794 (1962). [Online] Available at https://doi.org/10.1103/PhysRev.126.1794.
[687] A. W. Obst, T. B. Grandy, and J. L. Weil, "Reaction $Be^9(\alpha, n)$ C^{12} from 1.7 to 6.4 MeV," Phys. Rev. C **5**, 738 (1972). [Online] Available at https://doi.org/10.1103/PhysRevC.5.738.
[688] K. W. Geiger and L. Van Der Zwan, "Radioactive neutron source spectra from ^{9}Be(α, n) cross section data," Nucl. Inst. Meth. **131**, 315 (1975). [Online] Available at https://doi.org/10.1016/0029-554X(75)90336-5.
[689] K. W. Geiger and L. Van Der Zwan, "An evaluation of the ^{9}Be (α, n) cross section," Natl. Res. Counc. Can. Report, NRCC-15303 (1976).
[690] M. E. Anderson and R. A. Neff, "Neutron energy spectra of different size ^{239}Pu-Be (α, n) sources," Nucl. instruments Meth. **99**, 231 (1972). [Online] Available at https://doi.org/10.1016/0029-554X(72)90781-1.
[691] D. P. Griesheimer, A. T. Pavlou, J. T. Thompson, J. C. Holmes, M. L. Zerkle, E. Caro, and H. Joo, "In-line (α, n) source sampling methodology for Monte Carlo radiation transport simulations," Nucl. Eng. Techn. **49**, 1199 (2017). [Online] Available at https://doi.org/10.1016/j.net.2017.08.004.
[692] J. W. Marsh, D. J. Thomas, and M. Burke, "High resolution measurements of neutron energy spectra from Am-Be and Am-B neutron sources," Nucl. Inst. Meth. Phys. Res. Sect. A: Accel. Spectrometers, Detect. Assoc. Equip. **366**, 340 (1995). [Online] Available at https://doi.org/10.1016/0168-9002(95)00613-3.
[693] J. H. Gibbons and R. L. Macklin, "Total cross section for ^{9}Be(α, n)," Phys. Rev. **137**, B1508 (1965). [Online] Available at https://link.aps.org/doi/10.1103/PhysRev.137.B1508.
[694] L. Van der Zwan and K. W. Geiger, "The ^{9}Be (α, n) ^{12}C cross section between 1.5 and 7.8 MeV," Nucl. Phys. A **152**, 481 (1970).
[695] E. F. Shores, G. E. Mueller, and G. A. Schlapper, "A new ^{9}Be (α, n) cross-section evaluation for use in the SOURCES computer code," Appl. radiation isotopes **59**, 151 (2003).
[696] G. J. H. Jacobs and H. Liskien, "Energy spectra of neutrons produced by α-particles in thick targets of light elements," Ann. Nucl. En. **10**, 541 (1983).
[697] T. R. Herold, "Neutron spectrum of $^{238}PuO_2$," Nucl. Appl. **4**, 19 (1968).
[698] M. E. Anderson, "Neutron energy spectra of ^{239}Pu–Be, ^{238}Pu–F, and ^{238}Pu–^{18}O (α, n) sources," Tech. Rep. **MLM-1422**, Mound Plant (MOUND), Miamisburg, OH (United States) (1967).
[699] M. Anderson, "Neutron energy spectra of a ^{238}Pu–^{18}O (α, n) source – unmoderated and polyethylene moderated," Heal. Phys. **39**, 537 (1980).
[700] Ian Thompson, "Candidate evaluation for He3 + He4 scattering from R-matrix theory." https://indico.bnl.gov/event/15497/contributions/69761/attachments/44289/74713/Thompson-NDW22-Rmatrix-v1+IM.pdf (2022). Presentation at the 2022 CSEWG Meeting.
[701] G. Hale, R. E. Brown, and N. Jarmie, "Pole structure of the Jpi=3/2+ resonance in He-5," Phys. Rev. Lett. **59**, 763 (1987). [Online] Available at https://doi.org/10.1103/PhysRevLett.59.763.
[702] M. Chadwick, P. Oblozinsky, M. Herman, *et al.*, "ENDF/B-VII.0: Next generation evaluated nuclear data library for nuclear science and technology," Nucl. Data Sh. **107**, 2931 (2006). [Online] Available at https://doi.org/10.1016/j.nds.2006.11.001.
[703] M. W. Paris, P. Talou, J. L. Conlin, N. A. Gibson, W. Haeck, G. M. Hale, E. T. Norris, D. K. Parsons, and T. Saller, "Charged Particle Transport Libraries (Final Report FY2020 Level-2 Milestone #7127)," Tech. Rep.

LA-UR-20-26607-Rev.01, Los Alamos National Laboratory, Los Alamos, NM, USA (2021). [Online] Available at https://www.osti.gov/biblio/1770083.

[704] R. J. S. Brown, K. F. Famularo, H. D. Holmgren, D. Rankin, and T. F. Stratton, "Elastic scattering of deuterons by ^{3}He," Phys. Rev. **96**, 80 (1954). [Online] Available at http://dx.doi.org/10.1103/PhysRev.96.80.

[705] J. E. Brolley, T. M. Putnam, L. Rosen, and L. Stewart, "Hydrogen-helium isotope elastic scattering processes at intermediate energies," Phys. Rev. **117**, 1307 (1960). [Online] Available at http://dx.doi.org/10.1103/PhysRev.117.1307.

[706] T. A. Tombrello, R. J. Spiger, and A. D. Bacher, "Deuteron elastic scattering from ^{3}He and ^{3}H," Phys. Rev. **154**, 935 (1967). [Online] Available at http://dx.doi.org/10.1103/PhysRev.154.935.

[707] N. Jarmie and J. H. Jett, "Various cross sections for $A \leq 3$ nuclei," Phys. Rev. **C10**, 54 (1974). [Online] Available at http://dx.doi.org/10.1103/PhysRevC.10.54.

[708] B. Jenny, W. Gruebler, V. Konig, P. A. Schmelzbach, R. Risler, H. R. Burgi, and D. O. Boerma, "Analyzing-power and cross-section measurements for ^{3}He(d,d)^{3}He scattering," Nucl. Phys. **A324**, 99 (1979). [Online] Available at http://dx.doi.org/10.1016/0375-9474(79)90080-0.

[709] L. Ruby, R. V. Pyle, and Y.-C. Wong, "Cross sections for ^{6}Li(^{6}Li,^{5}He)^{7}Be, ^{6}Li(d,n)^{7}Be, and ^{19}F(^{6}Li,p)^{24}Na," Nucl. Sci. Eng. **71**, 280 (1979). [Online] Available at https://doi.org/10.13182/NSE79-A19064.

[710] B. J. Guzhovskij, S. N. Abramovich, A. G. Zvenigorodskij, V. P. Protopopov, G. N. Slepcov, and S. V. Trusillo, "Total Cross Sections for the Reactions ^{6}Li(d,n)^{7}Be,^{7}Li(d,2n)^{7}Be,and ^{6}Li(t,2n)^{7}Be," Izv. Ross. Akad. Nauk, Ser. Fiz. Engl. translation: Bull. Russ. Acad. Sci. - Phys. 44, p.168, 1980 **44**, 1983 (1980).

[711] C. R. McClenahan and R. E. Segel, "Cross sections for the ^{7}Li$(d,p)^8$Li, ^{6}Li$(^3$He$,n)^8$B, ^{6}Li$(d,\alpha)^4$He, ^{6}Li$(d,p)^7$Li, and ^{6}Li$(d,n)^7$Be reactions," Phys. Rev. **C11**, 370 (1975). [Online] Available at https://link.aps.org/doi/10.1103/PhysRevC.11.370.

[712] S. N. Paneru, H. Y. Lee, R. J. deBoer, *et al.*, "R-matrix analysis of the ^{8}Be system," Phys. Rev. C **111**, 064609 (2025). [Online] Available at https://link.aps.org/doi/10.1103/msrx-3fjr.

[713] S. N. Paneru, H. Y. Lee, C. Prokop, *et al.*, "Comprehensive study of $d+^6$Li via observing simultaneous outgoing neutrons, γ rays, and charged particles," Phys. Rev. C **110**, 044603 (2024). [Online] Available at https://link.aps.org/doi/10.1103/PhysRevC.110.044603.

[714] Z. Bödy, J. Szabó, and M. M. Várnagy, "Low-energy cross sections for ^{6}Li$(d,\alpha)^4$He and ^{6}Li$(d,p)^7$Li reactions," Nucl. Phys. **A330**, 495 (1979). [Online] Available at https://www.sciencedirect.com/science/article/pii/037594747990068X.

[715] A. J. Elwyn, R. E. Holland, C. N. Davids, L. Meyer-Schutzmeister, J. E. Monahan, F. P. Mooring, and W. Ray, "Absolute cross sections for deuteron-induced reactions on ^{6}Li at energies below 1 MeV," Phys. Rev. **C16**, 1744 (1977). [Online] Available at https://link.aps.org/doi/10.1103/PhysRevC.16.1744.

[716] F. Bertrand, G. Grenier, and J.Pornet, "^{6}Li(p,α)^{3}He, ^{6}Li(d,α)^{4}He, ^{6}Li(d,p_0)^{7}Li, ^{6}Li(d,p_1)^{7}Li* reaction investigation in the energy interval from 300 keV to 1000 keV," Tech. Rep. **3428**, Centre d'Etudes de Limeil, CEN Saclay, Villeneuve-Saint-Georges, France (1968).

[717] C. R. Gould, J. M. Joyce, and J. R. Boyce, "Cross section measurements for charged particle induced reactions on Li-6," in *Nuclear cross sections and technology. Volume II. Proceedings of a conference, Washington, D.C., March 3–7, 1975*, 697, US Department of Commerce, National Bureau of Standards, NBS Special Publication 425 (1975).

[718] J. Szabó, Z. Bödy, S. Szegedi, and M. Várnagy, "Low-energy cross section for ^{6}Li(d,n)^{7}Be," Nucl. Phys. **A289**, 526 (1977). [Online] Available at https://doi.org/10.1016/0375-9474(77)90049-5.

[719] I. J. F. Hirst and M. Poole, "LXXXV. the d-^{6}Li reactions," The London, Edinburgh, Dublin Philos. Mag. J. Sci. **45**, 762 (1954). [Online] Available at https://doi.org/10.1080/14786440708520486.

[720] G. Haouat, "Measurements of the ^{6}Li(d,n)^{7}Be cross section." personal communication to G. Hale (1985).

[721] S. T. Perkins and D. E. Cullen, "Elastic nuclear plus interference cross sections for light-charged particles," Nucl. Sci. Eng. **77**, 20 (1981). [Online] Available at https://doi.org/10.13182/NSE81-A21336.

[722] Gerald M. Hale, D. Kent Parsons, and Morgan White, "ACE Library CP2011 Charged Particles Incident on Light Isotopes," Memorandum **XCP-5: MCW-12-004(U)**, Los Alamos National Laboratory, NM, USA (2011).

[723] Gerald M. Hale and Morgan White, "NDI MG Library CP2011 Charged Particles Emissions from Neutrons Incident on Light Isotopes," Memorandum **XCP-5: MCW-12-005(U)**, Los Alamos National Laboratory, NM, USA (2011).

[724] M. Devlin, T. N. Taddeucci, G. M. Hale, R. C. Haight, and J. M. O'Donnell, "Differential Cross Section Measurements for the ^{6}Li(n,t)α Reaction in the Few MeV Region," Conference Report **1090**, Los Alamos National Laboratory, NM, USA (2009). EXFOR 14159, [Online] Available at http://dx.doi.org/10.1063/1.3087015.

[725] A. Mattera and A. Sonzogni, "Revision of fission yields uncertainties in ENDF/B-VIII.0," Tech. Rep. **BNL-220804-2021-INRE**, Brookhaven National Laboratory (BNL), Upton, NY (United States) (2021). [Online] Available at https://www.osti.gov/biblio/1762758.

[726] T. England and B. Rider, "Evaluation and Compilation of Fission Product Yields," Tech. Rep. **LA-UR-94-3106 (ENDF-349)**, Los Alamos National Laboratory, NM, USA (1994). [Online] Available at https://t2.lanl.gov/nis/publications/endf349.pdf.

[727] M. Chadwick, T. Kawano, D. Barr, *et al.*, "Fission product yields from fission spectrum n+ ^{239}Pu for ENDF/B-VII.1," Nucl. Data Sh. **111**, 2923 (2010). [Online] Available at https://doi.org/10.1016/j.nds.2010.11.003.

[728] S. Kumar, J. Chen, and F. Kondev, "Nuclear data sheets for A = 109," Nucl. Data Sh. **137**, 1 (2016). [Online] Available at https://www.sciencedirect.com/science/article/pii/S0090375216300321.

[729] A. Mattera, "Independent and cumulative thermal neutron-induced fission yields of ^{241}Pu for ENDF/B-VIII.1," Tech. Rep. **BNL-225087-2023-INRE**, Brookhaven National Laboratory (BNL), Upton, NY (United States) (2023). [Online] Available at https://www.osti.gov/servlets/purl/2267571.

[730] B. Rider and T. England, "Evaluation of fission product yields for the USA National Nuclear Data files," in *Proceedings of a Specialists' meeting on Data for Decay Heat Predictions*, 21, Nuclear Energy Agency, Committee on Reactor Physics and Nuclear Data Committee (1987).

[731] "From ENSDF database as of June, 2012. version available at http://www.nndc.bnl.gov/ensarchivals/."

[732] D. E. Cullen, "EPICS2023: August 2023 Status Report," Tech. Rep. **IAEA-NDS-0242**, IAEA, Vienna, Austria (2023). [Online] Available at https://nds.iaea.org/publications/nds/iaea-nds-0242/.

[733] D. E. Cullen, "EPICS2023: Electron Photon Interaction Cross Sections (2023)." https://www-nds.iaea.org/epics/ (2023).

[734] A. Carlson, V. Pronyaev, R. Capote, *et al.*, "Results of a New Evaluation of the Neutron Standards," in *Reactor Dosimetry: 16th International Symposium, ASTM STP1608, M.H. Sparks, K.R. DePriest, and D.W. Vehar, Eds.*, (West Conshohocken, PA, USA), 91, ASTM International (2018). [Online] Available at http://dx.doi.org/10.1520/STP16082017006.

[735] (Cross Section Evaluation Working Group (CSEWG)), "ENDF-6 Formats Manual - Data Formats and Procedures for the Evaluated Nuclear Data Files ENDF/B-VI, ENDF/B-VII and ENDF/B-VIII," Tech. Rep. **BNL-203218-2018-INRE, ENDF Report ENDF-102**, Brookhaven National Laboratory (2018). [Online] Available at https://www.osti.gov/biblio/1425114.

[736] Nuclear Energy Agency, OECD, *Specifications for the Generalised Nuclear Database Structure (GNDS)*. OECD Publishing (2023). [Online] Available at https://www.oecd-ilibrary.org/content/publication/5f05e3db-en.

[737] Nuclear Energy Agency, Working Party on Evaluation Cooperation, Expert Group GNDS, *Specifications for the Generalised Nuclear Database Structure (GNDS)*. Paris: OECD Publishing (2020).

[738] DataCite Metadata Working Group, "Datacite metadata schema for the publication and citation of research data and other research outputs. Version 4.5.," (2024). [Online] Available at https://doi.org/10.14454/g8e5-6293.

[739] J. A. Kulesza *et al.*, "MCNP Code Version 6.3.0 Theory & User Manual," Tech. Rep. **LA-UR-22-30006, Rev. 1**, Los Alamos National Laboratory, NM, USA (2022).

[740] J. L. Conlin, P. Romano, and W. Haeck, "A Compact ENDF (ACE) Format Specification," Tech. Rep. **LA-UR-19-29016**, Los Alamos National Laboratory, NM, USA (2019).

[741] F. Fröhner, "Applied Neutron Resonance Theory," Tech. Rep. **KFK 2669**, Kernforschungszentrum, Karlsruhe, Germany (1978). [Online] Available at https:/doi.org/10.5445/IR/270012145.

[742] F. Fröhner, "New Techniques for Multi-Level Cross Section Calculation and Fitting," Tech. Rep. **BNL-NCS-51363**, Brookhaven National Lab., Upton, NY, USA (1981). [Online] Available at https://www.osti.gov/biblio/5972980.

[743] C. M. Mattoon, B. R. Beck, and G. Gert, "Managing and Processing Nuclear Data Libraries with FUDGE," EPJ. Web. Conf. **284**, 14010 (2023). [Online] Available at https://doi.org/10.1051/epjconf/202328414010.

[744] P. Vranas, T. Bailey, B. Beck, M.-A. Descalle, A. Dreyfuss, and D. Brown, "Metis, the verification and validation test suite," Technical report **LLNL-SM-733021**, Lawrence Livermore National Laboratory, CA, USA (2017).

[745] P. Brantley *et al.*, "Mercury User Guide: Version 5.40.0," Tech. Rep. **LLNL-SM-560687**, Lawrence Livermore National Laboratory, CA, USA (2024).

[746] U. Hanebutte and P. N. Brown, "ARDRA, Scalable Parallel Code System to Perform Neutron and Radiation Transport Calculations," Tech. Rep. **UCRL-TB-132078**, Lawrence Livermore National Laboratory, CA, USA (1999).

[747] B. R. Beck, C. M. Mattoon, and G. Gert, "GIDI+: A GNDS 2.0 suite of C++ APIs to access nuclear and atomic data for use in radiation transport codes," EPJ. Web. Conf. **284**, 14004 (2023). [Online] Available at https://doi.org/10.1051/epjconf/202328414004.

[748] W. A. Wieselquist and R. A. Lefebvre, "SCALE 6.3.1 User Manual," Tech. Rep. **ORNL/TM-SCALE-6.3.1**, Oak Ridge National Laboratory (ORNL), Oak Ridge, TN (United States) (2023). [Online] Available at https://doi.org/10.2172/1959594.

[749] "SCALE-Public." https://code.ornl.gov/scale/code/scale-public (2023). [Online] Available at https://code.ornl.gov/scale/code/scale-public.

[750] K. S. Kim, D. Wiarda, C. Chapman, J. McDonnell, and W. Wieselquist, "Improvement of the SCALE-6.3/XSProc Pointwise Slowing-Down Capability with the Bound Thermal Scattering Data Including High Forward Peaks," Trans. Am. Nucl. Soc. **129**, 817 (2023).

[751] R. A. Lefebvre, J. Brown, C. Celik, T. Evans, B. Jeon, J. McDonnell, K. Royston, D. Wiarda, and W. Wieselquist, "Photonuclear Physics in SCALE," Tech. Rep. **ORNL/TM-2023/3201**, Oak Ridge National Laboratory (ORNL), Oak Ridge, TN (United States) (2024). [Online] Available at https://doi.org/10.2172/1959594.

[752] B. Pritychenko, "Tables of neutron thermal cross sections, Westcott factors, resonance integrals, Maxwellian averaged cross sections, astrophysical reaction rates, and r-process abundances calculated from the ENDF/B-VIII.1, JEFF-3.3, JENDL-5.0, BROND-3.1, and CENDL-3.2 evaluated data libraries," Atom. Data Nucl. Data Tables **163**, 101708 (2025). [Online] Available at https://www.sciencedirect.com/science/article/pii/S0092640X25000014.

[753] R. Mosteller, F. Brown, and B. Kiedrowski, "An Expanded Criticality Validation Suite for MCNP," Tech. Rep. **LA-UR-11-04170**, Los Alamos National Laboratory, NM, USA (2011). [Online] Available at https://mcnp.lanl.gov/pdf_files/TechReport_2011_LANL_LA-UR-11-04170_MostellerBrownEtAl.pdf.

[754] S. C. van der Marck, "Benchmarking ENDF/B-VII.0," Nucl. Data Sh. **107**, 3061 (2006).

[755] D. P. Griesheimer and N. A. Gibson, "Simplified method for estimating the effective delayed neutron fraction with Monte Carlo correlated sampling," in *Proceedings of International Conference on Mathematics and Computational Methods Applied to Nuclear Science and Engineering (M&C 2019)*, (Portland, Oregon (USA)), 886 (2019).

[756] K. Ivanov, M. Avramova, S. Kamerow, I. Kodeli, E. Sartori, E. Ivanov, and O. Cabellos, "Benchmark for Uncertainty Analysis in Modelling (UAM) for Design, Oper-

ation and Safety Analysis of LWRs, Volume I: Specification and Support Data for the Neutronics Cases (Phase I)," Tech. Rep. **NEA/NSC/DOC(2013)7**, NEA (2013).

[757] J. Leppänen, M. Pusa, T. Viitanen, V. Valtavirta, and T. Kaltiaisenaho, "The Serpent Monte Carlo code: Status, development and applications in 2013," Ann. Nucl. En. **82**, 142 (2015). [Online] Available at https://doi.org/10.1016/j.anucene.2014.08.024.

[758] R. Tuominen, V. Valtavirta, and J. Leppänen, "New energy deposition treatment in the Serpent 2 Monte Carlo transport code," Ann. Nucl. En. **129**, 224 (2019). [Online] Available at https://doi.org/10.1016/j.anucene.2019.02.003.

[759] B. Becker, R. Dagan, and G. Lohnert, "Proof and implementation of the stochastic formula for ideal gas, energy dependent scattering kernel," Ann. Nucl. En. **36**, 470 (2009). [Online] Available at http://dx.doi.org/10.1016/j.anucene.2008.12.001.

[760] E. Georgieva and T. Bahadir, "NEA/OECD TVA Watts Bar Unit 1 multi-physics multi-cycle depletion benchmark with CASMO5 and SIMULATE5," in *Proceedings of the International Conference on Physics of Reactors (PHYSOR 2024)*, (San Francisco, CA), 1208, American Nuclear Society (2024). [Online] Available at https://www.ans.org/pubs/proceedings/article-55591/.

[761] OECD/NEA, "International Handbook of Evaluated Reactor Physics Benchmark Experiments," NEA report (2016). [Online] Available at https://www.oecd-ilibrary.org/content/data/d863e360-en.

[762] G. G. Davidson, T. M. Pandya, S. R. Johnson, T. M. Evans, A. E. Isotalo, C. A. Gentry, and W. A. Wieselquist, "Nuclide depletion capabilities in the Shift Monte Carlo code," Ann. Nucl. En. **114**, 259 (2018). [Online] Available at https://www.sciencedirect.com/science/article/pii/S0306454917304322.

[763] G. Ilas, J. R. Burns, B. D. Hiscox, and U. Mertyurek, "SCALE 6.2.4 Validation: Reactor Physics," Tech. Rep. **ORNL/TM-2020/1500 v3**, Oak Ridge National Laboratory (ORNL), Oak Ridge, TN (United States) (2022). [Online] Available at https://doi.org/10.2172/1902818.

[764] S. W. D. Hart, G. I. Maldonado, S. Goluoglu, and B. Rearden, "Implementation of the Doppler broadening rejection correction in KENO," Trans. Am. Nucl. Soc. **108**, 423 (2013).

[765] J. Rhodes, K. Smith, and D. Lee, "CASMO-5 development and applications," in *Proceedings of PHYSOR-2006, Vancouver, BC, Canada*, American Nuclear Society (2006). [Online] Available at https://www.osti.gov/biblio/22039682.

[766] R. Ferrer, C. Wemple, and J. Hykes, "Initial Benchmarking of a New ENDF/B-VIII.1 . β2-based CASMO5 Neutron Data Library," in *PHYSOR2024, San Francisco, CA, USA*, (San Francisco, USA), American Nuclear Society (2024).

[767] A. Trkov, "CORD-2 package user's guide, rev.5," Tech. Rep. **IJS-DP-6948**, Jozef Stefan Institute, Ljubljana, Slovenia (2009). [Online] Available at https://www.rcp.ijs.si/bojan/cord2/cd2man.pdf.

[768] J. R. Askew, F. J. Fayers, and P. B. Kemshell, "General description of the lattice code WIMS," The J. Br. Nucl. En. Soc. **5**, 564 (1966). [Online] Available at https://www.osti.gov/biblio/4462252.

[769] ANSWERS Software Service, AEA Technology, "WIMSD5: Deterministic Multigroup Reactor Lattice Calculations," (2004). Tested version: 25-FEB-2004. Available for various platforms including Windows and UNIX., [Online] Available at https://www.oecd-nea.org/tools/abstract/detail/nea-1507/.

[770] D. Lopez Aldama and A. Trkov, "WIMS-D IAEA library," (2007). [Online] Available at https://nds.iaea.org/wimsd/.

[771] F. Leszczynski, D. Lopez Aldama, and A. Trkov, "WIMS-D Library Update," Tech. Rep. **STI/PUB/1264**, International Atomic Energy Agency, Vienna, Austria (2007). [Online] Available at https://www-pub.iaea.org/MTCD/Publications/PDF/Pub1264_web.pdf.

[772] D. L. Aldama, "Documentation for WIMSD-formatted libraries based on ENDF/B-VII.1 evaluated nuclear data files with extended actinide burnup chains and cross section data up to 2000 K for fuel materials," Tech. Rep. **INDC(NDS)-0674**, International Atomic Energy Agency, Vienna, Austria (2014). [Online] Available at https://nds.iaea.org/publications/indc/indc-nds-0674/.

[773] D. Neudecker, O. Cabellos, A. Clark, W. Haeck, R. Capote, A. Trkov, M. C. White, and M. E. Rising, "Which nuclear data can be validated with LLNL pulsed-sphere experiments?," Ann. Nucl. En. **159**, 108345 (2021).

[774] J. Alwin, A. Clark, T. Cutler, *et al.*, "EUCLID sensitivity database," Tech. Rep. **LA-UR-22-21534**, Los Alamos National Laboratory, NM, USA (2022).

[775] M. Divadeenam and J. Stehn, "A least-squares fit of thermal data for fissile nuclei," Ann. Nucl. En. **11**, 375 (1984). [Online] Available at https://doi.org/10.1016/0306-4549(84)90002-1.

[776] H. Alter, R. B. Kidman, R. LaBauve, R. Prostik, and B. A. Zolotar, "Cross section evaluation working group benchmark specifications," Tech. Rep. **BNL-19302; ENDF-202**, Brookhaven National Laboratory (1974). [Online] Available at https://www.osti.gov/biblio/4202823.

[777] H. Selby, M. Mac Innes, D. Barr, A. Keksis, R. Meade, C. Burns, M. Chadwick, and T. Wallstrom, "Fission Product Data Measured at Los Alamos for Fission Spectrum and Thermal Neutrons on 239Pu, 235U, 238U," Nucl. Data Sh. **111**, 2891 (2010). [Online] Available at https://www.sciencedirect.com/science/article/pii/S0090375210001018.

Appendix A: Provenance of evaluations in ENDF/B-VIII.1

To facilitate future reference, we document the provenance and update information of each individual file in the ENDF/B-VIII.1 release for the following sublibraries: neutrons (Table XLIX), thermal-neutron scattering law (Table L), photonuclear (Table LI), neutron-induced fission yields (Table LII), spontaneous fission yields (Table LIII), protons (Table LIV), deuterons (Table LV), tritons (Table LVI), ^{3}He (Table LVII), and alphas (Table LVIII).

As indicated in the main text, both the neutron-induced and spontaneous fission-yield libraries were updated. The nature of the fission yield changes imply that *every* fission yield evaluation was impacted as reflected in Tables LII and LIII.

TABLE XLIX: Summary of the origins of and recent changes to the neutrons sublibrary. For each file we list the library source, the year when the last significant evaluation effort or impactful modification was performed, and the evaluation source and year for each incident-neutron energy range: Resolved Resonance Range (RRR), Unresolved Resonance Range (URR), fast-neutron range below 20 MeV (Fast), and High Energy above 20 MeV (HE). We also provide additional comments, where relevant. Evaluations updated in ENDF/B-VIII.1 are in bold.

File name (.endf)	Source	Last updated	RRR		URR		Fast		HE		Comments
			Inst.	Year	Inst.	Year	Inst.	Year	Inst.	Year	
n-000_n_001	ENDF/B-VIII.0	2024					LANL	2016			
n-001_H_001	ENDF/B-VIII.0; CIELO 2017; Standards 2017	2023					LANL	2016			R-matrix analysis; COMMARA-2.0 covariances added in 2011
n-001_H_002	ENDF/B-VIII.0	2024					LANL	1994	LANL	1997	JEFF-3.2 ang dists; otw. B-VI below 50MeV; COMMARA-2.0 covariances added in 2011
n-001_H_003	ENDF/B-VII.0	2024					LANL	2001			R-matrix analysis
n-002_He_003	ENDF/B-VIII.0; Standards 2017	2024					LANL	2011			Originally from ENDF/B-III; capture replaced in 2011; (n,p) in 1990; exit distributions added
n-002_He_004	ENDF/B-VII.1	2024					LANL	2010			R-matrix analysis
n-003_Li_006	**ENDF/B-VIII.1; Standards 2017**	**2023**	**LANL**	**2023**			**LANL**	**2023**			**R-matrix analysis; EGAF primary gammas**
n-003_Li_007	ENDF/B-VI	2023					LANL	1988			EGAF primary gammas;IRDFF-II mod.
n-004_Be_007	ENDF/B-VIII.0	2024					LANL; LLNL	2017			ENDF/B-VII.1 R-matrix analysis up to 8.1 MeV; TALYS calc. above; EGAF primary gammas; Low-fidelity covariances added in 2011
n-004_Be_009	ENDF/B-VIII.0	2023					LANL; LLNL; JAEA	2011			Capture updated for VII.1; JENDL-4 energy and angular dists.; Various fixes including some to improve criticality
n-005_B_010	ENDF/B-VIII.0; Standards 2017	2023					LANL	2017			R-matrix analysis
n-005_B_011	ENDF/B-VIII.0	2024					LANL	2015			Angular dist. recalculated; EGAF primary gammas
n-006_C_012	ENDF/B-VIII.0; Standards 2017	2023					LANL	2016	LANL	2006	R-matrix analysis
n-006_C_013	ENDF/B-VIII.0; Standards 2017	2023					LANL	2017	LANL	2006	R-matrix analysis
n-007_N_014	ENDF/B-VI	2024					LANL	1994	LANL	1997	
n-007_N_015	ENDF/B-VI	2024					LANL	1983			
n-008_O_016	**ENDF/B-VIII.1; INDEN**	**2023**					**LANL; IAEA**	**2022**	**LANL; IAEA**	**2022**	**INDEN evaluation; R-matrix analysis below 7 MeV; elastic and (n, alpha) changed**
n-008_O_017	ENDF/B-V	2023	BNL	1978			BNL	1978			
n-008_O_018	**ENDF/B-VIII.1; INDEN**	**2024**	**JSI; BNL**	**2024**			**IPPE**	**2006**			**INDEN evaluation; capture from EAF-2010**
n-009_F_019	**ENDF/B-VIII.1; INDEN**	**2024**	**ORNL**	**2003**			**IAEA; LANL; LLNL**	**2023**			**INDEN evaluation.; EGAF primary gammas; IRDFF-II mod.; Documentation need updates**
n-010_Ne_020	TENDL-2015	2023	TENDL	2015			TENDL	2015	TENDL	2015	TENDL+EMPIRE
n-010_Ne_021	TENDL-2015	2023	TENDL	2015			TENDL	2015	TENDL	2015	TENDL+EMPIRE
n-010_Ne_022	TENDL-2015	2023	TENDL	2015			TENDL	2015	TENDL	2015	TENDL+EMPIRE
n-011_Na_022	JEF-2.2	2023	BNL	1981	BNL	1982	ECN	1982			Exit dist. added from TENDL
n-011_Na_023	ENDF/B-V	2023	ORNL	1977			ORNL	1977			EGAF primary gammas; IRDFF-II mod.; Exit dist. added from TENDL
n-012_Mg_024	JENDL-3	2023	JNDC	1987			JNDC	1987			COMMARA-2.0 covariances added in 2011; IRDFF-II mod.; Exit dist. added from TENDL

Continued on the next page

TABLE XLIX: (continued) Provenance for the neutrons sublibrary.

File name (.endf)	Source	Last updated	RRR		URR		Fast		HE		Comments
			Inst.	Year	Inst.	Year	Inst.	Year	Inst.	Year	
n-012_Mg_025	JENDL-3	2023	JNDC	1987			JNDC	1987			Low-fidelity covariances added in 2011; Exit dist. added from TENDL
n-012_Mg_026	JENDL-3	2023	JNDC	1987			JNDC	1987			Low-fidelity covariances added in 2011; Exit dist. added from TENDL
n-013_Al_026m1	ENDF/B-VIII.0	2023	BNL	2017			BNL	2017			TENDL+EMPIRE
n-013_Al_027	ENDF/B-VI	2023	ORNL	2023			LANL	1994	LANL	1997	EGAF primary gammas; IRDFF-II mod.; Exit dist. from KAERI/LANL
n-014_Si_028	**ENDF/B-VIII.1; INDEN**	**2023**	**ORNL; IAEA**	**2018**			**ORNL**	**1996**	**LANL**	**2002**	**EGAF primary gammas; IRDFF-II mod.; Exit dist. added from TENDL; INDEN evaluation**
n-014_Si_029	**ENDF/B-VIII.1; INDEN**	**2023**	**ORNL; IAEA**	**2018**			**LANL**	**2002**	**LANL**	**2002**	**INDEN evaluation; IRDFF-II mod.; Exit dist. from KAERI/LANL**
n-014_Si_030	**ENDF/B-VIII.1; INDEN**	**2023**	**ORNL; IAEA**	**2018**			**LANL**	**2002**	**LANL**	**2002**	**INDEN evaluation; Exit dist. from KAERI/LANL**
n-014_Si_031	ENDF/B-VIII.0	2024	BNL	2017			BNL	2017			TENDL+EMPIRE; Exit dist. from KAERI/LANL
n-014_Si_032	ENDF/B-VIII.0	2024	TENDL	2015			BNL	2017			TENDL+EMPIRE; Exit dist. from KAERI/LANL
n-015_P_031	ENDF/B-V	2023					LLNL	1977	LANL	1997	No RRR parameters given; IRDFF-II mod.; Exit dist. added from TENDL
n-016_S_032	JENDL-3.2	2024	JNDC	1987			JNDC	1994			IRDFF-II mod.; Exit dist. added from TENDL
n-016_S_033	JENDL-3.2	2024	JNDC	1987			JNDC	1994			Exit dist. added from TENDL
n-016_S_034	JENDL-3.2	2024	JNDC	1987			JNDC	1994			Exit dist. added from TENDL
n-016_S_035	ENDF/B-VIII.0	2023	TENDL	2015			BNL	2017			TENDL+EMPIRE
n-016_S_036	JENDL-3.2	2023					JNDC	1994			No RRR parameters given; Exit dist. added from TENDL
n-017_Cl_035	ENDF/B-VIII.0	2024	ORNL	2017			LANL	2000			EGAF primary gammas; Exit dist. from KAERI/LANL
n-017_Cl_036	ENDF/B-VIII.0	2024	TENDL	2015			BNL	2017			TENDL+EMPIRE; Exit dist. from KAERI/LANL
n-017_Cl_037	ENDF/B-VIII.0	2024	ORNL	2007			LANL	2016			EGAF primary gammas; Exit dist. from KAERI/LANL
n-018_Ar_036	JEF-2.2	2023	ECN	1982	ECN	1982	ECN	1982			Exit dist. added from TENDL
n-018_Ar_037	TENDL-2015	2023	TENDL	2015			TENDL	2015	TENDL	2015	TENDL+EMPIRE
n-018_Ar_038	JEF-2.2	2023	ECN	1982	ECN	1982	ECN	1982			Exit dist. added from TENDL
n-018_Ar_039	ENDF/B-VIII.0	2023	BNL	2017			BNL	2017			TENDL+EMPIRE
n-018_Ar_040	ENDF/B-VIII.0	2024	JNDC	1994			LANL	2011			
n-018_Ar_041	TENDL-2015	2023	TENDL	2015			TENDL	2015	TENDL	2015	TENDL+EMPIRE
n-019_K_039	JENDL-3.2	2024	ORNL	2007			JNDC	1994			Exit dist. from KAERI/LANL
n-019_K_040	JENDL-3.2	2024					JNDC	1994			No RRR parameters given; Exit dist. from KAERI/LANL
n-019_K_041	JENDL-3.2	2024	ORNL	2007			JNDC	1994			Exit dist. from KAERI/LANL
n-020_Ca_040	ENDF/B-VIII.0	2024	ORNL	2016			NRG	2004	NRG	2004	
n-020_Ca_041	ENDF/B-VIII.0	2023	BNL	2017			BNL	2017			TENDL+EMPIRE
n-020_Ca_042	JEFF-3.1	2024	JNDC	1987			NRG	2004	NRG	2004	
n-020_Ca_043	JEFF-3.1	2024	JNDC	1987			NRG	2004	NRG	2004	
n-020_Ca_044	JEFF-3.1	2024	JNDC	1987			NRG	2004	NRG	2004	
n-020_Ca_045	TENDL-2015	2024	TENDL	2015			TENDL	2015	TENDL	2015	TENDL+EMPIRE
n-020_Ca_046	JEFF-3.1	2024					NRG	2004	NRG	2004	No RRR parameters given
n-020_Ca_047	TENDL-2015	2024	TENDL	2015			TENDL	2015	TENDL	2015	TENDL+EMPIRE
n-020_Ca_048	JEFF-3.1	2024	JNDC	1987			NRG	2004	NRG	2004	
n-021_Sc_045	ENDF/B-VI	2023	BNL	1981			ANL; LLNL	1992			LANL corrections in 2000 and 2016; Exit dist. added from TENDL
n-022_Ti_046	ENDF/B-VII.1	2024	ORNL	2009			LANL	2008			IRDFF-II mod.; Exit dist. from KAERI/LANL
n-022_Ti_047	ENDF/B-VII.1	2024	ORNL	2009			LANL	2008			IRDFF-II mod.; Exit dist. from KAERI/LANL
n-022_Ti_048	ENDF/B-VII.1	2024	ORNL	2009			LANL	2008			IRDFF-II mod.; Exit dist. from KAERI/LANL
n-022_Ti_049	ENDF/B-VII.1	2024	ORNL	2009			LANL	2008			Exit dist. from KAERI/LANL
n-022_Ti_050	ENDF/B-VII.1	2024	ORNL	2009			LANL	2008			Exit dist. from KAERI/LANL
n-023_V_049	ENDF/B-VIII.0	2024	TENDL	2015			BNL	2017			TENDL+EMPIRE; Exit dist. from KAERI/LANL
n-023_V_050	JENDL-4.0	2024	JNDC	2010			JNDC	2010			Exit dist. from KAERI/LANL
n-023_V_051	**ENDF/B-VII.1**	**2024**	**JNDC**	**2010**	**ORNL**	**2023**	**LANL**	**2010**			**IRDFF-II mod.; Exit dist. from KAERI/LANL**
n-024_Cr_050	**ENDF/B-VIII.1; INDEN**	**2024**	**ORNL; IAEA; JSI**	**2020**			**BNL; ORNL; IAEA; JSI**	**2020**	**BNL; IAEA; JSI**	**2020**	**INDEN evaluation**

Continued on the next page

TABLE XLIX: (continued) Provenance for the neutrons sublibrary.

File name (.endf)	Source	Last updated	RRR		URR		Fast		HE		Comments
			Inst.	Year	Inst.	Year	Inst.	Year	Inst.	Year	
n-024_Cr_051	**ENDF/B-VIII.1; INDEN**	**2024**	**TENDL**	**2015**			**BNL; IAEA**	**2020**	**BNL; IAEA**	**2020**	**INDEN evaluation; Exit dist. from KAERI/LANL**
n-024_Cr_052	**ENDF/B-VIII.1; INDEN**	**2024**	**ORNL; IAEA; JSI**	**2020**			**BNL; ORNL; IAEA; JSI**	**2020**	**BNL; IAEA; JSI**	**2020**	**INDEN evaluation**
n-024_Cr_053	**ENDF/B-VIII.1; INDEN**	**2024**	**ORNL; IAEA; JSI**	**2020**			**BNL; ORNL; IAEA; JSI**	**2020**	**BNL; IAEA; JSI**	**2020**	**INDEN evaluation**
n-024_Cr_054	**ENDF/B-VIII.1; INDEN**	**2024**	**ORNL; IAEA; JSI**	**2020**			**BNL; ORNL; IAEA; JSI**	**2020**	**BNL; IAEA; JSI**	**2020**	**INDEN evaluation**
n-025_Mn_054	TENDL-2015	2023	TENDL	2015			TENDL	2015	TENDL	2015	TENDL+EMPIRE
n-025_Mn_055	**ENDF/B-VIII.1; INDEN**	**2023**	**IAEA; ORNL**	**2023**	**ORNL**	**2008**	**IAEA**	**2011**	**IAEA**	**2011**	**INDEN evaluations; Max energy 60 MeV; IRDFF-II mod.**
n-026_Fe_054	**ENDF/B-VIII.1; INDEN; CIELO 2017**	**2023**	**IAEA; BNL; IRSN**	**2023**			**BNL; IAEA**	**2017**	**BNL; IAEA**	**2017**	**INDEN evaluations; IRDFF-II mod.**
n-026_Fe_055	TENDL-2015	2023	TENDL	2015			TENDL	2015	TENDL	2015	TENDL+EMPIRE
n-026_Fe_056	ENDF/B-VIII.0; INDEN; CIELO 2017	2017	JAEA	2011			IAEA; BNL	2023	IAEA; BNL	2023	INDEN evaluation; Correct inelastic/elastic; Improved documentation.
n-026_Fe_057	**ENDF/B-VIII.0; INDEN; CIELO 2017**	**2023**	**IAEA; BNL**	**2023**			**BNL; IAEA**	**2017**	**BNL; IAEA**	**2017**	**INDEN evaluation**
n-026_Fe_058	ENDF/B-VIII.0; CIELO 2017	2024	IAEA	2005	IAEA	2005	BNL; IAEA	2017	BNL; IAEA	2017	
n-027_Co_058	ENDF/B-VIII.0; CIELO 2017	2024	BNL	2011	BNL	2011	BNL	2011			Exit dist. from KAERI/LANL
n-027_Co_058m1	JEF-2.2	2023	ECN	1982			ECN	1982			Evaluation year unknown but mods. In 1984 and 1985 and 1987
n-027_Co_059	ENDF/B-VIII.0	2024	ORNL	1992			LANL	2016			IRDFF-II mod.; Exit dist. from KAERI/LANL
n-027_Co_58m1	ENDF/B-VIII.1	2023									
n-028_Ni_058	ENDF/B-VIII.0	2023	ORNL	2009			LANL	2012	LANL	1997	COMMARA-2.0 covariances added in 2011; IRDFF-II mod.; Exit dist. from KAERI/LANL
n-028_Ni_059	ENDF/B-VIII.0	2024	JAEA	2009	JAEA	2009	LANL	2012	LANL	1997	JENDL-4.0 RRR and URR; Exit dist. from KAERI/LANL
n-028_Ni_060	ENDF/B-VIII.0	2023	ORNL	2009			LANL	2012	LANL	1997	COMMARA-2.0 covariances added in 2011; IRDFF-II mod.; Exit dist. from KAERI/LANL
n-028_Ni_061	ENDF/B-VIII.0	2024	JAERI	1992			LANL	2012	LANL	1997	JENDL-3.2 RRR; Exit dist. from KAERI/LANL
n-028_Ni_062	ENDF/B-VIII.0	2024	BNL; JSI	2011	BNL; JSI	2011	LANL	2012	LANL	1997	Resonance reevaluation year between 2009-2011; Exit dist. from KAERI/LANL
n-028_Ni_063	ENDF/B-VIII.0	2024	TENDL	2015			BNL	2017			TENDL+EMPIRE; Exit dist. from KAERI/LANL
n-028_Ni_064	ENDF/B-VIII.0	2024	JNDC	1987			LANL	2012	LANL	1997	RRR from JENDL-4.0 which is JENDL-2; Exit dist. from KAERI/LANL
n-029_Cu_063	**ENDF/B-VIII.1; INDEN**	**2023**	**ORNL; IAEA; JSI; CVR**	**2023**			**LANL; IAEA; JSI; CVR**	**2016**	**LANL; IAEA; JSI; CVR**	**1998**	**INDEN evaluation; IRDFF-II mod.; Exit dist. from KAERI/LANL**
n-029_Cu_064	ENDF/B-VIII.0	2024	BNL	2017			BNL	2017			TENDL+EMPIRE; Exit dist. from KAERI/LANL
n-029_Cu_065	**ENDF/B-VIII.1; INDEN**	**2023**	**ORNL; IAEA; JSI; CVR**	**2023**			**LANL; IAEA; JSI; CVR**	**2016**	**LANL; IAEA; JSI; CVR**	**1998**	**INDEN evaluation; IRDFF-II mod.; Exit dist. from KAERI/LANL**
n-030_Zn_064	JENDL-4.0	2023	JAEA	2009	JAEA	2009	JAEA	2009			IRDFF-II mod.; Exit dist. from KAERI/LANL
n-030_Zn_065	JENDL-4.0	2024			JAEA	2009	JAEA	2009			No RRR parameters given; only URR parameters; Exit dist. from KAERI/LANL
n-030_Zn_066	JENDL-4.0	2024	JAEA	2009	JAEA	2009	JAEA	2009			Exit dist. from KAERI/LANL
n-030_Zn_067	JENDL-4.0	2024	JAEA	2009	JAEA	2009	JAEA	2009			IRDFF-II mod.; Exit dist. from KAERI/LANL
n-030_Zn_068	JENDL-4.0	2024	JAEA	2009	JAEA	2009	JAEA	2009			IRDFF-II mod.; Exit dist. from KAERI/LANL
n-030_Zn_069	ENDF/B-VIII.0	2024	BNL	2017			BNL	2017			TENDL+EMPIRE; Exit dist. from KAERI/LANL
n-030_Zn_070	JENDL-4.0	2024	JAEA	2009	JAEA	2009	JAEA	2009			Exit dist. from KAERI/LANL

Continued on the next page

TABLE XLIX: (continued) Provenance for the neutrons sublibrary.

File name (.endf)	Source	Last updated	RRR		URR		Fast		HE		Comments
			Inst.	Year	Inst.	Year	Inst.	Year	Inst.	Year	
n-031_Ga_069	JENDL-3.3; WPEC/SG-23	2023	BNL	2006			JNDC	1994			Exit dist. added from TENDL
n-031_Ga_070	ENDF/B-VIII.0	2023	BNL	2017			BNL	2017			TENDL+EMPIRE
n-031_Ga_071	CENDL-3; WPEC/SG-23	2023	JNDC	1994			CNDC	2001			Exit dist. added from TENDL
n-032_Ge_070	ENDF/B-VII.0; WPEC/SG-23	2023	BNL	2004	BNL	2004	BNL; JAERI	2004			Exit dist. added from TENDL
n-032_Ge_071	ENDF/B-VIII.0	2023	TENDL	2015			BNL	2017			TENDL+EMPIRE
n-032_Ge_072	ENDF/B-VII.0; WPEC/SG-23	2023	BNL	2004	BNL	2004	BNL; JAERI	2004			Exit dist. added from TENDL
n-032_Ge_073	ENDF/B-VII.0; WPEC/SG-23	2023	BNL	2004	BNL	2004	BNL; JAERI	2004			Exit dist. added from TENDL
n-032_Ge_074	ENDF/B-VII.0; WPEC/SG-23	2023	BNL	2004	BNL	2004	BNL; JAERI	2004			Exit dist. added from TENDL
n-032_Ge_075	ENDF/B-VIII.0	2023	BNL	2017			BNL	2017			TENDL+EMPIRE
n-032_Ge_076	ENDF/B-VII.0; WPEC/SG-23	2023	BNL	2004	BNL	2004	BNL; JAERI	2004			Exit dist. added from TENDL
n-033_As_073	ENDF/B-VIII.0	2024	LANL	2010			LANL	2010			RRR is simple picket fence; Exit dist. from KAERI/LANL
n-033_As_074	ENDF/B-VIII.0	2023	BNL	2006	BNL	2006	LANL; LLNL; KAERI	2016			Exit dist. from KAERI/LANL
n-033_As_075	ENDF/B-VIII.0	2023	JNDC	1990	JNDC	1990	LANL	2010			IRDFF-II mod.
n-034_Se_074	JENDL-3; WPEC/SG-23	2023	JNDC	1990	JNDC	1990	JNDC	1990			Newer JENDL-4.0 (2009) evaluation available; Exit dist. added from TENDL
n-034_Se_075	TENDL-2015	2023	TENDL	2015			TENDL	2015	TENDL	2015	TENDL+EMPIRE
n-034_Se_076	JENDL-3; WPEC/SG-23	2023	JNDC	1990	JNDC	1990	JNDC	1990			Newer JENDL-4.0 (2009) evaluation available; Exit dist. added from TENDL
n-034_Se_077	JENDL-3; WPEC/SG-23	2023	JNDC	1990	JNDC	1990	JNDC	1990			Newer JENDL-4.0 (2009) evaluation available; Exit dist. added from TENDL
n-034_Se_078	JENDL-3; WPEC/SG-23	2023	JNDC	1990	JNDC	1990	JNDC	1990			Newer JENDL-4.0 (2009) evaluation available; Updates in the URR (RQW); Exit dist. added from TENDL
n-034_Se_079	JENDL-3; WPEC/SG-23	2023	JNDC	1990	JNDC	1990	JNDC	1990			Newer JENDL-4.0 (2009) evaluation available; Exit dist. added from TENDL
n-034_Se_080	JENDL-3; WPEC/SG-23	2023	JNDC	1990	JNDC	1990	JNDC	1990			Newer JENDL-4.0 (2009) evaluation available; Exit dist. added from TENDL
n-034_Se_081	ENDF/B-VIII.0	2023	BNL	2017			BNL	2017			TENDL+EMPIRE
n-034_Se_082	JENDL-3; WPEC/SG-23	2023	BNL	2006	BNL	1990	JNDC	1990			Newer JENDL-4.0 (2009) evaluation available; Exit dist. added from TENDL
n-035_Br_079	JENDL-3.2; WPEC/SG-23	2023	JNDC	1990	JNDC	1993	JNDC	1990			Newer JENDL-4.0 (2009) evaluation available; Exit dist. added from TENDL
n-035_Br_080	ENDF/B-VIII.0	2023	BNL	2017			BNL	2017			TENDL+EMPIRE
n-035_Br_081	JENDL-3.2; WPEC/SG-23	2023	BNL	2006	BNL	1993	JNDC	1990			Newer JENDL-4.0 (2009) evaluation available; Exit dist. added from TENDL
n-036_Kr_078	ENDF/B-VIII.0	2016	JAEA	2009	JAEA	2009	LANL	2016			Resonances from JENDL-4.0
n-036_Kr_079	ENDF/B-VIII.0	2023	BNL	2017			BNL	2017			TENDL+EMPIRE
n-036_Kr_080	JENDL-3; WPEC/SG-23	2023	JNDC	1990	JNDC	1990	JNDC	1990			Exit dist. added from TENDL
n-036_Kr_081	TENDL-2015	2023	TENDL	2015			TENDL	2015	TENDL	2015	TENDL+EMPIRE
n-036_Kr_082	JENDL-3; WPEC/SG-23	2023	BNL	2006	BNL	1990	JNDC	1990			Exit dist. added from TENDL
n-036_Kr_083	CENDL-3; WPEC/SG-23	2023	CNDC	2001	CNDC	2001	CNDC	2001			Exit dist. added from TENDL
n-036_Kr_084	**JENDL-4**	**2009**	**JAEA**	**2009**	**JAEA**	**2009**	**JAEA**	**2009**			**Updates in the URR (RQW); Exit dist. added from TENDL**
n-036_Kr_085	ENDF/B-VII.0; WPEC/SG-23	2024	BNL	2006	BNL	2006	BNL	2006			
n-036_Kr_086	**ENDF/B-VIII.1; WPEC/SG-23**	**2023**	**BNL**	**2006**			**BNL**	**2021**			
n-037_Rb_085	JENDL-3; WPEC/SG-23	2023	BNL	2006	BNL	1990	JNDC	1990			Updates in the URR (RQW); Exit dist. added from TENDL
n-037_Rb_086	ENDF/B-VII.0; WPEC/SG-23	2024	BNL	2006	BNL	2006	BNL	2006			
n-037_Rb_087	JENDL-3; WPEC/SG-23	2023	JNDC	1990	JNDC	1990	JNDC	1990			Exit dist. added from TENDL
n-038_Sr_084	ENDF/B-VII.0; WPEC/SG-23	2024	BNL	2006	BNL	2006	BNL	2006			

Continued on the next page

TABLE XLIX: (continued) Provenance for the neutrons sublibrary.

File name (.endf)	Source	Last updated	RRR		URR		Fast		HE		Comments
			Inst.	Year	Inst.	Year	Inst.	Year	Inst.	Year	
n-038_Sr_085	ENDF/B-VIII.0	2023	BNL	2017			BNL	2017			TENDL+EMPIRE
n-038_Sr_086	JENDL-3; WPEC/SG-23	2023	BNL	2006	JNDC	1990	JNDC	1990			Exit dist. added from TENDL
n-038_Sr_087	JENDL-3; WPEC/SG-23	2023	JNDC	1990	JNDC	1990	JNDC	1990			Exit dist. added from TENDL
n-038_Sr_088	CENDL-3; WPEC/SG-23	2024	ORNL	2023	ORNL	2023	CNDC	2001			Exit dist. added from TENDL
n-038_Sr_089	CENDL-3; WPEC/SG-23	2023			JNDC	1990	CNDC	2001			No RRR parameters given; only URR parameters; Exit dist. added from TENDL
n-038_Sr_090	JENDL-3.2; WPEC/SG-23	2023			JNDC	1990	JNDC	1993			No RRR parameters given; only URR parameters; Exit dist. added from TENDL
n-039_Y_089	ENDF/B-VII.1	2023	BNL	2006			LANL	2009			IRDFF-II mod.
n-039_Y_090	ENDF/B-VII.0; WPEC/SG-23	2024	BNL	2006	BNL	2006	BNL	2006			
n-039_Y_091	JENDL-3; WPEC/SG-23	2023			JNDC	1990	JNDC	1990			No RRR parameters given; only URR parameters; Exit dist. added from TENDL
n-040_Zr_090	ENDF/B-VII.1	2023	BNL	2011	BNL	2013	BNL; KAERI	2011			COMMARA-2.0 covariances added in 2011; IRDFF-II mod.; Exit dist. from KAERI/LANL
n-040_Zr_091	ENDF/B-VII.1	2023	BNL	2013	BNL	2011	BNL; KAERI	2011			COMMARA-2.0 covariances added in 2011; Exit dist. from KAERI/LANL
n-040_Zr_092	ENDF/B-VII.1	2024	BNL	2013	BNL	2011	BNL; KAERI	2011			COMMARA-2.0 covariances added in 2011; Exit dist. from KAERI/LANL
n-040_Zr_093	ENDF/B-VII.1	2024	BNL	2011	BNL	2011	BNL; KAERI	2011			COMMARA-2.0 covariances added in 2011; Exit dist. from KAERI/LANL
n-040_Zr_094	ENDF/B-VII.1	2024	BNL	2011	BNL	2011	BNL; KAERI	2011			COMMARA-2.0 covariances added in 2011; RRR revised 2013; RRR and URR matching fixed 2016; Exit dist. from KAERI/LANL
n-040_Zr_095	ENDF/B-VII.1	2023	BNL	2011	BNL	2011	BNL; KAERI	2011			COMMARA-2.0 covariances added in 2011; Exit dist. from KAERI/LANL
n-040_Zr_096	ENDF/B-VII.1	2024	BNL	2011	BNL	2011	BNL; KAERI	2016			COMMARA-2.0 covariances added in 2011; Exit dist. from KAERI/LANL
n-041_Nb_093	ENDF/B-VI	2023	JAEA	2009	JAEA	2009	LANL	1997	LANL	1997	RRR and URR from JENDL-4.0; Exit dist. added from TENDL
n-041_Nb_094	JENDL-3; WPEC/SG-23	2023	JNDC	1990	JNDC	1990	JNDC	1990			Exit dist. added from TENDL
n-041_Nb_095	JENDL-3; WPEC/SG-23	2023			JNDC	1990	JNDC	1990			No RRR parameters given; only URR parameters; COMMARA-2.0 covariances added in 2011; Exit dist. added from TENDL
n-042_Mo_092	JENDL-3.2; WPEC/SG-23	2023	JNDC	1993	JNDC	1993	JNDC	1993			IRDFF-II mod.; Exit dist. added from TENDL
n-042_Mo_093	TENDL-2015	2023	TENDL	2015			TENDL	2015	TENDL	2015	TENDL+EMPIRE
n-042_Mo_094	JENDL-3.2; WPEC/SG-23	2023	BNL	2006	BNL	1993	JNDC	1993			COMMARA-2.0 covariances added in 2011; Exit dist. added from TENDL
n-042_Mo_095	ENDF/B-VII.1	2024	BNL	2010	BNL	2010	BNL; KAERI	2010			COMMARA-2.0 covariances added in 2011; Exit dist. added from TENDL
n-042_Mo_096	JENDL-3.2; WPEC/SG-23	2023	JNDC	1993	JNDC	1993	JNDC	1993			COMMARA-2.0 covariances added in 2011; Exit dist. added from TENDL
n-042_Mo_097	JENDL-3.3; WPEC/SG-23	2023	BNL	2006	JNDC	2001	JNDC	2001			COMMARA-2.0 covariances added in 2011; Updates in the URR (RQW); Exit dist. added from TENDL
n-042_Mo_098	JENDL-3.3; WPEC/SG-23	2023	JNDC	1993	JNDC	1993	JNDC	2001			COMMARA-2.0 covariances added in 2011; Exit dist. added from TENDL
n-042_Mo_099	JENDL-3; WPEC/SG-23	2023			JNDC	1990	JNDC	1990			No RRR parameters given; only URR parameters; Exit dist. added from TENDL
n-042_Mo_100	CENDL-3; WPEC/SG-23	2024	JNDC	1989	JNDC	1989	CNDC	2001			RRR & URR from JENDL-3; COMMARA-2.0 covariances added in 2011; Exit dist. added from TENDL
n-043_Tc_098	TENDL-2015	2023	TENDL	2015			TENDL	2015	TENDL	2015	TENDL+EMPIRE
n-043_Tc_099	ENDF/B-VII.1	2023	BNL	2010	BNL	2010	BNL	2006			Covariances from BNL-LANL collaboration 2006; Updates in the URR (RQW)

Continued on the next page

TABLE XLIX: (continued) Provenance for the neutrons sublibrary.

File name (.endf)	Source	Last updated	RRR		URR		Fast		HE		Comments
			Inst.	Year	Inst.	Year	Inst.	Year	Inst.	Year	
n-044_Ru_096	JENDL-3; WPEC/SG-23	2023			JNDC	1990	JNDC	1990			No RRR parameters given; only URR parameters; Exit dist. added from TENDL
n-044_Ru_097	TENDL-2015	2023	TENDL	2015			TENDL	2015	TENDL	2015	TENDL+EMPIRE
n-044_Ru_098	JENDL-3; WPEC/SG-23	2023			JNDC	1990	JNDC	1990			No RRR parameters given; only URR parameters; Exit dist. added from TENDL
n-044_Ru_099	JENDL-3.2; WPEC/SG-23	2023	JNDC	2001	JNDC	1993	JNDC	1993			Exit dist. added from TENDL
n-044_Ru_100	JENDL-3; WPEC/SG-23	2023	BNL	2006	JNDC	1990	JNDC	1990			Exit dist. added from TENDL
n-044_Ru_101	ENDF/B-VII.0; WPEC/SG-23	2024	BNL; KAERI	1999	BNL; KAERI	1999	BNL; KAERI	2006			COMMARA-2.0 covariances added in 2011
n-044_Ru_102	CENDL-3; WPEC/SG-23	2023	BNL	2006	CNDC	2001	CNDC	2001			COMMARA-2.0 covariances added in 2011; Exit dist. added from TENDL
n-044_Ru_103	CENDL-3; WPEC/SG-23	2023	BNL	2006	CNDC	2001	CNDC	2001			COMMARA-2.0 covariances added in 2011; Exit dist. added from TENDL
n-044_Ru_104	CENDL-3; WPEC/SG-23	2023	JNDC	1990	JNDC	2001	CNDC	2001			RRR & URR from JENDL-3; COMMARA-2.0 covariances added in 2011; Exit dist. added from TENDL
n-044_Ru_105	CENDL-3; WPEC/SG-23	2023					CNDC	2001			No RRR parameters given; Exit dist. added from TENDL
n-044_Ru_106	JENDL-3; WPEC/SG-23	2023			JNDC	1990	JNDC	1990			No RRR parameters given; only URR parameters; COMMARA-2.0 covariances added in 2011; Exit dist. added from TENDL
n-045_Rh_103	**ENDF/B-VIII.1**	**2023**	**IRSN; NNL**	**2021**	**IRSN; NNL**	**2021**	**BNL; KAERI**	**2006**			**COMMARA-2.0 covariances added in 2011; IRDFF-II mod.; Exit dist. added from TENDL**
n-045_Rh_104	ENDF/B-VIII.0	2023	BNL	2017			BNL	2017			TENDL+EMPIRE
n-045_Rh_105	ENDF/B-VIII.0	2023	JAEA	2016	JNDC	1990	JNDC	1990			RRR now MLBW; Exit dist. added from TENDL
n-046_Pd_102	ENDF/B-VI; WPEC/SG-23	2023	BNL	2006			LANL	1996			Updates in the URR (RQW)
n-046_Pd_103	ENDF/B-VIII.0	2023	TENDL	2015			BNL	2017			TENDL+EMPIRE
n-046_Pd_104	ENDF/B-VI; WPEC/SG-23	2024	BNL	2006			LANL	1996			
n-046_Pd_105	ENDF/B-VII.0; WPEC/SG-23	2024	BNL; KAERI	1999	BNL; KAERI	1999	BNL; KAERI	2006			COMMARA-2.0 covariances added in 2011
n-046_Pd_106	ENDF/B-VI; WPEC/SG-23	2024	BNL	2006			LANL	1996			COMMARA-2.0 covariances added in 2011
n-046_Pd_107	JENDL-3.2; WPEC/SG-23	2023	JNDC	1993	JNDC	1993	JNDC	1993			COMMARA-2.0 covariances added in 2011; Exit dist. added from TENDL
n-046_Pd_108	ENDF/B-VI; WPEC/SG-23	2024	BNL	2006			LANL	1996			COMMARA-2.0 covariances added in 2011
n-046_Pd_109	ENDF/B-VIII.0	2023	BNL	2017			BNL	2017			TENDL+EMPIRE
n-046_Pd_110	ENDF/B-VI; WPEC/SG-23	2024	BNL	2006			LANL	1996			
n-047_Ag_107	JENDL-3.2; WPEC/SG-23	2023	BNL	2006	JNDC	1993	JNDC	1993			Exit dist. from KAERI/LANL
n-047_Ag_108	ENDF/B-VIII.0	2023	BNL	2017			BNL	2017			TENDL+EMPIRE
n-047_Ag_109	ENDF/B-VII.1; WPEC/SG-23	2023	BNL	2010	BNL	2010	BNL; KAERI	2006			Low-fidelity covariances added in 2011; Updates in the URR (RQW); Exit dist. from KAERI/LANL
n-047_Ag_110m1	JENDL-3.3; WPEC/SG-23	2023	BNL	2006	JNDC	1990	JNDC	1990			Exit dist. added from TENDL
n-047_Ag_111	ENDF/B-VII.0; WPEC/SG-23	2024	BNL	2006	BNL	2006	BNL	2006			
n-047_Ag_112	ENDF/B-VIII.0	2023	BNL	2017			BNL	2017			TENDL+EMPIRE
n-047_Ag_113	ENDF/B-VIII.0	2023	BNL	2017			BNL	2017			TENDL+EMPIRE
n-047_Ag_114	ENDF/B-VIII.0	2023	BNL	2017			BNL	2017			TENDL+EMPIRE
n-047_Ag_115	ENDF/B-VIII.0	2023	BNL	2017			BNL	2017			TENDL+EMPIRE
n-047_Ag_116	ENDF/B-VIII.0	2023	BNL	2017			BNL	2017			TENDL+EMPIRE
n-047_Ag_117	ENDF/B-VIII.0	2023	BNL	2017			BNL	2017			TENDL+EMPIRE
n-047_Ag_118m1	ENDF/B-VIII.0	2023	BNL	2017			BNL	2017			TENDL+EMPIRE
n-048_Cd_106	JENDL-3.3; WPEC/SG-23	2023	IRRM	2010	JNDC	2001	JNDC	2001			Exit dist. added from TENDL; LANL scatt. rad. fix
n-048_Cd_107	ENDF/B-VIII.0	2023	BNL	2017			BNL	2017			TENDL+EMPIRE
n-048_Cd_108	ENDF/B-VI; WPEC/SG-23	2023	IRRM	2010	ORNL	1991	ANL	1994			Exit dist. added from TENDL; LANL scatt. rad. fix
n-048_Cd_109	TENDL-2015	2023	TENDL	2015			TENDL	2015	TENDL	2015	TENDL+EMPIRE
n-048_Cd_110	ENDF/B-VI; WPEC/SG-23	2023	IRRM	2010	ORNL	1991	ANL	1994			Exit dist. added from TENDL; LANL scatt. rad. fix
n-048_Cd_111	JENDL-3.3; WPEC/SG-23	2023	IRRM	2010	JNDC	1994	JNDC	1994			Exit dist. added from TENDL; LANL scatt. rad. fix

Continued on the next page

TABLE XLIX: (continued) Provenance for the neutrons sublibrary.

File name (.endf)	Source	Last updated	RRR		URR		Fast		HE		Comments
			Inst.	Year	Inst.	Year	Inst.	Year	Inst.	Year	
n-048_Cd_112	ENDF/B-VI; WPEC/SG-23	2023	IRRM	2010	ORNL	1991	ANL	1994			Exit dist. added from TENDL; LANL scatt. rad. fix
n-048_Cd_113	CENDL-3	2023	BNL	2010	BNL	2010	CNDC	2001			Exit dist. added from TENDL
n-048_Cd_114	ENDF/B-VI; WPEC/SG-23	2023	IRRM	2010	ORNL	1991	ANL	1994			Exit dist. added from TENDL; LANL scatt. rad. fix
n-048_Cd_115m1	ENDF/B-VII.0; WPEC/SG-23	2024	BNL	2006	BNL	2006	BNL	2006			
n-048_Cd_116	ENDF/B-VI; WPEC/SG-23	2023	IRRM	2010	ORNL	1991	ANL	1994			Exit dist. added from TENDL; LANL scatt. rad. fix
n-049_In_113	JENDL-3; WPEC/SG-23	2023	BNL	2006	JNDC	1990	JNDC	1990			IRDFF-II mod.; Updates in the URR (RQW); Exit dist. added from TENDL
n-049_In_114	ENDF/B-VIII.0	2023	BNL	2017			BNL	2017			TENDL+EMPIRE
n-049_In_115	JENDL-3.2; WPEC/SG-23	2023	BNL	2006	JNDC	1982	JNDC	1993			IRDFF-II mod.; Updates in the URR (RQW); Exit dist. added from TENDL
n-050_Sn_112	JENDL-3; WPEC/SG-23	2023	BNL	2006	JNDC	1990	JNDC	1990			Exit dist. added from TENDL
n-050_Sn_113	ENDF/B-VII.0; WPEC/SG-23	2006	BNL	2006	BNL	2006	BNL	2006			
n-050_Sn_114	JENDL-3; WPEC/SG-23	2023	BNL	2006	JNDC	1990	JNDC	1990			Exit dist. added from TENDL
n-050_Sn_115	JENDL-3; WPEC/SG-23	2023	BNL	2006	JNDC	1990	JNDC	1990			Updates in the URR (RQW); Exit dist. added from TENDL
n-050_Sn_116	JENDL-3; WPEC/SG-23	2023	BNL	2006	JNDC	1990	JNDC	1990			Exit dist. added from TENDL
n-050_Sn_117	JENDL-3.2; WPEC/SG-23	2023	BNL	2006	JNDC	1993	JNDC	1993			Exit dist. added from TENDL
n-050_Sn_118	JENDL-3; WPEC/SG-23	2023	BNL	2006	JNDC	1990	JNDC	1990			Exit dist. added from TENDL
n-050_Sn_119	JENDL-3; WPEC/SG-23	2023	BNL	2006	JNDC	1990	JNDC	1990			Updates in the URR (RQW); Exit dist. added from TENDL
n-050_Sn_120	JENDL-3; WPEC/SG-23	2024	BNL	2006	JNDC	1990	LANL	2015			
n-050_Sn_121m1	ENDF/B-VIII.0	2023	BNL	2017			BNL	2017			TENDL+EMPIRE
n-050_Sn_122	JENDL-3; WPEC/SG-23	2023	BNL	2006			JNDC	1990			Exit dist. added from TENDL
n-050_Sn_123	JENDL-3; WPEC/SG-23	2023			JNDC	1990	JNDC	1990			No RRR parameters given; only URR parameters; Exit dist. added from TENDL
n-050_Sn_124	JENDL-3.2; WPEC/SG-23	2023	BNL	2006			JNDC	1993			Exit dist. added from TENDL
n-050_Sn_125	ENDF/B-VII.0; WPEC/SG-23	2024	BNL	2006	BNL	2006	BNL	2006			
n-050_Sn_126	JENDL-3; WPEC/SG-23	2023			JNDC	1990	JNDC	1990			No RRR parameters given; only URR parameters; Exit dist. added from TENDL
n-051_Sb_121	CENDL-3; WPEC/SG-23	2023	BNL	2006	JNDC	1994	CNDC	2001			CENDL eval year uncertain; Exit dist. added from TENDL
n-051_Sb_122	ENDF/B-VIII.0	2023	BNL	2017			BNL	2017			TENDL+EMPIRE
n-051_Sb_123	CENDL-3; WPEC/SG-23	2023	BNL	2006	JNDC	1994	CNDC	2001			CENDL eval year uncertain; Exit dist. added from TENDL
n-051_Sb_124	JENDL-3; WPEC/SG-23	2023			JNDC	1990	JNDC	1990			No RRR parameters given; only URR parameters; xit dist. added from TENDL
n-051_Sb_125	JENDL-3; WPEC/SG-23	2023			JNDC	1990	JNDC	1990			Exit dist. added from TENDL
n-051_Sb_126	ENDF/B-VII.0; WPEC/SG-23	2024	BNL	2006	BNL	2006	BNL	2006			
n-052_Te_120	JENDL-3; WPEC/SG-23	2023			JNDC	1990	JNDC	1990			No RRR parameters given; only URR parameters; Exit dist. added from TENDL
n-052_Te_121	ENDF/B-VIII.0	2023	BNL	2017			BNL	2017			TENDL+EMPIRE
n-052_Te_121m1	ENDF/B-VIII.0	2023	BNL	2017			BNL	2017			TENDL+EMPIRE
n-052_Te_122	JENDL-3.2; WPEC/SG-23	2023	BNL	2006	JNDC	1993	JNDC	1993			Updates in the URR (RQW); Exit dist. added from TENDL
n-052_Te_123	JENDL-3.2; WPEC/SG-23	2023	BNL	2006	JNDC	1993	JNDC	1993			Exit dist. added from TENDL
n-052_Te_124	JENDL-3.2; WPEC/SG-23	2023	BNL	2006	JNDC	1993	JNDC	1993			Updates in the URR (RQW); Exit dist. added from TENDL
n-052_Te_125	JENDL-3; WPEC/SG-23	2023	BNL	2006	JNDC	1990	JNDC	1990			Exit dist. added from TENDL
n-052_Te_126	JENDL-3.2; WPEC/SG-23	2023	BNL	2006	JNDC	1993	JNDC	1993			Exit dist. added from TENDL
n-052_Te_127m1	JENDL-3; WPEC/SG-23	2023			JNDC	1990	JNDC	1990			No RRR parameters given; only URR parameters; Exit dist. added from TENDL
n-052_Te_128	JENDL-3; WPEC/SG-23	2023	BNL	2006	JNDC	1990	JNDC	1990			Exit dist. added from TENDL

Continued on the next page

TABLE XLIX: (continued) Provenance for the neutrons sublibrary.

File name (.endf)	Source	Last updated	RRR		URR		Fast		HE		Comments
			Inst.	Year	Inst.	Year	Inst.	Year	Inst.	Year	
n-052_Te_129m1	JENDL-3; WPEC/SG-23	2023			JNDC	1990	JNDC	1990			No RRR parameters given; only URR parameters; Exit dist. added from TENDL
n-052_Te_130	CENDL-3; WPEC/SG-23	2023	BNL	2006	JNDC	1994	CNDC	2001			Exit dist. added from TENDL
n-052_Te_131	ENDF/B-VIII.0	2023	BNL	2017			BNL	2017			TENDL+EMPIRE
n-052_Te_131m1	ENDF/B-VIII.0	2023	BNL	2017			BNL	2017			TENDL+EMPIRE
n-052_Te_132	ENDF/B-VIII.0; WPEC/SG-23	2024	BNL	2006	BNL	2006	LANL	2016			
n-053_I_127	ENDF/B-VI; WPEC/SG-23	2016	BNL	2023			LANL	2005			COMMARA-2.0 covariances added in 2011; IRDFF-II mod.; Updates in the URR (RQW)
n-053_I_128	ENDF/B-VIII.0	2023	BNL	2017			BNL	2017			TENDL+EMPIRE
n-053_I_129	JENDL-3; WPEC/SG-23	2023	BNL	2006	JNDC	1990	JNDC	1990			COMMARA-2.0 covariances added in 2011; Exit dist. added from TENDL
n-053_I_130	ENDF/B-VII.0; WPEC/SG-23	2024	BNL	2006	BNL	2006	BNL	2006			
n-053_I_131	JENDL-3; WPEC/SG-23	2024			JNDC	1990	JNDC	1990			No RRR parameters given; only URR parameters; Exit dist. added from TENDL
n-053_I_132	ENDF/B-VIII.0	2023	BNL	2017			BNL	2017			TENDL+EMPIRE
n-053_I_132m1	ENDF/B-VIII.0	2023	BNL	2017			BNL	2017			TENDL+EMPIRE
n-053_I_133	ENDF/B-VIII.0	2023	BNL	2017			BNL	2017			TENDL+EMPIRE
n-053_I_134	ENDF/B-VIII.0	2023	BNL	2017			BNL	2017			TENDL+EMPIRE
n-053_I_135	CENDL-3; WPEC/SG-23	2023					CNDC	2001			No RRR parameters given; Exit dist. added from TENDL
n-054_Xe_123	ENDF/B-VII.1	2024					LLNL	2011			No RRR parameters given
n-054_Xe_124	ENDF/B-VIII.0	2024	JAEA	2009	JAEA	2009	LANL	2016			
n-054_Xe_125	ENDF/B-VIII.0	2023	BNL	2017			BNL	2017			TENDL+EMPIRE
n-054_Xe_126	JENDL-3; WPEC/SG-23	2023	BNL	2006	JNDC	1990	JNDC	1990			Exit dist. added from TENDL
n-054_Xe_127	ENDF/B-VIII.0	2023	BNL	2017			BNL	2017			TENDL+EMPIRE
n-054_Xe_128	JENDL-3; WPEC/SG-23	2023	BNL	2006	JNDC	1990	JNDC	1990			Exit dist. added from TENDL
n-054_Xe_129	JENDL-3; WPEC/SG-23	2023	BNL	2006	JNDC	1990	JNDC	1990			Exit dist. added from TENDL
n-054_Xe_130	ENDF/B-V; WPEC/SG-23	2023	BNL	2006			BNL	1978			Exit dist. added from TENDL
n-054_Xe_131	ENDF/B-VII.0; WPEC/SG-23	2024	BNL; KAERI	1999	BNL; KAERI	1999	BNL; KAERI	2006			COMMARA-2.0 covariances added in 2011
n-054_Xe_132	CENDL-3; WPEC/SG-23	2023	BNL	2006	JNDC	1990	CNDC	2001			COMMARA-2.0 covariances added in 2011; Exit dist. added from TENDL
n-054_Xe_133	JENDL-3; WPEC/SG-23	2024			JNDC	1990	JNDC	1990			No RRR parameters given; only URR parameters; Exit dist. added from TENDL
n-054_Xe_134	CENDL-3; WPEC/SG-23	2023	BNL	2006	JNDC	1990	CNDC	2001			COMMARA-2.0 covariances added in 2011; Exit dist. added from TENDL
n-054_Xe_135	JENDL-3; WPEC/SG-23	2023	JNDC	1990	JNDC	1990	JNDC	1990			Convert RRR from SLBW to MLBW in 2016; Exit dist. added from TENDL
n-054_Xe_136	CENDL-3; WPEC/SG-23	2023	BNL	2006			CNDC	2000			Exit dist. added from TENDL
n-055_Cs_133	ENDF/B-VII.1	2023	BNL	2010	BNL	2010	BNL	2006			COMMARA-2.0 covariances added in 2011; Updates in the URR (RQW)
n-055_Cs_134	**JENDL-4**	**2006**	**JAEA**	**2009**	**JAEA**	**2009**	**JAEA**	**2009**			**Updates in the URR (RQW); Exit dist. added from TENDL**
n-055_Cs_135	JENDL-3; WPEC/SG-23	2023	BNL	2006	JNDC	1990	JNDC	1990			COMMARA-2.0 covariances added in 2011; Exit dist. added from TENDL
n-055_Cs_136	JENDL-3; WPEC/SG-23	2023			JNDC	1990	JNDC	1990			No RRR parameters given; only URR parameters; Exit dist. added from TENDL
n-055_Cs_137	JENDL-3; WPEC/SG-23	2023			JNDC	1990	JNDC	1990			No RRR parameters given; only URR parameters; Exit dist. added from TENDL
n-056_Ba_130	JENDL-3; WPEC/SG-23	2023	BNL	2006	JNDC	1990	JNDC	1990			Updates in the URR (RQW); Exit dist. added from TENDL
n-056_Ba_131	ENDF/B-VIII.0	2023	BNL	2017			BNL	2017			TENDL+EMPIRE
n-056_Ba_132	JENDL-3; WPEC/SG-23	2023	BNL	2006	JNDC	1990	JNDC	1990			Exit dist. added from TENDL
n-056_Ba_133	ENDF/B-VII.0; WPEC/SG-23	2024	BNL	2006	BNL	2006	BNL	2006			
n-056_Ba_134	JENDL-3; WPEC/SG-23	2006	BNL	2006	JNDC	1990	JNDC	1990			Updates in the URR (RQW); Exit dist. added from TENDL
n-056_Ba_135	JENDL-3; WPEC/SG-23	2006	BNL	2006	JNDC	1990	JNDC	1990			Exit dist. added from TENDL

Continued on the next page

TABLE XLIX: (continued) Provenance for the neutrons sublibrary.

File name (.endf)	Source	Last updated	RRR		URR		Fast		HE		Comments
			Inst.	Year	Inst.	Year	Inst.	Year	Inst.	Year	
n-056_Ba_136	JENDL-3; WPEC/SG-23	2023	BNL	2006	JNDC	1990	JNDC	1990			Exit dist. added from TENDL
n-056_Ba_137	JENDL-3; WPEC/SG-23	2023	BNL	2006	JNDC	1990	JNDC	1990			Updates in the URR (RQW); Exit dist. added from TENDL
n-056_Ba_138	CENDL-3; WPEC/SG-23	2023	BNL	2006			CNDC	2001			Exit dist. added from TENDL
n-056_Ba_139	ENDF/B-VIII.0	2023	BNL	2017			BNL	2017			TENDL+EMPIRE
n-056_Ba_140	JEF-2; WPEC/SG-23	2023	ENEA	1977	ENEA	1977	ENEA	1989			RRR randomly generated; Exit dist. added from TENDL
n-057_La_138	JENDL-3; WPEC/SG-23	2023	JNDC	1990	JNDC	1990	JNDC	1990			Updates in the URR (RQW); Exit dist. added from TENDL
n-057_La_139	**FENDL-3.2**	**2023**	**BNL**	**2006**	**JNDC**	**1993**	**TENDL**	**2014**			
n-057_La_140	ENDF/B-VII.0; WPEC/SG-23	2024	BNL	2006	BNL	2006	BNL	2006			
n-058_Ce_136	ENDF/B-VII.0; WPEC/SG-23	2024	BNL	2006	BNL	2006	BNL	2006			
n-058_Ce_137	ENDF/B-VIII.0	2023	BNL	2017			BNL	2017			TENDL+EMPIRE
n-058_Ce_137m1	ENDF/B-VIII.0	2023	BNL	2017			BNL	2017			TENDL+EMPIRE
n-058_Ce_138	ENDF/B-VII.0; WPEC/SG-23	2024	BNL	2006	BNL	2006	BNL	2006			
n-058_Ce_139	ENDF/B-VII.0	2024	BNL	2006	BNL	2006	BNL	2006			
n-058_Ce_140	JENDL-3; WPEC/SG-23	2023	ORNL	2021	ORNL	2021	JNDC	1990			Exit dist. added from TENDL
n-058_Ce_141	CENDL-3; WPEC/SG-23	2023	BNL	2006	JNDC	1990	CNDC	2000			Exit dist. added from TENDL
n-058_Ce_142	**JENDL-3.2; WPEC/SG-23**	**2023**	**ORNL**	**2021**	**ORNL**	**2021**	**JNDC**	**1993**			**Exit dist. added from TENDL**
n-058_Ce_143	ENDF/B-VII.0; WPEC/SG-23	2024	BNL	2006	BNL	2006	BNL	2006			
n-058_Ce_144	JENDL-3; WPEC/SG-23	2023			JNDC	1990	JNDC	1990			No RRR parameters given; only URR parameters; Exit dist. added from TENDL
n-059_Pr_141	ENDF/B-VII.0; WPEC/SG-23	2023	BNL	2006	BNL	2006	BNL; KAERI	2006			COMMARA-2.0 covariances added in 2011; IRDFF-II mod.
n-059_Pr_142	ENDF/B-VII.0; WPEC/SG-23	2024	BNL	2006	BNL	2006	BNL	2006			
n-059_Pr_143	JENDL-3; WPEC/SG-23	2023	BNL	2006	JNDC	1990	JNDC	1990			Exit dist. added from TENDL
n-060_Nd_142	ENDF/B-VII.0; WPEC/SG-23	2024	BNL	2006	BNL	2006	BNL; KAERI	2006			
n-060_Nd_143	ENDF/B-VII.0; WPEC/SG-23	2023	BNL; KAERI	1999	BNL; KAERI	1999	BNL; KAERI	2006			COMMARA-2.0 covariances added in 2011; Exit dist. added from TENDL
n-060_Nd_144	ENDF/B-VII.0; WPEC/SG-23	2024	BNL	2006	BNL	2006	BNL; KAERI	2006			
n-060_Nd_145	ENDF/B-VII.0	2023	BNL	2010	BNL	2010	BNL; KAERI	2006			COMMARA-2.0 covariances added in 2011; Exit dist. added from TENDL
n-060_Nd_146	ENDF/B-VII.0; WPEC/SG-23	2024	BNL	2006	BNL	2006	BNL; KAERI	2006			COMMARA-2.0 covariances added in 2011
n-060_Nd_147	ENDF/B-VII.0; WPEC/SG-23	2024	BNL	2006	BNL	2006	BNL; KAERI	2006			
n-060_Nd_148	ENDF/B-VII.0; WPEC/SG-23	2023	BNL	2006	BNL	2006	BNL; KAERI	2006			COMMARA-2.0 covariances added in 2011; Updates in the URR (RQW)
n-060_Nd_149	ENDF/B-VIII.0	2023	BNL	2017			BNL	2017			TENDL+EMPIRE
n-060_Nd_150	ENDF/B-VII.0; WPEC/SG-23	2023	BNL	2006	BNL	2006	BNL; KAERI	2006			Updates in the URR (RQW)
n-061_Pm_143	TENDL-2015	2023	TENDL	2015			TENDL	2015	TENDL	2015	TENDL+EMPIRE
n-061_Pm_144	TENDL-2015	2023	TENDL	2015			TENDL	2015	TENDL	2015	TENDL+EMPIRE
n-061_Pm_145	TENDL-2015	2023	TENDL	2015			TENDL	2015	TENDL	2015	TENDL+EMPIRE
n-061_Pm_146	ENDF/B-VIII.0	2023	TENDL	2015			BNL	2017			TENDL+EMPIRE
n-061_Pm_147	JENDL-3; WPEC/SG-23	2023	JNDC	1990	JNDC	1990	JNDC	1990			COMMARA-2.0 covariances added in 2011; Updates in the URR (RQW); Exit dist. added from TENDL
n-061_Pm_148	JENDL-3; WPEC/SG-23	2023			JNDC	1990	JNDC	1990			No RRR parameters given; only URR parameters; Exit dist. added from TENDL
n-061_Pm_148m1	CENDL-3; WPEC/SG-23	2023	BNL	1973			CNDC	2001			Lone resonance converted from SLBW to MLBW; Exit dist. added from TENDL
n-061_Pm_149	JENDL-3; WPEC/SG-23	2006			JNDC	1990	JNDC	1990			No RRR parameters given; only URR parameters; Exit dist. added from TENDL
n-061_Pm_150	ENDF/B-VIII.0	2023	BNL	2017			BNL	2017			TENDL+EMPIRE
n-061_Pm_151	ENDF/B-VII.0; WPEC/SG-23	2024	BNL	2006	BNL	2006	BNL	2006			

Continued on the next page

TABLE XLIX: (continued) Provenance for the neutrons sublibrary.

File name (.endf)	Source	Last updated	RRR		URR		Fast		HE		Comments
			Inst.	Year	Inst.	Year	Inst.	Year	Inst.	Year	
n-062_Sm_144	ENDF/B-VII.0; WPEC/SG-23	2024	BNL	2006	BNL	2006	BNL; KAERI	2006			Fix URR grid in 2016
n-062_Sm_145	TENDL-2015	2023	TENDL	2015			TENDL	2015	TENDL	2015	TENDL+EMPIRE
n-062_Sm_146	ENDF/B-VIII.0	2023	BNL	2017			BNL	2017			TENDL+EMPIRE
n-062_Sm_147	ENDF/B-VII.0; WPEC/SG-23	2023	BNL	2006	BNL	2006	BNL; KAERI	2006			Exit dist. added from TENDL
n-062_Sm_148	ENDF/B-VII.0; WPEC/SG-23	2024	BNL	2006	BNL	2006	BNL; KAERI	2006			
n-062_Sm_149	ENDF/B-VII.0; WPEC/SG-23	2023	BNL	2006	BNL	2006	BNL; KAERI	2006			COMMARA-2.0 covariances added in 2011; Exit dist. added from TENDL
n-062_Sm_150	ENDF/B-VII.0; WPEC/SG-23	2024	BNL	2006	BNL	2006	BNL; KAERI	2006			
n-062_Sm_151	ENDF/B-VII.0; WPEC/SG-23	2024	BNL	2006	BNL	2006	BNL; KAERI	2006			COMMARA-2.0 covariances added in 2011
n-062_Sm_152	ENDF/B-VII.0; WPEC/SG-23	2024	BNL	2006	BNL	2006	BNL; KAERI	2006			COMMARA-2.0 covariances added in 2011; Fix spectra in 2015
n-062_Sm_153	ENDF/B-VII.0; WPEC/SG-23	2023	BNL	2006	BNL	2006	BNL; KAERI	2006			Updates in the URR (RQW); Exit dist. added from TENDL
n-062_Sm_154	ENDF/B-VII.0; WPEC/SG-23	2024	BNL	2006	BNL	2006	BNL; KAERI	2006			
n-063_Eu_151	CENDL-3; WPEC/SG-23	2023	BNL	2006	JNDC	1989	CNDC	2001			Exit dist. added from TENDL
n-063_Eu_152	JENDL-3; WPEC/SG-23	2023	ORNL	1988	JNDC	1990	JNDC	1990			Exit dist. added from TENDL
n-063_Eu_153	ENDF/B-VII.0	2023	BNL	2011	BNL	2011	BNL; KAERI	2006			COMMARA-2.0 covariances added in 2011; Exit dist. added from TENDL
n-063_Eu_154	CENDL-3; WPEC/SG-23	2023	BNL	2006	JNDC	1990	CNDC	2001			Exit dist. added from TENDL
n-063_Eu_155	CENDL-3; WPEC/SG-23	2023	JNDC	1990	JNDC	1990	CNDC	2001			COMMARA-2.0 covariances added in 2011; Updates in the URR (RQW); Exit dist. added from TENDL
n-063_Eu_156	JENDL-3; WPEC/SG-23	2023			JNDC	1990	JNDC	1990			No RRR parameters given; only URR parameters; Exit dist. added from TENDL
n-063_Eu_157	ENDF/B-VII.0; WPEC/SG-23	2024	BNL	2006	BNL	2006	BNL	2006			
n-064_Gd_152	ENDF/B-VII.0; WPEC/SG-23	2023	BNL	2006	BNL	2006	BNL	2006			Covariances from ORNL (RR) and LANL (Fast); Exit dist. added from TENDL
n-064_Gd_153	ENDF/B-VII.0; WPEC/SG-23	2023	BNL	2006	BNL	2006	BNL	2006			Covariances from ORNL (RR) and LANL (Fast): Exit dist. added from TENDL
n-064_Gd_154	ENDF/B-VII.0; WPEC/SG-23	2024	BNL	2006	BNL	2006	BNL	2006			Covariances from ORNL (RR) and LANL (Fast)
n-064_Gd_155	ENDF/B-VII.0; WPEC/SG-23	2023	BNL	2006	BNL	2006	BNL	2006			Covariances from ORNL (RR) and LANL (Fast); Exit dist. added from TENDL
n-064_Gd_156	ENDF/B-VII.0; WPEC/SG-23	2023	BNL	2006	BNL	2006	BNL	2006			COMMARA-2.0 covariances added in 2011
n-064_Gd_157	ENDF/B-VII.0; WPEC/SG-23	2023	BNL	2006	BNL	2006	BNL	2006			COMMARA-2.0 covariances added in 2011; Exit dist. added from TENDL
n-064_Gd_158	ENDF/B-VII.0; WPEC/SG-23	2024	BNL	2006	BNL	2006	BNL	2006			COMMARA-2.0 covariances added in 2011
n-064_Gd_159	ENDF/B-VIII.0	2023	BNL	2017			BNL	2017			TENDL+EMPIRE
n-064_Gd_160	ENDF/B-VII.0; WPEC/SG-23	2023	BNL	2006	BNL	2006	BNL	2006			COMMARA-2.0 covariances added in 2011; Updates in the URR (RQW)
n-065_Tb_158	ENDF/B-VIII.0	2023	TENDL	2015			BNL	2017			TENDL+EMPIRE
n-065_Tb_159	JENDL-3; WPEC/SG-23	2023	BNL	2006	JNDC	1990	JNDC	1990			Exit dist. added from TENDL; Updates in the URR (RQW)
n-065_Tb_160	ENDF/B-VII.0; WPEC/SG-23	2024	BNL	2006	BNL	2006	BNL	2006			
n-065_Tb_161	ENDF/B-VIII.0	2023	TENDL	2015			BNL	2017			TENDL+EMPIRE
n-066_Dy_154	JENDL-4.0	2023			JAEA	2009	JAEA	2009			No RRR parameters given; only URR parameters; Exit dist. added from TENDL
n-066_Dy_155	ENDF/B-VIII.0	2023	BNL	2017			BNL	2017			TENDL+EMPIRE
n-066_Dy_156	**ENDF/B-VIII.1; WPEC/SG-23**	**2023**	**ORNL**	**2023**	**BNL**	**2006**	**BNL; KAERI**	**2006**			
n-066_Dy_157	ENDF/B-VIII.0	2023	BNL	2017			BNL	2017			TENDL+EMPIRE
n-066_Dy_158	**ENDF/B-VIII.1; WPEC/SG-23**	**2006**	**ORNL**	**2023**	**BNL**	**2006**	**BNL; KAERI**	**2006**			
n-066_Dy_159	JENDL-4.0	2023			JAEA	2009	JAEA	2009			No RRR parameters given; only URR parameters; Exit dist. added from TENDL

Continued on the next page

TABLE XLIX: (continued) Provenance for the neutrons sublibrary.

File name (.endf)	Source	Last updated	RRR		URR		Fast		HE		Comments
			Inst.	Year	Inst.	Year	Inst.	Year	Inst.	Year	
n-066_Dy_160	**ENDF/B-VIII.1; WPEC/SG-23**	**2023**	**ORNL**	**2018**	**ORNL**	**2018**	**BNL; KAERI**	**2006**			
n-066_Dy_161	**ENDF/B-VIII.1; WPEC/SG-23**	**2023**	**ORNL**	**2018**	**ORNL**	**2018**	**BNL; KAERI**	**2006**			
n-066_Dy_162	**ENDF/B-VIII.1; WPEC/SG-23**	**2023**	**ORNL**	**2018**	**ORNL**	**2018**	**BNL; KAERI**	**2006**			
n-066_Dy_163	**ENDF/B-VIII.1; WPEC/SG-23**	**2023**	**ORNL**	**2018**	**ORNL**	**2018**	**BNL; KAERI**	**2006**			
n-066_Dy_164	**ENDF/B-VIII.1; WPEC/SG-23**	**2023**	**ORNL**	**2018**	**ORNL**	**2018**	**BNL; KAERI**	**2006**			
n-067_Ho_165	ENDF/B-VI; WPEC/SG-23	2024	BNL	2006			LANL	1988			
n-067_Ho_166m1	ENDF/B-VII.0; WPEC/SG-23	2024	BNL	2006	BNL	2006	BNL	2006			
n-068_Er_162	JENDL-3.3; WPEC/SG-23	2023	TIT; JAERI	2001			TIT; JAERI	2001			Exit dist. added from TENDL
n-068_Er_163	ENDF/B-VIII.0	2023	BNL	2017			BNL	2017			TENDL+EMPIRE
n-068_Er_164	JENDL-3.3; WPEC/SG-23	2023	TIT; JAERI	2001			TIT; JAERI	2001			Exit dist. added from TENDL
n-068_Er_165	ENDF/B-VIII.0	2023	BNL	2017			BNL	2017			TENDL+EMPIRE
n-068_Er_166	JENDL-3.3; WPEC/SG-23	2023	BNL	2006			TIT; JAERI	2001			COMMARA-2.0 covariances added in 2011; Updates in the URR (RQW); Exit dist. added from TENDL
n-068_Er_167	JENDL-3.3; WPEC/SG-23	2023	BNL	2006	TIT; JAERI	2001	TIT; JAERI	2001			COMMARA-2.0 covariances added in 2011; Exit dist. added from TENDL
n-068_Er_168	JENDL-3.3; WPEC/SG-23	2023	BNL	2006			TIT; JAERI	2001			COMMARA-2.0 covariances added in 2011; Updates in the URR (RQW); Exit dist. added from TENDL
n-068_Er_169	ENDF/B-VIII.0	2023	TENDL	2015			BNL	2017			TENDL+EMPIRE
n-068_Er_170	JENDL-3.3; WPEC/SG-23	2023	BNL	2006	IPPE	2006	TIT; JAERI	2001			COMMARA-2.0 covariances added in 2011; Updates in the URR (RQW); Exit dist. added from TENDL
n-069_Tm_168	ENDF/B-VII.1	2023	BNL	2011			BNL	2011			
n-069_Tm_169	ENDF/B-VII.1	2023	BNL	2011	BNL	2011	BNL	2011			IRDFF-II mod.
n-069_Tm_170	ENDF/B-VII.1	2023	BNL	2011	BNL	2011	BNL	2011			
n-069_Tm_171	ENDF/B-VIII.0	2023	TENDL	2015			BNL	2017			TENDL+EMPIRE
n-070_Yb_168	JENDL-4.0	2023	JAEA	2010	JAEA	2010	JAEA	2010			Updates in the URR (RQW); Exit dist. added from TENDL
n-070_Yb_169	ENDF/B-VIII.0	2023	BNL	2017			BNL	2017			TENDL+EMPIRE
n-070_Yb_170	JENDL-4.0	2023	JAEA	2010	JAEA	2010	JAEA	2010			Exit dist. added from TENDL
n-070_Yb_171	JENDL-4.0	2023	JAEA	2010	JAEA	2010	JAEA	2010			Exit dist. added from TENDL
n-070_Yb_172	JENDL-4.0	2023	JAEA	2010	JAEA	2010	JAEA	2010			Exit dist. added from TENDL
n-070_Yb_173	JENDL-4.0	2023	JAEA	2010	JAEA	2010	JAEA	2010			Exit dist. added from TENDL
n-070_Yb_174	JENDL-4.0	2023	JAEA	2010	JAEA	2010	JAEA	2010			Exit dist. added from TENDL
n-070_Yb_175	ENDF/B-VIII.0	2023	TENDL	2015			BNL	2017			TENDL+EMPIRE
n-070_Yb_176	JENDL-4.0	2023	JAEA	2010	JAEA	2010	JAEA	2010			Updates in the URR (RQW); Exit dist. added from TENDL
n-071_Lu_175	ENDF/B-VI	2023	BNL	1984	BNL	1998	ORNL	1998			Updates in the URR (RQW); Exit dist. added from TENDL
n-071_Lu_176	ENDF/B-VI	2023	BNL	1984	BNL	1998	ORNL	1998			Updates in the URR (RQW); Exit dist. added from TENDL
n-072_Hf_174	ENDF/B-VIII.0	2023	ORNL	2009	ORNL	2009	LANL	2016			RR source is JEFF-3.1 and ENDF/B-VI; Updates in the URR (RQW); Exit dist. added from TENDL
n-072_Hf_175	ENDF/B-VIII.0	2023	BNL	2017			BNL	2017			TENDL+EMPIRE
n-072_Hf_176	ENDF/B-VIII.0	2023	ORNL	2009	ORNL	2009	LANL	2016			RR source is JEFF-3.1 and ENDF/B-VI; Updates in the URR (RQW); Exit dist. added from TENDL
n-072_Hf_177	ENDF/B-VIII.0	2017	ORNL	2009	ORNL	2009	LANL	2016			RR source is JENDL-3.3 and ENDF/B-VI; Updates in the URR (RQW)
n-072_Hf_178	ENDF/B-VIII.0	2017	ORNL	2009	ORNL	2009	LANL	2016			RR source is JEFF-3.1 and ENDF/B-VIUpdates in the URR (RQW); Exit dist. added from TENDL
n-072_Hf_179	ENDF/B-VIII.0	2023	ORNL	2009	ORNL	2009	LANL	2016			RR source is JENDL-3.3 and ENDF/B-VI; Updates in the URR (RQW); Exit dist. added from TENDL

Continued on the next page

TABLE XLIX: (continued) Provenance for the neutrons sublibrary.

File name (.endf)	Source	Last updated	RRR		URR		Fast		HE		Comments
			Inst.	Year	Inst.	Year	Inst.	Year	Inst.	Year	
n-072_Hf_180	ENDF/B-VIII.0	2023	ORNL	2009	ORNL	2009	LANL	2016			RR source is JEFF-3.1 and ENDF/B-VI; Exit dist. added from TENDL; Updates in the URR (RQW)
n-072_Hf_181	JENDL-4.0	2023			JAEA	2010	JAEA	2010			No RRR parameters given; Only URR parameters; Exit dist. added from TENDL
n-072_Hf_182	JENDL-4.0	2023			JAEA	2010	JAEA	2010			No RRR parameters given; Only URR parameters; Exit dist. added from TENDL
n-073_Ta_180	ENDF/B-VII.1	2024					LLNL	2011			No RRR parameters given; Exit dist. from KAERI/LANL
n-073_Ta_180m1	JENDL-5	2024	ORNL	1975	JAEA	2014	JAEA	2014			
n-073_Ta_181	**ENDF/B-VII.1**	**2024**	**RPI; ORNL**	**2024**	**RPI; ORNL**	**2024**	**LANL**	**2023**			**Exit dist. from KAERI/LANL**
n-073_Ta_182	ENDF/B-IV	2023	BNL	1971	BNL	1971	BNL	1971			Exit dist. added from TENDL
n-074_W_180	IAEA W CRP	2024	BNL	2006			IAEA	2011			
n-074_W_181	ENDF/B-VIII.0	2023	TENDL	2015			BNL	2017			TENDL+EMPIRE
n-074_W_182	ENDF/B-VIII.0	2024	ORNL	2014			IAEA	2011			
n-074_W_183	IAEA W CRP	2024	ORNL	2014			IAEA	2011			
n-074_W_184	IAEA W CRP	2024	ORNL	2014	ORNL		IAEA	2011			
n-074_W_185	ENDF/B-VIII.0	2023	BNL	2017			BNL	2017			TENDL+EMPIRE
n-074_W_186	IAEA W CRP	2024	ORNL	2014	ORNL		IAEA	2011			
n-075_Re_185	ENDF/B-VII.1	2024	BNL	1984	BNL	1984	LLNL	2011			R' in RRR corrected in 2015
n-075_Re_186m1	ENDF/B-VIII.0	2023	BNL	2017			BNL	2017			TENDL+EMPIRE
n-075_Re_187	ENDF/B-VII.1	2023	BNL	1984	BNL	1984	LLNL	2011			R' in RRR corrected in 2015
n-076_Os_184	ENDF/B-VIII.0	2023			JAEA	2010	JAEA	2010			No RRR parameters given; only URR parameters; Exit dist. added from TENDL
n-076_Os_185	ENDF/B-VIII.0	2023	TENDL	2015			BNL	2017			TENDL+EMPIRE
n-076_Os_186	JENDL-4.0	2023	JAEA	2010	JAEA	2010	JAEA	2010			Exit dist. added from TENDL
n-076_Os_187	JENDL-4.0	2023	JAEA	2010	JAEA	2010	JAEA	2010			Exit dist. added from TENDL
n-076_Os_188	JENDL-4.0	2023	JAEA	2010	JAEA	2010	JAEA	2010			Exit dist. added from TENDL
n-076_Os_189	JENDL-4.0	2023	JAEA	2010	JAEA	2010	JAEA	2010			Exit dist. added from TENDL
n-076_Os_190	JENDL-4.0	2023	JAEA	2010	JAEA	2010	JAEA	2010			Exit dist. added from TENDL
n-076_Os_191	TENDL-2015	2023	TENDL	2015			TENDL	2015	TENDL	2015	TENDL+EMPIRE
n-076_Os_192	ENDF/B-VIII.0	2023	JAEA	2010	JAEA	2010	JAEA	2010			Exit dist. added from TENDL
n-077_Ir_191	ENDF/B-VII.0	2024	BNL	2006			LANL; BNL	2006			
n-077_Ir_192	TENDL-2015	2023	TENDL	2015			TENDL	2015	TENDL	2015	TENDL+EMPIRE
n-077_Ir_193	ENDF/B-VII.0	2024	BNL	2006	BNL	2006	LANL	2006			
n-077_Ir_194m1	ENDF/B-VIII.0	2023	BNL	2017			BNL	2017			TENDL+EMPIRE
n-078_Pt_190	**ENDF/B-VIII.1**	**2024**	**TENDL**	**2015**			**LANL**	**2024**	**LANL**	**2024**	
n-078_Pt_191	**ENDF/B-VIII.1**	**2024**	**TENDL**	**2015**			**LANL**	**2024**	**LANL**	**2024**	
n-078_Pt_192	**ENDF/B-VIII.1**	**2024**	**TENDL**	**2015**			**LANL**	**2024**	**LANL**	**2024**	**Fixed remaining gaps between fast and RRR; Fixed domain mismatch between different L/J sections in URR; moving lowest point in L>0 sections down to match L=0.**
n-078_Pt_193	**ENDF/B-VIII.1**	**2024**	**TENDL**	**2015**			**LANL**	**2024**	**LANL**	**2024**	
n-078_Pt_194	**ENDF/B-VIII.1**	**2024**	**TENDL**	**2015**			**LANL**	**2024**	**LANL**	**2024**	
n-078_Pt_195	**ENDF/B-VIII.1**	**2024**	**TENDL**	**2015**			**LANL**	**2024**	**LANL**	**2024**	
n-078_Pt_196	**ENDF/B-VIII.1**	**2024**	**TENDL**	**2015**			**LANL**	**2024**	**LANL**	**2024**	
n-078_Pt_197	**ENDF/B-VIII.1**	**2024**	**TENDL**	**2015**			**LANL**	**2024**	**LANL**	**2024**	
n-078_Pt_198	**ENDF/B-VIII.1**	**2024**	**TENDL**	**2015**			**LANL**	**2024**	**LANL**	**2024**	
n-079_Au_197	ENDF/B-VII.0; Standards 2017	2023	IRMM	2017	IRMM	2017	LANL	1984			TENDL+EMPIRE; IRDFF-II mod.; Exit dist. from KAERI/LANL
n-080_Hg_196	JENDL-3.3	2023	JNDC	1997			JNDC	1997	LANL	1998	Exit dist. added from TENDL
n-080_Hg_197	ENDF/B-VIII.0	2023	BNL	2017			BNL	2017			TENDL+EMPIRE
n-080_Hg_197m1	ENDF/B-VIII.0	2023	BNL	2017			BNL	2017			TENDL+EMPIRE
n-080_Hg_198	JENDL-3.3	2023	JNDC	1997			JNDC	1997	LANL	2004	Exit dist. added from TENDL
n-080_Hg_199	JENDL-3.3	2023	JNDC	1997			JNDC	1997	LANL	2004	IRDFF-II mod.; Exit dist. added from TENDL
n-080_Hg_200	JENDL-3.3	2023	JNDC	1997			JNDC	1997	LANL	2004	Exit dist. added from TENDL
n-080_Hg_201	JENDL-3.3	2023	JNDC	1997			JNDC	1997	LANL	2004	Exit dist. added from TENDL
n-080_Hg_202	JENDL-3.3	2023	JNDC	1997			JNDC	1997	LANL	2004	Exit dist. added from TENDL
n-080_Hg_203	TENDL-2015	2023	TENDL	2015			TENDL	2015	TENDL	2015	TENDL+EMPIRE
n-080_Hg_204	JENDL-3.3	2023					JNDC	1997	LANL	1998	No RRR parameters given; Exit dist. added from TENDL
n-081_Tl_203	ENDF/B-VII.1	2023	BNL	2011	BNL	2011	BNL	2011			
n-081_Tl_204	TENDL-2015	2023	TENDL	2015			TENDL	2015	TENDL	2015	TENDL+EMPIRE
n-081_Tl_205	ENDF/B-VII.1	2011	BNL	2011	BNL	2011	BNL	2011			
n-082_Pb_204	**ENDF/B-VIII.1**	**2023**	**RPI**	**2023**			**NRG**	**2004**	**NRG**	**2004**	**NEUP evaluation from P.J. Brain; IRDFF-II mod.**

Continued on the next page

TABLE XLIX: (continued) Provenance for the neutrons sublibrary.

File name (.endf)	Source	Last updated	RRR		URR		Fast		HE		Comments
			Inst.	Year	Inst.	Year	Inst.	Year	Inst.	Year	
n-082_Pb_205	TENDL-2015	2023	TENDL	2015			TENDL	2015	TENDL	2015	TENDL+EMPIRE
n-082_Pb_206	**ENDF/B-VIII.1**	**2023**	**RPI**	**2023**			**LANL; RPI**	**2023**	**LANL; RPI**	**2023**	**NEUP evaluation from P.J. Brain**
n-082_Pb_207	**ENDF/B-VIII.1**	**2023**	**RPI**	**2023**			**LANL; RPI**	**2023**	**LANL; RPI**	**2023**	**NEUP evaluation from P.J. Brain**
n-082_Pb_208	**ENDF/B-VIII.1**	**2023**	**RPI**	**2023**			**LANL; RPI**	**2023**	**LANL; RPI**	**2023**	**NEUP evaluation from P.J. Brain**
n-083_Bi_209	ENDF/B-VI	2023	BNL	1984			ANL	1989	LANL	1999	COMMARA-2.0 covariances added in 2011; Exit dist. added from TENDL; IRDFF-II mod.
n-083_Bi_210m1	ENDF/B-VIII.0	2023	BNL	2017			BNL	2017			TENDL+EMPIRE
n-084_Po_208	TENDL-2015	2023	TENDL	2015			TENDL	2015	TENDL	2015	TENDL+EMPIRE
n-084_Po_209	ENDF/B-VIII.0	2023	TENDL	2015			BNL	2017			TENDL+EMPIRE
n-084_Po_210	TENDL-2015	2023	TENDL	2015			TENDL	2015	TENDL	2015	TENDL+EMPIRE
n-088_Ra_223	JENDL-3	2023					TIT; JAERI	1988			No RRR parameters given; Exit dist. added from TENDL
n-088_Ra_224	JENDL-3	2023					TIT; JAERI	1988			No RRR parameters given; Exit dist. added from TENDL
n-088_Ra_225	JENDL-3	2023					TIT; JAERI	1988			No RRR parameters given; Exit dist. added from TENDL
n-088_Ra_226	JENDL-3	2023	TIT; JAERI	1988			TIT; JAERI	1988			Exit dist. added from TENDL
n-089_Ac_225	JENDL-4.0	2023					JAEA	2010			No RRR parameters given
n-089_Ac_226	JENDL-4.0	2023					JAEA	2010			No RRR parameters given
n-089_Ac_227	JENDL-4.0	2023					JAEA	2010			No RRR parameters given
n-090_Th_227	JENDL-4.0	2023					JAEA	2010			
n-090_Th_228	JENDL-4.0	2023	JAEA	2010	JAEA	2010	JAEA	2010			
n-090_Th_229	JENDL-4.0	2023	JAEA	2010	JAEA	2010	JAEA	2010			
n-090_Th_230	JENDL-4.0	2023	JAEA	2010	JAEA	2010	JAEA	2010			
n-090_Th_231	JENDL-4.0	2023					JAEA	2010			
n-090_Th_232	IAEA Th-U CRP	2023	ORNL	2005	IRMM	2005	IAEA	2006	IAEA	2006	
n-090_Th_233	JENDL-4.0	2023					JAEA	2010			
n-090_Th_234	JENDL-4.0	2023					JAEA	2010			
n-091_Pa_229	JENDL-4.0	2023					JAEA	2010			No RRR parameters given
n-091_Pa_230	JENDL-4.0	2024					JAEA	2010			No RRR parameters given; prompt nubar update (RQW)
n-091_Pa_231	IAEA Th-U CRP	2023	ORNL; BNL	2006	ORNL	2006	IAEA	2006	IAEA	2006	
n-091_Pa_232	JENDL-4.0	2023	JAEA	2010	JAEA	2010	JAEA	2010			prompt nubar update (RQW)
n-091_Pa_233	IAEA Th-U CRP	2023	ORNL	2006	IAEA	2003	IAEA	2006	IAEA	2006	
n-092_U_230	JENDL-4.0	2023					JAEA	2010			No RRR parameters given; prompt nubar update (RQW)
n-092_U_231	JENDL-4.0	2023					JAEA	2010			No RRR parameters given; prompt nubar update (RQW)
n-092_U_232	JENDL-4.0	2023	JAEA	2010	JAEA	2010	JAEA	2010			prompt nubar update (RQW)
n-092_U_233	**ENDF/B-VIII.1**	**2023**	**ORNL**	**2023**	**JAEA**	**2010**	**JAEA**	**2010**			**Nubar updates**
n-092_U_234	**ENDF/B-VII.0**	**2023**	**LANL**	**2006**	**LANL**	**2006**	**LANL; IAEA**	**2023**			**COMMARA-2.0 covariances added in 2011**
n-092_U_235	**ENDF/B-VIII.1; INDEN; Standards 2017**	**2024**	**ORNL; IAEA**	**2017**	**ORNL**	**1997**	**IAEA; LANL**	**2023**			**INDEN evaluation; Exit dist. added from TENDL**
n-092_U_236	**ENDF/B-VII.0**	**2023**	**BNL**	**1989**	**BNL**	**1978**	**LANL**	**2023**			**COMMARA-2.0 covariances added in 2011**
n-092_U_237	ENDF/B-VII.0	2023	JNDC	1993	JNDC	1993	LANL	2010			
n-092_U_238	**ENDF/B-VIII.1; INDEN; Standards 2017**	**2023**	**ORNL; IAEA**	**2023**	**ORNL; IAEA**	**2023**	**IAEA; LANL**	**2023**			**INDEN evaluation**
n-092_U_239	ENDF/B-VII.1	2023	LLNL	2016	LLNL	2011	LLNL	2011			
n-092_U_240	ENDF/B-VII.0	2023	LANL	2003	LANL	2003	LANL	2003			Resonances from ENDF/B-VI 242Pu evaluation
n-092_U_241	ENDF/B-VII.0	2023	LANL; BNL	2016	LANL	2000	LANL	2005			
n-093_Np_234	JENDL-4.0	2023					JAEA	2010			No RRR parameters given
n-093_Np_235	JENDL-4.0	2023					JAEA	2010			No RRR parameters given
n-093_Np_236	JENDL-4.0	2023	JAEA	2010	JAEA	2010	JAEA	2010			RQ Wright nubars added in 2016
n-093_Np_236m1	ENDF/B-VIII.0	2023	JAEA	2010			LANL	2017			
n-093_Np_237	ENDF/B-VII.0	2023	LANL	2010	LANL	2006	LANL	2010			COMMARA-2.0 covariances added in 2011
n-093_Np_238	JENDL-4.0	2023	JAEA	2010	JAEA	2010	JAEA	2010			RQ Wright nubars added in 2016
n-093_Np_239	JENDL-4.0	2023					JAEA	2010			No RRR parameters given
n-094_Pu_236	JENDL-4.0	2023	JAEA	2010	JAEA	2010	JAEA	2010			
n-094_Pu_237	JENDL-4.0	2024					JAEA	2010			No RRR parameters given; prompt nubar update (RQW)
n-094_Pu_238	ENDF/B-VII.1	2023	JAEA	2010	JAEA	2010	LANL	2010			Exit dist. added from TENDL
n-094_Pu_239	**ENDF/B-VIII.1; INDEN; Standards 2017**	**2024**	**ORNL**	**2023**	**ORNL**	**1993**	**IAEA; LANL; LLNL**	**2023**			**INDEN evaluation**

Continued on the next page

TABLE XLIX: (continued) Provenance for the neutrons sublibrary.

File name (.endf)	Source	Last updated	RRR		URR		Fast		HE		Comments
			Inst.	Year	Inst.	Year	Inst.	Year	Inst.	Year	
n-094_Pu_240	**ENDF/B-VIII.1; INDEN**	**2023**	**ORNL**	**2017**	**ORNL**	**1986**	**LANL**	**2009**			**INDEN evaluation; Unclear when URR evaluated; Adj. to RRR to improve perf. in depletion; Improved documentation**
n-094_Pu_241	**ENDF/B-VIII.1; INDEN**	**2023**	**ORNL**	**2023**	**ORNL; CEA**	**1988**	**ORNL**	**1988**			**Fission cross section covariance added in 2010 by LANL; Adj. to RRR to improve perf. in depletion**
n-094_Pu_242	JENDL-4.0	2023	BNL	2011	BNL	2011	JAEA	2010			COMMARA-2.0 covariances added in 2011
n-094_Pu_243	ENDF/B-V	2023	LLNL	1976	LLNL	1976	LLNL	1976			RQ Wright nubars added in 2016
n-094_Pu_244	JENDL-4.0	2023	JAEA	2010	JAEA	2010	JAEA	2010			RQ Wright nubars added in 2016
n-094_Pu_245	ENDF/B-VIII.0	2023	BNL	2017			BNL	2017			TENDL+EMPIRE
n-094_Pu_246	JENDL-4.0	2023					JAEA	2010			No RRR parameters given; RQ Wright nubars added in 2016
n-095_Am_240	JENDL-4.0	2024					JAEA	2010			No RRR parameters given; prompt nubar update (RQW)
n-095_Am_241	ENDF/B-VII.0	2023	JAEA	2010	JAEA	2010	LANL	2017			(n;2n) and capture changed
n-095_Am_242	ENDF/B-VII.0	2023	JAEA	2000	JAEA	2000	LANL	2004			Exit dist. added from TENDL
n-095_Am_242m1	ENDF/B-VII.0	2023	JAEA	2000	JAEA	2000	LANL	2005			COMMARA-2.0 covariances added in 2011; Exit dist. added from TENDL
n-095_Am_243	ENDF/B-VII.0	2023	BNL	2011	BNL	2011	LANL	2006			COMMARA-2.0 covariances added in 2011
n-095_Am_244	JENDL-3	2024					JAEA	1988			No RRR parameters given; prompt nubar update (RQW); Exit dist. added from TENDL
n-095_Am_244m1	JENDL-3	2023					JAEA	1988			No RRR parameters given; Exit dist. added from TENDL
n-096_Cm_240	JENDL-4.0	2023					JAEA	2010			No RRR parameters given; prompt nubar update (RQW)
n-096_Cm_241	JENDL-4.0	2023					JAEA	2010			No RRR parameters given; RQ Wright nubars added in 2016
n-096_Cm_242	JENDL-4.0	2023	JAEA	2010	JAEA	2010	JAEA	2010			RQ Wright nubars added in 2016
n-096_Cm_243	JENDL-4.0	2023	JAEA	2010	JAEA	2010	JAEA	2010			
n-096_Cm_244	JENDL-4.0	2023	JAEA	2010	JAEA	2010	JAEA	2010			RQ Wright nubars added in 2016
n-096_Cm_245	JENDL-4.0	2023	JAEA	2010	JAEA	2010	JAEA	2010			
n-096_Cm_246	JENDL-4.0	2023	JAEA	2010	JAEA	2010	JAEA	2010			RQ Wright nubars added in 2016
n-096_Cm_247	JENDL-4.0	2023	JAEA	2010	JAEA	2010	JAEA	2010			RQ Wright nubars added in 2016
n-096_Cm_248	JENDL-4.0	2023	JAEA	2010	JAEA	2010	JAEA	2010			RQ Wright nubars added in 2016
n-096_Cm_249	JENDL-4.0	2023					JAEA	2010			No RRR parameters given; RQ Wright nubars added in 2016
n-096_Cm_250	JENDL-4.0	2023	JAEA	2010	JAEA	2010	JAEA	2010			RQ Wright nubars added in 2016
n-097_Bk_245	JENDL-4.0	2023					JAEA	2010			No RRR parameters given; RQ Wright nubars added in 2016
n-097_Bk_246	JENDL-4.0	2023					JAEA	2010			No RRR parameters given; RQ Wright nubars added in 2016
n-097_Bk_247	JENDL-4.0	2023					JAEA	2010			No RRR parameters given; RQ Wright nubars added in 2016
n-097_Bk_248	JENDL-4.0	2023					JAEA	2010			No RRR parameters given; RQ Wright nubars added in 2016
n-097_Bk_249	JENDL-4.0	2023	JAEA	2010	JAEA	2010	JAEA	2010			RQ Wright nubars added in 2016
n-097_Bk_250	JENDL-4.0	2023					JAEA	2010			No RRR parameters given; RQ Wright nubars added in 2016
n-098_Cf_246	JENDL-4.0	2024					JAEA	2010			No RRR parameters given; prompt nubar update (RQW)
n-098_Cf_247	ENDF/B-VIII.0	2023	BNL	2017			BNL	2017			TENDL+EMPIRE
n-098_Cf_248	JENDL-4.0	2024					JAEA	2010			No RRR parameters given; prompt nubar update (RQW)
n-098_Cf_249	JENDL-4.0	2024	JAEA	2010	JAEA	2010	JAEA	2010			prompt nubar update (RQW)
n-098_Cf_250	JENDL-4.0	2024	JAEA	2010	JAEA	2010	JAEA	2010			prompt nubar update (RQW)
n-098_Cf_251	JENDL-4.0	2024	JAEA	2010	JAEA	2010	JAEA	2010			prompt nubar update (RQW)
n-098_Cf_252	JENDL-4.0	2024	JAEA	2010	JAEA	2010	JAEA	2010			prompt nubar update (RQW)
n-098_Cf_253	JENDL-4.0	2024					JAEA	2010			No RRR parameters given; prompt nubar update (RQW)
n-098_Cf_254	JENDL-4.0	2024					JAEA	2010			No RRR parameters given; prompt nubar update (RQW)
n-099_Es_251	JENDL-4.0	2023					JAEA	2010			No RRR parameters given; RQ Wright nubars added in 2016
n-099_Es_252	JENDL-4.0	2023					JAEA	2010			No RRR parameters given; RQ Wright nubars added in 2016
n-099_Es_253	JENDL-4.0	2023	JAEA	2010			JAEA	2010			Artificial resonance added to match capture RI; RQ Wright nubars added in 2016
n-099_Es_254	JENDL-4.0	2023					JAEA	2010			No RRR parameters given; RQ Wright nubars added in 2016
n-099_Es_254m1	JENDL-4.0	2024					JAEA	2010			No RRR parameters given; prompt nubar update (RQW)
n-099_Es_255	JENDL-4.0	2023					JAEA	2010			No RRR parameters given; RQ Wright nubars added in 2016

Continued on the next page

TABLE XLIX: (continued) Provenance for the neutrons sublibrary.

File name (.endf)	Source	Last updated	RRR		URR		Fast		HE		Comments
			Inst.	Year	Inst.	Year	Inst.	Year	Inst.	Year	
n-100_Fm_255	JENDL-4.0	2023					JAEA	2010			No RRR parameters given; RQ Wright nubars added in 2016

TABLE L: Summary of the origins of and recent changes to the thermal-neutron scattering law sublibrary. For each file we list the library source, the year when the last significant evaluation effort or impactful modification was performed, the institution responsible for its most recent evaluation and the corresponding year said evaluation was completed. Evaluations updated in ENDF/B-VIII.1 are in bold.

File name (.endf)	Source	Last updated	Institution	Year
tsl-013_Al_027	ENDF/B-VII.0	2024	LANL	2005
tsl-AlinAl2O3	**ENDF/B-VIII.1**	**2024**	**LEIP**	**2020**
tsl-OinAl2O3	**ENDF/B-VIII.1**	**2023**	**LEIP**	**2020**
tsl-Be-metal	**ENDF/B-VIII.1**	**2024**	**LEIP**	**2021**
tsl-Be-metal+Sd	**ENDF/B-VIII.1**	**2024**	**LEIP**	**2021**
tsl-BeinBe2C	**ENDF/B-VIII.1**	**2023**	**NNL**	**2023**
tsl-CinBe2C	**ENDF/B-VIII.1**	**2023**	**NNL**	**2023**
tsl-BeinBeF2	**ENDF/B-VIII.1**	**2023**	**UoS**	**2021**
tsl-FinBeF2	**ENDF/B-VIII.1**	**2023**	**UoS**	**2023**
tsl-BeinBeO	**ENDF/B-VIII.1**	**2023**	**LEIP**	**2022**
tsl-OinBeO	**ENDF/B-VIII.1**	**2023**	**LEIP**	**2022**
tsl-benzene	ENDF-269	2017	GA	1969
tsl-CainCaH2	**ENDF/B-VIII.1**	**2023**	**LEIP**	**2021**
tsl-H1inCaH2	**ENDF/B-VIII.1**	**2023**	**LEIP**	**2021**
tsl-H2inCaH2	**ENDF/B-VIII.1**	**2023**	**LEIP**	**2021**
tsl-CinCF2	**ENDF/B-VIII.1**	**2023**	**ORNL/RPI**	**2022**
tsl-FinCF2	**ENDF/B-VIII.1**	**2023**	**ORNL/RPI**	**2022**
tsl-HinCH2	ENDF/B-VIII.0	2023	LEIP	2017
tsl-l-CH4	ENDF/B-VII.0	2023	LANL	1993
tsl-s-CH4	ENDF/B-VII.0	2016	LANL	1993
tsl-CinC8H8	**ENDF/B-VIII.1**	**2023**	**ORNL/RPI**	**2022**
tsl-HinC8H8	**ENDF/B-VIII.1**	**2023**	**ORNL/RPI**	**2022**
tsl-CinC5O2H8	**ENDF/B-VIII.1**	**2023**	**ORNL/RPI**	**2022**
tsl-HinC5O2H8	**ENDF/B-VIII.1**	**2023**	**ORNL/RPI**	**2022**
tsl-OinC5O2H8	**ENDF/B-VIII.1**	**2023**	**ORNL/RPI**	**2022**
tsl-ortho-D	**ENDF/B-VIII.1**	**2023**	**ESS**	**2023**
tsl-para-D	**ENDF/B-VIII.1**	**2023**	**ESS**	**2023**
tsl-DinD2O	ENDF/B-VIII.0	2023	ARCAB	2017
tsl-OinD2O	ENDF/B-VIII.0	2023	ARCAB	2017
tsl-026_Fe_056	ENDF/B-VII.0	2024	LANL	2005
tsl-BeinFLiBe	**ENDF/B-VIII.1**	**2023**	**LEIP**	**2020**
tsl-FinFLiBe	**ENDF/B-VIII.1**	**2023**	**LEIP**	**2020**
tsl-LiinFLiBe	**ENDF/B-VIII.1**	**2023**	**LEIP**	**2020**
tsl-crystalline-graphite	ENDF/B-VIII.0	2023	LEIP	2017
tsl-reactor-graphite-10P	ENDF/B-VIII.0	2023	LEIP	2017
tsl-reactor-graphite-20P	**ENDF/B-VIII.1**	**2023**	**LEIP**	**2020**
tsl-reactor-graphite-30P	ENDF/B-VIII.0	2023	LEIP	2017
tsl-graphiteSd	**ENDF/B-VIII.1**	**2023**	**LEIP**	**2022**
tsl-ortho-H	**ENDF/B-VIII.1**	**2023**	**ESS**	**2023**
tsl-para-H	**ENDF/B-VIII.1**	**2023**	**ESS**	**2023**
tsl-FinHF	**ENDF/B-VIII.1**	**2023**	**LEIP**	**2022**
tsl-HinHF	**ENDF/B-VIII.1**	**2023**	**LEIP**	**2022**
tsl-HinH2O	**ENDF/B-VIII.1**	**2023**	**ESS**	**2023**
tsl-HinIceIh	ENDF/B-VIII.0	2023	BAPL	2016
tsl-OinIceIh	ENDF/B-VIII.0	2016	BAPL	2016
tsl-7Liin7LiD-mixed	**ENDF/B-VIII.1**	**2023**	**NNL**	**2023**
tsl-Din7LiD-mixed	**ENDF/B-VIII.1**	**2023**	**NNL**	**2023**
tsl-7Liin7LiH-mixed	**ENDF/B-VIII.1**	**2023**	**NNL**	**2023**
tsl-Hin7LiH-mixed	**ENDF/B-VIII.1**	**2023**	**NNL**	**2023**
tsl-FinMgF2	**ENDF/B-VIII.1**	**2023**	**UoS**	**2021**
tsl-MginMgF2	**ENDF/B-VIII.1**	**2023**	**UoS**	**2021**
tsl-MginMgO	**ENDF/B-VIII.1**	**2023**	**UoS**	**2021**
tsl-OinMgO	**ENDF/B-VIII.1**	**2023**	**UoS**	**2021**
tsl-HinParaffinicOil	**ENDF/B-VIII.1**	**2023**	**ESS**	**2023**
tsl-OinPuO2	**ENDF/B-VIII.1**	**2023**	**LEIP**	**2023**

Continued on the next page

TABLE L: (continued) Provenance for the thermal-neutron scattering law sublibrary.

File name (.endf)	Source	Last updated	Institution	Year
tsl-PuinPuO2	**ENDF/B-VIII.1**	**2023**	**LEIP**	**2023**
tsl-CinSiC	**ENDF/B-VIII.1**	**2023**	**LEIP**	**2022**
tsl-SiinSiC	**ENDF/B-VIII.1**	**2023**	**LEIP**	**2022**
tsl-OinSiO2-alpha	**ENDF/B-VIII.1**	**2023**	**LEIP**	**2022**
tsl-SiinSiO2-alpha	**ENDF/B-VIII.1**	**2023**	**LEIP**	**2022**
tsl-SiO2-beta	ENDF/B-VIII.0	2016	LEIP	2011
tsl-U-metal-100P	**ENDF/B-VIII.1**	**2023**	**LEIP**	**2023**
tsl-U-metal-10P	**ENDF/B-VIII.1**	**2023**	**LEIP**	**2023**
tsl-U-metal-5P	**ENDF/B-VIII.1**	**2023**	**LEIP**	**2023**
tsl-U-metal-HALEU	**ENDF/B-VIII.1**	**2023**	**LEIP**	**2023**
tsl-U-metal-HEU	**ENDF/B-VIII.1**	**2023**	**LEIP**	**2023**
tsl-U-metal	**ENDF/B-VIII.1**	**2023**	**LEIP**	**2023**
tsl-CinUC-100P	**ENDF/B-VIII.1**	**2023**	**LEIP**	**2022**
tsl-UinUC-100P	**ENDF/B-VIII.1**	**2023**	**LEIP**	**2022**
tsl-CinUC-10P	**ENDF/B-VIII.1**	**2023**	**LEIP**	**2022**
tsl-UinUC-10P	**ENDF/B-VIII.1**	**2023**	**LEIP**	**2022**
tsl-CinUC-5P	**ENDF/B-VIII.1**	**2023**	**LEIP**	**2022**
tsl-UinUC-5P	**ENDF/B-VIII.1**	**2023**	**LEIP**	**2022**
tsl-CinUC-HALEU	**ENDF/B-VIII.1**	**2023**	**LEIP**	**2022**
tsl-UinUC-HALEU	**ENDF/B-VIII.1**	**2023**	**LEIP**	**2022**
tsl-CinUC-HEU	**ENDF/B-VIII.1**	**2023**	**LEIP**	**2022**
tsl-UinUC-HEU	**ENDF/B-VIII.1**	**2023**	**LEIP**	**2022**
tsl-CinUC	**ENDF/B-VIII.1**	**2023**	**LEIP**	**2022**
tsl-UinUC	**ENDF/B-VIII.1**	**2023**	**LEIP**	**2022**
tsl-HinUH3	**ENDF/B-VIII.1**	**2023**	**NNL**	**2018**
tsl-NinUN-100P	**ENDF/B-VIII.1**	**2023**	**LEIP**	**2022**
tsl-UinUN-100P	**ENDF/B-VIII.1**	**2023**	**LEIP**	**2022**
tsl-NinUN-10P	**ENDF/B-VIII.1**	**2023**	**LEIP**	**2022**
tsl-UinUN-10P	**ENDF/B-VIII.1**	**2023**	**LEIP**	**2022**
tsl-NinUN-5P	**ENDF/B-VIII.1**	**2023**	**LEIP**	**2022**
tsl-UinUN-5P	**ENDF/B-VIII.1**	**2023**	**LEIP**	**2022**
tsl-NinUN-HALEU	**ENDF/B-VIII.1**	**2023**	**LEIP**	**2022**
tsl-UinUN-HALEU	**ENDF/B-VIII.1**	**2023**	**LEIP**	**2022**
tsl-NinUN-HEU	**ENDF/B-VIII.1**	**2023**	**LEIP**	**2022**
tsl-UinUN-HEU	**ENDF/B-VIII.1**	**2023**	**LEIP**	**2022**
tsl-NinUN	**ENDF/B-VIII.1**	**2023**	**LEIP**	**2022**
tsl-UinUN	**ENDF/B-VIII.1**	**2023**	**LEIP**	**2022**
tsl-OinUO2-100P	**ENDF/B-VIII.1**	**2023**	**LEIP**	**2022**
tsl-UinUO2-100P	**ENDF/B-VIII.1**	**2023**	**LEIP**	**2022**
tsl-OinUO2-10P	**ENDF/B-VIII.1**	**2023**	**LEIP**	**2022**
tsl-UinUO2-10P	**ENDF/B-VIII.1**	**2023**	**LEIP**	**2022**
tsl-OinUO2-5P	**ENDF/B-VIII.1**	**2023**	**LEIP**	**2022**
tsl-UinUO2-5P	**ENDF/B-VIII.1**	**2023**	**LEIP**	**2022**
tsl-OinUO2-HALEU	**ENDF/B-VIII.1**	**2023**	**LEIP**	**2022**
tsl-UinUO2-HALEU	**ENDF/B-VIII.1**	**2023**	**LEIP**	**2022**
tsl-OinUO2-HEU	**ENDF/B-VIII.1**	**2023**	**LEIP**	**2022**
tsl-UinUO2-HEU	**ENDF/B-VIII.1**	**2023**	**LEIP**	**2022**
tsl-OinUO2	**ENDF/B-VIII.1**	**2023**	**LEIP**	**2022**
tsl-UinUO2	**ENDF/B-VIII.1**	**2023**	**LEIP**	**2022**
tsl-HinYH2	**ENDF/B-VIII.1**	**2024**	**NNL**	**2024**
tsl-YinYH2	**ENDF/B-VIII.1**	**2024**	**NNL**	**2024**
tsl-CinZrC	**ENDF/B-VIII.1**	**2023**	**NNL**	**2023**
tsl-ZrinZrC	**ENDF/B-VIII.1**	**2023**	**NNL**	**2023**
tsl-HinZrH	ENDF/B-VII.0	2023	LANL	1993
tsl-ZrinZrH	ENDF/B-VII.0	2023	LANL	1993
tsl-HinZrH2	**ENDF/B-VIII.1**	**2023**	**NNL**	**2023**
tsl-ZrinZrH2	**ENDF/B-VIII.1**	**2023**	**NNL**	**2023**
tsl-HinZrHx	**ENDF/B-VIII.1**	**2023**	**NNL**	**2023**
tsl-ZrinZrHx	**ENDF/B-VIII.1**	**2023**	**NNL**	**2023**

TABLE LI: Summary of the origins of and recent changes to the photonuclear sublibrary. For each file we list the library source, the year when the last significant evaluation effort or impactful modification was performed, the institution responsible for its most recent evaluation and the corresponding year said evaluation was completed. We also provide additional comments, where relevant. Evaluations updated in ENDF/B-VIII.1 are in bold.

File name (.endf)	Source	Last updated	Institution	Year	Comments
g-001_H_002	ENDF/B-VII.0	2023	LANL	2005	2019 IAEA Photonuclear CRP
g-002_He_003	**JENDL-5**	**2023**	**JAEA**	**2003**	**2019 IAEA Photonuclear CRP**
g-003_Li_006	**JENDL-5**	**2023**	**JAEA**	**2013**	**2019 IAEA Photonuclear CRP**
g-003_Li_007	**JENDL-5**	**2023**	**JAEA**	**2013**	**2019 IAEA Photonuclear CRP**
g-004_Be_009	**CENDL-3**	**2023**	**CNDC**	**2018**	**2019 IAEA Photonuclear CRP**

Continued on the next page

TABLE LI: (continued) Provenance for the photonuclear sublibrary.

File name (.endf)	Source	Last updated	Institution	Year	Comments
g-006_C_012	LANL150u	2023	LANL	1999	2019 IAEA Photonuclear CRP
g-006_C_013	KAERI/G-1	2023	KAERI	1999	2019 IAEA Photonuclear CRP
g-006_C_014	**TENDL2012**	**2023**	**KAERI/NRG**	**2019**	**2019 IAEA Photonuclear CRP**
g-007_N_014	**ENDF/B-VII.0**	**2024**	**KAERI**	**1999**	**2019 IAEA Photonuclear CRP; added missing photon distributions**
g-007_N_015	KAERI/G-1	2023	KAERI	1999	2019 IAEA Photonuclear CRP
g-008_O_016	LANL150u	2023	LANL	1999	2019 IAEA Photonuclear CRP
g-008_O_017	KAERI/G-1	2023	KAERI	1999	2019 IAEA Photonuclear CRP
g-008_O_018	KAERI/G-1	2023	KAERI	1999	2019 IAEA Photonuclear CRP
g-009_F_019	**JENDL-5**	**2023**	**JAEA**	**2013**	**2019 IAEA Photonuclear CRP**
g-011_Na_023	KAERI/G-1	2023	KAERI	1999	2019 IAEA Photonuclear CRP
g-012_Mg_024	KAERI/G-1	2023	KAERI	1999	2019 IAEA Photonuclear CRP
g-012_Mg_025	KAERI/G-1	2023	KAERI	1999	2019 IAEA Photonuclear CRP
g-012_Mg_026	KAERI/G-1	2023	KAERI	1999	2019 IAEA Photonuclear CRP
g-013_Al_027	LANL150u	2023	LANL	1999	2019 IAEA Photonuclear CRP
g-014_Si_027	KAERI/G-1	2023	KAERI	1999	2019 IAEA Photonuclear CRP
g-014_Si_028	ENDF/B-VII.0	2023	LANL	1999	2019 IAEA Photonuclear CRP
g-014_Si_029	KAERI/G-1	2023	KAERI	1999	2019 IAEA Photonuclear CRP
g-014_Si_030	KAERI/G-1	2023	KAERI	1999	2019 IAEA Photonuclear CRP
g-016_S_032	KAERI/G-1	2023	KAERI	1999	2019 IAEA Photonuclear CRP
g-016_S_033	KAERI/G-1	2023	KAERI	1999	2019 IAEA Photonuclear CRP
g-016_S_034	KAERI/G-1	2023	KAERI	1999	2019 IAEA Photonuclear CRP
g-016_S_036	KAERI/G-1	2023	KAERI	1999	2019 IAEA Photonuclear CRP
g-017_Cl_035	**JENDL-5**	**2023**	**JAEA**	**2019**	**2019 IAEA Photonuclear CRP**
g-017_Cl_037	**JENDL-5**	**2023**	**JAEA**	**2019**	**2019 IAEA Photonuclear CRP**
g-018_Ar_036	**JENDL-5**	**2023**	**JAEA**	**2019**	**2019 IAEA Photonuclear CRP**
g-018_Ar_038	**JENDL-5**	**2023**	**JAEA**	**2019**	**2019 IAEA Photonuclear CRP**
g-018_Ar_040	**JENDL-5**	**2023**	**JAEA**	**2019**	**2019 IAEA Photonuclear CRP**
g-019_K_039	**JENDL-5**	**2023**	**JAEA**	**2019**	**2019 IAEA Photonuclear CRP**
g-019_K_040	**JENDL-5**	**2023**	**JAEA**	**2019**	**2019 IAEA Photonuclear CRP**
g-019_K_041	**JENDL-5**	**2023**	**JAEA**	**2019**	**2019 IAEA Photonuclear CRP**
g-020_Ca_040	LANL150u	2024	LANL	1998	2019 IAEA Photonuclear CRP; correct masses
g-020_Ca_042	KAERI/G-1	2023	KAERI	1999	2019 IAEA Photonuclear CRP
g-020_Ca_043	KAERI/G-1	2023	KAERI	1999	2019 IAEA Photonuclear CRP
g-020_Ca_044	**JENDL-5**	**2023**	**JAEA**	**2013**	**2019 IAEA Photonuclear CRP**
g-020_Ca_046	KAERI/G-1	2023	KAERI	1999	2019 IAEA Photonuclear CRP
g-020_Ca_048	**JENDL-5**	**2023**	**JAEA**	**2013**	**2019 IAEA Photonuclear CRP**
g-021_Sc_045	**JENDL-5**	**2023**	**JAEA**	**2019**	**2019 IAEA Photonuclear CRP**
g-022_Ti_046	**JENDL-5**	**2023**	**JAEA**	**2019**	**2019 IAEA Photonuclear CRP**
g-022_Ti_047	**JENDL-5**	**2023**	**JAEA**	**2019**	**2019 IAEA Photonuclear CRP**
g-022_Ti_048	**JENDL-5**	**2023**	**JAEA**	**2019**	**2019 IAEA Photonuclear CRP**
g-022_Ti_049	**JENDL-5**	**2023**	**JAEA**	**2019**	**2019 IAEA Photonuclear CRP**
g-022_Ti_050	**JENDL-5**	**2023**	**JAEA**	**2019**	**2019 IAEA Photonuclear CRP**
g-023_V_050	**JENDL-5**	**2023**	**JAEA**	**2019**	**2019 IAEA Photonuclear CRP**
g-023_V_051	**JENDL-5**	**2023**	**JAEA**	**2019**	**2019 IAEA Photonuclear CRP**
g-024_Cr_050	**CENDL-3**	**2023**	**CNDC**	**2018**	**2019 IAEA Photonuclear CRP**
g-024_Cr_052	**JENDL-5**	**2023**	**JAEA**	**2019**	**2019 IAEA Photonuclear CRP**
g-024_Cr_053	**CENDL-3**	**2023**	**CNDC**	**2018**	**2019 IAEA Photonuclear CRP**
g-024_Cr_054	**CENDL-3**	**2023**	**CNDC**	**2018**	**2019 IAEA Photonuclear CRP**
g-025_Mn_055	**JENDL-5**	**2023**	**JAEA**	**2019**	**2019 IAEA Photonuclear CRP**
g-026_Fe_054	**JENDL-5**	**2023**	**JAEA**	**2019**	**2019 IAEA Photonuclear CRP**
g-026_Fe_056	**JENDL-5**	**2023**	**JAEA**	**2019**	**2019 IAEA Photonuclear CRP**
g-026_Fe_057	**JENDL-5**	**2023**	**JAEA**	**2019**	**2019 IAEA Photonuclear CRP**
g-026_Fe_058	**JENDL-5**	**2023**	**JAEA**	**2019**	**2019 IAEA Photonuclear CRP**
g-027_Co_059	**2019 Photonuclear CRP**	**2023**	**IFIN-HH**	**2019**	**2019 IAEA Photonuclear CRP**
g-028_Ni_058	**JENDL-5**	**2023**	**JAEA**	**2019**	**2019 IAEA Photonuclear CRP**
g-028_Ni_060	**JENDL-5**	**2023**	**JAEA**	**2019**	**2019 IAEA Photonuclear CRP**
g-028_Ni_061	**JENDL-5**	**2023**	**JAEA**	**2019**	**2019 IAEA Photonuclear CRP**
g-028_Ni_062	**JENDL-5**	**2023**	**JAEA**	**2019**	**2019 IAEA Photonuclear CRP**
g-028_Ni_064	**JENDL-5**	**2023**	**JAEA**	**2019**	**2019 IAEA Photonuclear CRP**
g-029_Cu_063	LANL150u	2023	LANL	1999	2019 IAEA Photonuclear CRP
g-029_Cu_065	**JENDL-5**	**2023**	**JAEA**	**2019**	**2019 IAEA Photonuclear CRP**
g-030_Zn_064	**TENDL2012**	**2023**	**KAERI/NRG**	**2019**	**2019 IAEA Photonuclear CRP**
g-030_Zn_066	**JENDL-5**	**2023**	**JAEA**	**2019**	**2019 IAEA Photonuclear CRP**
g-030_Zn_067	**JENDL-5**	**2023**	**JAEA**	**2019**	**2019 IAEA Photonuclear CRP**
g-030_Zn_068	**JENDL-5**	**2023**	**JAEA**	**2019**	**2019 IAEA Photonuclear CRP**
g-030_Zn_070	**JENDL-5**	**2023**	**JAEA**	**2019**	**2019 IAEA Photonuclear CRP**
g-032_Ge_070	**JENDL-5**	**2023**	**JAEA**	**2019**	**2019 IAEA Photonuclear CRP**
g-032_Ge_072	**JENDL-5**	**2023**	**JAEA**	**2019**	**2019 IAEA Photonuclear CRP**

Continued on the next page

TABLE LI: (continued) Provenance for the photonuclear sublibrary.

File name (.endf)	Source	Last updated	Institution	Year	Comments
g-032_Ge_073	JENDL-5	2023	JAEA	2019	2019 IAEA Photonuclear CRP
g-032_Ge_074	JENDL-5	2023	JAEA	2019	2019 IAEA Photonuclear CRP
g-032_Ge_076	JENDL-5	2023	JAEA	2019	2019 IAEA Photonuclear CRP
g-033_As_075	TENDL2012	2023	KAERI/NRG	2019	2019 IAEA Photonuclear CRP
g-034_Se_076	TENDL2012	2023	KAERI/NRG	2019	2019 IAEA Photonuclear CRP
g-034_Se_078	TENDL2012	2023	KAERI/NRG	2019	2019 IAEA Photonuclear CRP
g-034_Se_080	TENDL2012	2023	KAERI/NRG	2019	2019 IAEA Photonuclear CRP
g-034_Se_082	TENDL2012	2023	KAERI/NRG	2019	2019 IAEA Photonuclear CRP
g-038_Sr_084	JENDL-5	2023	JAEA	2019	2019 IAEA Photonuclear CRP
g-038_Sr_086	JENDL-5	2023	JAEA	2019	2019 IAEA Photonuclear CRP
g-038_Sr_087	JENDL-5	2023	JAEA	2019	2019 IAEA Photonuclear CRP
g-038_Sr_088	JENDL-5	2023	JAEA	2019	2019 IAEA Photonuclear CRP
g-038_Sr_090	JENDL-5	2023	JAEA	2019	2019 IAEA Photonuclear CRP
g-039_Y_089	2019 Photonuclear CRP	2023	IFIN-HH	2019	2019 IAEA Photonuclear CRP; Fix yields for gammas and residuals
g-040_Zr_090	CENDL/G-3	2023	CNDC	2018	2019 IAEA Photonuclear CRP
g-040_Zr_091	TENDL2012	2023	KAERI/NRG	2019	2019 IAEA Photonuclear CRP
g-040_Zr_092	JENDL-5	2023	JAEA	2019	2019 IAEA Photonuclear CRP
g-040_Zr_093	JENDL-5	2023	JAEA	2019	2019 IAEA Photonuclear CRP
g-040_Zr_094	TENDL2012	2023	KAERI/NRG	2019	2019 IAEA Photonuclear CRP
g-040_Zr_096	JENDL-5	2023	JAEA	2019	2019 IAEA Photonuclear CRP
g-041_Nb_093	JENDL-5	2023	JAEA	2019	2019 IAEA Photonuclear CRP
g-041_Nb_094	JENDL-5	2023	JAEA	2019	2019 IAEA Photonuclear CRP
g-042_Mo_092	JENDL-5	2023	JAEA	2019	2019 IAEA Photonuclear CRP
g-042_Mo_094	JENDL-5	2023	JAEA	2019	2019 IAEA Photonuclear CRP
g-042_Mo_095	JENDL-5	2023	JAEA	2019	2019 IAEA Photonuclear CRP
g-042_Mo_096	JENDL-5	2023	JAEA	2019	2019 IAEA Photonuclear CRP
g-042_Mo_097	JENDL-5	2023	JAEA	2019	2019 IAEA Photonuclear CRP
g-042_Mo_098	JENDL-5	2023	JAEA	2019	2019 IAEA Photonuclear CRP
g-042_Mo_100	JENDL-5	2023	JAEA	2019	2019 IAEA Photonuclear CRP
g-044_Ru_098	JENDL-5	2023	JAEA	2019	2019 IAEA Photonuclear CRP
g-045_Rh_103	2019 Photonuclear CRP	2023	IFIN-HH	2019	2019 IAEA Photonuclear CRP; Fix yields for gammas and residuals
g-046_Pd_102	JENDL-5	2023	JAEA	2019	2019 IAEA Photonuclear CRP
g-046_Pd_104	JENDL-5	2023	JAEA	2019	2019 IAEA Photonuclear CRP
g-046_Pd_105	JENDL-5	2023	JAEA	2019	2019 IAEA Photonuclear CRP
g-046_Pd_106	JENDL-5	2023	JAEA	2019	2019 IAEA Photonuclear CRP
g-046_Pd_107	JENDL-5	2023	JAEA	2019	2019 IAEA Photonuclear CRP
g-046_Pd_108	JENDL-5	2023	JAEA	2019	2019 IAEA Photonuclear CRP
g-046_Pd_110	JENDL-5	2023	JAEA	2019	2019 IAEA Photonuclear CRP
g-047_Ag_107	JENDL-5	2023	JAEA	2019	2019 IAEA Photonuclear CRP
g-047_Ag_108	JENDL-5	2023	JAEA	2019	2019 IAEA Photonuclear CRP
g-047_Ag_109	JENDL-5	2023	JAEA	2019	2019 IAEA Photonuclear CRP
g-048_Cd_106	JENDL-5	2023	JAEA	2019	2019 IAEA Photonuclear CRP
g-048_Cd_108	JENDL-5	2023	JAEA	2019	2019 IAEA Photonuclear CRP
g-048_Cd_110	JENDL-5	2023	JAEA	2019	2019 IAEA Photonuclear CRP
g-048_Cd_111	JENDL-5	2023	JAEA	2019	2019 IAEA Photonuclear CRP
g-048_Cd_112	JENDL-5	2023	JAEA	2019	2019 IAEA Photonuclear CRP
g-048_Cd_113	JENDL-5	2023	JAEA	2019	2019 IAEA Photonuclear CRP
g-048_Cd_114	JENDL-5	2023	JAEA	2019	2019 IAEA Photonuclear CRP
g-048_Cd_116	JENDL-5	2023	JAEA	2019	2019 IAEA Photonuclear CRP
g-049_In_115	TENDL2012	2023	KAERI/NRG	2019	2019 IAEA Photonuclear CRP
g-050_Sn_112	JENDL-5	2023	JAEA	2019	2019 IAEA Photonuclear CRP
g-050_Sn_114	JENDL-5	2023	JAEA	2019	2019 IAEA Photonuclear CRP
g-050_Sn_115	JENDL-5	2023	JAEA	2019	2019 IAEA Photonuclear CRP
g-050_Sn_116	TENDL2012	2023	KAERI/NRG	2019	2019 IAEA Photonuclear CRP
g-050_Sn_117	JENDL-5	2023	JAEA	2019	2019 IAEA Photonuclear CRP
g-050_Sn_118	2019 Photonuclear CRP	2023	CNDC	2017	2019 IAEA Photonuclear CRP
g-050_Sn_119	JENDL-5	2023	JAEA	2019	2019 IAEA Photonuclear CRP
g-050_Sn_120	JENDL-5	2023	JAEA	2019	2019 IAEA Photonuclear CRP
g-050_Sn_122	JENDL-5	2023	JAEA	2019	2019 IAEA Photonuclear CRP
g-050_Sn_124	JENDL-5	2023	JAEA	2019	2019 IAEA Photonuclear CRP
g-051_Sb_121	JENDL-5	2023	JAEA	2019	2019 IAEA Photonuclear CRP
g-051_Sb_123	JENDL-5	2023	JAEA	2019	2019 IAEA Photonuclear CRP
g-052_Te_120	JENDL-5	2023	JAEA	2019	2019 IAEA Photonuclear CRP
g-052_Te_122	JENDL-5	2023	JAEA	2019	2019 IAEA Photonuclear CRP
g-052_Te_123	JENDL-5	2023	JAEA	2019	2019 IAEA Photonuclear CRP
g-052_Te_124	JENDL-5	2023	JAEA	2019	2019 IAEA Photonuclear CRP
g-052_Te_125	JENDL-5	2023	JAEA	2019	2019 IAEA Photonuclear CRP
g-052_Te_126	JENDL-5	2023	JAEA	2019	2019 IAEA Photonuclear CRP
g-052_Te_128	JENDL-5	2023	JAEA	2019	2019 IAEA Photonuclear CRP
g-052_Te_130	JENDL-5	2023	JAEA	2019	2019 IAEA Photonuclear CRP

Continued on the next page

TABLE LI: (continued) Provenance for the photonuclear sublibrary.

File name (.endf)	Source	Last updated	Institution	Year	Comments
g-053_I_127	**JENDL-5**	**2023**	**JAEA**	**2019**	**2019 IAEA Photonuclear CRP**
g-053_I_129	**JENDL-5**	**2023**	**JAEA**	**2019**	**2019 IAEA Photonuclear CRP**
g-054_Xe_132	**JENDL-5**	**2023**	**JAEA**	**2019**	**2019 IAEA Photonuclear CRP**
g-055_Cs_133	**TENDL2012**	**2023**	**KAERI/NRG**	**2019**	**2019 IAEA Photonuclear CRP**
g-055_Cs_135	**JENDL-5**	**2023**	**JAEA**	**2019**	**2019 IAEA Photonuclear CRP**
g-055_Cs_137	**JENDL-5**	**2023**	**JAEA**	**2019**	**2019 IAEA Photonuclear CRP**
g-056_Ba_138	**TENDL2012**	**2023**	**KAERI/NRG**	**2019**	**2019 IAEA Photonuclear CRP**
g-057_La_139	**JENDL-5**	**2023**	**JAEA**	**2019**	**2019 IAEA Photonuclear CRP**
g-058_Ce_140	**TENDL2012**	**2023**	**KAERI/NRG**	**2019**	**2019 IAEA Photonuclear CRP**
g-058_Ce_142	**TENDL2012**	**2023**	**KAERI/NRG**	**2019**	**2019 IAEA Photonuclear CRP**
g-059_Pr_141	**JENDL-5**	**2023**	**JAEA**	**2019**	**2019 IAEA Photonuclear CRP**
g-060_Nd_142	**TENDL2012**	**2023**	**KAERI/NRG**	**2019**	**2019 IAEA Photonuclear CRP**
g-060_Nd_143	**TENDL2012**	**2023**	**KAERI/NRG**	**2019**	**2019 IAEA Photonuclear CRP**
g-060_Nd_144	**TENDL2012**	**2023**	**KAERI/NRG**	**2019**	**2019 IAEA Photonuclear CRP**
g-060_Nd_145	**TENDL2012**	**2023**	**KAERI/NRG**	**2019**	**2019 IAEA Photonuclear CRP**
g-060_Nd_146	**TENDL2012**	**2023**	**KAERI/NRG**	**2019**	**2019 IAEA Photonuclear CRP**
g-060_Nd_148	**TENDL2012**	**2023**	**KAERI/NRG**	**2019**	**2019 IAEA Photonuclear CRP**
g-060_Nd_150	**TENDL2012**	**2023**	**KAERI/NRG**	**2019**	**2019 IAEA Photonuclear CRP**
g-062_Sm_144	**JENDL-5**	**2023**	**JAEA**	**2019**	**2019 IAEA Photonuclear CRP**
g-062_Sm_147	**JENDL-5**	**2023**	**JAEA**	**2019**	**2019 IAEA Photonuclear CRP**
g-062_Sm_148	**JENDL-5**	**2023**	**JAEA**	**2019**	**2019 IAEA Photonuclear CRP**
g-062_Sm_149	**JENDL-5**	**2023**	**JAEA**	**2019**	**2019 IAEA Photonuclear CRP**
g-062_Sm_150	**JENDL-5**	**2023**	**JAEA**	**2019**	**2019 IAEA Photonuclear CRP**
g-062_Sm_151	**JENDL-5**	**2023**	**JAEA**	**2019**	**2019 IAEA Photonuclear CRP**
g-062_Sm_152	**JENDL-5**	**2023**	**JAEA**	**2019**	**2019 IAEA Photonuclear CRP**
g-062_Sm_154	**JENDL-5**	**2023**	**JAEA**	**2019**	**2019 IAEA Photonuclear CRP**
g-063_Eu_153	**TENDL2012**	**2023**	**KAERI/NRG**	**2019**	**2019 IAEA Photonuclear CRP**
g-064_Gd_156	**JENDL-5**	**2023**	**JAEA**	**2019**	**2019 IAEA Photonuclear CRP**
g-064_Gd_157	**JENDL-5**	**2023**	**JAEA**	**2019**	**2019 IAEA Photonuclear CRP**
g-064_Gd_158	**JENDL-5**	**2023**	**JAEA**	**2019**	**2019 IAEA Photonuclear CRP**
g-064_Gd_160	**JENDL-5**	**2023**	**JAEA**	**2019**	**2019 IAEA Photonuclear CRP**
g-065_Tb_158	**JENDL-5**	**2023**	**JAEA**	**2019**	**2019 IAEA Photonuclear CRP**
g-065_Tb_159	**2019 Photonuclear CRP**	**2023**	**IFIN-HH**	**2019**	**2019 IAEA Photonuclear CRP; Fix yields for gammas and residuals**
g-066_Dy_162	**JENDL-5**	**2023**	**JAEA**	**2019**	**2019 IAEA Photonuclear CRP**
g-066_Dy_163	**JENDL-5**	**2023**	**JAEA**	**2019**	**2019 IAEA Photonuclear CRP**
g-067_Ho_165	**2019 Photonuclear CRP**	**2023**	**IFIN-HH**	**2019**	**2019 IAEA Photonuclear CRP; Fix yields for gammas and residuals**
g-068_Er_166	**JENDL-5**	**2023**	**JAEA**	**2019**	**2019 IAEA Photonuclear CRP**
g-068_Er_170	**JENDL-5**	**2023**	**JAEA**	**2019**	**2019 IAEA Photonuclear CRP**
g-069_Tm_169	**2019 Photonuclear CRP**	**2023**	**IFIN-HH**	**2019**	**2019 IAEA Photonuclear CRP; Fix yields for gammas and residuals**
g-071_Lu_175	**TENDL2012**	**2023**	**KAERI/NRG**	**2019**	**2019 IAEA Photonuclear CRP**
g-072_Hf_174	**JENDL-5**	**2023**	**JAEA**	**2019**	**2019 IAEA Photonuclear CRP**
g-072_Hf_176	**JENDL-5**	**2023**	**JAEA**	**2019**	**2019 IAEA Photonuclear CRP**
g-072_Hf_177	**JENDL-5**	**2023**	**JAEA**	**2019**	**2019 IAEA Photonuclear CRP**
g-072_Hf_178	**JENDL-5**	**2023**	**JAEA**	**2019**	**2019 IAEA Photonuclear CRP**
g-072_Hf_179	**JENDL-5**	**2023**	**JAEA**	**2019**	**2019 IAEA Photonuclear CRP**
g-072_Hf_180	**JENDL-5**	**2023**	**JAEA**	**2019**	**2019 IAEA Photonuclear CRP**
g-073_Ta_181	**2019 Photonuclear CRP**	**2023**	**IFIN-HH**	**2019**	**2019 IAEA Photonuclear CRP; Fix yields for gammas and residuals**
g-074_W_180	CENDL/G	2023	CNDC	1997	IAEA Photonuclear Data Library
g-074_W_182	ENDF/B-VII.0	2023	CNDC	1997	
g-074_W_183	CENDL/G	2023	CNDC	1997	IAEA Photonuclear Data Library
g-074_W_184	LANL150u	2023	LANL	1998	IAEA Photonuclear Data Library
g-074_W_186	ENDF/B-VII.0	2023	CNDC	1997	
g-075_Re_185	**JENDL-5**	**2024**	**JAEA**	**2019**	**2019 IAEA Photonuclear CRP; Minor fixes**
g-075_Re_187	**JENDL-5**	**2024**	**JAEA**	**2019**	**2019 IAEA Photonuclear CRP; Minor fixes**
g-076_Os_186	**TENDL2012**	**2023**	**KAERI/NRG**	**2019**	**2019 IAEA Photonuclear CRP**
g-076_Os_188	**TENDL2012**	**2023**	**KAERI/NRG**	**2019**	**2019 IAEA Photonuclear CRP**
g-076_Os_189	**TENDL2012**	**2023**	**KAERI/NRG**	**2019**	**2019 IAEA Photonuclear CRP**
g-076_Os_190	**TENDL2012**	**2023**	**KAERI/NRG**	**2019**	**2019 IAEA Photonuclear CRP**
g-076_Os_192	**TENDL2012**	**2023**	**KAERI/NRG**	**2019**	**2019 IAEA Photonuclear CRP**
g-078_Pt_194	**JENDL-5**	**2024**	**JAEA**	**2019**	**2019 IAEA Photonuclear CRP; Minor fixes**
g-079_Au_197	**JENDL-5**	**2024**	**JAEA**	**2019**	**2019 IAEA Photonuclear CRP; Minor fixes**
g-082_Pb_206	LANL150u	2023	LANL	1998	2019 IAEA Photonuclear CRP
g-082_Pb_207	LANL150u	2023	LANL	1998	2019 IAEA Photonuclear CRP

Continued on the next page

TABLE LI: (continued) Provenance for the photonuclear sublibrary.

File name (.endf)	Source	Last updated	Institution	Year	Comments
g-082_Pb_208	LANL150u	2023	LANL	1998	2019 IAEA Photonuclear CRP
g-083_Bi_209	**TENDL2012**	**2023**	**KAERI/NRG**	**2019**	**2019 IAEA Photonuclear CRP**
g-088_Ra_226	**JENDL-5**	**2024**	**JAEA**	**2019**	**2019 IAEA Photonuclear CRP; Minor fixes**
g-090_Th_232	**JENDL-5**	**2024**	**JAEA**	**2019**	**2019 IAEA Photonuclear CRP; Minor fixes**
g-092_U_233	**JENDL-5**	**2024**	**JAEA**	**2019**	**2019 IAEA Photonuclear CRP; Minor fixes**
g-092_U_234	**JENDL-5**	**2024**	**JAEA**	**2019**	**2019 IAEA Photonuclear CRP; Minor fixes**
g-092_U_235	ENDF/B-VII.0	2023	LANL	2005	
g-092_U_236	**JENDL-5**	**2024**	**JAEA**	**2019**	**2019 IAEA Photonuclear CRP; Minor fixes**
g-092_U_238	ENDF/B-VII.0	2023	LANL	2005	
g-093_Np_237	ENDF/B-VII.0	2023	LANL	2005	
g-094_Pu_238	**JENDL-5**	**2024**	**JAEA**	**2019**	**2019 IAEA Photonuclear CRP; Minor fixes**
g-094_Pu_239	ENDF/B-VII.0	2023	LANL	2005	
g-094_Pu_240	ENDF/B-VII.0	2024	LANL	2005	Minor fixes
g-094_Pu_241	**JENDL-5**	**2024**	**JAEA**	**2019**	**2019 IAEA Photonuclear CRP; Minor fixes**
g-094_Pu_242	**JENDL-5**	**2023**	**JAEA**	**2019**	
g-095_Am_241	ENDF/B-VII.0	2024	LANL	2005	Minor fixes

TABLE LII: Summary of the origins of and recent changes to the neutron-induced fission yields sublibrary. For each file we list the library source, the year when the last significant evaluation effort or impactful modification was performed, the institution responsible for its most recent evaluation and the corresponding year said evaluation was completed. We also provide additional comments, where relevant. Evaluations updated in ENDF/B-VIII.1 are in bold.

File name (.endf)	Source	Last updated	Institution	Year	Comments
nfy-090_Th_227	**ENDF/B-VI.0**	**2023**	**LANL**	**1989**	**England Rider evaluation (ENDF-349); Corrected uncertainties**
nfy-090_Th_229	**ENDF/B-VI.0**	**2023**	**LANL**	**1989**	**England Rider evaluation (ENDF-349); Corrected uncertainties**
nfy-090_Th_232	**ENDF/B-VI.0**	**2023**	**LANL**	**1989**	**England Rider evaluation (ENDF-349); Corrected uncertainties**
nfy-091_Pa_231	**ENDF/B-VI.0**	**2023**	**LANL**	**1989**	**England Rider evaluation (ENDF-349); Corrected uncertainties**
nfy-092_U_232	**ENDF/B-VI.0**	**2023**	**LANL**	**1989**	**England Rider evaluation (ENDF-349); Corrected uncertainties**
nfy-092_U_233	**ENDF/B-VI.0**	**2023**	**LANL**	**1989**	**England Rider evaluation (ENDF-349); Corrected uncertainties**
nfy-092_U_234	**ENDF/B-VI.0**	**2023**	**LANL**	**1989**	**England Rider evaluation (ENDF-349); Corrected uncertainties**
nfy-092_U_235	**ENDF/B-VI.0**	**2023**	**LANL**	**1989**	**England Rider evaluation (ENDF-349); Corrected uncertainties**
nfy-092_U_236	**ENDF/B-VI.0**	**2023**	**LANL**	**1989**	**England Rider evaluation (ENDF-349); Corrected uncertainties**
nfy-092_U_237	**ENDF/B-VI.0**	**2023**	**LANL**	**1989**	**England Rider evaluation (ENDF-349); Corrected uncertainties**
nfy-092_U_238	**ENDF/B-VI.0**	**2023**	**LANL**	**1989**	**England Rider evaluation (ENDF-349); Corrected uncertainties**
nfy-093_Np_237	**ENDF/B-VI.0**	**2023**	**LANL**	**1989**	**England Rider evaluation (ENDF-349); Corrected uncertainties**
nfy-093_Np_238	**ENDF/B-VI.0**	**2023**	**LANL**	**1989**	**England Rider evaluation (ENDF-349); Corrected uncertainties**
nfy-094_Pu_238	**ENDF/B-VI.0**	**2023**	**LANL**	**1989**	**England Rider evaluation (ENDF-349); Corrected uncertainties**
nfy-094_Pu_239	**ENDF/B-VII.1**	**2023**	**LANL**	**2011**	**Revised from England Rider; Corrected uncertainties**
nfy-094_Pu_240	**ENDF/B-VI.0**	**2023**	**LANL**	**1989**	**England Rider evaluation (ENDF-349); Corrected uncertainties**
nfy-094_Pu_241	**ENDF/B-VI.0**	**2024**	**LANL**	**1989**	**England Rider evaluation (ENDF-349); Corrected uncertainties**
nfy-094_Pu_242	**ENDF/B-VI.0**	**2023**	**LANL**	**1989**	**England Rider evaluation (ENDF-349); Corrected uncertainties**
nfy-095_Am_241	**ENDF/B-VI.0**	**2023**	**LANL**	**1989**	**England Rider evaluation (ENDF-349); Corrected uncertainties**
nfy-095_Am_242m1	**ENDF/B-VI.0**	**2023**	**LANL**	**1989**	**England Rider evaluation (ENDF-349); Corrected uncertainties**
nfy-095_Am_243	**ENDF/B-VI.0**	**2023**	**LANL**	**1989**	**England Rider evaluation (ENDF-349); Corrected uncertainties**
nfy-096_Cm_242	**ENDF/B-VI.0**	**2023**	**LANL**	**1989**	**England Rider evaluation (ENDF-349); Corrected uncertainties**
nfy-096_Cm_243	**ENDF/B-VI.0**	**2023**	**LANL**	**1989**	**England Rider evaluation (ENDF-349); Corrected uncertainties**
nfy-096_Cm_244	**ENDF/B-VI.0**	**2023**	**LANL**	**1989**	**England Rider evaluation (ENDF-349); Corrected uncertainties**
nfy-096_Cm_245	**ENDF/B-VI.0**	**2023**	**LANL**	**1989**	**England Rider evaluation (ENDF-349); Corrected uncertainties**
nfy-096_Cm_246	**ENDF/B-VI.0**	**2023**	**LANL**	**1989**	**England Rider evaluation (ENDF-349); Corrected uncertainties**
nfy-096_Cm_248	**ENDF/B-VI.0**	**2023**	**LANL**	**1989**	**England Rider evaluation (ENDF-349); Corrected uncertainties**
nfy-098_Cf_249	**ENDF/B-VI.0**	**2023**	**LANL**	**1989**	**England Rider evaluation (ENDF-349); Corrected uncertainties**
nfy-098_Cf_251	**ENDF/B-VI.0**	**2023**	**LANL**	**1989**	**England Rider evaluation (ENDF-349); Corrected uncertainties**
nfy-099_Es_254	**ENDF/B-VI.0**	**2023**	**LANL**	**1989**	**England Rider evaluation (ENDF-349); Corrected uncertainties**
nfy-100_Fm_255	**ENDF/B-VI.0**	**2023**	**LANL**	**1989**	**England Rider evaluation (ENDF-349); Corrected uncertainties**

TABLE LIII: Summary of the origins of and recent changes to the spontaneous fission yields sublibrary. For each file we list the library source, the year when the last significant evaluation effort or impactful modification was performed, the institution responsible for its most recent evaluation and the corresponding year said evaluation was completed. We also provide additional comments, where relevant. Evaluations updated in ENDF/B-VIII.1 are in bold.

File name (.endf)	Source	Last updated	Institution	Year	Comments
sfy-092_U_238	**ENDF/B-VI.0**	**2023**	**LANL**	**1989**	**England Rider evaluation (ENDF-349); Corrected uncertainties**

Continued on the next page

TABLE LIII: (continued) Provenance for the spontaneous fission yields sublibrary.

File name (.endf)	Source	Last updated	Institution	Year	Comments
sfy-096_Cm_244	**ENDF/B-VI.0**	**2023**	**LANL**	**1989**	**England Rider evaluation (ENDF-349); Corrected uncertainties**
sfy-096_Cm_246	**ENDF/B-VI.0**	**2023**	**LANL**	**1989**	**England Rider evaluation (ENDF-349); Corrected uncertainties**
sfy-096_Cm_248	**ENDF/B-VI.0**	**2023**	**LANL**	**1989**	**England Rider evaluation (ENDF-349); Corrected uncertainties**
sfy-098_Cf_250	**ENDF/B-VI.0**	**2023**	**LANL**	**1989**	**England Rider evaluation (ENDF-349); Corrected uncertainties**
sfy-098_Cf_252	**ENDF/B-VI.0**	**2023**	**LANL**	**1989**	**England Rider evaluation (ENDF-349); Corrected uncertainties**
sfy-099_Es_253	**ENDF/B-VI.0**	**2023**	**LANL**	**1989**	**England Rider evaluation (ENDF-349); Corrected uncertainties**
sfy-100_Fm_254	**ENDF/B-VI.0**	**2023**	**LANL**	**1989**	**England Rider evaluation (ENDF-349); Corrected uncertainties**
sfy-100_Fm_256	**ENDF/B-VI.0**	**2023**	**LANL**	**1989**	**England Rider evaluation (ENDF-349); Corrected uncertainties**

TABLE LIV: Summary of the origins of and recent changes to the protons sublibrary. For each file we list the library source, the year when the last significant evaluation effort or impactful modification was performed, the institution responsible for its most recent evaluation and the corresponding year said evaluation was completed. We also provide additional comments, where relevant. Evaluations updated in ENDF/B-VIII.1 are in bold.

File name (.endf)	Source	Last updated	Institution	Year	Comments
p-001_H_001	ENDF/B-VI.6	2006	LANL	1998	R-matrix analysis
p-001_H_002	ENDF/B-VI.6	2006	LANL/ECN	1997	R-matrix analysis; primary gamma fix
p-001_H_003	ENDF/B-VII.0	2006	LANL	2001	R-matrix analysis
p-002_He_003	ENDF/B-VII.0	2006	LANL	1983	R-matrix analysis
p-002_He_004	**ECPL**	**2024**	**LLNL**	**1999**	**Minor corrections**
p-003_Li_006	ENDF/B-VII.0	2006	LANL	2001	R-matrix analysis
p-003_Li_007	ENDF/B-VII.0	2016	LANL/LLNL	2010	R-matrix analysis; modifications from ENDL2009
p-004_Be_009	ENDF/B-VI.0	2006	LANL	1988	LA-11753-MS
p-005_B_010	ENDF/B-VII.0	2006	LANL	2005	R-matrix analysis
p-006_C_012	ENDF/B-VI.6	2006	LANL/ECN	1996	LA150
p-006_C_013	**ENDF/B-VII.0**	**2024**	**LANL**	**2004**	**R-matrix analysis; Minor corrections**
p-007_N_014	ENDF/B-VI.6	2006	LANL/ECN	1997	LA150
p-008_O_016	ENDF/B-VI.6	2006	LANL/ECN	1996	LA150
p-013_Al_027	ENDF/B-VII.0	2006	LANL/ECN	1997	LA150; MF6/MT5 correction
p-014_Si_028	ENDF/B-VII.0	2016	LANL/ECN	1997	LA150; MF6/MT5 correction
p-014_Si_029	ENDF/B-VII.0	2006	LANL/ECN	1997	LA150; MF6/MT5 correction
p-014_Si_030	ENDF/B-VII.0	2006	LANL/ECN	1997	LA150; MF6/MT5 correction
p-015_P_031	ENDF/B-VII.0	2006	LANL/ECN	1997	LA150; MF6/MT5 correction
p-020_Ca_040	ENDF/B-VII.0	2006	LANL/ECN	1997	LA150; MF6/MT5 correction
p-024_Cr_050	ENDF/B-VII.0	2006	LANL/ECN	1997	LA150; MF6/MT5 correction
p-024_Cr_052	ENDF/B-VII.0	2006	LANL	1997	LA150; MF6/MT5 correction
p-024_Cr_053	ENDF/B-VII.0	2006	LANL/ECN	1997	LA150; MF6/MT5 correction
p-024_Cr_054	ENDF/B-VII.0	2006	LANL/ECN	1997	LA150; MF6/MT5 correction
p-026_Fe_054	ENDF/B-VII.0	2006	LANL/ECN	1996	LA150; MF6/MT5 correction
p-026_Fe_056	ENDF/B-VII.0	2006	LANL/ECN	1996	LA150; MF6/MT5 correction
p-026_Fe_057	ENDF/B-VII.0	2006	LANL/ECN	1996	LA150; MF6/MT5 correction
p-028_Ni_058	ENDF/B-VII.0	2006	LANL/ECN	1997	LA150; MF6/MT5 correction
p-028_Ni_060	ENDF/B-VII.0	2006	LANL/ECN	1997	LA150; MF6/MT5 correction
p-028_Ni_061	ENDF/B-VII.0	2006	LANL/ECN	1997	LA150; MF6/MT5 correction
p-028_Ni_062	ENDF/B-VII.0	2006	LANL/ECN	1997	LA150; MF6/MT5 correction
p-028_Ni_064	ENDF/B-VII.0	2006	LANL/ECN	1997	LA150; MF6/MT5 correction
p-029_Cu_063	ENDF/B-VII.0	2006	LANL/ECN	1998	LA150; MF6/MT5 correction
p-029_Cu_065	ENDF/B-VII.0	2006	LANL/ECN	1998	LA150; MF6/MT5 correction
p-041_Nb_093	ENDF/B-VII.0	2006	LANL	1997	LA150; MF6/MT5 correction
p-074_W_182	ENDF/B-VI.6	2006	LANL	1996	LA150
p-074_W_183	ENDF/B-VII.0	2006	LANL	1996	LA150; MF6/MT5 correction
p-074_W_184	ENDF/B-VII.0	2006	LANL	1996	LA150; MF6/MT5 correction
p-074_W_186	ENDF/B-VI.6	2006	LANL	1996	LA150
p-080_Hg_196	ENDF/B-VII.0	2006	LANL/JAERI	1998	LA150; MF6/MT5 correction
p-080_Hg_198	ENDF/B-VII.0	2006	LANL/JAERI	1998	LA150; MF6/MT5 correction
p-080_Hg_199	ENDF/B-VII.0	2006	LANL/JAERI	1998	LA150; MF6/MT5 correction
p-080_Hg_200	ENDF/B-VII.0	2006	LANL/JAERI	1998	LA150; MF6/MT5 correction
p-080_Hg_201	ENDF/B-VII.0	2006	LANL/JAERI	1998	LA150; MF6/MT5 correction
p-080_Hg_202	ENDF/B-VII.0	2006	LANL/JAERI	1998	LA150; MF6/MT5 correction
p-080_Hg_204	ENDF/B-VII.0	2006	LANL/JAERI	1998	LA150; MF6/MT5 correction
p-082_Pb_206	ENDF/B-VI.6	2006	LANL/ECN	1996	LA150
p-082_Pb_207	ENDF/B-VII.0	2006	LANL/ECN	1996	LA150; MF6/MT5 correction
p-082_Pb_208	ENDF/B-VII.0	2006	LANL/ECN	1996	LA150; MF6/MT5 correction
p-083_Bi_209	ENDF/B-VI.7	2006	LANL	1998	LA150

TABLE LV. Summary of the origins of and recent changes to the deuterons sublibrary. For each file we list the library source, the year when the last significant evaluation effort or impactful modification was performed, the institution responsible for its most recent evaluation and the corresponding year said evaluation was completed. We also provide additional comments, where relevant. Evaluations updated in ENDF/B-VIII.1 are in bold.

File name (.endf)	Source	Last updated	Institution	Year	Comments
d-001_H_002	ENDF/B-VII.0	2024	LLNL/LANL	1992	Updated ECPL
d-001_H_003	**ENDF/B-VIII.1**	**2023**	**LANL**	**2023**	**R-matrix analysis**
d-002_He_003	**ENDF/B-VIII.1**	**2024**	**LANL**	**2020**	**R-matrix analysis**
d-002_He_004	ENDF/B-VII.0	2024	LANL	2001	R-matrix analysis
d-003_Li_006	**ENDF/B-VIII.1**	**2024**	**LANL**	**2020**	**R-matrix analysis**
d-003_Li_007	ENDL2010	2024	LLNL	2010	Updated ECPL

TABLE LVI. Summary of the origins of and recent changes to the tritons sublibrary. For each file we list the library source, the year when the last significant evaluation effort or impactful modification was performed, the institution responsible for its most recent evaluation and the corresponding year said evaluation was completed. We also provide additional comments, where relevant. Evaluations updated in ENDF/B-VIII.1 are in bold.

File name (.endf)	Source	Last updated	Institution	Year	Comments
t-001_H_003	ENDF/B-VII.0	2006	LANL	2001	R-matrix analysis
t-002_He_003	**ENDF/B-VII.0**	**2023**	**LANL**	**2001**	**R-matrix analysis**
t-002_He_004	**ECPL**	**2023**	**LLNL**	**1999**	
t-003_Li_006	**ENDF/B-VII.0**	**2023**	**LANL**	**2001**	**R-matrix analysis**
t-003_Li_007	ENDL2011	2016	LLNL	2016	Updated ECPL

TABLE LVII. Summary of the origins of and recent changes to the helions (^{3}He) sublibrary. For each file we list the library source, the year when the last significant evaluation effort or impactful modification was performed, the institution responsible for its most recent evaluation and the corresponding year said evaluation was completed. We also provide additional comments, where relevant. Evaluations updated in ENDF/B-VIII.1 are in bold.

File name (.endf)	Source	Last updated	Institution	Year	Comments
h-002_He_003	ENDL2011	2016	LLNL/LANL	2010	Updated ENDF/B-VII.0
h-002_He_004	**ENDF/B-VIII.1**	**2024**	**LLNL/INDEN**	**2022**	**R-matrix analysis**
h-003_Li_006	**ENDF/B-VII.0+ECPL**	**2024**	**LANL/LLNL**	**2002**	**R-matrix analysis**
h-003_Li_007	**ECPL**	**2024**	**LLNL**	**1985**	

TABLE LVIII. Summary of the origins of and recent changes to the alphas (^{4}He) sublibrary. For each file we list the library source, the year when the last significant evaluation effort or impactful modification was performed, the institution responsible for its most recent evaluation and the corresponding year said evaluation was completed. We also provide additional comments, where relevant. Evaluations updated in ENDF/B-VIII.1 are in bold.

File name (.endf)	Source	Last updated	Institution	Year	Comments
a-002_He_004	**ENDF/B-VII.1**	**2024**	**LANL/LLNL**	**2010**	**R-matrix analysis**
a-003_Li_006	ECPL	2024	LLNL	1985	Minor revisions
a-004_Be_009	ENDF/B-VIII.1	2024	NNL	2018	Based on JENDL/AN-2005
a-008_O_017	ENDF/B-VIII.1	2024	NNL	2018	Based on JENDL/AN-2005
a-008_O_018	**ENDF/B-VIII.1**	**2024**	**NNL**	**2018**	**Based on JENDL/AN-2005**

Appendix B: Summary of criticality k_{eff} C/E Changes Between ENDF/B-VIII.0 and ENDF/B-VIII.1 validation results

The calculated results for multiple benchmark suites presented in Section XIV A 2 are listed in Table LIX. The benchmark name listed in this table is the name used in the International Criticality Safety Benchmark Evaluation Project (ICSBEP) Handbook [158]. The results include the use of the following scattering kernels: (1) water (h-h2o), (2) heavy water (d-d2o), (3) polyethylene (h-poly), (4) beryllium metal (be-met), (5) beryllium-oxide (be-beo, o-beo), and (6) reactor graphite (grph, grph10). The "S_d" versions of beryllium metal and reactor graphite scattering kernels were used. In the table, benchmark names include an "s" for simplified models and "d" for detailed models (e.g., the Jezebel benchmark PU-MET-FAST-001 includes simplified "PU-MET-FAST-001-001s" and detailed "PU-MET-FAST-001-001-d-rev5" models).

For the convenience of potential users of the data in Table LIX, we provide the corresponding data in a comma-separated-value (CSV) formatted file in the ENDF/B-VIII.1 release page hosted by the NNDC [19].

TABLE LIX: Complete list of validation results of ENDF/B-VIII.1 in criticality benchmarks performed by Los Alamos National Laboratory.

Benchmark	E	unc.$_E$	ENDF/B-VIII.1			ENDF/B-VIII.0		
			C	unc.$_C$	C/E	C	unc.$_C$	C/E
HEU-MET-FAST-101-001	1.00065	0.00078	1.00002	0.00002	0.99937	1.00041	0.00002	0.99976
HEU-MET-FAST-101-002	1.00345	0.00079	1.00285	0.00002	0.99940	1.00321	0.00002	0.99976
HEU-MET-FAST-101-003	1.00017	0.00081	0.99974	0.00002	0.99957	1.00016	0.00002	0.99999
HEU-MET-FAST-101-004	1.00048	0.00076	0.99991	0.00002	0.99943	1.00027	0.00002	0.99979
HEU-MET-FAST-101-005	1.00189	0.00076	1.00135	0.00002	0.99946	1.00175	0.00002	0.99987
HEU-MET-FAST-104-001-d	1.00072	0.00118	1.00013	0.00001	0.99941	1.00023	0.00002	0.99951
HEU-MET-FAST-104-002-d	1.00091	0.00098	0.99998	0.00002	0.99907	1.00013	0.00002	0.99922
HEU-MET-INTER-006-001-rev4	0.99770	0.00080	0.99750	0.00001	0.99980	0.99578	0.00001	0.99807
HEU-MET-INTER-006-002-rev4	1.00010	0.00080	1.00122	0.00001	1.00112	1.00023	0.00001	1.00013
HEU-MET-INTER-006-003-rev4	1.00150	0.00090	1.00335	0.00001	1.00184	1.00317	0.00001	1.00167
HEU-MET-INTER-006-004-rev4	1.00160	0.00080	1.00440	0.00001	1.00279	1.00537	0.00001	1.00376
HEU-MET-INTER-011-001	1.00107	0.00101	1.00762	0.00002	1.00654	1.01850	0.00002	1.01742
HEU-MET-INTER-011-002	1.00008	0.00123	1.00670	0.00002	1.00662	1.01841	0.00002	1.01833
HEU-MET-INTER-011-003	1.00143	0.00115	1.00543	0.00002	1.00399	1.01803	0.00002	1.01658
HEU-MET-INTER-011-004	1.00061	0.00097	1.00492	0.00002	1.00431	1.01824	0.00002	1.01762
HEU-MET-INTER-011-005	1.00007	0.00095	1.00237	0.00002	1.00230	1.01611	0.00002	1.01604
PU-MET-FAST-001-001-d-rev5	0.99999	0.00110	1.00003	0.00002	1.00004	1.00049	0.00002	1.00050
PU-MET-FAST-001-002-d-rev5	1.00016	0.00110	1.00057	0.00002	1.00041	1.00104	0.00002	1.00088
PU-MET-FAST-001-003-d-rev5	1.00020	0.00110	1.00030	0.00002	1.00010	1.00066	0.00002	1.00046
PU-MET-FAST-001-004-d-rev5	1.00128	0.00110	1.00130	0.00002	1.00002	1.00171	0.00002	1.00043
PU-MET-FAST-038-001-rev0	1.00070	0.00190	1.00129	0.00003	1.00059	1.00087	0.00003	1.00017
PU-MET-FAST-047-001	1.00067	0.00186	1.00370	0.00002	1.00303	1.00137	0.00002	1.00069
PU-MET-FAST-047-002	1.00050	0.00186	1.00346	0.00002	1.00295	1.00115	0.00002	1.00065
PU-MET-FAST-047-003	1.00028	0.00186	1.00314	0.00002	1.00286	1.00087	0.00002	1.00059
PU-MET-MIXED-002-001-d-rev1	1.00073	0.00260	1.00222	0.00008	1.00149	1.00321	0.00008	1.00247
PU-MET-MIXED-002-002-d-rev1	1.00024	0.00236	0.99805	0.00009	0.99781	1.00045	0.00009	1.00021
PU-MET-MIXED-002-003-d-rev1	1.00072	0.00220	1.00745	0.00009	1.00672	1.01110	0.00009	1.01037
PU-MET-MIXED-002-004-d-rev1	1.00083	0.00287	1.00066	0.00009	0.99983	1.00337	0.00009	1.00254
PU-MET-MIXED-002-005-d-rev1	0.99940	0.00193	1.00348	0.00009	1.00408	1.00568	0.00009	1.00628
PU-MET-MIXED-003-001-d-rev0	0.99953	0.00195	1.00281	0.00007	1.00329	1.00928	0.00007	1.00975
PU-MET-MIXED-003-002-d-rev0	0.99938	0.00154	1.00023	0.00007	1.00085	1.00765	0.00008	1.00827
PU-MET-MIXED-003-003-d-rev0	1.00008	0.00154	0.99748	0.00008	0.99740	1.00726	0.00008	1.00718
PU-MET-MIXED-003-004-d-rev0	1.00078	0.00142	0.99538	0.00008	0.99460	1.00290	0.00008	1.00212
PU-MET-MIXED-003-005-d-rev0	0.99871	0.00121	0.99515	0.00008	0.99644	0.99965	0.00008	1.00094
HEU-MET-FAST-001-001	1.00000	0.00100	0.99988	0.00008	0.99988	1.00005	0.00008	1.00005
HEU-MET-FAST-002-002	1.00000	0.00300	1.00026	0.00009	1.00026	1.00012	0.00009	1.00012
HEU-MET-FAST-002-003	1.00000	0.00300	0.99846	0.00009	0.99846	0.99842	0.00009	0.99842
HEU-MET-FAST-002-004	1.00000	0.00300	0.99757	0.00009	0.99757	0.99772	0.00009	0.99772
HEU-MET-FAST-002-005	1.00000	0.00300	0.99784	0.00009	0.99784	0.99782	0.00009	0.99782
HEU-MET-FAST-002-006	1.00000	0.00300	0.99918	0.00009	0.99918	0.99923	0.00009	0.99923
HEU-MET-FAST-003-001	1.00000	0.00500	0.99301	0.00009	0.99301	0.99303	0.00009	0.99303
HEU-MET-FAST-003-002	1.00000	0.00500	0.99208	0.00009	0.99208	0.99214	0.00009	0.99214
HEU-MET-FAST-003-003	1.00000	0.00500	0.99672	0.00009	0.99672	0.99669	0.00009	0.99669
HEU-MET-FAST-003-004	1.00000	0.00300	0.99489	0.00009	0.99489	0.99481	0.00009	0.99481
HEU-MET-FAST-003-005	1.00000	0.00300	0.99924	0.00009	0.99924	0.99939	0.00009	0.99939
HEU-MET-FAST-003-006	1.00000	0.00300	0.99957	0.00009	0.99957	0.99972	0.00009	0.99972
HEU-MET-FAST-003-007	1.00000	0.00300	1.00015	0.00009	1.00015	1.00029	0.00009	1.00029
HEU-MET-FAST-003-008	1.00000	0.00500	1.00029	0.00009	1.00029	1.00046	0.00009	1.00046
HEU-MET-FAST-003-009	1.00000	0.00500	1.00035	0.00009	1.00035	1.00055	0.00009	1.00055
HEU-MET-FAST-003-010	1.00000	0.00500	1.00359	0.00009	1.00359	1.00381	0.00009	1.00381
HEU-MET-FAST-003-011	1.00000	0.00500	1.00833	0.00009	1.00833	1.00851	0.00009	1.00851
HEU-MET-FAST-003-012	1.00000	0.00300	0.99909	0.00009	0.99909	0.99948	0.00009	0.99948

Continued on the next page

TABLE LIX: (continued) ENDF-6 ENDF/B-VIII.1 criticality validation.

Benchmark	E	unc.$_E$	ENDF/B-VIII.1			ENDF/B-VIII.0		
			C	unc.$_C$	C/E	C	unc.$_C$	C/E
HEU-MET-FAST-004-001	1.00200	0.00000	1.00233	0.00011	1.00033	1.00227	0.00011	1.00027
HEU-MET-FAST-005-001	1.00000	0.00360	0.99586	0.00009	0.99586	0.99565	0.00009	0.99565
HEU-MET-FAST-005-002	1.00070	0.00360	0.99732	0.00010	0.99662	0.99784	0.00010	0.99714
HEU-MET-FAST-005-003	0.99960	0.00360	0.99918	0.00010	0.99958	0.99945	0.00010	0.99985
HEU-MET-FAST-005-004	0.99890	0.00360	0.99227	0.00010	0.99336	0.99275	0.00010	0.99384
HEU-MET-FAST-005-005	0.99800	0.00360	0.99784	0.00010	0.99983	0.99799	0.00010	0.99999
HEU-MET-FAST-005-006	0.99870	0.00360	0.99666	0.00009	0.99796	0.99708	0.00009	0.99838
HEU-MET-FAST-007-001	0.99500	0.00240	0.99328	0.00009	0.99827	0.99327	0.00009	0.99826
HEU-MET-FAST-007-002	0.99640	0.00140	0.99839	0.00010	1.00200	0.99867	0.00009	1.00228
HEU-MET-FAST-007-003	0.99900	0.00130	1.00011	0.00010	1.00111	1.00007	0.00010	1.00107
HEU-MET-FAST-007-004	0.99480	0.00130	0.99834	0.00010	1.00356	0.99864	0.00010	1.00386
HEU-MET-FAST-007-005	0.99780	0.00180	1.00069	0.00010	1.00290	1.00090	0.00010	1.00311
HEU-MET-FAST-007-006	1.00060	0.00130	1.00599	0.00010	1.00539	1.00566	0.00010	1.00506
HEU-MET-FAST-007-007	0.99740	0.00140	1.00190	0.00010	1.00451	1.00204	0.00010	1.00465
HEU-MET-FAST-007-008	0.99730	0.00130	1.00017	0.00010	1.00287	1.00008	0.00010	1.00279
HEU-MET-FAST-007-009	0.99950	0.00560	1.00381	0.00010	1.00431	1.00362	0.00010	1.00412
HEU-MET-FAST-007-010	0.99810	0.00120	1.00020	0.00011	1.00210	0.99944	0.00011	1.00134
HEU-MET-FAST-007-011	0.99580	0.00130	0.99942	0.00012	1.00363	0.99853	0.00012	1.00274
HEU-MET-FAST-007-012	0.99320	0.00120	0.99461	0.00012	1.00142	0.99356	0.00012	1.00036
HEU-MET-FAST-007-013	0.99900	0.00120	1.00012	0.00012	1.00112	0.99924	0.00012	1.00024
HEU-MET-FAST-007-014	0.99640	0.00120	0.99867	0.00012	1.00228	0.99754	0.00012	1.00114
HEU-MET-FAST-007-015	0.99590	0.00120	0.99680	0.00012	1.00091	0.99604	0.00012	1.00014
HEU-MET-FAST-007-016	0.99690	0.00120	0.99741	0.00012	1.00051	0.99665	0.00012	0.99975
HEU-MET-FAST-007-017	0.99530	0.00120	0.99638	0.00013	1.00109	0.99479	0.00012	0.99949
HEU-MET-FAST-007-018	0.99720	0.00120	0.99874	0.00013	1.00154	0.99711	0.00013	0.99991
HEU-MET-FAST-007-019	0.99560	0.00150	0.99664	0.00009	1.00105	0.99690	0.00009	1.00131
HEU-MET-FAST-007-020	0.99500	0.00170	0.99829	0.00010	1.00330	0.99838	0.00010	1.00340
HEU-MET-FAST-007-021	0.99560	0.00180	0.99892	0.00010	1.00334	0.99913	0.00010	1.00355
HEU-MET-FAST-007-022	0.99630	0.00190	0.99993	0.00010	1.00364	0.99993	0.00010	1.00364
HEU-MET-FAST-007-023	0.99620	0.00170	0.99932	0.00011	1.00313	0.99898	0.00011	1.00279
HEU-MET-FAST-007-024	0.99700	0.00180	0.99961	0.00011	1.00262	0.99920	0.00011	1.00221
HEU-MET-FAST-007-025	0.99590	0.00180	0.99824	0.00011	1.00235	0.99785	0.00011	1.00196
HEU-MET-FAST-007-026	0.99660	0.00170	0.99851	0.00011	1.00192	0.99815	0.00011	1.00156
HEU-MET-FAST-007-035	1.00030	0.00180	0.99961	0.00011	0.99931	0.99906	0.00011	0.99876
HEU-MET-FAST-007-036	0.99990	0.00070	1.00128	0.00011	1.00138	1.00123	0.00012	1.00133
HEU-MET-FAST-007-037	0.99880	0.00080	1.00043	0.00012	1.00163	1.00009	0.00011	1.00129
HEU-MET-FAST-007-038	1.00000	0.00080	1.00185	0.00012	1.00185	1.00149	0.00011	1.00149
HEU-MET-FAST-007-039	1.00180	0.00140	1.00439	0.00012	1.00258	1.00366	0.00011	1.00186
HEU-MET-FAST-007-040	1.00130	0.00080	1.00485	0.00012	1.00355	1.00431	0.00011	1.00301
HEU-MET-FAST-007-041	0.99940	0.00090	1.00015	0.00012	1.00075	0.99922	0.00012	0.99982
HEU-MET-FAST-007-042	1.00160	0.00090	1.00255	0.00012	1.00095	1.00127	0.00012	0.99967
HEU-MET-FAST-007-043	0.99980	0.00080	1.00035	0.00012	1.00055	0.99818	0.00012	0.99838
HEU-MET-FAST-008-001	0.99890	0.00160	0.99567	0.00009	0.99676	0.99544	0.00009	0.99654
HEU-MET-FAST-009-001	0.99920	0.00150	0.99612	0.00009	0.99692	0.99619	0.00009	0.99699
HEU-MET-FAST-009-002	0.99920	0.00150	0.99524	0.00009	0.99604	0.99506	0.00009	0.99586
HEU-MET-FAST-010-001	0.99920	0.00150	0.99761	0.00009	0.99841	0.99777	0.00009	0.99857
HEU-MET-FAST-010-002	0.99920	0.00150	0.99691	0.00009	0.99771	0.99717	0.00009	0.99797
HEU-MET-FAST-011-001	0.99890	0.00150	0.99686	0.00011	0.99796	0.99690	0.00011	0.99800
HEU-MET-FAST-012-001	0.99920	0.00180	0.99806	0.00009	0.99886	0.99802	0.00009	0.99882
HEU-MET-FAST-013-001	0.99900	0.00150	0.99899	0.00009	0.99999	0.99867	0.00009	0.99967
HEU-MET-FAST-014-001	0.99890	0.00170	0.99531	0.00009	0.99640	0.99516	0.00009	0.99626
HEU-MET-FAST-015-001	0.99960	0.00170	0.99472	0.00009	0.99511	0.99477	0.00008	0.99517
HEU-MET-FAST-016-001	0.99960	0.00180	1.00033	0.00009	1.00073	1.00036	0.00009	1.00076
HEU-MET-FAST-016-002	0.99960	0.00180	1.00133	0.00009	1.00173	1.00132	0.00009	1.00172
HEU-MET-FAST-017-001	0.99930	0.00140	0.99860	0.00010	0.99930	0.99880	0.00010	0.99950
HEU-MET-FAST-018-001	1.00000	0.00140	1.00037	0.00009	1.00037	0.99998	0.00008	0.99998
HEU-MET-FAST-019-001	1.00000	0.00280	1.00550	0.00009	1.00550	1.00587	0.00009	1.00587
HEU-MET-FAST-020-001	1.00000	0.00280	1.00027	0.00010	1.00027	1.00019	0.00009	1.00019
HEU-MET-FAST-021-001	1.00000	0.00240	0.99994	0.00009	0.99994	0.99947	0.00009	0.99947
HEU-MET-FAST-022-001	1.00000	0.00190	0.99752	0.00009	0.99752	0.99746	0.00009	0.99746
HEU-MET-FAST-024-001	0.99900	0.00150	0.99777	0.00010	0.99877	0.99757	0.00010	0.99857
HEU-MET-FAST-025-001	0.99870	0.00140	0.99890	0.00009	1.00020	0.99897	0.00009	1.00027
HEU-MET-FAST-025-002	0.99900	0.00160	1.00117	0.00009	1.00217	1.00119	0.00009	1.00219
HEU-MET-FAST-025-003	0.99910	0.00160	1.00382	0.00009	1.00472	1.00371	0.00009	1.00461
HEU-MET-FAST-025-004	0.99950	0.00160	1.00541	0.00009	1.00591	1.00557	0.00009	1.00607
HEU-MET-FAST-025-005	0.99910	0.00160	1.00570	0.00009	1.00660	1.00573	0.00009	1.00664

Continued on the next page

TABLE LIX: (continued) ENDF-6 ENDF/B-VIII.1 criticality validation.

Benchmark	E	unc.$_E$	ENDF/B-VIII.1			ENDF/B-VIII.0		
			C	unc.$_C$	C/E	C	unc.$_C$	C/E
HEU-MET-FAST-027-001	1.00000	0.00250	1.00321	0.00009	1.00321	1.00059	0.00009	1.00059
HEU-MET-FAST-028-001	1.00000	0.00300	1.00071	0.00009	1.00071	1.00090	0.00009	1.00090
HEU-MET-FAST-029-001	1.00000	0.00200	1.00350	0.00009	1.00350	1.00358	0.00009	1.00358
HEU-MET-FAST-030-001	1.00000	0.00090	0.99948	0.00010	0.99948	1.00057	0.00010	1.00057
HEU-MET-FAST-031-001	1.00000	0.00590	1.00251	0.00011	1.00251	1.00179	0.00011	1.00179
HEU-MET-FAST-032-001	1.00000	0.00160	1.00158	0.00009	1.00158	1.00176	0.00009	1.00176
HEU-MET-FAST-032-002	1.00000	0.00270	1.00227	0.00009	1.00227	1.00249	0.00009	1.00249
HEU-MET-FAST-032-003	1.00000	0.00170	0.99811	0.00009	0.99811	0.99829	0.00009	0.99829
HEU-MET-FAST-032-004	1.00000	0.00170	0.99977	0.00009	0.99977	0.99995	0.00008	0.99995
HEU-MET-FAST-033-001	0.99910	0.00140	1.00088	0.00011	1.00178	1.00063	0.00011	1.00153
HEU-MET-FAST-033-002	0.99910	0.00140	0.99771	0.00012	0.99860	0.99747	0.00012	0.99837
HEU-MET-FAST-034-001	0.99900	0.00120	0.99674	0.00011	0.99774	0.99619	0.00011	0.99719
HEU-MET-FAST-034-002	0.99900	0.00120	0.99853	0.00011	0.99953	0.99769	0.00011	0.99869
HEU-MET-FAST-034-003	0.99900	0.00120	0.99792	0.00011	0.99892	0.99763	0.00011	0.99863
HEU-MET-FAST-036-001	0.99930	0.00150	0.99762	0.00011	0.99832	0.99661	0.00011	0.99731
HEU-MET-FAST-036-002	0.99930	0.00130	0.99670	0.00011	0.99740	0.99624	0.00010	0.99694
HEU-MET-FAST-037-001	0.99970	0.00110	0.99885	0.00011	0.99915	0.99847	0.00011	0.99877
HEU-MET-FAST-037-002	0.99970	0.00110	0.99584	0.00010	0.99614	0.99536	0.00011	0.99566
HEU-MET-FAST-038-001	0.99990	0.00070	1.00021	0.00010	1.00031	1.00133	0.00010	1.00143
HEU-MET-FAST-038-002	0.99990	0.00090	1.00062	0.00010	1.00072	1.00167	0.00010	1.00177
HEU-MET-FAST-040-001	0.99910	0.00110	1.00464	0.00009	1.00555	1.00463	0.00009	1.00553
HEU-MET-FAST-041-001	1.00130	0.00300	1.00474	0.00010	1.00344	1.00500	0.00010	1.00370
HEU-MET-FAST-041-002	1.00220	0.00430	1.00239	0.00011	1.00019	1.00226	0.00011	1.00006
HEU-MET-FAST-041-003	1.00060	0.00290	1.00096	0.00009	1.00036	1.00090	0.00009	1.00030
HEU-MET-FAST-041-004	1.00060	0.00250	1.00551	0.00009	1.00491	1.00571	0.00009	1.00511
HEU-MET-FAST-041-005	1.00060	0.00310	1.00116	0.00010	1.00056	1.00115	0.00009	1.00055
HEU-MET-FAST-041-006	1.00060	0.00450	1.00252	0.00010	1.00192	1.00247	0.00010	1.00187
HEU-MET-FAST-043-001	0.99950	0.00180	0.99945	0.00009	0.99995	0.99960	0.00009	1.00010
HEU-MET-FAST-043-002	0.99950	0.00190	0.99898	0.00009	0.99948	0.99909	0.00009	0.99959
HEU-MET-FAST-043-003	0.99950	0.00210	0.99994	0.00009	1.00044	1.00020	0.00009	1.00070
HEU-MET-FAST-043-004	0.99950	0.00150	0.99897	0.00009	0.99947	0.99913	0.00009	0.99963
HEU-MET-FAST-043-005	0.99950	0.00150	1.00005	0.00009	1.00055	1.00016	0.00009	1.00066
HEU-MET-FAST-044-001	0.99950	0.00190	0.99999	0.00009	1.00049	1.00027	0.00009	1.00077
HEU-MET-FAST-044-002	0.99950	0.00170	0.99944	0.00009	0.99994	0.99964	0.00009	1.00014
HEU-MET-FAST-044-003	0.99950	0.00190	0.99981	0.00009	1.00031	0.99999	0.00009	1.00049
HEU-MET-FAST-044-004	0.99950	0.00140	0.99953	0.00009	1.00003	0.99957	0.00009	1.00007
HEU-MET-FAST-044-005	0.99950	0.00150	1.00007	0.00009	1.00057	1.00029	0.00009	1.00079
HEU-MET-FAST-049-001	0.99900	0.00160	0.99785	0.00009	0.99885	0.99803	0.00009	0.99903
HEU-MET-FAST-049-002	0.99940	0.00150	0.99933	0.00009	0.99993	0.99952	0.00009	1.00012
HEU-MET-FAST-049-003	0.99940	0.00160	0.99856	0.00009	0.99916	0.99850	0.00009	0.99910
HEU-MET-FAST-050-001	0.99900	0.00120	0.99840	0.00009	0.99940	0.99861	0.00009	0.99961
HEU-MET-FAST-051-001	0.99690	0.00050	0.99518	0.00009	0.99827	0.99540	0.00009	0.99850
HEU-MET-FAST-051-002	0.99660	0.00050	0.99540	0.00009	0.99879	0.99560	0.00009	0.99900
HEU-MET-FAST-051-003	0.99710	0.00050	0.99502	0.00009	0.99791	0.99523	0.00008	0.99812
HEU-MET-FAST-051-004	0.99660	0.00050	0.99529	0.00009	0.99868	0.99528	0.00008	0.99868
HEU-MET-FAST-051-009	0.99780	0.00020	0.99505	0.00009	0.99724	0.99521	0.00009	0.99740
HEU-MET-FAST-051-014	0.99960	0.00020	0.99902	0.00009	0.99942	0.99885	0.00009	0.99925
HEU-MET-FAST-051-015	0.99970	0.00010	0.99798	0.00009	0.99828	0.99811	0.00009	0.99841
HEU-MET-FAST-051-016	0.99790	0.00010	0.99631	0.00009	0.99840	0.99658	0.00009	0.99868
HEU-MET-FAST-051-017	0.99650	0.00010	0.99563	0.00009	0.99912	0.99549	0.00009	0.99899
HEU-MET-FAST-051-018	0.99790	0.00020	0.99395	0.00009	0.99604	0.99428	0.00009	0.99637
HEU-MET-FAST-052-001	0.99930	0.00110	1.00202	0.00010	1.00272	1.00335	0.00010	1.00405
HEU-MET-FAST-055-001	0.99550	0.00280	0.99739	0.00009	1.00190	0.99716	0.00008	1.00167
HEU-MET-FAST-057-001	1.00000	0.00200	0.99334	0.00009	0.99334	0.98940	0.00009	0.98940
HEU-MET-FAST-057-002	1.00000	0.00230	1.00223	0.00009	1.00223	0.99791	0.00009	0.99791
HEU-MET-FAST-057-003	1.00000	0.00320	1.02124	0.00009	1.02124	1.01687	0.00009	1.01687
HEU-MET-FAST-057-004	1.00000	0.00400	0.99147	0.00009	0.99147	0.98775	0.00009	0.98775
HEU-MET-FAST-057-005	1.00000	0.00190	1.02590	0.00009	1.02590	1.02159	0.00009	1.02159
HEU-MET-FAST-057-006	1.00000	0.00290	1.00079	0.00009	1.00079	0.99637	0.00009	0.99637
HEU-MET-FAST-058-001	1.00000	0.00260	1.00138	0.00011	1.00138	1.00017	0.00011	1.00017
HEU-MET-FAST-058-002	1.00000	0.00350	1.00240	0.00010	1.00240	1.00264	0.00010	1.00264
HEU-MET-FAST-058-003	1.00000	0.00270	1.00073	0.00010	1.00073	1.00093	0.00010	1.00093
HEU-MET-FAST-058-004	1.00000	0.00210	1.00009	0.00009	1.00009	1.00018	0.00009	1.00018
HEU-MET-FAST-058-005	1.00000	0.00330	0.99941	0.00009	0.99941	0.99953	0.00009	0.99953

Continued on the next page

TABLE LIX: (continued) ENDF-6 ENDF/B-VIII.1 criticality validation.

Benchmark	E	unc.$_E$	ENDF/B-VIII.1			ENDF/B-VIII.0		
			C	unc.$_C$	C/E	C	unc.$_C$	C/E
HEU-MET-FAST-059-001	0.99290	0.00280	0.99013	0.00009	0.99721	0.99010	0.00009	0.99718
HEU-MET-FAST-059-002	0.99520	0.00160	0.99289	0.00009	0.99768	0.99304	0.00009	0.99783
HEU-MET-FAST-060-001	0.99550	0.00240	1.00206	0.00008	1.00659	1.00215	0.00008	1.00668
HEU-MET-FAST-061-001	0.99980	0.00250	1.00252	0.00010	1.00272	1.00336	0.00010	1.00356
HEU-MET-FAST-063-001	0.99930	0.00400	1.00320	0.00009	1.00391	1.00308	0.00009	1.00378
HEU-MET-FAST-063-002	0.99880	0.00470	1.00341	0.00009	1.00462	1.00381	0.00009	1.00502
HEU-MET-FAST-064-001	0.99960	0.00080	0.99984	0.00009	1.00024	0.99526	0.00009	0.99566
HEU-MET-FAST-064-002	0.99960	0.00100	0.99992	0.00009	1.00032	0.99532	0.00009	0.99572
HEU-MET-FAST-064-003	0.99960	0.00090	0.99779	0.00009	0.99819	0.99351	0.00009	0.99391
HEU-MET-FAST-065-001	0.99950	0.00130	0.99823	0.00008	0.99873	0.99829	0.00009	0.99879
HEU-MET-FAST-066-001	1.00300	0.00330	1.00065	0.00011	0.99765	1.00096	0.00010	0.99797
HEU-MET-FAST-066-002	1.00230	0.00290	0.99902	0.00010	0.99672	0.99928	0.00010	0.99699
HEU-MET-FAST-066-003	1.00230	0.00260	1.00219	0.00010	0.99989	1.00242	0.00009	1.00012
HEU-MET-FAST-066-004	1.00430	0.00430	1.00208	0.00011	0.99779	1.00191	0.00011	0.99762
HEU-MET-FAST-066-005	1.00300	0.00330	1.00132	0.00010	0.99833	1.00156	0.00010	0.99856
HEU-MET-FAST-066-006	1.00280	0.00300	1.00063	0.00010	0.99784	1.00105	0.00010	0.99825
HEU-MET-FAST-066-007	1.00480	0.00390	1.00265	0.00011	0.99786	1.00297	0.00010	0.99818
HEU-MET-FAST-066-008	1.00390	0.00400	1.00168	0.00011	0.99779	1.00166	0.00011	0.99777
HEU-MET-FAST-066-009	1.00270	0.00360	1.00014	0.00011	0.99744	1.00047	0.00011	0.99778
HEU-MET-FAST-067-001	0.99590	0.00240	1.00026	0.00008	1.00438	1.00131	0.00008	1.00543
HEU-MET-FAST-067-002	0.99380	0.00240	0.99554	0.00008	1.00175	0.99527	0.00008	1.00148
HEU-MET-FAST-069-001	0.99940	0.00040	0.99820	0.00009	0.99880	0.99842	0.00009	0.99902
HEU-MET-FAST-070-001	1.00050	0.00130	1.00649	0.00008	1.00599	1.00630	0.00008	1.00580
HEU-MET-FAST-070-002	0.99950	0.00130	1.00012	0.00009	1.00062	1.00031	0.00008	1.00081
HEU-MET-FAST-070-003	1.00130	0.00130	1.00467	0.00008	1.00336	1.00485	0.00008	1.00355
HEU-MET-FAST-072-001	0.99910	0.00240	1.00175	0.00009	1.00266	1.00398	0.00009	1.00488
HEU-MET-FAST-072-003	1.00160	0.00690	1.01110	0.00010	1.00948	1.01145	0.00010	1.00983
HEU-MET-FAST-073-001	1.00040	0.00160	0.99863	0.00009	0.99823	0.99965	0.00009	0.99925
HEU-MET-FAST-075-001	0.99850	0.00270	1.00078	0.00009	1.00228	1.00174	0.00009	1.00324
HEU-MET-FAST-077-001	1.00010	0.00310	0.99801	0.00010	0.99791	0.99805	0.00010	0.99795
HEU-MET-FAST-077-002	0.99950	0.00270	0.99809	0.00010	0.99859	0.99846	0.00010	0.99896
HEU-MET-FAST-077-003	0.99950	0.00400	0.99516	0.00011	0.99566	0.99454	0.00011	0.99504
HEU-MET-FAST-077-004	0.99980	0.00320	0.99555	0.00010	0.99575	0.99591	0.00010	0.99611
HEU-MET-FAST-077-005	0.99940	0.00270	0.99758	0.00010	0.99818	0.99763	0.00010	0.99823
HEU-MET-FAST-077-006	0.99960	0.00330	0.99697	0.00010	0.99737	0.99721	0.00010	0.99761
HEU-MET-FAST-077-007	0.99940	0.00560	0.99815	0.00010	0.99875	0.99844	0.00009	0.99904
HEU-MET-FAST-077-008	0.99940	0.00350	0.99549	0.00010	0.99609	0.99588	0.00010	0.99648
HEU-MET-FAST-078-001	0.99950	0.00180	0.99430	0.00010	0.99479	0.99400	0.00010	0.99450
HEU-MET-FAST-078-003	0.99940	0.00220	0.99547	0.00010	0.99607	0.99547	0.00010	0.99607
HEU-MET-FAST-078-005	0.99910	0.00190	0.99526	0.00010	0.99616	0.99494	0.00010	0.99584
HEU-MET-FAST-078-007	1.00000	0.00190	0.99646	0.00011	0.99646	0.99613	0.00011	0.99613
HEU-MET-FAST-078-009	0.99970	0.00220	0.99433	0.00010	0.99462	0.99420	0.00010	0.99450
HEU-MET-FAST-078-011	0.99950	0.00150	0.99426	0.00010	0.99476	0.99434	0.00010	0.99484
HEU-MET-FAST-078-013	1.00000	0.00170	0.99572	0.00010	0.99572	0.99548	0.00010	0.99548
HEU-MET-FAST-078-015	0.99910	0.00180	0.99512	0.00010	0.99602	0.99494	0.00010	0.99584
HEU-MET-FAST-078-017	0.99950	0.00180	0.99496	0.00010	0.99545	0.99473	0.00010	0.99523
HEU-MET-FAST-078-023	0.99920	0.00220	0.99781	0.00009	0.99861	0.99797	0.00009	0.99877
HEU-MET-FAST-078-025	0.99920	0.00250	0.99689	0.00009	0.99769	0.99680	0.00009	0.99760
HEU-MET-FAST-078-027	0.99920	0.00210	0.99524	0.00009	0.99604	0.99529	0.00009	0.99609
HEU-MET-FAST-078-029	1.00000	0.00250	1.00057	0.00010	1.00057	1.00068	0.00010	1.00068
HEU-MET-FAST-078-031	0.99940	0.00200	0.99439	0.00010	0.99498	0.99450	0.00009	0.99510
HEU-MET-FAST-078-033	0.99960	0.00260	0.99445	0.00010	0.99485	0.99451	0.00010	0.99491
HEU-MET-FAST-078-035	0.99910	0.00220	0.99364	0.00009	0.99453	0.99392	0.00009	0.99482
HEU-MET-FAST-078-037	0.99860	0.00210	0.99555	0.00009	0.99695	0.99564	0.00009	0.99704
HEU-MET-FAST-078-039	0.99890	0.00210	0.99604	0.00009	0.99714	0.99613	0.00009	0.99723
HEU-MET-FAST-078-041	0.99920	0.00250	0.99684	0.00009	0.99764	0.99691	0.00009	0.99771
HEU-MET-FAST-078-043	1.00000	0.00190	0.99715	0.00010	0.99715	0.99704	0.00009	0.99704
HEU-MET-FAST-079-001	0.99960	0.00150	0.99974	0.00009	1.00014	0.99979	0.00009	1.00019
HEU-MET-FAST-079-002	0.99960	0.00140	0.99891	0.00009	0.99931	0.99928	0.00009	0.99968
HEU-MET-FAST-079-003	0.99960	0.00150	0.99991	0.00009	1.00031	1.00032	0.00009	1.00072
HEU-MET-FAST-079-004	0.99960	0.00140	1.00059	0.00009	1.00099	1.00092	0.00009	1.00132
HEU-MET-FAST-079-005	0.99960	0.00150	0.99935	0.00009	0.99975	0.99964	0.00009	1.00004
HEU-MET-FAST-082-001	0.99920	0.00130	0.99584	0.00010	0.99664	0.99590	0.00010	0.99670
HEU-MET-FAST-082-002	0.99890	0.00130	0.99516	0.00010	0.99626	0.99554	0.00010	0.99664
HEU-MET-FAST-082-003	0.99890	0.00130	0.99738	0.00010	0.99847	0.99760	0.00010	0.99870
HEU-MET-FAST-084-001	0.99940	0.00190	0.99896	0.00009	0.99956	0.99915	0.00009	0.99975
HEU-MET-FAST-084-002	0.99940	0.00210	0.99883	0.00009	0.99943	0.99899	0.00009	0.99959
HEU-MET-FAST-084-003	0.99930	0.00210	0.99845	0.00009	0.99915	0.99857	0.00009	0.99927

Continued on the next page

TABLE LIX: (continued) ENDF-6 ENDF/B-VIII.1 criticality validation.

Benchmark	E	unc.$_E$	ENDF/B-VIII.1			ENDF/B-VIII.0		
			C	unc.$_C$	C/E	C	unc.$_C$	C/E
HEU-MET-FAST-084-004	0.99940	0.00200	0.99761	0.00009	0.99821	0.99803	0.00009	0.99863
HEU-MET-FAST-084-005	0.99930	0.00210	1.00611	0.00009	1.00682	1.00629	0.00009	1.00699
HEU-MET-FAST-084-006	0.99940	0.00240	0.99859	0.00009	0.99919	0.99475	0.00009	0.99535
HEU-MET-FAST-084-007	0.99950	0.00200	0.99868	0.00009	0.99918	0.99873	0.00009	0.99923
HEU-MET-FAST-084-008	0.99940	0.00340	1.00839	0.00009	1.00900	1.00849	0.00009	1.00910
HEU-MET-FAST-084-009	0.99930	0.00540	1.00208	0.00009	1.00278	1.00207	0.00009	1.00277
HEU-MET-FAST-084-010	0.99930	0.00220	0.99616	0.00009	0.99686	0.99632	0.00009	0.99702
HEU-MET-FAST-084-011	0.99950	0.00190	1.00063	0.00010	1.00113	1.00059	0.00010	1.00109
HEU-MET-FAST-084-012	0.99940	0.00200	0.99691	0.00009	0.99751	0.99703	0.00009	0.99763
HEU-MET-FAST-084-013	0.99940	0.00220	0.99756	0.00009	0.99816	0.99772	0.00009	0.99832
HEU-MET-FAST-084-014	0.99940	0.00190	0.99847	0.00009	0.99907	0.99844	0.00009	0.99904
HEU-MET-FAST-084-015	0.99950	0.00210	0.99781	0.00009	0.99831	0.99778	0.00009	0.99828
HEU-MET-FAST-084-016	0.99940	0.00200	0.99827	0.00009	0.99887	0.99833	0.00009	0.99893
HEU-MET-FAST-084-017	0.99950	0.00190	1.00095	0.00009	1.00145	1.00115	0.00009	1.00165
HEU-MET-FAST-084-018	0.99950	0.00220	0.99758	0.00009	0.99808	0.99536	0.00009	0.99586
HEU-MET-FAST-084-019	0.99960	0.00190	0.99833	0.00009	0.99873	0.99845	0.00009	0.99885
HEU-MET-FAST-084-020	0.99950	0.00250	1.00305	0.00009	1.00356	1.00305	0.00009	1.00355
HEU-MET-FAST-084-021	0.99950	0.00450	1.00017	0.00009	1.00067	1.00008	0.00009	1.00058
HEU-MET-FAST-084-022	0.99940	0.00200	0.99514	0.00009	0.99573	0.99511	0.00009	0.99571
HEU-MET-FAST-084-023	0.99930	0.00240	0.99897	0.00009	0.99967	0.99906	0.00009	0.99976
HEU-MET-FAST-084-024	0.99960	0.00180	0.99779	0.00009	0.99819	0.99789	0.00009	0.99829
HEU-MET-FAST-084-025	0.99950	0.00200	0.99759	0.00009	0.99809	0.99721	0.00009	0.99771
HEU-MET-FAST-084-026	0.99930	0.00220	0.99985	0.00009	1.00055	0.99980	0.00009	1.00050
HEU-MET-FAST-084-027	0.99940	0.00200	0.99705	0.00009	0.99765	0.99704	0.00009	0.99764
HEU-MET-FAST-085-001	0.99980	0.00290	1.00002	0.00009	1.00022	0.99453	0.00009	0.99473
HEU-MET-FAST-085-002	0.99970	0.00310	1.00287	0.00009	1.00317	0.99688	0.00009	0.99718
HEU-MET-FAST-085-003	0.99950	0.00460	0.99835	0.00009	0.99885	0.99844	0.00009	0.99894
HEU-MET-FAST-085-004	0.99960	0.00290	0.99701	0.00009	0.99741	0.99515	0.00009	0.99555
HEU-MET-FAST-085-005	0.99950	0.00240	1.00022	0.00009	1.00073	1.00025	0.00009	1.00075
HEU-MET-FAST-085-006	0.99970	0.00290	1.00366	0.00009	1.00396	1.00362	0.00009	1.00392
HEU-MET-FAST-087-001	0.99870	0.00130	0.99996	0.00009	1.00126	1.00013	0.00009	1.00143
HEU-MET-FAST-088-001	0.99930	0.00080	0.99662	0.00011	0.99732	0.99679	0.00011	0.99749
HEU-MET-FAST-088-002	0.99930	0.00070	0.99611	0.00011	0.99680	0.99546	0.00011	0.99616
HEU-MET-FAST-089-001	0.99910	0.00140	1.00009	0.00009	1.00099	1.00018	0.00009	1.00108
HEU-MET-FAST-090-001	0.99940	0.00070	1.00320	0.00011	1.00381	1.00265	0.00011	1.00325
HEU-MET-FAST-090-002	0.99930	0.00070	0.99984	0.00011	1.00054	0.99917	0.00011	0.99987
HEU-MET-FAST-091-001	0.99960	0.00090	0.99727	0.00011	0.99767	0.99681	0.00011	0.99721
HEU-MET-FAST-092-001	0.99860	0.00110	1.00136	0.00009	1.00276	1.00141	0.00009	1.00281
HEU-MET-FAST-092-002	0.99890	0.00130	1.00306	0.00009	1.00417	1.00308	0.00009	1.00418
HEU-MET-FAST-092-003	0.99930	0.00120	1.00440	0.00009	1.00511	1.00426	0.00009	1.00496
HEU-MET-FAST-092-004	0.99930	0.00130	1.00371	0.00009	1.00441	1.00375	0.00009	1.00445
HEU-MET-FAST-093-001	0.99780	0.00120	1.00411	0.00009	1.00632	1.00391	0.00009	1.00612
HEU-MET-FAST-094-001	0.99940	0.00120	1.00047	0.00010	1.00107	1.00114	0.00010	1.00174
HEU-MET-FAST-094-002	0.99930	0.00100	1.00114	0.00010	1.00184	1.00184	0.00010	1.00254
HEU-MET-FAST-100-001	1.00310	0.00070	1.00496	0.00008	1.00185	1.00509	0.00009	1.00198
HEU-MET-FAST-100-002	0.99660	0.00070	0.99885	0.00009	1.00226	0.99887	0.00008	1.00228
HEU-MET-INTER-001-001	0.99660	0.00260	0.99844	0.00010	1.00184	0.99870	0.00009	1.00211
HEU-MET-INTER-006-001	0.99770	0.00080	0.99743	0.00011	0.99972	0.99585	0.00011	0.99815
HEU-MET-INTER-006-002	1.00010	0.00080	1.00118	0.00011	1.00108	1.00018	0.00011	1.00008
HEU-MET-INTER-006-003	1.00150	0.00090	1.00342	0.00011	1.00191	1.00309	0.00011	1.00159
HEU-MET-INTER-006-004	1.00160	0.00080	1.00431	0.00010	1.00271	1.00532	0.00010	1.00371
HEU-MET-MIXED-001-001	0.99950	0.00130	1.00032	0.00011	1.00082	0.99984	0.00011	1.00034
HEU-MET-MIXED-002-001	1.00000	0.00370	1.00310	0.00011	1.00310	1.00245	0.00011	1.00245
HEU-MET-MIXED-003-001	1.00000	0.00380	1.00403	0.00011	1.00403	1.00347	0.00011	1.00347
HEU-MET-MIXED-004-001	0.99990	0.00090	0.99896	0.00010	0.99906	0.99824	0.00010	0.99834
HEU-MET-MIXED-012-001	1.00420	0.00240	1.01056	0.00010	1.00633	1.00931	0.00009	1.00509
HEU-MET-MIXED-015-001	0.99960	0.00080	0.99500	0.00012	0.99540	0.99342	0.00012	0.99382
HEU-MET-MIXED-016-001	0.99950	0.00080	0.99995	0.00012	1.00045	0.99831	0.00012	0.99881
HEU-MET-MIXED-016-002	0.99950	0.00070	1.00010	0.00012	1.00060	0.99874	0.00012	0.99924
HEU-MET-MIXED-017-001	1.00000	0.00080	0.99377	0.00012	0.99377	0.99250	0.00012	0.99250
HEU-MET-MIXED-020-001	0.99900	0.00050	1.00165	0.00012	1.00265	1.00024	0.00012	1.00124
HEU-MET-MIXED-020-002	0.99910	0.00070	0.99939	0.00012	1.00029	0.99832	0.00011	0.99922
HEU-MET-THERM-010-001-s	1.00300	0.00720	1.00771	0.00012	1.00469	1.00738	0.00012	1.00437
HEU-MET-THERM-012-001-s	0.99710	0.00250	1.00834	0.00012	1.01127	1.00730	0.00012	1.01023

Continued on the next page

TABLE LIX: (continued) ENDF-6 ENDF/B-VIII.1 criticality validation.

Benchmark	E	unc.$_E$	ENDF/B-VIII.1			ENDF/B-VIII.0		
			C	unc.$_C$	C/E	C	unc.$_C$	C/E
HEU-MET-THERM-014-001-s	0.99390	0.00150	1.00552	0.00013	1.01169	1.00522	0.00013	1.01139
HEU-MET-THERM-031-001-s	1.00370	0.00240	1.00838	0.00012	1.00467	1.00788	0.00012	1.00416
HEU-SOL-THERM-001-001	1.00040	0.00600	0.99961	0.00015	0.99921	0.99831	0.00015	0.99791
HEU-SOL-THERM-001-002	1.00210	0.00720	0.99687	0.00015	0.99478	0.99492	0.00015	0.99284
HEU-SOL-THERM-001-003	1.00030	0.00350	1.00241	0.00015	1.00211	1.00169	0.00015	1.00139
HEU-SOL-THERM-001-004	1.00080	0.00530	0.99899	0.00015	0.99819	0.99739	0.00015	0.99659
HEU-SOL-THERM-001-005	1.00010	0.00490	0.99980	0.00013	0.99970	0.99896	0.00013	0.99886
HEU-SOL-THERM-001-006	1.00020	0.00460	1.00292	0.00013	1.00272	1.00246	0.00013	1.00226
HEU-SOL-THERM-001-007	1.00080	0.00400	0.99889	0.00015	0.99809	0.99800	0.00015	0.99720
HEU-SOL-THERM-001-008	0.99980	0.00380	0.99930	0.00015	0.99950	0.99818	0.00015	0.99838
HEU-SOL-THERM-001-009	1.00080	0.00540	0.99486	0.00015	0.99406	0.99319	0.00015	0.99240
HEU-SOL-THERM-001-010	0.99930	0.00540	0.99323	0.00013	0.99393	0.99273	0.00013	0.99343
HEU-SOL-THERM-004-001	1.00000	0.00330	0.99250	0.00013	0.99250	0.99030	0.00012	0.99030
HEU-SOL-THERM-004-002	1.00000	0.00360	0.98666	0.00013	0.98666	0.98420	0.00013	0.98420
HEU-SOL-THERM-004-003	1.00000	0.00390	0.99303	0.00013	0.99303	0.99025	0.00013	0.99025
HEU-SOL-THERM-004-004	1.00000	0.00460	0.99474	0.00013	0.99474	0.99243	0.00013	0.99243
HEU-SOL-THERM-004-005	1.00000	0.00520	0.99298	0.00014	0.99298	0.99110	0.00014	0.99110
HEU-SOL-THERM-004-006	1.00000	0.00590	0.98962	0.00014	0.98962	0.98815	0.00014	0.98815
HEU-SOL-THERM-006-001	0.99730	0.00500	0.98260	0.00015	0.98526	0.98132	0.00014	0.98398
HEU-SOL-THERM-006-002	0.99860	0.00540	0.98828	0.00014	0.98967	0.98712	0.00014	0.98850
HEU-SOL-THERM-006-003	1.00000	0.00650	1.00059	0.00013	1.00059	0.99977	0.00013	0.99977
HEU-SOL-THERM-006-004	1.00000	0.00780	1.00314	0.00013	1.00314	1.00199	0.00012	1.00199
HEU-SOL-THERM-006-005	1.00000	0.00910	1.01009	0.00012	1.01009	1.00924	0.00012	1.00924
HEU-SOL-THERM-006-006	1.00000	0.00870	1.00177	0.00011	1.00177	1.00037	0.00012	1.00037
HEU-SOL-THERM-006-007	1.00000	0.00880	1.00339	0.00011	1.00339	1.00244	0.00011	1.00244
HEU-SOL-THERM-006-008	0.99730	0.00500	0.98267	0.00014	0.98533	0.98099	0.00014	0.98365
HEU-SOL-THERM-006-009	0.99860	0.00540	0.98840	0.00013	0.98979	0.98644	0.00014	0.98782
HEU-SOL-THERM-006-010	1.00000	0.00650	1.00024	0.00013	1.00024	0.99914	0.00013	0.99914
HEU-SOL-THERM-006-011	1.00000	0.00880	1.00339	0.00011	1.00339	1.00257	0.00011	1.00257
HEU-SOL-THERM-006-012	0.99730	0.00500	0.98148	0.00015	0.98413	0.98031	0.00014	0.98296
HEU-SOL-THERM-006-013	0.99860	0.00540	0.98633	0.00014	0.98771	0.98485	0.00014	0.98623
HEU-SOL-THERM-006-014	1.00000	0.00780	1.00181	0.00013	1.00181	1.00065	0.00012	1.00065
HEU-SOL-THERM-006-015	1.00000	0.00910	1.00963	0.00012	1.00963	1.00806	0.00012	1.00806
HEU-SOL-THERM-006-016	1.00000	0.00870	1.00120	0.00011	1.00120	1.00015	0.00011	1.00015
HEU-SOL-THERM-006-017	1.00000	0.00880	1.00312	0.00011	1.00312	1.00197	0.00011	1.00197
HEU-SOL-THERM-006-018	1.00000	0.00780	1.00266	0.00012	1.00266	1.00141	0.00012	1.00141
HEU-SOL-THERM-006-019	1.00000	0.00910	1.00966	0.00012	1.00966	1.00867	0.00012	1.00867
HEU-SOL-THERM-006-020	1.00000	0.00870	1.00148	0.00011	1.00148	1.00034	0.00011	1.00034
HEU-SOL-THERM-006-021	1.00000	0.00880	1.00352	0.00011	1.00352	1.00244	0.00011	1.00244
HEU-SOL-THERM-006-022	1.00000	0.00650	1.00090	0.00013	1.00090	0.99961	0.00013	0.99961
HEU-SOL-THERM-006-023	1.00000	0.00780	1.00310	0.00012	1.00310	1.00194	0.00012	1.00194
HEU-SOL-THERM-006-024	1.00000	0.00910	1.01018	0.00012	1.01018	1.00903	0.00012	1.00903
HEU-SOL-THERM-006-025	1.00000	0.00870	1.00169	0.00011	1.00169	1.00068	0.00011	1.00068
HEU-SOL-THERM-006-026	1.00000	0.00880	1.00376	0.00011	1.00376	1.00276	0.00011	1.00276
HEU-SOL-THERM-006-027	0.99730	0.00500	0.98376	0.00014	0.98642	0.98174	0.00014	0.98440
HEU-SOL-THERM-006-028	0.99860	0.00540	0.98732	0.00013	0.98871	0.98615	0.00014	0.98753
HEU-SOL-THERM-006-029	1.00000	0.00880	1.00385	0.00011	1.00385	1.00274	0.00011	1.00274
HEU-SOL-THERM-009-001	0.99900	0.00430	1.00197	0.00013	1.00297	1.00110	0.00014	1.00210
HEU-SOL-THERM-009-002	1.00000	0.00390	1.00308	0.00013	1.00308	1.00171	0.00014	1.00171
HEU-SOL-THERM-009-003	1.00000	0.00360	1.00290	0.00014	1.00290	1.00218	0.00014	1.00218
HEU-SOL-THERM-009-004	0.99860	0.00350	0.99760	0.00013	0.99900	0.99697	0.00014	0.99837
HEU-SOL-THERM-010-001	1.00000	0.00290	1.00286	0.00013	1.00286	1.00226	0.00013	1.00226
HEU-SOL-THERM-011-001	1.00000	0.00230	1.00609	0.00011	1.00609	1.00539	0.00011	1.00539
HEU-SOL-THERM-011-002	1.00000	0.00230	1.00210	0.00012	1.00210	1.00155	0.00011	1.00155
HEU-SOL-THERM-012-001	0.99990	0.00580	1.00114	0.00008	1.00125	1.00082	0.00008	1.00092
HEU-SOL-THERM-013-001	1.00120	0.00260	0.99881	0.00008	0.99761	0.99829	0.00008	0.99709
HEU-SOL-THERM-019-001	1.00000	0.00410	0.99870	0.00014	0.99870	0.99692	0.00014	0.99692
HEU-SOL-THERM-019-002	1.00000	0.00410	1.00117	0.00014	1.00117	0.99986	0.00013	0.99986
HEU-SOL-THERM-019-003	1.00000	0.00670	0.99739	0.00013	0.99739	0.99577	0.00013	0.99577
HEU-SOL-THERM-020-001	0.99660	0.01160	0.99698	0.00015	1.00038	0.99420	0.00015	0.99759
HEU-SOL-THERM-020-002	0.99560	0.00930	1.00153	0.00016	1.00595	0.99933	0.00016	1.00374
HEU-SOL-THERM-020-003	0.99570	0.00790	1.00887	0.00016	1.01322	1.00759	0.00016	1.01195
HEU-SOL-THERM-020-004	0.99550	0.00780	1.00864	0.00016	1.01320	1.00741	0.00016	1.01196
HEU-SOL-THERM-020-005	0.99590	0.00770	1.01458	0.00016	1.01876	1.01405	0.00015	1.01823
HEU-SOL-THERM-025-001	1.00020	0.00250	1.00181	0.00011	1.00161	1.00167	0.00011	1.00147
HEU-SOL-THERM-025-002	1.00070	0.00250	1.00153	0.00011	1.00083	1.00086	0.00011	1.00016
HEU-SOL-THERM-025-003	1.00020	0.00640	0.99649	0.00011	0.99629	0.99585	0.00011	0.99565
HEU-SOL-THERM-025-004	1.00030	0.00270	1.00177	0.00012	1.00147	1.00165	0.00012	1.00135
HEU-SOL-THERM-025-005	1.00130	0.00300	1.00425	0.00013	1.00295	1.00366	0.00013	1.00236
HEU-SOL-THERM-025-006	1.00020	0.00670	1.00925	0.00010	1.00905	1.00874	0.00010	1.00854
HEU-SOL-THERM-025-007	1.00090	0.00730	1.01354	0.00011	1.01262	1.01333	0.00011	1.01242

Continued on the next page

TABLE LIX: (continued) ENDF-6 ENDF/B-VIII.1 criticality validation.

Benchmark	E	unc.$_E$	ENDF/B-VIII.1			ENDF/B-VIII.0		
			C	unc.$_C$	C/E	C	unc.$_C$	C/E
HEU-SOL-THERM-025-008	1.00000	0.00670	1.01110	0.00010	1.01110	1.01071	0.00011	1.01071
HEU-SOL-THERM-025-009	1.00020	0.00650	1.00530	0.00011	1.00510	1.00508	0.00011	1.00488
HEU-SOL-THERM-025-010	1.00030	0.00430	1.00968	0.00012	1.00938	1.00939	0.00011	1.00909
HEU-SOL-THERM-025-011	1.00020	0.00450	1.00869	0.00011	1.00849	1.00851	0.00011	1.00831
HEU-SOL-THERM-025-012	1.00020	0.00450	1.00752	0.00011	1.00732	1.00714	0.00011	1.00694
HEU-SOL-THERM-025-013	1.00090	0.00470	1.01547	0.00010	1.01455	1.01523	0.00010	1.01432
HEU-SOL-THERM-025-014	1.00080	0.00530	1.00660	0.00011	1.00579	1.00642	0.00011	1.00562
HEU-SOL-THERM-025-015	1.00020	0.00580	1.00064	0.00011	1.00044	1.00038	0.00011	1.00018
HEU-SOL-THERM-025-016	1.00000	0.00490	1.01099	0.00011	1.01099	1.01043	0.00011	1.01043
HEU-SOL-THERM-025-017	1.00000	0.00550	1.00292	0.00011	1.00292	1.00265	0.00011	1.00265
HEU-SOL-THERM-025-018	1.00000	0.00610	1.00029	0.00011	1.00029	0.99999	0.00011	0.99999
HEU-SOL-THERM-027-001	1.00000	0.00460	0.99722	0.00014	0.99722	0.99633	0.00015	0.99633
HEU-SOL-THERM-027-002	1.00000	0.00430	0.99779	0.00014	0.99779	0.99657	0.00014	0.99657
HEU-SOL-THERM-027-003	1.00000	0.00370	0.99845	0.00014	0.99845	0.99748	0.00014	0.99748
HEU-SOL-THERM-027-004	1.00000	0.00370	0.99920	0.00014	0.99920	0.99798	0.00014	0.99798
HEU-SOL-THERM-027-005	1.00000	0.00440	0.99698	0.00014	0.99698	0.99625	0.00014	0.99625
HEU-SOL-THERM-027-006	1.00000	0.00430	0.99239	0.00014	0.99239	0.99168	0.00014	0.99168
HEU-SOL-THERM-027-007	1.00000	0.00380	0.99862	0.00014	0.99862	0.99756	0.00014	0.99756
HEU-SOL-THERM-027-008	1.00000	0.00350	1.00135	0.00014	1.00135	1.00027	0.00014	1.00027
HEU-SOL-THERM-027-009	1.00000	0.00390	0.99865	0.00014	0.99865	0.99772	0.00014	0.99772
HEU-SOL-THERM-028-001	1.00000	0.00230	0.99766	0.00012	0.99766	0.99723	0.00012	0.99723
HEU-SOL-THERM-028-002	1.00000	0.00340	0.99796	0.00012	0.99796	0.99759	0.00012	0.99759
HEU-SOL-THERM-028-003	1.00000	0.00260	0.99953	0.00013	0.99953	0.99925	0.00012	0.99925
HEU-SOL-THERM-028-004	1.00000	0.00280	0.99983	0.00012	0.99983	0.99903	0.00012	0.99903
HEU-SOL-THERM-028-005	1.00000	0.00310	0.99508	0.00013	0.99508	0.99475	0.00013	0.99475
HEU-SOL-THERM-028-006	1.00000	0.00230	0.99820	0.00012	0.99820	0.99791	0.00012	0.99791
HEU-SOL-THERM-028-007	1.00000	0.00380	0.99915	0.00013	0.99915	0.99860	0.00012	0.99860
HEU-SOL-THERM-028-008	1.00000	0.00270	0.99871	0.00012	0.99871	0.99837	0.00012	0.99837
HEU-SOL-THERM-028-009	1.00000	0.00490	0.99712	0.00014	0.99712	0.99599	0.00014	0.99599
HEU-SOL-THERM-028-010	1.00000	0.00530	0.99508	0.00013	0.99508	0.99381	0.00013	0.99381
HEU-SOL-THERM-028-011	1.00000	0.00510	0.99929	0.00014	0.99929	0.99763	0.00014	0.99763
HEU-SOL-THERM-028-012	1.00000	0.00460	0.99567	0.00013	0.99567	0.99458	0.00013	0.99458
HEU-SOL-THERM-028-013	1.00000	0.00580	0.99801	0.00014	0.99801	0.99653	0.00014	0.99653
HEU-SOL-THERM-028-014	1.00000	0.00460	0.99737	0.00013	0.99737	0.99641	0.00014	0.99641
HEU-SOL-THERM-028-015	1.00000	0.00640	1.00574	0.00014	1.00574	1.00470	0.00014	1.00470
HEU-SOL-THERM-028-016	1.00000	0.00520	1.00187	0.00014	1.00187	1.00058	0.00014	1.00058
HEU-SOL-THERM-028-017	1.00000	0.00660	0.99715	0.00014	0.99715	0.99637	0.00014	0.99637
HEU-SOL-THERM-028-018	1.00000	0.00600	0.99820	0.00014	0.99820	0.99683	0.00014	0.99683
HEU-SOL-THERM-032-001	1.00150	0.00260	0.99906	0.00005	0.99756	0.99864	0.00005	0.99714
HEU-SOL-THERM-038-001	1.00000	0.00250	0.99584	0.00014	0.99584	0.99469	0.00014	0.99469
HEU-SOL-THERM-038-002	1.00000	0.00250	0.99740	0.00013	0.99740	0.99611	0.00014	0.99611
HEU-SOL-THERM-038-003	1.00000	0.00250	0.99831	0.00014	0.99831	0.99722	0.00014	0.99722
HEU-SOL-THERM-038-004	1.00000	0.00250	0.99602	0.00014	0.99602	0.99501	0.00014	0.99501
HEU-SOL-THERM-038-005	1.00000	0.00250	0.99602	0.00014	0.99602	0.99512	0.00014	0.99512
HEU-SOL-THERM-038-006	1.00000	0.00250	0.99699	0.00014	0.99699	0.99569	0.00014	0.99569
HEU-SOL-THERM-038-007	1.00000	0.00320	0.99867	0.00014	0.99867	0.99735	0.00014	0.99735
HEU-SOL-THERM-038-008	1.00000	0.00260	0.99861	0.00014	0.99861	0.99747	0.00014	0.99747
HEU-SOL-THERM-038-009	1.00000	0.00330	0.99866	0.00014	0.99866	0.99702	0.00014	0.99702
HEU-SOL-THERM-038-010	1.00000	0.00260	0.99757	0.00014	0.99757	0.99658	0.00014	0.99658
HEU-SOL-THERM-038-011	1.00000	0.00250	0.99724	0.00014	0.99724	0.99600	0.00014	0.99600
HEU-SOL-THERM-038-012	1.00000	0.00250	0.99680	0.00014	0.99680	0.99587	0.00014	0.99587
HEU-SOL-THERM-038-013	1.00000	0.00500	1.00159	0.00014	1.00159	1.00049	0.00014	1.00049
HEU-SOL-THERM-038-014	1.00000	0.00500	1.00177	0.00014	1.00177	1.00058	0.00014	1.00058
HEU-SOL-THERM-038-015	1.00000	0.00500	1.00134	0.00014	1.00134	1.00010	0.00014	1.00010
HEU-SOL-THERM-038-016	1.00000	0.00500	1.00019	0.00014	1.00019	0.99917	0.00014	0.99917
HEU-SOL-THERM-038-017	1.00000	0.00260	0.99702	0.00014	0.99702	0.99576	0.00014	0.99576
HEU-SOL-THERM-038-018	1.00000	0.00320	0.99583	0.00014	0.99583	0.99439	0.00014	0.99439
HEU-SOL-THERM-038-019	1.00000	0.00320	0.99820	0.00014	0.99820	0.99662	0.00014	0.99662
HEU-SOL-THERM-038-020	1.00000	0.00320	0.99813	0.00014	0.99813	0.99681	0.00014	0.99681
HEU-SOL-THERM-038-021	1.00000	0.00250	0.99796	0.00014	0.99796	0.99702	0.00013	0.99702
HEU-SOL-THERM-038-022	1.00000	0.00270	0.99788	0.00014	0.99788	0.99688	0.00014	0.99688
HEU-SOL-THERM-038-023	1.00000	0.00270	0.99738	0.00014	0.99738	0.99599	0.00014	0.99599
HEU-SOL-THERM-038-024	1.00000	0.00260	0.99756	0.00014	0.99756	0.99615	0.00014	0.99615
HEU-SOL-THERM-038-025	1.00000	0.00320	0.99797	0.00014	0.99797	0.99668	0.00014	0.99668
HEU-SOL-THERM-038-026	1.00000	0.00320	0.99813	0.00014	0.99813	0.99690	0.00014	0.99690
HEU-SOL-THERM-038-027	1.00000	0.00320	0.99788	0.00014	0.99788	0.99679	0.00014	0.99679
HEU-SOL-THERM-038-028	1.00000	0.00250	0.99838	0.00014	0.99838	0.99690	0.00014	0.99690
HEU-SOL-THERM-042-001	0.99570	0.00390	0.99656	0.00006	1.00087	0.99601	0.00007	1.00031
HEU-SOL-THERM-042-002	0.99650	0.00360	0.99644	0.00006	0.99994	0.99590	0.00006	0.99940
HEU-SOL-THERM-042-003	0.99940	0.00280	1.00038	0.00005	1.00098	0.99979	0.00005	1.00039
HEU-SOL-THERM-042-004	1.00000	0.00340	1.00161	0.00005	1.00161	1.00129	0.00005	1.00129
HEU-SOL-THERM-042-005	1.00000	0.00340	0.99962	0.00004	0.99962	0.99919	0.00004	0.99919
HEU-SOL-THERM-042-006	1.00000	0.00370	0.99976	0.00004	0.99976	0.99928	0.00004	0.99928
HEU-SOL-THERM-042-007	1.00000	0.00360	1.00090	0.00004	1.00090	1.00027	0.00004	1.00027
HEU-SOL-THERM-042-008	1.00000	0.00350	1.00127	0.00003	1.00127	1.00081	0.00003	1.00081

Continued on the next page

TABLE LIX: (continued) ENDF-6 ENDF/B-VIII.1 criticality validation.

Benchmark	E	unc.$_E$	ENDF/B-VIII.1			ENDF/B-VIII.0		
			C	unc.$_C$	C/E	C	unc.$_C$	C/E
HEU-SOL-THERM-043-001	0.99860	0.00310	0.99564	0.00015	0.99704	0.99470	0.00015	0.99609
HEU-SOL-THERM-043-002	0.99950	0.00260	1.00567	0.00009	1.00617	1.00517	0.00009	1.00567
HEU-SOL-THERM-043-003	0.99900	0.00250	1.00114	0.00008	1.00214	1.00069	0.00008	1.00169
HEU-SOL-THERM-049-001	1.00120	0.00260	0.99989	0.00014	0.99869	0.99839	0.00014	0.99719
HEU-SOL-THERM-049-002	1.00120	0.00290	0.99149	0.00014	0.99031	0.98914	0.00014	0.98795
HEU-SOL-THERM-049-003	1.00120	0.00260	0.99993	0.00014	0.99873	0.99824	0.00013	0.99704
HEU-SOL-THERM-049-004	1.00120	0.00250	1.00173	0.00013	1.00053	1.00004	0.00013	0.99884
HEU-SOL-THERM-049-005	1.00120	0.00250	1.00432	0.00013	1.00311	1.00277	0.00013	1.00157
HEU-SOL-THERM-049-006	1.00120	0.00250	1.00792	0.00013	1.00671	1.00597	0.00013	1.00476
HEU-SOL-THERM-049-007	1.00120	0.00240	1.00851	0.00013	1.00730	1.00664	0.00013	1.00543
HEU-SOL-THERM-049-008	1.00120	0.00240	1.00725	0.00012	1.00605	1.00556	0.00012	1.00435
HEU-SOL-THERM-049-009	1.00120	0.00200	0.99968	0.00014	0.99848	0.99782	0.00014	0.99662
HEU-SOL-THERM-049-010	1.00120	0.00240	0.98987	0.00015	0.98868	0.98771	0.00015	0.98653
HEU-SOL-THERM-049-011	1.00120	0.00220	0.99448	0.00014	0.99329	0.99249	0.00014	0.99130
HEU-SOL-THERM-049-012	1.00120	0.00210	0.99769	0.00014	0.99649	0.99582	0.00014	0.99463
HEU-SOL-THERM-049-013	1.00120	0.00210	0.99927	0.00014	0.99807	0.99740	0.00014	0.99620
HEU-SOL-THERM-049-014	1.00120	0.00200	1.00062	0.00014	0.99942	0.99887	0.00013	0.99767
HEU-SOL-THERM-049-015	1.00120	0.00210	1.00294	0.00013	1.00174	1.00136	0.00013	1.00016
HEU-SOL-THERM-049-016	1.00120	0.00200	1.00160	0.00013	1.00040	0.99965	0.00013	0.99845
HEU-SOL-THERM-049-017	1.00120	0.00210	1.00104	0.00013	0.99984	0.99953	0.00013	0.99833
HEU-SOL-THERM-049-018	1.00120	0.00200	1.00291	0.00013	1.00170	1.00152	0.00013	1.00032
HEU-SOL-THERM-049-019	1.00120	0.00200	1.00413	0.00012	1.00293	1.00275	0.00012	1.00155
HEU-SOL-THERM-049-020	1.00120	0.00190	1.00266	0.00012	1.00146	1.00125	0.00012	1.00005
HEU-SOL-THERM-050-001	0.99530	0.00860	1.00624	0.00015	1.01099	1.00568	0.00015	1.01043
HEU-SOL-THERM-050-002	0.99870	0.00830	1.00165	0.00015	1.00296	1.00122	0.00015	1.00252
HEU-SOL-THERM-050-003	0.99840	0.00790	1.00246	0.00015	1.00407	1.00247	0.00015	1.00408
HEU-SOL-THERM-050-004	0.99870	0.00840	1.00314	0.00015	1.00444	1.00300	0.00015	1.00431
HEU-SOL-THERM-050-005	0.99850	0.00850	1.00042	0.00015	1.00192	0.99995	0.00015	1.00145
HEU-SOL-THERM-050-006	0.99850	0.00810	1.00805	0.00015	1.00957	1.00754	0.00015	1.00905
HEU-SOL-THERM-050-007	0.99780	0.00780	0.99579	0.00015	0.99799	0.99606	0.00015	0.99826
HEU-SOL-THERM-050-008	0.99750	0.00840	0.99686	0.00015	0.99936	0.99624	0.00015	0.99874
HEU-SOL-THERM-050-009	0.99660	0.00820	0.99507	0.00014	0.99847	0.99534	0.00014	0.99874
HEU-SOL-THERM-050-010	0.99600	0.00900	0.97930	0.00015	0.98323	0.97862	0.00015	0.98255
HEU-SOL-THERM-050-011	0.99640	0.00890	0.99101	0.00015	0.99459	0.99026	0.00015	0.99384
IEU-MET-FAST-001-001	0.99880	0.00090	0.99892	0.00009	1.00012	0.99887	0.00009	1.00007
IEU-MET-FAST-001-002	0.99880	0.00090	0.99935	0.00009	1.00055	0.99892	0.00009	1.00012
IEU-MET-FAST-001-003	0.99900	0.00030	0.99865	0.00009	0.99965	0.99826	0.00009	0.99926
IEU-MET-FAST-001-004	0.99900	0.00030	0.99964	0.00009	1.00064	0.99948	0.00009	1.00048
IEU-MET-FAST-002-001	1.00000	0.00300	0.99650	0.00008	0.99650	0.99619	0.00008	0.99619
IEU-MET-FAST-003-001	1.00000	0.00170	0.99991	0.00009	0.99991	0.99961	0.00009	0.99961
IEU-MET-FAST-004-001	1.00000	0.00300	1.00523	0.00009	1.00523	1.00493	0.00009	1.00493
IEU-MET-FAST-005-001	1.00000	0.00210	1.00199	0.00009	1.00199	1.00094	0.00009	1.00094
IEU-MET-FAST-006-001	1.00000	0.00230	0.99435	0.00009	0.99435	0.99386	0.00009	0.99386
IEU-MET-FAST-007-001-D	1.00450	0.00070	1.00466	0.00007	1.00016	1.00421	0.00007	0.99971
IEU-MET-FAST-008-001	1.00000	0.00180	1.00245	0.00009	1.00245	1.00243	0.00009	1.00243
IEU-MET-FAST-009-001	1.00000	0.00530	1.00760	0.00011	1.00760	1.00701	0.00010	1.00701
IEU-MET-FAST-010-001	0.99540	0.00240	0.99706	0.00007	1.00167	0.99622	0.00007	1.00082
IEU-MET-FAST-012-001	1.00070	0.00270	1.00256	0.00007	1.00185	1.00151	0.00007	1.00081
IEU-MET-FAST-013-001	0.99410	0.00230	0.99700	0.00007	1.00292	0.99643	0.00007	1.00234
IEU-MET-FAST-014-001	0.99580	0.00220	0.99711	0.00007	1.00132	0.99672	0.00007	1.00092
IEU-MET-FAST-014-002	0.99270	0.00220	0.99423	0.00007	1.00154	0.99422	0.00007	1.00153
IEU-MET-FAST-015-001	0.99560	0.00150	0.99789	0.00008	1.00230	0.99733	0.00008	1.00174
IEU-MET-FAST-016-001	0.99740	0.00160	0.99604	0.00007	0.99864	0.99537	0.00007	0.99796
LEU-COMP-THERM-001-001	0.99980	0.00310	0.99987	0.00009	1.00007	0.99986	0.00009	1.00006
LEU-COMP-THERM-001-002	0.99980	0.00310	0.99916	0.00009	0.99936	0.99894	0.00009	0.99914
LEU-COMP-THERM-001-003	0.99980	0.00310	0.99890	0.00009	0.99910	0.99852	0.00009	0.99872
LEU-COMP-THERM-001-004	0.99980	0.00310	0.99943	0.00009	0.99963	0.99907	0.00009	0.99927
LEU-COMP-THERM-001-005	0.99980	0.00310	0.99732	0.00009	0.99752	0.99706	0.00009	0.99726
LEU-COMP-THERM-001-006	0.99980	0.00310	0.99932	0.00009	0.99952	0.99897	0.00009	0.99917
LEU-COMP-THERM-001-007	0.99980	0.00310	0.99859	0.00009	0.99879	0.99832	0.00009	0.99852
LEU-COMP-THERM-001-008	0.99980	0.00310	0.99755	0.00009	0.99775	0.99744	0.00009	0.99764
LEU-COMP-THERM-002-001	0.99970	0.00200	0.99882	0.00011	0.99912	0.99835	0.00010	0.99865
LEU-COMP-THERM-002-002	0.99970	0.00200	0.99999	0.00011	1.00029	0.99980	0.00011	1.00010
LEU-COMP-THERM-002-003	0.99970	0.00200	0.99958	0.00011	0.99988	0.99909	0.00011	0.99939
LEU-COMP-THERM-002-004	0.99970	0.00200	0.99951	0.00011	0.99981	0.99886	0.00010	0.99916
LEU-COMP-THERM-002-005	0.99970	0.00200	0.99802	0.00010	0.99832	0.99776	0.00010	0.99806

Continued on the next page

TABLE LIX: (continued) ENDF-6 ENDF/B-VIII.1 criticality validation.

Benchmark	E	unc.$_E$	ENDF/B-VIII.1			ENDF/B-VIII.0		
			C	unc.$_C$	C/E	C	unc.$_C$	C/E
LEU-COMP-THERM-005-001	1.00000	0.00230	1.00289	0.00011	1.00289	1.00255	0.00011	1.00255
LEU-COMP-THERM-005-002	1.00000	0.00210	0.99979	0.00011	0.99979	0.99936	0.00011	0.99936
LEU-COMP-THERM-005-003	1.00000	0.00290	0.99931	0.00011	0.99931	0.99911	0.00011	0.99911
LEU-COMP-THERM-005-004	1.00000	0.00250	0.99809	0.00011	0.99809	0.99762	0.00011	0.99762
LEU-COMP-THERM-005-005	1.00000	0.00470	1.00420	0.00011	1.00420	1.00303	0.00011	1.00303
LEU-COMP-THERM-005-006	1.00000	0.00420	1.00408	0.00011	1.00408	1.00332	0.00011	1.00332
LEU-COMP-THERM-005-007	1.00000	0.00430	1.00020	0.00011	1.00020	0.99937	0.00011	0.99937
LEU-COMP-THERM-005-008	1.00000	0.00210	1.00107	0.00011	1.00107	0.99986	0.00011	0.99986
LEU-COMP-THERM-005-009	1.00000	0.00400	1.00185	0.00011	1.00185	1.00060	0.00011	1.00060
LEU-COMP-THERM-005-010	1.00000	0.00280	1.00094	0.00010	1.00094	1.00009	0.00010	1.00009
LEU-COMP-THERM-005-011	1.00000	0.00430	1.00148	0.00010	1.00148	1.00026	0.00011	1.00026
LEU-COMP-THERM-005-012	1.00000	0.00660	1.00533	0.00010	1.00533	1.00377	0.00010	1.00377
LEU-COMP-THERM-005-013	1.00000	0.00640	1.01105	0.00011	1.01105	1.00900	0.00011	1.00900
LEU-COMP-THERM-006-001	1.00000	0.00300	0.99979	0.00010	0.99979	0.99948	0.00010	0.99948
LEU-COMP-THERM-006-002	1.00000	0.00300	1.00042	0.00010	1.00042	0.99968	0.00010	0.99968
LEU-COMP-THERM-006-003	1.00000	0.00300	1.00007	0.00010	1.00007	0.99934	0.00010	0.99934
LEU-COMP-THERM-006-004	1.00000	0.00300	0.99987	0.00010	0.99987	0.99944	0.00010	0.99944
LEU-COMP-THERM-006-005	1.00000	0.00300	0.99970	0.00010	0.99970	0.99942	0.00010	0.99942
LEU-COMP-THERM-006-006	1.00000	0.00300	1.00009	0.00010	1.00009	0.99983	0.00010	0.99983
LEU-COMP-THERM-006-007	1.00000	0.00300	0.99980	0.00010	0.99980	0.99944	0.00010	0.99944
LEU-COMP-THERM-006-008	1.00000	0.00300	0.99994	0.00010	0.99994	0.99944	0.00010	0.99944
LEU-COMP-THERM-006-009	1.00000	0.00300	1.00004	0.00010	1.00004	0.99965	0.00010	0.99965
LEU-COMP-THERM-006-010	1.00000	0.00300	1.00013	0.00010	1.00013	0.99974	0.00010	0.99974
LEU-COMP-THERM-006-011	1.00000	0.00300	0.99993	0.00010	0.99993	0.99968	0.00010	0.99968
LEU-COMP-THERM-006-012	1.00000	0.00300	0.99971	0.00010	0.99971	0.99914	0.00010	0.99914
LEU-COMP-THERM-006-013	1.00000	0.00300	0.99954	0.00010	0.99954	0.99926	0.00010	0.99926
LEU-COMP-THERM-006-014	1.00000	0.00300	1.00012	0.00010	1.00012	0.99969	0.00010	0.99969
LEU-COMP-THERM-006-015	1.00000	0.00300	0.99989	0.00010	0.99989	0.99930	0.00010	0.99930
LEU-COMP-THERM-006-016	1.00000	0.00300	0.99986	0.00010	0.99986	0.99957	0.00010	0.99957
LEU-COMP-THERM-006-017	1.00000	0.00300	0.99967	0.00010	0.99967	0.99937	0.00010	0.99937
LEU-COMP-THERM-006-018	1.00000	0.00300	0.99970	0.00010	0.99970	0.99939	0.00010	0.99939
LEU-COMP-THERM-007-001	1.00000	0.00140	0.99736	0.00011	0.99736	0.99685	0.00011	0.99685
LEU-COMP-THERM-007-002	1.00000	0.00080	0.99913	0.00011	0.99913	0.99900	0.00011	0.99900
LEU-COMP-THERM-007-003	1.00000	0.00070	0.99816	0.00010	0.99816	0.99799	0.00010	0.99799
LEU-COMP-THERM-007-004	1.00000	0.00080	0.99865	0.00009	0.99865	0.99856	0.00009	0.99856
LEU-COMP-THERM-007-005	1.00000	0.00140	0.99671	0.00011	0.99671	0.99615	0.00011	0.99615
LEU-COMP-THERM-007-006	1.00000	0.00080	0.99902	0.00011	0.99902	0.99891	0.00011	0.99891
LEU-COMP-THERM-007-007	1.00000	0.00070	0.99910	0.00010	0.99910	0.99871	0.00010	0.99871
LEU-COMP-THERM-007-008	1.00000	0.00140	0.99818	0.00011	0.99818	0.99725	0.00011	0.99725
LEU-COMP-THERM-007-009	1.00000	0.00080	0.99858	0.00011	0.99858	0.99819	0.00011	0.99819
LEU-COMP-THERM-007-010	1.00000	0.00070	0.99895	0.00010	0.99895	0.99886	0.00010	0.99886
LEU-COMP-THERM-008-001	1.00070	0.00120	1.00104	0.00009	1.00034	1.00067	0.00009	0.99997
LEU-COMP-THERM-008-002	1.00070	0.00120	1.00100	0.00009	1.00030	1.00103	0.00009	1.00033
LEU-COMP-THERM-008-005	1.00070	0.00120	1.00062	0.00009	0.99992	1.00016	0.00009	0.99946
LEU-COMP-THERM-008-007	1.00070	0.00120	1.00019	0.00009	0.99949	0.99994	0.00009	0.99924
LEU-COMP-THERM-008-008	1.00070	0.00120	0.99946	0.00010	0.99876	0.99949	0.00009	0.99879
LEU-COMP-THERM-008-011	1.00070	0.00120	1.00144	0.00009	1.00074	1.00149	0.00009	1.00079
LEU-COMP-THERM-009-001	1.00000	0.00210	0.99963	0.00010	0.99963	0.99946	0.00010	0.99946
LEU-COMP-THERM-009-002	1.00000	0.00210	0.99932	0.00011	0.99932	0.99883	0.00011	0.99883
LEU-COMP-THERM-009-003	1.00000	0.00210	0.99876	0.00010	0.99876	0.99843	0.00010	0.99843
LEU-COMP-THERM-009-004	1.00000	0.00210	0.99982	0.00010	0.99982	0.99900	0.00010	0.99900
LEU-COMP-THERM-009-005	1.00000	0.00210	1.00001	0.00010	1.00001	0.99973	0.00010	0.99973
LEU-COMP-THERM-009-006	1.00000	0.00210	0.99910	0.00011	0.99910	0.99903	0.00011	0.99903
LEU-COMP-THERM-009-007	1.00000	0.00210	0.99999	0.00011	0.99999	0.99994	0.00010	0.99994
LEU-COMP-THERM-009-008	1.00000	0.00210	0.99916	0.00010	0.99916	0.99891	0.00010	0.99891
LEU-COMP-THERM-009-010	1.00000	0.00210	0.99920	0.00010	0.99920	0.99894	0.00010	0.99894
LEU-COMP-THERM-009-011	1.00000	0.00210	0.99923	0.00011	0.99923	0.99891	0.00011	0.99891
LEU-COMP-THERM-009-013	1.00000	0.00210	0.99964	0.00010	0.99964	0.99919	0.00010	0.99919
LEU-COMP-THERM-009-015	1.00000	0.00210	0.99977	0.00010	0.99977	0.99949	0.00011	0.99949
LEU-COMP-THERM-009-016	1.00000	0.00210	0.99946	0.00010	0.99946	0.99876	0.00010	0.99876
LEU-COMP-THERM-009-017	1.00000	0.00210	1.00004	0.00010	1.00004	0.99965	0.00010	0.99965
LEU-COMP-THERM-009-018	1.00000	0.00210	0.99864	0.00010	0.99864	0.99858	0.00011	0.99858
LEU-COMP-THERM-009-019	1.00000	0.00210	0.99977	0.00010	0.99977	0.99948	0.00010	0.99948
LEU-COMP-THERM-009-020	1.00000	0.00210	0.99919	0.00011	0.99919	0.99887	0.00010	0.99887
LEU-COMP-THERM-009-021	1.00000	0.00210	0.99985	0.00010	0.99985	0.99952	0.00010	0.99952
LEU-COMP-THERM-009-022	1.00000	0.00210	0.99928	0.00010	0.99928	0.99908	0.00011	0.99908
LEU-COMP-THERM-009-023	1.00000	0.00210	0.99996	0.00010	0.99996	0.99970	0.00010	0.99970
LEU-COMP-THERM-009-024	1.00000	0.00210	0.99915	0.00011	0.99915	0.99877	0.00010	0.99877
LEU-COMP-THERM-009-025	1.00000	0.00210	0.99944	0.00011	0.99944	0.99926	0.00010	0.99926
LEU-COMP-THERM-009-026	1.00000	0.00210	0.99958	0.00010	0.99958	0.99920	0.00010	0.99920
LEU-COMP-THERM-009-027	1.00000	0.00210	0.99977	0.00010	0.99977	0.99931	0.00010	0.99931
LEU-COMP-THERM-010-001	1.00000	0.00210	1.00682	0.00010	1.00682	1.00490	0.00010	1.00490
LEU-COMP-THERM-010-002	1.00000	0.00210	1.00685	0.00010	1.00685	1.00494	0.00010	1.00494
LEU-COMP-THERM-010-003	1.00000	0.00210	1.00562	0.00011	1.00562	1.00421	0.00010	1.00421
LEU-COMP-THERM-010-004	1.00000	0.00210	0.99739	0.00010	0.99739	0.99683	0.00010	0.99683

Continued on the next page

TABLE LIX: (continued) ENDF-6 ENDF/B-VIII.1 criticality validation.

Benchmark	E	unc.$_E$	ENDF/B-VIII.1			ENDF/B-VIII.0		
			C	unc.$_C$	C/E	C	unc.$_C$	C/E
LEU-COMP-THERM-010-005	1.00000	0.00210	0.99917	0.00010	0.99917	0.99911	0.00010	0.99911
LEU-COMP-THERM-010-006	1.00000	0.00210	1.00020	0.00010	1.00020	0.99990	0.00010	0.99990
LEU-COMP-THERM-010-007	1.00000	0.00210	1.00130	0.00010	1.00130	1.00110	0.00010	1.00110
LEU-COMP-THERM-010-008	1.00000	0.00210	0.99837	0.00010	0.99837	0.99798	0.00010	0.99798
LEU-COMP-THERM-010-009	1.00000	0.00210	1.00093	0.00011	1.00093	1.00003	0.00010	1.00003
LEU-COMP-THERM-010-010	1.00000	0.00210	1.00094	0.00011	1.00094	1.00038	0.00010	1.00038
LEU-COMP-THERM-010-011	1.00000	0.00210	1.00120	0.00010	1.00120	1.00027	0.00010	1.00027
LEU-COMP-THERM-010-012	1.00000	0.00210	1.00031	0.00010	1.00031	0.99945	0.00011	0.99945
LEU-COMP-THERM-010-013	1.00000	0.00210	0.99794	0.00010	0.99794	0.99773	0.00010	0.99773
LEU-COMP-THERM-010-014	1.00000	0.00280	1.00218	0.00011	1.00218	1.00105	0.00011	1.00105
LEU-COMP-THERM-010-015	1.00000	0.00280	1.00253	0.00011	1.00253	1.00138	0.00011	1.00138
LEU-COMP-THERM-010-016	1.00000	0.00280	1.00310	0.00011	1.00310	1.00210	0.00011	1.00210
LEU-COMP-THERM-010-017	1.00000	0.00280	1.00225	0.00011	1.00225	1.00132	0.00011	1.00132
LEU-COMP-THERM-010-018	1.00000	0.00280	1.00211	0.00011	1.00211	1.00121	0.00011	1.00121
LEU-COMP-THERM-010-019	1.00000	0.00280	1.00158	0.00011	1.00158	1.00061	0.00011	1.00061
LEU-COMP-THERM-010-020	1.00000	0.00280	1.00458	0.00011	1.00458	1.00273	0.00011	1.00273
LEU-COMP-THERM-010-021	1.00000	0.00280	1.00467	0.00011	1.00467	1.00334	0.00011	1.00334
LEU-COMP-THERM-010-022	1.00000	0.00280	1.00401	0.00011	1.00401	1.00272	0.00011	1.00272
LEU-COMP-THERM-010-023	1.00000	0.00280	1.00219	0.00011	1.00219	1.00093	0.00011	1.00093
LEU-COMP-THERM-010-024	1.00000	0.00280	0.99960	0.00011	0.99960	0.99889	0.00010	0.99889
LEU-COMP-THERM-010-025	1.00000	0.00280	1.00123	0.00010	1.00123	1.00041	0.00010	1.00041
LEU-COMP-THERM-010-026	1.00000	0.00280	1.00153	0.00011	1.00153	1.00087	0.00011	1.00087
LEU-COMP-THERM-010-027	1.00000	0.00280	1.00176	0.00011	1.00176	1.00104	0.00010	1.00104
LEU-COMP-THERM-010-028	1.00000	0.00280	1.00225	0.00011	1.00225	1.00155	0.00010	1.00155
LEU-COMP-THERM-010-029	1.00000	0.00280	1.00155	0.00011	1.00155	1.00082	0.00011	1.00082
LEU-COMP-THERM-010-030	1.00000	0.00280	1.00019	0.00010	1.00019	0.99982	0.00011	0.99982
LEU-COMP-THERM-011-002	1.00090	0.00320	0.99832	0.00010	0.99742	0.99803	0.00010	0.99713
LEU-COMP-THERM-011-003	1.00090	0.00320	0.99829	0.00010	0.99740	0.99817	0.00010	0.99727
LEU-COMP-THERM-011-007	1.00090	0.00320	0.99856	0.00010	0.99767	0.99816	0.00009	0.99726
LEU-COMP-THERM-011-009	1.00090	0.00320	0.99847	0.00010	0.99758	0.99824	0.00010	0.99734
LEU-COMP-THERM-011-015	1.00100	0.00180	0.99711	0.00009	0.99611	0.99662	0.00009	0.99562
LEU-COMP-THERM-017-001	1.00000	0.00310	1.00257	0.00009	1.00257	1.00145	0.00009	1.00145
LEU-COMP-THERM-017-002	1.00000	0.00310	1.00231	0.00009	1.00231	1.00120	0.00009	1.00120
LEU-COMP-THERM-017-003	1.00000	0.00310	1.00040	0.00009	1.00040	0.99974	0.00009	0.99974
LEU-COMP-THERM-017-004	1.00000	0.00310	0.99830	0.00009	0.99830	0.99777	0.00009	0.99777
LEU-COMP-THERM-017-005	1.00000	0.00310	0.99996	0.00009	0.99996	0.99965	0.00009	0.99965
LEU-COMP-THERM-017-006	1.00000	0.00310	1.00020	0.00009	1.00020	0.99981	0.00009	0.99981
LEU-COMP-THERM-017-007	1.00000	0.00310	1.00024	0.00009	1.00024	0.99989	0.00009	0.99989
LEU-COMP-THERM-017-008	1.00000	0.00310	0.99871	0.00009	0.99871	0.99837	0.00009	0.99837
LEU-COMP-THERM-017-009	1.00000	0.00310	0.99798	0.00009	0.99798	0.99760	0.00009	0.99760
LEU-COMP-THERM-017-010	1.00000	0.00310	0.99868	0.00009	0.99868	0.99824	0.00009	0.99824
LEU-COMP-THERM-017-011	1.00000	0.00310	0.99894	0.00009	0.99894	0.99864	0.00009	0.99864
LEU-COMP-THERM-017-012	1.00000	0.00310	0.99887	0.00009	0.99887	0.99840	0.00009	0.99840
LEU-COMP-THERM-017-013	1.00000	0.00310	0.99927	0.00009	0.99927	0.99876	0.00009	0.99876
LEU-COMP-THERM-017-014	1.00000	0.00310	0.99939	0.00009	0.99939	0.99907	0.00009	0.99907
LEU-COMP-THERM-022-001	1.00000	0.00460	1.00223	0.00011	1.00223	1.00180	0.00011	1.00180
LEU-COMP-THERM-022-002	1.00000	0.00460	1.00713	0.00011	1.00713	1.00645	0.00011	1.00645
LEU-COMP-THERM-022-003	1.00000	0.00360	1.00793	0.00011	1.00793	1.00804	0.00011	1.00804
LEU-COMP-THERM-022-004	1.00000	0.00370	1.00860	0.00011	1.00860	1.00885	0.00011	1.00885
LEU-COMP-THERM-022-005	1.00000	0.00380	1.00394	0.00011	1.00394	1.00378	0.00010	1.00378
LEU-COMP-THERM-022-006	1.00000	0.00460	1.00174	0.00009	1.00174	1.00189	0.00009	1.00189
LEU-COMP-THERM-022-007	1.00000	0.00460	1.00430	0.00009	1.00430	1.00432	0.00009	1.00432
LEU-COMP-THERM-024-001	1.00000	0.00540	1.00062	0.00011	1.00062	0.99992	0.00011	0.99992
LEU-COMP-THERM-024-002	1.00000	0.00400	1.00897	0.00011	1.00897	1.00901	0.00011	1.00901
LEU-COMP-THERM-025-001	1.00000	0.00410	0.98807	0.00011	0.98807	0.98787	0.00011	0.98787
LEU-COMP-THERM-025-002	1.00000	0.00440	0.99591	0.00011	0.99591	0.99618	0.00011	0.99618
LEU-COMP-THERM-025-003	1.00000	0.00470	1.00084	0.00011	1.00084	1.00119	0.00011	1.00119
LEU-COMP-THERM-025-004	1.00000	0.00520	1.00299	0.00010	1.00299	1.00329	0.00010	1.00329
LEU-COMP-THERM-027-001	1.00140	0.00150	1.00681	0.00011	1.00540	1.00425	0.00011	1.00285
LEU-COMP-THERM-027-002	1.00140	0.00120	1.00887	0.00011	1.00746	1.00645	0.00011	1.00504
LEU-COMP-THERM-027-003	1.00140	0.00150	1.00915	0.00011	1.00774	1.00706	0.00011	1.00565
LEU-COMP-THERM-027-004	1.00140	0.00150	1.01092	0.00011	1.00951	1.00919	0.00011	1.00778
LEU-COMP-THERM-028-001	0.99977	0.00472	0.99752	0.00010	0.99775	0.99760	0.00010	0.99783
LEU-COMP-THERM-028-002	1.00012	0.00540	0.99881	0.00010	0.99869	0.99887	0.00010	0.99875
LEU-COMP-THERM-028-003	0.99992	0.00511	0.99838	0.00010	0.99846	0.99844	0.00010	0.99852
LEU-COMP-THERM-028-004	1.00000	0.00432	1.00056	0.00010	1.00056	1.00081	0.00011	1.00081
LEU-COMP-THERM-028-005	1.00022	0.00477	0.99957	0.00010	0.99935	0.99955	0.00010	0.99933
LEU-COMP-THERM-028-006	1.00009	0.00452	1.00079	0.00010	1.00070	1.00070	0.00010	1.00061
LEU-COMP-THERM-028-007	0.99978	0.00467	0.99543	0.00011	0.99565	0.99562	0.00010	0.99584
LEU-COMP-THERM-028-008	0.99978	0.00515	0.99368	0.00010	0.99390	0.99406	0.00010	0.99428
LEU-COMP-THERM-028-009	0.99980	0.00470	0.99243	0.00010	0.99263	0.99242	0.00010	0.99262
LEU-COMP-THERM-028-010	1.00039	0.00453	0.99729	0.00010	0.99690	0.99782	0.00010	0.99743
LEU-COMP-THERM-028-011	1.00022	0.00450	0.99787	0.00010	0.99765	0.99819	0.00010	0.99797
LEU-COMP-THERM-028-012	1.00003	0.00489	0.99627	0.00010	0.99624	0.99645	0.00010	0.99642

Continued on the next page

TABLE LIX: (continued) ENDF-6 ENDF/B-VIII.1 criticality validation.

Benchmark	E	unc.$_E$	ENDF/B-VIII.1			ENDF/B-VIII.0		
			C	unc.$_C$	C/E	C	unc.$_C$	C/E
LEU-COMP-THERM-028-013	0.99980	0.00496	0.99519	0.00010	0.99539	0.99548	0.00010	0.99568
LEU-COMP-THERM-028-014	1.00006	0.00474	0.99284	0.00010	0.99278	0.99339	0.00010	0.99333
LEU-COMP-THERM-028-015	0.99967	0.00443	0.99811	0.00009	0.99843	0.99824	0.00009	0.99857
LEU-COMP-THERM-028-016	1.00000	0.00491	0.99836	0.00009	0.99836	0.99878	0.00009	0.99878
LEU-COMP-THERM-028-017	1.00000	0.00466	0.99856	0.00009	0.99856	0.99879	0.00009	0.99879
LEU-COMP-THERM-028-018	0.99988	0.00469	0.99900	0.00009	0.99912	0.99917	0.00009	0.99929
LEU-COMP-THERM-028-019	1.00017	0.00464	0.99814	0.00009	0.99797	0.99864	0.00009	0.99847
LEU-COMP-THERM-028-020	1.00007	0.00456	0.99615	0.00009	0.99608	0.99620	0.00009	0.99613
LEU-COMP-THERM-035-001	1.00000	0.00180	0.99987	0.00011	0.99987	0.99974	0.00010	0.99974
LEU-COMP-THERM-035-002	1.00000	0.00190	0.99905	0.00010	0.99905	0.99853	0.00010	0.99853
LEU-COMP-THERM-035-003	1.00000	0.00220	0.99533	0.00010	0.99533	0.99472	0.00010	0.99472
LEU-COMP-THERM-039-001	1.00000	0.00140	0.99699	0.00011	0.99699	0.99632	0.00011	0.99632
LEU-COMP-THERM-039-002	1.00000	0.00140	0.99778	0.00011	0.99778	0.99731	0.00011	0.99731
LEU-COMP-THERM-039-003	1.00000	0.00140	0.99731	0.00011	0.99731	0.99660	0.00011	0.99660
LEU-COMP-THERM-039-004	1.00000	0.00140	0.99647	0.00011	0.99647	0.99613	0.00011	0.99613
LEU-COMP-THERM-039-005	1.00000	0.00090	0.99770	0.00011	0.99770	0.99722	0.00011	0.99722
LEU-COMP-THERM-039-006	1.00000	0.00090	0.99760	0.00011	0.99760	0.99700	0.00011	0.99700
LEU-COMP-THERM-039-007	1.00000	0.00120	0.99701	0.00011	0.99701	0.99628	0.00011	0.99628
LEU-COMP-THERM-039-008	1.00000	0.00120	0.99694	0.00011	0.99694	0.99674	0.00011	0.99674
LEU-COMP-THERM-039-009	1.00000	0.00120	0.99700	0.00011	0.99700	0.99637	0.00011	0.99637
LEU-COMP-THERM-039-010	1.00000	0.00120	0.99759	0.00011	0.99759	0.99714	0.00011	0.99714
LEU-COMP-THERM-042-001	1.00000	0.00160	0.99860	0.00010	0.99860	0.99765	0.00010	0.99765
LEU-COMP-THERM-042-002	1.00000	0.00160	0.99811	0.00010	0.99811	0.99737	0.00010	0.99737
LEU-COMP-THERM-042-003	1.00000	0.00160	0.99882	0.00010	0.99882	0.99824	0.00010	0.99824
LEU-COMP-THERM-042-004	1.00000	0.00170	0.99832	0.00010	0.99832	0.99770	0.00010	0.99770
LEU-COMP-THERM-042-005	1.00000	0.00330	0.99944	0.00010	0.99944	0.99881	0.00010	0.99881
LEU-COMP-THERM-042-006	1.00000	0.00160	0.99955	0.00010	0.99955	0.99876	0.00010	0.99876
LEU-COMP-THERM-042-007	1.00000	0.00180	0.99791	0.00010	0.99791	0.99718	0.00010	0.99718
LEU-COMP-THERM-060-001	0.99900	0.00260	1.00121	0.00009	1.00221	1.00087	0.00009	1.00187
LEU-COMP-THERM-060-002	0.99770	0.00260	1.00061	0.00009	1.00292	1.00091	0.00009	1.00322
LEU-COMP-THERM-060-003	1.00010	0.00260	1.00214	0.00009	1.00204	1.00205	0.00009	1.00195
LEU-COMP-THERM-060-004	1.00170	0.00260	1.00184	0.00010	1.00014	1.00247	0.00009	1.00077
LEU-COMP-THERM-060-005	1.00090	0.00260	1.00341	0.00009	1.00251	1.00303	0.00010	1.00213
LEU-COMP-THERM-060-006	0.98940	0.00270	0.99113	0.00010	1.00174	0.99148	0.00010	1.00210
LEU-COMP-THERM-078-001	0.99950	0.00100	0.99772	0.00012	0.99822	0.99671	0.00012	0.99721
LEU-COMP-THERM-078-002	0.99990	0.00100	0.99845	0.00011	0.99855	0.99744	0.00012	0.99754
LEU-COMP-THERM-078-003	0.99900	0.00100	0.99741	0.00012	0.99841	0.99639	0.00012	0.99739
LEU-COMP-THERM-078-004	0.99860	0.00100	0.99716	0.00012	0.99856	0.99616	0.00012	0.99756
LEU-COMP-THERM-078-005	0.99800	0.00100	0.99667	0.00012	0.99866	0.99565	0.00012	0.99765
LEU-COMP-THERM-078-006	0.99740	0.00100	0.99627	0.00012	0.99887	0.99481	0.00012	0.99740
LEU-COMP-THERM-078-007	0.99940	0.00100	0.99782	0.00012	0.99842	0.99672	0.00012	0.99732
LEU-COMP-THERM-078-008	0.99870	0.00100	0.99739	0.00012	0.99869	0.99615	0.00012	0.99745
LEU-COMP-THERM-078-009	0.99780	0.00100	0.99626	0.00012	0.99845	0.99532	0.00012	0.99751
LEU-COMP-THERM-078-010	0.99690	0.00100	0.99470	0.00012	0.99780	0.99411	0.00012	0.99720
LEU-COMP-THERM-078-011	0.99940	0.00100	0.99786	0.00012	0.99846	0.99681	0.00012	0.99741
LEU-COMP-THERM-078-012	0.99930	0.00100	0.99782	0.00012	0.99852	0.99676	0.00012	0.99746
LEU-COMP-THERM-078-013	0.99930	0.00100	0.99790	0.00012	0.99860	0.99648	0.00012	0.99718
LEU-COMP-THERM-078-014	0.99910	0.00100	0.99762	0.00012	0.99852	0.99645	0.00012	0.99735
LEU-COMP-THERM-078-015	0.99960	0.00100	0.99846	0.00012	0.99886	0.99760	0.00012	0.99800
LEU-COMP-THERM-079-001	0.99990	0.00102	0.99772	0.00011	0.99782	0.99676	0.00011	0.99686
LEU-COMP-THERM-079-002	1.00020	0.00102	0.99813	0.00011	0.99793	0.99724	0.00011	0.99704
LEU-COMP-THERM-079-003	1.00050	0.00102	0.99846	0.00011	0.99796	0.99776	0.00011	0.99726
LEU-COMP-THERM-079-004	1.00040	0.00102	0.99865	0.00011	0.99825	0.99807	0.00011	0.99767
LEU-COMP-THERM-079-005	1.00040	0.00102	0.99880	0.00011	0.99840	0.99823	0.00011	0.99783
LEU-COMP-THERM-079-006	0.99940	0.00073	0.99880	0.00011	0.99940	0.99858	0.00010	0.99918
LEU-COMP-THERM-079-007	1.00030	0.00073	0.99804	0.00010	0.99774	0.99770	0.00010	0.99740
LEU-COMP-THERM-079-008	1.00080	0.00073	0.99929	0.00011	0.99850	0.99921	0.00010	0.99841
LEU-COMP-THERM-079-009	1.00030	0.00073	0.99873	0.00011	0.99843	0.99877	0.00010	0.99847
LEU-COMP-THERM-079-010	1.00090	0.00073	0.99961	0.00010	0.99871	0.99967	0.00010	0.99877
LEU-COMP-THERM-080-001	0.99760	0.00100	0.99551	0.00012	0.99791	0.99458	0.00012	0.99697
LEU-COMP-THERM-080-002	0.99820	0.00100	0.99583	0.00012	0.99763	0.99511	0.00012	0.99690
LEU-COMP-THERM-080-003	0.99840	0.00100	0.99649	0.00012	0.99809	0.99496	0.00012	0.99655
LEU-COMP-THERM-080-004	0.99810	0.00100	0.99598	0.00012	0.99788	0.99456	0.00012	0.99645
LEU-COMP-THERM-080-005	0.99790	0.00100	0.99571	0.00012	0.99781	0.99460	0.00012	0.99669
LEU-COMP-THERM-080-006	0.99750	0.00100	0.99552	0.00012	0.99801	0.99420	0.00012	0.99669
LEU-COMP-THERM-080-007	0.99930	0.00100	0.99731	0.00012	0.99801	0.99595	0.00012	0.99665
LEU-COMP-THERM-080-008	0.99870	0.00100	0.99668	0.00012	0.99798	0.99552	0.00012	0.99682
LEU-COMP-THERM-080-009	0.99820	0.00100	0.99634	0.00012	0.99814	0.99488	0.00012	0.99667
LEU-COMP-THERM-080-010	0.99720	0.00100	0.99547	0.00012	0.99826	0.99424	0.00012	0.99703
LEU-COMP-THERM-080-011	0.99840	0.00100	0.99698	0.00012	0.99857	0.99570	0.00012	0.99730
LEU-SOL-THERM-004-001	0.99940	0.00080	1.00139	0.00009	1.00199	1.00077	0.00009	1.00137
LEU-SOL-THERM-004-002	0.99990	0.00090	1.00237	0.00009	1.00247	1.00203	0.00009	1.00213
LEU-SOL-THERM-004-003	0.99990	0.00090	1.00027	0.00009	1.00037	0.99976	0.00009	0.99986
LEU-SOL-THERM-004-004	0.99990	0.00100	1.00249	0.00008	1.00259	1.00201	0.00008	1.00211

Continued on the next page

TABLE LIX: (continued) ENDF-6 ENDF/B-VIII.1 criticality validation.

Benchmark	E	unc.$_E$	ENDF/B-VIII.1			ENDF/B-VIII.0		
			C	unc.$_C$	C/E	C	unc.$_C$	C/E
LEU-SOL-THERM-004-005	0.99990	0.00100	1.00224	0.00008	1.00234	1.00214	0.00008	1.00224
LEU-SOL-THERM-004-006	0.99940	0.00110	1.00140	0.00008	1.00200	1.00117	0.00008	1.00177
LEU-SOL-THERM-004-007	0.99960	0.00110	1.00158	0.00008	1.00198	1.00119	0.00008	1.00159
LEU-SOL-THERM-007-001	0.99610	0.00090	0.99546	0.00010	0.99936	0.99531	0.00010	0.99921
LEU-SOL-THERM-007-002	0.99730	0.00090	0.99792	0.00010	1.00062	0.99731	0.00010	1.00001
LEU-SOL-THERM-007-003	0.99850	0.00100	0.99665	0.00009	0.99814	0.99614	0.00009	0.99764
LEU-SOL-THERM-007-004	0.99880	0.00110	0.99932	0.00009	1.00052	0.99880	0.00009	1.00000
LEU-SOL-THERM-007-005	0.99830	0.00110	0.99786	0.00008	0.99956	0.99723	0.00008	0.99893
LEU-SOL-THERM-020-001	0.99950	0.00100	1.00014	0.00008	1.00064	1.00005	0.00008	1.00055
LEU-SOL-THERM-020-002	0.99960	0.00100	0.99985	0.00008	1.00025	0.99946	0.00008	0.99986
LEU-SOL-THERM-020-003	0.99970	0.00120	0.99922	0.00007	0.99952	0.99867	0.00008	0.99897
LEU-SOL-THERM-020-004	0.99980	0.00120	1.00020	0.00007	1.00040	0.99982	0.00007	1.00002
LEU-SOL-THERM-021-001	0.99830	0.00090	0.99837	0.00009	1.00007	0.99782	0.00009	0.99952
LEU-SOL-THERM-021-002	0.99850	0.00100	0.99872	0.00008	1.00022	0.99821	0.00008	0.99971
LEU-SOL-THERM-021-003	0.99890	0.00110	0.99765	0.00008	0.99874	0.99734	0.00008	0.99844
LEU-SOL-THERM-021-004	0.99930	0.00120	0.99956	0.00007	1.00026	0.99910	0.00007	0.99980
MIX-MET-FAST-001-001	1.00000	0.00160	0.99915	0.00009	0.99915	0.99924	0.00008	0.99924
MIX-MET-FAST-002-001	1.00000	0.00420	1.00333	0.00010	1.00333	1.00342	0.00010	1.00342
MIX-MET-FAST-002-002	1.00000	0.00440	1.00376	0.00010	1.00376	1.00356	0.00010	1.00356
MIX-MET-FAST-002-003	1.00000	0.00480	1.00410	0.00010	1.00410	1.00391	0.00009	1.00391
MIX-MET-FAST-003-001	0.99930	0.00160	1.00080	0.00009	1.00150	1.00058	0.00009	1.00128
MIX-MET-FAST-004-001	0.99930	0.00130	0.99986	0.00009	1.00056	0.99961	0.00009	1.00031
MIX-MET-FAST-004-002	0.99930	0.00130	0.99887	0.00009	0.99957	0.99893	0.00009	0.99963
MIX-MET-FAST-005-001	0.99900	0.00170	1.00376	0.00009	1.00476	1.00368	0.00009	1.00468
MIX-MET-FAST-007-001	1.00000	0.00450	1.00218	0.00011	1.00218	1.00069	0.00011	1.00069
MIX-MET-FAST-007-002	1.00000	0.00230	1.00668	0.00011	1.00668	1.00596	0.00011	1.00596
MIX-MET-FAST-007-003	1.00000	0.00280	1.00446	0.00010	1.00446	1.00435	0.00010	1.00435
MIX-MET-FAST-007-004	1.00000	0.00280	1.00371	0.00010	1.00371	1.00335	0.00010	1.00335
MIX-MET-FAST-007-005	1.00000	0.00320	1.00137	0.00009	1.00137	1.00130	0.00009	1.00130
MIX-MET-FAST-007-006	1.00000	0.00350	1.00026	0.00009	1.00026	1.00033	0.00009	1.00033
MIX-MET-FAST-007-007	1.00000	0.00320	1.00521	0.00011	1.00521	1.00415	0.00011	1.00415
MIX-MET-FAST-007-008	1.00000	0.00300	1.00360	0.00011	1.00360	1.00295	0.00010	1.00295
MIX-MET-FAST-007-009	1.00000	0.00280	1.00364	0.00010	1.00364	1.00293	0.00010	1.00293
MIX-MET-FAST-007-010	1.00000	0.00270	1.00357	0.00010	1.00357	1.00319	0.00010	1.00319
MIX-MET-FAST-007-011	1.00000	0.00260	1.00230	0.00010	1.00230	1.00187	0.00009	1.00187
MIX-MET-FAST-007-012	1.00000	0.00300	1.00152	0.00009	1.00152	1.00157	0.00009	1.00157
MIX-MET-FAST-007-013	1.00000	0.00330	1.00045	0.00009	1.00045	1.00010	0.00009	1.00010
MIX-MET-FAST-007-014	1.00000	0.00320	1.00686	0.00010	1.00686	1.00625	0.00010	1.00625
MIX-MET-FAST-007-015	1.00000	0.00320	1.00630	0.00010	1.00630	1.00573	0.00010	1.00573
MIX-MET-FAST-007-016	1.00000	0.00280	1.00483	0.00009	1.00483	1.00422	0.00010	1.00422
MIX-MET-FAST-007-017	1.00000	0.00280	1.00470	0.00009	1.00470	1.00448	0.00009	1.00448
MIX-MET-FAST-007-018	1.00000	0.00300	1.00693	0.00009	1.00693	1.00693	0.00009	1.00693
MIX-MET-FAST-007-019	1.00000	0.00340	1.00607	0.00009	1.00607	1.00554	0.00009	1.00554
MIX-MET-FAST-007-020	1.00000	0.00300	1.00378	0.00009	1.00378	1.00388	0.00009	1.00388
MIX-MET-FAST-007-021	1.00000	0.00310	1.00422	0.00009	1.00422	1.00440	0.00009	1.00440
MIX-MET-FAST-007-022	1.00000	0.00300	1.00301	0.00009	1.00301	1.00281	0.00009	1.00281
MIX-MET-FAST-007-023	1.00000	0.00280	1.00261	0.00009	1.00261	1.00257	0.00009	1.00257
MIX-MET-FAST-009-001	1.00000	0.00100	0.99913	0.00008	0.99913	0.99964	0.00008	0.99964
MIX-MET-FAST-010-001	1.00000	0.00090	0.99945	0.00009	0.99945	0.99924	0.00008	0.99924
MIX-MET-FAST-011-001-B	0.98970	0.00230	0.99053	0.00010	1.00084	0.98970	0.00010	1.00000
MIX-MET-FAST-011-001-C	0.99980	0.00230	0.99610	0.00010	0.99630	0.99591	0.00010	0.99611
MIX-MET-FAST-011-001-D	1.00180	0.00240	1.00057	0.00010	0.99878	1.00078	0.00010	0.99898
MIX-MET-FAST-011-001-E	1.00120	0.00240	1.00185	0.00010	1.00065	1.00246	0.00010	1.00126
MIX-MET-INTER-003-001	0.96380	0.00270	0.96817	0.00010	1.00454	0.97059	0.00010	1.00705
MIX-MET-INTER-004-001	0.97570	0.00230	0.97555	0.00009	0.99985	0.97969	0.00009	1.00409
MIX-MET-MIXED-001-001	0.99910	0.00130	1.00063	0.00012	1.00153	1.00007	0.00012	1.00097
PU-MET-FAST-001-001-s	1.00000	0.00110	1.00010	0.00001	1.00010	1.00065	0.00008	1.00065
PU-MET-FAST-002-001	1.00000	0.00200	1.00075	0.00008	1.00075	1.00147	0.00008	1.00147
PU-MET-FAST-005-001	1.00000	0.00130	0.99991	0.00009	0.99991	0.99922	0.00009	0.99922
PU-MET-FAST-006-001	1.00000	0.00300	0.99997	0.00010	0.99997	0.99975	0.00010	0.99975
PU-MET-FAST-008-001	1.00000	0.00060	0.99759	0.00009	0.99759	0.99740	0.00009	0.99740
PU-MET-FAST-009-001	1.00000	0.00270	1.00483	0.00009	1.00483	1.00482	0.00009	1.00482
PU-MET-FAST-010-001	1.00000	0.00180	0.99809	0.00009	0.99809	0.99779	0.00009	0.99779
PU-MET-FAST-011-001	1.00000	0.00100	1.00044	0.00011	1.00044	1.00077	0.00011	1.00077

Continued on the next page

TABLE LIX: (continued) ENDF-6 ENDF/B-VIII.1 criticality validation.

Benchmark	E	unc.$_E$	ENDF/B-VIII.1			ENDF/B-VIII.0		
			C	unc.$_C$	C/E	C	unc.$_C$	C/E
PU-MET-FAST-012-001	1.00090	0.00210	1.00265	0.00010	1.00175	1.00216	0.00010	1.00126
PU-MET-FAST-013-001	1.00340	0.00230	0.99976	0.00009	0.99637	0.99769	0.00009	0.99431
PU-MET-FAST-014-001	1.00370	0.00310	0.99099	0.00009	0.98734	0.99046	0.00009	0.98681
PU-MET-FAST-015-001	1.00410	0.00260	1.00477	0.00009	1.00066	1.00367	0.00009	0.99957
PU-MET-FAST-016-001	0.99740	0.00420	1.01783	0.00011	1.02048	1.02079	0.00011	1.02345
PU-MET-FAST-016-002	1.00000	0.00380	1.00727	0.00011	1.00727	1.01017	0.00011	1.01017
PU-MET-FAST-016-003	1.00000	0.00330	1.00546	0.00011	1.00546	1.00847	0.00011	1.00847
PU-MET-FAST-016-004	1.00000	0.00300	1.00509	0.00011	1.00509	1.00796	0.00011	1.00796
PU-MET-FAST-016-005	1.00000	0.00340	1.00488	0.00011	1.00488	1.00769	0.00011	1.00769
PU-MET-FAST-016-006	1.00000	0.00320	1.00722	0.00011	1.00722	1.01010	0.00011	1.01010
PU-MET-FAST-018-001	1.00000	0.00300	0.99859	0.00009	0.99859	0.99818	0.00009	0.99818
PU-MET-FAST-019-001	0.99920	0.00150	1.00016	0.00009	1.00096	0.99966	0.00009	1.00046
PU-MET-FAST-020-001	0.99930	0.00170	0.99655	0.00009	0.99724	0.99654	0.00009	0.99724
PU-MET-FAST-021-001	1.00000	0.00260	1.00374	0.00010	1.00374	1.00375	0.00009	1.00375
PU-MET-FAST-021-002	1.00000	0.00260	0.99227	0.00009	0.99227	0.99239	0.00009	0.99239
PU-MET-FAST-022-001	1.00000	0.00210	0.99782	0.00008	0.99782	0.99802	0.00008	0.99802
PU-MET-FAST-023-001	1.00000	0.00200	0.99830	0.00009	0.99830	0.99816	0.00009	0.99816
PU-MET-FAST-024-001	1.00000	0.00200	1.00081	0.00009	1.00081	1.00104	0.00009	1.00104
PU-MET-FAST-025-001	1.00000	0.00200	0.99935	0.00009	0.99935	0.99954	0.00009	0.99954
PU-MET-FAST-026-001	1.00000	0.00240	1.00147	0.00009	1.00147	1.00147	0.00009	1.00147
PU-MET-FAST-027-001	1.00000	0.00220	1.00258	0.00011	1.00258	1.00274	0.00011	1.00274
PU-MET-FAST-028-001	1.00000	0.00220	1.00328	0.00009	1.00328	1.00304	0.00009	1.00304
PU-MET-FAST-029-001	1.00000	0.00200	0.99558	0.00008	0.99558	0.99611	0.00008	0.99611
PU-MET-FAST-030-001	1.00000	0.00210	1.00188	0.00009	1.00188	1.00207	0.00009	1.00207
PU-MET-FAST-031-001	1.00000	0.00210	1.00419	0.00010	1.00419	1.00433	0.00010	1.00433
PU-MET-FAST-032-001	1.00000	0.00200	1.00055	0.00009	1.00055	1.00104	0.00009	1.00104
PU-MET-FAST-033-001	0.99670	0.00260	0.99593	0.00010	0.99922	0.99503	0.00010	0.99832
PU-MET-FAST-035-001	1.00000	0.00160	1.00223	0.00009	1.00223	0.99728	0.00009	0.99728
PU-MET-FAST-036-001	1.00000	0.00310	1.00621	0.00010	1.00621	1.00591	0.00009	1.00591
PU-MET-FAST-038-001-D	1.00070	0.00190	1.00132	0.00010	1.00062	1.00111	0.00010	1.00041
PU-MET-FAST-039-001	1.00000	0.00220	0.99149	0.00009	0.99149	0.99143	0.00009	0.99143
PU-MET-FAST-040-001	1.00000	0.00380	0.99684	0.00009	0.99684	0.99399	0.00009	0.99399
PU-MET-FAST-041-001	1.00000	0.00160	1.00520	0.00010	1.00520	1.00491	0.00010	1.00491
PU-MET-FAST-044-001	0.99770	0.00210	1.00007	0.00010	1.00238	1.00049	0.00010	1.00280
PU-MET-FAST-044-002	0.99800	0.00220	1.00092	0.00010	1.00292	1.00155	0.00010	1.00356
PU-MET-FAST-044-003	0.99770	0.00210	0.99894	0.00010	1.00124	0.99878	0.00010	1.00108
PU-MET-FAST-044-004	0.99780	0.00260	0.99969	0.00010	1.00190	0.99994	0.00010	1.00214
PU-MET-FAST-044-005	0.99770	0.00240	0.99850	0.00010	1.00080	0.99848	0.00010	1.00078
PU-MET-FAST-045-001	1.00000	0.00340	0.99477	0.00009	0.99477	0.99606	0.00009	0.99606
PU-MET-FAST-045-002	1.00000	0.00340	1.00176	0.00009	1.00176	1.00313	0.00009	1.00313
PU-MET-FAST-045-003	1.00000	0.00350	1.00054	0.00009	1.00054	1.00183	0.00009	1.00183
PU-MET-FAST-045-004	1.00000	0.00350	1.00060	0.00009	1.00060	1.00173	0.00009	1.00173
PU-MET-FAST-045-005	1.00000	0.00360	1.00174	0.00009	1.00174	1.00223	0.00009	1.00223
PU-MET-FAST-045-006	1.00000	0.00380	1.00579	0.00009	1.00579	1.00743	0.00009	1.00743
PU-MET-FAST-045-007	1.00000	0.00380	1.00531	0.00009	1.00531	1.00688	0.00010	1.00688
PU-MET-INTER-002-001	0.98780	0.00230	0.99362	0.00010	1.00589	1.00387	0.00010	1.01627
PU-MET-INTER-003-001	0.98420	0.00160	0.98331	0.00010	0.99909	0.98563	0.00010	1.00145
PU-MET-INTER-004-001	0.97230	0.00250	0.96980	0.00012	0.99743	0.97136	0.00011	0.99903
PU-SOL-THERM-001-001	1.00000	0.00500	1.00465	0.00013	1.00465	1.00114	0.00013	1.00114
PU-SOL-THERM-001-002	1.00000	0.00500	1.00661	0.00013	1.00661	1.00340	0.00013	1.00340
PU-SOL-THERM-001-003	1.00000	0.00500	1.00991	0.00013	1.00991	1.00640	0.00013	1.00640
PU-SOL-THERM-001-004	1.00000	0.00500	1.00413	0.00013	1.00413	1.00099	0.00013	1.00099
PU-SOL-THERM-001-005	1.00000	0.00500	1.00824	0.00013	1.00824	1.00525	0.00013	1.00525
PU-SOL-THERM-001-006	1.00000	0.00500	1.01005	0.00013	1.01005	1.00830	0.00013	1.00830
PU-SOL-THERM-002-001	1.00000	0.00470	1.00222	0.00012	1.00222	0.99820	0.00012	0.99820
PU-SOL-THERM-002-002	1.00000	0.00470	1.00308	0.00012	1.00308	0.99971	0.00012	0.99971
PU-SOL-THERM-002-003	1.00000	0.00470	1.00219	0.00012	1.00219	0.99842	0.00013	0.99842

Continued on the next page

TABLE LIX: (continued) ENDF-6 ENDF/B-VIII.1 criticality validation.

Benchmark	E	unc.$_E$	ENDF/B-VIII.1			ENDF/B-VIII.0		
			C	unc.$_C$	C/E	C	unc.$_C$	C/E
PU-SOL-THERM-002-004	1.00000	0.00470	1.00520	0.00013	1.00520	1.00122	0.00012	1.00122
PU-SOL-THERM-002-005	1.00000	0.00470	1.00800	0.00013	1.00800	1.00428	0.00013	1.00428
PU-SOL-THERM-002-006	1.00000	0.00470	1.00399	0.00012	1.00399	1.00018	0.00013	1.00018
PU-SOL-THERM-002-007	1.00000	0.00470	1.00642	0.00013	1.00642	1.00260	0.00013	1.00260
PU-SOL-THERM-003-001	1.00000	0.00470	1.00037	0.00012	1.00037	0.99672	0.00011	0.99672
PU-SOL-THERM-003-002	1.00000	0.00470	1.00023	0.00011	1.00023	0.99648	0.00011	0.99648
PU-SOL-THERM-003-003	1.00000	0.00470	1.00291	0.00012	1.00291	0.99913	0.00012	0.99913
PU-SOL-THERM-003-004	1.00000	0.00470	1.00215	0.00012	1.00215	0.99863	0.00012	0.99863
PU-SOL-THERM-003-005	1.00000	0.00470	1.00321	0.00012	1.00321	0.99968	0.00012	0.99968
PU-SOL-THERM-003-006	1.00000	0.00470	1.00383	0.00012	1.00383	1.00020	0.00012	1.00020
PU-SOL-THERM-003-007	1.00000	0.00470	1.00460	0.00012	1.00460	1.00077	0.00012	1.00077
PU-SOL-THERM-003-008	1.00000	0.00470	1.00328	0.00012	1.00328	1.00000	0.00012	1.00000
PU-SOL-THERM-004-001	1.00000	0.00470	1.00151	0.00011	1.00151	0.99775	0.00011	0.99775
PU-SOL-THERM-004-002	1.00000	0.00470	0.99640	0.00011	0.99640	0.99253	0.00011	0.99253
PU-SOL-THERM-004-003	1.00000	0.00470	0.99873	0.00011	0.99873	0.99478	0.00011	0.99478
PU-SOL-THERM-004-004	1.00000	0.00470	0.99674	0.00011	0.99674	0.99263	0.00011	0.99263
PU-SOL-THERM-004-005	1.00000	0.00470	0.99732	0.00011	0.99732	0.99366	0.00011	0.99366
PU-SOL-THERM-004-006	1.00000	0.00470	0.99892	0.00011	0.99892	0.99559	0.00011	0.99559
PU-SOL-THERM-004-007	1.00000	0.00470	1.00300	0.00011	1.00300	0.99930	0.00011	0.99930
PU-SOL-THERM-004-008	1.00000	0.00470	0.99879	0.00011	0.99879	0.99565	0.00011	0.99565
PU-SOL-THERM-004-009	1.00000	0.00470	0.99791	0.00011	0.99791	0.99468	0.00011	0.99468
PU-SOL-THERM-004-010	1.00000	0.00470	0.99994	0.00011	0.99994	0.99616	0.00011	0.99616
PU-SOL-THERM-004-011	1.00000	0.00470	0.99836	0.00012	0.99836	0.99486	0.00011	0.99486
PU-SOL-THERM-004-012	1.00000	0.00470	1.00013	0.00011	1.00013	0.99674	0.00011	0.99674
PU-SOL-THERM-004-013	1.00000	0.00470	0.99782	0.00011	0.99782	0.99418	0.00011	0.99418
PU-SOL-THERM-005-001	1.00000	0.00470	0.99994	0.00011	0.99994	0.99658	0.00011	0.99658
PU-SOL-THERM-005-002	1.00000	0.00470	1.00022	0.00011	1.00022	0.99696	0.00011	0.99696
PU-SOL-THERM-005-003	1.00000	0.00470	1.00101	0.00011	1.00101	0.99784	0.00011	0.99784
PU-SOL-THERM-005-004	1.00000	0.00470	1.00256	0.00011	1.00256	0.99943	0.00011	0.99943
PU-SOL-THERM-005-005	1.00000	0.00470	1.00400	0.00011	1.00400	1.00051	0.00012	1.00051
PU-SOL-THERM-005-006	1.00000	0.00470	1.00342	0.00011	1.00342	1.00009	0.00012	1.00009
PU-SOL-THERM-005-007	1.00000	0.00470	1.00191	0.00012	1.00191	0.99849	0.00012	0.99849
PU-SOL-THERM-005-008	1.00000	0.00470	0.99662	0.00011	0.99662	0.99356	0.00011	0.99356
PU-SOL-THERM-005-009	1.00000	0.00470	0.99960	0.00011	0.99960	0.99616	0.00011	0.99616
PU-SOL-THERM-006-001	1.00000	0.00350	0.99767	0.00011	0.99767	0.99454	0.00011	0.99454
PU-SOL-THERM-006-002	1.00000	0.00350	0.99907	0.00011	0.99907	0.99590	0.00011	0.99590
PU-SOL-THERM-006-003	1.00000	0.00350	0.99897	0.00011	0.99897	0.99549	0.00011	0.99549
PU-SOL-THERM-007-002	1.00000	0.00470	1.00952	0.00013	1.00952	1.00710	0.00013	1.00710
PU-SOL-THERM-007-003	1.00000	0.00470	1.00393	0.00013	1.00393	1.00127	0.00013	1.00127
PU-SOL-THERM-007-005	1.00000	0.00470	1.00852	0.00013	1.00852	1.00507	0.00013	1.00507
PU-SOL-THERM-007-006	1.00000	0.00470	1.00242	0.00013	1.00242	0.99910	0.00013	0.99910
PU-SOL-THERM-007-007	1.00000	0.00470	1.00444	0.00013	1.00444	1.00101	0.00013	1.00101
PU-SOL-THERM-007-008	1.00000	0.00470	0.99792	0.00013	0.99792	0.99476	0.00013	0.99476
PU-SOL-THERM-007-009	1.00000	0.00470	0.99659	0.00013	0.99659	0.99302	0.00013	0.99302
PU-SOL-THERM-007-010	1.00000	0.00470	1.00029	0.00013	1.00029	0.99656	0.00013	0.99656
PU-SOL-THERM-009-003-A	1.00030	0.00330	1.01369	0.00006	1.01339	1.01305	0.00006	1.01275
PU-SOL-THERM-010-001	1.00000	0.00480	1.01718	0.00013	1.01718	1.01351	0.00013	1.01351
PU-SOL-THERM-010-002	1.00000	0.00480	1.01335	0.00013	1.01335	1.00962	0.00013	1.00962
PU-SOL-THERM-010-003	1.00000	0.00480	1.00692	0.00012	1.00692	1.00304	0.00012	1.00304
PU-SOL-THERM-010-004	1.00000	0.00480	1.01071	0.00012	1.01071	1.00728	0.00012	1.00728
PU-SOL-THERM-010-005	1.00000	0.00480	1.00829	0.00012	1.00829	1.00476	0.00012	1.00476
PU-SOL-THERM-010-006	1.00000	0.00480	1.00725	0.00012	1.00725	1.00389	0.00012	1.00389
PU-SOL-THERM-010-007	1.00000	0.00480	1.00059	0.00012	1.00059	0.99677	0.00012	0.99677
PU-SOL-THERM-010-008	1.00000	0.00480	1.00136	0.00012	1.00136	0.99820	0.00011	0.99820
PU-SOL-THERM-010-009	1.00000	0.00480	1.01354	0.00012	1.01354	1.00963	0.00013	1.00963
PU-SOL-THERM-010-010	1.00000	0.00480	1.00073	0.00012	1.00073	0.99718	0.00012	0.99718
PU-SOL-THERM-010-011	1.00000	0.00480	1.00824	0.00012	1.00824	1.00444	0.00012	1.00444
PU-SOL-THERM-010-012	1.00000	0.00480	1.00777	0.00012	1.00777	1.00412	0.00012	1.00412
PU-SOL-THERM-010-013	1.00000	0.00480	1.01382	0.00012	1.01382	1.01008	0.00012	1.01008
PU-SOL-THERM-010-014	1.00000	0.00480	1.00681	0.00011	1.00681	1.00354	0.00011	1.00354
PU-SOL-THERM-011-16-1	1.00000	0.00520	1.00721	0.00013	1.00721	1.00353	0.00013	1.00353
PU-SOL-THERM-011-16-2	1.00000	0.00520	1.01212	0.00013	1.01212	1.00817	0.00013	1.00817
PU-SOL-THERM-011-16-3	1.00000	0.00520	1.01395	0.00013	1.01395	1.01039	0.00013	1.01039
PU-SOL-THERM-011-16-4	1.00000	0.00520	1.00652	0.00013	1.00652	1.00269	0.00013	1.00269
PU-SOL-THERM-011-16-5	1.00000	0.00520	1.00362	0.00013	1.00362	0.99992	0.00013	0.99992
PU-SOL-THERM-011-18-1	1.00000	0.00520	0.99085	0.00011	0.99085	0.98766	0.00011	0.98766
PU-SOL-THERM-011-18-2	1.00000	0.00520	0.99709	0.00011	0.99709	0.99375	0.00011	0.99375
PU-SOL-THERM-011-18-3	1.00000	0.00520	0.99352	0.00011	0.99352	0.99043	0.00011	0.99043
PU-SOL-THERM-011-18-4	1.00000	0.00520	0.99047	0.00011	0.99047	0.98666	0.00011	0.98666
PU-SOL-THERM-011-18-5	1.00000	0.00520	1.00015	0.00012	1.00015	0.99711	0.00011	0.99711
PU-SOL-THERM-011-18-6	1.00000	0.00520	0.99719	0.00012	0.99719	0.99369	0.00012	0.99369
PU-SOL-THERM-011-18-7	1.00000	0.00520	0.99644	0.00011	0.99644	0.99318	0.00011	0.99318
PU-SOL-THERM-012-001	1.00000	0.00430	1.00183	0.00009	1.00183	0.99997	0.00009	0.99997

Continued on the next page

TABLE LIX: (continued) ENDF-6 ENDF/B-VIII.1 criticality validation.

Benchmark	E	unc.$_E$	ENDF/B-VIII.1			ENDF/B-VIII.0		
			C	unc.$_C$	C/E	C	unc.$_C$	C/E
PU-SOL-THERM-012-002	1.00000	0.00430	1.00211	0.00008	1.00211	1.00053	0.00008	1.00053
PU-SOL-THERM-012-003	1.00000	0.00580	1.00339	0.00008	1.00339	1.00199	0.00008	1.00199
PU-SOL-THERM-012-004	1.00000	0.00580	1.00342	0.00007	1.00342	1.00234	0.00007	1.00234
PU-SOL-THERM-012-005	1.00000	0.00580	1.00519	0.00006	1.00519	1.00435	0.00006	1.00435
PU-SOL-THERM-012-006	1.00000	0.00070	1.00577	0.00013	1.00577	1.00420	0.00013	1.00420
PU-SOL-THERM-012-007	1.00000	0.00130	1.00395	0.00013	1.00395	1.00262	0.00013	1.00262
PU-SOL-THERM-012-008	1.00000	0.00130	1.00218	0.00012	1.00218	1.00048	0.00012	1.00048
PU-SOL-THERM-012-009	1.00000	0.00430	1.00676	0.00011	1.00676	1.00492	0.00011	1.00492
PU-SOL-THERM-012-010	1.00000	0.00430	1.00072	0.00010	1.00072	0.99886	0.00010	0.99886
PU-SOL-THERM-012-011	1.00000	0.00430	1.00301	0.00009	1.00301	1.00121	0.00009	1.00121
PU-SOL-THERM-012-012	1.00000	0.00430	1.00318	0.00009	1.00318	1.00148	0.00009	1.00148
PU-SOL-THERM-012-013	1.00000	0.00580	1.00511	0.00006	1.00511	1.00420	0.00006	1.00420
PU-SOL-THERM-018-001	1.00000	0.00340	1.01049	0.00012	1.01049	1.00915	0.00012	1.00915
PU-SOL-THERM-018-002	1.00000	0.00340	1.01307	0.00012	1.01307	1.01206	0.00012	1.01206
PU-SOL-THERM-018-003	1.00000	0.00320	1.01101	0.00012	1.01101	1.00950	0.00012	1.00950
PU-SOL-THERM-018-004	1.00000	0.00300	1.00844	0.00012	1.00844	1.00688	0.00012	1.00688
PU-SOL-THERM-018-005	1.00000	0.00300	1.00739	0.00012	1.00739	1.00574	0.00012	1.00574
PU-SOL-THERM-018-006	1.00000	0.00310	1.00508	0.00011	1.00508	1.00304	0.00011	1.00304
PU-SOL-THERM-018-007	1.00000	0.00320	1.00428	0.00011	1.00428	1.00232	0.00011	1.00232
PU-SOL-THERM-018-008	1.00000	0.00330	1.00365	0.00011	1.00365	1.00125	0.00010	1.00125
PU-SOL-THERM-018-009	1.00000	0.00340	1.00176	0.00010	1.00176	0.99946	0.00010	0.99946
PU-SOL-THERM-022-001	1.00000	0.00200	0.99972	0.00013	0.99972	0.99882	0.00013	0.99882
PU-SOL-THERM-022-002	1.00000	0.00160	1.00161	0.00013	1.00161	1.00008	0.00013	1.00008
PU-SOL-THERM-022-003	1.00000	0.00150	0.99920	0.00012	0.99920	0.99765	0.00012	0.99765
PU-SOL-THERM-022-004	1.00000	0.00170	0.99950	0.00012	0.99950	0.99774	0.00012	0.99774
PU-SOL-THERM-022-005	1.00000	0.00190	0.99970	0.00011	0.99970	0.99804	0.00011	0.99804
PU-SOL-THERM-022-006	1.00000	0.00210	1.00045	0.00011	1.00045	0.99842	0.00011	0.99842
PU-SOL-THERM-022-007	1.00000	0.00210	1.00161	0.00011	1.00161	0.99990	0.00010	0.99990
PU-SOL-THERM-022-008	1.00000	0.00230	1.00198	0.00010	1.00198	1.00015	0.00010	1.00015
PU-SOL-THERM-022-009	1.00000	0.00240	1.00043	0.00010	1.00043	0.99893	0.00010	0.99893
PU-SOL-THERM-028-001	1.00000	0.00120	1.00617	0.00012	1.00617	1.00350	0.00012	1.00350
PU-SOL-THERM-028-002	1.00000	0.00120	1.00529	0.00012	1.00529	1.00255	0.00012	1.00255
PU-SOL-THERM-028-003	1.00000	0.00120	1.00656	0.00012	1.00656	1.00409	0.00012	1.00409
PU-SOL-THERM-028-004	1.00000	0.00120	1.00605	0.00012	1.00605	1.00387	0.00012	1.00387
PU-SOL-THERM-028-005	1.00000	0.00120	1.00695	0.00011	1.00695	1.00470	0.00011	1.00470
PU-SOL-THERM-028-006	1.00000	0.00120	1.00772	0.00011	1.00772	1.00520	0.00011	1.00520
PU-SOL-THERM-028-007	1.00000	0.00120	1.00651	0.00012	1.00651	1.00406	0.00012	1.00406
PU-SOL-THERM-028-008	1.00000	0.00120	1.00647	0.00012	1.00647	1.00374	0.00012	1.00374
PU-SOL-THERM-028-009	1.00000	0.00120	1.00792	0.00011	1.00792	1.00544	0.00011	1.00544
PU-SOL-THERM-032-001	1.00000	0.00193	0.99387	0.00013	0.99387	0.99156	0.00013	0.99156
PU-SOL-THERM-032-002	1.00000	0.00193	0.99923	0.00012	0.99923	0.99714	0.00012	0.99714
PU-SOL-THERM-032-003	1.00000	0.00193	1.00011	0.00012	1.00011	0.99802	0.00012	0.99802
PU-SOL-THERM-032-004	1.00000	0.00193	0.99972	0.00012	0.99972	0.99753	0.00012	0.99753
PU-SOL-THERM-032-005	1.00000	0.00193	1.00131	0.00011	1.00131	0.99940	0.00011	0.99940
PU-SOL-THERM-032-006	1.00000	0.00193	1.00140	0.00011	1.00140	0.99930	0.00011	0.99930
PU-SOL-THERM-032-007	1.00000	0.00193	1.00178	0.00011	1.00178	0.99995	0.00011	0.99995
PU-SOL-THERM-032-008	1.00000	0.00193	1.00098	0.00011	1.00098	0.99906	0.00011	0.99906
PU-SOL-THERM-032-009	1.00000	0.00193	0.99958	0.00011	0.99958	0.99770	0.00010	0.99770
PU-SOL-THERM-032-010	1.00000	0.00193	1.00130	0.00010	1.00130	0.99941	0.00010	0.99941
PU-SOL-THERM-032-011	1.00000	0.00193	1.00072	0.00010	1.00072	0.99898	0.00010	0.99898
PU-SOL-THERM-032-012	1.00000	0.00193	0.99970	0.00010	0.99970	0.99786	0.00010	0.99786
PU-SOL-THERM-032-013	1.00000	0.00193	0.99965	0.00012	0.99965	0.99786	0.00012	0.99786
PU-SOL-THERM-032-014	1.00000	0.00193	0.99925	0.00012	0.99925	0.99696	0.00012	0.99696
PU-SOL-THERM-032-015	1.00000	0.00193	1.00127	0.00011	1.00127	0.99914	0.00011	0.99914
PU-SOL-THERM-032-016	1.00000	0.00193	1.00066	0.00011	1.00066	0.99892	0.00011	0.99892
PU-SOL-THERM-032-017	1.00000	0.00193	1.00074	0.00011	1.00074	0.99907	0.00011	0.99907
PU-SOL-THERM-034-001	1.00000	0.00620	0.99889	0.00013	0.99889	0.99681	0.00013	0.99681
PU-SOL-THERM-034-002	1.00000	0.00440	0.99998	0.00013	0.99998	0.99795	0.00012	0.99795
PU-SOL-THERM-034-003	1.00000	0.00400	0.99719	0.00012	0.99719	0.99539	0.00012	0.99539
PU-SOL-THERM-034-004	1.00000	0.00390	0.99972	0.00011	0.99972	0.99807	0.00011	0.99807
PU-SOL-THERM-034-005	1.00000	0.00400	0.99651	0.00011	0.99651	0.99541	0.00010	0.99541
PU-SOL-THERM-034-006	1.00000	0.00420	0.99752	0.00010	0.99752	0.99654	0.00010	0.99654
PU-SOL-THERM-034-007	1.00000	0.00570	0.99753	0.00012	0.99753	0.99876	0.00012	0.99876
PU-SOL-THERM-034-008	1.00000	0.00550	0.99754	0.00012	0.99754	0.99847	0.00012	0.99847
PU-SOL-THERM-034-009	1.00000	0.00520	0.99591	0.00011	0.99591	0.99708	0.00012	0.99708
PU-SOL-THERM-034-010	1.00000	0.00520	0.99508	0.00011	0.99508	0.99678	0.00012	0.99678
PU-SOL-THERM-034-011	1.00000	0.00480	0.99647	0.00011	0.99647	0.99825	0.00011	0.99825
PU-SOL-THERM-034-012	1.00000	0.00420	0.99601	0.00011	0.99601	0.99748	0.00011	0.99748
PU-SOL-THERM-034-013	1.00000	0.00430	0.99365	0.00011	0.99365	0.99576	0.00011	0.99576
PU-SOL-THERM-034-014	1.00000	0.00440	0.99361	0.00011	0.99361	0.99578	0.00011	0.99578
PU-SOL-THERM-034-015	1.00000	0.00420	0.99421	0.00011	0.99421	0.99587	0.00011	0.99587
PU-SOL-THERM-038-001	1.00050	0.00150	0.99874	0.00009	0.99824	0.99778	0.00009	0.99728
PU-SOL-THERM-038-002	1.00050	0.00150	0.99913	0.00009	0.99863	0.99785	0.00009	0.99735
PU-SOL-THERM-038-003	1.00050	0.00180	0.99741	0.00007	0.99691	0.99706	0.00007	0.99656
PU-SOL-THERM-038-004	1.00050	0.00130	0.99614	0.00007	0.99564	0.99599	0.00007	0.99549

Continued on the next page

TABLE LIX: (continued) ENDF-6 ENDF/B-VIII.1 criticality validation.

Benchmark	E	unc.$_E$	ENDF/B-VIII.1			ENDF/B-VIII.0		
			C	unc.$_C$	C/E	C	unc.$_C$	C/E
PU-SOL-THERM-038-005	1.00050	0.00130	0.99669	0.00007	0.99619	0.99619	0.00007	0.99569
U233-COMP-THERM-001-001	1.00060	0.00270	0.99860	0.00013	0.99800	0.99666	0.00013	0.99606
U233-COMP-THERM-001-002	1.00150	0.00250	1.00512	0.00015	1.00362	0.99912	0.00015	0.99762
U233-COMP-THERM-001-003	1.00000	0.00240	1.00615	0.00014	1.00615	1.00057	0.00014	1.00057
U233-COMP-THERM-001-004	1.00070	0.00250	1.00237	0.00012	1.00167	0.99795	0.00012	0.99725
U233-COMP-THERM-001-005	1.00150	0.00260	0.99944	0.00011	0.99795	0.99795	0.00011	0.99646
U233-COMP-THERM-001-006	1.00150	0.00280	0.99786	0.00013	0.99637	0.99686	0.00013	0.99537
U233-COMP-THERM-001-007	0.99950	0.00270	1.00256	0.00014	1.00306	0.99810	0.00014	0.99860
U233-COMP-THERM-001-008	1.00040	0.00280	1.00002	0.00013	0.99962	0.99553	0.00013	0.99513
U233-COMP-THERM-004-001	1.00170	0.00200	1.00005	0.00009	0.99835	0.99938	0.00008	0.99768
U233-MET-FAST-001-001	1.00000	0.00100	0.99991	0.00008	0.99991	1.00056	0.00008	1.00056
U233-MET-FAST-002-001	1.00000	0.00100	0.99989	0.00008	0.99989	1.00008	0.00008	1.00008
U233-MET-FAST-002-002	1.00000	0.00110	1.00124	0.00008	1.00124	1.00158	0.00009	1.00158
U233-MET-FAST-003-001	1.00000	0.00100	0.99964	0.00009	0.99964	0.99967	0.00008	0.99967
U233-MET-FAST-003-002	1.00000	0.00100	1.00008	0.00009	1.00008	1.00025	0.00009	1.00025
U233-MET-FAST-004-001	1.00000	0.00070	0.99971	0.00009	0.99971	0.99950	0.00009	0.99950
U233-MET-FAST-004-002	1.00000	0.00080	0.99689	0.00009	0.99689	0.99638	0.00009	0.99638
U233-MET-FAST-005-001	1.00000	0.00300	0.99778	0.00009	0.99778	0.99759	0.00009	0.99759
U233-MET-FAST-005-002	1.00000	0.00300	0.99861	0.00009	0.99861	0.99720	0.00009	0.99720
U233-MET-FAST-006-001	1.00000	0.00140	1.00019	0.00010	1.00019	0.99988	0.00010	0.99988
U233-SOL-INTER-001-001	1.00000	0.00830	0.98811	0.00015	0.98811	0.98201	0.00015	0.98201
U233-SOL-INTER-001-002	1.00000	0.00850	0.98426	0.00015	0.98426	0.97771	0.00015	0.97771
U233-SOL-INTER-001-003	1.00000	0.00660	0.98519	0.00015	0.98519	0.97902	0.00015	0.97902
U233-SOL-INTER-001-004	1.00000	0.00610	0.99720	0.00015	0.99720	0.99127	0.00015	0.99127
U233-SOL-INTER-001-005	1.00000	0.00820	0.98839	0.00015	0.98839	0.98228	0.00016	0.98228
U233-SOL-INTER-001-006	1.00000	0.00610	0.99075	0.00015	0.99075	0.98458	0.00015	0.98458
U233-SOL-INTER-001-007	1.00000	0.00590	0.98586	0.00016	0.98586	0.97964	0.00015	0.97964
U233-SOL-INTER-001-008	1.00000	0.00560	0.98555	0.00015	0.98555	0.97996	0.00015	0.97996
U233-SOL-INTER-001-009	1.00000	0.00680	0.98379	0.00016	0.98379	0.97770	0.00015	0.97770
U233-SOL-INTER-001-010	1.00000	0.00530	0.98242	0.00016	0.98242	0.97691	0.00016	0.97691
U233-SOL-INTER-001-011	1.00000	0.00570	0.98421	0.00016	0.98421	0.97849	0.00016	0.97849
U233-SOL-INTER-001-012	1.00000	0.00910	0.98442	0.00015	0.98442	0.97806	0.00015	0.97806
U233-SOL-INTER-001-013	1.00000	0.00710	0.98542	0.00015	0.98542	0.97903	0.00015	0.97903
U233-SOL-INTER-001-014	1.00000	0.00520	0.99523	0.00015	0.99523	0.98866	0.00015	0.98866
U233-SOL-INTER-001-015	1.00000	0.00750	0.98347	0.00015	0.98347	0.97732	0.00016	0.97732
U233-SOL-INTER-001-016	1.00000	0.00280	0.98469	0.00015	0.98469	0.97881	0.00015	0.97881
U233-SOL-INTER-001-017	1.00000	0.00550	0.99330	0.00015	0.99330	0.98728	0.00015	0.98728
U233-SOL-INTER-001-018	1.00000	0.00570	0.98224	0.00015	0.98224	0.97596	0.00016	0.97596
U233-SOL-INTER-001-019	1.00000	0.00830	0.97897	0.00016	0.97897	0.97313	0.00015	0.97313
U233-SOL-INTER-001-020	1.00000	0.00560	0.98460	0.00015	0.98460	0.97874	0.00015	0.97874
U233-SOL-INTER-001-021	1.00000	0.00500	0.97676	0.00016	0.97676	0.97098	0.00015	0.97098
U233-SOL-INTER-001-022	1.00000	0.00490	0.98195	0.00016	0.98195	0.97569	0.00016	0.97569
U233-SOL-INTER-001-023	1.00000	0.00470	0.99392	0.00016	0.99392	0.98839	0.00016	0.98839
U233-SOL-INTER-001-024	1.00000	0.00810	0.99476	0.00015	0.99476	0.98906	0.00016	0.98906
U233-SOL-INTER-001-025	1.00000	0.00810	0.98830	0.00015	0.98830	0.98214	0.00016	0.98214
U233-SOL-INTER-001-026	1.00000	0.00650	0.99211	0.00015	0.99211	0.98629	0.00016	0.98629
U233-SOL-INTER-001-027	1.00000	0.00510	0.99483	0.00015	0.99483	0.98875	0.00015	0.98875
U233-SOL-INTER-001-028	1.00000	0.00610	0.98678	0.00016	0.98678	0.98102	0.00016	0.98102
U233-SOL-INTER-001-029	1.00000	0.00980	0.98090	0.00016	0.98090	0.97473	0.00016	0.97473
U233-SOL-INTER-001-030	1.00000	0.00530	0.98275	0.00016	0.98275	0.97689	0.00016	0.97689
U233-SOL-INTER-001-031	1.00000	0.00710	0.99447	0.00016	0.99447	0.98822	0.00016	0.98822
U233-SOL-INTER-001-032	1.00000	0.00530	0.97898	0.00016	0.97898	0.97317	0.00016	0.97317
U233-SOL-INTER-001-033	1.00000	0.00460	0.99731	0.00016	0.99731	0.99167	0.00016	0.99167
U233-SOL-THERM-001-001	1.00000	0.00310	1.00046	0.00008	1.00046	0.99946	0.00008	0.99946
U233-SOL-THERM-001-002	1.00050	0.00330	1.00037	0.00008	0.99987	0.99930	0.00008	0.99880
U233-SOL-THERM-001-003	1.00060	0.00330	0.99979	0.00008	0.99919	0.99931	0.00008	0.99871
U233-SOL-THERM-001-004	0.99980	0.00330	0.99999	0.00008	1.00019	0.99903	0.00008	0.99923
U233-SOL-THERM-001-005	0.99990	0.00330	0.99942	0.00009	0.99952	0.99859	0.00009	0.99869
U233-SOL-THERM-005-001	1.00000	0.00400	1.00419	0.00013	1.00419	0.99994	0.00013	0.99994
U233-SOL-THERM-005-002	1.00000	0.00490	1.00686	0.00013	1.00686	1.00319	0.00012	1.00319
U233-SOL-THERM-008-001	1.00060	0.00290	0.99934	0.00005	0.99874	0.99983	0.00005	0.99923
U233-SOL-THERM-009-001	0.99660	0.00440	0.99433	0.00006	0.99772	0.99428	0.00006	0.99767
U233-SOL-THERM-009-002	0.99810	0.00400	0.99738	0.00006	0.99928	0.99765	0.00006	0.99955
U233-SOL-THERM-009-003	0.99890	0.00380	0.99835	0.00005	0.99945	0.99891	0.00005	1.00001
U233-SOL-THERM-009-004	0.99980	0.00380	0.99659	0.00005	0.99679	0.99771	0.00005	0.99791
U233-SOL-THERM-012-001	1.00000	0.00280	1.00457	0.00014	1.00457	0.99911	0.00015	0.99911
U233-SOL-THERM-012-002	1.00000	0.00250	1.00367	0.00014	1.00367	0.99807	0.00014	0.99807
U233-SOL-THERM-012-003	1.00000	0.00230	1.01319	0.00014	1.01319	1.00748	0.00015	1.00748
U233-SOL-THERM-012-004	1.00000	0.00150	1.00591	0.00014	1.00591	1.00107	0.00014	1.00107
U233-SOL-THERM-012-005	1.00000	0.00710	1.00799	0.00014	1.00799	1.00288	0.00014	1.00288

Continued on the next page

TABLE LIX: (continued) ENDF-6 ENDF/B-VIII.1 criticality validation.

Benchmark	E	unc.$_E$	ENDF/B-VIII.1			ENDF/B-VIII.0		
			C	unc.$_C$	C/E	C	unc.$_C$	C/E
U233-SOL-THERM-012-006	1.00000	0.00100	1.00860	0.00014	1.00860	1.00392	0.00014	1.00392
U233-SOL-THERM-012-007	1.00000	0.00380	1.00359	0.00012	1.00359	0.99982	0.00012	0.99982
U233-SOL-THERM-012-008	1.00000	0.00480	1.00075	0.00012	1.00075	0.99702	0.00012	0.99702
U233-SOL-THERM-013-001	0.99920	0.00730	1.00796	0.00016	1.00877	1.00194	0.00016	1.00274
U233-SOL-THERM-013-002	0.99920	0.00700	1.00819	0.00016	1.00900	1.00243	0.00016	1.00323
U233-SOL-THERM-013-003	0.99920	0.00690	1.00890	0.00016	1.00971	1.00283	0.00016	1.00363
U233-SOL-THERM-013-004	0.99920	0.00730	1.00896	0.00016	1.00976	1.00321	0.00016	1.00401
U233-SOL-THERM-013-005	0.99920	0.00670	1.00995	0.00016	1.01076	1.00425	0.00016	1.00505
U233-SOL-THERM-013-006	0.99920	0.00500	1.00912	0.00016	1.00993	1.00292	0.00016	1.00372
U233-SOL-THERM-013-007	0.99920	0.00540	1.00918	0.00016	1.00999	1.00300	0.00016	1.00380
U233-SOL-THERM-013-008	0.99920	0.00500	1.00976	0.00016	1.01057	1.00408	0.00016	1.00488
U233-SOL-THERM-013-009	0.99920	0.00450	1.01035	0.00016	1.01116	1.00451	0.00016	1.00531
U233-SOL-THERM-013-010	0.99920	0.00460	1.01079	0.00016	1.01160	1.00507	0.00016	1.00587
U233-SOL-THERM-013-011	0.99920	0.00540	1.00790	0.00016	1.00871	1.00216	0.00016	1.00296
U233-SOL-THERM-013-012	0.99920	0.00500	1.00904	0.00016	1.00985	1.00318	0.00016	1.00398
U233-SOL-THERM-013-013	0.99920	0.00620	1.00610	0.00016	1.00691	1.00045	0.00016	1.00125
U233-SOL-THERM-013-014	0.99920	0.00510	1.00913	0.00016	1.00994	1.00370	0.00016	1.00450
U233-SOL-THERM-013-015	0.99960	0.00770	1.02327	0.00015	1.02368	1.01832	0.00015	1.01873
U233-SOL-THERM-013-016	0.99960	0.00690	0.99610	0.00015	0.99650	0.99067	0.00015	0.99107
U233-SOL-THERM-013-017	0.99960	0.00520	0.99891	0.00015	0.99931	0.99347	0.00015	0.99387
U233-SOL-THERM-013-018	0.99960	0.00200	1.00236	0.00015	1.00276	0.99753	0.00015	0.99793
U233-SOL-THERM-013-019	0.99960	0.00890	0.99848	0.00015	0.99888	0.99365	0.00015	0.99405
U233-SOL-THERM-013-020	0.99960	0.00560	1.00123	0.00014	1.00163	0.99675	0.00014	0.99715
U233-SOL-THERM-013-021	0.99960	0.00340	1.00359	0.00013	1.00400	0.99958	0.00013	0.99998
U233-SOL-THERM-015-001	1.00000	0.00750	0.99227	0.00015	0.99227	0.98683	0.00015	0.98683
U233-SOL-THERM-015-002	1.00000	0.00700	0.98777	0.00015	0.98777	0.98245	0.00016	0.98245
U233-SOL-THERM-015-003	1.00000	0.00680	0.98940	0.00015	0.98940	0.98352	0.00015	0.98352
U233-SOL-THERM-015-004	1.00000	0.00410	0.99363	0.00015	0.99363	0.98797	0.00015	0.98797
U233-SOL-THERM-015-005	1.00000	0.00550	0.98926	0.00015	0.98926	0.98321	0.00016	0.98321
U233-SOL-THERM-015-006	1.00000	0.00990	0.97999	0.00016	0.97999	0.97370	0.00016	0.97370
U233-SOL-THERM-015-007	1.00000	0.00700	0.99133	0.00015	0.99133	0.98575	0.00015	0.98575
U233-SOL-THERM-015-008	1.00000	0.00670	0.97623	0.00016	0.97623	0.97045	0.00016	0.97045
U233-SOL-THERM-015-009	1.00000	0.00500	0.97184	0.00016	0.97184	0.96602	0.00016	0.96602
U233-SOL-THERM-015-010	1.00000	0.00510	0.99359	0.00016	0.99359	0.98757	0.00016	0.98757
U233-SOL-THERM-015-011	1.00000	0.00750	0.99510	0.00015	0.99510	0.98994	0.00015	0.98994
U233-SOL-THERM-015-012	1.00000	0.00690	0.99613	0.00015	0.99613	0.99058	0.00015	0.99058
U233-SOL-THERM-015-013	1.00000	0.00690	0.99437	0.00016	0.99437	0.98877	0.00015	0.98877
U233-SOL-THERM-015-014	1.00000	0.00360	1.00189	0.00015	1.00189	0.99561	0.00015	0.99561
U233-SOL-THERM-015-015	1.00000	0.00600	0.99225	0.00015	0.99225	0.98663	0.00016	0.98663
U233-SOL-THERM-015-016	1.00000	0.00430	0.99147	0.00016	0.99147	0.98571	0.00016	0.98571
U233-SOL-THERM-015-017	1.00000	0.00290	1.00178	0.00015	1.00178	0.99595	0.00015	0.99595
U233-SOL-THERM-015-018	1.00000	0.00560	0.97725	0.00016	0.97725	0.97188	0.00016	0.97188
U233-SOL-THERM-015-019	1.00000	0.00520	0.97785	0.00016	0.97785	0.97226	0.00016	0.97226
U233-SOL-THERM-015-020	1.00000	0.00790	0.99697	0.00015	0.99697	0.99187	0.00015	0.99187
U233-SOL-THERM-015-021	1.00000	0.00700	0.99995	0.00015	0.99995	0.99509	0.00015	0.99509
U233-SOL-THERM-015-022	1.00000	0.00620	0.99847	0.00015	0.99847	0.99320	0.00015	0.99320
U233-SOL-THERM-015-023	1.00000	0.00550	0.99674	0.00016	0.99674	0.99122	0.00015	0.99122
U233-SOL-THERM-015-024	1.00000	0.00510	0.99317	0.00015	0.99317	0.98746	0.00015	0.98746
U233-SOL-THERM-015-025	1.00000	0.00230	1.00153	0.00015	1.00153	0.99636	0.00015	0.99636
U233-SOL-THERM-015-026	1.00000	0.00660	0.99591	0.00015	0.99591	0.99170	0.00014	0.99170
U233-SOL-THERM-015-027	1.00000	0.00630	1.00047	0.00014	1.00047	0.99613	0.00015	0.99613
U233-SOL-THERM-015-028	1.00000	0.00580	0.99894	0.00014	0.99894	0.99441	0.00014	0.99441
U233-SOL-THERM-015-029	1.00000	0.00510	0.99755	0.00015	0.99755	0.99292	0.00015	0.99292
U233-SOL-THERM-015-030	1.00000	0.00480	0.99726	0.00015	0.99726	0.99239	0.00015	0.99239
U233-SOL-THERM-015-031	1.00000	0.00550	0.99667	0.00015	0.99667	0.99137	0.00015	0.99137
U233-SOL-THERM-016-001	0.99870	0.00370	1.00628	0.00016	1.00759	1.00072	0.00016	1.00202
U233-SOL-THERM-016-002	0.99830	0.00440	1.00766	0.00016	1.00937	1.00188	0.00016	1.00359
U233-SOL-THERM-016-003	0.99920	0.00360	1.00719	0.00016	1.00800	1.00144	0.00016	1.00224
U233-SOL-THERM-016-006	0.99930	0.00340	0.99946	0.00016	1.00016	0.99290	0.00016	0.99360
U233-SOL-THERM-016-007	1.00080	0.00340	0.99977	0.00016	0.99897	0.99362	0.00016	0.99283
U233-SOL-THERM-016-008	1.00110	0.00280	0.99954	0.00016	0.99845	0.99335	0.00016	0.99226
U233-SOL-THERM-016-010	1.00000	0.00300	1.00807	0.00016	1.00807	1.00159	0.00017	1.00159
U233-SOL-THERM-016-011	0.99920	0.00410	1.00812	0.00016	1.00893	1.00139	0.00017	1.00219
U233-SOL-THERM-016-012	0.99920	0.00470	1.00823	0.00016	1.00903	1.00152	0.00017	1.00232
U233-SOL-THERM-016-013	0.99930	0.00360	1.00754	0.00016	1.00825	1.00237	0.00016	1.00307
U233-SOL-THERM-016-014	1.00000	0.00260	1.00824	0.00016	1.00824	1.00238	0.00016	1.00238
U233-SOL-THERM-016-015	1.00000	0.00270	1.00924	0.00015	1.00924	1.00369	0.00016	1.00369
U233-SOL-THERM-016-016	0.99940	0.00310	1.01202	0.00015	1.01263	1.00674	0.00016	1.00734
U233-SOL-THERM-016-017	1.00000	0.00280	0.99771	0.00015	0.99771	0.99241	0.00015	0.99241
U233-SOL-THERM-016-018	0.99880	0.00360	0.99796	0.00016	0.99916	0.99307	0.00016	0.99426
U233-SOL-THERM-016-021	1.00000	0.00280	1.01249	0.00016	1.01249	1.00663	0.00016	1.00663
U233-SOL-THERM-016-022	1.00000	0.00340	1.01220	0.00016	1.01220	1.00673	0.00016	1.00673
U233-SOL-THERM-016-023	1.00000	0.00310	1.01255	0.00016	1.01255	1.00677	0.00016	1.00677
U233-SOL-THERM-016-025	0.99810	0.00400	1.00250	0.00015	1.00441	0.99735	0.00015	0.99925
U233-SOL-THERM-016-026	0.99800	0.00340	1.00767	0.00015	1.00969	1.00264	0.00015	1.00465
U233-SOL-THERM-016-027	0.99880	0.00370	1.00550	0.00015	1.00671	1.00095	0.00015	1.00215
U233-SOL-THERM-016-028	0.99860	0.00370	1.00126	0.00015	1.00266	0.99611	0.00015	0.99751

Continued on the next page

TABLE LIX: (continued) ENDF-6 ENDF/B-VIII.1 criticality validation.

Benchmark	E	unc.$_E$	ENDF/B-VIII.1			ENDF/B-VIII.0		
			C	unc.$_C$	C/E	C	unc.$_C$	C/E
U233-SOL-THERM-016-029	0.99850	0.00310	1.00185	0.00015	1.00335	0.99723	0.00015	0.99873
U233-SOL-THERM-016-030	0.99930	0.00320	1.00151	0.00015	1.00222	0.99648	0.00014	0.99718
U233-SOL-THERM-016-031	0.99900	0.00340	1.01188	0.00013	1.01289	1.00817	0.00013	1.00918
U233-SOL-THERM-016-032	0.99850	0.00320	1.01360	0.00013	1.01512	1.00972	0.00013	1.01124
U233-SOL-THERM-016-033	0.99860	0.00390	1.01379	0.00013	1.01521	1.00970	0.00013	1.01112
U233-SOL-THERM-017-001	0.99970	0.00320	1.00707	0.00015	1.00737	1.00235	0.00014	1.00265
U233-SOL-THERM-017-002	1.00000	0.00250	1.00332	0.00014	1.00332	0.99853	0.00014	0.99853
U233-SOL-THERM-017-003	1.00010	0.00350	1.00861	0.00015	1.00851	1.00344	0.00014	1.00334
U233-SOL-THERM-017-004	0.99940	0.00400	1.00801	0.00014	1.00862	1.00336	0.00014	1.00396
U233-SOL-THERM-017-005	1.00000	0.00290	1.00452	0.00014	1.00452	0.99985	0.00014	0.99985
U233-SOL-THERM-017-006	1.00000	0.00290	1.00231	0.00012	1.00231	0.99860	0.00013	0.99860
U233-SOL-THERM-017-007	1.00000	0.00370	1.00188	0.00013	1.00188	0.99824	0.00013	0.99824

Appendix C: Complete validation results from GNDS files

LLNL tested ENDF/B-VIII.1 in the GNDS format against a wide range of fast criticality and fission ratio benchmarks from the ICSBEP [158] using the Metis Validation and Verification platform [744] and the Monte Carlo transport code Mercury [745]. These tests were performed by first translating the evaluations into GNDS-2.0 format, processing with `FUDGE` [743], and using the `GIDI+` API [747] within Mercury to read and sample data. See section XIII B for more detail on `FUDGE`, `GIDI+` and Metis. Mercury tests of 17 LLNL pulsed spheres available in Metis were consistent with the MCNP6 results presented in the text.

For the convenience of potential users of the data in Tables LX and LXI, we provide the corresponding data in comma-separated-value (CSV) formatted files in the ENDF/B-VIII.1 release page hosted by the NNDC [19].

TABLE LX: Validation of the ENDF/B-VIII.1 nuclear data library in GNDS-2.0 format against effective multiplication factors (keff) of criticality benchmarks published in the ICSBEP handbook [158]. Simulation results were obtained with the LLNL Monte Carlo code Mercury version 5.42.0 with `GIDI+` API version 3.31.0. Results for the released version of ENDF/B-VIII.0 in GNDS-2.0 format are also provided. The ENDF/B-VIII.0 and ENDF/B-VIII.1 libraries were processed with the `FUDGE` processing code at a temperature of 293.6K, and include thermal neutron scattering laws and unresolved region probability tables.

GNDS-2.0 library Case Name	ENDF/B-VIII.1 at 293.6K Calculated keff	uncertainty	ENDF/B-VIII.0 at 293.6K Calculated keff	uncertainty	Experimental Benchmark keff	uncertainty
HEU-MET-FAST-001	0.99995	0.00010	1.00007	0.00010	1.00000	0.00100
HEU-MET-FAST-002	0.99951	0.00010	0.99961	0.00010	1.00000	0.00300
HEU-MET-FAST-002-002	0.99991	0.00014	0.99975	0.00014	1.00000	0.00300
HEU-MET-FAST-003	0.99893	0.00010	0.99906	0.00010	1.00000	0.00300
HEU-MET-FAST-003-001	0.99294	0.00013	0.99297	0.00013	1.00000	0.00500
HEU-MET-FAST-003-010	1.00362	0.00013	1.00398	0.00013	1.00000	0.00500
HEU-MET-FAST-003-011	1.00864	0.00013	1.00886	0.00013	1.00000	0.00500
HEU-MET-FAST-003-002	0.99196	0.00013	0.99235	0.00013	1.00000	0.00500
HEU-MET-FAST-003-003	0.99673	0.00014	0.99661	0.00014	1.00000	0.00500
HEU-MET-FAST-010-001	0.99769	0.00016	0.99765	0.00016	0.99920	0.00100
HEU-MET-FAST-010-002	0.99708	0.00016	0.99724	0.00016	0.99920	0.00100
HEU-MET-FAST-012	0.99805	0.00016	0.99808	0.00016	0.99920	0.00180
HEU-MET-FAST-014-001	0.99727	0.00013	0.99697	0.00013	0.99890	0.00170
HEU-MET-FAST-017	0.99630	0.00010	0.99667	0.00010	0.99930	0.00140
HEU-MET-FAST-018	0.99951	0.00010	0.99963	0.00010	1.00000	0.00160
HEU-MET-FAST-019	1.00566	0.00010	1.00557	0.00010	1.00000	0.00300
HEU-MET-FAST-020	0.99979	0.00010	0.99997	0.00010	1.00000	0.00300
HEU-MET-FAST-028	1.00048	0.00010	1.00037	0.00010	1.00000	0.00300
HEU-MET-FAST-032-001	1.00165	0.00014	1.00173	0.00014	1.00000	0.00160
HEU-MET-FAST-032-002	1.00232	0.00013	1.00238	0.00014	1.00000	0.00270
HEU-MET-FAST-032-003	0.99823	0.00013	0.99830	0.00013	1.00000	0.00170
HEU-MET-FAST-032-004	0.99999	0.00013	0.99984	0.00013	1.00000	0.00170
HEU-MET-FAST-038	0.99963	0.00010	1.00101	0.00010	0.99990	0.00070
HEU-MET-FAST-041-001	1.00448	0.00010	1.00463	0.00010	1.00130	0.00300
HEU-MET-FAST-041-002	1.00223	0.00010	1.00231	0.00010	1.00220	0.00430
HEU-MET-FAST-041-003	1.00093	0.00010	1.00088	0.00010	1.00060	0.00290
HEU-MET-FAST-041-004	1.00551	0.00010	1.00533	0.00010	1.00060	0.00250
HEU-MET-FAST-041-005	1.00091	0.00010	1.00117	0.00010	1.00060	0.00310
HEU-MET-FAST-041-006	1.00363	0.00010	1.00374	0.00010	1.00060	0.00450

Continued on the next page

TABLE LX: (continued) GNDS ENDF/B-VIII.1 criticality validation

GNDS-2.0 library Case Name	ENDF/B-VIII.1 at 293.6K Calculated keff	uncertainty	ENDF/B-VIII.0 at 293.6K Calculated keff	uncertainty	Experimental Benchmark keff	uncertainty
HEU-MET-FAST-055	0.99683	0.00010	0.99667	0.00010	0.99550	0.00280
HEU-MET-FAST-057-001	0.99357	0.00010	0.98919	0.00010	1.00000	0.00200
HEU-MET-FAST-057-002	1.00173	0.00010	0.99787	0.00010	1.00000	0.00230
HEU-MET-FAST-060	1.00284	0.00010	1.00314	0.00010	0.99550	0.00240
HEU-MET-FAST-064	0.99995	0.00010	0.99539	0.00010	0.99960	0.00080
HEU-MET-FAST-073	1.00230	0.00010	1.00302	0.00010	1.00040	0.00160
HEU-MET-FAST-079-001	0.99867	0.00010	0.99876	0.00010	0.99960	0.00150
HEU-MET-FAST-079-002	0.99886	0.00010	0.99905	0.00010	0.99960	0.00140
HEU-MET-FAST-079-003	0.99708	0.00010	0.99699	0.00010	0.99960	0.00150
HEU-MET-FAST-079-004	1.00043	0.00010	1.00058	0.00010	0.99960	0.00140
HEU-MET-FAST-079-005	0.99955	0.00010	1.00002	0.00010	0.99960	0.00150
HEU-MET-FAST-084-001	0.99880	0.00010	0.99899	0.00010	0.99940	0.00190
HEU-MET-FAST-084-010	0.99597	0.00010	0.99597	0.00010	0.99930	0.00220
HEU-MET-FAST-084-011	1.00084	0.00010	1.00078	0.00010	0.99950	0.00190
HEU-MET-FAST-084-012	0.99688	0.00010	0.99716	0.00010	0.99940	0.00200
HEU-MET-FAST-084-013	0.99760	0.00010	0.99740	0.00010	0.99940	0.00220
HEU-MET-FAST-084-014	1.10044	0.00011	1.09898	0.00011	0.99940	0.00190
HEU-MET-FAST-084-015	0.99789	0.00010	0.99763	0.00010	0.99950	0.00210
HEU-MET-FAST-084-016	0.99814	0.00010	0.99837	0.00010	0.99940	0.00200
HEU-MET-FAST-084-017	1.00080	0.00010	1.00093	0.00010	0.99950	0.00190
HEU-MET-FAST-084-018	0.99769	0.00010	0.99514	0.00010	0.99950	0.00220
HEU-MET-FAST-084-019	0.99835	0.00010	0.99838	0.00010	0.99960	0.00190
HEU-MET-FAST-084-002	0.99909	0.00010	0.99888	0.00010	0.99940	0.00210
HEU-MET-FAST-084-020	1.00323	0.00010	1.00327	0.00010	0.99950	0.00250
HEU-MET-FAST-084-021	1.00014	0.00010	1.00011	0.00010	0.99950	0.00450
HEU-MET-FAST-084-022	0.99496	0.00010	0.99511	0.00010	0.99940	0.00200
HEU-MET-FAST-084-023	0.99497	0.00010	0.99516	0.00010	0.99930	0.00240
HEU-MET-FAST-084-024	0.99764	0.00010	0.99778	0.00010	0.99960	0.00180
HEU-MET-FAST-084-025	1.06350	0.00010	1.06236	0.00011	0.99950	0.00200
HEU-MET-FAST-084-026	0.99992	0.00010	0.99997	0.00010	0.99930	0.00220
HEU-MET-FAST-084-027	0.98372	0.00010	0.98401	0.00010	0.99940	0.00200
HEU-MET-FAST-084-003	0.99820	0.00010	0.99850	0.00010	0.99930	0.00210
HEU-MET-FAST-084-004	0.99769	0.00010	0.99788	0.00010	0.99940	0.00200
HEU-MET-FAST-084-005	1.00601	0.00010	1.00601	0.00010	0.99930	0.00210
HEU-MET-FAST-084-006	0.99876	0.00010	0.99496	0.00010	0.99940	0.00240
HEU-MET-FAST-084-007	0.99878	0.00010	0.99896	0.00010	0.99950	0.00200
HEU-MET-FAST-084-008	1.00845	0.00010	1.00848	0.00010	0.99940	0.00340
HEU-MET-FAST-084-009	1.00296	0.00010	1.00272	0.00010	0.99930	0.00540
HEU-MET-FAST-085-001	0.99969	0.00010	0.99457	0.00010	0.99980	0.00290
HEU-MET-FAST-085-002	1.00263	0.00010	0.99671	0.00010	0.99970	0.00310
HEU-MET-FAST-085-003	0.99844	0.00010	0.99827	0.00010	0.99950	0.00460
HEU-MET-FAST-085-004	0.99692	0.00010	0.99486	0.00010	0.99960	0.00290
HEU-MET-FAST-085-005	1.00027	0.00010	1.00018	0.00010	0.99950	0.00240
HEU-MET-FAST-085-006	1.00359	0.00010	1.00365	0.00010	0.99970	0.00290
IEU-MET-FAST-004	1.00498	0.00010	1.00476	0.00010	1.00000	0.00300
IEU-MET-FAST-005	1.00198	0.00010	1.00074	0.00010	1.00000	0.00210
IEU-MET-FAST-007	1.00400	0.00010	1.00352	0.00010	1.00450	0.00070
IEU-MET-FAST-010-001	0.99682	0.00016	0.99561	0.00016	0.99540	0.00240
IEU-MET-FAST-012-001	1.00214	0.00013	1.00089	0.00013	1.00070	0.00270
IEU-MET-FAST-013-001	0.99662	0.00016	0.99578	0.00016	0.99410	0.00230
IEU-MET-FAST-014-002	0.99492	0.00016	0.99459	0.00016	0.99270	0.00220
IEU-MET-FAST-020-01d	1.00080	0.00016	1.00150	0.00016	1.00060	0.00130
IEU-MET-FAST-020-01s	1.00230	0.00016	1.00282	0.00016	1.00200	0.00130
IEU-MET-FAST-020-02d	1.00279	0.00016	1.00161	0.00016	1.00150	0.00130
IEU-MET-FAST-020-02s	1.00514	0.00016	1.00386	0.00016	1.00410	0.00130
IEU-MET-FAST-020-03d	1.00197	0.00016	1.00038	0.00016	1.00040	0.00130
IEU-MET-FAST-020-03s	1.00543	0.00016	1.00371	0.00016	1.00400	0.00130
IEU-MET-FAST-020-04d	1.00341	0.00016	1.00099	0.00016	1.00080	0.00130
IEU-MET-FAST-020-04s	1.00761	0.00016	1.00520	0.00016	1.00530	0.00130
IEU-MET-FAST-020-05d	1.00438	0.00016	1.00097	0.00016	1.00140	0.00130
IEU-MET-FAST-020-05s	1.00936	0.00016	1.00598	0.00016	1.00670	0.00130
IEU-MET-FAST-020-06d	1.00401	0.00016	1.00044	0.00016	1.00120	0.00130
IEU-MET-FAST-020-06s	1.00872	0.00016	1.00533	0.00016	1.00650	0.00130
IEU-MET-FAST-020-07d	1.00364	0.00016	1.00064	0.00016	1.00110	0.00140
IEU-MET-FAST-020-07s	1.01238	0.00016	1.00949	0.00016	1.01040	0.00140
IEU-MET-FAST-020-08d	1.00093	0.00016	1.00178	0.00016	1.00030	0.00130
IEU-MET-FAST-020-09d	1.00032	0.00016	1.00114	0.00016	1.00070	0.00130
IEU-MET-FAST-021-01d	1.00207	0.00017	1.00192	0.00016	1.00000	0.00145
IEU-MET-FAST-021-01s	1.01030	0.00016	1.00987	0.00016	1.00839	0.00145

Continued on the next page

TABLE LX: (continued) GNDS ENDF/B-VIII.1 criticality validation

GNDS-2.0 library Case Name	ENDF/B-VIII.1 at 293.6K Calculated keff	uncertainty	ENDF/B-VIII.0 at 293.6K Calculated keff	uncertainty	Experimental Benchmark keff	uncertainty
IEU-MET-FAST-022-01d	1.00089	0.00016	1.00253	0.00016	1.00570	0.00134
IEU-MET-FAST-022-01s	1.00104	0.00016	1.00277	0.00016	1.00077	0.00134
IEU-MET-FAST-022-02d	0.99869	0.00016	0.99888	0.00016	1.00042	0.00110
IEU-MET-FAST-022-02s	0.99300	0.00016	0.99368	0.00016	0.99400	0.00114
IEU-MET-FAST-022-03d	0.99612	0.00016	0.99596	0.00016	1.00131	0.00110
IEU-MET-FAST-022-03s	0.98328	0.00016	0.98331	0.00016	0.98748	0.00114
IEU-MET-FAST-022-04d	0.99847	0.00016	0.99921	0.00016	1.00100	0.00107
IEU-MET-FAST-022-04s	0.98511	0.00016	0.98596	0.00016	0.98629	0.00236
IEU-MET-FAST-022-05d	0.99808	0.00016	1.00004	0.00016	1.00022	0.00123
IEU-MET-FAST-022-05s	0.99668	0.00016	0.99862	0.00016	0.99782	0.00126
IEU-MET-FAST-022-06d	1.00344	0.00015	1.00543	0.00016	1.00056	0.00172
IEU-MET-FAST-022-06s	0.99945	0.00016	1.00171	0.00016	1.00121	0.00193
IEU-MET-FAST-022-07d	1.00185	0.00016	1.00281	0.00016	0.99758	0.00193
IEU-MET-FAST-022-07s	0.99862	0.00016	0.99932	0.00016	1.00147	0.00126
MIX-MET-FAST-001	0.99910	0.00010	0.99910	0.00010	1.00000	0.00160
MIX-MET-FAST-002-001	1.00366	0.00010	1.00327	0.00010	1.00000	0.00420
MIX-MET-FAST-002-002	1.00359	0.00010	1.00352	0.00010	1.00000	0.00440
MIX-MET-FAST-002-003	1.00381	0.00010	1.00378	0.00010	1.00000	0.00480
MIX-MET-FAST-005	1.00353	0.00018	1.00381	0.00018	0.99900	0.00170
MIX-MET-FAST-007-001	1.00288	0.00010	1.00156	0.00010	1.00000	0.00450
MIX-MET-FAST-007-010	1.00303	0.00010	1.00255	0.00010	1.00000	0.00270
MIX-MET-FAST-007-011	1.00181	0.00010	1.00176	0.00010	1.00000	0.00260
MIX-MET-FAST-007-012	1.00137	0.00010	1.00131	0.00010	1.00000	0.00300
MIX-MET-FAST-007-013	1.00028	0.00010	1.00025	0.00010	1.00000	0.00330
MIX-MET-FAST-007-014	1.00613	0.00010	1.00541	0.00010	1.00000	0.00320
MIX-MET-FAST-007-015	1.00568	0.00010	1.00514	0.00010	1.00000	0.00320
MIX-MET-FAST-007-016	1.00448	0.00010	1.00385	0.00010	1.00000	0.00280
MIX-MET-FAST-007-017	1.00449	0.00010	1.00434	0.00010	1.00000	0.00280
MIX-MET-FAST-007-018	1.00689	0.00010	1.00699	0.00010	1.00000	0.00300
MIX-MET-FAST-007-019	1.00542	0.00010	1.00509	0.00010	1.00000	0.00340
MIX-MET-FAST-007-002	1.00669	0.00010	1.00564	0.00010	1.00000	0.00230
MIX-MET-FAST-007-020	1.00364	0.00010	1.00365	0.00010	1.00000	0.00300
MIX-MET-FAST-007-021	1.00431	0.00010	1.00432	0.00010	1.00000	0.00310
MIX-MET-FAST-007-022	1.00278	0.00010	1.00247	0.00010	1.00000	0.00300
MIX-MET-FAST-007-023	1.00259	0.00010	1.00248	0.00010	1.00000	0.00280
MIX-MET-FAST-007-003	1.00439	0.00010	1.00389	0.00010	1.00000	0.00280
MIX-MET-FAST-007-004	1.00338	0.00010	1.00344	0.00010	1.00000	0.00280
MIX-MET-FAST-007-005	1.00119	0.00010	1.00098	0.00010	1.00000	0.00320
MIX-MET-FAST-007-006	1.00010	0.00010	1.00011	0.00010	1.00000	0.00350
MIX-MET-FAST-007-007	1.00511	0.00010	1.00429	0.00010	1.00000	0.00320
MIX-MET-FAST-007-008	1.00350	0.00010	1.00257	0.00010	1.00000	0.00300
MIX-MET-FAST-007-009	1.00326	0.00010	1.00262	0.00010	1.00000	0.00280
MIX-MET-FAST-009	0.99947	0.00010	0.99980	0.00010	1.00000	0.00100
MIX-MET-FAST-010	0.99960	0.00010	0.99931	0.00010	1.00000	0.00090
PU-MET-FAST-001-r5s	1.00012	0.00010	1.00057	0.00010	1.00000	0.00129
PU-MET-FAST-002	1.00075	0.00010	1.00126	0.00010	1.00000	0.00200
PU-MET-FAST-005	0.99961	0.00010	0.99903	0.00010	1.00000	0.00130
PU-MET-FAST-006	0.99972	0.00010	0.99954	0.00010	1.00000	0.00300
PU-MET-FAST-008a	0.99791	0.00010	0.99786	0.00010	1.00000	0.00060
PU-MET-FAST-009	1.00520	0.00010	1.00532	0.00010	1.00000	0.00270
PU-MET-FAST-010	0.99768	0.00010	0.99780	0.00010	1.00000	0.00180
PU-MET-FAST-018	0.99820	0.00010	0.99771	0.00010	1.00000	0.00300
PU-MET-FAST-019	0.99978	0.00010	0.99924	0.00010	0.99920	0.00150
PU-MET-FAST-020	0.99660	0.00019	0.99635	0.00018	0.99930	0.00170
PU-MET-FAST-022	0.99750	0.00010	0.99825	0.00010	1.00000	0.00210
PU-MET-FAST-023	0.99808	0.00010	0.99821	0.00010	1.00000	0.00200
PU-MET-FAST-024	1.00077	0.00010	1.00081	0.00010	1.00000	0.00200
PU-MET-FAST-025	0.99910	0.00010	0.99988	0.00010	1.00000	0.00200
PU-MET-FAST-026	1.00148	0.00010	1.00150	0.00010	1.00000	0.00240
PU-MET-FAST-028	1.00321	0.00010	1.00282	0.00010	1.00000	0.00220
PU-MET-FAST-029	0.99535	0.00010	0.99605	0.00010	1.00000	0.00200
PU-MET-FAST-030	1.00211	0.00010	1.00250	0.00010	1.00000	0.00210
PU-MET-FAST-032	1.00054	0.00010	1.00091	0.00010	1.00000	0.00200

Continued on the next page

TABLE LX: (continued) GNDS ENDF/B-VIII.1 criticality validation

GNDS-2.0 library Case Name	ENDF/B-VIII.1 at 293.6K Calculated keff	uncertainty	ENDF/B-VIII.0 at 293.6K Calculated keff	uncertainty	Experimental Benchmark keff	uncertainty
PU-MET-FAST-035	1.00180	0.00010	0.99682	0.00010	1.00000	0.00160
PU-MET-FAST-036	1.00041	0.00010	1.00038	0.00010	1.00000	0.00310
PU-MET-FAST-039	0.99149	0.00010	0.99129	0.00010	1.00000	0.00220
PU-MET-FAST-040	0.99682	0.00010	0.99393	0.00010	1.00000	0.00380
PU-MET-FAST-041	1.00506	0.00010	1.00483	0.00010	1.00000	0.00160
U233-MET-FAST-001	0.99994	0.00010	0.99996	0.00010	1.00000	0.00100
U233-MET-FAST-002	0.99975	0.00010	0.99970	0.00010	1.00000	0.00100
U233-MET-FAST-003	0.99958	0.00010	0.99910	0.00010	1.00000	0.00100
U233-MET-FAST-004	0.99952	0.00010	0.99902	0.00010	1.00000	0.00070
U233-MET-FAST-006	1.00005	0.00010	0.99908	0.00010	1.00000	0.00140

TABLE LXI. Comparison of calculated fission ratios for the ENDF/B-VIII.1 nuclear data library in GNDS-2.0 format with measured values in the center of critical assemblies, where fission ratio is defined as the fission rate for an actinide normalized by the ^{235}U fission rate. Calculated fission ratios were obtained from fission rates simulated with LLNL's Mercury Monte Carlo transport code. Experimental fission ratios for Exp-A and Exp-B are taken from Ref. [68, Table XXXIX]. Note that Exp-A and Exp-B refer to the same experimental data. Values for Exp-A are found in the CSEWG Fast Reactor Benchmark Compilation, BNL 19302 (June 1973) [776]. These measurements were later reevaluated and transmitted to R. Mc Farlane in 1984 (personal communication): the reevaluated fission ratios are named Exp-B. Calc/Exp Ratio were calculated with Exp-B values when available. Experimental values for IMF007 are from Ref. [777]. These LLNL-calculated values can be compared to LANL MCNP calculated values in Table XLVIII. They are similar.

Assembly	Quantity	^{238}U(n,f)/^{235}U(n,f) value	unc.	^{237}Np(n,f)/^{235}U(n,f) value	unc.	^{233}U(n,f)/^{235}U(n,f) value	unc.	^{239}Pu(n,f)/^{235}U(n,f) value	unc.
Godiva (HMF001)	Calculated	0.1581		0.8307		1.5794		1.383	
	Exp-B	0.1643	0.0018	0.8516	0.012			1.4152	0.014
	Exp-A	0.1642	0.0018	0.837	0.013	1.59	0.03	1.402	0.025
	Calc/Exp	0.9623		0.9755		0.9933		0.9772	
Jezebel (PMF001)	Calculated	0.2109		0.9714		1.5663		1.4244	
	Exp-B	0.2133	0.0023	0.9835	0.014			1.4609	0.013
	Exp-A	0.2137	0.0023	0.962	0.016	1.578	0.027	1.448	0.029
	Calc/Exp	0.9887		0.9877		0.9926		0.975	
Jezebel-23 (UMF001)	Calculated	0.2112		0.9842					
	Exp-B	0.2131	0.0026	0.997	0.015				
	Exp-A	0.2131	0.0023	0.977	0.016				
	Calc/Exp	0.9912		0.9872					
Flattop-25 (HMF028)	Calculated	0.1447		0.7719		1.5779		1.3603	
	Exp-B	0.1492	0.0016	0.7804	0.01	1.608	0.003	1.3847	0.012
	Exp-A	0.149	0.002	0.76	0.01	1.6	0.003	1.37	0.02
	Calc/Exp	0.9699		0.9892		0.9813		0.9824	
Flattop-Pu (PMF006)	Calculated	0.1779		0.8508					
	Exp-B	0.1799	0.002	0.8561	0.012				
	Exp-A	0.18	0.003	0.84	0.01				
	Calc/Exp	0.9889		0.9938					
Flattop-23 (UMF006)	Calculated	0.1872		0.8992					
	Exp-B	0.1916	0.0021	0.9103	0.013				
	Exp-A	0.191	0.003	0.89	0.01				
	Calc/Exp	0.9771		0.9878					